TECHNISCHE UNIVERSITÄT MÜNCHEN

Lehrstuhl für Numerische Mechanik

Computational Methods for Fluid-Structure Interaction including Porous Media and Solid Contact

Christoph Franz Ager

Vollständiger Abdruck der von der Fakultät für Maschinenwesen der Technischen Universität München zur Erlangung des akademischen Grades eines

Doktor-Ingenieurs (Dr.-Ing.)

genehmigten Dissertation.

Vorsitzende: Prof. Dr. Julija Zavadlav

Prüfer der Dissertation:

1. Prof. Dr.-Ing. Wolfgang A. Wall
2. Prof. Marek Behr, Ph.D.

Die Dissertation wurde am 21.10.2019 bei der Technischen Universität München eingereicht und durch die Fakultät für Maschinenwesen am 18.02.2021 angenommen.

Abstract

This thesis deals with the computational prediction of systems which are characterized by the interaction of fluid and deformable bodies, with a special emphasis on the contact interaction of these bodies. Besides engineering configurations such as seals and bearings, various biomechanical systems including heart valves and synovial joints belong to this group of problems, which are denoted as fluid-structure-contact interaction (FSCI). In order to provide accurate physical models for the different fields of application, not only impermeable solids, but also fluid-saturated poroelastic medium is considered within this thesis, leading to so-called fluid-poroelasticity-structure-contact interaction (FPSCI). Since the underlying physical processes for contact of bodies surrounded by fluid vary significantly depending on the surface microstructure, different physical models for rough and smooth surface contact are developed and serve as a basis for all presented computational approaches. For rough surface contact, a model which is based on an averaged representation of the microstructure by a poroelastic layer is introduced.

A major challenge for the consistent numerical treatment of FSCI problems using interface-fitted moving mesh approaches is the distortion of fluid elements due to the vanishing fluid in the contact zone. This problem can be avoided by the cut finite element method (CutFEM), which enables the use of computational fluid meshes that are not fitted to the structural interface, while ensuring an accurate and sharp representation of the interface. Therefore, a numerical formulation for fluid-structure interaction (FSI) problems utilizing the CutFEM, which serves as a basis for all subsequent developments, is numerically validated and extended by a novel Nitsche-based formulation exploiting the solid stress. To extend this formulation to poroelastic bodies by a general formulation for poroelastic medium, an interface-unfitted computational approach for fluid-poroelasticity interaction (FPI) including a novel Nitsche-based formulation, which allows incorporating the tangential Beavers-Joseph-Saffmann condition for an extended range of problem parameters compared to traditional approaches, is developed.

To extend these approaches by the numerical treatment of contacting bodies, particular attention on the determination of the fluid stress in the zone of closed contact is required, since it is essential for a physically correct contact lift-off behavior and for ensuring continuity of the associated change of conditions. For this purpose, a novel computational approach for general FSCI, in which not only the FSI interface conditions but also the contact conditions are incorporated by a Nitsche-based method, is introduced. Therein, the general Navier interface condition is applied to ensure continuity in tangential interface orientation and an extension approach is utilized to determine the fluid state in the contact zone. Subsequently, this computational approach for FSCI is extended to FPSCI by additionally including a poroelastic formulation and especially incorporating the interface conditions of FPI, solid-poroelastic contact, and poroelastic-poroelastic contact by Nitsche-based methods. Techniques to ensure a smooth transition between the porous flow conditions of FPI and contact and using the porous fluid pressure to determine the fluid stress in the contact zone are the essential aspects of this formulation.

Various numerical tests and examples are presented to analyze and validate aspects such as the spatial convergence behavior, the sensitivity and the proper scaling of the numerical parameters, the robustness for varying parameters which characterize the problem, and the correct prediction of the basic processes of contact and lift-off. In addition, more challenging configurations including frequent topological changes, large contacting areas, and 3D configurations demonstrate the general applicability of the developed computational methods.

Zusammenfassung

Diese Arbeit beschäftigt sich mit der Simulation des mechanischen Verhaltens von Systemen, welche durch die Wechselwirkung von deformierbaren Körpern und Fluiden gekennzeichnet sind. Ein besonderer Schwerpunkt liegt dabei auf dem Kontakt von Körpern in Fluidumgebung. Diese Fluid-Struktur-Kontakt-Interaktion (FSCI) tritt sowohl in technischen Problemstellungen wie Dichtungen und Lagern als auch in verschiedenen bio-mechanischen Systemen wie Herzklappen und Synovialgelenken auf. Um genaue physikalische Modelle für die verschiedensten Anwendungsbereiche zu entwickeln, werden nicht nur impermeable Strukturen, sondern auch fluidgesättigte poroelastische Strukturen betrachtet, was zu einer sogenannten Fluid-Poroelastizität-Struktur-Kontakt-Interaktion (FPSCI) führt. Da sich die zugrunde liegenden physikalischen Prozesse für Kontakt in Fluidumgebung abhängig von der Oberflächenmikrostruktur stark unterscheiden, werden verschiedene physikalische Modelle für den rauen und glatten Oberflächenkontakt entwickelt. Diese physikalischen Modelle bilden die Grundlage für alle vorgestellten Berechnungsansätze. Für den rauen Oberflächenkontakt wird ein Modell präsentiert, das auf einer gemittelten Darstellung der rauen Mikrostruktur durch eine fluidgesättigte poroelastische Schicht basiert.

Eine zentrale Herausforderung für die konsistente numerische Behandlung von FSCI-Problemen liegt darin, dass Fluidelemente stark verzerrt werden, wenn der Fluidspalt in der Kontaktzone sehr klein wird und das Rechennetz des Fluides an die Strukturoberfläche gekoppelt ist. Dieses Problem kann durch die Anwendung der Cut-Finite-Elemente-Methode (CutFEM), bei der das Rechennetz des Fluidgebiets unabhängig von der Strukturoberfläche ist, vermieden werden. Deshalb dient in dieser Arbeit eine numerische Formulierung für Fluid-Struktur-Interaktionsprobleme (FSI) unter Verwendung der CutFEM als Grundlage für alle weiteren Entwicklungen. Diese Formulierung wird numerisch validiert und um eine neuartige Nitsche-basierte Formulierung, welche Strukturspannungen nutzt, erweitert. Um auch die Anwendung auf Fluid-Poroelastizität-Interaktionsprobleme (FPI) zu ermöglichen, wird eine numerische Formulierung für nicht passende Rechennetze unter Verwendung einer allgemeinen Formulierung für poroelastisches Medium eingeführt. Ein neuartiger Nitsche-basierter Ansatz zum Aufbringen der tangentialen Beavers-Joseph-Saffmann Bedingung vergrößert den Bereich anwendbarer Systemparameter im Vergleich zu herkömmlichen Ansätzen.

Bei der Erweiterung dieser numerischen Formulierungen zur Berücksichtigung von Kontakt ist besonderes Augenmerk auf die Bestimmung der Fluidspannung in der Zone des geschlossenen Kontakts zu legen, da diese essentiell für ein physikalisch korrektes Kontakablöseverhalten der Körper sowie die Kontinuität des Übergangs zwischen den damit verbundenen Interfacebedingungen ist. Deshalb wird ein neuartiger Berechnungsansatz für allgemeine FSCI, bei dem nicht nur die FSI-Interfacebedingung, sondern auch die Kontaktbedingungen durch eine Nitsche-basierte Methode berücksichtigt werden, entwickelt. Darin wird die allgemeine Navier-Interfacebedingung angewendet, um die Kontinuität in tangentialer Interfaceausrichtung zu gewährleisten, und es wird ein Fortsetzungsansatz verwendet, um den Fluidzustand in der Kontaktzone zu bestimmen. Anschließend wird dieser numerische Ansatz von FSCI auf FPSCI erweitert, indem eine poroelastische Formulierung berücksichtigt wird. Diese Entwicklung beinhaltet insbesondere die Einbeziehung der Interfacebedingung von FPI, Struktur-Poroelastischem Kontakt, und Poroelastisch-Poroelastischem Kontakt durch Nitsche-basierte Methoden. Wesentliche Aspekte dieser Formulierung sind Techniken, um einen kontinuierlichen Übergang zwi-

schen den Interfacebedingung der porösen Strömung von FPI und dem Kontakt zu gewährleisten, und die Verwendung des porösen Fluiddrucks zur Bestimmung der Fluidspannung in der Kontaktzone.

Anhand verschiedener numerischer Tests und Beispiele werden unter anderem das räumliche Konvergenzverhalten, die Sensitivität und die richtige Skalierung der numerischen Parameter, die Robustheit der Methoden bei Variation unterschiedlicher Parametern die das Problem charakterisieren, und die korrekte Vorhersage der grundlegenden Prozesse von Kontakt und Kontaktablösung analysiert und validiert. Darüber hinaus zeigen anspruchsvollere Konfigurationen mit häufigen topologischen Änderungen des Fluidgebietes, großen Kontaktflächen und dreidimensionalen Systemen die allgemeine Anwendbarkeit der entwickelten Berechnungsmethoden.

Contents

Nomenclature

Quantities and Mathematical Operators

$*$	Scalar quantity
$\underline{*}$	Vector, tensor quantity
$\underline{\mathbf{0}}$	Zero vector
$\underline{\boldsymbol{I}}$	Second order identity tensor
$(\underline{*})^{\mathsf{T}}$	Transpose of a tensor
$(\underline{*})^{-1}$	Inverse of a tensor
$(\underline{*})^{-\mathsf{T}}$	Inverse transpose of a tensor
$\boldsymbol{\nabla}_0 *$, $\boldsymbol{\nabla} *$	Material, spatial gradient operator
$\boldsymbol{\nabla}_0 \cdot *$, $\boldsymbol{\nabla} \cdot *$	Material, spatial divergence operator
$\boldsymbol{\Delta} *$	Laplace operator
tr $(\underline{*})$	Trace of a tensor
$\mathrm{span}[*]$	Linear span of a set
δ_{ij}	Kronecker delta
$\min[*,*]$	Minimum operator
$\max[*,*]$	Maximum operator
$[\![*]\!]$	Jump operator
$\mathcal{D}_{\underline{\boldsymbol{v}}}[*]$	Directional derivative in direction $\underline{\boldsymbol{v}}$
$\underline{*} \cdot \underline{*}$	Single contraction
$\underline{*} : \underline{*}$	Double contraction
$\underline{*} \odot \underline{*}$	Alternative scalar product
const.	Constant function
$\|\| * \|\|_{\Omega}$	$\mathcal{L}^2$-norm in Ω
$\|\|*\|\|_{\infty,\Omega}$	$\mathcal{L}^\infty$-norm in Ω
$\|\|\underline{*}\|\|$	$\mathcal{L}^2$-norm of a vector or tensor
$\|\|\underline{*}\|\|_{\infty}$	$\mathcal{L}^\infty$-norm of a vector or tensor
$\mathcal{O}(*)$	Order of $*$
$(\underline{*},\underline{*})_{\Omega}$	$\mathcal{L}^2$-inner product in Ω
$\langle \underline{*},\underline{*} \rangle_{\Gamma}$	$\mathcal{L}^2$-inner product on Γ

Overall Problem

Ω	Domain of interest
$\partial\Omega$	Boundary of domain Ω
$\Omega^{\mathrm{S}}, \Omega^{\mathrm{F}}, \Omega^{\mathrm{P}}$	Solid, fluid, and poroelastic domain
$\partial\Omega^{\mathrm{S}}, \partial\Omega^{\mathrm{F}}, \partial\Omega^{\mathrm{P}}$	Boundary of solid, fluid, and poroelastic domain

d	Number of spatial dimension
$\underline{\boldsymbol{x}}$	Position vector in spatial configuration
$\underline{\boldsymbol{X}}$	Position vector in material configuration
$\underline{\boldsymbol{\chi}}$	Position vector in reference configuration
t	Time
t_0	Initial point in time
t_E	Final point in time
$\mathcal{T}$	Time interval of interest

Interfaces and Boundaries

$\underline{\boldsymbol{n}}$	Normal vector
$\underline{\boldsymbol{t}}$	Tangential vector
$\underline{\boldsymbol{P}}^n$	Normal projection matrix
$\underline{\boldsymbol{P}}^t$	Tangential projection matrix
$\underline{\tilde{\boldsymbol{n}}}$	Nodal smoothed normal vector
Γ	Interface, Boundary
$\Gamma^{\mathrm{S,N}}, \Gamma^{\mathrm{F,N}}, \Gamma^{\mathrm{P,N}}, \Gamma^{\mathrm{P^F,N}}$	Neumann boundary
$\Gamma^{\mathrm{S,D}}, \Gamma^{\mathrm{F,D}}, \Gamma^{\mathrm{P,D}}, \Gamma^{\mathrm{P^F,D}}$	Dirichlet boundary
$\Gamma^{\mathrm{S,I}}, \Gamma^{\mathrm{F,I}}, \Gamma^{\mathrm{P,I}}, \Gamma^{\mathrm{P^F,I}}$	General Interface of corresponding domain
Γ^{FS}	Fluid-structure interface
Γ^{FP}	Fluid-poroelasticity interface
Γ^{FF}	Fluid-fluid interface
Γ^{PS}	Poroelasticity-solid interface
$\Gamma^{\mathrm{S},c}$	Solid contact interface
$\Gamma^{\mathrm{P},c}$	Poroelasticity contact interface
$\Gamma^{\mathrm{SS},c}$	Solid-solid contact interface
$\Gamma^{\mathrm{PS},c}$,$\Gamma^{\mathrm{SP},c}$	Poroelasticity-solid contact interface
$\Gamma^{\mathrm{PP},c}$	Poroelasticity-poroelasticity contact interface
$\breve{\Gamma}^{*,c}$	Potential contact interface

Continuum Mechanics and Governing Equations

Φ	Mapping from material to current domain
Ξ	Mapping from reference to current domain
Ψ	Mapping from reference to material domain
$\underline{\boldsymbol{F}}^{\mathrm{S}}, \underline{\boldsymbol{F}}^{\mathrm{P}}$	Deformation gradient
$J^{\mathrm{S}}, J^{\mathrm{P}}$	Determinate of the deformation gradient
$\underline{\boldsymbol{E}}^{\mathrm{S}}, \underline{\boldsymbol{E}}^{\mathrm{P}}$	Green-Lagrange strain tensor
$\underline{\boldsymbol{C}}^{\mathrm{S}}, \underline{\boldsymbol{C}}^{\mathrm{P}}$	Right Cauchy-Green deformation tensor
$\underline{\boldsymbol{\sigma}}, \underline{\boldsymbol{\sigma}}^{\mathrm{S}}, \underline{\boldsymbol{\sigma}}^{\mathrm{F}}, \underline{\boldsymbol{\sigma}}^{\mathrm{P}}$	Cauchy stress
$\underline{\boldsymbol{\sigma}}^{\mathrm{S/P}}$	Combined solid, poroelastic Cauchy stress
σ_{nn}	Normal Cauchy stress

$\underline{\boldsymbol{P}}^{\mathrm{S}}, \underline{\boldsymbol{P}}^{\mathrm{P}}$	First Piola Kirchhoff stress tensor
$\underline{\boldsymbol{S}}^{\mathrm{S}}, \underline{\boldsymbol{S}}^{\mathrm{P}}$	Second Piola Kirchhoff stress tensor
$\underline{\boldsymbol{\epsilon}}^{\mathrm{F}}(\underline{\boldsymbol{v}}^{\mathrm{F}}), \underline{\boldsymbol{\epsilon}}^{\mathrm{F}}$	Strain-rate tensor
$\underline{\hat{\boldsymbol{b}}}_0^{\mathrm{S}}, \underline{\hat{\boldsymbol{b}}}^{\mathrm{F}}, \underline{\hat{\boldsymbol{b}}}^{\mathrm{PF}}, \underline{\hat{\boldsymbol{b}}}_0^{\mathrm{P}}$	Body force per unit mass
$\underline{\hat{\boldsymbol{h}}}^{\mathrm{S,N}}, \underline{\hat{\boldsymbol{h}}}^{\mathrm{F,N}}, \underline{\hat{\boldsymbol{h}}}^{\mathrm{P,N}}$	Traction on Neumann boundary
$\hat{h}^{\mathrm{PF,N}}$	Normal traction on porous fluid Neumann boundary
$\underline{\boldsymbol{h}}^{\mathrm{S,I}}, \underline{\boldsymbol{h}}^{\mathrm{F,I}}, \underline{\boldsymbol{h}}^{P,I}$	Traction on general interface
$h^{\mathrm{PF,I}}$	Normal traction on general porous fluid interface
g^n	Normal gap

Physical Quantities and Parameters

$\rho^{\mathrm{S}}, \rho^{\mathrm{F}}$	Density
$\tilde{\rho}_0^{\mathrm{PS}}$	Macroscopic averaged density of the solid phase
μ^{F}	Dynamic viscosity
ϕ	Porosity
K	Scalar material permeability value for isotropic permeability tensor
$\underline{\boldsymbol{k}}$	Spatial permeability tensor
$\underline{\boldsymbol{K}}$	Material permeability tensor
ψ	Strain energy density function
ψ_{NH}	Strain energy density function of Neo-Hookean material model
$\psi^{\mathrm{P},skel}$	Strain energy density function for macroscopic deformation
$\psi^{\mathrm{P},vol}$	Strain energy density function for volume change of the solid phase
$\psi^{\mathrm{P},pen}$	Strain energy density function to ensure positive porosity
E	Young's modulus
ν	Poisson ratio
κ^{P}	Bulk modulus
α^{P}	Parameter of penalty strain energy density function
β_{BJ}	Beavers-Joseph-Saffmann condition indicator
α_{BJ}	Beavers-Joseph model parameter
κ	Slip length of BJ condition or general Navier condition
κ_{BJ}	Slip length of BJ condition
κ_0	Reference slip length
κ^c	Slip length of constraint relaxation for FSCI and FPSCI

System States

$\underline{\boldsymbol{u}}^{\mathrm{S}}, \underline{\boldsymbol{u}}^{\mathrm{P}}, \underline{\boldsymbol{u}}^{\mathrm{G}}$	Displacement field
$\underline{\boldsymbol{v}}^{\mathrm{F}}, \underline{\boldsymbol{v}}^{\mathrm{P}}$	Velocity field
$p^{\mathrm{F}}, p^{\mathrm{P}}$	Pressure field

$\underline{\boldsymbol{v}}^G$	Mesh velocity field
$\underline{\boldsymbol{v}}^{\mathrm{P},seepage}$	Poroelastic seepage velocity field
$\underline{\boldsymbol{\lambda}}$	Contact Lagrange multiplier field
$\underline{\boldsymbol{\lambda}}^{\mathcal{A}}$	Active contact Lagrange multiplier field
$\underline{\boldsymbol{x}}^*$	State vector of the coupled problem
$\underline{\mathbf{u}}^{\mathrm{S}}, \underline{\mathbf{u}}^{\mathrm{P}}, \underline{\mathbf{u}}^{\mathrm{G}}$	Nodal displacement vector
$\underline{\mathbf{v}}^{\mathrm{F}}, \underline{\mathbf{v}}^{\mathrm{P}}$	Nodal fluid velocity vector
$\underline{\mathbf{p}}^{\mathrm{F}}, \underline{\mathbf{p}}^{\mathrm{P}}$	Nodal fluid pressure vector
$\underline{\boldsymbol{\lambda}}^{\mathcal{A}}$	Nodal active contact Lagrange multiplier vector
$\underline{\mathbf{x}}^*$	Nodal state vector of the coupled problem
$\underline{\tilde{\mathbf{v}}}^{\mathrm{F}}$	Nodal fluid velocity vector projected to the current solution space (CutFEM)
$\underline{\tilde{\mathbf{p}}}^{\mathrm{F}}$	Nodal fluid pressure vector projected to the current solution space (CutFEM)
$\underline{\tilde{\mathbf{x}}}^*$	Nodal state vector of the coupled problem projected to the current solution space (CutFEM)

Test Functions

$\delta*$	Test function
$\delta\underline{\boldsymbol{u}}^{\mathrm{S}}, \delta\underline{\boldsymbol{u}}^{\mathrm{P}}$	Displacement test function
$\delta\underline{\boldsymbol{v}}^{\mathrm{F}}, \delta\underline{\boldsymbol{v}}^{\mathrm{P}}$	Velocity test function
$\delta p^{\mathrm{F}}, \delta p^{\mathrm{P}}$	Pressure test function
$\delta\underline{\boldsymbol{v}}^{\mathrm{F}}_{\emptyset}, \delta p^{\mathrm{F}}_{\emptyset}$	Fluid test functions vanishing outside of the fluid domain
$\delta\underline{\boldsymbol{\lambda}}$	Contact Lagrange multiplier test function
$\delta\underline{\boldsymbol{\lambda}}^{\mathcal{A}}$	Active contact Lagrange multiplier function

Solution and Test Function Spaces

$\mathcal{S}_{\underline{\boldsymbol{u}}^{\mathrm{S}}}, \mathcal{T}_{\delta\underline{\boldsymbol{u}}^{\mathrm{S}}}$	Displacement solution and test function space
$\mathcal{S}_{\underline{\boldsymbol{v}}^{\mathrm{F}}}, \mathcal{T}_{\delta\underline{\boldsymbol{v}}^{\mathrm{F}}}$	Fluid velocity solution and test function space
$\mathcal{S}_{p^{\mathrm{F}}}, \mathcal{T}_{\delta p^{\mathrm{F}}}$	Fluid pressure solution and test function space
$\mathcal{S}_{\underline{\boldsymbol{u}}^{\mathrm{P}}}, \mathcal{T}_{\delta\underline{\boldsymbol{u}}^{\mathrm{P}}}$	Poroelastic displacement solution and test function space
$\mathcal{S}_{\underline{\boldsymbol{v}}^{\mathrm{P}}}, \mathcal{T}_{\delta\underline{\boldsymbol{v}}^{\mathrm{P}}}$	Poroelastic fluid velocity solution and test function space
$\mathcal{S}_{p^{\mathrm{P}}}, \mathcal{T}_{\delta p^{\mathrm{P}}}$	Poroelastic fluid pressure solution and test function space
$\mathcal{S}_{\underline{\boldsymbol{\lambda}}^{\mathcal{A}}}, \mathcal{T}_{\delta\underline{\boldsymbol{\lambda}}^{\mathcal{A}}}$	Active contact Lagrange mult. solution and test function space
$\mathcal{S}_{\underline{\boldsymbol{x}}^*}, \mathcal{T}_{\delta\underline{\boldsymbol{x}}^*}$	Solution and test function space of coupled problem

Temporal Discretization

Δt	Time step length
n_{t}	Number of time intervals

θ	Parameter of the One-Step-θ-scheme
$\tilde{\partial}_t\,[*]$	First order discrete time derivative
$\tilde{\partial}_t^2\,[*]$	Second order discrete time derivative
$(\underline{*}, \underline{*})_{\Omega_{n+1},n+\theta}$	$\mathcal{L}^2$-inner product in Ω_{n+1}, evaluated for time-discrete quantities at $t = t_{n+\theta}$
$\langle \underline{*}, \underline{*} \rangle_{\Gamma_{n+1},n+\theta}$	$\mathcal{L}^2$-inner product on Γ_{n+1}, evaluated for time-discrete quantities at $t = t_{n+\theta}$

Spatial Discretization

n_{ele}	Number of elements in a discretization
n_{nod}	Number of nodes in a discretization
$\underline{\mathbf{x}}_i$	Position of node i
N_i	Shape function of node i
$\tilde{N}_i$	Shape function of local node i in element local coordinate system
ψ_i	Contact Lagrange multiplier shape function of node i
$\psi_{\delta,i}$	Contact Lagrange multiplier test function shape function of node i
$\underline{\boldsymbol{\xi}}$	Element local coordinate
$\underline{\Upsilon}_e$	Mapping from the element local to the global coordinate system for element e
h, h_Γ	Mesh size parameter
$\Omega_{\mathcal{T}_\mathrm{h},e}$	Domain covered by element e
$\breve{\Omega}_{\mathcal{T}_\mathrm{h}}$	Domain covered by the elements of a discretization
$\breve{\Omega}_{\mathcal{T}_\mathrm{h},\mathcal{A}}$	Domain covered by active elements (CutFEM)
$\breve{\Omega}_{\mathcal{T}_\mathrm{h},\mathcal{I}}$	Domain covered by inactive elements (CutFEM)
$\breve{\Omega}_{\mathcal{T}_\mathrm{h},\Gamma^{\mathrm{F,I}}}, \breve{\Omega}_{\mathcal{T}_\mathrm{h},\Gamma^{\mathrm{FS}}}, \breve{\Omega}_{\mathcal{T}_\mathrm{h},\Gamma^{\mathrm{FP}}}$	Domain covered by intersected elements (CutFEM)
$\breve{\Omega}_{\mathcal{T}_\mathrm{h},\setminus\Gamma^{\mathrm{F,I}}}, \breve{\Omega}_{\mathcal{T}_\mathrm{h},\setminus\Gamma^{\mathrm{FS}}}, \breve{\Omega}_{\mathcal{T}_\mathrm{h},\setminus\Gamma^{\mathrm{FP}}}$	Domain covered by not intersected elements (CutFEM)
$\Omega^{\mathrm{F}}_{\mathrm{h},\Gamma^{\mathrm{F,I}}}, \Omega^{\mathrm{F}}_{\mathrm{h},\Gamma^{\mathrm{FS}}}, \Omega^{\mathrm{F}}_{\mathrm{h},\Gamma^{\mathrm{FP}}}$	Fluid domain covered by intersected elements (CutFEM)
$\Omega^{\mathrm{F}}_{\mathrm{h},\Gamma^{\mathrm{F,I}},\mathcal{I}}, \Omega^{\mathrm{F}}_{\mathrm{h},\Gamma^{\mathrm{FS}},\mathcal{I}}, \Omega^{\mathrm{F}}_{\mathrm{h},\Gamma^{\mathrm{FP}},\mathcal{I}}$	Non-Fluid domain covered by intersected elements (CutFEM)
$\mathcal{F}_{i,j}$	Common face of element i and element j
$\mathcal{F}_{\breve{\Omega}^*_{\mathcal{T}_\mathrm{h}}}$	Set of all inner faces of a discretization
$\mathcal{F}^{\mathcal{G}}_{\breve{\Omega}^{\mathrm{F}}_{\mathcal{T}_\mathrm{h},\mathcal{A}}}$	Set of faces which is utilized for the ghost penalty stabilization (CutFEM)
$\mathcal{N}$	Discrete space

Discrete Weak Form

$\mathcal{W}^{\mathrm{S}}_{\mathrm{h},n+1}$	... for the structural problem
$\mathcal{W}^{\mathrm{F}}_{\mathrm{h},n+1}$	... for the fluid problem
$\mathcal{W}^{\mathrm{F}}_{\mathcal{S}_\mathrm{h},n+1}$	... for the stabilization of the fluid problem

$\mathcal{W}_{\mathrm{h},n+1}^{\mathrm{F,CUT}}$	... for the fluid problem discretized by CutFEM
$\mathcal{W}_{\mathcal{G}_\mathrm{h},n+1}^{\mathrm{F}}$	... for the ghost penalty stabilization (CutFEM)
$\mathcal{W}_{\mathrm{h},n+1}^{\mathrm{P}}$	... for the poroelastic problem
$\mathcal{W}_{\mathcal{S}_\mathrm{h},n+1}^{\mathrm{P}}$	... for the stabilization of the porous fluid problem
$\mathcal{W}_{\mathrm{h},n+1}^{\mathrm{FSI,F}}$	... for the Nitsche-based incorporation of the FSI-interface conditions utilizing fluid-sided interface stress representation
$\mathcal{W}_{\mathrm{h},n+1}^{\mathrm{FSI,S}}$	... for the Nitsche-based incorporation of the FSI-interface conditions utilizing solid-sided interface stress representation
$\mathcal{W}_{\mathrm{h},n+1}^{\mathrm{FFI}}$	... for the Nitsche-based incorporation of the fluid-fluid-interface conditions
$\mathcal{W}_{\mathrm{h},n+1}^{\mathrm{FPI},n}$	... for the Nitsche-based incorporation of the normal FPI-interface conditions
$\mathcal{W}_{\mathrm{h},n+1}^{\mathrm{FPI},t,Nit}$	... for the Nitsche-based incorporation of the tangential FPI-interface conditions
$\mathcal{W}_{\mathrm{h},n+1}^{\mathrm{FPI},t,Sub}$	... for the substitution-based incorporation of the tangential FPI-interface conditions
$\mathcal{W}_{\mathrm{h},n+1}^{\mathrm{PS},c}$	... for the dual Mortar Lagrange multiplier incorporation of the solid-poroelastic contact conditions
$\mathcal{W}_{\mathrm{h},n+1}^{\mathrm{PS},f}$	... for the Nitsche-based incorporation of porous fluid mass balance on the solid-poroelastic contact interface
$\mathcal{W}_{\mathrm{h},\Gamma,n+1}^{\mathrm{FS},n} + \mathcal{W}_{\mathrm{h},\Gamma,\mathrm{Adj},n+1}^{\mathrm{FS},n}$	... for the Nitsche-based incorporation of the normal FSCI conditions
$\mathcal{W}_{\mathrm{h},\Gamma,n+1}^{\mathrm{FS},t} + \mathcal{W}_{\mathrm{h},\Gamma,\mathrm{Adj},n+1}^{\mathrm{FS},t}$	... for the Nitsche-based incorporation of the tangential FSCI conditions
$\mathcal{W}_{\mathrm{h},\Gamma,n+1}^{\mathrm{FPS},n} + \mathcal{W}_{\mathrm{h},\Gamma,\mathrm{Adj},n+1}^{\mathrm{FPS},n}$	... for the Nitsche-based incorporation of the normal FPSCI conditions
$\mathcal{W}_{\mathrm{h},\Gamma,n+1}^{\mathrm{FPS},t} + \mathcal{W}_{\mathrm{h},\Gamma,\mathrm{Adj},n+1}^{\mathrm{FPS},t}$	... for the Nitsche-based incorporation of the tangential FPSCI conditions
$\mathcal{W}_{\mathrm{h},\Gamma,n+1}^{\mathrm{P^F},c} + \mathcal{W}_{\mathrm{h},\Gamma,\mathrm{Adj},n+1}^{\mathrm{P^F},c}$	... for the Nitsche-based incorporation of viscous fluid porous fluid coupling condition for FPSCI

Nitsche-based Methods

$\gamma^{\mathrm{S},c}, \gamma^{\mathrm{S/P},c}, \gamma^{\mathrm{FSI}}$	Nitsche penalty parameter
$\gamma_0^{\mathrm{S},c}, \gamma_0^{\mathrm{S/P},c}, \gamma_0^{\mathrm{FSI}}, \gamma_0^{\mathrm{FPI},n}, \gamma_0^{\mathrm{FPI},t}$	Nitsche penalty constant
$\phi_\Gamma^{\mathrm{F}}, \phi_\Gamma^{\mathrm{S}}, \phi^{\mathrm{S},c}$	Scaling of Nitsche penalty parameter
$\xi, \xi^{\mathrm{FSI}}, \xi^{\mathrm{FPI}}$	Sign of adjoint-consistency term
λ_e	Maximum eigenvalue of the generalized local eigenvalue problem for element e

$\underline{\boldsymbol{A}}_e, \underline{\boldsymbol{B}}_e$	Element matrices utilized for the generalized local eigenvalue problem for element e
ω^c	Contact interface stress weighting factor
$\underline{\hat{\boldsymbol{g}}}_v^{\mathrm{FS}}, \underline{\hat{\boldsymbol{g}}}^{\mathrm{FP},n}, \underline{\hat{\boldsymbol{g}}}^{\mathrm{FP},t}$	Interface constraint jump vector
$\underline{\hat{\boldsymbol{g}}}_\sigma^{\mathrm{FS}}, \underline{\hat{\boldsymbol{g}}}_\sigma^{\mathrm{FP}}, \hat{g}_\sigma^{\mathrm{FP},n}$	Interface traction jump value, vector

Nonlinear Solution Procedure

$\underline{\mathsf{A}}^*$	Vector of the nonlinear system of equations depending on the unknown state
$\underline{\mathsf{F}}^*$	Vector of the nonlinear system of equations depending on the known state
$\underline{\mathsf{R}}^*$	Residual vector of the nonlinear system of equations
$\underline{\mathsf{C}}$	Linearization matrix
ω^i	Damping parameter in iteration i
$\epsilon_{\underline{\mathsf{R}}}, \epsilon_{\Delta\underline{\mathsf{x}}}, \epsilon_{\mathrm{geom}}$	Tolerances for the nonlinear solution procedure

Nitsche-based FSCI and FPSCI

$\underline{\boldsymbol{v}}^{\mathrm{S/P},rel}$	Relative interface velocity
$v^{rel,n}, v^{\mathrm{S/P},rel,n}$	Normal relative interface velocity
$\underline{\boldsymbol{x}}_{\mathcal{E}}$	Extension origin position
$\mathcal{E}_{\underline{\boldsymbol{x}}}\left[*\right]$	Extension of a quantities $*$ to position $\underline{\boldsymbol{x}}$
$\mathcal{E}_{\underline{\boldsymbol{x}}}^{const.}\left[*\right]$	Constant extension of a quantities $*$ to position $\underline{\boldsymbol{x}}$
$\mathcal{E}_{\underline{\boldsymbol{x}}}^{\overline{\mathrm{F}}-stress}\left[*\right]$	Physically motivated extension of the numerical fluid stress to position $\underline{\boldsymbol{x}}$
$\overline{\underline{\boldsymbol{\sigma}}}_{\mathrm{h}}^n$	Unique interface traction
$\overline{\sigma}_{\mathrm{h}}^{nn}$	Normal unique interface traction
$\overline{p}_{\mathrm{h}}^{\mathrm{P}}$	Representative of porous fluid pressure for FPSCI
$\overline{\sigma}_{\mathrm{h}}^{\mathrm{S},nn}$	Representative solid contact stress for FSCI
$\overline{\sigma}_{\mathrm{h}}^{\mathrm{S/P},nn}$	Representative solid/poroelastic contact stress for FPSCI
$\alpha_*^{\mathrm{P}}, \alpha_{sharp}^{\mathrm{P}}, \alpha_{smooth}^{\mathrm{P}}$	Porous interface type indicator

Subscripts and Superscripts

$(*)^{\mathrm{F}}$	Quantity corresponding to the fluid domain
$(*)^{\mathrm{S}}$	Quantity corresponding to the solid domain
$(*)^{\mathrm{P}}$	Quantity corresponding to the poroelastic domain
$(*)^{\mathrm{P^F}}$	Quantity corresponding to the poroelastic fluid phase

$(*)^{\mathrm{PS}}$	Quantity corresponding to the poroelastic solid phase
$(*)^{\mathrm{G}}$	Quantity corresponding to the mesh motion
$(*)^{c}$	Quantity related to contact
$(*)^{n}$	Quantity in interface normal direction
$(*)^{t}$	Quantity in interface tangential orientation
$(*)^{i}$	Quantity evaluated at i-th iteration of the nonlinear solution procedure
$(*)_{0}$	Quantity in material configuration
$(*)_{\mathrm{h}}$	Space-discrete quantity
$\hat{(*)}$	Prescribed quantity
$\mathring{(*)}$	Initial quantity
$(*)_{\mathcal{E}}$	Extension of a quantity from the fluid domain
$(*)_{n}$,$(*)_{n+1}$,$(*)_{n+\theta}$	Time-discrete quantity at $t = t_n, t = t_{n+1}, t = t_{n+\theta}$
$\check{(*)}$	Projection onto the opposite interface
$(*)_{\mathcal{A}}$	Analytic solution

Abbreviations

ALE	Arbitrary Lagrangian-Eulerian
AMG	Algebraic multigrid
BDF	Backward differentiation formula
BG	Bubnov Galerkin
BJ	Beavers-Joseph (condition)
BJS	Beavers-Joseph-Saffmann (condition)
cG-FEM	Continuous Galerkin finite element method
CIP	Continuous interior penalty
CutFEM	Cut finite element method
DG	Discontinuous Galerkin
DOF	Degree of freedom
DOFSet	Set of degrees of freedom
EHL	Elastohydrodynamic lubrication
EOS	Edge-oriented stabilization
FD	Fictitious domain (method)
FE	Finite element (method)
FEM	Finite element method
FOS	Face-oriented stabilization
FPI	Fluid-poroelasticity interaction
FPSCI	Fluid-poroelasticity-structure-contact interaction
FPSI	Fluid-poroelasticity-structure interaction
FSCI	Fluid-structure-contact interaction
FSI	Fluid-structure interaction
GMRES	Generalized minimal residual method
HSM	Hertz–Signiorini–Moreau (conditions)
IB	Immersed boundary (method)
IBVP	Initial boundary value problem
ILU	Incomplete LU factorization
IP	Integration point
NURBS	Non-Uniform Rational B-Spline
OST	One-Step-θ (scheme)
PDE	Partial differential equations
PG	Petrov Galerkin
XFEM	eXtended finite element method

1 Introduction

From the beginning of our solar system and the formation of first structural bodies from a giant molecular cloud, many contact events of these bodies characterize significant turning points in the fate of the world. The impact of structures of impressive dimensions on the planet earth most likely led to the formation of our permanent companion, the moon [117], and abruptly ended the existence of the earth's greatest land creatures, the dinosaurs [194]. To varying degrees these processes were influenced by the presence of surrounding fluid such as the gas atmosphere surrounding the earth. The deceleration of bodies by atmospheric gas or the propagation of pressure waves as a result of an impact can have a crucial influence on the environmental effect of these processes. While these extraordinary phenomena occur very rarely and are almost impossible to be influenced by the human being, a closer look reveals that numerous similar processes, which include contacting solid bodies in interaction with fluid, permanently occur on a smaller length scale in various natural and technical setups. The ability to accurately predict this type of physical processes is essential in various fields, such as engineering, biomechanics, and medical technology in order to obtain a profound understanding and thus make innovations possible in the first place.

1.1 Motivation[1]

The development of computational methods to predict challenging mechanical processes which include the interaction of contacting solid bodies with surrounding fluid is the focus of this work. Whereas the still challenging numerical treatment of fluid-structure interaction (FSI) as well as the numerical treatment of solid contact mechanics are active research fields since decades, first developments to solve fluid-structure-contact interaction (FSCI) systems numerically have been started only a short time ago. Taking solid body contact for FSI systems into account significantly increases the complexity of the physical modeling and the computational approaches. As a result, all numerical formulations presented for this type of problem so far suffer from various restrictions prohibiting the application to general FSCI systems. Due to the varying underlying physical processes on the contact surfaces, e.g. due to differences for smooth and rough surface contact, different physical models for FSCI on a macroscopic scale are necessary. The computational approaches should meet the requirements to solve these types of problems as general as possible in order to account for the wide range of applications.

In the field of biomechanics, the solution of FSCI problems can help to understand various underlying physical processes better, which can hardly be accessed by experiments. Most of the so far presented computational approaches for FSCI-like problems are motivated by the prediction of the heart valve processes (see e.g. [70, 169]). In the development and selection of

[1] Certain parts of this paragraph are adapted from the author's publications [1, 3]

replacements for diseased human heart valves, a deep insight into the mechanical state and the fluid flow during the pumping operation is required. But also for the mechanical prediction of an complete human heart, the included fluid in the heart pericardium leads to FSCI-like problems (see e.g. [168] for a discussion on boundary conditions on the heart pericardium for the computational analysis). For the contact processes of the poroelastic tissues in articulating joints (such as the knee joint) [107, 158], the relevance of the surrounding synovial fluid on the mechanical response can be analyzed by a numerical approach for fluid-poroelasticity-structure-contact interaction (FPSCI). A last topic related to the human body mentioned herein, is the investigation of the mechanical digestion processes in the stomach. Contact processes between solid food particles and self-contact of the gastric wall in the surrounding of the digesta characterize these complex mechanical processes (for an overview see e.g. [35]). As large deformations often occur when analyzing soft tissue in complex FSI processes for biomechanical applications, contact cannot be excluded beforehand in many scenarios. An illustrative example is the computational prediction of biofilms [66, 207], where contact with itself might occur when taking the real complex 3D geometry [29] into account. Depending on the objective of the respective study, considering the porosity of the corresponding biological tissue might or might not be essential.

Many technical devices are based on processes of FSCI systems. In the field of tribology, essential machine parts, such as bearings and seals, have to be analyzed [162, 164, 182]. Also the contact of vehicle tires on wet roads is an FSCI configuration of large relevance. The inflation of parachutes including massive self-contact of the canopy is analyzed in [125]. Finally, in conventional lithium-ion batteries, self-contact of the electrodes within the liquid electrolyte might occur due to essential volumetric changes of the active material during the charging and discharging process (see [98] for the principle structure of such a battery).

As motivated by these examples, the subsequent examinations will be carried out at a system scale, at which the relevant physics can be well represented by means of the continuum mechanics theory.

A major challenge of the development of a consistent physical model for fluid-structure interaction including contact is the multiscale nature of the considered problem. While at the macroscopic scale the fluid physics are governed by the well-known Navier-Stokes equations supplemented by a no-slip condition on the fluid-structure interface, this does not necessarily hold true when solid bodies come into contact. Solving simply this classical macroscopic physical model for FSI does not lead to contact of submersed smooth solid bodies due to the increasing viscous stress when the fluid gap gets smaller. Therefore, a finite fluid gap would remain, which is not in agreement with the observation of contacting bodies. This "no-collision" paradox, which states that contact between smooth surfaces with no velocity slip on the interface between the fluid and the involved structures cannot occur in an incompressible, viscous fluid in finite time (see the works of Hillairet and Takahashi [119] and Gérard-Varet *et al.* [92]), is contrary to the macroscopic observation. Interface conditions allowing for a certain amount of velocity slip on the colliding surfaces (shown by e.g. Hocking [122]) or for non-smooth surfaces (analyzed by e.g. Cawthorn and Balmforth [56] and Gérard-Varet and Hillairet [91]), contact between the corresponding bodies is possible. A physical explanation for this paradox is the lack of consideration of the surface microstructure. As soon as the microscopic roughness is treated, solid-solid contact can occur, as shown by Davis *et al.* [69]. Whether roughness effects play a significant role in the overall problem depends on the specific purpose of investigation, the macroscopic problem setup, as well as the ratio of the relevant problem size to the characteristic roughness height.

Thus, for contacting surfaces with a small height of the microstructure, the roughness effect can still be essential in the case of small scale problems and vice versa. A deeper insight into the underlying physical processes of contacting submersed bodies and the non-exact nature of computational approaches allows identifying different ways out of this dilemma. For clarification, it should be pointed out that the "no-collision" paradox does not apply in the case poroelastic permeable bodies approach each other in surrounding fluid since the fluid mass enters the poroelastic domains.

For absolutely smooth contacting solid bodies, the fluid gap between approaching solid bodies at some point will fall below the validity limit of the classical fluid dynamics models used in continuum mechanics. The actual geometric size of this limit depends on the considered type of fluid and its molecular free path length. As a first consequence when the remaining fluid gap becomes smaller than this limit, a transition of the no-slip interface condition to a slip interface condition (including in general a surface roughness dependent slip length) into the so called "Slip-Flow Regime" (see e.g. the work of Barber and Emerson [16]), while retaining the validity of the Navier-Stokes equations in the fluid domain, serves as a good fluid dynamics model. Therefore, this local relaxation of the tangential no-slip condition has to be incorporated into the physical model, while retaining the no-slip condition for the remaining part of the interface. This results in a consistent physical model to consider contact of smooth solid bodies with fluid between the contacting surfaces. It should be pointed out, that the only exception is the case of two parallel plates, where due to the required acceleration of the fluid mass no contact occurs in finite time.

Second, taking into account that any real surface has a microstructure, this contacting process can change fundamentally. As soon as the height of the fluid film between rough surfaces is in the same order of magnitude as surface asperities, surface roughness has an essential impact on the physical response of such a system. If single asperities come into contact before the validity of the classical fluid equations is lost, the contacting process described first cannot hold anymore. From a macroscopic point of view, contact is enabled in this case via a fluid mass transfer from the fluid domain into the rough microstructure. Therefore, considering the rough microstructure of contacting surfaces can be essential for a consistent FSCI model. This is the case when the characteristic roughness height is larger than the limiting size of classical fluid equations. To account for this rough surface configuration, which is relevant for many problems of interest, a model that takes this rough surfaces in an average manner into account, can be beneficial.

Finally, even for the computational analysis of FSCI configurations where these two physical effects are not essential on the considered length scale, contact still has to be considered to provide sufficient robustness with respect to numerical errors. This is a result of the fact that numerical solution approaches are always accompanied by approximations of the underlying physical model when considering general configurations. As a result, the "no-collision" paradox does not apply for the numerical solution of contacting bodies in the surrounding of fluid. In the case there is no explicit contact treatment within the discrete FSI formulation, only fluid forces in the gap keep the bodies apart. As soon as an artificial collision of solid bodies occurs, e.g. during an iterative nonlinear solution procedure, there is no separation force acting since there is no remaining fluid between these bodies. This is shown in the works of De Hart *et al.* [70] and Astorino *et al.* [9], where a penetration of surfaces can be observed as no contact formulation is considered. An FSI formulation including contact ensures that the corresponding computational approach provides a physical meaningful response even on a macroscopic scale.

Thus, the different emerging numerical errors, which are potentially even small, do not change the system behavior fundamentally.

1.2 Research Objective

The overall research objective of this thesis lies in the development of physical models and corresponding numerical approaches to predict the processes of FSI and fluid-poroelasticity interaction (FPI) systems including contact of the elastic bodies as general as possible. In order to achieve this, suitable methods are chosen which have been successfully developed for problems of reduced complexity in the preceding works. The extension of these well known approaches and the development of novel approaches allows unifying these components into a coherent FSCI and FPSCI framework. To account for the different causes which require an explicit treatment of contact, such as a small gap size and corresponding slip interface conditions, the microstructure of rough surfaces, or simply to provide sufficient robustness with respect to numerical errors, different physical models and corresponding numerical formulations are required.

1.2.1 Specification of Requirements

In the following, the most essential requirements to develop approaches for the efficient numerical prediction of FSCI and FPSCI systems are briefly discussed.

No Limitations Concerning the Flow Regime and the Geometric Configuration A general formulation to solve FSCI problems must not be limited to a specific configuration such as the flow regime, the geometric setup, or specific boundary conditions. Such formulations, which are often used to model thin viscous film flows by utilizing the Reynolds equation [6, 179], allow to reduce the computational complexity and cost. Nevertheless, for a general formulation of FSCI and FPSCI, the spatially fully resolved Navier-Stokes equations have to be utilized.

Handling of Topological Changes of the Fluid Domain As soon as contact between elastic bodies cannot be ruled out, there is no lower limit for the size of the gap between the surfaces involved. Since the gap is directly related to the dimensions of the fluid domain between both contacting bodies for FSCI configurations, the fluid domain potentially vanishes at certain positions. This process corresponds to a topological change of the fluid domain and needs to be treated in a robust way by the utilized numerical method. Classical numerical approaches for FSI where a moving computational mesh matches the fluid domain reach their limits for such processes. The application of unfitted FEMs, which utilize a fixed computational mesh that does not fit the boundaries of the fluid domain, enable the numerical treatment of these processes without specific modifications to the fluid formulation. Due to its properties such as consistency and accuracy, the Cut Finite Element Method (CutFEM) provides a beneficial methodology to discretize the governing equations in the fluid domain [51].

Flexible Computation Framework for Unfitted FSI A well-tested and flexible computation framework for interface-unfitted FSI is required as a basis to be extended to FPI, FSCI,

and FPSCI. Flexibility includes the application of an unfitted numerical formulation for the fluid domain which is essentially independent of the embedded structural domain. Additionally, the incorporation of interface conditions should only have an effect locally and do not require any modifications to the discrete evaluation of the governing equations in the involved physical fields. These aspects ensure that the formulation can be utilized to embed other physical domains than structures, such as a poroelastic domain, and take into account different conditions on the respective interfaces.

Continuity of the Discrete Formulation Dynamic FSCI problems go along with time dependent changes of the interface conditions from FSI conditions to contact conditions. In the development of formulations for FSCI, it has to be ensured that the change of interface conditions is continuous and does not introduce abrupt changes to the discrete system. Thereby, the introduction of errors arising from corresponding nonphysical temporal changes is avoided. Additionally this is an essential property for the application of gradient-based nonlinear solution procedures.

Robust Formulation for Strongly Interacting Domains The general formulation to solve FSCI and FPSCI needs to be robust also for systems including a strong interaction between the fluid and the elastic structures. It is well known that a simultaneous, monolithic solution of the entire system of equations is beneficial concerning the accuracy and the numerical robustness for such configurations. Thus, a monolithic solution procedure should be applied for all formulations [115, 154].

Physical Model for Rough Surface Contact in FSCI As already noted previously, the effects arising from the roughness of surfaces can, but not necessarily does, dominate the macroscopic overall physical response of an FSCI system. Whenever the surface roughness has to be considered in the physical model, a direct resolution of the microstructure by the computational discretization is most often not practicable for engineering applications. Therein, the focus is mostly on averaged quantities such as the average velocity in the fluid gap of a valve or the average pressure in the fluid gap of a bearing. With such computed averaged quantities, predictions for global quantities such as the leakage flow of a valve or the load capacity of a bearing can be deduced. Resolving the potentially complex fluid flow between single roughness asperities is generally not necessary for these types of applications besides the fact that the exact microstructure is not known at all in most cases. Thus, a physical model which takes the effect of rough contacting surfaces by a homogenized, poroelastic layer of fluid and structure into account, has to be developed.

Computation Framework for Unfitted FPI Based on the flexible FSI framework, an interface-unfitted FPI formulation is necessary to serve as a basic computational approach for the rough surface FSCI model. This formulation has to include a general and flexible poroelastic formulation in order to take essential physical effects into account such as e.g. the increase of flow resistance when the porous medium is compressed, the expansion of the medium for an increasing fluid pressure, and the proper mechanical response to external loads. Furthermore,

various constitutive models are required to adapt the formulation to different rough microstructures and solid materials. The formulation for the incorporation of interface conditions has ensure a robust operation for a large range of physical parameters and be well suited for the extension to general FPSCI.

Computational Approach for General FSCI A computational approach for general FSCI has to combine an unfitted FSI formulation with contact mechanics. Specific attention is required for the formulation of the temporally changing interface conditions of FSI and contact. As no fluid domain remains in the zone of solid-solid contact, and thus, no fluid state is directly available thereon, appropriate and physically reasonable techniques are required to ensure a continuous transition between the different interface conditions. Specific numerical approaches have to guarantee this continuity also for the discrete formulation.

Computational Approach for General FPSCI The extension of FSCI to FPSCI requires the incorporation of the more complex coupling conditions between viscous fluids and the poroelastic structure and its temporal dependent transition to the contact conditions. Contact between poroelastic structures requires the fulfillment of the porous fluid mass balance in addition to the classical contact conditions. To ensure a physical formulation for the FPSCI problem, the porous fluid, which is also present in the zone of contact, should be utilized to formulate the transition of conditions.

1.3 Numerical Approaches as a Basis for FSCI and FPSCI

Within this thesis, numerical approaches to treat the different aspects of the FSCI and FPSCI problems are based on approaches known from literature as far as they are available. In the following paragraphs, a brief overview on preceding work in the most essential fields, which are related to the formulations for FSCI and FPSCI developed in this work, is given.

eXtended FEM and CutFEM for Unfitted Discretizations In the eXtended finite element method (XFEM) the discrete solution space is enriched by prior knowledge of the solution. This approach was first introduced in the works of Belytschko and Black [22], Belytschko *et al.* [24], Moës *et al.* [157], and Sukumar *et al.* [206] to incorporate the discontinuity and singularity of brittle cracks into the numerical formulation. This is enabled by incorporating enrichment functions in addition to the standard FE shape functions, which are accompanied by additionally introduced unknowns.

For unfitted formulations, where the computational mesh does not match the outer boundaries of the considered domains, this prior knowledge is the position of a boundary of the respective domain. Specifying a Heaviside function or a Step function aligned to the boundary as an enrichment function, separates the physical from the non-physcial part of the computational mesh in the XFEM, which equals in principle a CutFEM formulation. In the context of unfitted discretizations, the CutFEM can be considered as a special case of the XFEM. For the CutFEM

point of view, the part of the computational mesh outside of the boundary is "cut" away. Both terms, which are used alternately, include the modification of the solution space.

The development of the CutFEM for the application to the fluid equations, started by analyses on the Poisson equation by Burman and Hansbo [46], the Stokes equation by Burman and Hansbo [47], Massing *et al.* [150], and finally, including advection, the Oseen equation by Massing *et al.* [149]. The application to the Navier-Stokes equation was presented by Schott and Wall [188]. In these works, the techniques to enforce conditions on boundaries which are unfitted to the computational mesh are based on the method introduced by Nitsche [161]. Due to the arbitrary intersection of the computational mesh and the boundary a proper treatment of critical intersections to ensure a stable formulation is required. Most often used and also applied within this thesis, is a ghost penalty stabilization which was first presented by Burman [38]. Recently, an alternative approach to this stabilization where intersected elements are strongly coupled to patches, the aggregated finite element method, was presented by Badia *et al.* [14, 15]. The shifted boundary method, which was introduced by Main and Scovazzi [147, 148], directly avoids the intersection of elements by making use of a surrogate boundary along element boundaries.

The CutFEM with moving interfaces has been successfully applied to various applications including two-phase flow Groß and Reusken [104], Hansbo *et al.* [112], and Schott *et al.* [189] and FSI, which will be discussed in the subsequent paragraph.

Fluid-Structure Interaction The computational study of mechanical systems where deformable structures interact with fluid attracts a lot of attention. As a result, a large amount of literature deals with various aspects of this problem and, hence, in the following, only certain selected contributions to FSI, which help to categorize the approach applied in this thesis, will be discussed. So far, the most widely used approach consists of the application of interface- and boundary-fitted fluid and structural discretizations, which is enabled by the combination with an arbitrary Lagrangian-Eulerian (ALE) formulation for the fluid domain. The basis for this strategy has already been presented in the works of Belytschko *et al.* [23], Donea *et al.* [74], and Hirt *et al.* [121]. The simultaneous monolithic solution of both, the solid and the fluid domain (see e.g. the work of Heil [115]), requires advanced approaches for solving the resulting system of equations. This aspect has been addressed e.g. in the works of Gee *et al.* [90], Mayr [153], Mayr *et al.* [154] and for general n-field coupled problems by Verdugo and Wall [214]. A comparison of different FSI coupling strategies by Küttler *et al.* [135] indicates that monolithic coupling schemes are superior to sequential approaches in the case of strong interaction between the solid and the fluid. Klöppel *et al.* [134] presented a dual mortar interface coupling approach, which extends the applicability of ALE-based FSI to non-conforming interfaces. Many FSI problems, especially in the field of biomechanics, include large motions and deformations of the solid bodies, which potentially even lead to topological changes of the fluid domain. For these type of problems, all previously mentioned approaches rapidly reach their limit of efficient application due to the occurring distortion of the fluid discretization.

Such challenging configurations led to the development of numerical approaches where the fluid discretization is not fitted to the solid bodies. For most of these approaches, a fixed computational grid for the discretization of the fluid domain is utilized, and thus, an Eulerian fluid observer is applied. One approach, which is realized in various ways, is the immersed boundary (IB) method. The IB concept was initially introduced for flow simulation in the heart by Peskin

[165, 166] and a summary of the IB method was presented by Peskin [167]. In this approach, a smoothed approximation of the interaction equations on the interface link the Eulerian fluid variables and the Lagrangian structural variables. The coupling is performed by volumetric force terms. Another approach, which was used several times in attempts to formulate FSI including solid body contact, is the fictitious domain method (FD) originally presented for embedded boundaries in fluid flows by Glowinski *et al.* [96, 97] and extended to FSI by Baaijens [11]. Therein, the interface conditions are incorporated on the FSI interface by a Lagrange multiplier which is in general not fitted to the fixed-grid fluid discretization. Due to the arbitrary alignment of the fluid and the structural discretization, the specification of an accurate but numerically stable discrete space for the Lagrange multiplier in general is still an open issue (see e.g. the discussion by van Loon *et al.* [213]). As time-dependent changes of the fluid domain due to the motion of the structural domain are not taken into account, the FD method is applied to slender structural bodies with negligible thickness for FSI configurations. Still, a spatially continuous solution space in the entire fluid domain is utilized, which can lead to difficulties e.g. in the case of a different fluid pressure level on the two sides of the slender structure (see the discussion in the work of Kamensky *et al.* [133]). This aspect is critical as this kind of discontinuous pressure is typical for any valve-type configuration. Recently, this issue was analyzed by Boilevin-Kayl *et al.* [28], who provided a comparison of an interface-fitted moving fluid mesh approach, a FD method, and a Nitsche-XFEM, which is identical to the CutFEM, for FSI with thin-walled structures.

A formulation for the interaction of rigid particles with Stokes flow based on the XFEM and including enrichment functions to account for the lubrication solution between these particles is presented by Wagner *et al.* [219]. The application of Lagrange multipliers to weakly enforce the FSI interface conditions based on the XFEM framework was analyzed by Gerstenberger and Wall [94]. Wall *et al.* [220] presented a comparison of this formulation with an alternative fluid domain decomposition approach for FSI based on a moving fluid mesh close to the structure which overlaps with a fixed background mesh. By developing a stress-based Lagrange multiplier method, Gerstenberger [93] could resolve the otherwise critical choice of the discrete Lagrange multiplier space. On the basis of the CutFEM framework, which includes the weak imposition of interface conditions by a Nitsche-based approach in combination with ghost penalty stabilization, recently, formulations for the treatment of unfitted FSI were presented. In the work of Burman and Fernández [42], the interaction of Stokes flow and linear elastic structures is analyzed. Alauzet *et al.* [5] presented a comparison of different coupling schemes for FSI with immersed thin-walled structures based on a closely related numerical approach. An approach based on the XFEM for FSI with thick structures utilizing discontinuous Galerkin (DG) mortaring to connect the enriched and the not enriched fluid domain was presented by Zonca *et al.* [239] for moderate Reynolds numbers.

An unfitted fully implicit approach for FSI based on the CutFEM framework including nonlinear structural materials and large deformation is introduced in the thesis of Schott [187]. The formulations therein serve as a starting point for the developments regarding unfitted FSI in this thesis. The extension of a closely related approach to FSI including fracture of the structures is presented by Sudhakar and Wall [202]. Making use of a moving ALE fluid discretization, various approaches combining the advantages of fitted and unfitted FSI-formulations are presented by Schott *et al.* [192].

A critical aspect of all unfitted formulations, especially for high Reynolds number flows, is the sufficient resolution of the boundary layer flows close to the FSI interface. To track boundary layers in turbulent FSI, Farhat and Lakshminarayan [83] presented an ALE approach where the unfitted computational mesh is rigidly translated and rotated. A Hybrid Fixed-Grid-ALE Approach is presented in the thesis of Shahmiri [198] to enable the application of an interface-fitted moving fluid discretization close to the interface, whereas a fixed fluid mesh is utilized in the remaining fluid domain. Therein, the background discretization is intersected by the boundary of a moving fluid mesh and coupling conditions are enforced on this sharp domain decomposition interface. A similar approach applied to the steady state FSI problem with Stokes flow is presented by Massing *et al.* [151]. A fully monolithic formulation of hybrid Eulerian-ALE fluid domain decomposition, which is based exclusively on the Nitsche method to enforce all interface conditions, is presented by Schott *et al.* [191].

Fluid-Poroelasticity Interaction[1] The interaction of an incompressible fluid with a permeable, elastic, and fluid-saturated structure is of great interest for various fields, such as geomechanics, biomechanics, and, which is the incentive for developing an unfitted FPI formulation in this thesis, is rough surface modeling in the context of FSCI (see Chapter 5).

Several formulations to solve the interface-coupled problem of incompressible flow and poroelasticity were presented by Ambartsumyan *et al.* [7], Badia *et al.* [12], Bukač *et al.* [37], Luo *et al.* [146], Showalter [200], and Zakerzadeh *et al.* [234] in the recent years. Novel approaches are still being developed to meet the arising challenges. Therein, the governing equations inside of the poroelastic domain are usually based on the Biot-system (see the work of Biot [26]), where the fluid flow through the poroelastic matrix is modeled by a Darcy-like flow equation that is volume-coupled to a linear solid mechanics model for small deformations. In the fluid domain, the Stokes equations [7, 37, 146, 200] or, including the effect of convection, the Navier-Stokes equations [12, 234] are applied. On the fluid-poroelastic interface, either the Beavers-Joseph-Saffmann [7, 12, 37, 200] or a no-slip condition [37, 146, 234] in tangential interface direction are considered. Details on these interface conditions for the coupling of fluid and (rigid-) porous flow can be found in the works of Beavers and Joseph [20], Cao *et al.* [55], D'Angelo and Zunino [68], Discacciati and Quarteroni [71], Saffman [181], and the references therein.

Contact Mechanics[2] Classical computational approaches for contact mechanics treat the interface conditions of contact between multiple structural bodies. These conditions consist of the no-penetration between contacting bodies, the dynamic equilibrium on the interface between both bodies, and potentially include frictional models. The effect of surrounding fluid is typically neglected for these methods. Similar to the field of FSI, a large amount of numerical approaches was developed to treat this type of problem. Thus, in the following, only the works directly related to the methods utilized in this thesis will be discussed. For a broader overview on the field of contact mechanics, the reader is referred to the textbooks of e.g. Wriggers [230] and Laursen [139] and the theses of Farah [81], Gitterle [95], Popp [170], and Seitz [195]. Especially the last two works provide the starting point related to contact mechanics for the developments presented herein.

[1] This paragraph is adapted from the author's publication [2]

[2] Certain parts of this paragraph are adapted from the author's publication [3]

The first developed contact formulations, which are based on so-called node-to-segment contact, are not utilized in this thesis. Therein, the penetration of the computational nodes on a specific interface into the discrete surface of the opposite interface is prevented. An imposition of the contact conditions in an integral sense is enabled by Mortar methods. This type of formulation was first introduced for non-overlapping domain decomposition (see e.g. the work of Belgacem [21]). Different variants for Mortar contact based on penalty methods or on Lagrange multipliers to enforce the contact constraints were presented e.g. by Fischer and Wriggers [84], Hild [118], Puso and Laursen [176], Tur *et al.* [212], and Yang *et al.* [232]. The construction of the discrete space of the Lagrange multiplier based on biorthogonal/dual shape functions was proposed by Wohlmuth [227, 228]. Due to the associated localization of the nodal coupling in comparison to the standard Mortar method, an efficient elimination of the Lagrange multiplier from the final system of equations is enabled. Contact formulations based on this dual discrete space for discretization of the contact Lagrange multiplier are presented e.g. by Hartmann *et al.* [113], Hüeber and Wohlmuth [126], and Popp *et al.* [171, 172]. Based on this type of dual Mortar contact formulation, the numerical approach to treat rough surface contact in FSCI, which is presented in Chapter 5, is developed.

As an alternative to Lagrange multipliers, the Nitsche method gathers increasing attention to develop consistent contact formulations. A first application of the Nitsche method to contact problems is presented in Wriggers and Zavarise [229]. Chouly [60], Chouly and Hild [61], and Chouly *et al.* [62] provide a mathematical analysis of symmetric and skew-symmetric Nitsche methods for small deformation frictionless and frictional contact problems. A penalty-free formulation for the Signiorini problem is given by Burman *et al.* [52]. The extension of these works to nonlinear elasticity at finite deformations and nonlinear thermomechanical problems are given by Mlika *et al.* [156] and by Seitz *et al.* [196], respectively. In contrast to the most common formulations that require the definition of a master and a slave contact interface prior to the computation, Chouly *et al.* [63] and Mlika *et al.* [156] presented unbiased variants that do not required this arbitrary specification. In the work of Seitz *et al.* [196], a harmonic weighting of the contact stress is applied, which results in an almost unbiased approach as the only bias is introduced by the applied integration rule on the contact interface. In this thesis, the formulation will by extended to a completely unbiased approach by integration on both contact interfaces, which is similar to so-called two-half-pass algorithms (see e.g. the work of Sauer and De Lorenzis [184]).

Fluid-Structure-Contact Interaction[1] When looking at the available literature, one can note that a large portion of the available literature on FSCI formulations is either interested in the analysis of heart valves as given by Astorino *et al.* [9], Borazjani [31], De Hart *et al.* [70], Dos Santos *et al.* [76], Espino *et al.* [79, 80], Kamensky *et al.* [133], Laadhari and Quarteroni [136], Meschini *et al.* [155], and van Loon *et al.* [213] and only a smaller set in solving a more general problem setup of FSCI given by Bogaers *et al.* [27], Burman *et al.* [53], Liu and Liu [144], Mayer *et al.* [152], Sathe and Tezduyar [183], Tezduyar and Sathe [208], and Wick [225]. However, while most of those formulations work well for certain selected problem setups, they suffer from some restrictions preventing their application to more general complex problem classes. In the following, a brief overview on the aforementioned formulations is given.

[1] Certain parts of this paragraph are adapted from the author's publication [3]

Therein, the different approach will not be discussed in detail but rather classified regarding certain features and especially regarding assumptions or restrictions.

In [79, 80] contact in surrounding fluid does not need to be considered due to the chosen problem setup with geometrically separated contact and fluid-structure interfaces. A penetration of the solid bodies is accepted in [70] since contact is not treated explicitly. In [31], contact is included, but in the presented computations only the valve opening phase without significant influence of the contact formulation is analyzed. In [225], no explicit contact formulation is considered and a minimal distance of one mesh cell still remains between two flaps. Using reduced modeling with included contact of the heart valve, [136] avoids the requirement for a general FSCI formulation. A general formulation for FSCI is very powerful and also well motivated by the involved physical phenomena, but it is also more complex and not always needed.

Explicit treatment of the contact is considered in [9, 76, 152, 213] by Lagrange multiplier based contact methods, in [27, 31, 133, 183, 208] by methods based on penalty contact contributions, in [155] by an approach based on enforcement of equal structural velocity, and in [144] by a separating force based on the potential of the Lennard-Jones model.

Interface-fitted computational meshes for discretization of the fluid domain are enabled by approaches that require to enforce a non-vanishing fluid gap between approaching bodies and therefore avoid topological changes in the fluid domain preventing degenerated elements [27, 183, 208]. Approaches enabling the use of a non-interface-fitted discretization, which allow the consideration of "real" contact scenarios and the resulting topological changes of the fluid domain directly, are applied in [9, 31, 70, 76, 133, 136, 144, 152, 155, 213, 225]. The majority of these formulations consider dimensionally reduced structural models (i.e. membranes and shells) [9, 31, 70, 76, 133, 136, 155, 213], whereas bulky structures (i.e. structures of significant thickness as compared to the spatial resolution of the computational discretization in the fluid domain) are considered in [53, 144, 152, 225]. The restriction to slender bodies of the non-interface-fitted approaches is often related to issues concerning system conditioning and mass conservation errors close to the fluid-structure interface. This is due to the fact that the discontinuity of the fluid stress between two sides of a submersed solid is typically not represented by the discrete formulation (see e.g. [133, 136]), which prevents the analysis of configurations including large pressure jumps. This issue is not a fundamental limitation for non-interface-fitted FSI as shown e.g. in the works of Alauzet *et al.* [5], Burman and Fernández [42] (without contact), but increases the complexity of such a formulation including the underlying algorithm.

Contact of Saturated Poroelastic Medium[1] Most research concerning computational modeling of contact between poroelastic structures, which is often also denoted as biphasic contact, is dedicated to the study of contacting articular cartilage in articulating joints such as the knee (see e.g. the work of Guo *et al.* [107]). Numerical formulations to handle contact between poroelastic structure were presented by Ateshian *et al.* [10], Chen *et al.* [58], Donzelli and Spilker [75], Guo and Spilker [105, 106], Guo *et al.* [107], Sabetamal *et al.* [180] and Yang and Spilker [233] and are based on the interface conditions discussed by Hou *et al.* [124]. Two scalar Lagrange multipliers are utilized in [75] and extended to 3D in [233] to represent the solid and fluid contact interface traction. The formulation for biphasic contact presented in [58] is also

[1] This paragraph is adapted from the author's publication [4]

based on Lagrange multipliers. An augmented Lagranean formulation for this type of problem is utilized in [10, 105, 180], and for 3D configurations in [106]. This formulation is applied to the analysis of knee joints in [107]. A comparison of different selected computational approaches contact of poroelastic tissues is given by Galbusera *et al.* [88]. None of the previously mentioned formulations takes into account the interaction with an ambient fluid, but a vanishing porous fluid pressure on the boundary to the surrounding is assumed.

Thin Film Flows for Rough Surfaces[1] To analyze and predict tribological systems for thin fluid films, the Reynolds equation introduced by Reynolds [179], which can be derived from the Navier-Stokes equation by utilizing assumptions valid for thin film flows only, is widely used. To incorporate the effect of surface roughness without resolving the surfaces, an averaged Reynolds equation is often used to determine the averaged fluid pressure, see e.g. the works of Bayada and Chambat [18], Christensen and Tonder [64], Patir and Cheng [163], Prat *et al.* [174], and Tripp [211]. Bou-Said [32] and Jai and Bou-Said [129] show that significantly fewer degrees of freedom are required for solving the homogenized equations compared to the direct equations in order to obtain the pressure field between rough surfaces. A framework to consider the effects of deformation of structural bodies that are interacting via a thin fluid film is presented by Budt *et al.* [36] and Yang and Laursen [231] .

Almqvist *et al.* [6] compare the numerical solution of the full spatially discretized fluid momentum and continuity equations to the Reynolds approach on a problem with valid thin film approximation and show that there is no significant deviation of the results between both approaches. Nevertheless, with increasing film size this result does not hold any longer, as the underlying geometrical assumptions of the Reynolds equation become invalid. In this case, the solution of the full fluid equations seems to be absolutely essential, even though the computational cost is higher due to the increased number of degrees of freedom as compared to the Reynolds approach. As a consequence, the general Navier-Stokes equations to describe the physics of fluids are applied exclusively within this thesis.

1.4 Contribution of this Work

The methods presented in this thesis address the requirements specified in Section 1.2.1. The major scientific contributions are summarized in the following:

- **Validation and Extension of the CutFEM FSI** Since the interface-unfitted CutFEM FSI formulation serves as a fundamental workhorse for all developments within this thesis, a validation by various numerical tests including spatial convergence and challenging numerical examples is performed. In addition to the incorporation of the interface conditions by the Nitsche-based approach making use of a fluid-sided interface stress, the formulation is extended by a Nitsche-based formulation utilizing the solid-sided interface stress.

- **A Nitsche-based CutFEM FPI Approach** (see also Ager *et al.* [2]) Motivated by the specific requirements on a FPI formulation to model rough surface contact in FSI, the range of applicability of existing FPI formulations is extended by several aspects. These are the

[1] This paragraph is adapted from the author's publication [1]

application of a very general poroelastic formulation, the usage of an interface-unfitted fluid discretization by the CutFEM, and the incorporation of the interface conditions by a novel Nitsche-based method. The application of a Hybrid Eulerian-ALE fluid domain decomposition approach for FPI to increase the spatial computational resolution close the interface demonstrates the excellent extensibility of the formulation.

- **A Consistent Approach for Rough Surface FSCI** (see also Ager *et al.* [1]) To take into account the roughness of surfaces which are contacting in FSCI, without spatially resolving the microstructure, a homogenized model of the rough layer is proposed. This layer consist of a mixture of fluid and solid, and thus, can be described by the governing equations of poroelastic medium. From an abstract point of view, a fluid-poroelasticity-solid interaction (FPSI) problem including contact between a solid and poroelastic bodies has to be solved. A computational approach based on the CutFEM in conjunction with a dual mortar Lagrange multiplier contact formulation is developed.

- **A Nitsche-based Approach for General FSCI** (see also Ager *et al.* [3]) For FSCI configurations with a negligible effect of the surface roughness, a computational approach exclusively utilizing Nitsche-based approaches for the incorporation of all interface conditions is developed. A single set of conditions on the interface which already includes the transition between FSI and contact is formulated . An extension approach for the fluid state provides the FSI traction in the zone of closed contact, and thus, ensures a continuous transition between the different types of interface conditions. The general Navier interface condition with a variable amount of velocity slip is applied as FSI condition in tangential interface orientation. This allows taking physical slip due to the small absolute gap into account and to facilitate an equal interface stress for FSI and contact.

- **A Nitsche-based Approach for General FPSCI** (see also Ager *et al.* [4]) The computational approach developed for FSCI is extended to the more general configuration of FPSCI. This also includes the contact of multiple impermeable and permeable bodies. Again, all interface conditions, which are present for FSI, FPI, solid-solid contact, solid-poroelastic contact, and poroelastic-poroelastic contact are incorporated by a Nitsche-based approach. This also includes a smooth transition from the conditions on an FPI interface to the porous fluid mass balance on the interface zone of closed contact in the case a poroelastic bodies is involved. The fluid state in the contact zone determined by the extension approach is enriched far from the fluid domain by the physically more meaningful poroelastic fluid pressure. In addition to classical configurations of FPSCI, this computational approach can be applied to solve the rough surface FSCI model developed beforehand.

As indicated, essential parts of this thesis have been already published in peer-reviewed journals. All the computational approaches have been implemented in the parallel in-house software environment BACI [221] of the Institute for Computational Mechanics. As much as possible, algorithms and general functionalities were reused. In that respect, especially the developments of Dr.-Ing. Benedikt Schott for the CutFEM FSI and Dr.-Ing. Anh-Tu Vuong concerning the general poroelastic formulation are highlighted. Further, the code-related contributions of Dipl.-Ing.

Michael Hiermeier, Dr.-Ing. Ulrich Küttler, Dmytro Sashko, M.Sc.(hons), Prof. Dr.-Ing. Sudhakar Yogaraj, and Andy Wirtz, M.Sc. for the geometric intersection library, of Raffaela Kruse, M.Sc. for the CutFEM framework, of Prof. Dr.-Ing. Alexander Popp for the dual Mortar based contact formulations, of Christoph Schmidt, M.Sc. and Dr.-Ing. Alexander Seitz for the Nitsche-based contact formulations, and of Magnus Winter, M.Sc. for the Nitsche-based general Navier condition are gratefully acknowledged.

1.5 Outline

The physical models and the computational approaches developed in this work, as well as a large number of numerical validation and demonstration examples, are presented with increasing complexity herein. Thus, the remainder of the thesis is organized as follows.

In **Chapter 2**, the most relevant fundamentals of continuum mechanics and all models in terms of the governing equations and condition for the different physical fields structure, fluid, and poroelasticity are introduced. The conditions of the different types of interfaces are discussed in the following. The second part of this chapter is denoted to the numerical solution of these field equations, still neglecting their interaction, by temporal and spatial discretization with the One-Step-θ scheme and the FEM, respectively. The resulting discrete weak forms in all domains and potential stabilization techniques, whenever required, are depicted. Finally, the nonlinear solution procedure is presented.

The CutFEM and its application to FSI is introduced in **Chapter 3**. This includes an explanation of the representation of unfitted interfaces, the concept of the unfitted fluid discretization, the required ghost penalty stabilization, and the numerical integration of geometrically intersected elements. The extension to treat moving interfaces is given in the following. The subsequent sections are devoted to the weak imposition of interface conditions by Nitsche-based approaches. A brief introduction to Nitsche's method is followed by two variants to incorporate the FSI interface conditions. Additionally to the commonly utilized representation of the interface stress by the fluid state, a novel formulation based on the state of the solid domain is presented. The nonlinear solution procedure for the coupled CutFEM FSI formulation including temporally changing fluid solution spaces and, as a result, a varying number of degrees of freedom, is depicted subsequently. Numerical tests analyze the spatial convergence, the sensitivity of numerical parameters, and corresponding parameter scalings. The general applicability of both CutFEM FSI approaches is demonstrated by a more complex problem configuration.

In **Chapter 4**, the novel CutFEM FPI formulation is presented. A brief summary of the essential aspects for the CutFEM FPI already discussed in the preceding chapters including the embedding of the poroelastic domain into the fluid domain by the CutFEM is given at first. The novel Nitsche-based approach for the incorporation of all interface conditions, which is presented for the normal and the tangential interface orientation separately, is introduced subsequently. In the following, the resulting discrete coupled formulation for the numerical solution of the general FPI problem is depicted. By a wide variety of numerical tests, the properties of the presented approach, such as the spatial convergence, the sensitivity with respect to the Nitsche penalty parameters, and the applicability compared to the classical approach for the incorporation of the interface conditions, are analyzed. The additional numerical examples demonstrate the flexibil-

ity of the formulation by applying a Hybrid Eulerian-ALEfluid domain decomposition approach and the applicability for more complex 3D configurations.

The rough surface model for FSCI based on an poroelastic layer is introduced in **Chapter 5**. A detailed description of the proposed model is followed by the formulation of interface conditions on a solid-poroelastic contact interface and the continuous change of all involved interface conditions. A review of all previously introduced approaches used for the numerical solution of the rough surface FSCI problem and a depiction of the utilized dual mortar formulation for contact between solids and the poroelastic layer is given in the following. The proposed model is validated by a comparison of the computed results with experimental data from literature for a leakage flow configuration. Two additional numerical examples demonstrate the proper contacting and lift-off behavior predicted by the formulation, and analyze a more general configuration of a non-return valve.

In **Chapter 6**, a numerical formulation for general FSCI problems, where the surface roughness does not need to be considered directly, is presented. Therein, one set of conditions on the interface is formulated which includes already all transitions between the different types of conditions. These conditions include the general Navier condition on the fluid-structure interface, which allows formulating a continuous transition to frictionless contact. The numerical approach is based on the CutFEM in combination with a novel Nitsche-based formulation to weakly incorporate all interface conditions of the FSCI problem. A detailed discussion on the different interface contributions of the formulation is given. Various numerical examples analyze the prediction of the fundamental processes for simple configurations and demonstrate the general applicability for more challenging configurations.

The extension of this formulation for FSCI to FPSCI problems is presented in **Chapter 7**. Thus, a poroelastic domain and the corresponding interface conditions of solid-poroelastic contact, poroelastic-poroelastic contact, and viscous flow-poroelasticity interaction are introduced. A set of interface conditions which includes already the transition between the different types of interface conditions is formulated. The CutFEM is utilized for the discretization of the fluid equations and Nitsche-based formulations are used to weakly incorporate all interface conditions of the FPSCI problem. Three numerical examples analyze the prediction of basic FPSCI processes and demonstrate the applicability for more general problem setups.

Finally, in **Chapter 8**, the most important results and developments in this theses are summarized and an outlook to promising future fields of research is given.

2 Fundamentals for the Finite Element Solution of FSCI and FPSCI

In this chapter, the fundamentals for solving the problems of fluid-structure interaction with solid body contact (fluid-structure-contact interaction, FSCI) and fluid-poroelasticity-structure interaction with contact (fluid-poroelasticity-structure-contact interaction, FPSCI) numerically are discussed. In Section 2.1, the essential fundamentals to formulate the coupled continuous problem in the framework of continuum mechanics are given. Besides the basic notation, this includes a brief explanation of the governing equations of all involved physical fields and the conditions at the interjacent interfaces. Section 2.2 is dedicated to the numerical solution of the aforementioned problems. The numerical approaches to treat the interaction of the different fields are not discussed in this chapter. These formulations will be introduced successively in the following chapters when required. Still, these problems and the presented numerical approaches build the basis for solving all considered coupled problems of increasing complexity in the subsequent chapters. For the temporal discretization the One-Step-θ method and for the spatial discretization the boundary-fitted FEM is applied to make the continuous problem accessible to the numerical solution. Finally, the procedure to solve for the resulting nonlinear system of equations is presented.

2.1 The Continuous Problem: Continuum Mechanics

Within this section, the continuous problem, which is the mathematically expressed model for the physical systems of interest, is formulated. A generic overall problem configuration including the basic notation of all potential domains and interfaces is presented first. This is followed by a review of the different considered configurations to formulate the governing equations in continuum mechanics as well as their relations. After a brief recapitulation of the fundamental physical balances, which have to apply to all physical fields and interfaces, the governing equations of the structural field, the fluid field, and the poroelastic field are discussed. Finally, the underlying conditions on the fluid-structure interface, the fluid-poroelastic interface, the fluid-fluid interface, and the solid-solid contact interface with surrounding fluid are presented. Contact interfaces including poroelastic bodies are not discussed within this chapter, as this will be introduced in Chapter 5 and 7.

2.1.1 Generic Overall Problem Configuration and Basic Notation

The overall FPSCI problem, which includes also potential rough surface modeling from an abstract perspective, is composed of three fields following differing physics: a structural, a fluid, and a poroelastic domain. The spatial domain of interest of the overall problem is specified by

$\Omega \subset \mathbb{R}^d$ with its outer boundary $\partial\Omega$. The considered spatial problem dimension is $d = 2$ or $d = 3$.

This domain Ω is split into the structural domain Ω^{S}, the fluid domain Ω^{F} and the poroelastic domain Ω^{P}. The governing equations and conditions of these domain will be given in Sections 2.1.4, 2.1.5 and 2.1.6, which are all based on the same fundamental physical balances that are briefly discussed in Section 2.1.3. All boundaries (green) and interfaces (red) connected to these domains and the principal setup are visualized in Figure 2.1. Different conditions have to be fulfilled on the interfaces $\Gamma^{\mathrm{S,I}}$, $\Gamma^{\mathrm{F,I}}$, and $\Gamma^{\mathrm{P,I}}$ depending on the adjacent domains and specific modeling assumptions due to the underlying physics. The basic interfaces are the fluid-fluid interface Γ^{FF}, the fluid-structure interface Γ^{FS}, the fluid-poroelastic interface Γ^{FP}, the poroelastic-solid interface Γ^{PS}, the solid-solid contact interface $\Gamma^{\mathrm{SS},c}$, the poroelastic-solid contact interface $\Gamma^{\mathrm{PS},c}$, and the poroelastic-poroelastic contact interface $\Gamma^{\mathrm{PP},c}$.

In the case of multiple subdomains $\Omega^{*_1}, \Omega^{*_2}, ..., \Omega^{*_n}$, which are not overlappling ($\Omega^{*_i} \cap \Omega^{*_j} = \emptyset \, \forall \, i, j; \; 1 \leq i, j \leq n; \; i \neq j$), of a certain domain Ω^* are explicitly denoted by an index $1, 2, ..., n$ (n number of subdomains), the union of all subdomains $\Omega^* = \Omega^{*_1} \cup \Omega^{*_2} ... \cup \Omega^{*_n}$ is always indicated by an omitted index. This also applies to interfaces and boundaries (e.g. for the fluid-structure interface $\Gamma^{\mathrm{FS}} = \Gamma^{\mathrm{FS}_1} \cup \Gamma^{\mathrm{FS}_2} ... \cup \Gamma^{\mathrm{FS}_n}$).

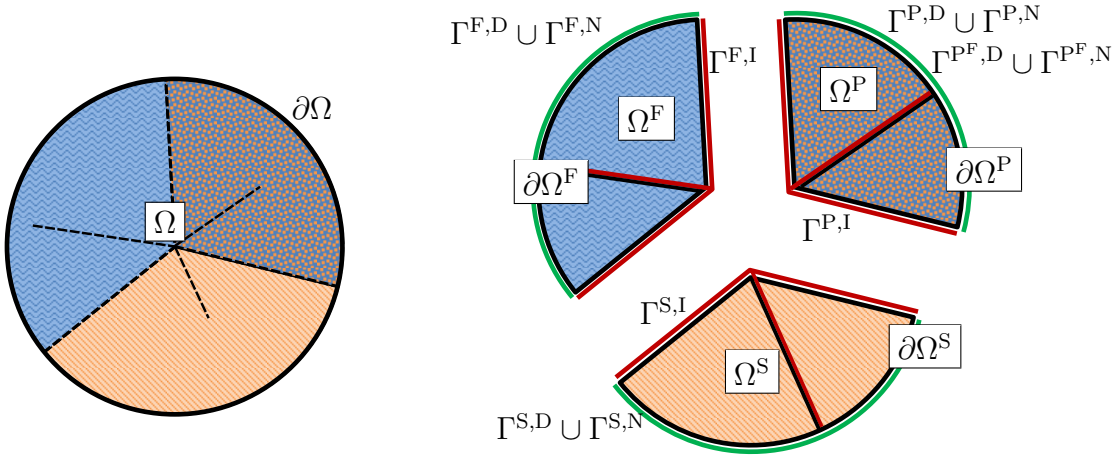

Figure 2.1: The overall problem is specified in the domain Ω with the outer boundary $\partial\Omega$. This problem is split into three domains $\Omega^{\mathrm{S}}, \Omega^{\mathrm{F}}$, and Ω^{P} with their respective outer boundaries $\partial\Omega^{\mathrm{S}}, \partial\Omega^{\mathrm{F}}$, and $\partial\Omega^{\mathrm{P}}$ (marked by the black lines). The occurring interfaces between these domain are denoted by $\Gamma^{\mathrm{S,I}}, \Gamma^{\mathrm{F,I}}$, and $\Gamma^{\mathrm{P,I}}$ (marked by the red lines). On the outer boundary of the overall problem $\partial\Omega$, Dirichlet-type boundary conditions on $\Gamma^{\mathrm{S,D}}, \Gamma^{\mathrm{F,D}}, \Gamma^{\mathrm{P,D}}, \Gamma^{\mathrm{P^F,D}}$ or Neumann-type boundary conditions on $\Gamma^{\mathrm{S,N}}, \Gamma^{\mathrm{F,N}}, \Gamma^{\mathrm{P,N}}, \Gamma^{\mathrm{P^F,N}}$ are applied (marked by the green lines).

The time t of interest is given by the interval $t \in]t_0, t_{\mathrm{E}}]$. At the initial point in time t_0, all states of the system states have to be specified. The last state of interest of the system corresponds to the end-time t_{E}. To shorten the notation in the following, this interval is denoted as $\mathcal{T} =]t_0, t_{\mathrm{E}}]$. It should be emphasized that all domains $\Omega^* = \Omega^*(t)$ and interfaces/boundaries $\Gamma^* = \Gamma^*(t)$ depend on time. To keep the notation clear, this is not explicitly denoted in the following presentation anymore.

Various equations and conditions that are formulated locally at a specific spatial position $\underline{\boldsymbol{x}}$ and time t have to be fulfilled in/on the entire domain/interface/boundary for the entire time interval

of interest. The recurring specification $\forall\,(\underline{\boldsymbol{x}},t) \in \bigcup_{t\in\mathcal{T}} \Omega^*(t) \times \{t\}$ and $\forall\,(\underline{\boldsymbol{x}},t) \in \bigcup_{t\in\mathcal{T}} \Gamma^*(t) \times \{t\}$ is mostly denoted in the short version "in $\bigcup_{t\in\mathcal{T}} \Omega^* \times \{t\}$" and "on $\bigcup_{t\in\mathcal{T}} \Gamma^* \times \{t\}$" or the very short version "in Ω^*" and "on Γ^*". To enable a clear presentation, all three variants should be considered as equivalent to the first most precise variant. For domains/interfaces/boundaries which do not change in time this is equivalent to the frequently used notations $\forall\,(\underline{\boldsymbol{x}},t) \in \Omega^* \times \mathcal{T}$ or $\forall\,(\underline{\boldsymbol{x}},t) \in \Gamma^* \times \mathcal{T}$ and the short versions "in $\Omega^* \times \mathcal{T}$" or "on $\Gamma^* \times \mathcal{T}$".

The expressions $(*,*)_{\Omega^*}$, $\langle *,*\rangle_{\partial\Omega^*}$ denote the $\mathcal{L}^2$-inner product integrated in the domain Ω^* and on the boundary or interface $\partial\Omega^*$, respectively.

$$(*,*)_{\Omega^*} = \int_{\Omega^*} (* \odot *)\ \mathrm{d}\Omega^*, \quad \langle *,*\rangle_{\partial\Omega^*} = \int_{\partial\Omega^*} (* \odot *)\ \mathrm{d}\partial\Omega^* \tag{2.1}$$

Herein, the operator $\odot$ denotes the scalar product, with its definition depending on the tensorial order of $*$.

The undeformed, reference/material configuration of a quantity is specified by the "zero"-index: $*_0$ or $\underline{*}_0$, whereas a missing index refers to the current/spatial configuration (see following Section 2.1.2 for details). Potentially time-dependent prescribed quantities at a boundary, an interface or in the domain are indicated by the "hat"-symbol: $\hat{*}$ or $\underline{\hat{*}}$. Quantities prescribed at t_0 are specified by the "ring"-symbol: $\mathring{*}$ or $\underline{\mathring{*}}$.

2.1.2 Material, Spatial and Reference Configuration

Independent of the underlying physics in each domain, different observers and configurations can be considered to formulate the governing equations based on the concept of continuum mechanics. The domain in material configuration Ω_0^* is given by all material points with position $\underline{\boldsymbol{X}}$ at the initial point in time $t = t_0$. The underlying physical process leads to a motion of these material points to the current position $\underline{\boldsymbol{x}}$ and results in the domain in current, spatial or actual configuration $\Omega^*\,(t)$ at every point in time t. This motion is given by the bijective, smooth, orientation-preserving mapping Φ from the material domain Ω_0^* to the time-dependent current domain $\Omega^*\,(t)$.

$$\Phi\,(\underline{\boldsymbol{X}},t) : \begin{cases} \Omega_0^* \to \Omega^*\,(t) \\ (\underline{\boldsymbol{X}},t) \mapsto \Phi\,(\underline{\boldsymbol{X}},t) = \underline{\boldsymbol{x}}\,(\underline{\boldsymbol{X}},t) \end{cases} \tag{2.2}$$

Governing equations have to be formulated with respect to a specific configuration. While a Lagrangian observer describes processes for a specific material point $\underline{\boldsymbol{X}}$ and therefore is linked to the material configuration, the Eulerian observer represents changes on a spatial point $\underline{\boldsymbol{x}}$ and therefore acts in the spatial configuration. Because of the different deformation characteristics, problems in structural mechanics are typically formulated in an Lagrangian framework whereas problems in fluid mechanics are often formulated in an Eulerian way. Besides these configurations, a generalization with an arbitrary reference configuration with associated reference domain Ω_{ref}^* is considered to account for challenges arising in the modeling of e.g. interface-coupled or volume coupled (poroelastic medium) fluid-structure interaction. The position in the coordiante system of the reference configuration is denoted by $\underline{\boldsymbol{\chi}}$. Hereby, in general, the motion of the Arbitrary-Lagrangian-Eulerian observer is independent of the physical motion of material

particles. The motion from the time-dependent reference domain $\Omega^*_{\mathrm{ref}}(t)$ to the time-dependent current domain $\Omega^*(t)$ is given by the bijective, smooth, orientation-preserving mapping Ξ.

$$\Xi\left(\underline{\boldsymbol{\chi}}, t\right) : \begin{cases} \Omega^*_{\mathrm{ref}}(t) \rightarrow \Omega^*(t) \\ \left(\underline{\boldsymbol{\chi}}, t\right) \mapsto \Xi\left(\underline{\boldsymbol{\chi}}, t\right) = \underline{\boldsymbol{x}}\left(\underline{\boldsymbol{\chi}}, t\right) \end{cases} \tag{2.3}$$

Finally, by combination of the mappings (2.2) and (2.3), the bijective, smooth, orientation-preserving mapping Ψ from the time-dependent reference domain $\Omega^*_{\mathrm{ref}}(t)$ to the material domain Ω^*_0 is given.

$$\Psi\left(\underline{\boldsymbol{\chi}}, t\right) = \Phi^{-1}\left(\underline{\boldsymbol{x}}, t\right) \circ \Xi\left(\underline{\boldsymbol{\chi}}, t\right) : \begin{cases} \Omega^*_{\mathrm{ref}}(t) \rightarrow \Omega^*_0 \\ \left(\underline{\boldsymbol{\chi}}, t\right) \mapsto \Psi\left(\underline{\boldsymbol{\chi}}, t\right) = \underline{\boldsymbol{X}}\left(\underline{\boldsymbol{\chi}}, t\right) \end{cases} \tag{2.4}$$

A visualization of all three configurations and the mappings between them is given in Figure 2.2. For computations by the FEM, the motion Ψ^{-1} of the reference configuration typically coin-

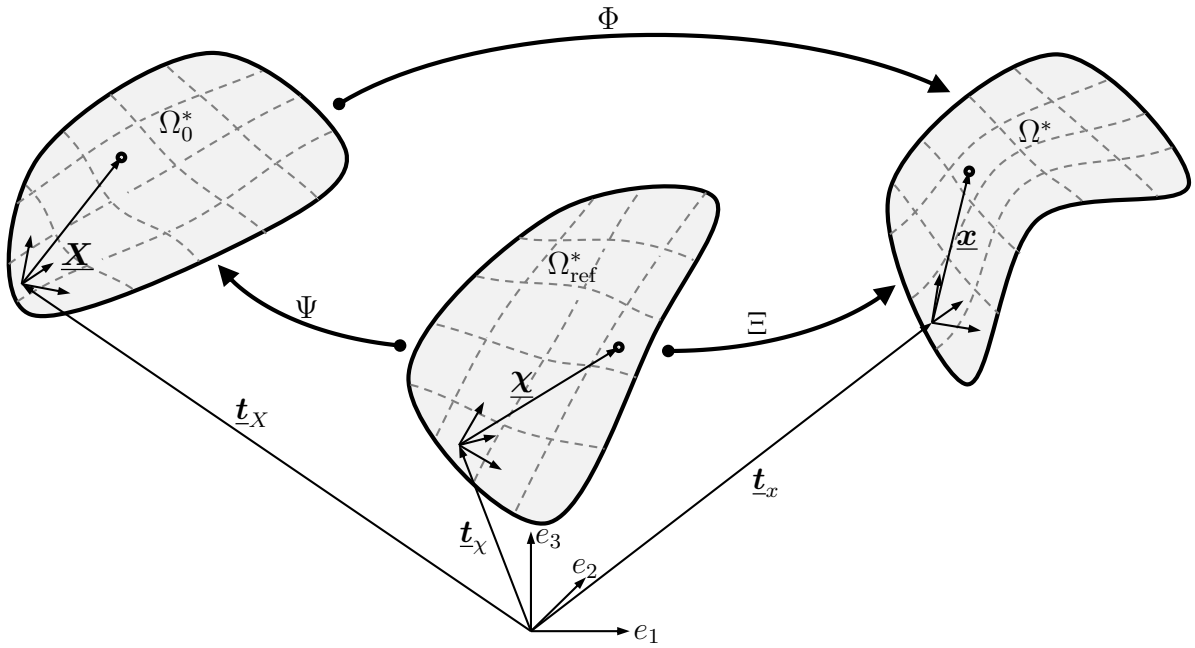

Figure 2.2: Visualization of the three configurations material domain Ω^*_0, spatial domain Ω^*, and reference domain Ω_{ref} and the bijective mappings Φ, Ξ, Φ between these configurations. Positions in the different configurations are described by the vectors $\underline{\boldsymbol{x}}, \underline{\boldsymbol{X}}, \underline{\boldsymbol{\chi}}$ and are in general based on different coordinate systems (the global position of the respective coordinate system is given by $\underline{\boldsymbol{t}}_x, \underline{\boldsymbol{t}}_X, \underline{\boldsymbol{t}}_\chi$) for every configuration.

cides with the motion of the computational mesh. To enable the use of classical time integration schemes, total time derivatives, which occur in the physical equations, have to be formulated as partial time derivative for a point that is constant in the reference configuration $\underline{\boldsymbol{\chi}}$ (equal to a

specific point on the computational mesh). The total time derivative of a quantity a is:

$$\frac{\mathrm{d}a\left(\underline{\boldsymbol{x}},t\right)}{\mathrm{d}t} = \left.\frac{\partial a\left(\underline{\boldsymbol{X}},t\right)}{\partial t}\right|_{\underline{\boldsymbol{X}}} = \left.\frac{\partial a\left(\underline{\boldsymbol{\chi}},t\right)}{\partial t}\right|_{\underline{\boldsymbol{\chi}}} + \underbrace{\left.\frac{\partial a\left(\underline{\boldsymbol{\chi}},t\right)}{\partial \underline{\boldsymbol{\chi}}}\right|_{t}}_{=\left.\frac{\partial a\left(\underline{\boldsymbol{x}},t\right)}{\partial \underline{\boldsymbol{x}}}\right|_{t}\left.\frac{\partial \underline{\boldsymbol{x}}\left(\underline{\boldsymbol{\chi}},t\right)}{\partial \underline{\boldsymbol{\chi}}}\right|_{t}} \cdot \left.\frac{\partial \underline{\boldsymbol{\chi}}\left(\underline{\boldsymbol{X}},t\right)}{\partial t}\right|_{\underline{\boldsymbol{X}}} . \tag{2.5}$$

The application of expression (2.5) onto the current coordinate $\underline{\boldsymbol{x}}$ of a particle, gives the total velocity of this material particle.

$$\frac{\mathrm{d}\underline{\boldsymbol{x}}\left(t\right)}{\mathrm{d}t} = \left.\frac{\partial \underline{\boldsymbol{x}}\left(\underline{\boldsymbol{X}},t\right)}{\partial t}\right|_{\underline{\boldsymbol{X}}} = \left.\frac{\partial \underline{\boldsymbol{x}}\left(\underline{\boldsymbol{\chi}},t\right)}{\partial t}\right|_{\underline{\boldsymbol{\chi}}} + \left.\frac{\partial \underline{\boldsymbol{x}}\left(\underline{\boldsymbol{\chi}},t\right)}{\partial \underline{\boldsymbol{\chi}}}\right|_{t}\left.\frac{\partial \underline{\boldsymbol{\chi}}\left(\underline{\boldsymbol{X}},t\right)}{\partial t}\right|_{\underline{\boldsymbol{X}}} \tag{2.6}$$

By inserting the last term in expression (2.6) into the total time derivative (2.5), an expression independent of derivatives of the reference coordinate $\underline{\boldsymbol{\chi}}$ can be constructed:

$$\frac{\mathrm{d}a\left(\underline{\boldsymbol{x}},t\right)}{\mathrm{d}t} = \left.\frac{\partial a\left(\underline{\boldsymbol{\chi}},t\right)}{\partial t}\right|_{\underline{\boldsymbol{\chi}}} + \left.\frac{\partial a\left(\underline{\boldsymbol{x}},t\right)}{\partial \underline{\boldsymbol{x}}}\right|_{t}\left(\frac{\mathrm{d}\underline{\boldsymbol{x}}\left(t\right)}{\mathrm{d}t} - \left.\frac{\partial \underline{\boldsymbol{x}}\left(\underline{\boldsymbol{\chi}},t\right)}{\partial t}\right|_{\underline{\boldsymbol{\chi}}}\right) . \tag{2.7}$$

Finally, equation (2.7) allows expressing all total time derivatives that occur in the fundamental physical balances as partial time derivatives for a constant reference coordinate $\underline{\boldsymbol{\chi}}$ with an additional convective or advective contribution. All partial time derivatives presented in the following are formulated for a constant reference coordinate and are therefore applicable to classical time integration procedures. In the case an Eulerian or Lagrangian observer is considered, this is not explicitly marked in the time derivative.

2.1.3 Fundamental Physical Balances

In the following, the governing equations for a structural, fluid and poroelastic system will be presented. For all the different mechanical fields, the fundamental physical balances that describe the behavior are, the balance of mass, linear momentum, angular momentum and energy. The balance of angular momentum is directly incorporated into the formulations by the symmetry of the Cauchy stress tensor. The balance of energy is automatically fulfilled for the isothermal case by the balance of linear momentum. The actual formulation to take into account the balance of mass and linear momentum depends on the choice of the reference configuration and the underlying physics. No derivation of the governing equations in local point-wise form, which build the basis for the weak form presented subsequently and the discretized equations of these fundamental physical balances, is shown in the following. These derivations and further details can be found e.g. in the textbooks of Bonet and Wood [30], Holzapfel [123] and Donea and Huerta [73].

2.1.4 Structure

In this section, the set of equations and conditions of the initial boundary value problem (IBVP) to describe the transient behavior of an elastic solid including nonlinearities, arising from geometric changes and the constitutive relation, are presented. The structural problem is formulated in a Lagrangian reference configuration and therefore the motion of the domain of interest Ω^{S} is given by the displacement of the material particles. Due to the choice to formulate the balance of linear momentum in the material domain Ω_0^{S}, the consideration of time-dependent deforming domains can be avoided for the computations.

The position of a point in the material configuration $\underline{\boldsymbol{X}}^{\mathrm{S}}$ and in the current configuration $\underline{\boldsymbol{x}}^{\mathrm{S}}$ is described in the same global Cartesian coordinate system. Thus, the displacement vector $\underline{\boldsymbol{u}}^{\mathrm{S}}$ of a material point can be computed as the difference between these positions $\underline{\boldsymbol{u}}^{\mathrm{S}} = \underline{\boldsymbol{x}}^{\mathrm{S}} - \underline{\boldsymbol{X}}^{\mathrm{S}}$. The material gradient of the current position is denoted as the deformation gradient

$$\underline{\boldsymbol{F}}^{\mathrm{S}} = \frac{\partial \underline{\boldsymbol{x}}^{\mathrm{S}}\left(\underline{\boldsymbol{X}}^{\mathrm{S}}, t\right)}{\partial \underline{\boldsymbol{X}}^{\mathrm{S}}} = \underline{\boldsymbol{I}} + \frac{\partial \underline{\boldsymbol{u}}^{\mathrm{S}}\left(\underline{\boldsymbol{X}}^{\mathrm{S}}, t\right)}{\partial \underline{\boldsymbol{X}}^{\mathrm{S}}}, \tag{2.8}$$

which equals the identity in the undeformed state. The deformation of an infinitesimal vector given in material configuration to its current configuration is given by the deformation gradient $\mathrm{d}\underline{\boldsymbol{x}}^{\mathrm{S}} = \underline{\boldsymbol{F}}^{\mathrm{S}}\,\mathrm{d}\underline{\boldsymbol{X}}^{\mathrm{S}}$. The change of an infinitesimal volume from material configuration to current configuration is given by the determinate of the deformation gradient: $\mathrm{d}\Omega^{\mathrm{S}} = J^{\mathrm{S}}\mathrm{d}\Omega_0^{\mathrm{S}}$, with $J^{\mathrm{S}} = \det\left(\underline{\boldsymbol{F}}^{\mathrm{S}}\right)$. The deformation gradient builds the basis for the definition of a strain measure. In the following, the Green-Lagrange strain tensor

$$\underline{\boldsymbol{E}}^{\mathrm{S}} = \frac{1}{2}\left(\underline{\boldsymbol{C}}^{\mathrm{S}} - \underline{\boldsymbol{I}}\right), \quad \text{with} \quad \underline{\boldsymbol{C}}^{\mathrm{S}} = \left(\underline{\boldsymbol{F}}^{\mathrm{S}}\right)^{\mathsf{T}} \cdot \underline{\boldsymbol{F}}^{\mathrm{S}}, \tag{2.9}$$

which is based on the right Cauchy-Green deformation tensor $\underline{\boldsymbol{C}}^{\mathrm{S}}$, is applied. As required for a strain measure, the Green-Lagrange strain tensor is a zero tensor for the undeformed state $\left(\underline{\boldsymbol{F}}^{\mathrm{S}} = \underline{\boldsymbol{I}} \rightarrow \underline{\boldsymbol{C}}^{\mathrm{S}} = \underline{\boldsymbol{I}}\right)$. The spatial traction acting on a specific deformed boundary $\underline{\boldsymbol{h}}^{\mathrm{S}}$, which equals the force per area, is represented by the Cauchy stress tensor $\underline{\boldsymbol{\sigma}}^{\mathrm{S}}$ and the outward-pointing unit normal vector on the boundary $\underline{\boldsymbol{n}}^{\mathrm{S}}$.

$$\underline{\boldsymbol{h}}^{\mathrm{S}} = \underline{\boldsymbol{\sigma}}^{\mathrm{S}} \cdot \underline{\boldsymbol{n}}^{\mathrm{S}} \tag{2.10}$$

As already mentioned in Section 2.1.3, the Cauchy stress tensor is a symmetric tensor and therefore directly fulfills the balance of angular momentum. An alternative stress representation is given by the first Piola-Kirchhoff stress tensor

$$\underline{\boldsymbol{P}}^{\mathrm{S}} = J^{\mathrm{S}}\underline{\boldsymbol{\sigma}}^{\mathrm{S}} \cdot \left(\underline{\boldsymbol{F}}^{\mathrm{S}}\right)^{-\mathsf{T}}, \tag{2.11}$$

which represents the spatial traction $\underline{\boldsymbol{h}}_0^{\mathrm{S}}$ acting on the undeformed boundary

$$\underline{\boldsymbol{h}}_0^{\mathrm{S}} = \underline{\boldsymbol{P}}^{\mathrm{S}} \cdot \underline{\boldsymbol{n}}_0^{\mathrm{S}}, \tag{2.12}$$

with $\underline{\boldsymbol{n}}_0^{\mathrm{S}}$ being the outward-pointing unit normal vector in material configuration. Finally, the second Piola-Kirchhoff stress tensor $\underline{\boldsymbol{S}}^{\mathrm{S}}$ allows representing the stress purely based on the material configuration

$$\underline{\boldsymbol{S}}^{\mathrm{S}} = \left(\underline{\boldsymbol{F}}^{\mathrm{S}}\right)^{-1} \cdot \underline{\boldsymbol{P}}^{\mathrm{S}} = J^{\mathrm{S}}\left(\underline{\boldsymbol{F}}^{\mathrm{S}}\right)^{-1} \cdot \underline{\boldsymbol{\sigma}}^{\mathrm{S}} \cdot \left(\underline{\boldsymbol{F}}^{\mathrm{S}}\right)^{-\mathsf{T}}. \tag{2.13}$$

Balance of Mass Due to the Lagrangian reference frame, the balance of mass reduces to the statement that the material solid density ρ_0^{S} does not change in time.

$$\rho_0^{\mathrm{S}} = J^{\mathrm{S}}\rho^{\mathrm{S}} = \text{const.} \quad \text{or} \quad \frac{\partial \rho_0^{\mathrm{S}}}{\partial t} = \frac{\partial\left(J^{\mathrm{S}}\rho^{\mathrm{S}}\right)}{\partial t} = 0 \quad \text{in } \Omega_0^{\mathrm{S}} \times \mathcal{T} \tag{2.14}$$

Herein, the current solid density is denoted by ρ^{S}. By considering ρ_0^{S} as a constant in the final computational model, the balance of mass is automatically fulfilled and therefore no explicit treatment of (2.14) is required.

Balance of Linear Momentum The PDE to be solved in the structural domain is the local point-wise form of the balance of linear momentum, which can be written as:

$$\rho_0^{\mathrm{S}} \frac{\partial^2 \underline{\boldsymbol{u}}^{\mathrm{S}}}{\partial t^2} - \boldsymbol{\nabla}_0 \cdot \underline{\boldsymbol{P}}^{\mathrm{S}} - \rho_0^{\mathrm{S}} \hat{\underline{\boldsymbol{b}}}_0^{\mathrm{S}} = \underline{\mathbf{0}} \quad \text{in } \Omega_0^{\mathrm{S}} \times \mathcal{T}. \tag{2.15}$$

Herein, the inertia contribution by the first term, the elastic contributions from the second term and a potential volume body force (e.g. gravity or magnetic forces) in the last term have to be in balance. The body force per unit mass is denoted by $\hat{\underline{\boldsymbol{b}}}_0^{\mathrm{S}}$. The material divergence operator is denoted by $\boldsymbol{\nabla}_0 \cdot \underline{*} = \sum_{i=1}^{d} \frac{\partial *_i}{\partial X_i}$.

For the closure of equation (2.15), a constitutive law, which gives a stress-strain relation, has to be formulated. This nonlinear constitutive law is formulated by a strain energy density function ψ^{S}, which depends solely on the deformation state for a hyperelastic material.

$$\underline{\boldsymbol{S}}^{\mathrm{S}} = \frac{\partial \psi^{\mathrm{S}}\left(\underline{\boldsymbol{E}}^{\mathrm{S}}\right)}{\partial \underline{\boldsymbol{E}}^{\mathrm{S}}} = 2\frac{\partial \psi^{\mathrm{S}}\left(\underline{\boldsymbol{C}}^{\mathrm{S}}\right)}{\partial \underline{\boldsymbol{C}}^{\mathrm{S}}} \tag{2.16}$$

Since it will be applied for most of the presented numerical examples, the strain energy density function for a Neo-Hookean material model $\psi_{NH}^{\mathrm{S}} = \psi_{NH}(\underline{\boldsymbol{C}}^{\mathrm{S}}, J^{\mathrm{S}})$ is given exemplary.

$$\psi_{NH}(\underline{\boldsymbol{C}}, J) = c\left[\mathrm{tr}\left(\underline{\boldsymbol{C}}\right) - 3\right] + \frac{c}{\beta}\left(J^{-2\beta} - 1\right), \quad c = \frac{E}{4(1+\nu)}, \quad \beta = \frac{\nu}{1-2\nu} \tag{2.17}$$

The constants c and β can be expressed by the Young's modulus E and the Poisson ration ν, which are normally used in linear theory.

Further, adequate initial conditions with a prescribed displacement field $\mathring{\underline{\boldsymbol{u}}}^{\mathrm{S}}$ and velocity field $\mathring{\underline{\boldsymbol{v}}}^{\mathrm{S}}$ are defined:

$$\underline{\boldsymbol{u}}^{\mathrm{S}} = \mathring{\underline{\boldsymbol{u}}}^{\mathrm{S}} \quad \text{in } \Omega_0^{\mathrm{S}} \times \{t_0\}, \qquad \frac{\partial \underline{\boldsymbol{u}}^{\mathrm{S}}}{\partial t} = \mathring{\underline{\boldsymbol{v}}}^{\mathrm{S}} \quad \text{in } \Omega_0^{\mathrm{S}} \times \{t_0\}. \tag{2.18}$$

Finally, suitable boundary conditions on the outer boundary $\partial\Omega_0 \cap \partial\Omega_0^{\mathrm{S}}$ must be specified to complete the description of the IBVP for nonlinear elastodynamics. These are the predefined displacement $\hat{\underline{\boldsymbol{u}}}^{\mathrm{S}}$ on the Dirichlet boundary $\Gamma_0^{\mathrm{S,D}}$ and the given traction $\hat{\underline{\boldsymbol{h}}}_0^{\mathrm{S,N}}$ on the Neumann boundary $\Gamma_0^{\mathrm{S,N}}$.

$$\underline{\boldsymbol{u}}^{\mathrm{S}} = \hat{\underline{\boldsymbol{u}}}^{\mathrm{S}} \quad \text{on } \Gamma_0^{\mathrm{S,D}}, \qquad \underline{\boldsymbol{P}}^{\mathrm{S}} \cdot \underline{\boldsymbol{n}}_0^{\mathrm{S}} = \hat{\underline{\boldsymbol{h}}}_0^{\mathrm{S,N}} \quad \text{on } \Gamma_0^{\mathrm{S,N}} \tag{2.19}$$

The conditions on the structural interface

$$\Gamma_0^{\mathrm{S,I}} = \partial\Omega_0^{\mathrm{S}} \setminus \left(\Gamma_0^{\mathrm{S,D}} \cup \Gamma_0^{\mathrm{S,N}}\right), \tag{2.20}$$

which is the subset of the structural boundary where the structural domain is coupled to the other fields, are not treated so far. This interface is not part of the outer boundary of the overall problem $\partial\Omega_0 \cap \Gamma_0^{\mathrm{S,I}} = \emptyset$. The different types of interface conditions will be discussed in Sections 2.1.7, 2.1.10, and the subsequent chapters.

Continuous Weak Form The weak form builds the basis for the application of the FEM to the structural problem. Therefore, equation (2.15) is multiplied with an arbitrary test function $\delta\underline{\boldsymbol{u}}^{\mathrm{S}}$ and integrated in the material domain Ω_0^{S}. A subsequent partial integration of the resulting integral arising from the second term in equation (2.15) leads to the weak form.
Find $\underline{\boldsymbol{u}}^{\mathrm{S}} \in \mathcal{S}_{\underline{\boldsymbol{u}}^{\mathrm{S}}}$ *such that for all* $\delta\underline{\boldsymbol{u}}^{\mathrm{S}} \in \mathcal{T}_{\delta\underline{\boldsymbol{u}}^{\mathrm{S}}}$:

$$\mathcal{W}^{\mathrm{S}}\left[\delta\underline{\boldsymbol{u}}^{\mathrm{S}}, \underline{\boldsymbol{u}}^{\mathrm{S}}\right] = 0, \tag{2.21}$$

with the form $\mathcal{W}^{\mathrm{S}}$ resulting from the derivation

$$\begin{aligned}\mathcal{W}^{\mathrm{S}}\left[\delta\underline{\boldsymbol{u}}^{\mathrm{S}}, \underline{\boldsymbol{u}}^{\mathrm{S}}\right] = \left(\delta\underline{\boldsymbol{u}}^{\mathrm{S}}, \rho_0^{\mathrm{S}}\frac{\partial^2\underline{\boldsymbol{u}}^{\mathrm{S}}}{\partial t^2}\right)_{\Omega_0^{\mathrm{S}}} + \left(\boldsymbol{\nabla}_0\delta\underline{\boldsymbol{u}}^{\mathrm{S}}, \boldsymbol{P}^{\mathrm{S}}\right)_{\Omega_0^{\mathrm{S}}} - \left(\delta\underline{\boldsymbol{u}}^{\mathrm{S}}, \rho_0^{\mathrm{S}}\hat{\underline{\boldsymbol{b}}}_0^{\mathrm{S}}\right)_{\Omega_0^{\mathrm{S}}} \\ - \left\langle\delta\underline{\boldsymbol{u}}^{\mathrm{S}}, \hat{\underline{\boldsymbol{h}}}_0^{\mathrm{S,N}}\right\rangle_{\Gamma_0^{\mathrm{S,N}}} - \left\langle\delta\underline{\boldsymbol{u}}^{\mathrm{S}}, \underline{\boldsymbol{h}}_0^{\mathrm{S,I}}\right\rangle_{\Gamma_0^{\mathrm{S,I}}}.\end{aligned} \tag{2.22}$$

Herein, also the boundary integral arising from partial integration on the boundary $\Gamma_0^{\mathrm{S,I}}$ is considered. If such a boundary (interface) exists, proper incorporation of the traction $\underline{\boldsymbol{h}}_0^{\mathrm{S,I}}$ has to be performed to result in a solvable system. This aspect will be discussed in the subsequent chapters for all considered types of interfaces. For the pure structural problem, this boundary does not exist ($\Gamma_0^{\mathrm{S,I}} = \emptyset$).

The solution space $\mathcal{S}_{\underline{\boldsymbol{u}}^{\mathrm{S}}}$ and the test function space $\mathcal{T}_{\delta\underline{\boldsymbol{u}}^{\mathrm{S}}}$ are sufficiently smooth for the problem formulation (2.21) to make sense. Additionally, Dirichlet-type boundary conditions are directly incorporated into the solution and test function spaces:

$$\underline{\boldsymbol{u}}^{\mathrm{S}} = \hat{\underline{\boldsymbol{u}}}^{\mathrm{S}} \quad \text{on } \Gamma_0^{\mathrm{S,D}} \;\forall\; \underline{\boldsymbol{u}}^{\mathrm{S}} \in \mathcal{S}_{\underline{\boldsymbol{u}}^{\mathrm{S}}}, \qquad \delta\underline{\boldsymbol{u}}^{\mathrm{S}} = \underline{\boldsymbol{0}} \quad \text{on } \Gamma_0^{\mathrm{S,D}} \;\forall\; \delta\underline{\boldsymbol{u}}^{\mathrm{S}} \in \mathcal{T}_{\delta\underline{\boldsymbol{u}}^{\mathrm{S}}}. \tag{2.23}$$

2.1.5 Fluid

In the following section, the problem formulation for a transient, incompressible, viscous flow is discussed. The governing equations of this flow are given by the well known Navier–Stokes equations. The fluid problem is typically formulated in a fixed Eulerian reference configuration. Following the fluid particle motion by the reference configuration (Lagrangian reference) for flow problems typically leads to large distortion of the computational meshes and is therefore not applied to flow problems in general. The current domain of interest for the fluid problem is given by Ω^{F}.

For moving boundary problems such as fluid-structure interaction or free surface flow, an arbitrary Lagrangian-Eulerian (ALE) formulation, where the domain change is treated by a moving

reference configuration, can be applied. In this case, the motion of the reference configuration is given by the motion of the boundaries and a suitable motion inside of the domain. One possibility is to solve a pseudo-elasticity problem (as presented in the previous section) for given displacements at the boundary. The displacement of the reference configuration is denoted by $\underline{\boldsymbol{u}}^{\mathrm{G}}$, and thus, the velocity of points in the reference domain is given as

$$\frac{\partial \underline{\boldsymbol{u}}^{\mathrm{G}}}{\partial t} = \left.\frac{\partial \underline{\boldsymbol{x}}\left(\underline{\boldsymbol{\chi}}, t\right)}{\partial t}\right|_{\underline{\boldsymbol{\chi}}}. \tag{2.24}$$

The mechanical state of the considered fluid is given by the fluid velocity $\underline{\boldsymbol{v}}^{\mathrm{F}}$ and the fluid pressure p^{F}. The constant fluid density is denoted by ρ^{F} and the dynamic viscosity by μ^{F}. To measure the rate of deformation, the symmetric strain-rate tensor is considered

$$\underline{\boldsymbol{\epsilon}}^{\mathrm{F}}(\underline{\boldsymbol{v}}^{\mathrm{F}}) = \frac{1}{2}\left[\boldsymbol{\nabla}\underline{\boldsymbol{v}}^{\mathrm{F}} + \left(\boldsymbol{\nabla}\underline{\boldsymbol{v}}^{\mathrm{F}}\right)^{\mathsf{T}}\right]. \tag{2.25}$$

Using the strain rate-tensor $\underline{\boldsymbol{\epsilon}}^{\mathrm{F}}$ to formulate the viscous stress contribution, the Cauchy stress tensor $\underline{\boldsymbol{\sigma}}^{\mathrm{F}}$ for the viscous fluid is given by

$$\underline{\boldsymbol{\sigma}}^{\mathrm{F}} = -p^{\mathrm{F}}\underline{\boldsymbol{I}} + 2\mu^{\mathrm{F}}\underline{\boldsymbol{\epsilon}}^{\mathrm{F}}(\underline{\boldsymbol{v}}^{\mathrm{F}}). \tag{2.26}$$

Balance of Mass Due to the incompressibility of the considered fluid the balance of mass reduces to:

$$\boldsymbol{\nabla}\cdot\underline{\boldsymbol{v}}^{\mathrm{F}} = 0 \quad \text{in} \bigcup_{t\in\mathcal{T}} \Omega^{\mathrm{F}} \times \{t\}. \tag{2.27}$$

Balance of Linear Momentum For the balance of linear momentum, which is formulated in the current domain Ω^{F}, the general ALE formulation considering a moving reference configuration is presented:

$$\begin{aligned}\rho^{\mathrm{F}}\left.\frac{\partial \underline{\boldsymbol{v}}^{\mathrm{F}}}{\partial t}\right|_{\underline{\boldsymbol{\chi}}} \circ \Xi^{-1} + \rho^{\mathrm{F}}\left(\underline{\boldsymbol{v}}^{\mathrm{F}} - \frac{\partial \underline{\boldsymbol{u}}^{\mathrm{G}}}{\partial t}\right)\cdot\boldsymbol{\nabla}\underline{\boldsymbol{v}}^{\mathrm{F}} \\ +\boldsymbol{\nabla}p^{\mathrm{F}} - \boldsymbol{\nabla}\cdot(2\mu^{\mathrm{F}}\underline{\boldsymbol{\epsilon}}^{\mathrm{F}}(\underline{\boldsymbol{v}}^{\mathrm{F}})) - \rho^{\mathrm{F}}\hat{\underline{\boldsymbol{b}}}^{\mathrm{F}} = \underline{\mathbf{0}} \quad \text{in} \bigcup_{t\in\mathcal{T}} \Omega^{\mathrm{F}} \times \{t\}.\end{aligned} \tag{2.28}$$

Herein, the inertia contribution considered by the first term, the contribution due to convection in the second term, the contribution due to the pressure and the viscous stress in the following terms and a potential volumetric body force accounted for in the last term have to be in balance. The body force per unit mass is denoted by $\hat{\underline{\boldsymbol{b}}}^{\mathrm{F}}$.

Remark 2.1 (Eulerian observer)**.** *In the case an Eulerian observer is considered, the reference configuration and the current configuration are equal* ($\underline{\boldsymbol{\chi}} = \underline{\boldsymbol{x}}$)*, which results in a vanishing velocity* $\dfrac{\partial \underline{\boldsymbol{u}}^{\mathrm{G}}}{\partial t} = \underline{\mathbf{0}}$ *and a vanishing effect of the mapping* Ξ*. Therefore the balance of momentum* (2.28) *reduces to the classical Eulerian form.*

$$\rho^{\mathrm{F}}\frac{\partial \underline{\boldsymbol{v}}^{\mathrm{F}}}{\partial t} + \rho^{\mathrm{F}}\underline{\boldsymbol{v}}^{\mathrm{F}}\cdot\boldsymbol{\nabla}\underline{\boldsymbol{v}}^{\mathrm{F}} + \boldsymbol{\nabla}p^{\mathrm{F}} - \boldsymbol{\nabla}\cdot(2\mu^{\mathrm{F}}\underline{\boldsymbol{\epsilon}}^{\mathrm{F}}(\underline{\boldsymbol{v}}^{\mathrm{F}})) - \rho^{\mathrm{F}}\hat{\underline{\boldsymbol{b}}}^{\mathrm{F}} = \underline{\mathbf{0}} \quad \textit{in} \bigcup_{t\in\mathcal{T}} \Omega^{\mathrm{F}} \times \{t\}. \tag{2.29}$$

As an adequate initial condition of the transient fluid problem, the initial velocity field $\mathring{\underline{\boldsymbol{v}}}^{\mathrm{F}}$, which fulfills the balance of mass (2.27), is prescribed.

$$\underline{\boldsymbol{v}}^{\mathrm{F}} = \mathring{\underline{\boldsymbol{v}}}^{\mathrm{F}} \quad \text{with } \boldsymbol{\nabla}\cdot\mathring{\underline{\boldsymbol{v}}}^{\mathrm{F}} = 0 \quad \text{in } \Omega^{\mathrm{F}} \times \{t_0\} \tag{2.30}$$

Boundary conditions on the subset of the outer boundary $\Gamma^{\mathrm{F,D}} \cup \Gamma^{\mathrm{F,N}} = \partial\Omega \cap \partial\Omega^{\mathrm{F}}$ have to be specified to finalize the description of the fluid problem. Hereby, the fluid velocity $\hat{\underline{\boldsymbol{v}}}^{\mathrm{F}}$ on Dirichlet boundaries $\Gamma^{\mathrm{F,D}}$ and the fluid traction $\hat{\underline{\boldsymbol{h}}}^{\mathrm{F,N}}$ on Neumann boundaries $\Gamma^{\mathrm{F,N}}$ are prescribed.

$$\underline{\boldsymbol{v}}^{\mathrm{F}} = \hat{\underline{\boldsymbol{v}}}^{\mathrm{F}} \quad \text{on } \Gamma^{\mathrm{F,D}}, \qquad \underline{\boldsymbol{\sigma}}^{\mathrm{F}} \cdot \underline{\boldsymbol{n}}^{\mathrm{F}} = \hat{\underline{\boldsymbol{h}}}^{\mathrm{F,N}} \quad \text{on } \Gamma^{\mathrm{F,N}}, \tag{2.31}$$

with $\underline{\boldsymbol{n}}^{\mathrm{F}}$ being the outward-pointing unit normal vector of the fluid domain. The conditions on the fluid interface

$$\Gamma^{\mathrm{F,I}} = \partial\Omega^{\mathrm{F}} \setminus \left(\Gamma^{\mathrm{F,D}} \cup \Gamma^{\mathrm{F,N}}\right), \tag{2.32}$$

which is not part of the outer boundary of the overall problem $\partial\Omega \cap \Gamma^{\mathrm{F,I}} = \emptyset$, were still not specified and will be discussed in Sections 2.1.7, 2.1.8, 2.1.9, and the subsequent chapters.

Continuous Weak Form In the following, the continuous weak form of the fluid problem, which is equivalent to the problem formulated previously, is presented. This formulation builds the basis for the application of spatial discretization by the FEM. It should be stated that the derivation of the discrete fluid problem formulation is based on the time-discrete problem weak form. Still, since this procedure is equal to the derivation from the continuous problem, the continuous weak form is already presented here.

Similar to the structural problem, the point-wise balance equations (2.27) and (2.28) are multiplied by suitable test functions $\delta\underline{\boldsymbol{v}}^{\mathrm{F}}$ and δp^{F} and integrated in the current domain Ω^{F}. Additionally, a partial integration of the pressure and viscous stress terms in the resulting balance of linear momentum is performed. This reduces the occurring order of spatial derivatives to one and leads to additional boundary integrals in the weak form of the fluid problem.
$Find\ \left(\underline{\boldsymbol{v}}^{\mathrm{F}}, p^{\mathrm{F}}\right) \in \mathcal{S}_{\underline{\boldsymbol{v}}^{\mathrm{F}}} \times \mathcal{S}_{p^{\mathrm{F}}}\ such\ that\ for\ all\ \left(\delta\underline{\boldsymbol{v}}^{\mathrm{F}}, \delta p^{\mathrm{F}}\right) \in \mathcal{T}_{\delta\underline{\boldsymbol{v}}^{\mathrm{F}}} \times \mathcal{T}_{\delta p^{\mathrm{F}}}$:

$$\mathcal{W}^{\mathrm{F}}\left[\left(\delta\underline{\boldsymbol{v}}^{\mathrm{F}}, \delta p^{\mathrm{F}}\right), \left(\underline{\boldsymbol{v}}^{\mathrm{F}}, p^{\mathrm{F}}\right)\right] = 0, \tag{2.33}$$

with the form $\mathcal{W}^{\mathrm{F}}$ resulting from the derivation

$$\begin{aligned}
\mathcal{W}^{\mathrm{F}}\left[\left(\delta\underline{\boldsymbol{v}}^{\mathrm{F}}, \delta p^{\mathrm{F}}\right), \left(\underline{\boldsymbol{v}}^{\mathrm{F}}, p^{\mathrm{F}}\right)\right] = {} & \left(\delta\underline{\boldsymbol{v}}^{\mathrm{F}}, \rho^{\mathrm{F}} \left.\frac{\partial \underline{\boldsymbol{v}}^{\mathrm{F}}}{\partial t}\right|_{\underline{\boldsymbol{\chi}}} \circ \Xi^{-1}\right)_{\Omega^{\mathrm{F}}} \\
+ \left(\delta\underline{\boldsymbol{v}}^{\mathrm{F}}, \rho^{\mathrm{F}} \left(\underline{\boldsymbol{v}}^{\mathrm{F}} - \frac{\partial \underline{\boldsymbol{u}}^{\mathrm{G}}}{\partial t}\right) \cdot \boldsymbol{\nabla}\underline{\boldsymbol{v}}^{\mathrm{F}}\right)_{\Omega^{\mathrm{F}}} & - \left(\boldsymbol{\nabla}\cdot\delta\underline{\boldsymbol{v}}^{\mathrm{F}}, p^{\mathrm{F}}\right)_{\Omega^{\mathrm{F}}} + \left(\underline{\boldsymbol{\epsilon}}^{\mathrm{F}}(\delta\underline{\boldsymbol{v}}^{\mathrm{F}}), 2\mu^{\mathrm{F}}\underline{\boldsymbol{\epsilon}}^{\mathrm{F}}(\underline{\boldsymbol{v}}^{\mathrm{F}})\right)_{\Omega^{\mathrm{F}}} \\
& - \left(\delta\underline{\boldsymbol{v}}^{\mathrm{F}}, \rho^{\mathrm{F}}\hat{\underline{\boldsymbol{b}}}^{\mathrm{F}}\right)_{\Omega^{\mathrm{F}}} - \left\langle \delta\underline{\boldsymbol{v}}^{\mathrm{F}}, \hat{\underline{\boldsymbol{h}}}^{\mathrm{F,N}}\right\rangle_{\Gamma^{\mathrm{F,N}}} - \left\langle \delta\underline{\boldsymbol{v}}^{\mathrm{F}}, \underline{\boldsymbol{h}}^{\mathrm{F,I}}\right\rangle_{\Gamma^{\mathrm{F,I}}} + \left(\delta p^{\mathrm{F}}, \boldsymbol{\nabla}\cdot\underline{\boldsymbol{v}}^{\mathrm{F}}\right)_{\Omega^{\mathrm{F}}}.
\end{aligned} \tag{2.34}$$

Herein, the boundary integral on $\Gamma^{\mathrm{F,I}}$ arises from partial integration and occurs only in case of an interface-coupled problem. The interface stress $\underline{\boldsymbol{h}}^{\mathrm{F,I}}$ therein serves as a placeholder and will be specified in the subsequent chapters for the different possible interface types.

The solution spaces $\mathcal{S}_{\underline{\boldsymbol{v}}^{\mathrm{F}}}, \mathcal{S}_{p^{\mathrm{F}}}$ and the test function spaces $\mathcal{T}_{\delta\underline{\boldsymbol{v}}^{\mathrm{F}}}, \mathcal{T}_{\delta p^{\mathrm{F}}}$ are sufficiently smooth for the problem formulation (2.33) to make sense. Additionally, Dirichlet-type boundary conditions are directly incorporated into the solution and test function spaces:

$$\underline{\boldsymbol{v}}^{\mathrm{F}} = \underline{\hat{\boldsymbol{v}}}^{\mathrm{F}} \quad \text{on } \Gamma^{\mathrm{F,D}} \; \forall \; \underline{\boldsymbol{v}}^{\mathrm{F}} \in \mathcal{S}_{\underline{\boldsymbol{v}}^{\mathrm{F}}}, \qquad \delta\underline{\boldsymbol{v}}^{\mathrm{F}} = \underline{\mathbf{0}} \quad \text{on } \Gamma^{\mathrm{F,D}} \; \forall \; \delta\underline{\boldsymbol{v}}^{\mathrm{F}} \in \mathcal{T}_{\delta\underline{\boldsymbol{v}}^{\mathrm{F}}}. \tag{2.35}$$

2.1.6 Poroelasticity

As illustrated in Figure 2.3 (left), a poroelastic medium consists of an impermeable structural phase and a fluid phase. The structural phase is often also referred to as skeleton phase. Due to the complex geometrical configuration of both phases and the resulting fluid-structure interface, obtaining a direct solution of such a problem is challenging and computational expensive in general. Another problematic aspect for the direct solution of such problems is the uncertain location of the fluid-structure interface for many applications of practical interest.

However, computing the direct solution of the interface-coupled problem is not necessary in many cases as the knowledge of an averaged solution is often sufficient. This is where poroelastic formulations come into play. In the following, the geometric scale that resolves the fluid-structure interface of the microstructure is denoted as the microscopic scale, whereas the scale of the overall problem is denoted as the macroscopic scale. A continuum mechanics poroelastic

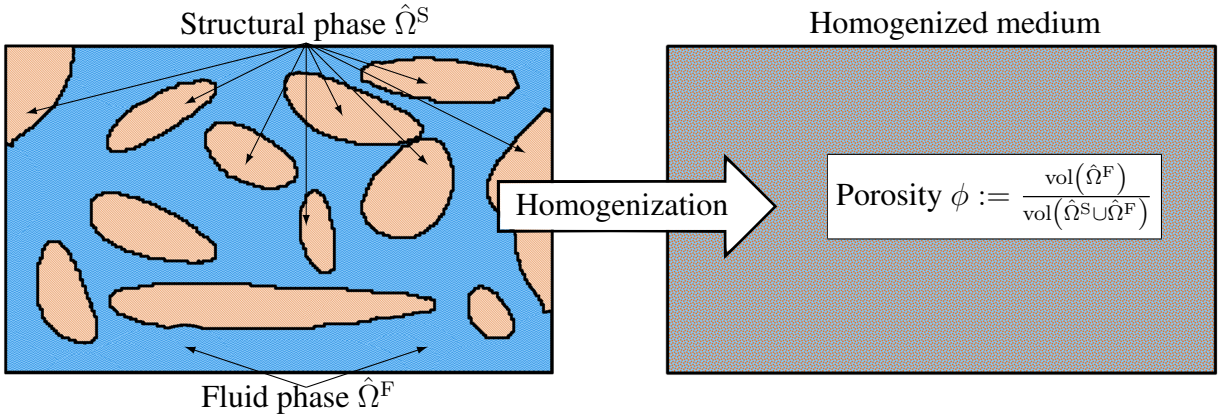

Figure 2.3: Basic steps in the derivation of a continuum mechanics formulation for poroelasticity: A homogenization or averaging procedure is applied to the direct problem consisting of a resolve structural phase and a resolved fluid phase (left). This results in a formulation of the homogenized medium in the domain occupied by the structural and fluid phase (right).

formulation represents the average behavior of such a system on the macroscopic scale, which is larger than the microscopic scale. The basic concept for deriving poroelastic formulations is shown in Figure 2.3. Starting from the resolved interface-coupled FSI problem, including a separated structural phase $\hat{\Omega}^{\mathrm{S}}$ and fluid phase $\hat{\Omega}^{\mathrm{F}}$, an averaging procedure is applied. This results in a volume coupled problem on the overall domain ($\Omega^{\mathrm{P}} = \hat{\Omega}^{\mathrm{S}} \cup \hat{\Omega}^{\mathrm{F}}$) occupied by both phases, wherein the interface between the two phases is not spatially resolved anymore. As the main emphasis of this thesis is not in the derivation of continuum mechanics formulations for porous medium, the reader is referred to e.g. Whitaker [222, 223, 224] for volume averaging, and to e.g. Gray and Schrefler [99], Gray and Miller [100, 101], and Gray *et al.* [102] for the thermodynamically constrained averaging theory, for details on these different procedures.

The respective volume ratio of structure and fluid at every point in the resulting homogenized medium is described by the porosity ϕ. The fluid flow equation is an extension of Darcy's law, which implies a proportionality of the fluid pressure gradient and the porous fluid velocity. The proportionality constant therein includes the permeability tensor $\underline{\boldsymbol{k}}$, which characterizes the average macroscopic flow resistance due to the viscous flow through the porous microstructure. Additional effects resulting in macroscopic flow resistance occur due to fluid acceleration on the microscopic scale and are typically captured by the tortuosity (see e.g. the works Boudreau [33], Coussy [67], and references therein).

The underlying incentive for presenting this poroelastic formulation, is the application of a homogenized poroelastic medium for modeling the fluid-saturated rough microstructure of contacting surfaces in Chapter 5. The formulation for two phase fluid-saturated poroelastic medium which is presented in the following is chosen to fulfill the requirements of the rough surface contact model briefly introduces in Section 1.1. Nevertheless, no specific aspects concerning the application of the poroelastic formulation to rough surface modeling will be discussed in this section. The formulation is capable of representing all essential physical effects, such as incompressible flow on the micro scale, finite deformations of the poroelastic matrix, deformation-dependent and variable porosity, as well as arbitrary strain energy functions for the skeleton. The addressed formulation was developed and successfully applied by Chapelle and Moireau [57], Vuong [215], and Vuong *et al.* [216, 217, 218]. Further details and a general introduction to porous medium can be found, e.g., in the textbooks of Coussy [67] and Lewis and Schrefler [142]. In the following the basics for poroelastic medium, the governing equations, the appropriate initial and boundary conditions as well as the continuous weak form will be presented.

To formulate the fundamental physical balances of Section 2.1.3 for the poroelastic problem on macroscopic scale, in a first step all relevant quantities are introduced. They describe the averaged state from a macroscopic or microscopic view and, therefore, no fluctuations due to the microstructure are present. In this context, macroscopic view corresponds to averaging over the domain $\mathrm{d}\Omega^{\mathrm{P}}$, whereas microscopic view refers to an averaging over the portion of the domain of the corresponding phase (fluid phase $\phi\,\mathrm{d}\Omega^{\mathrm{P}}$ or solid phase $(1-\phi)\,\mathrm{d}\Omega^{\mathrm{P}}$). Still, a macroscopic fluid phase, structural phase and the mixture which includes both phases can be differentiated.

The domain of interest Ω^{P} is specified by the initial domain of interest Ω_0^{P} at $t = t_0$ and the deformation of the skeleton. Therefore, a Lagrangian observer is considered for a skeleton particle, whereas an ALE observer is considered for the fluid particles. The reference configuration for the fluid is given by the material configuration of the skeleton. Therefore, the mappings between the configurations defined in Section 2.1.2 correspond to the motion of the skeleton particles.

The averaged velocity and pressure in a microscopic view of the fluid phase is specified by $\underline{\boldsymbol{v}}^{\mathrm{P}}$ and p^{P}, respectively. To describe the elastic behavior of the structural phase, in the following, a few quantities already known from Section 2.1.4 for the pure structural problem will be redefined for the poroelastic problem. The position of a skeleton particle in material configuration $\underline{\boldsymbol{X}}^{\mathrm{P}}$ and its position in spatial configuration $\underline{\boldsymbol{x}}^{\mathrm{P}}$ are described by a single global Cartesian coordinate system. The macroscopic displacement of the poroelastic domain is then given by $\underline{\boldsymbol{u}}^{\mathrm{P}} = \underline{\boldsymbol{x}}^{\mathrm{P}} - \underline{\boldsymbol{X}}^{\mathrm{P}}$. The material gradient of the current position is depicted as the macroscopic deformation gradient

$$\underline{\boldsymbol{F}}^{\mathrm{P}} = \frac{\partial \underline{\boldsymbol{x}}^{\mathrm{P}}\left(\underline{\boldsymbol{X}}^{\mathrm{P}}, t\right)}{\partial \underline{\boldsymbol{X}}^{\mathrm{P}}} = \underline{\boldsymbol{I}} + \frac{\partial \underline{\boldsymbol{u}}^{\mathrm{P}}\left(\underline{\boldsymbol{X}}^{\mathrm{P}}, t\right)}{\partial \underline{\boldsymbol{X}}^{\mathrm{P}}}, \tag{2.36}$$

which equals the identity in the undeformed state. Analogous to the structural problem, the deformation of an infinitesimal vector and the change of an infinitesimal volume between material and current configuration is given by $\underline{\mathrm{d}\boldsymbol{x}}^{\mathrm{P}} = \underline{\boldsymbol{F}}^{\mathrm{P}}\,\underline{\mathrm{d}\boldsymbol{X}}^{\mathrm{P}}$ and $\mathrm{d}\Omega^{\mathrm{P}} = J^{\mathrm{P}}\mathrm{d}\Omega_0^{\mathrm{P}}$ with $J^{\mathrm{P}} = \det\left(\underline{\boldsymbol{F}}^{\mathrm{P}}\right)$. The macroscopic Green-Lagrange strain tensor $\underline{\boldsymbol{E}}^{\mathrm{P}}$ serves as a strain measure

$$\underline{\boldsymbol{E}}^{\mathrm{P}} = \frac{1}{2}\left(\underline{\boldsymbol{C}}^{\mathrm{P}} - \underline{\boldsymbol{I}}\right) \quad \text{with} \quad \underline{\boldsymbol{C}}^{\mathrm{P}} = \left(\underline{\boldsymbol{F}}^{\mathrm{P}}\right)^{\mathsf{T}} \cdot \underline{\boldsymbol{F}}^{\mathrm{P}}, \tag{2.37}$$

and is based on the macroscopic right Cauchy-Green deformation tensor $\underline{\boldsymbol{C}}^{\mathrm{P}}$. As required for a strain measure, the macroscopic Green-Lagrange strain tensor is a zero tensor for the undeformed state $\left(\underline{\boldsymbol{F}}^{\mathrm{P}} = \underline{\boldsymbol{I}} \rightarrow \underline{\boldsymbol{C}}^{\mathrm{P}} = \underline{\boldsymbol{I}}\right)$. The spatial traction acting on a specific deformed boundary $\underline{\boldsymbol{h}}^{\mathrm{P}}$, which equals the force per area, is represented by the homogenized Cauchy stress tensor $\underline{\boldsymbol{\sigma}}^{\mathrm{P}}$ of the mixture and the outward-pointing unit normal vector on the boundary $\underline{\boldsymbol{n}}^{\mathrm{P}}$:

$$\underline{\boldsymbol{h}}^{\mathrm{P}} = \underline{\boldsymbol{\sigma}}^{\mathrm{P}} \cdot \underline{\boldsymbol{n}}^{\mathrm{P}}. \tag{2.38}$$

The symmetry of the Cauchy stress tensor to fulfill the balance of angular momentum directly also applies for the poroelastic mixture. An alternative stress representation is given by the homogenized first Piola-Kirchhoff stress tensor of the mixture

$$\underline{\boldsymbol{P}}^{\mathrm{P}} = J^{\mathrm{P}}\underline{\boldsymbol{\sigma}}^{\mathrm{P}} \cdot \left(\underline{\boldsymbol{F}}^{\mathrm{P}}\right)^{-\mathsf{T}}, \tag{2.39}$$

which represents the spatial traction $\underline{\boldsymbol{h}}_0^{\mathrm{P}}$ acting on the undeformed boundary

$$\underline{\boldsymbol{h}}_0^{\mathrm{P}} = \underline{\boldsymbol{P}}^{\mathrm{P}} \cdot \underline{\boldsymbol{n}}_0^{\mathrm{P}}, \tag{2.40}$$

with $\underline{\boldsymbol{n}}_0^{\mathrm{P}}$ being the outward-pointing unit normal vector in material configuration. Finally, the homogenized second Piola-Kirchhoff stress tensor of the mixture $\underline{\boldsymbol{S}}^{\mathrm{P}}$ is a stress representation purely based on the material configuration

$$\underline{\boldsymbol{S}}^{\mathrm{P}} = \left(\underline{\boldsymbol{F}}^{\mathrm{P}}\right)^{-1} \cdot \underline{\boldsymbol{P}}^{\mathrm{P}} = J^{\mathrm{P}}\left(\underline{\boldsymbol{F}}^{\mathrm{P}}\right)^{-1} \cdot \underline{\boldsymbol{\sigma}}^{\mathrm{P}} \cdot \left(\underline{\boldsymbol{F}}^{\mathrm{P}}\right)^{-\mathsf{T}}. \tag{2.41}$$

In the following, the governing equations for the balance of mass and the balance of linear momentum are presented without a derivation. A step-by-step derivation is given by Vuong [215].

Balance of Mass Due to the choice of a Lagrangian reference frame for the structural phase, the balance of mass for the skeleton reduces to

$$\tilde{\rho}_0^{\mathrm{P^S}} = J^{\mathrm{P}}\tilde{\rho}^{\mathrm{P^S}} = \text{const.} \quad \text{or} \quad \frac{\partial \tilde{\rho}_0^{\mathrm{P^S}}}{\partial t} = \frac{\partial\left(J^{\mathrm{P}}\tilde{\rho}^{\mathrm{P^S}}\right)}{\partial t} = 0 \quad \text{in } \Omega_0^{\mathrm{P}} \times \mathcal{T}, \tag{2.42}$$

where $\tilde{\rho}_0^{\mathrm{P^S}} = (1 - \mathring{\phi})\rho_0^{\mathrm{S}}$ is the macroscopic averaged initial density of the solid phase and $\tilde{\rho}^{\mathrm{P^S}} = (1 - \phi)\rho^{\mathrm{S}}$ the macroscopic averaged density of the solid phase. Therein, the initial porosity is denoted by $\mathring{\phi}$. It should be noted that the densities ρ^{S} and ρ_0^{S} correspond to the quantities introduced for the pure structural problem. As the density ρ_0^{S}, and thus also $\tilde{\rho}_0^{\mathrm{P^S}}$, is considered

as a constant in the final computational model, analogous to the pure structural problem, the balance of mass (2.42) is automatically fulfilled and therefore no explicit treatment is required.

Considering incompressible flow on the microscopic scale and a temporally and spatially varying porosity the balance of mass for the fluid phase formulated in the current domain Ω^{P} is given as

$$\left.\frac{\partial \phi}{\partial t}\right|_{\underline{\boldsymbol{X}}^{\mathrm{P}}} \circ \Phi^{-1} + \phi \boldsymbol{\nabla} \cdot \frac{\partial \underline{\boldsymbol{u}}^{\mathrm{P}}}{\partial t} + \boldsymbol{\nabla} \cdot \left[\phi \left(\underline{\boldsymbol{v}}^{\mathrm{P}} - \frac{\partial \underline{\boldsymbol{u}}^{\mathrm{P}}}{\partial t} \right) \right] = 0 \quad \text{in} \bigcup_{t \in \mathcal{T}} \Omega^{\mathrm{P}} \times \{t\}. \tag{2.43}$$

Therein, the mapping Φ is related to the skeleton deformation and not the fluid motion and thus represents the mapping between the reference configuration and the current configuration for the fluid phase.

Balance of Linear Momentum The considered balance of linear momentum for the fluid phase formulated in the current domain Ω^{P} is given as

$$\begin{aligned} &\rho^{\mathrm{F}} \left.\frac{\partial \underline{\boldsymbol{v}}^{\mathrm{P}}}{\partial t}\right|_{\underline{\boldsymbol{X}}^{\mathrm{P}}} \circ \Phi^{-1} - \rho^{\mathrm{F}} \frac{\partial \underline{\boldsymbol{u}}^{\mathrm{P}}}{\partial t} \cdot \boldsymbol{\nabla} \underline{\boldsymbol{v}}^{\mathrm{P}} + \boldsymbol{\nabla} p^{\mathrm{P}} - \rho^{\mathrm{F}} \hat{\underline{\boldsymbol{b}}}^{\mathrm{P}^{\mathrm{F}}} \\ &+ \mu^{\mathrm{F}} \phi \underline{\boldsymbol{k}}^{-1} \cdot \left(\underline{\boldsymbol{v}}^{\mathrm{P}} - \frac{\partial \underline{\boldsymbol{u}}^{\mathrm{P}}}{\partial t} \right) = \underline{\mathbf{0}} \quad \text{in} \bigcup_{t \in \mathcal{T}} \Omega^{\mathrm{P}} \times \{t\}, \end{aligned} \tag{2.44}$$

with $\hat{\underline{\boldsymbol{b}}}^{\mathrm{P}^{\mathrm{F}}}$ being the body force acting on the embedded fluid per unit mass, and ρ^{F} being the microscopic averaged fluid density. The density ρ^{F} equals the fluid density introduced in Section 2.1.5 in the case of solving a coupled problem including porous flow and a viscous fluid simultaneously. As the observer deforms with the with the solid domain (see the time derivative in the first term), the second term, which accounts for the advection, occurs. This governing equation is an extension of the Darcy's law as the pressure gradient is balanced by the last term, which includes the seepage velocity $\left(\underline{\boldsymbol{v}}^{\mathrm{P}} - \partial \underline{\boldsymbol{u}}^{\mathrm{P}} / \partial t\right)$, and thus accounts for the flow resistance cause by the relative motion of the fluid to the skeleton. The macroscopic flow resistance is characterized by the inverse of the positive definite, symmetric, second-order spatial permeability tensor

$$\underline{\boldsymbol{k}} = \left(J^{\mathrm{P}}\right)^{-1} \underline{\boldsymbol{F}}^{\mathrm{P}} \cdot \underline{\boldsymbol{K}} \cdot \left(\underline{\boldsymbol{F}}^{\mathrm{P}}\right)^{\mathsf{T}}, \tag{2.45}$$

which can be expressed for a given deformation by means of the corresponding positive definite, symmetric, second-order material permeability tensor $\underline{\boldsymbol{K}}$. In principal, equation (2.44) physically makes sense only for the fluid portion of the porous mixture. Nevertheless, to avoid superfluous complexity, the presented form results from a division by the porosity ϕ in the derivation of the equation.

Finally, the balance of linear momentum for the whole porous mixture formulated in reference configuration Ω_0^{P} is given as:

$$\begin{aligned} &\tilde{\rho}_0^{\mathrm{P}^{\mathrm{S}}} \frac{\partial^2 \underline{\boldsymbol{u}}^{\mathrm{P}}}{\partial t^2} - \boldsymbol{\nabla}_0 \cdot \underline{\boldsymbol{P}}^{\mathrm{P}} - \tilde{\rho}_0^{\mathrm{P}^{\mathrm{S}}} \hat{\underline{\boldsymbol{b}}}_0^{\mathrm{P}} - J^{\mathrm{P}} \phi \left(\underline{\boldsymbol{F}}^{\mathrm{P}}\right)^{-\mathsf{T}} \cdot \boldsymbol{\nabla}_0 p^{\mathrm{P}} \\ &- \mu^{\mathrm{F}} J^{\mathrm{P}} \phi^2 \underline{\boldsymbol{k}}^{-1} \cdot \left(\underline{\boldsymbol{v}}^{\mathrm{P}} - \frac{\partial \underline{\boldsymbol{u}}^{\mathrm{P}}}{\partial t} \right) = \underline{\mathbf{0}} \quad \text{in } \Omega_0^{\mathrm{P}} \times \mathcal{T}, \end{aligned} \tag{2.46}$$

with $\hat{\underline{\boldsymbol{b}}}_0^{\mathrm{P}}$ being the body force acting on the poroelastic mixture per unit averaged solid mass.

To complete the system of equations, a constitutive law based on the strain energy density function ψ^{P}, which provides the relation of stress and known quantities (for the poroelastic problem these are the deformation by $\underline{\boldsymbol{u}}^{\mathrm{P}}$ and the porous fluid pressure p^{P}), has to be formulated. Three different contributions give poroelastic strain energy density function

$$\psi^{\mathrm{P}}(\underline{\boldsymbol{E}}^{\mathrm{P}}, J^{\mathrm{P}}(1-\phi)) = \psi^{\mathrm{P},skel}(\underline{\boldsymbol{E}}^{\mathrm{P}}) + \psi^{\mathrm{P},vol}(J^{\mathrm{P}}(1-\phi)) + \psi^{\mathrm{P},pen}(\underline{\boldsymbol{E}}^{\mathrm{P}}, J^{\mathrm{P}}(1-\phi)), \tag{2.47}$$

with $\psi^{\mathrm{P},skel}$ accounting for the strain energy due to macroscopic deformation of the solid phase, $\psi^{\mathrm{P},vol}$ arises from the volume change of the solid phase due to changing fluid pressure, and finally $\psi^{\mathrm{P},pen}$ guarantees positive porosity of the poroelastic model (see [57, 216]). For $\psi^{\mathrm{P},skel} = \psi_{NH}(\underline{\boldsymbol{C}}^{\mathrm{P}}, J^{\mathrm{P}})$, a Neo-Hookean material model as given in equation (2.17) is applied for most numerical examples presented in this thesis. If not denoted otherwise $\psi^{\mathrm{P},vol}$ is specified as

$$\psi^{\mathrm{P},vol}(J^{\mathrm{P}}(1-\phi)) = \kappa^{\mathrm{P}} \left[\frac{(1-\phi)J^{\mathrm{P}}}{1-\mathring{\phi}} - 1 - \ln\left(\frac{(1-\phi)J^{\mathrm{P}}}{1-\mathring{\phi}} \right) \right], \tag{2.48}$$

with bulk modulus κ^{P}. In the case a problem requires a penalty contribution, the following strain energy density function

$$\psi^{\mathrm{P},pen}(\underline{\boldsymbol{E}}^{\mathrm{P}}, J^{\mathrm{P}}(1-\phi)) = \eta^{\mathrm{P}} \left[\frac{J^{\mathrm{P}}\phi}{\mathring{\phi}} - \frac{1}{\mathring{\phi}} - \ln\left(\frac{J^{\mathrm{P}}\phi}{\mathring{\phi}} \right) \right], \tag{2.49}$$

with the parameter η^{P} is added.

Remark 2.2 (A physical interpretation of $\psi^{\mathrm{P},pen}$)**.** *Depending on the load that acts on the poroelastic medium in combination with considering solely the strain energy density contributions $\psi^{\mathrm{P},skel}$ and $\psi^{\mathrm{P},vol}$ can lead to negative porosities, which is definitely non-physical. To avoid negative porosities, the penalty contribution $\psi^{\mathrm{P},pen}$ can be added. From a physical point of view, this can be interpreted as contact between the skeleton walls of vanishing fluid cells on the microscopic scale.*

Making use of the Green-Lagrange strain tensor $\underline{\boldsymbol{E}}^{\mathrm{P}}$ as the strain measure gives two constitutive relations to complete the system of equations for poroelasticity

$$\underline{\boldsymbol{S}}^{\mathrm{P}} = \frac{\partial \psi^{\mathrm{P}}(\underline{\boldsymbol{E}}^{\mathrm{P}}, J^{\mathrm{P}}(1-\phi) = \text{const.})}{\partial \underline{\boldsymbol{E}}^{\mathrm{P}}} - p^{\mathrm{P}} J^{\mathrm{P}} \left(\underline{\boldsymbol{F}}^{\mathrm{P}}\right)^{-1} \cdot \left(\underline{\boldsymbol{F}}^{\mathrm{P}}\right)^{-\mathsf{T}}, \tag{2.50}$$

$$p^{\mathrm{P}} = -\frac{\partial \psi^{\mathrm{P}}(\underline{\boldsymbol{E}}^{\mathrm{P}} = \text{const.}, J^{\mathrm{P}}(1-\phi))}{\partial (J^{\mathrm{P}}(1-\phi))}. \tag{2.51}$$

To sum up, when considering a constant density $\tilde{\rho}_0^{\mathrm{PS}} = \text{const.}$, equations (2.43), (2.44), and (2.46) describe the averaged state from a macroscopic view in the poroelastic domain. The constitutive equation (2.51) allows expressing the porosity ϕ by the fluid pressure p^{P} and the displacement $\underline{\boldsymbol{u}}^{\mathrm{P}}$, which will be used in the following to formulate the poroelastic problem by the primal unknowns fluid pressure p^{P}, fluid velocity $\underline{\boldsymbol{v}}^{\mathrm{P}}$, and skeleton displacement $\underline{\boldsymbol{u}}^{\mathrm{P}}$.

The necessary initial conditions given by the initial displacement $\mathring{\underline{\boldsymbol{u}}}^{\mathrm{P}}$, the initial solid phase velocity $\mathring{\underline{\boldsymbol{v}}}^{\mathrm{P^S}}$, the initial porosity $\mathring{\phi}$, and the initial fluid velocity field $\mathring{\underline{\boldsymbol{v}}}^{\mathrm{P}}$ for the poroelastic problem are:

$$\begin{aligned} &\underline{\boldsymbol{u}}^{\mathrm{P}} = \mathring{\underline{\boldsymbol{u}}}^{\mathrm{P}} \quad \text{in } \Omega_0^{\mathrm{P}} \times \{t_0\}\,, && \frac{\partial \underline{\boldsymbol{u}}^{\mathrm{P}}}{\partial t} = \mathring{\underline{\boldsymbol{v}}}^{\mathrm{P^S}} \quad \text{in } \Omega_0^{\mathrm{P}} \times \{t_0\}\,, \\ &\phi = \mathring{\phi} \quad \text{in } \Omega^{\mathrm{P}} \times \{t_0\}\,, && \underline{\boldsymbol{v}}^{\mathrm{P}} = \mathring{\underline{\boldsymbol{v}}}^{\mathrm{P}} \quad \text{in } \Omega^{\mathrm{P}} \times \{t_0\}\,. \end{aligned} \tag{2.52}$$

To complete the problem description of poroelasticity, adequate boundary conditions on the outer boundary $\partial\Omega \cap \partial\Omega^{\mathrm{P}}$ have to be prescribed:

$$\underline{\boldsymbol{v}}^{\mathrm{P}} \cdot \underline{\boldsymbol{n}}^{\mathrm{P}} = \hat{v}^{\mathrm{P},n} \quad \text{on } \Gamma^{\mathrm{P^F,D}}, \qquad -p^{\mathrm{P}} \underline{\boldsymbol{n}}^{\mathrm{P}} = \hat{h}^{\mathrm{P^F,N}} \underline{\boldsymbol{n}}^{\mathrm{P}} \quad \text{on } \Gamma^{\mathrm{P^F,N}}, \tag{2.53}$$

$$\underline{\boldsymbol{u}}^{\mathrm{P}} = \hat{\underline{\boldsymbol{u}}}^{\mathrm{P}} \quad \text{on } \Gamma_0^{\mathrm{P,D}}, \qquad \underline{\boldsymbol{P}}^{\mathrm{P}} \cdot \underline{\boldsymbol{n}}_0^{\mathrm{P}} = \hat{\underline{\boldsymbol{h}}}_0^{\mathrm{P,N}} \quad \text{on } \Gamma_0^{\mathrm{P,N}}. \tag{2.54}$$

Therein, $\hat{v}^{\mathrm{P},n}$ is the scalar normal fluid velocity of the Darcy-like flow on Dirichlet boundaries $\Gamma^{\mathrm{P^F,D}}$, $\hat{h}^{\mathrm{P^F,N}}$ is the traction in normal direction on the Neumann boundaries $\Gamma^{\mathrm{P^F,N}}$, $\hat{\underline{\boldsymbol{u}}}^{\mathrm{P}}$ is the displacement of the poroelastic domain on the Dirichlet boundaries $\Gamma_0^{\mathrm{P,D}}$, and $\hat{\underline{\boldsymbol{h}}}_0^{\mathrm{P,N}}$ is the traction on the poroelastic mixture on the Neumann boundaries $\Gamma_0^{\mathrm{P,N}}$. Conditions on remaining part of the poroelastic boundary

$$\Gamma^{\mathrm{P,I}} = \partial\Omega^{\mathrm{P}} \setminus \left(\Gamma^{\mathrm{P^F,D}} \cup \Gamma^{\mathrm{P^F,N}}\right) = \partial\Omega^{\mathrm{P}} \setminus \left(\Gamma^{\mathrm{P,D}} \cup \Gamma^{\mathrm{P,N}}\right), \tag{2.55}$$

have not yet been considered. This interface is not part of the outer boundary $\partial\Omega \cap \Gamma^{\mathrm{P,I}} = \emptyset$ and will be discussed in Section 2.1.8 and the subsequent chapters.

Continuous Weak Form As the weak form of the poroelastic problem formulation builds the basis for the numerical treatment by the FEM, it is presented in the following. To derive this form of the governing equations, the balance equations (2.43), (2.44), and (2.46) to be solved are multiplied by the test functions δp^{P}, $\delta \underline{\boldsymbol{v}}^{\mathrm{P}}$, and $\delta \underline{\boldsymbol{u}}^{\mathrm{P}}$ respectively. Equations (2.43), (2.44) are integrated in the current domain Ω^{P} and (2.46) is integrated in the material domain Ω_0^{P}. An additional boundary integral is introduced by a partial integration of the porosity gradient term in (2.43) to avoid spatial derivatives of ϕ in the formulation. Similar to the derivations in Sections 2.1.4 and 2.1.5, a partial integration of the stress terms is performed for the balances of linear momentum (2.44) and (2.46) as this reduces the order of spatial derivatives of $\underline{\boldsymbol{v}}^{\mathrm{P}}$ and $\underline{\boldsymbol{u}}^{\mathrm{P}}$ in the formulation to one. This aforementioned procedure finally results in the weak formulation of the poroelastic problem.
$Find\ \left(\underline{\boldsymbol{v}}^{\mathrm{P}}, \underline{\boldsymbol{u}}^{\mathrm{P}}, p^{\mathrm{P}}\right) \in \mathcal{S}_{\underline{\boldsymbol{v}}^{\mathrm{P}}} \times \mathcal{S}_{\underline{\boldsymbol{u}}^{\mathrm{P}}} \times \mathcal{S}_{p^{\mathrm{P}}}\ such\ that\ for\ all\ \left(\delta\underline{\boldsymbol{v}}^{\mathrm{P}}, \delta\underline{\boldsymbol{u}}^{\mathrm{P}}, \delta p^{\mathrm{P}}\right) \in \mathcal{T}_{\delta\underline{\boldsymbol{v}}^{\mathrm{P}}} \times \mathcal{T}_{\delta\underline{\boldsymbol{u}}^{\mathrm{P}}} \times \mathcal{T}_{\delta p^{\mathrm{P}}}$:

$$\mathcal{W}^{\mathrm{P}}\left[\left(\delta\underline{\boldsymbol{v}}^{\mathrm{P}}, \delta\underline{\boldsymbol{u}}^{\mathrm{P}}, \delta p^{\mathrm{P}}\right), \left(\underline{\boldsymbol{v}}^{\mathrm{P}}, \underline{\boldsymbol{u}}^{\mathrm{P}}, p^{\mathrm{P}}\right)\right] = 0. \tag{2.56}$$

The form $\mathcal{W}^{\mathrm{P}}$ which results from the derivation is:

$$\begin{aligned}
\mathcal{W}^{\mathrm{P}}\left[\left(\delta\underline{\boldsymbol{v}}^{\mathrm{P}},\delta\underline{\boldsymbol{u}}^{\mathrm{P}},\delta p^{\mathrm{P}}\right),\left(\underline{\boldsymbol{v}}^{\mathrm{P}},\underline{\boldsymbol{u}}^{\mathrm{P}},p^{\mathrm{P}}\right)\right] = &\left(\delta p^{\mathrm{P}},\left.\frac{\partial\phi}{\partial t}\right|_{\underline{\boldsymbol{X}}^{\mathrm{P}}}\circ\Phi^{-1}\right)_{\Omega^{\mathrm{P}}}+\left(\delta p^{\mathrm{P}},\phi\boldsymbol{\nabla}\cdot\frac{\partial\underline{\boldsymbol{u}}^{\mathrm{P}}}{\partial t}\right)_{\Omega^{\mathrm{P}}}\\
&-\left(\boldsymbol{\nabla}\delta p^{\mathrm{P}},\phi\left(\underline{\boldsymbol{v}}^{\mathrm{P}}-\frac{\partial\underline{\boldsymbol{u}}^{\mathrm{P}}}{\partial t}\right)\right)_{\Omega^{\mathrm{P}}}+\left\langle\delta p^{\mathrm{P}},\phi\underline{\boldsymbol{n}}^{\mathrm{P}}\cdot\left(\underline{\boldsymbol{v}}^{\mathrm{P}}-\frac{\partial\underline{\boldsymbol{u}}^{\mathrm{P}}}{\partial t}\right)\right\rangle_{\partial\Omega^{\mathrm{P}}}\\
&+\left(\delta\underline{\boldsymbol{v}}^{\mathrm{P}},\rho^{\mathrm{F}}\left.\frac{\partial\underline{\boldsymbol{v}}^{\mathrm{P}}}{\partial t}\right|_{\underline{\boldsymbol{X}}^{\mathrm{P}}}\circ\Phi^{-1}\right)_{\Omega^{\mathrm{P}}}-\left(\boldsymbol{\nabla}\cdot\delta\underline{\boldsymbol{v}}^{\mathrm{P}},p^{\mathrm{P}}\right)_{\Omega^{\mathrm{P}}}-\left(\delta\underline{\boldsymbol{v}}^{\mathrm{P}},\rho^{\mathrm{F}}\frac{\partial\underline{\boldsymbol{u}}^{\mathrm{P}}}{\partial t}\cdot\boldsymbol{\nabla}\underline{\boldsymbol{v}}^{\mathrm{P}}\right)_{\Omega^{\mathrm{P}}}\\
&+\left(\delta\underline{\boldsymbol{v}}^{\mathrm{P}},\mu^{\mathrm{F}}\phi\underline{\boldsymbol{k}}^{-1}\cdot\underline{\boldsymbol{v}}^{\mathrm{P}}\right)_{\Omega^{\mathrm{P}}}-\left(\delta\underline{\boldsymbol{v}}^{\mathrm{P}},\mu^{\mathrm{F}}\phi\underline{\boldsymbol{k}}^{-1}\cdot\frac{\partial\underline{\boldsymbol{u}}^{\mathrm{P}}}{\partial t}\right)_{\Omega^{\mathrm{P}}}-\left(\delta\underline{\boldsymbol{v}}^{\mathrm{P}},\rho^{\mathrm{F}}\hat{\underline{\boldsymbol{b}}}^{\mathrm{P^F}}\right)_{\Omega^{\mathrm{P}}}\\
&-\left\langle\delta\underline{\boldsymbol{v}}^{\mathrm{P}},\hat{h}^{\mathrm{P^F,N}}\underline{\boldsymbol{n}}^{\mathrm{P}}\right\rangle_{\Gamma^{\mathrm{P^F,N}}}-\left\langle\delta\underline{\boldsymbol{v}}^{\mathrm{P}},h^{\mathrm{P^F,I}}\underline{\boldsymbol{n}}^{\mathrm{P}}\right\rangle_{\Gamma^{\mathrm{P,I}}}\\
&+\left(\delta\underline{\boldsymbol{u}}^{\mathrm{P}},\tilde{\rho}_0^{\mathrm{P^S}}\frac{\partial^2\underline{\boldsymbol{u}}^{\mathrm{P}}}{\partial t^2}\right)_{\Omega_0^{\mathrm{P}}}+\left(\boldsymbol{\nabla}_0\delta\underline{\boldsymbol{u}}^{\mathrm{P}},\underline{\boldsymbol{P}}^{\mathrm{P}}\right)_{\Omega_0^{\mathrm{P}}}+\left(\delta\underline{\boldsymbol{u}}^{\mathrm{P}},\mu^{\mathrm{F}}J^{\mathrm{P}}\phi^2\underline{\boldsymbol{k}}^{-1}\cdot\frac{\partial\underline{\boldsymbol{u}}^{\mathrm{P}}}{\partial t}\right)_{\Omega_0^{\mathrm{P}}}\\
&-\left(\delta\underline{\boldsymbol{u}}^{\mathrm{P}},\mu^{\mathrm{F}}J^{\mathrm{P}}\phi^2\underline{\boldsymbol{k}}^{-1}\cdot\underline{\boldsymbol{v}}^{\mathrm{P}}\right)_{\Omega_0^{\mathrm{P}}}-\left(\delta\underline{\boldsymbol{u}}^{\mathrm{P}},J^{\mathrm{P}}\phi\left(\underline{\boldsymbol{F}}^{\mathrm{P}}\right)^{-\mathsf{T}}\cdot\boldsymbol{\nabla}_0 p^{\mathrm{P}}\right)_{\Omega_0^{\mathrm{P}}}\\
&-\left(\delta\underline{\boldsymbol{u}}^{\mathrm{P}},\tilde{\rho}_0^{\mathrm{P^S}}\hat{\underline{\boldsymbol{b}}}_0^{\mathrm{P}}\right)_{\Omega_0^{\mathrm{P}}}-\left\langle\delta\underline{\boldsymbol{u}}^{\mathrm{P}},\hat{\underline{\boldsymbol{h}}}_0^{\mathrm{P,N}}\right\rangle_{\Gamma_0^{\mathrm{P,N}}}-\left\langle\delta\underline{\boldsymbol{u}}^{\mathrm{P}},\underline{\boldsymbol{h}}_0^{P,I}\right\rangle_{\Gamma_0^{\mathrm{P,I}}}.
\end{aligned}\tag{2.57}$$

Herein, the boundary integrals on $\Gamma^{\mathrm{P,I}}$ or $\Gamma_0^{\mathrm{P,I}}$ arise from the partial integration in the derivation of the weak form and occur only in case of an interface-coupled problem. The interface stresses $h^{\mathrm{P^F,I}}$ and $\underline{\boldsymbol{h}}_0^{P,I}$ serve as a placeholder therein and will be specified in the subsequent chapters for the different possible interface types.

The solution spaces $\mathcal{S}_{\underline{\boldsymbol{v}}^{\mathrm{P}}},\mathcal{S}_{\underline{\boldsymbol{u}}^{\mathrm{P}}},\mathcal{S}_{p^{\mathrm{P}}}$ and test function spaces $\mathcal{T}_{\delta\underline{\boldsymbol{v}}^{\mathrm{P}}},\mathcal{T}_{\delta\underline{\boldsymbol{u}}^{\mathrm{P}}},\mathcal{T}_{\delta p^{\mathrm{P}}}$ are sufficiently smooth for the problem formulation (2.56) to make sense. Additionally, the Dirichlet-type boundary conditions are directly incorporated into the solution and test function spaces:

$$\begin{aligned}
\underline{\boldsymbol{v}}^{\mathrm{P}}\cdot\underline{\boldsymbol{n}}^{\mathrm{P}}=\hat{v}^{\mathrm{P},n}\quad&\text{on }\Gamma^{\mathrm{P^F,D}}\ \forall\ \underline{\boldsymbol{v}}^{\mathrm{P}}\in\mathcal{S}_{\underline{\boldsymbol{v}}^{\mathrm{P}}},\qquad \delta\underline{\boldsymbol{v}}^{\mathrm{P}}\cdot\underline{\boldsymbol{n}}^{\mathrm{P}}=0\quad\text{on }\Gamma^{\mathrm{P^F,D}}\ \forall\ \delta\underline{\boldsymbol{v}}^{\mathrm{P}}\in\mathcal{T}_{\delta\underline{\boldsymbol{v}}^{\mathrm{P}}},\\
\underline{\boldsymbol{u}}^{\mathrm{P}}=\hat{\underline{\boldsymbol{u}}}^{\mathrm{P}}\quad&\text{on }\Gamma_0^{\mathrm{P,D}}\ \forall\ \underline{\boldsymbol{u}}^{\mathrm{P}}\in\mathcal{S}_{\underline{\boldsymbol{u}}^{\mathrm{P}}},\qquad \delta\underline{\boldsymbol{u}}^{\mathrm{P}}=\underline{\boldsymbol{0}}\quad\text{on }\Gamma_0^{\mathrm{P,D}}\ \forall\ \delta\underline{\boldsymbol{u}}^{\mathrm{P}}\in\mathcal{T}_{\delta\underline{\boldsymbol{u}}^{\mathrm{P}}}.
\end{aligned}\tag{2.58}$$

Remark 2.3 (Smoothness of the solution spaces for the primary unknowns of the poroelastic problem)**.** *Within this thesis, solely a Darcy-based equation for the porous flow as presented previously is considered. This allows removing all spatial derivatives of the porosity in* (2.57) *and therefore reducing the smoothness requirements of the solution space. When considering a Darcy-Brinkmann-based flow equation this is not possible anymore. The arising issue can be tackled by a NURBS-based finite element discretization or a "mixed" approach where the porosity ϕ is chosen as an additional primary variable as discussed by Vuong [215], Vuong* et al. *[217].*

2.1.7 Interface of Viscous Fluids and Elastic Structures

The interface between the viscous fluid domain and the structural domain $\Gamma^{\mathrm{FS}}=\partial\Omega^{\mathrm{F}}\cap\partial\Omega^{\mathrm{S}}=\Gamma^{\mathrm{F,I}}\cap\Gamma^{\mathrm{S,I}}$ needs to fulfill the dynamic stress balance (2.59) as well as the no-slip condition (2.60)

which includes already mass conservation on the interface.

$$\underline{\boldsymbol{\sigma}}^{\mathrm{F}} \cdot \underline{\boldsymbol{n}}^{\mathrm{F}} = \underline{\boldsymbol{\sigma}}^{\mathrm{S}} \cdot \underline{\boldsymbol{n}}^{\mathrm{F}} + \underline{\hat{\boldsymbol{g}}}_{\sigma}^{\mathrm{FS}} \qquad \text{on } \Gamma^{\mathrm{FS}} \tag{2.59}$$

$$\underline{\boldsymbol{v}}^{\mathrm{F}} = \frac{\partial \underline{\boldsymbol{u}}^{\mathrm{S}}}{\partial t} - \underline{\hat{\boldsymbol{g}}}_{v}^{\mathrm{FS}} \qquad \text{on } \Gamma^{\mathrm{FS}} \tag{2.60}$$

Remark 2.4 (Occurring jump contributions in conditions (2.59) and (2.60))**.** *The jump vectors introduced in these conditions have to vanish when considering the physical correct conditions:* $\underline{\hat{\boldsymbol{g}}}_{\sigma}^{\mathrm{FS}} = \underline{\mathbf{0}}$ *and* $\underline{\hat{\boldsymbol{g}}}_{v}^{\mathrm{FS}} = \underline{\mathbf{0}}$*. Nevertheless, non-vanishing jump vectors will be prescribed in Chapter 3, Section 3.5, to validate the presented numerical approach by the method of manufactured solutions.*

Remark 2.5 (Validity of the no-slip condition)**.** *The no-slip condition is non-controversial accepted on a fluid-structure interface for a macroscopic problem setup. Nevertheless, due to characteristics such as surface roughness or wettability, an interfacial velocity slip can be observed in a large number of experiments (see e.g. the work of Neto* et al. *[160]). Thus, this effect can get relevant for contacting scenarios. In Chapter 6 and Chapter 7, such a velocity slip is taken into account by a general Navier boundary condition on the fluid-structure interface.*

2.1.8 Interface of Viscous Fluids and Permeable Elastic Structures[1]

The conditions on the common interface between a viscous fluid and the poroelastic domain are specified in analogy to the frequently analyzed coupling of viscous flow and porous flow. Hereby, the conditions (2.61)-(2.64) need to be fulfilled on the interface $\Gamma^{\mathrm{FP}} = \partial\Omega^{\mathrm{F}} \cap \partial\Omega^{\mathrm{P}} = \Gamma^{\mathrm{F,I}} \cap \Gamma^{\mathrm{P,I}}$.

$$\underline{\mathbf{0}} = \underline{\boldsymbol{\sigma}}^{\mathrm{F}} \cdot \underline{\boldsymbol{n}}^{\mathrm{F}} - \underline{\boldsymbol{\sigma}}^{\mathrm{P}} \cdot \underline{\boldsymbol{n}}^{\mathrm{F}} - \underline{\hat{\boldsymbol{g}}}_{\sigma}^{\mathrm{FP}} \qquad \text{on } \Gamma^{\mathrm{FP}} \tag{2.61}$$

$$0 = \underline{\boldsymbol{n}}^{\mathrm{F}} \cdot \underline{\boldsymbol{\sigma}}^{\mathrm{F}} \cdot \underline{\boldsymbol{n}}^{\mathrm{F}} + p^{\mathrm{P}} - \hat{g}_{\sigma}^{\mathrm{FP},n} \qquad \text{on } \Gamma^{\mathrm{FP}} \tag{2.62}$$

$$0 = \left[\underline{\boldsymbol{v}}^{\mathrm{F}} - \frac{\partial \underline{\boldsymbol{u}}^{\mathrm{P}}}{\partial t} - \phi \left(\underline{\boldsymbol{v}}^{\mathrm{P}} - \frac{\partial \underline{\boldsymbol{u}}^{\mathrm{P}}}{\partial t} \right) - \underline{\hat{\boldsymbol{g}}}^{\mathrm{FP},n} \right] \cdot \underline{\boldsymbol{n}}^{\mathrm{F}} \qquad \text{on } \Gamma^{\mathrm{FP}} \tag{2.63}$$

$$0 = \left[\underline{\boldsymbol{v}}^{\mathrm{F}} - \frac{\partial \underline{\boldsymbol{u}}^{\mathrm{P}}}{\partial t} - \beta_{\mathrm{BJ}} \phi \left(\underline{\boldsymbol{v}}^{\mathrm{P}} - \frac{\partial \underline{\boldsymbol{u}}^{\mathrm{P}}}{\partial t} \right) + \kappa \underline{\boldsymbol{n}}^{\mathrm{F}} \cdot \underline{\boldsymbol{\sigma}}^{\mathrm{F}} - \underline{\hat{\boldsymbol{g}}}^{\mathrm{FP},t} \right] \cdot \underline{\boldsymbol{t}}_{i}, \quad \text{with } i = 1, 2 \qquad \text{on } \Gamma^{\mathrm{FP}} \tag{2.64}$$

The dynamic stress balance in the current configuration between the Cauchy stresses of fluid and the entire poroelastic mixture is represented by (2.61). Furthermore, a dynamic stress balance between the fluid pressure inside of the poroelastic domain and the stress components of the viscous fluid, in normal direction, are enforced by (2.62). The kinematic constraint in interface normal direction (2.63) guarantees mass-balance on the interface. A constraint in tangential direction on the viscous fluid is still missing. To include effects arising from the boundary layer in the porous flow, which cannot be represented by the Darcy equation, the so-called Beavers-Joseph (BJ) condition ($\beta_{\mathrm{BJ}} = 1$), which has been introduced by Beavers and Joseph [20], is included in (2.64). Herein, a proportionality of the viscous shear stress and the relative velocity slip in tangential direction between the adjacent fluids on both sides of the interface is proposed. The

[1] This section is adapted from the author's publication [2].

tangential vectors $\underline{\boldsymbol{t}}_i$, which are orthogonal to the normal vector $\underline{\boldsymbol{n}}^{\mathrm{F}}$, define the tangential plane of the interface. The proportionality constant κ depends on the permeability $\underline{\boldsymbol{k}}$ of the porous structure, the fluid viscosity μ^{F}, and the positive model parameter α_{BJ} which has to be verified experimentally. Then, κ can be computed as:

$$\kappa = \left(\alpha_{\mathrm{BJ}}\mu^{\mathrm{F}}\sqrt{3}\right)^{-1}\sqrt{\mathrm{tr}(\underline{\boldsymbol{k}})}. \tag{2.65}$$

In cases with small permeability, a simplified condition, which does not include the seepage velocity, the Beavers-Joseph-Saffmann (BJS) condition ($\beta_{\mathrm{BJ}} = 0$), which has been analyzed by Saffman [181] and Jones [131], can be applied. Due to the nonexistent tangential stress contribution on the boundaries/interfaces of the Darcy equation (see boundary/interface term of porous flow equation in (2.57)), this condition - which does not include the tangential porous fluid velocity - is mostly analyzed and applied. For the Beavers-Joseph condition it is shown by Cao *et al.* [55] that well-posedness is established for small α_{BJ}. In the works of Gartling *et al.* [89] and Burman and Hansbo [45], numerical computations for a "no-slip" condition between viscous and porous fluid velocity (Beavers-Joseph condition with $\alpha_{\mathrm{BJ}}^{-1} = 0$) show oscillations of the porous velocity close to the interface. To analyze the behavior of the two different approaches ($\beta_{\mathrm{BJ}} = 1$ and $\beta_{\mathrm{BJ}} = 0$), a comparison of both methods when varying the parameter α_{BJ} is presented in Chapter 4, Section 4.4.5.

Remark 2.6 (Occurring jump contributions in conditions (2.61) - (2.64))**.** *In all conditions* (2.61) - (2.64)*, additional jump contributions* $\hat{\underline{\boldsymbol{g}}}_{\sigma}^{\mathrm{FP}}$, $\hat{g}_{\sigma}^{\mathrm{FP},n}$, $\hat{\underline{\boldsymbol{g}}}^{\mathrm{FP},n}$, *and* $\hat{\underline{\boldsymbol{g}}}^{\mathrm{FP},t}$ *are incorporated. In general, these contributions have to vanish when considering the physical correct conditions, but they will be employed in Section 4.4 for the application of the method of manufactured solutions. This simplifies the choice of possible prescribed analytic solutions, as non-vanishing physical conditions can be considered.*

2.1.9 Interface between Viscous Fluids

In the case the fluid domain Ω^{F} is partitioned in two separate domains $\Omega^{\mathrm{F}} = \Omega^{\mathrm{F}_1} \cup \Omega^{\mathrm{F}_2}$ ($\Omega^{\mathrm{F}_1} \cap \Omega^{\mathrm{F}_2} = \emptyset$) and the outer boundaries of both fluid domains have a common interface $\Gamma^{\mathrm{FF}} = \partial\Omega^{\mathrm{F}_1} \cap \partial\Omega^{\mathrm{F}_2}$, the kinematic continuity (2.66) and the dynamic equilibrium (2.67) have to be enforced on the interface Γ^{FF}.

$$\underline{\boldsymbol{\sigma}}^{\mathrm{F}_1} \cdot \underline{\boldsymbol{n}} = \underline{\boldsymbol{\sigma}}^{\mathrm{F}_2} \cdot \underline{\boldsymbol{n}} \qquad \text{on } \Gamma^{\mathrm{FF}} \tag{2.66}$$

$$\underline{\boldsymbol{v}}^{\mathrm{F}_1} = \underline{\boldsymbol{v}}^{\mathrm{F}_2} \qquad \text{on } \Gamma^{\mathrm{FF}} \tag{2.67}$$

Herein, the vector $\underline{\boldsymbol{n}}$ is a unit normal vector on the interface Γ^{FF} which equals either the normal vector on $\partial\Omega^{\mathrm{F}_1}$ or $\partial\Omega^{\mathrm{F}_2}$. The fluid stress $\underline{\boldsymbol{\sigma}}^{\mathrm{F}_1}$, $\underline{\boldsymbol{\sigma}}^{\mathrm{F}_2}$ and the velocity $\underline{\boldsymbol{v}}^{\mathrm{F}_1}$, $\underline{\boldsymbol{v}}^{\mathrm{F}_2}$ correspond to the fluid domain Ω^{F_1}, Ω^{F_2}, respectively.

2.1.10 Contact Interfaces

In the following section, interfaces where contact between two elastic structures occurs are discussed. For a clear presentation, only impermeable solid structures (Section 2.1.4) are considered

herein. The extension to the contact of poroelastic bodies including details on the applied numerical approaches is given in Chapter 5 and 7. Only the most important aspects of contact for this work are discussed in the following. For a more general overview on contact mechanics the reader is referred to the textbooks of e.g. Wriggers [230] and Laursen [139] and to the theses of Popp [170] and Seitz [195], which provide deep insight to the specific underlying numerical approaches to treat contact of solid bodies.

First, the basic notation and contact kinematics are discussed. To start with, two solid bodies (domains Ω^{S_1} and Ω^{S_2}) which potentially come into contact, as visualized in Figure 2.4, are considered. The potential contacting interfaces $\breve{\Gamma}^{\mathrm{S}_1,c}$ and $\breve{\Gamma}^{\mathrm{S}_2,c}$ are a subset of the corresponding

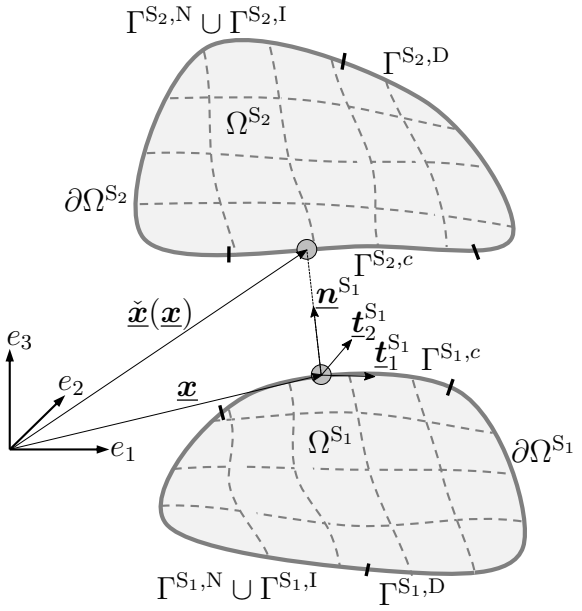

Figure 2.4: Basic configuration for two body contact.

outer boundaries $\breve{\Gamma}^{\mathrm{S}_1,c} \subseteq \Gamma^{\mathrm{S}_1,c} \cup \Gamma^{\mathrm{S}_1,\mathrm{N}} \cup \Gamma^{\mathrm{S}_1,\mathrm{I}} \subseteq \partial\Omega^{\mathrm{S}_1}$ and $\breve{\Gamma}^{\mathrm{S}_2,c} \subseteq \Gamma^{\mathrm{S}_2,c} \cup \Gamma^{\mathrm{S}_2,\mathrm{N}} \cup \Gamma^{\mathrm{S}_2,\mathrm{I}} \subseteq \partial\Omega^{\mathrm{S}_2}$. Herein, the "active" contact interfaces, which are typically unknown prior to the computation, are denoted as $\Gamma^{\mathrm{S}_1,c}$ and $\Gamma^{\mathrm{S}_2,c}$ on the respective sides. These contact interfaces are non-overlapping with the remaining interfaces: $\Gamma^{\mathrm{S}_i,c} \cap \Gamma^{\mathrm{S}_i,\mathrm{D}} = \emptyset$, $\Gamma^{\mathrm{S}_i,c} \cap \Gamma^{\mathrm{S}_i,\mathrm{N}} = \emptyset$, and $\Gamma^{\mathrm{S}_i,c} \cap \Gamma^{\mathrm{S}_i,\mathrm{I}} = \emptyset$ with $i, j = 1, 2$. To formulate the kinematic relations between contacting bodies, a projection $\breve{\mathcal{P}}_{ij}^{\boldsymbol{n}}$ of any specific point $\underline{\boldsymbol{x}}$ on the interface $\breve{\Gamma}^{\mathrm{S}_i,c}$ to a point $\underline{\breve{\boldsymbol{x}}}\,(\underline{\boldsymbol{x}})$ on the opposite interface $\breve{\Gamma}^{\mathrm{S}_j,c}$ is defined.

$$\breve{\mathcal{P}}_{ij}^{\boldsymbol{n}}\,(\underline{\boldsymbol{x}}) : \begin{cases} \breve{\Gamma}^{\mathrm{S}_i,c} \rightarrow \breve{\Gamma}^{\mathrm{S}_j,c} \\ \underline{\boldsymbol{x}} \mapsto \breve{\mathcal{P}}_{ij}^{\boldsymbol{n}}\,(\underline{\boldsymbol{x}}) = \underline{\breve{\boldsymbol{x}}}\,(\underline{\boldsymbol{x}}) \end{cases} \quad \text{with} \quad i, j = 1, 2 \quad \text{and} \quad i \neq j \tag{2.68}$$

The direction along which this projection is preformed is specified by the outward normal vector $\underline{\boldsymbol{n}}^{\mathrm{S}_i}$ on the potential contacting boundary $\breve{\Gamma}^{\mathrm{S}_i,c}$. For the projection $\breve{\mathcal{P}}_{12}^{\boldsymbol{n}}\,(\underline{\boldsymbol{x}})$ in Figure 2.4 the utilized normal vector is $\underline{\boldsymbol{n}}^{\mathrm{S}_1}$. The normal vector $\underline{\boldsymbol{n}}^{\mathrm{S}_i}$ is orthogonal onto the tangential vectors $\underline{\boldsymbol{t}}_1^{\mathrm{S}_i}$ and $\underline{\boldsymbol{t}}_2^{\mathrm{S}_i}$, which represent the tangential plane on $\breve{\Gamma}^{\mathrm{S}_i,c}$. It is assumed that this projection $\breve{\mathcal{P}}_{ij}^{\boldsymbol{n}}\,(\underline{\boldsymbol{x}})$ exists on the overall interface $\breve{\Gamma}^{\mathrm{S}_i,c}$. This assumption is not a general limitation and can be treated in an easy way by the computational algorithm, since for sufficiently smooth bodies contact does not occur on parts of the interface $\breve{\Gamma}^{\mathrm{S}_i,c}$ where this projection does not exist. For all quantities

$*, \underline{*}$ evaluated at the projected point, the short notation $\breve{*} = \breve{*}(\underline{\boldsymbol{x}}) = *(\breve{\underline{\boldsymbol{x}}}(\underline{\boldsymbol{x}}))$, $\underline{\breve{*}} = \underline{\breve{*}}(\underline{\boldsymbol{x}}) = \underline{*}(\breve{\underline{\boldsymbol{x}}}(\underline{\boldsymbol{x}}))$ is used. Making use of the projection allows defining the geometric gap between two potentially contacting interfaces

$$g^n(\underline{\boldsymbol{x}}) := (\breve{\underline{\boldsymbol{x}}}(\underline{\boldsymbol{x}}) - \underline{\boldsymbol{x}}) \cdot \underline{\boldsymbol{n}}^{\mathrm{S}}(\underline{\boldsymbol{x}}) \quad \underline{\boldsymbol{x}} \in \breve{\Gamma}^{\mathrm{S}_1,c} \cup \breve{\Gamma}^{\mathrm{S}_2,c}. \tag{2.69}$$

A positive gap g^n indicates that both solid bodies are separated. On the "active" contact interface $\Gamma^{\mathrm{SS},c} := \Gamma^{\mathrm{S}_1,c} = \Gamma^{\mathrm{S}_2,c}$, the contact interfaces of both solid bodies coincide and thus the gap has to vanish ($g^n = 0$). It should be noted that such a unique "active" contact interface $\Gamma^{\mathrm{SS},c}$ of both sides in general does only exist for the continuous problem but not the discretized problem. A visualization of the different interfaces is given in Figure 2.5 (left).

To fulfill the balance of linear momentum, the traction $\underline{\boldsymbol{h}}^{\mathrm{S}_1,\mathrm{I}} (= \underline{\boldsymbol{\sigma}}^{\mathrm{S}_1} \cdot \underline{\boldsymbol{n}}^{\mathrm{S}_1})$ on the interface $\Gamma^{\mathrm{S}_1,c}$ and the traction $\underline{\boldsymbol{h}}^{\mathrm{S}_2,\mathrm{I}} (= \underline{\boldsymbol{\sigma}}^{\mathrm{S}_2} \cdot \underline{\boldsymbol{n}}^{\mathrm{S}_2})$ on the interface $\Gamma^{\mathrm{S}_2,c}$ have to be in balance

$$\underline{\boldsymbol{h}}^{\mathrm{S,I}} := \underline{\boldsymbol{h}}^{\mathrm{S}_1,\mathrm{I}} = -\underline{\boldsymbol{h}}^{\mathrm{S}_2,\mathrm{I}} \quad \text{on} \quad \Gamma^{\mathrm{SS},c}. \tag{2.70}$$

The choice to define the traction corresponding to the solid body Ω^{S_1} as the positive contact traction $\underline{\boldsymbol{h}}^{\mathrm{S,I}}$ is done arbitrarily and could be chosen vice versa.

Within this work, frictionless contact is considered exclusively

$$\underline{\boldsymbol{h}}^{\mathrm{S,I}} \cdot \underline{\boldsymbol{P}}^t = \underline{\boldsymbol{0}} \quad \text{on} \quad \Gamma^{\mathrm{SS},c}, \tag{2.71}$$

with the tangential projection matrix $\underline{\boldsymbol{P}}^t = \underline{\boldsymbol{I}} - \underline{\boldsymbol{n}}^{\mathrm{S}} \otimes \underline{\boldsymbol{n}}^{\mathrm{S}}$. This is a reasonable assumption for many problem configurations and enables the answering of various relevant questions. Still, the present work should also be seen as a solid basis for the extension towards frictional contact.

2.1.10.1 Contact without Surrounding Fluid

In classical contact mechanics, the influence of surrounding fluid on the solid bodies is not considered and zero interface traction is assumed outside of the contact zone. In the case that the interface condition on the remaining part of the interface $\breve{\Gamma}^{\mathrm{S}_1,c} \setminus \Gamma^{\mathrm{S}_1,c} \subseteq \Gamma^{\mathrm{S}_1,\mathrm{N}}$ and $\breve{\Gamma}^{\mathrm{S}_2,c} \setminus \Gamma^{\mathrm{S}_2,c} \subseteq \Gamma^{\mathrm{S}_2,\mathrm{N}}$ equals a zero-traction Neumann boundary condition ($\hat{\underline{\boldsymbol{h}}}^{\mathrm{S}_1,\mathrm{N}} = \hat{\underline{\boldsymbol{h}}}^{\mathrm{S}_2,\mathrm{N}} = \underline{\boldsymbol{0}}$), as shown in Figure 2.5 (right), the balance of linear momentum (2.70) is automatically valid for the overall potential contact interface $\breve{\Gamma}^{\mathrm{S}_1,c} \cup \breve{\Gamma}^{\mathrm{S}_2,c}$ and not only on $\Gamma^{\mathrm{SS},c}$. Considering no adhesive forces on the contact interface, the conditions in normal direction on the potential contact interface are given by the classical set Karush-Kuhn-Tucker (KKT) conditions, also referred to as Herz-Signorini-Moreau (HSM) conditions.

$$g^n \geq 0 \quad \text{on} \quad \breve{\Gamma}^{\mathrm{S}_1,c} \cup \breve{\Gamma}^{\mathrm{S}_2,c} \tag{2.72}$$

$$h^{\mathrm{S},*,n} \leq 0 \quad \text{on} \quad \breve{\Gamma}^{\mathrm{S}_1,c} \cup \breve{\Gamma}^{\mathrm{S}_2,c} \tag{2.73}$$

$$g^n h^{\mathrm{S},*,n} = 0 \quad \text{on} \quad \breve{\Gamma}^{\mathrm{S}_1,c} \cup \breve{\Gamma}^{\mathrm{S}_2,c} \tag{2.74}$$

Therein, the normal contact traction $h^{\mathrm{S},*,n}$ on the different parts of the potential contact interface $\breve{\Gamma}^{\mathrm{S}_1,c} \cup \breve{\Gamma}^{\mathrm{S}_2,c}$ is specified by

$$h^{\mathrm{S},*,n} = \begin{cases} \underline{\boldsymbol{h}}^{\mathrm{S,I}} \cdot \underline{\boldsymbol{n}}^{\mathrm{S}_1} & \text{on} \quad \Gamma^{\mathrm{SS},c} \\ \hat{\underline{\boldsymbol{h}}}^{\mathrm{S}_1,\mathrm{N}} \cdot \underline{\boldsymbol{n}}^{\mathrm{S}_1} = 0 & \text{on} \quad \Gamma^{\mathrm{S}_1,\mathrm{N}} \\ \hat{\underline{\boldsymbol{h}}}^{\mathrm{S}_2,\mathrm{N}} \cdot \underline{\boldsymbol{n}}^{\mathrm{S}_2} = 0 & \text{on} \quad \Gamma^{\mathrm{S}_2,\mathrm{N}}. \end{cases} \tag{2.75}$$

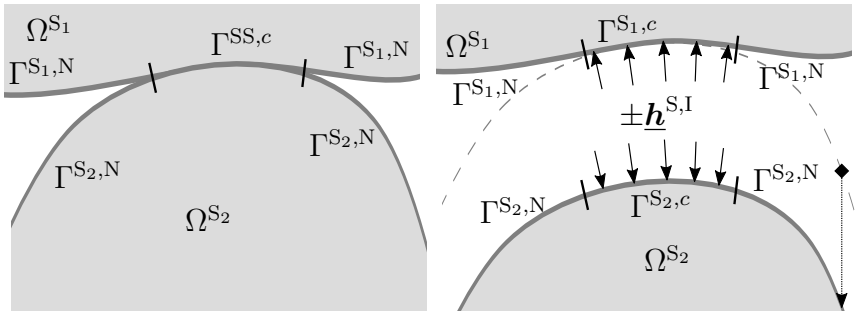

Figure 2.5: Contact of two bodies without surrounding fluid. The involved interfaces and domains for contacting configuration are shown (left). Visualization of the contact with separated solid bodies and demonstration of the contact traction $\underline{\boldsymbol{h}}^{S,I}$ (right).

Condition (2.72) represents the solely geometry-based no-penetration condition between both solid bodies. The limitation to no-adhesive stress in the contact zone is given by condition (2.73). Finally, the complementary condition (2.74) exclusively ensures a vanishing gap (contact zone on $\Gamma^{SS,c}$) or a vanish interface traction (zero-traction zone on $\Gamma^{S,N}$).

2.1.10.2 Contact with Surrounding Fluid

In contrast to the discussion in the previous section, the influence of the surrounding fluid is not neglected within this thesis. Figure 2.6 shows an exemplary configuration for such an FSCI problem. The interface conditions on the non-contacting part of the interface $\breve{\Gamma}^{S_1,c} \setminus \Gamma^{S_1,c} \subseteq \Gamma^{FS_1}$ and $\breve{\Gamma}^{S_2,c} \setminus \Gamma^{S_2,c} \subseteq \Gamma^{FS_2}$ are given by the FSI interface conditions, which were already discussed in Section 2.1.7. As the interface traction on an FSI interface does not vanish in general, the relation (2.70) is not fulfilled on the entire potential contact interface $\breve{\Gamma}^{S_1,c} \cup \breve{\Gamma}^{S_2,c}$, which is in contrast to the classical contact configuration. Thus, either the balance of linear momentum solely on the "active" contact interface can be enforced (see Chapter 5) or an alternative formulation of condition (2.70) is considered (see Chapter 6 and 7). To formulate a continuous problem, the

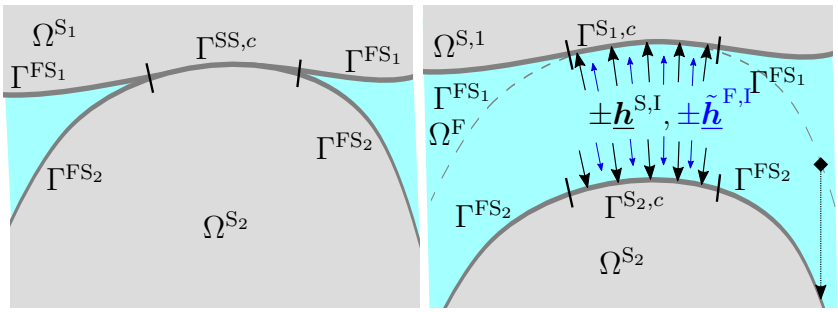

Figure 2.6: Contact of two bodies with surrounding fluid. The involved interfaces and domains for contacting configuration are shown (left). Visualization of the contact with separated solid bodies and demonstration of the contact traction $\underline{\boldsymbol{h}}^{S,I}$ and the "fictive" fluid traction $\tilde{\underline{\boldsymbol{h}}}^{F,I}$ (right).

"fictive" fluid traction $\tilde{\underline{\boldsymbol{h}}}^{F,I} (\approx \underline{\boldsymbol{\sigma}}^{F} \cdot \underline{\boldsymbol{n}}^{S_1})$ is introduced in the contact zone $\Gamma^{SS,c}$. It represents the fluid traction in the contact zone and is denoted differently as the fluid traction $\underline{\boldsymbol{h}}^{F,I} (= \underline{\boldsymbol{\sigma}}^{F} \cdot \underline{\boldsymbol{n}}^{F})$ on the interface of the fluid domain $\Gamma^{F,I}$. This distinction is due to the non-existent fluid domain

in the contact zone when analyzing the FSCI configuration on a macroscopic scale. On the line separating the contact and fluid-structure interface, the traction $\underline{\tilde{\boldsymbol{h}}}^{\mathrm{F,I}}$ has to coincide with the fluid interface traction and as a result of the dynamic equilibrium on the fluid-structure interface (2.59) has to be equal to the solid interface traction

$$\underline{\tilde{\boldsymbol{h}}}^{\mathrm{F,I}} = \underline{\boldsymbol{h}}^{\mathrm{F,I}} \left(\underline{\boldsymbol{n}}^{\mathrm{F}} \cdot \underline{\boldsymbol{n}}^{\mathrm{S}_1} \right) = \underline{\boldsymbol{h}}^{\mathrm{S,I}} \quad \text{on} \quad \overline{\Gamma^{\mathrm{SS},c}} \cap \overline{\Gamma^{\mathrm{FS}}}. \tag{2.76}$$

By taking criteria (2.76) for the specification of $\underline{\tilde{\boldsymbol{h}}}^{\mathrm{F,I}}$ into account, the definition of $\underline{\tilde{\boldsymbol{h}}}^{\mathrm{F,I}}$ allows incorporating the effect of fluid flow between the contacting bodies. Depending on the problem configuration and the quantities of interest, different approaches to specify this traction $\underline{\tilde{\boldsymbol{h}}}^{\mathrm{F,I}}$ can be applied. To model rough surface contact, in Chapter 5, a poroelastic layer is added to the contact interface, which allows specifying the fluid traction inside of the contact zone by the porous fluid pressure. In Chapter 6, a simpler and less complex extension-based approach is considered to define the fluid traction $\underline{\tilde{\boldsymbol{h}}}^{\mathrm{F,I}}$. Finally, in Chapter 7, a combination of the previously mentioned approaches based on extension close to the fluid domain and based on the porous fluid pressure far from the fluid domain is applied. In the following, the traction $\underline{\tilde{\boldsymbol{h}}}^{\mathrm{F,I}}$ is assumed to be defined and the discussion of the different variants is left to the previously referenced chapters.

Assuming that the solid bodies in contact do not transmit adhesive forces, the contact conditions in normal direction including the effect of surrounding fluid on the potential contact interface are given as

$$g^n \geq 0 \quad \text{on} \quad \breve{\Gamma}^{\mathrm{S}_1,c} \cup \breve{\Gamma}^{\mathrm{S}_2,c} \tag{2.77}$$

$$h^{\mathrm{S},*,n} - h^{\mathrm{F},*,n} \leq 0 \quad \text{on} \quad \breve{\Gamma}^{\mathrm{S}_1,c} \cup \breve{\Gamma}^{\mathrm{S}_2,c} \tag{2.78}$$

$$g^n \left(h^{\mathrm{S},*,n} - h^{\mathrm{F},*,n} \right) = 0 \quad \text{on} \quad \breve{\Gamma}^{\mathrm{S}_1,c} \cup \breve{\Gamma}^{\mathrm{S}_2,c}. \tag{2.79}$$

Therein, the relative normal contact traction $h^{\mathrm{S},*,n} - h^{\mathrm{F},*,n}$ on the different parts of the potential contact interface $\breve{\Gamma}^{\mathrm{S}_1,c} \cup \breve{\Gamma}^{\mathrm{S}_2,c}$ is specified by

$$h^{\mathrm{S},*,n} - h^{\mathrm{F},*,n} = \begin{cases} \underline{\boldsymbol{h}}^{\mathrm{S,I}} \cdot \underline{\boldsymbol{n}}^{\mathrm{S}_1} - \underline{\tilde{\boldsymbol{h}}}^{\mathrm{F,I}} \cdot \underline{\boldsymbol{n}}^{\mathrm{S}_1} & \text{on} \quad \Gamma^{\mathrm{SS},c} \\ \underline{\boldsymbol{h}}^{\mathrm{S}_1,\mathrm{I}} \cdot \underline{\boldsymbol{n}}^{\mathrm{S}_1} - \underline{\boldsymbol{h}}^{\mathrm{F,I}} \cdot \underline{\boldsymbol{n}}^{\mathrm{F}} & \text{on} \quad \Gamma^{\mathrm{FS}_1} \\ \underline{\boldsymbol{h}}^{\mathrm{S}_2,\mathrm{I}} \cdot \underline{\boldsymbol{n}}^{\mathrm{S}_2} - \underline{\boldsymbol{h}}^{\mathrm{F,I}} \cdot \underline{\boldsymbol{n}}^{\mathrm{F}} & \text{on} \quad \Gamma^{\mathrm{FS}_2}. \end{cases} \tag{2.80}$$

The purely geometry-based no-penetration condition (2.77), equals condition (2.72) for contact without surrounding fluid. The negativity of the relative contact traction in condition (2.78) guarantees that no adhesive forces directly act between the solid bodies. As a result, contacting solid bodies will "lift-off" if the fluid pressure in the contact zone exceeds the solid contact traction. Finally, the complementary condition (2.79) guarantees the exclusiveness of a vanishing gap (contact zone on $\Gamma^{\mathrm{SS},c}$) or a vanishing relative interface traction (dynamic equilibrium (2.59) fulfilled on Γ^{FS}).

Remark 2.7 (Consideration of contact as an additional constraint)**.** *In contrast to this presentation of contact with surrounding flow by splitting the potential contact interface into the "active" contact interface part $\Gamma^{\mathrm{SS},c}$ and the fluid-structure interaction part Γ^{FS}, an alternative view on this situation is often pursued. Therein, the potential deformation but not the topological change*

of the fluid-structure interface is considered. To include contact, in addition to the traction arising from fluid-structure interaction a contact traction is applied in the contact zone. Interpreting contact as an additional constraint to a FSI configuration naturally results in this point of view. While such an approach can still result in sound or even similar numerical formulations, some aspects should be discussed at this stage.

- *Most often there is no discussion concerning the "fictive" fluid stress in the contact zone. However, as no topological changes of* Γ^{FS} *are considered, to enforce the FSI conditions (*(2.59) *and* (2.60)*) on* $\Gamma^{\mathrm{SS},c}$*, a "fictive" fluid state is required on this part of the interface. In the case that a numerical approach provides such a fluid state outside of the physical fluid domain* Ω^{F} *and as a result also on* $\Gamma^{\mathrm{SS},c}$ *by default, the discussion on this "fictive" fluid state does not automatically show up. It should be pointed out that such a fluid state evaluated outside of the physical fluid domain* Ω^{F} *(*$\partial\Omega^{\mathrm{F}} \cap \Gamma^{\mathrm{SS},c} = \emptyset$*) is always non-physical. Depending on the question of interest and the underlying numerical approach, this automatically given "fictive" fluid state might not be a sufficiently good implicit model of fluid in the contact zone.*

- *For this type of approach, two accumulating interface stress contributions, namely the FSI traction and the contact traction, are added on* $\Gamma^{\mathrm{SS},c}$*. Especially for large contacting areas and as a result large distances of points on* $\Gamma^{\mathrm{SS},c}$ *to the fluid domain* Ω^{F}*, the utilized FSI traction can be very sensitive with respect to the system state variables. This aspect can become critical when finally solving the nonlinear FSCI problem by a numerical approach.*

- *The FSI traction on* $\Gamma^{\mathrm{SS},c}$ *already includes a tangential stress component. Thus, the application of classical frictional laws for contact, such as the Coulomb friction laws, which cover the entire tangential tension and not the difference to a tangential FSI traction, is difficult. This difficulty arises already for the formulation of frictionless contact.*

2.2 The Discrete Problem: Discretization of the Continuous Problem

The formulations presented in the previous sections include infinite-dimensional (continuous) solution spaces. To make this problem accessible for the numerical solution, an approximation leading to a finite-dimensional problem has to be performed. Within this thesis, a separate discretization of the spatial and temporal components of the PDEs is used. Therefore, by the temporal discretization a semi-discrete formulation of the physical problem is derived. With a subsequently applied spatial discretization the fully discrete problem can be obtained. Alternative approaches, such as Space-time approaches which pursue for a simultaneous discretization in space and time are not considered in this thesis.

For the temporal discretization, the one-step θ-scheme is applied, which is used in all numerical examples presented in this thesis. Section 2.2.1 gives a compact description of the temporal discretization procedure for systems including first and second order derivatives in time. Alternative schemes such as the generalized α-scheme (see the related works of Chung and Hulbert [65], Jansen *et al.* [130]) for the discretization in time are not considered in this thesis.

For the spatial discretization the continuous Finite Element Method (FEM) is applied exclusively. In Section 2.2.2, a compact discussion of all essential steps for application of the FEM is given. For further insight, the reader is referred to one of the numerous textbooks for solid mechanics, e.g., Belytschko *et al.* [25], Zienkiewicz *et al.* [236, 238], for fluid dynamics, e.g., Donea and Huerta [73], Zienkiewicz *et al.* [237], and for poroelasticity, e.g., Lewis and Schrefler [142]. Alternative types of spatial discretization techniques such as the Finite Volume approach, the Discontinuous Galerkin method, the Finite Differences approach or meshfree methods are beyond the scope of this thesis. The discretization of the continuous problems presented in Sections 2.1.4, 2.1.5 and 2.1.6 is given in the subsequent Sections 2.2.3, 2.2.4 and 2.2.5, respectively.

2.2.1 Temporal Discretization

For temporal discretization, the time interval of interest $t \in]t_0, t_\mathrm{E}]$ is split into a finite number (n_t) of time intervals $t \in \bigcup_{n=0}^{n_\mathrm{t}-1}]t_n, t_{n+1}]$ with $t_\mathrm{E} = t_{n_\mathrm{t}}$. The time step size represents the length of each time interval $\Delta t_n = t_{n+1} - t_n$. If no additional index n is given for the time step size, an equal time step size for all intervals is considered.

The One-Step-θ scheme includes a scalar parameter $\theta \in [0.0, 1.0]$. For a "small" parameter $\theta \in [0.0, 0.5[$ the scheme is conditionally stable, whereas for $\theta \in [0.5, 1.0]$ the resulting scheme is unconditionally stable for linear problems. Depending on the parameter θ, different well-known schemes for the temporal discretization are recovered. For $\theta = 0.0$ the first order accurate in time $(\mathrm{Err}_\mathrm{t} \sim \mathcal{O}(\Delta t))$ explicit Euler scheme is recovered. The Crank-Nicolson method ($\theta = 0.5$) enables second order convergence of the temporal error $(\mathrm{Err}_\mathrm{t} \sim \mathcal{O}(\Delta t^2))$. As a last special case, selecting $\theta = 1.0$, the fully implicit backward Euler scheme, which is first order accurate in time $(\mathrm{Err}_\mathrm{t} \sim \mathcal{O}(\Delta t))$, is recovered. In the following, solely the unconditionally stable implicit range of parameter θ will be applied.

2.2.1.1 System including First Order Time Derivatives

Considering the following system which includes a first order time derivative and is valid for the time interval $]t_n, t_{n+1}]$,with constant matrix $\underline{\mathsf{M}}$, time- and state-dependent vector-valued function $\underline{\mathbf{f}}$, and the unknown time-depend vector-valued velocity vector $\underline{\mathbf{v}}$,

$$\underline{\mathsf{M}} \frac{\partial \underline{\mathbf{v}}(t)}{\partial t} = -\underline{\mathbf{f}}(\underline{\mathbf{v}}(t), t) \quad \text{in } t \in]t_n, t_{n+1}], \tag{2.81}$$

the One-Step-θ scheme approximates time derivatives in the interval $t \in]t_n, t_{n+1}]$ by

$$\underline{\mathsf{M}} \frac{\underline{\mathbf{v}}_{n+1} - \underline{\mathbf{v}}_n}{\Delta t} = -\theta \underline{\mathbf{f}}(\underline{\mathbf{v}}_{n+1}, t_{n+1}) - (1-\theta)\, \underline{\mathbf{f}}(\underline{\mathbf{v}}_n, t_n). \tag{2.82}$$

Herein, $\underline{\mathbf{v}}_{n+1} = \underline{\mathbf{v}}\,(t_{n+1})$ and $\underline{\mathbf{v}}_n = \underline{\mathbf{v}}\,(t_n)$ is the velocity at the start and end point of the interval. The velocity $\underline{\mathbf{v}}_n$ is either known from the initial conditions or the solution of a previous time interval. Therefore, the unknown velocity $\underline{\mathbf{v}}_{n+1}$ can be computed from

$$\underline{\mathsf{M}}\, \underline{\mathbf{v}}_{n+1} + \Delta t \theta \underline{\mathbf{f}}(\underline{\mathbf{v}}_{n+1}, t_{n+1}) = \underline{\mathsf{M}}\, \underline{\mathbf{v}}_n - (1-\theta)\, \Delta t \underline{\mathbf{f}}(\underline{\mathbf{v}}_n, t_n). \tag{2.83}$$

The application of expression (2.83) for the previous time interval $t \in]t_{n-1}, t_n]$ allows formulating a One-Step-θ scheme avoiding explicit computation of contributions arising from the last time step

$$-\Delta t \underline{\mathbf{f}}(\underline{\mathbf{v}}_n, t_n) = \theta^{-1} \left(\underline{\mathsf{M}}\, \underline{\mathbf{v}}_n - \underline{\mathsf{M}}\, \underline{\mathbf{v}}_{n-1} \right) + \theta^{-1} (1-\theta)\, \Delta t \underline{\mathbf{f}}(\underline{\mathbf{v}}_{n-1}, t_{n-1}). \tag{2.84}$$

For application of this approach, the vector $\underline{\mathbf{f}}_0 := \underline{\mathbf{f}}(\underline{\mathbf{v}}_0, t_0)$ has to be given for the first time interval $t \in]t_0, t_1]$, if an implicit scheme $\theta \neq 1$ is considered, whereas for all subsequent intervals, expression (2.84) is applied.

2.2.1.2 System including Second Order Time Derivatives

For systems including second order time derivatives, two systems with first order time derivatives, which are equivalent, are formulated

$$\underline{\mathsf{M}} \frac{\partial^2 \underline{\mathbf{u}}(t)}{\partial t^2} = -\underline{\mathbf{f}}(\underline{\mathbf{u}}(t), t) \quad \text{in }]t_n, t_{n+1}], \tag{2.85}$$

$$\Leftrightarrow \frac{\partial \underline{\mathbf{u}}(t)}{\partial t} = \underline{\mathbf{v}}(t) \quad \text{and} \quad \underline{\mathsf{M}} \frac{\partial \underline{\mathbf{v}}(t)}{\partial t} = -\underline{\mathbf{f}}(\underline{\mathbf{u}}(t), t) \quad \text{in }]t_n, t_{n+1}]. \tag{2.86}$$

This system includes the constant matrix $\underline{\mathsf{M}}$, the time- and state-dependent vector-valued function $\underline{\mathbf{f}}$, and the unknown time-depend vector-valued state vectors displacement $\underline{\mathbf{u}}$ and velocity $\underline{\mathbf{v}}$. Introducing the approximation (2.82) for the time derivatives of velocity $\underline{\mathbf{v}}(t)$ and displacement $\underline{\mathbf{u}}(t)$ and eliminating of the velocity $\underline{\mathbf{v}}_{n+1}$ leads to the following relation for the unknown displacement $\underline{\mathbf{u}}_{n+1}$

$$\underline{\mathsf{M}}\, \underline{\mathbf{u}}_{n+1} + (\theta \Delta t)^2\, \underline{\mathbf{f}}(\underline{\mathbf{u}}_{n+1}, t_{n+1}) = \underline{\mathsf{M}}\, (\underline{\mathbf{u}}_n + \Delta t \underline{\mathbf{v}}_n) - (1-\theta)\, \theta \Delta t^2 \underline{\mathbf{f}}(\underline{\mathbf{u}}_n, t_n). \tag{2.87}$$

Herein, the displacement $\underline{\mathbf{u}}_n$ is again either known from the initial conditions or the solution of a previous time interval and the velocity $\underline{\mathbf{v}}_n$ can be computed by

$$\underline{\mathbf{v}}_n = -\frac{(1-\theta)}{\theta} \underline{\mathbf{v}}_{n-1} + \frac{\underline{\mathbf{u}}_n - \underline{\mathbf{u}}_{n-1}}{\theta \Delta t}. \tag{2.88}$$

2.2.1.3 Notation for Temporal Discretization

To allow for a compact presentation of the time-discrete formulations, the following notation is used. The evaluation of a state $\underline{\mathbf{u}}(t)$ or the function $\underline{\mathbf{f}}(\underline{\mathbf{u}}(t), t)$ at the intermediate point in time $t_{n+\theta} = \theta t_{n+1} + (1-\theta)\, t_n$ is defined as follows

$$\underline{\mathbf{u}}_{n+\theta} := \theta \underline{\mathbf{u}}_{n+1} + (1-\theta)\, \underline{\mathbf{u}}_n, \tag{2.89}$$

$$\underline{\mathbf{f}}_{n+\theta} := \theta \underline{\mathbf{f}}(\underline{\mathbf{u}}_{n+1}, t_{n+1}) + (1-\theta)\, \underline{\mathbf{f}}(\underline{\mathbf{u}}_n, t_n). \tag{2.90}$$

The discrete first and second order time derivatives at the intermediate point in time are denoted by

$$\tilde{\partial}_t \left[\underline{\mathbf{v}}\right]_{n+\theta} := \frac{\underline{\mathbf{v}}_{n+1} - \underline{\mathbf{v}}_n}{\Delta t} = \theta \tilde{\partial}_t \left[\underline{\mathbf{v}}\right]_{n+1} + (1-\theta)\, \tilde{\partial}_t \left[\underline{\mathbf{v}}\right]_n, \tag{2.91}$$

$$\tilde{\partial}_t^2 \left[\underline{\mathbf{u}}\right]_{n+\theta} := \frac{\underline{\mathbf{u}}_{n+1} - \underline{\mathbf{u}}_n}{\theta \Delta t^2} - \frac{\underline{\mathbf{v}}_n}{\theta \Delta t} = \theta \tilde{\partial}_t^2 \left[\underline{\mathbf{u}}\right]_{n+1} + (1-\theta)\, \tilde{\partial}_t^2 \left[\underline{\mathbf{u}}\right]_n. \tag{2.92}$$

The discrete time derivatives at the end point in time t_{n+1} are given, according to the One-Step-θ scheme, as

$$\tilde{\partial}_t \left[\underline{\mathbf{v}}\right]_{n+1} := \frac{\underline{\mathbf{v}}_{n+1} - \underline{\mathbf{v}}_n}{\theta \Delta t} - \frac{1-\theta}{\theta} \tilde{\partial}_t \left[\underline{\mathbf{v}}\right]_n , \tag{2.93}$$

$$\tilde{\partial}_t^2 \left[\underline{\mathbf{u}}\right]_{n+1} := \frac{\underline{\mathbf{u}}_{n+1} - \underline{\mathbf{u}}_n}{\theta^2 \Delta t^2} - \frac{\underline{\mathbf{v}}_n}{\theta^2 \Delta t} - \frac{1-\theta}{\theta} \tilde{\partial}_t^2 \left[\underline{\mathbf{u}}\right]_n . \tag{2.94}$$

For time-discrete $\mathcal{L}^2$-inner products integrated on time-dependent current domains, the following notation is used

$$\begin{aligned} (\underline{\boldsymbol{a}}, \underline{\boldsymbol{b}})_{\Omega^*_{n+1}, n+\theta} :=& \int_{\Omega^*(t_{n+1})} \left((\underline{\boldsymbol{a}} \circ \Xi) \odot (\underline{\boldsymbol{b}} \circ \Xi) \right)_{n+\theta} \circ \Xi_{n+1}^{-1} \, \mathrm{d}\Omega^* \\ =& \theta \int_{\Omega^*(t_{n+1})} \left((\underline{\boldsymbol{a}} \circ \Xi) \odot (\underline{\boldsymbol{b}} \circ \Xi) \right)_{n+1} \circ \Xi_{n+1}^{-1} \, \mathrm{d}\Omega^* \\ &+ (1-\theta) \int_{\Omega^*(t_{n+1})} \left((\underline{\boldsymbol{a}} \circ \Xi) \odot (\underline{\boldsymbol{b}} \circ \Xi) \right)_{n} \circ \Xi_{n+1}^{-1} \, \mathrm{d}\Omega^* . \end{aligned} \tag{2.95}$$

Herein, $\Xi_n := \Xi\left(\underline{\boldsymbol{\chi}}, t_n\right)$ denotes the mapping between reference and current configuration at a specific point in time $t = t_n$. When using the compact notation (2.95), occurring discrete time derivatives have to be evaluated as: $(\tilde{\partial}_t \left[\underline{\boldsymbol{b}}\right] \circ \Xi)_{n^*} = \tilde{\partial}_t \left[\underline{\boldsymbol{b}} \circ \Xi\right]_{n^*}$. For time-discrete $\mathcal{L}^2$-inner products integrated on the material domains, the following notation is used

$$\begin{aligned} (\underline{\boldsymbol{a}}, \underline{\boldsymbol{b}})_{\Omega^*_0, n+\theta} :=& \int_{\Omega^*_0} (\underline{\boldsymbol{a}} \odot \underline{\boldsymbol{b}})_{n+\theta} \, \mathrm{d}\Omega^*_0 \\ =& \theta \int_{\Omega^*_0} (\underline{\boldsymbol{a}} \odot \underline{\boldsymbol{b}})_{n+1} \, \mathrm{d}\Omega^*_0 + (1-\theta) \int_{\Omega^*_0} (\underline{\boldsymbol{a}} \odot \underline{\boldsymbol{b}})_{n} \, \mathrm{d}\Omega^*_0 . \end{aligned} \tag{2.96}$$

This simplified form of (2.95) results from the mapping $\Psi = const(t)$ between reference configuration and material configuration for the Lagrangian observer that is constant in time.

Application of the presented notation to the systems introduced in Sections 2.2.1.1 and 2.2.1.2 results in the compact notation

$$\underbrace{\underline{\mathsf{M}} \, \tilde{\partial}_t \left[\underline{\mathbf{v}}\right]_{n+\theta} = -\underline{\mathbf{f}}_{n+\theta}}_{\text{equivalent to (2.82)}} \quad \text{and} \quad \underbrace{\underline{\mathsf{M}} \, \tilde{\partial}_t^2 \left[\underline{\mathbf{u}}\right]_{n+\theta} = -\underline{\mathbf{f}}_{n+\theta}}_{\text{equivalent to (2.87)}} . \tag{2.97}$$

2.2.2 Spatial Discretization: The Boundary-Fitted Finite Element Method

In the following section, the spatial discretization of the weak forms (2.21), (2.33), and (2.56) by the continuous Galerkin Finite Element Method (cG-FEM) for boundary-fitted discretizations is discussed. This serves as a basis for the unfitted Finite Element Method, the CutFEM, which will be discussed in Chapter 3.

To discretize the continuous problem, the domain of interest Ω^*(i.e., $\Omega^{\mathrm{S}}_0, \Omega^{\mathrm{F}}, \Omega^{\mathrm{P}}$, or Ω^{P}_0), on which the weak form is integrated, is approximated by a discrete domain $\Omega^*_{\mathrm{h}} \approx \Omega^*$. Automatically, the resulting discrete outer boundary $\partial\Omega^*_{\mathrm{h}}$ leads to a discrete representation of all boundaries such as $\Gamma^{*,\mathrm{N}}_{\mathrm{h}}$ and $\Gamma^{*,\mathrm{D}}_{\mathrm{h}}$.

To enable numerical calculations using the FEM, a computation mesh is required. This mesh consists of a set of n^*_{ele} elements with non-overlapping domain $\Omega^*_{\mathcal{T}_\mathrm{h},e}$ of every element e. Mostly, the element types are triangles, tetrahedra, quadrilaterals or hexahedrals depending on the spatial dimension of the considered problem. The characteristic geometric length of an element (e.g. a specific edge length or the volume equivalent diameter) is called the element size h. The domain covered by the computational mesh $\breve{\Omega}^*_{\mathcal{T}_\mathrm{h}}$ results from the union of all element domains $\Omega^*_{\mathcal{T}_\mathrm{h},e}$.

$$\breve{\Omega}^*_{\mathcal{T}_\mathrm{h}} = \bigcup_{e=1}^{n^*_{\mathrm{ele}}} \Omega^*_{\mathcal{T}_\mathrm{h},e} \tag{2.98}$$

In the case of a boundary-fitted mesh, the approximated discrete domain Ω^*_h and the domain represented by the elements $\breve{\Omega}^*_{\mathcal{T}_\mathrm{h}}$ are equal.

$$\text{boundary-fitted: } \Omega^*_\mathrm{h} = \quad \breve{\Omega}^*_{\mathcal{T}_\mathrm{h}}. \tag{2.99}$$

The geometry of an element $\Omega^*_{\mathcal{T}_\mathrm{h},e}$ is specified by the position $\underline{\mathbf{x}}_i$ of node $i = 1...n^*_{\mathrm{nod},e}$ of $n^*_{\mathrm{nod},e}$ element nodes, which are specific points inside the element or on its boundary. For the cG-FEM, neighboring elements share their nodes at common faces or edges, which results in a smaller number of global nodes n^*_{nod} in $\breve{\Omega}^*_{\mathcal{T}_\mathrm{h}}$ as the sum of all element nodes $n^*_{\mathrm{nod}} \leq \sum_{e=1}^{n^*_{\mathrm{ele}}} n^*_{\mathrm{nod},e}$. A common edge ($d = 2$) or a common face ($d = 3$) of element i and element j is given by the common part of the element outer boundary: $\mathcal{F}^*_{i,j} = \partial\Omega^*_{\mathcal{T}_\mathrm{h},i} \cap \partial\Omega^*_{\mathcal{T}_\mathrm{h},j}$, $i \neq j$, $i,j = 1...n^*_{\mathrm{ele}}$. The set of all inner faces of a discretization is denoted by $\mathcal{F}_{\breve{\Omega}^*_{\mathcal{T}_\mathrm{h}}} = \left\{\mathcal{F}^*_{i,j} : i,j = 1...n^*_{\mathrm{ele}}, i < j\right\}$.

For each element domain $\Omega^*_{\mathcal{T}_\mathrm{h},e}$, a local coordinate system with coordinate $\underline{\boldsymbol{\xi}}$ and a specific coordinate range in the domain $\Omega^*_{\mathcal{T}_\mathrm{h},e,\mathrm{loc}}$ (which solely depends on the element type), is defined. Based on this local coordinate $\underline{\boldsymbol{\xi}}$, $n^*_{\mathrm{nod},e}$ Lagrange polynomials $\tilde{N}_i\left(\underline{\boldsymbol{\xi}}\right)$ of polynomial degree p with $i = 1...n^*_{\mathrm{nod},e}$ are defined for all element types. The Lagrange polynomials fulfill: $\sum_{i=1}^{n^*_{\mathrm{nod},i}} \tilde{N}_i\left(\underline{\boldsymbol{\xi}}\right) = 1$, $\tilde{N}_i\left(\underline{\boldsymbol{\xi}}_i\right) = 1$, and as a result: $\tilde{N}_i\left(\underline{\boldsymbol{\xi}}_j\right) = 0$ with $i \neq j$, $i,j = 1...n^*_{\mathrm{nod},e}$. Herein, $\underline{\boldsymbol{\xi}}_i$ are the local coordinates at the respective element node i. The consideration of alternative functions to Lagrangian polynomials, such as NURBS, is beyond the scope of this thesis. Due to the aforementioned properties, these shape functions $\tilde{N}_i\left(\underline{\boldsymbol{\xi}}\right)$ can be applied to interpolate any quantity defined at the nodal positions inside of the element. Applying the isoparametric concept, any position $\underline{\boldsymbol{x}}$ of a given local coordinate $\underline{\boldsymbol{\xi}}$ inside the element can be computed by the nodal positions $\underline{\mathbf{x}}_i$

$$\underline{\boldsymbol{x}}\left(\underline{\boldsymbol{\xi}}\right) = \sum_{i=1}^{n^*_{\mathrm{nod},e}} \tilde{N}_i\left(\underline{\boldsymbol{\xi}}\right) \cdot \underline{\mathbf{x}}_i \quad \text{in} \quad \Omega^*_{\mathcal{T}_\mathrm{h},e}. \tag{2.100}$$

The element-specific mapping Υ_e from the element local coordinate system (coordinate $\underline{\boldsymbol{\xi}}$) to the global coordinate system (coordinate $\underline{\boldsymbol{x}}$) can therefore be defined as

$$\Upsilon_e\left(\underline{\boldsymbol{\xi}}\right) : \begin{cases} \Omega^*_{\mathcal{T}_\mathrm{h},e,\mathrm{loc}} \rightarrow \Omega_{\mathcal{T}_\mathrm{h},e}, \\ \underline{\boldsymbol{\xi}} \mapsto \Upsilon_e\left(\underline{\boldsymbol{\xi}}\right) = \underline{\boldsymbol{x}}\left(\underline{\boldsymbol{\xi}}\right). \end{cases} \tag{2.101}$$

Application of the mapping Υ_e on (2.100) for every element allows defining the shape function $N_j\left(\underline{\boldsymbol{x}}\right)$ in the global coordinate system

$$N_j\left(\underline{\boldsymbol{x}}\right) = \sum_{e=1}^{n^*_{\mathrm{ele}}} N_j\left(\underline{\boldsymbol{x}}\right)|_{\Omega^*_{\mathcal{T}_\mathrm{h},e}}, \quad \text{with} \quad N_j\left(\underline{\boldsymbol{x}}\right)|_{\Omega^*_{\mathcal{T}_\mathrm{h},e}} = \tilde{N}_i\left(\Upsilon_e^{-1}\left(\underline{\boldsymbol{x}}\right)\right)\Big|_{\Omega^*_{\mathcal{T}_\mathrm{h},e}}, \tag{2.102}$$

with the local index $i = 1...n^*_{\mathrm{nod},e}$ specifying the nodes of a single element $\Omega^*_{\mathcal{T}_\mathrm{h},e}$ and the global index $j = 1...n^*_{\mathrm{nod}}$ specifying all nodes in $\breve{\Omega}^*_{\mathcal{T}_\mathrm{h}}$. For all global nodes j which are not connected to the element e, the shape function of node j is zero in element e. Making use of (2.102), a finite-dimensional approximation of the continuous scalar field a or vector field $\underline{\boldsymbol{a}}$ can be obtained by its nodal values a_j and $\underline{\mathbf{a}}_j$, respectively.

$$a\left(\underline{\boldsymbol{x}}\right) \approx a_\mathrm{h}\left(\underline{\boldsymbol{x}}\right) = \sum_{j=1}^{n^*_{\mathrm{nod}}} N_j\left(\underline{\boldsymbol{x}}\right)\mathsf{a}_j \quad \text{and} \quad \underline{\boldsymbol{a}}\left(\underline{\boldsymbol{x}}\right) \approx \underline{\boldsymbol{a}}_\mathrm{h}\left(\underline{\boldsymbol{x}}\right) = \sum_{j=1}^{n^*_{\mathrm{nod}}} N_j\left(\underline{\boldsymbol{x}}\right)\underline{\mathbf{a}}_j \quad \text{in} \quad \breve{\Omega}^*_{\mathcal{T}_\mathrm{h}}. \tag{2.103}$$

If the quantity $a(t)$ or $\underline{\boldsymbol{a}}(t)$ is depending on time, for the approximation solely the nodal values $\mathsf{a}_j(t)$ or $\underline{\mathbf{a}}_j(t)$ depend on time but not the shape functions $N_j\left(\underline{\boldsymbol{x}}\right)$ as long as the domain $\Omega_{\mathcal{T}_\mathrm{h},e}$ and therefore the mapping Υ_e do not change in time. In the case the domain $\Omega_{\mathcal{T}_\mathrm{h},e}$ and therefore the mapping Υ_e is time-dependent (e.g. for an ALE fluid formulation as a result of the time-dependent domain Ω^F), there is still a constant reference configuration in which the nodal shape functions are constant in time. The discrete function space for the approximations (2.103) is then given by all shape functions

$$\mathcal{N}_\mathrm{h} = \left\{ a_\mathrm{h} \in \operatorname*{span}_{1\leq j\leq n^*_{\mathrm{nod}}} \left[N_j\left(\underline{\boldsymbol{x}}\right)\right] \right\} \quad \text{and} \quad \mathcal{N}^d_\mathrm{h} = \left\{ \underline{\boldsymbol{a}}_\mathrm{h} \in \operatorname*{span}_{1\leq j\leq n^*_{\mathrm{nod}}} \left[N_j\left(\underline{\boldsymbol{x}}\right)\right]^d \right\}. \tag{2.104}$$

It should be pointed out, that due to the shared boundary nodes of neighboring elements, there is only one shape function $N_j\left(\underline{\boldsymbol{x}}\right)$ per node, which leads to a continuous approximation space on the boundaries between elements.

In the following, the approximation (2.103) will be used to discretize the respective unknowns and the test functions of the structural, the fluid and the poroelastic weak form leading to a so-called Bubnov-Galerkin method. In general, the primal unknowns and the test functions could be discretized by different discrete approximation spaces leading to a so-called Petrov-Galerkin method. This will not be considered for the discretization of the governing equations in the domains, but for the discretization of the contact Lagrange multiplier on the interface (see Section 5.3.2). In the following, the spatial discretization approach will be applied to derive a discrete formulation in each domain separately, starting from a semi-discrete (time discrete) form.

2.2.2.1 Notation for Spatial Discretization

The expression $\langle *, * \rangle_{\mathcal{F}_*}$ indicates the sum of all $\mathcal{L}^2$-inner products integrated on all faces $\mathcal{F}$ of the set $\mathcal{F}_*$

$$\langle *, * \rangle_{\mathcal{F}_*} = \sum_{\mathcal{F}\in\mathcal{F}_*} \langle *, * \rangle_{\mathcal{F}}. \tag{2.105}$$

For quantities evaluated at a specific face $\mathcal{F}$, the jump operator is given by: $[\![*]\!]_{\mathcal{F}} = [\![*]\!] = \left(*_{\mathcal{F}}^{+} - *_{\mathcal{F}}^{-}\right)$. The "+" and "−" sign herein specifies the evaluation of quantity "$*$" in positive or negative face normal direction. As this jump operator evaluated on a face is solely applied for symmetric $\mathcal{L}^2$-inner products of type $\langle [\![*]\!], [\![*]\!] \rangle_{\mathcal{F}}$, the choice of the normal orientation is arbitrary as it cancels out.

2.2.3 Structure

For the discretization of the continuous structural problem presented in Section 2.1.4, first, the temporal discretization of the balance of momentum in the formulation of the equation (2.15) according to equation (2.87) is performed. To result in a discrete formulation, this semi-discrete formulation has to be additionally discretized in space. Therefore, a time-discrete weak formulation, similar to the time continuous weak form (2.21), is derived. Then, a spatial discretization of this formulation is performed by the FEM as presented in Section 2.2.2. The test function $\delta\underline{\boldsymbol{u}}^{\mathrm{S}}$ and semi-discrete displacement $\underline{\boldsymbol{u}}^{\mathrm{S}}_{n+1}$ are analogously discretized to (2.103) by a computational mesh consisting of $n^{\mathrm{S}}_{\mathrm{ele}}$ elements and $n^{\mathrm{S}}_{\mathrm{nod}}$ computational nodes. This approximation for the point in time $t = t_{n+1}$ is denoted by $\delta\underline{\boldsymbol{u}}^{\mathrm{S}}_{\mathrm{h}}$ (does not depend on time) and $\underline{\boldsymbol{u}}^{\mathrm{S}}_{\mathrm{h},n+1}$. The discrete counterpart of the derived quantities, defined as continuous quantities in Section 2.1.4, are indicated by an additional subscript h. The vector $\underline{\mathbf{u}}^{\mathrm{S}}_{n+1}$ includes all nodal displacements. At a specific node with a global index $j = 1...n^{\mathrm{S}}_{\mathrm{nod}}$, the nodal displacement is denoted as $\underline{\mathbf{u}}^{\mathrm{S}}_{j,n+1}$. The incorporation of Dirichlet boundary conditions on $\Gamma^{\mathrm{S,D}}_{0}$ leads to the following solution and test function spaces of the discrete approximation

$$\begin{aligned}
\mathcal{S}_{\underline{\boldsymbol{u}}^{\mathrm{S}},\mathrm{h},n+1} &= \left\{ \underline{\boldsymbol{u}}^{\mathrm{S}}_{\mathrm{h}} \in \mathcal{N}^{d}_{\mathrm{h}}\left(\Omega^{\mathrm{S}}_{0,\mathrm{h}}\right) \,\middle|\, \underline{\boldsymbol{u}}^{\mathrm{S}}_{\mathrm{h}} = \underline{\hat{\boldsymbol{u}}}^{\mathrm{S}}\left(t_{n+1}\right) \text{ on } \Gamma^{\mathrm{S,D}}_{0,\mathrm{h}} \right\}, \\
\mathcal{T}_{\delta\underline{\boldsymbol{u}}^{\mathrm{S}},\mathrm{h}} &= \left\{ \delta\underline{\boldsymbol{u}}^{\mathrm{S}}_{\mathrm{h}} \in \mathcal{N}^{d}_{\mathrm{h}}\left(\Omega^{\mathrm{S}}_{0,\mathrm{h}}\right) \,\middle|\, \delta\underline{\boldsymbol{u}}^{\mathrm{S}}_{\mathrm{h}} = \underline{\mathbf{0}} \text{ on } \Gamma^{\mathrm{S,D}}_{0,\mathrm{h}} \right\}.
\end{aligned} \tag{2.106}$$

Then, the resulting discrete structural problem can be formulated.
Find $\underline{\boldsymbol{u}}^{\mathrm{S}}_{\mathrm{h},n+1} \in \mathcal{S}_{\underline{\boldsymbol{u}}^{\mathrm{S}},\mathrm{h},n+1}$ *such that for all* $\delta\underline{\boldsymbol{u}}^{\mathrm{S}}_{\mathrm{h}} \in \mathcal{T}_{\delta\underline{\boldsymbol{u}}^{\mathrm{S}},\mathrm{h}}$:

$$\mathcal{W}^{\mathrm{S}}_{\mathrm{h},n+1}\left[\delta\underline{\boldsymbol{u}}^{\mathrm{S}}_{\mathrm{h}}, \underline{\boldsymbol{u}}^{\mathrm{S}}_{\mathrm{h},n+1}\right] = 0, \tag{2.107}$$

with the resulting discrete form

$$\begin{aligned}
\mathcal{W}^{\mathrm{S}}_{\mathrm{h},n+1}\left[\delta\underline{\boldsymbol{u}}^{\mathrm{S}}_{\mathrm{h}}, \underline{\boldsymbol{u}}^{\mathrm{S}}_{\mathrm{h},n+1}\right] = &\left(\delta\underline{\boldsymbol{u}}^{\mathrm{S}}_{\mathrm{h}}, \rho^{\mathrm{S}}_{0}\tilde{\partial}^{2}_{t}\left[\underline{\boldsymbol{u}}^{\mathrm{S}}_{\mathrm{h}}\right]\right)_{\Omega^{\mathrm{S}}_{0,\mathrm{h}},n+\theta} + \left(\boldsymbol{\nabla}_{0}\delta\underline{\boldsymbol{u}}^{\mathrm{S}}_{\mathrm{h}}, \underline{\boldsymbol{P}}^{\mathrm{S}}_{\mathrm{h}}\right)_{\Omega^{\mathrm{S}}_{0,\mathrm{h}},n+\theta} \\
&- \left(\delta\underline{\boldsymbol{u}}^{\mathrm{S}}_{\mathrm{h}}, \rho^{\mathrm{S}}_{0}\hat{\underline{\boldsymbol{b}}}^{\mathrm{S}}_{0}\right)_{\Omega^{\mathrm{S}}_{0,\mathrm{h}},n+\theta} - \left\langle \delta\underline{\boldsymbol{u}}^{\mathrm{S}}_{\mathrm{h}}, \hat{\underline{\boldsymbol{h}}}^{\mathrm{S,N}}_{0}\right\rangle_{\Gamma^{\mathrm{S,N}}_{0,\mathrm{h}},n+\theta}.
\end{aligned} \tag{2.108}$$

It should be highlighted that the potential interface term on $\Gamma^{\mathrm{S,I}}_{0,\mathrm{h}}$ is not included in the discrete weak form in contrast to the presented continuous weak form (2.22). For non-coupled problems, this term does not exist and for coupled problems a specific form of this contribution will be added depending on the applied numerical approach, as presented in the following chapters. To allow for a compact presentation of this weak form, the notation given in Section 2.2.1.3 is used. The resulting system depends solely on the displacement $\underline{\boldsymbol{u}}^{\mathrm{S}}_{\mathrm{h},n+1}$ at t_{n+1} for given displacement $\underline{\boldsymbol{u}}^{\mathrm{S}}_{\mathrm{h},n}$ and velocity $\tilde{\partial}_{t}\left[\underline{\boldsymbol{u}}^{\mathrm{S}}_{\mathrm{h}}\right]_{n}$ at $t = t_{n}$. Selecting $(n^{\mathrm{S}}_{\mathrm{nod}} \cdot d)$ independent discrete test functions

$\left(\delta\underline{\boldsymbol{u}}^{\mathrm{S}}_{\mathrm{h}}\right)_1 \ldots \left(\delta\underline{\boldsymbol{u}}^{\mathrm{S}}_{\mathrm{h}}\right)_{\left(n^{\mathrm{S}}_{\mathrm{nod}}\cdot d\right)}$ and expressing the discrete displacements by the vector of its nodal values $\underline{\mathbf{u}}^{\mathrm{S}}_{n+1}$ according to the definition (2.103), leads to a system of nonlinear equations, which can be written in vector notation as

$$\underline{\mathbf{R}}^{\mathrm{S}}_{n+1}\left(\underline{\mathbf{u}}^{\mathrm{S}}_{n+1}\right) := \underline{\mathbf{A}}^{\mathrm{S}}_{n+1}\left(\underline{\mathbf{u}}^{\mathrm{S}}_{n+1}\right) + \underline{\mathbf{F}}^{\mathrm{S}}_{n+1} = \underline{\mathbf{0}}. \tag{2.109}$$

The structural residual vector $\underline{\mathbf{R}}^{\mathrm{S}}_{n+1}$ consists of $\underline{\mathbf{A}}^{\mathrm{S}}_{n+1}$, which includes all displacement-dependent contributions at $t = t_{n+1}$, and $\underline{\mathbf{F}}^{\mathrm{S}}_{n+1}$, which includes prescribed non-displacement-dependent contributions (such as the Neumann load or the body force) and all contribution arising from the previous point in time $t = t_n$. Finally, this nonlinear system of equations has to be solved for the unknown displacement vector $\underline{\mathbf{u}}^{\mathrm{S}}_{n+1}$. This aspect will be discussed in Section 2.3.

2.2.4 Fluid

In this section, a numerically solvable finite-dimensional discrete formulation for the continuous fluid problem, discussed in Section 2.1.5, is presented. As a first step, temporal discretization of the point-wise equations (2.27) and (2.28) with the time-discrete relation (2.82), which is based on the One-Step-θ scheme, is performed. A subsequent derivation of a time-discrete weak formulation (similar to the continuous weak form (2.33)) followed by a discretization in space by the FEM according to Section 2.2.2 has to be performed. Therein, the test functions $\delta\underline{\boldsymbol{v}}^{\mathrm{F}}$ and δp^{F}, the semi-discrete velocity $\underline{\boldsymbol{v}}^{\mathrm{F}}_{n+1}$, and the semi-discrete pressure p^{F}_{n+1} are discretized by the approximations given in (2.103) with a corresponding computational mesh consisting of $n^{\mathrm{F}}_{\mathrm{ele}}$ elements and $n^{\mathrm{F}}_{\mathrm{nod}}$ computational nodes. These approximations are denoted by $\delta\underline{\boldsymbol{v}}^{\mathrm{F}}_{\mathrm{h}}$ and $\delta p^{\mathrm{F}}_{\mathrm{h}}$ for the test functions and $\underline{\boldsymbol{v}}^{\mathrm{F}}_{\mathrm{h},n+1}$ and $p^{\mathrm{F}}_{\mathrm{h},n+1}$ for velocity and pressure at $t = t_{n+1}$. The vectors consisting of all nodal velocities and nodal pressures are denoted by $\underline{\mathbf{v}}^{\mathrm{F}}_{n+1}$ and $\underline{\mathbf{p}}^{\mathrm{F}}_{n+1}$, respectively. At a specific node with a global index $j = 1 \ldots n^{\mathrm{F}}_{\mathrm{nod}}$, the nodal velocity vector and pressure is given as $\underline{\mathbf{v}}^{\mathrm{F}}_{j,n+1}$ and $\underline{\mathbf{p}}^{\mathrm{F}}_{j,n+1}$. The resulting discrete test function and solution spaces for velocity and pressure with incorporated Dirichlet boundary conditions on $\Gamma^{\mathrm{F,D}}$ are

$$\begin{aligned}
\mathcal{S}_{\underline{\boldsymbol{v}}^{\mathrm{F}},\mathrm{h},n+1} &= \left\{ \underline{\boldsymbol{v}}^{\mathrm{F}}_{\mathrm{h}} \in \mathcal{N}^d_{\mathrm{h}}\left(\Omega^{\mathrm{F}}_{\mathrm{h}}\right) \,\middle|\, \underline{\boldsymbol{v}}^{\mathrm{F}}_{\mathrm{h}} = \underline{\hat{\boldsymbol{v}}}^{\mathrm{F}}\left(t_{n+1}\right) \text{ on } \Gamma^{\mathrm{F,D}}_{\mathrm{h}} \right\}, \; \mathcal{S}_{p^{\mathrm{F}},\mathrm{h}} = \left\{ p^{\mathrm{F}}_{\mathrm{h}} \in \mathcal{N}_{\mathrm{h}}\left(\Omega^{\mathrm{F}}_{\mathrm{h}}\right) \right\}, \\
\mathcal{T}_{\delta\underline{\boldsymbol{v}}^{\mathrm{F}},\mathrm{h}} &= \left\{ \delta\underline{\boldsymbol{v}}^{\mathrm{F}}_{\mathrm{h}} \in \mathcal{N}^d_{\mathrm{h}}\left(\Omega^{\mathrm{F}}_{\mathrm{h}}\right) \,\middle|\, \delta\underline{\boldsymbol{v}}^{\mathrm{F}}_{\mathrm{h}} = \underline{\mathbf{0}} \text{ on } \Gamma^{\mathrm{F,D}}_{\mathrm{h}} \right\}, \qquad \mathcal{T}_{\delta p^{\mathrm{F}},\mathrm{h}} = \left\{ \delta p^{\mathrm{F}}_{\mathrm{h}} \in \mathcal{N}_{\mathrm{h}}\left(\Omega^{\mathrm{F}}_{\mathrm{h}}\right) \right\}.
\end{aligned} \tag{2.110}$$

Remark 2.8 (Time dependence of fluid test function and solution spaces)**.** *Applying the ALE formulation and including moving boundaries in principle results in time-dependent discrete test function and solution spaces due to the time-dependent domain $\Omega^{\mathrm{F}}_{\mathrm{h},n+1} \neq \Omega^{\mathrm{F}}_{\mathrm{h},n}$, if expressed in current configuration. Still, if formulated in the reference configuration, no time dependence of these spaces occurs due to the domain change and therefore the temporal index is omitted.*

Then, the resulting discrete formulation of the fluid problem is formulated.
$Find\ \left(\underline{\boldsymbol{v}}^{\mathrm{F}}_{\mathrm{h},n+1}, p^{\mathrm{F}}_{\mathrm{h},n+1}\right) \in \mathcal{S}_{\underline{\boldsymbol{v}}^{\mathrm{F}},\mathrm{h},n+1} \times \mathcal{S}_{p^{\mathrm{F}},\mathrm{h}}\ such\ that\ for\ all\ \left(\delta\underline{\boldsymbol{v}}^{\mathrm{F}}_{\mathrm{h}}, \delta p^{\mathrm{F}}_{\mathrm{h}}\right) \in \mathcal{T}_{\delta\underline{\boldsymbol{v}}^{\mathrm{F}},\mathrm{h}} \times \mathcal{T}_{\delta p^{\mathrm{F}},\mathrm{h}}$:

$$\mathcal{W}^{\mathrm{F}}_{\mathrm{h},n+1}\left[\left(\delta\underline{\boldsymbol{v}}^{\mathrm{F}}_{\mathrm{h}}, \delta p^{\mathrm{F}}_{\mathrm{h}}\right), \left(\underline{\boldsymbol{v}}^{\mathrm{F}}_{\mathrm{h},n+1}, p^{\mathrm{F}}_{\mathrm{h},n+1}\right)\right] = 0. \tag{2.111}$$

The form resulting from the derivation and including an additional stabilization contribution $\mathcal{W}^{\mathrm{F}}_{\mathcal{S}_{\mathrm{h}},n+1}$ is

$$\begin{aligned}
\mathcal{W}^{\mathrm{F}}_{\mathrm{h},n+1}\left[\left(\delta\underline{\boldsymbol{v}}^{\mathrm{F}}_{\mathrm{h}},\delta p^{\mathrm{F}}_{\mathrm{h}}\right),\left(\underline{\boldsymbol{v}}^{\mathrm{F}}_{\mathrm{h},n+1},p^{\mathrm{F}}_{\mathrm{h},n+1}\right)\right] &= \left(\delta\underline{\boldsymbol{v}}^{\mathrm{F}}_{\mathrm{h}},\rho^{\mathrm{F}}\tilde{\partial}_t\left[\underline{\boldsymbol{v}}^{\mathrm{F}}_{\mathrm{h}}\right]\right)_{\Omega^{\mathrm{F}}_{\mathrm{h},n+1},n+\theta} \\
&+\left(\delta\underline{\boldsymbol{v}}^{\mathrm{F}}_{\mathrm{h}},\rho^{\mathrm{F}}\left(\underline{\boldsymbol{v}}^{\mathrm{F}}_{\mathrm{h}}-\tilde{\partial}_t\left[\underline{\boldsymbol{u}}^{\mathrm{G}}_{\mathrm{h}}\right]\right)\cdot\boldsymbol{\nabla}\underline{\boldsymbol{v}}^{\mathrm{F}}_{\mathrm{h}}\right)_{\Omega^{\mathrm{F}}_{\mathrm{h},n+1},n+\theta}-\left(\boldsymbol{\nabla}\cdot\delta\underline{\boldsymbol{v}}^{\mathrm{F}}_{\mathrm{h}},p^{\mathrm{F}}_{\mathrm{h}}\right)_{\Omega^{\mathrm{F}}_{\mathrm{h},n+1},n+\theta} \\
&+\left(\underline{\boldsymbol{\epsilon}}^{\mathrm{F}}(\delta\underline{\boldsymbol{v}}^{\mathrm{F}}_{\mathrm{h}}),2\mu^{\mathrm{F}}\underline{\boldsymbol{\epsilon}}^{\mathrm{F}}(\underline{\boldsymbol{v}}^{\mathrm{F}}_{\mathrm{h}})\right)_{\Omega^{\mathrm{F}}_{\mathrm{h},n+1},n+\theta}-\left(\delta\underline{\boldsymbol{v}}^{\mathrm{F}}_{\mathrm{h}},\rho^{\mathrm{F}}\hat{\underline{\boldsymbol{b}}}^{\mathrm{F}}\right)_{\Omega^{\mathrm{F}}_{\mathrm{h},n+1},n+\theta}-\left\langle\delta\underline{\boldsymbol{v}}^{\mathrm{F}}_{\mathrm{h}},\hat{\underline{\boldsymbol{h}}}^{\mathrm{F,N}}\right\rangle_{\Gamma^{\mathrm{F,N}}_{\mathrm{h},n+1},n+\theta} \\
&+\left(\delta p^{\mathrm{F}}_{\mathrm{h}},\boldsymbol{\nabla}\cdot\underline{\boldsymbol{v}}^{\mathrm{F}}_{\mathrm{h}}\right)_{\Omega^{\mathrm{F}}_{\mathrm{h},n+1},n+\theta}+\mathcal{W}^{\mathrm{F}}_{\mathcal{S}_{\mathrm{h}},n+1}\left[\left(\delta\underline{\boldsymbol{v}}^{\mathrm{F}}_{\mathrm{h}},\delta p^{\mathrm{F}}_{\mathrm{h}}\right),\left(\underline{\boldsymbol{v}}^{\mathrm{F}}_{\mathrm{h},n+1},p^{\mathrm{F}}_{\mathrm{h},n+1}\right)\right]. \quad (2.112)
\end{aligned}$$

As for the structural problem, the potential interface term on $\Gamma^{\mathrm{F,I}}_{\mathrm{h}}$ is not included in the discrete weak form and specific formulations of this term will be added for the coupled problem in the subsequent chapters. Details on the stabilization of the discrete fluid problem by $\mathcal{W}^{\mathrm{F}}_{\mathcal{S}_{\mathrm{h}},n+1}$ are presented in Section 2.2.4.1. Insertion of all definition in Section 2.2.1.3, leads to a system solely depending on the discrete state $\left(\underline{\boldsymbol{v}}^{\mathrm{F}}_{\mathrm{h},n+1},p^{\mathrm{F}}_{\mathrm{h},n+1}\right)$ at a new point in time $t=t_{n+1}$ for a given state $\left(\underline{\boldsymbol{v}}^{\mathrm{F}}_{\mathrm{h},n},p^{\mathrm{F}}_{\mathrm{h},n}\right)$ at time $t=t_n$. In the case a moving mesh is applied, the grid motion is considered to be given.

Selecting $(n^{\mathrm{F}}_{\mathrm{nod}}\cdot(d+1))$ independent discrete test functions $\left(\delta\underline{\boldsymbol{v}}^{\mathrm{F}}_{\mathrm{h}},\delta p^{\mathrm{F}}_{\mathrm{h}}\right)_1 \ldots \left(\delta\underline{\boldsymbol{v}}^{\mathrm{F}}_{\mathrm{h}},\delta p^{\mathrm{F}}_{\mathrm{h}}\right)_{(n^{\mathrm{F}}_{\mathrm{nod}}\cdot(d+1))}$ and making use of definition (2.103) leads to a system of nonlinear equations which are depending on the vectors of nodal velocities $\underline{\mathbf{v}}^{\mathrm{F}}_{n+1}$ and nodal pressure vectors $\underline{\mathbf{p}}^{\mathrm{F}}_{n+1}$. In vector notation, this system can be written as

$$\underline{\mathbf{R}}^{\mathrm{F}}_{n+1}\left(\underline{\mathbf{v}}^{\mathrm{F}}_{n+1},\underline{\mathbf{p}}^{\mathrm{F}}_{n+1}\right):=\underline{\mathbf{A}}^{\mathrm{F}}_{n+1}\left(\underline{\mathbf{v}}^{\mathrm{F}}_{n+1},\underline{\mathbf{p}}^{\mathrm{F}}_{n+1}\right)+\underline{\mathbf{F}}^{\mathrm{F}}_{n+1}=\underline{\mathbf{0}}. \quad (2.113)$$

The fluid residual vector $\underline{\mathbf{R}}^{\mathrm{F}}_{n+1}$ is build up by $\underline{\mathbf{A}}^{\mathrm{F}}_{n+1}$, which contains all velocity and pressure-dependent contributions at $t=t_{n+1}$, and $\underline{\mathbf{F}}^{\mathrm{F}}_{n+1}$ which includes prescribed non-velocity and non-pressure-dependent contributions as well as contributions depending on the state of the previous point in time $t=t_n$. For solving the fluid problem, this system of nonlinear equations has to be solved for the state vectors $(\underline{\mathbf{v}}^{\mathrm{F}}_{n+1},\underline{\mathbf{p}}^{\mathrm{F}}_{n+1})$ at every time step, which will be discussed in Section 2.3.

2.2.4.1 Stabilization of the Discrete Fluid Problem

In contrast to the continuous weak form (2.27), the discrete weak form (2.111) has to contain an additional stabilization contribution $\mathcal{W}^{\mathrm{F}}_{\mathcal{S}_{\mathrm{h}},n+1}$. The necessity for these additional terms arises from different types of discrete instabilities. As it can be seen from the definition of the discrete spaces for velocity and pressure (2.110) and the underlying discrete spaces (2.104), shape functions of equal polynomial order p are utilized for velocity and pressure. For such equal-order interpolations the Ladyzhenskaya-Babuška-Breezi (LBB) condition is violated, prohibiting the convergence of the numerical error for such a scheme. Discretizations that directly lead to LBB-stable pairs of velocity and pressure are not considered within this thesis. Additionally, a local loss of control over the convective term in combination with the requirement to ensure sufficient control on the incompressibility can lead to computed solutions which are non-physical.

There are several approaches, which lead to different stabilization contributions $\mathcal{W}^{\mathrm{F}}_{\mathcal{S}_{\mathrm{h}},n+1}$, to overcome these issues. A comparison of the classical residual-based, the face-oriented and the local projection-based stabilization method for incompressible flow problems is given by Braack *et al.* [34]. Stabilization techniques based on the residual-based variational multiscale framework combine a streamline-upwind-Petrov-Galerkin (SUPG), a pressure-stabilizing-Petrov-Galerkin (PSPG) and a least-squares incompressibility constraint (Grad-Div) stabilization. Although residual-based stabilization provides one possible stabilization technique suitable for the considered problem, this technique is not applied in the numerical examples presented in this thesis. Further details on the residual-based variational multiscale framework can be found in e.g. Hughes *et al.* [128]. The reader is referred to the theses of Shahmiri [198], Rasthofer [177] and Schott [187] for the application of residual-based techniques on similar problem configurations (including CutFEM).

In this thesis, the face-oriented stabilization (FOS) for $d = 3$, also called edge-oriented stabilization (EOS) for $d = 2$ or continuous-interior penalty method (CIP) is applied exclusively. This technique goes back to Douglas and Dupont [77], where a penalty on the jump of normal derivatives on edges between elements was applied. An analysis of the FOS for the advection-diffusion problem was presented by Burman and Hansbo [43], for the Stokes problem by Burman and Hansbo [44], the linear fluid problem by Burman *et al.* [50], and for the time-dependent Navier–Stokes equations by Burman and Fernández [40].

In the FOS technique, the jumps of derivatives integrated on all inner faces of the fluid discretization $\mathcal{F}_{\Omega^{\mathrm{F}}_{\mathrm{h,n+1}}}$ are penalized. For a continuous velocity and pressure solution, such a stabilization approach is weakly consistent. A fully implicit treatment for the time-discretization of the stabilization as presented by Burman and Fernández [41] is applied. Then, the stabilization contribution are given as

$$\mathcal{W}^{\mathrm{F}}_{\mathcal{S}_{\mathrm{h}},n+1}\left[\left(\delta\underline{\boldsymbol{v}}^{\mathrm{F}}_{\mathrm{h}},\delta p^{\mathrm{F}}_{\mathrm{h}}\right),\left(\underline{\boldsymbol{v}}^{\mathrm{F}}_{\mathrm{h},n+1},p^{\mathrm{F}}_{\mathrm{h},n+1}\right)\right] = \tag{2.114}$$

$$\left\langle \tau^{\mathrm{F}}_{u}\left[\!\left[\boldsymbol{\nabla}\delta\underline{\boldsymbol{v}}^{\mathrm{F}}_{\mathrm{h}}\right]\!\right],\left[\!\left[\boldsymbol{\nabla}\underline{\boldsymbol{v}}^{\mathrm{F}}_{\mathrm{h}}\right]\!\right]\right\rangle_{\mathcal{F}_{\Omega^{\mathrm{F}}_{\mathrm{h},n+1}},n+1} \tag{2.115}$$

$$+\left\langle \tau^{\mathrm{F}}_{p}\left[\!\left[\boldsymbol{\nabla}\delta p^{\mathrm{F}}_{\mathrm{h}}\right]\!\right],\left[\!\left[\boldsymbol{\nabla}p^{\mathrm{F}}_{\mathrm{h}}\right]\!\right]\right\rangle_{\mathcal{F}_{\Omega^{\mathrm{F}}_{\mathrm{h},n+1}},n+1} \tag{2.116}$$

$$+\left\langle \tau^{\mathrm{F}}_{div}\left[\!\left[\boldsymbol{\nabla}\cdot\delta\underline{\boldsymbol{v}}^{\mathrm{F}}_{\mathrm{h}}\right]\!\right],\left[\!\left[\boldsymbol{\nabla}\cdot\underline{\boldsymbol{v}}^{\mathrm{F}}_{\mathrm{h}}\right]\!\right]\right\rangle_{\mathcal{F}_{\Omega^{\mathrm{F}}_{\mathrm{h},n+1}},n+1}. \tag{2.117}$$

Herein, line (2.115) accounts for convective instabilities, line (2.116) enables the use of equal order interpolation for velocity and pressure, and line (2.117) facilitates additional control on the incompressibility constraint. The occurring parameters $\tau^{\mathrm{F}}_{p},\tau^{\mathrm{F}}_{u}$ and τ^{F}_{div}, which are constant for each face $\mathcal{F}$, are defined as

$$\begin{aligned}
\tau^{\mathrm{F}}_{u} &= \gamma_{u}\left(\rho^{\mathrm{F}}\left|\left|\underline{\boldsymbol{v}}^{\mathrm{F}}_{\mathrm{h}}-\tilde{\partial}_{t}\left[\underline{\boldsymbol{u}}^{\mathrm{G}}_{\mathrm{h}}\right]\right|\right|_{\infty,\mathcal{F}}\right)^{2}h^{3}_{\mathcal{F}}\left(\Phi^{\mathrm{F}}_{\mathcal{F}}\right)^{-1},\\
\tau^{\mathrm{F}}_{p} &= \gamma_{p}h^{3}_{\mathcal{F}}\left(\Phi^{\mathrm{F}}_{\mathcal{F}}\right)^{-1},\quad \tau^{\mathrm{F}}_{div}=\gamma_{div}h_{\mathcal{F}}\Phi^{\mathrm{F}}_{\mathcal{F}},\\
\text{with}\quad \Phi^{\mathrm{F}}_{\mathcal{F}} &= \mu^{\mathrm{F}}+h_{\mathcal{F}}c_{v}\rho^{\mathrm{F}}\left|\left|\underline{\boldsymbol{v}}^{\mathrm{F}}_{\mathrm{h}}-\tilde{\partial}_{t}\left[\underline{\boldsymbol{u}}^{\mathrm{G}}_{\mathrm{h}}\right]\right|\right|_{\infty,\mathcal{F}}+h^{2}_{\mathcal{F}}c_{t}\frac{\rho^{\mathrm{F}}}{\theta\Delta t}.
\end{aligned}\tag{2.118}$$

The constants therein are set to $\gamma_{p}=0.05$, $\gamma_{u}=0.05$, $\gamma_{div}=10^{-3}\gamma_{p}$, $c_{t}=1/12$, $c_{k}=1$, $c_{v}=1/6$. This definition equals the choice in Schott *et al.* [189, 190] and Massing *et al.* [149]. The

norm of the convective velocity $\left|\left|\underline{\boldsymbol{v}}^{\mathrm{F}} - \tilde{\partial}_t \left[\underline{\boldsymbol{u}}_{\mathrm{h}}^{\mathrm{G}}\right]\right|\right|_{\infty,\mathcal{F},n+1}$ equals the maximal velocity component within both elements $\Omega^{\mathrm{F}}_{\mathcal{T}_{\mathrm{h}},i}$ and $\Omega^{\mathrm{F}}_{\mathcal{T}_{\mathrm{h}},j}$ connected to the face $\mathcal{F} = \mathcal{F}_{i,j}$. The mesh size parameter $h_{\mathcal{F}}$ characterizes the maximum diameter of both elements connected to the face $\mathcal{F}$.

2.2.5 Poroelasticity

As for the pure structural and fluid problem, a numerically solvable finite-dimensional formulation of the continuous poroelastic problem, given in Section 2.1.6, is presented. In this formulation the porosity ϕ is not considered as an additional primary unknown. It is based on one of the presented formulations by Vuong *et al.* [216] and Vuong [215], that are applying an alternative numerical stabilization approach (see Section 2.2.5.1). In a first step, the point-wise equations to be solved (2.43), (2.44) and (2.46) are discretized in time by the One-Step-θ scheme. Therefore, the time-discrete relations (2.82) and (2.86) are applied to approximate the temporal derivative of first- and second-order. Based on the resulting equations, a time-discrete weak formulation is derived (similar to the derivation of the continuous weak form (2.56)). Finally, the spatial discretization by the FEM according to Section 2.2.2 is performed. The test functions $\delta\underline{\boldsymbol{v}}^{\mathrm{P}}, \delta\underline{\boldsymbol{u}}^{\mathrm{P}}, \delta p^{\mathrm{P}}$ and the semi-discrete fluid velocity $\underline{\boldsymbol{v}}^{\mathrm{P}}_{n+1}$, skeleton displacement $\underline{\boldsymbol{u}}^{\mathrm{P}}_{n+1}$, fluid pressure p^{P}_{n+1} are discretized with approximation (2.103) by a computational mesh consisting of $n^{\mathrm{P}}_{\mathrm{ele}}$ elements and $n^{\mathrm{P}}_{\mathrm{nod}}$ computational nodes. The discretized poroelastic test functions are denoted by $\delta\underline{\boldsymbol{v}}^{\mathrm{P}}_{\mathrm{h}}, \delta\underline{\boldsymbol{u}}^{\mathrm{P}}_{\mathrm{h}}, \delta p^{\mathrm{P}}_{\mathrm{h}}$ and the primary unknowns by $\underline{\boldsymbol{v}}^{\mathrm{P}}_{\mathrm{h},n+1}, \underline{\boldsymbol{u}}^{\mathrm{P}}_{\mathrm{h},n+1}, p^{\mathrm{P}}_{\mathrm{h},n+1}$ at the point in time $t = t_{n+1}$. The discrete counterparts of all derived quantities, defined as continuous quantities in Section 2.1.6, are indicated by an additional subscript h. The vectors including all nodal velocities, nodal displacements and nodal pressures are denoted by $\underline{\mathbf{v}}^{\mathrm{P}}_{n+1}, \underline{\mathbf{u}}^{\mathrm{P}}_{n+1}$, and $\underline{\mathbf{p}}^{\mathrm{P}}_{n+1}$, respectively. At a specific node with a global index $j = 1...n^{\mathrm{P}}_{\mathrm{nod}}$, the nodal velocity vector, nodal displacement vector, and nodal pressures is given as $\underline{\mathbf{v}}^{\mathrm{P}}_{j,n+1}$,$\underline{\mathbf{u}}^{\mathrm{P}}_{j,n+1}$, and $\underline{\mathbf{p}}^{\mathrm{P}}_{j,n+1}$, respectively. Consequently, the resulting discrete test function and solution spaces for velocity, displacement and pressure including incorporated Dirichlet boundary conditions on $\Gamma^{\mathrm{P,D}}_0$ or $\Gamma^{\mathrm{P^F,D}}$ are

$$
\begin{aligned}
\mathcal{S}_{\underline{\boldsymbol{v}}^{\mathrm{P}},\mathrm{h},n+1} &= \left\{ \underline{\boldsymbol{v}}^{\mathrm{P}}_{\mathrm{h}} \in \mathcal{N}^d_{\mathrm{h}}\left(\Omega^{\mathrm{P}}_{\mathrm{h}}\right) \left| \underline{\boldsymbol{v}}^{\mathrm{P}}_{\mathrm{h}} \cdot \underline{\boldsymbol{n}}^{\mathrm{P}}_{\mathrm{h}} = \hat{v}^{\mathrm{P},n}\left(t_{n+1}\right) \text{ on } \Gamma^{\mathrm{P^F,D}}_{\mathrm{h}} \right.\right\}, \\
\mathcal{S}_{\underline{\boldsymbol{u}}^{\mathrm{P}},\mathrm{h},n+1} &= \left\{ \underline{\boldsymbol{u}}^{\mathrm{P}}_{\mathrm{h}} \in \mathcal{N}^d_{\mathrm{h}}\left(\Omega^{\mathrm{P}}_{0,\mathrm{h}}\right) \left| \underline{\boldsymbol{u}}^{\mathrm{P}}_{\mathrm{h}} = \hat{\underline{\boldsymbol{u}}}^{\mathrm{P}}\left(t_{n+1}\right) \text{ on } \Gamma^{\mathrm{P,D}}_{0,\mathrm{h}} \right.\right\}, \\
\mathcal{S}_{p^{\mathrm{P}},\mathrm{h}} &= \left\{ p^{\mathrm{P}}_{\mathrm{h}} \in \mathcal{N}_{\mathrm{h}}\left(\Omega^{\mathrm{P}}_{\mathrm{h}}\right) \right\}, \\
\mathcal{T}_{\delta\underline{\boldsymbol{v}}^{\mathrm{P}},\mathrm{h}} &= \left\{ \delta\underline{\boldsymbol{v}}^{\mathrm{P}}_{\mathrm{h}} \in \mathcal{N}^d_{\mathrm{h}}\left(\Omega^{\mathrm{P}}_{\mathrm{h}}\right) \left| \delta\underline{\boldsymbol{v}}^{\mathrm{P}}_{\mathrm{h}} \cdot \underline{\boldsymbol{n}}^{\mathrm{P}}_{\mathrm{h}} = 0 \text{ on } \Gamma^{\mathrm{P^F,D}}_{\mathrm{h}} \right.\right\}, \\
\mathcal{T}_{\delta\underline{\boldsymbol{u}}^{\mathrm{P}},\mathrm{h}} &= \left\{ \delta\underline{\boldsymbol{u}}^{\mathrm{S}}_{\mathrm{h}} \in \mathcal{N}^d_{\mathrm{h}}\left(\Omega^{\mathrm{P}}_{0,\mathrm{h}}\right) \left| \delta\underline{\boldsymbol{u}}^{\mathrm{P}}_{\mathrm{h}} = \underline{\mathbf{0}} \text{ on } \Gamma^{\mathrm{P,D}}_{0,\mathrm{h}} \right.\right\}, \\
\mathcal{T}_{\delta p^{\mathrm{P}},\mathrm{h}} &= \left\{ \delta p^{\mathrm{P}}_{\mathrm{h}} \in \mathcal{N}_{\mathrm{h}}\left(\Omega^{\mathrm{P}}_{\mathrm{h}}\right) \right\}.
\end{aligned}
\tag{2.119}
$$

In principle, all porous flow solution and test function spaces are time-dependent due to the deformation and formulation of the governing equations in the current configuration. Just as for the fluid discretization this is not indicated by an additional subscript as the function spaces are not depending on time if formulated in the corresponding reference configuration.

Then, the resulting discrete formulation of the poroelastic problem can be formulated.
$Find\ \left(\underline{\boldsymbol{v}}^{\mathrm{P}}_{\mathrm{h},n+1}, \underline{\boldsymbol{u}}^{\mathrm{P}}_{\mathrm{h},n+1}, p^{\mathrm{P}}_{\mathrm{h},n+1}\right) \in \mathcal{S}_{\underline{\boldsymbol{v}}^{\mathrm{P}},\mathrm{h},n+1} \times \mathcal{S}_{\underline{\boldsymbol{u}}^{\mathrm{P}},\mathrm{h},n+1} \times \mathcal{S}_{p^{\mathrm{P}},\mathrm{h}}\ such\ that\ for\ all\ \left(\delta\underline{\boldsymbol{v}}^{\mathrm{P}}_{\mathrm{h}}, \delta\underline{\boldsymbol{u}}^{\mathrm{P}}_{\mathrm{h}}, \delta p^{\mathrm{P}}_{\mathrm{h}}\right) \in$

$\mathcal{T}_{\delta\underline{\boldsymbol{v}}^{\mathrm{P}},\mathrm{h}} \times \mathcal{T}_{\delta\underline{\boldsymbol{u}}^{\mathrm{P}},\mathrm{h}} \times \mathcal{T}_{\delta p^{\mathrm{P}},\mathrm{h}}$:

$$\mathcal{W}^{\mathrm{P}}_{\mathrm{h},n+1}\left[\left(\delta\underline{\boldsymbol{v}}^{\mathrm{P}}_{\mathrm{h}},\delta\underline{\boldsymbol{u}}^{\mathrm{P}}_{\mathrm{h}},\delta p^{\mathrm{P}}_{\mathrm{h}}\right),\left(\underline{\boldsymbol{v}}^{\mathrm{P}}_{\mathrm{h},n+1},\underline{\boldsymbol{u}}^{\mathrm{P}}_{\mathrm{h},n+1},p^{\mathrm{P}}_{\mathrm{h},n+1}\right)\right]=0. \tag{2.120}$$

The form resulting from the derivation including an additional stabilization contribution $\mathcal{W}^{\mathrm{P}}_{\mathcal{S}_{\mathrm{h}},n+1}$ for the discrete problem is:

$$\begin{aligned}
\mathcal{W}^{\mathrm{P}}_{\mathrm{h},n+1}\left[\left(\delta\underline{\boldsymbol{v}}^{\mathrm{P}}_{\mathrm{h}},\delta\underline{\boldsymbol{u}}^{\mathrm{P}}_{\mathrm{h}},\delta p^{\mathrm{P}}_{\mathrm{h}}\right),\left(\underline{\boldsymbol{v}}^{\mathrm{P}}_{\mathrm{h},n+1},\underline{\boldsymbol{u}}^{\mathrm{P}}_{\mathrm{h},n+1},p^{\mathrm{P}}_{\mathrm{h},n+1}\right)\right] &= \left(\delta p^{\mathrm{P}}_{\mathrm{h}},\tilde{\partial}_t\left[\phi_{\mathrm{h}}\right]\right)_{\Omega^{\mathrm{P}}_{\mathrm{h},n+1},n+\theta} \\
&+\left(\delta p^{\mathrm{P}}_{\mathrm{h}},\phi_{\mathrm{h}}\boldsymbol{\nabla}\cdot\tilde{\partial}_t\left[\underline{\boldsymbol{u}}^{\mathrm{P}}_{\mathrm{h}}\right]\right)_{\Omega^{\mathrm{P}}_{\mathrm{h},n+1},n+\theta}-\left(\boldsymbol{\nabla}\delta p^{\mathrm{P}}_{\mathrm{h}},\phi_{\mathrm{h}}\left(\underline{\boldsymbol{v}}^{\mathrm{P}}_{\mathrm{h}}-\tilde{\partial}_t\left[\underline{\boldsymbol{u}}^{\mathrm{P}}_{\mathrm{h}}\right]\right)\right)_{\Omega^{\mathrm{P}}_{\mathrm{h},n+1},n+\theta} \\
&+\left\langle\delta p^{\mathrm{P}}_{\mathrm{h}},\phi_{\mathrm{h}}\underline{\boldsymbol{n}}^{\mathrm{P}}_{\mathrm{h}}\cdot\left(\underline{\boldsymbol{v}}^{\mathrm{P}}_{\mathrm{h}}-\tilde{\partial}_t\left[\underline{\boldsymbol{u}}^{\mathrm{P}}_{\mathrm{h}}\right]\right)\right\rangle_{\partial\Omega^{\mathrm{P}}_{\mathrm{h},n+1},n+\theta}+\left(\delta\underline{\boldsymbol{v}}^{\mathrm{P}}_{\mathrm{h}},\rho^{\mathrm{F}}\tilde{\partial}_t\left[\underline{\boldsymbol{v}}^{\mathrm{P}}_{\mathrm{h}}\right]\right)_{\Omega^{\mathrm{P}}_{\mathrm{h},n+1},n+\theta} \\
&-\left(\boldsymbol{\nabla}\cdot\delta\underline{\boldsymbol{v}}^{\mathrm{P}}_{\mathrm{h}},p^{\mathrm{P}}_{\mathrm{h}}\right)_{\Omega^{\mathrm{P}}_{\mathrm{h},n+1},n+\theta}-\left(\delta\underline{\boldsymbol{v}}^{\mathrm{P}}_{\mathrm{h}},\rho^{\mathrm{F}}\tilde{\partial}_t\left[\underline{\boldsymbol{u}}^{\mathrm{P}}_{\mathrm{h}}\right]\cdot\boldsymbol{\nabla}\underline{\boldsymbol{v}}^{\mathrm{P}}_{\mathrm{h}}\right)_{\Omega^{\mathrm{P}}_{\mathrm{h},n+1},n+\theta} \\
&+\left(\delta\underline{\boldsymbol{v}}^{\mathrm{P}}_{\mathrm{h}},\mu^{\mathrm{F}}\phi_{\mathrm{h}}\underline{\boldsymbol{k}}^{-1}_{\mathrm{h}}\cdot\underline{\boldsymbol{v}}^{\mathrm{P}}_{\mathrm{h}}\right)_{\Omega^{\mathrm{P}}_{\mathrm{h},n+1},n+\theta}-\left(\delta\underline{\boldsymbol{v}}^{\mathrm{P}}_{\mathrm{h}},\mu^{\mathrm{F}}\phi_{\mathrm{h}}\underline{\boldsymbol{k}}^{-1}_{\mathrm{h}}\cdot\tilde{\partial}_t\left[\underline{\boldsymbol{u}}^{\mathrm{P}}_{\mathrm{h}}\right]\right)_{\Omega^{\mathrm{P}}_{\mathrm{h},n+1},n+\theta} \\
&-\left(\delta\underline{\boldsymbol{v}}^{\mathrm{P}}_{\mathrm{h}},\rho^{\mathrm{F}}\hat{\underline{\boldsymbol{b}}}^{\mathrm{P}^{\mathrm{F}}}\right)_{\Omega^{\mathrm{P}}_{\mathrm{h},n+1},n+\theta}-\left\langle\delta\underline{\boldsymbol{v}}^{\mathrm{P}}_{\mathrm{h}},\hat{h}^{\mathrm{P}^{\mathrm{F}},\mathrm{N}}\underline{\boldsymbol{n}}^{\mathrm{P}}_{\mathrm{h}}\right\rangle_{\Gamma^{\mathrm{P}^{\mathrm{F}},\mathrm{N}}_{\mathrm{h},n+1},n+\theta} \\
&+\left(\delta\underline{\boldsymbol{u}}^{\mathrm{P}}_{\mathrm{h}},\tilde{\rho}^{\mathrm{P}^{\mathrm{S}}}_0\tilde{\partial}^2_t\left[\underline{\boldsymbol{u}}^{\mathrm{P}}_{\mathrm{h}}\right]\right)_{\Omega^{\mathrm{P}}_{0,\mathrm{h}},n+\theta}+\left(\boldsymbol{\nabla}_0\delta\underline{\boldsymbol{u}}^{\mathrm{P}}_{\mathrm{h}},\underline{\boldsymbol{P}}^{\mathrm{P}}_{\mathrm{h}}\right)_{\Omega^{\mathrm{P}}_{0,\mathrm{h}},n+\theta} \\
&+\left(\delta\underline{\boldsymbol{u}}^{\mathrm{P}}_{\mathrm{h}},\mu^{\mathrm{F}}J^{\mathrm{P}}_{\mathrm{h}}\phi^2_{\mathrm{h}}\underline{\boldsymbol{k}}^{-1}_{\mathrm{h}}\cdot\tilde{\partial}_t\left[\underline{\boldsymbol{u}}^{\mathrm{P}}_{\mathrm{h}}\right]\right)_{\Omega^{\mathrm{P}}_{0,\mathrm{h}},n+\theta}-\left(\delta\underline{\boldsymbol{u}}^{\mathrm{P}}_{\mathrm{h}},\mu^{\mathrm{F}}J^{\mathrm{P}}_{\mathrm{h}}\phi^2_{\mathrm{h}}\underline{\boldsymbol{k}}^{-1}_{\mathrm{h}}\cdot\underline{\boldsymbol{v}}^{\mathrm{P}}_{\mathrm{h}}\right)_{\Omega^{\mathrm{P}}_{0,\mathrm{h}},n+\theta} \\
&-\left(\delta\underline{\boldsymbol{u}}^{\mathrm{P}}_{\mathrm{h}},J^{\mathrm{P}}_{\mathrm{h}}\phi_{\mathrm{h}}\left(\underline{\boldsymbol{F}}^{\mathrm{P}}_{\mathrm{h}}\right)^{-\mathsf{T}}\cdot\boldsymbol{\nabla}_0 p^{\mathrm{P}}_{\mathrm{h}}\right)_{\Omega^{\mathrm{P}}_{0,\mathrm{h}},n+\theta}-\left(\delta\underline{\boldsymbol{u}}^{\mathrm{P}}_{\mathrm{h}},\tilde{\rho}^{\mathrm{P}^{\mathrm{S}}}_0\hat{\underline{\boldsymbol{b}}}^{\mathrm{P}}_0\right)_{\Omega^{\mathrm{P}}_{0,\mathrm{h}},n+\theta}-\left\langle\delta\underline{\boldsymbol{u}}^{\mathrm{P}}_{\mathrm{h}},\hat{\underline{\boldsymbol{h}}}^{\mathrm{P},\mathrm{N}}_0\right\rangle_{\Gamma^{\mathrm{P},\mathrm{N}}_{0,\mathrm{h}},n+\theta} \\
&+\mathcal{W}^{\mathrm{P}}_{\mathcal{S}_{\mathrm{h}},n+1}\left[\left(\delta\underline{\boldsymbol{v}}^{\mathrm{P}}_{\mathrm{h}},\delta p^{\mathrm{P}}_{\mathrm{h}}\right),\left(\underline{\boldsymbol{v}}^{\mathrm{P}}_{\mathrm{h},n+1},\underline{\boldsymbol{u}}^{\mathrm{P}}_{\mathrm{h},n+1},p^{\mathrm{P}}_{\mathrm{h},n+1}\right)\right].
\end{aligned} \tag{2.121}$$

Not included herein are the potential interface terms on $\Gamma^{\mathrm{P,I}}_{\mathrm{h}}$ and $\Gamma^{\mathrm{P,I}}_{0,\mathrm{h}}$ which have to be treated in the case of an interface-coupled problem. Whereas these terms do not exist for non-coupled problems, different numerical approaches to incorporate the interface conditions, which will be discussed in the following chapters, result in additional terms on these interfaces. The stabilization contribtuion of the discrete poroelastic problem $\mathcal{W}^{\mathrm{P}}_{\mathcal{S}_{\mathrm{h}},n+1}$ is discussed in Section 2.2.5.1. Insertion of all definitions in Section 2.2.1.3 as well as the relations for derived quantities in Section 2.1.6, leads to a system solely depending on the discrete state $\left(\underline{\boldsymbol{v}}^{\mathrm{P}}_{\mathrm{h},n+1},\underline{\boldsymbol{u}}^{\mathrm{P}}_{\mathrm{h},n+1},p^{\mathrm{P}}_{\mathrm{h},n+1}\right)$ at a new point in time $t=t_{n+1}$ for a given state $\left(\underline{\boldsymbol{v}}^{\mathrm{P}}_{\mathrm{h},n},\underline{\boldsymbol{u}}^{\mathrm{P}}_{\mathrm{h},n},p^{\mathrm{P}}_{\mathrm{h},n},\tilde{\partial}_t\left[\underline{\boldsymbol{u}}^{\mathrm{P}}_{\mathrm{h}}\right]_n\right)$ at time $t=t_n$.

Remark 2.9 (Discretization of the porosity time derivative $\tilde{\partial}_t\left[\phi_{\mathrm{h}}\right]$)**.** *Due to the implicit definition of the porosity $\phi_{\mathrm{h},n+1}$ via the constitutive relation* (2.51)*, and thus, by the dependence on the state $\left(\underline{\boldsymbol{v}}^{\mathrm{P}}_{\mathrm{h},n+1},\underline{\boldsymbol{u}}^{\mathrm{P}}_{\mathrm{h},n+1},p^{\mathrm{P}}_{\mathrm{h},n+1}\right)$, special attention has to be paid to the treatment of the discrete porosity time derivative $\tilde{\partial}_t\left[\phi_{\mathrm{h}}\right]$ in* (2.121)*. As presented by Vuong [215], the partial derivatives of the porosity ϕ_{h} w.r.t. the fluid pressure $p^{\mathrm{P}}_{\mathrm{h}}$ and the displacement $\underline{\boldsymbol{u}}^{\mathrm{P}}_{\mathrm{h}}$ and their corresponding temporal derivatives are computed to formulate $\tilde{\partial}_t\left[\phi_{\mathrm{h}}\right]$.*

In analogy to the previous sections, to test the weak form (2.120), selecting $(n_{\mathrm{nod}}^{\mathrm{P}} \cdot (2d+1))$ independent discrete test functions $\left(\delta\underline{\boldsymbol{v}}_{\mathrm{h}}^{\mathrm{P}}, \delta\underline{\boldsymbol{u}}_{\mathrm{h}}^{\mathrm{P}}, \delta p_{\mathrm{h}}^{\mathrm{P}}\right)_1 \ldots \left(\delta\underline{\boldsymbol{v}}_{\mathrm{h}}^{\mathrm{P}}, \delta\underline{\boldsymbol{u}}_{\mathrm{h}}^{\mathrm{P}}, \delta p_{\mathrm{h}}^{\mathrm{P}}\right)_{(n_{\mathrm{nod}}^{\mathrm{P}}\cdot(2d+1))}$ and making use of definition (2.103) leads to a system of nonlinear equations which are depending on the vectors of nodal velocities $\underline{\mathbf{v}}_{n+1}^{\mathrm{P}}$, nodal displacements $\underline{\mathbf{u}}_{n+1}^{\mathrm{P}}$, and nodal pressure vectors $\underline{\mathbf{p}}_{n+1}^{\mathrm{P}}$. In vector notation, this system can be written as

$$\underline{\mathbf{R}}_{n+1}^{\mathrm{P}}\left(\underline{\mathbf{v}}_{n+1}^{\mathrm{P}}, \underline{\mathbf{u}}_{n+1}^{\mathrm{P}}, \underline{\mathbf{p}}_{n+1}^{\mathrm{P}}\right) := \underline{\mathbf{A}}_{n+1}^{\mathrm{P}}\left(\underline{\mathbf{v}}_{n+1}^{\mathrm{P}}, \underline{\mathbf{u}}_{n+1}^{\mathrm{P}}, \underline{\mathbf{p}}_{n+1}^{\mathrm{P}}\right) + \underline{\mathbf{F}}_{n+1}^{\mathrm{P}} = \underline{\mathbf{0}}. \tag{2.122}$$

Herein, $\underline{\mathbf{A}}_{n+1}^{\mathrm{P}}$ includes all velocity, displacement, and pressure-dependent contributions at $t = t_{n+1}$. All prescribed non-velocity, non-displacement, and non-pressure-dependent contributions as well as contributions depending on the state of the previous point in time $t = t_n$ are contained in $\underline{\mathbf{F}}_{n+1}^{\mathrm{P}}$. The sum of both contributions, which is the poroelastic residual vector $\underline{\mathbf{R}}_{n+1}^{\mathrm{P}}$, has to vanish. For solving the poroelastic problem, this system of nonlinear equations has to be solved for the state vectors $(\underline{\mathbf{v}}_{n+1}^{\mathrm{P}}\underline{\mathbf{u}}_{n+1}^{\mathrm{P}}, \underline{\mathbf{p}}_{n+1}^{\mathrm{P}})$ at every time step, which will be discussed in Section 2.3.

2.2.5.1 Stabilization of the Discrete Poroelastic Fluid Problem[1]

Analogous to the discrete fluid problem, the discrete weak form (2.120) includes an additional stabilization contribution $\mathcal{W}_{\mathcal{S}_{\mathrm{h}},n+1}^{\mathrm{P}}$. This is necessary due to the discretization of velocity and pressure (2.119) with discrete spaces constructed by shape functions of equal polynomial order p and additionally to ensure control on the incompressibility. For the poroelastic problem, a CIP stabilization, similar to the stabilization for the discrete fluid problem in Section 2.2.4.1, is applied. With this technique, jumps of derivatives integrated on all inner faces of the poroelastic discretization $\mathcal{F}_{\Omega_{\mathrm{h,n+1}}^{\mathrm{P}}}$ are penalized. The stabilization contributions are given as

$$\begin{aligned}\mathcal{W}_{\mathcal{S}_{\mathrm{h}},n+1}^{\mathrm{P}}\left[\left(\delta\underline{\boldsymbol{v}}_{\mathrm{h}}^{\mathrm{P}}, \delta p_{\mathrm{h}}^{\mathrm{P}}\right), \left(\underline{\boldsymbol{v}}_{\mathrm{h},n+1}^{\mathrm{P}}, \underline{\boldsymbol{u}}_{\mathrm{h},n+1}^{\mathrm{P}}, p_{\mathrm{h},n+1}^{\mathrm{P}}\right)\right] = \\ \left\langle \tau_p^P \left[\!\left[\boldsymbol{\nabla}\delta p_{\mathrm{h}}^{\mathrm{P}}\right]\!\right], \left[\!\left[\boldsymbol{\nabla} p_{\mathrm{h}}^{\mathrm{P}}\right]\!\right]\right\rangle_{\mathcal{F}_{\Omega_{\mathrm{h,n+1}}^{\mathrm{P}}},n+1} + \left\langle \tau_{div}^P \left[\!\left[\boldsymbol{\nabla}\cdot\delta\underline{\boldsymbol{v}}_{\mathrm{h}}^{\mathrm{P}}\right]\!\right], \left[\!\left[\boldsymbol{\nabla}\cdot\underline{\boldsymbol{v}}_{\mathrm{h}}^{\mathrm{P}}\right]\!\right]\right\rangle_{\mathcal{F}_{\Omega_{\mathrm{h,n+1}}^{\mathrm{P}}},n+1}.\end{aligned} \tag{2.123}$$

Arising from the poroelastic equation (2.120), the reactive contribution is extended by the physical reaction coefficient herein. The stabilization parameters τ_p^P, and τ_{div}^P are constant on each face $\mathcal{F}$ and are defined as follows

$$\tau_p^P = \gamma_p h_{\mathcal{F}}^3 \left(\Phi_{\mathcal{F}}^P\right)^{-1}, \quad \tau_{div}^P = \gamma_{div} h_{\mathcal{F}} \Phi_{\mathcal{F}}^P, \quad \Phi_{\mathcal{F}}^P = h_{\mathcal{F}}^2 \left(c_k \frac{\mu^{\mathrm{F}}\mathring{\phi}}{\mathring{K}} + c_t \frac{\rho^{\mathrm{F}}}{\theta\Delta t}\right). \tag{2.124}$$

The constants are set to $\gamma_p = 0.05$, $\gamma_{div} = 10^{-3}\gamma_p$, $c_t = 1/12$, $c_k = 1$. The set of faces $\mathcal{F}_{\Omega_{\mathrm{h,n+1}}^{\mathrm{P}}}$ includes all inner faces between elements associated with the poroelastic discretization. The mesh size parameter $h_{\mathcal{F}}$ characterizes the maximum diameter of both elements connected to the face $\mathcal{F}$.

Remark 2.10 (Definition of the reactive contribution in the poroelastic stabilization (2.124))**.** *In this section and for all presented numerical examples, the constant initial scalar reactive contribution $(\mathring{\phi}, \mathring{K})$ for the reactive stabilization in the poroelastic domain is applied for simplicity.*

[1] This section is adapted from the author's publication [2].

In the case of large variations in porosity or permeability, the actual computed quantities ($\phi, \underline{\boldsymbol{k}}$) should be utilized. However, this will lead to an additional nonlinearity in the system. Also in case of a relevant anisotropy of the permeability tensor $\underline{\boldsymbol{k}}$, further adaptions to $\Phi_{\mathcal{F}}^{P}$ have to be considered (for residual-based stabilization, see e.g. the work of Barrios et al. *[17]).*

2.3 Nonlinear Solution Procedure

The discretized formulations for the structural, the fluid and the poroelastic domain lead to systems of nonlinear equations (2.109), (2.113) and (2.122), which have to be solved for every time step. Starting at the first time step with $t \in]t_0, t_1]$ with a given initial state vector at $t = t_0$, the unknown state at the first point in time $t = t_1$ is computed. In general, making use of the previously computed state at $t = t_n$ repeatedly allows computing the subsequent state at $t = t_{n+1}$. In the case a fluid-structure interaction, fluid-poroelastic interaction, or fluid-poroelastic-structure interaction problem is solved, some or all of the systems of nonlinear equations (2.109), (2.113) and (2.122) are coupled. As the focus of this thesis is on strongly interacting systems, a monolithic approach, where all discrete equations are solved simultaneously, is applied. Such a monolithic scheme has already been applied e.g. for FSI in the works of Gee *et al.* [90], Heil [115] and Küttler *et al.* [135]. The nonlinear system of equations to be solved, which corresponds to the generic overall problem presented in Section 2.1.1 still neglecting the interfaces, is given by

$$\begin{pmatrix} \underline{\mathbf{R}}^{\mathrm{S}}\left(\underline{\mathbf{u}}^{\mathrm{S}}_{n+1}\right) \\ \underline{\mathbf{R}}^{\mathrm{F}}\left(\underline{\mathbf{v}}^{\mathrm{F}}_{n+1}, \underline{\mathbf{p}}^{\mathrm{F}}_{n+1}\right) \\ \underline{\mathbf{R}}^{\mathrm{G}}\left(\underline{\mathbf{u}}^{\mathrm{G}}_{n+1}\right) \\ \underline{\mathbf{R}}^{\mathrm{P}}\left(\underline{\mathbf{u}}^{\mathrm{P}}_{n+1}, \underline{\mathbf{v}}^{\mathrm{P}}_{n+1}, \underline{\mathbf{p}}^{\mathrm{P}}_{n+1}\right) \end{pmatrix}_{n+1} = \underline{\mathbf{0}}. \tag{2.125}$$

Remark 2.11 (Mesh motion residual $\underline{\mathbf{R}}^{\mathrm{G}}\left(\underline{\mathbf{u}}^{\mathrm{G}}_{n+1}\right)$)**.** *The included mesh motion residual $\underline{\mathbf{R}}^{\mathrm{G}}\left(\underline{\mathbf{u}}^{\mathrm{G}}_{n+1}\right)$ was not discussed in detail before. In case of considering an ALE formulation in the fluid domain Ω^{F} this residual results from the governing equations of the grid motion. For all numerical examples presented in this thesis, a pseudo-structural mesh motion formulation was applied, and therefore the governing discrete equations to form the residual $\underline{\mathbf{R}}^{\mathrm{G}}\left(\underline{\mathbf{u}}^{\mathrm{G}}_{n+1}\right) \hat{=} \underline{\mathbf{R}}^{\mathrm{S}}\left(\underline{\mathbf{u}}^{\mathrm{G}}_{n+1}\right)$ are already presented in Section 2.2.3. For the mesh motion the inertia term and the body force term are omitted. This equation is solved for the vector of nodal displacements $\underline{\mathbf{u}}^{\mathrm{G}}_{n+1}$ of the computational fluid mesh.*

Remark 2.12 (Incorporation of mesh motion displacement continuity for interface matching discretizations)**.** *For all cases where interface matching discretization for the fluid domain and the structural or poroelastic domain are applied, all nodal grid displacements in $\underline{\mathbf{u}}^{\mathrm{G}}$ belonging to the corresponding interface $\Gamma_{\mathrm{h}}^{\mathrm{FS}}$ or $\Gamma_{\mathrm{h}}^{\mathrm{FP}}$ are directly replaced by corresponding "physical" displacements in $\underline{\mathbf{u}}^{\mathrm{S}}$ or $\underline{\mathbf{u}}^{\mathrm{P}}$. This condensation procedure directly allows incorporating the continuity of displacements on the interface in a strong sense and therefore reduces the number of equations that have to be solved since only grid displacements in the inside of the fluid domain are solved.*

To solve the system of equations (2.125) numerically, an iterative Newton-Raphson-based procedure is applied (with iteration counter $i = 0, 1, 2, ...$)

$$\text{Solve:} \quad \underline{\mathbf{C}}^{i}_{n+1} \cdot \Delta\underline{\mathbf{x}}^{i+1}_{n+1} = -\underline{\mathbf{R}}^{i}_{n+1}, \tag{2.126}$$

$$\text{Update:} \quad \underline{\mathbf{x}}^{i+1}_{n+1} = \underline{\mathbf{x}}^{i}_{n+1} + \omega^{i} \Delta\underline{\mathbf{x}}^{i+1}_{n+1}, \tag{2.127}$$

$$\text{Check Convergence:} \left|\left|\underline{\mathbf{R}}^{i+1}_{n+1}\right|\right| \leq \epsilon_{\underline{\mathbf{R}}} \quad \text{and/or} \quad \left|\left|\Delta\underline{\mathbf{x}}^{i+1}_{n+1}\right|\right| \leq \epsilon_{\Delta\underline{\mathbf{x}}}, \tag{2.128}$$

where the problem residual $\underline{\mathbf{R}}^{i}_{n+1}$ is defined as

$$\underline{\mathbf{R}}^{i}_{n+1} := \left[\underline{\mathbf{R}}^{\mathrm{S}}\left(\underline{\mathbf{u}}^{\mathrm{S},i}_{n+1}\right)^{\mathsf{T}}, \underline{\mathbf{R}}^{\mathrm{F}}\left(\underline{\mathbf{v}}^{\mathrm{F},i}_{n+1}, \underline{\mathbf{p}}^{\mathrm{F},i}_{n+1}\right)^{\mathsf{T}}, \underline{\mathbf{R}}^{\mathrm{G}}\left(\underline{\mathbf{u}}^{\mathrm{G},i}_{n+1}\right)^{\mathsf{T}}, \underline{\mathbf{R}}^{\mathrm{P}}\left(\underline{\mathbf{u}}^{\mathrm{P},i}_{n+1}, \underline{\mathbf{v}}^{\mathrm{P}}_{n+1}, \underline{\mathbf{p}}^{\mathrm{P},i}_{n+1}\right)^{\mathsf{T}}\right]^{\mathsf{T}}, \tag{2.129}$$

the overall state vector $\underline{\mathbf{x}}^{i}_{n+1}$ as

$$\underline{\mathbf{x}}^{i}_{n+1} := \left[\left(\underline{\mathbf{u}}^{\mathrm{S},i}_{n+1}\right)^{\mathsf{T}}, \left(\underline{\mathbf{v}}^{\mathrm{F},i}_{n+1}\right)^{\mathsf{T}}, \left(\underline{\mathbf{p}}^{\mathrm{F},i}_{n+1}\right)^{\mathsf{T}}, \left(\underline{\mathbf{u}}^{\mathrm{G},i}_{n+1}\right)^{\mathsf{T}}, \left(\underline{\mathbf{u}}^{\mathrm{P},i}_{n+1}\right)^{\mathsf{T}}, \left(\underline{\mathbf{v}}^{\mathrm{P}}_{n+1}\right)^{\mathsf{T}}, \left(\underline{\mathbf{p}}^{\mathrm{P},i}_{n+1}\right)^{\mathsf{T}}\right]^{\mathsf{T}}, \tag{2.130}$$

and the linearization matrix $\underline{\mathbf{C}}^{i}_{n+1}$ as

$$\underline{\mathbf{C}}^{i}_{n+1} := \frac{\mathrm{d}\underline{\mathbf{R}}^{i}_{n+1}}{\mathrm{d}\underline{\mathbf{x}}}. \tag{2.131}$$

The principal iterative solution procedure consist of the three steps “solve”, “update”, and “check convergence”.

Solve First, a linear system of equations has to be solved for the unknown state increments as defined in (2.126). Therein, the residual vector $\underline{\mathbf{R}}^{i}_{n+1}$ as well as the linearization matrix $\underline{\mathbf{C}}^{i}_{n+1}$ are computed by the state of the previous iteration $\underline{\mathbf{x}}^{i}_{n+1}$. For the first iteration step $i = 0$, a predictor computes an “initial guess” of the state $\underline{\mathbf{x}}^{0}_{n+1}$ which is based on the state of the previous time step(s). This linear system of equations has a block structure given from the underlying physical fields. While for “small” problem setups, a direct solution procedure of the entire system is performed, an iterative block Gauss-Seidel preconditioned GMRES solver is applied for the remaining systems. For preconditioning, each block Gauss-Seidel iteration is performed by incomplete LU factorization (ILU) type preconditioning or an efficient algebraic multigrid (AMG) type preconditioning in each matrix block. A unified framework for the solution of n-field coupled problems is presented by Verdugo and Wall [214].

Update As a consecutive step, an update of the previous state vector by the computed state increment is performed according to (2.127). This update involves a scalar damping parameter ω^{i}, chosen in the range $\omega^{i} \in]0, 1.0]$. In case $\omega^{i} = 1.0$ is chosen, a full Newton update strategy is performed, which leads to quadratic convergence of the residual close to the solution. Nevertheless, for the handling of strong nonlinearities, which means that the procedure may be started far from the solution, including a damping with parameter $\omega^{i} < 1.0$ in the update step can increase robustness of the solution procedure. Different variants for the definition of the damping parameter ω^{i} are possible. In all following numerical examples, simple strategies to specify the damping parameter in order to increase robustness of the solution procedure are utilized.

Check Convergence Finally, the convergence of the iterative procedure has to be checked. An appropriate norm of the residual vector $\left|\left|\underline{\mathbf{R}}_{n+1}^{i+1}\right|\right|$ and/or the state increment vector $\left|\left|\Delta\underline{\mathbf{x}}_{n+1}^{i+1}\right|\right|$ has to fall below a certain predefined tolerance ϵ_*. Then, the iterative procedure is stopped with the solution state $\underline{\mathbf{x}}_{n+1}^{i+1}$ and the computation of the subsequent time step is performed. Depending on the definition of the vector norm, the checks for all underlying physical fields can be performed separately.

Remark 2.13 (Dependencies of $\underline{\mathbf{R}}_{n+1}^{i}$ for coupled problems)**.** *Up to now, the coupling of the different physical domains was not treated explicitly and therefore the specific residuals* $\underline{\mathbf{R}}^{\mathrm{S}}, \underline{\mathbf{R}}^{\mathrm{F}}, \underline{\mathbf{R}}^{\mathrm{G}}$*, and* $\underline{\mathbf{R}}^{\mathrm{P}}$ *depend solely on the unknowns of the respective physical field. In general, due to the consideration of different coupling terms, additional dependencies arise. Considering, e.g., FSI with an ALE fluid formulation including Nitsche-based coupling with fluid-sided interface stress representation (see Section 3.3.2.1) leads to the following dependencies of the structural and the fluid residual:* $\underline{\mathbf{R}}^{\mathrm{S}}\left(\underline{\mathbf{u}}_{n+1}^{\mathrm{S},i}, \underline{\mathbf{v}}_{n+1}^{\mathrm{F},i}, \underline{\mathbf{p}}_{n+1}^{\mathrm{F},i}\right)$*,* $\underline{\mathbf{R}}^{\mathrm{G}}\left(\underline{\mathbf{u}}_{n+1}^{\mathrm{G},i}, \underline{\mathbf{u}}_{n+1}^{\mathrm{S},i}\right)$*, and* $\underline{\mathbf{R}}^{\mathrm{F}}\left(\underline{\mathbf{v}}_{n+1}^{\mathrm{F},i}, \underline{\mathbf{p}}_{n+1}^{\mathrm{F},i}, \underline{\mathbf{u}}_{n+1}^{\mathrm{S},i}, \underline{\mathbf{u}}_{n+1}^{\mathrm{G},i}\right)$*. Therefore, the linearization matrix* $\underline{\mathbf{C}}_{n+1}^{i}$ *includes main diagonal blocks arising from the discretization of the field equations and additional off-diagonal blocks due to the coupling between the different physical fields.*

Remark 2.14 (Neglecting contributions in $\underline{\mathbf{C}}_{n+1}^{i}$)**.** *From the definition* (2.131)*, the linearization of all different residuals with respect to all degrees of freedom should be considered. Nevertheless, it can be seen from the computed numerical examples that not all components of the linearization are required to solve the nonlinear system of equations. Therefore, to reduce the number of non-zero entries in the matrix* $\underline{\mathbf{C}}_{n+1}^{i}$ *and due to implementation reasons, some off-diagonal coupling terms are treated in a fix-point manner and are not considered in the linearization. Out of the formulations discussed in this chapter, the linearization of the fluid stabilization parameters, specified in* (2.118)*, are not considered.*

3 A Flexible Unfitted Formulation for Fluid-Structure Interaction and More

Within this chapter, a flexible formulation for interface-unfitted fluid-structure interaction is presented. The terms interface-unfitted or interface-fitted in this context denotes whether the boundary of the computational fluid mesh does not match or matches the common interface of the structure and the fluid respectively. The presented formulation serves also as basis for the interface-unfitted fluid-poroelastic interaction and different modeling variants and numerical approaches to incorporate contact. Certain notes discussing these extensions are included in this chapter. Still, the rigorous discussion of all additional aspects concerning these extensions is left to the following chapters.

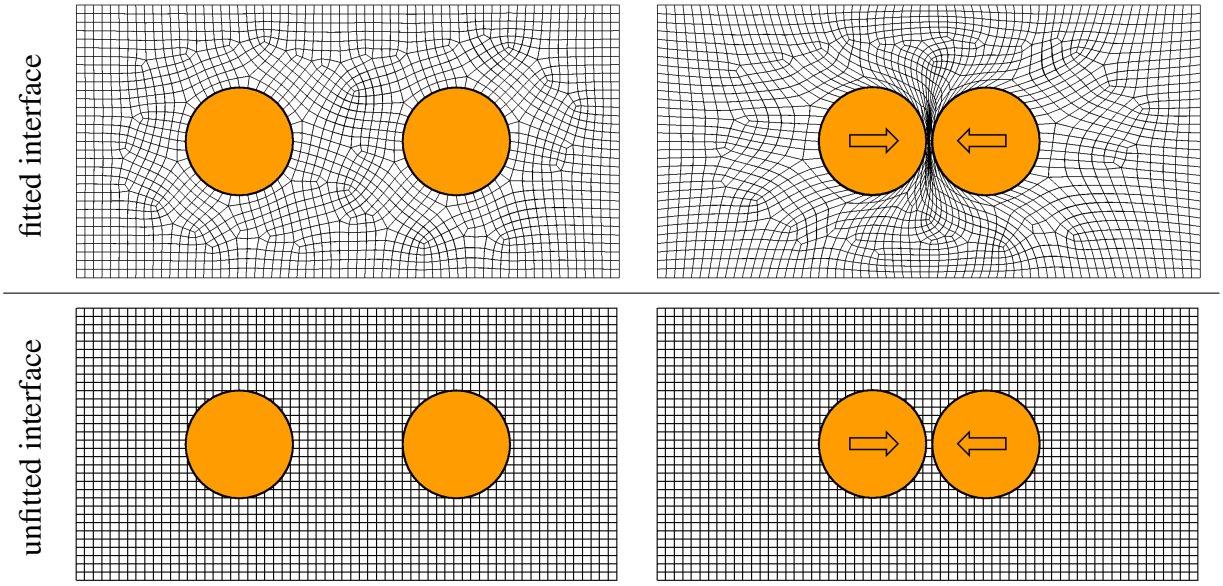

Figure 3.1: Comparison of an interface-fitted vs. interface-unfitted computational fluid mesh for the discretization of fluid-structure interaction problems in “close-to-contact” scenarios.

In Figure 3.1, the classical interface-fitted approach for FSI using a deforming computational mesh for the fluid discretization and the alternative approach for FSI utilizing unfitted interfaces and a fixed computational fluid mesh are compared for a “close-to-contact” scenario. Both approaches are suitable discretization approaches when considering moderate deformation and motion of the solid domain for standard FSI configurations (see Figure 3.1 (left)). As soon as potential contact between solid bodies has to be considered, this changes drastically. Hereby, applying an interface-fitted fluid discretization approach leads to a distortion of the fluid elements

between the approaching solid bodies. To some extent, re-meshing algorithms allow to enlarge the applicable range for such numerical approaches when considering "close-to-contact" scenarios. Nevertheless, when real contact occurs, and as a consequence thereof topological changes of the fluid domain arise, interface-fitted approaches are no longer applicable in practice. An illustrative example for topological changes is, for example, the separation of the fluid domain into two parts when analyzing the closing of a valve. Techniques which allow to use interface-unfitted fluid meshes do not suffer from these limitations on the other hand. Therefore, these approaches are the methods of choice for FSI computations including contact of solid bodies.

In the previous chapter, the basics for the numerical treatment of FSI problems by the FEM with boundary- and interface-fitted computational meshes were presented. In order to fulfill the requirements arising for the FSCI problem, in this chapter, an extension to unfitted fluid discretizations enabled by the CutFEM is given.

First, an introduction to all essential aspects for the application of the CutFEM on the fluid domain in Section 3.1 is given. This includes the representation of unfitted boundaries and interfaces, the underlying discretization, the ghost penalty stabilization, as well as selected details on the geometric intersection. In the subsequent part, Section 3.2, the extension to handle moving boundary/interface problems is discussed. The weak imposition of interface conditions by Nitsche-based methods and the resulting formulation of the overall coupled is presented in Section 3.3. In addition to the commonly applied fluid-sided interface stress representation for the incorporation of the conditions on an FSI interface also a solid-sided interface stress representation is introduced. Section 3.4 provides details on the applied nonlinear solution procedure for the CutFEM FSI problem. The chapter is concluded with numerical tests in Section 3.5 to validate the FSI formulation and a numerical example in Section 3.6 showing the general applicability of the formulation.

3.1 The CutFEM for the Discretization of the Fluid Domain

In this section all essential steps to discretize the Navier-Stokes equations (2.27) and (2.28) in the fluid domain Ω^{F} in the case of an unfitted computational mesh by the CutFEM are discussed.

3.1.1 Representation of Unfitted Boundaries and Interfaces

For boundary- and interface-fitted computational meshes, the location of present boundaries or interfaces is directly given by the outer boundary of the discretization. As this information is not directly available for unfitted computational meshes, an additional description of the boundaries/interfaces is required. Mainly two approaches are used for this purpose: the implicit and the explicit representation.

The implicit representation of an evolving interface is typically specified by a scalar phase indicator field (see e.g. the works of Hirt and Nichols [120] and Tezduyar *et al.* [209]) or by a so-called Level-Set function, where the zero-level of an artificial scalar field, which is defined in the overall computational domain, specifies the interface between different phases (see e.g. the works of Sethian [197] and Nagrath *et al.* [159]). This interface representation is often applied

for multi-phase flow computations, where typically one unfitted computational mesh is used for the discretization of all fluid phases and thus no explicit interface is available. Solving a scalar advection equation for a known velocity field allows taking moving interfaces into account. To increase the accuracy of these approaches, enhanced discretizations near the interface are used by Tezduyar *et al.* [209] and enriched discrete spaces (XFEM, CutFEM) are utilized by Chessa and Belytschko [59], Groß and Reusken [104], Rasthofer *et al.* [178], Sauerland and Fries [185] and Schott *et al.* [189].

In contrast to that, for applications where an embedded domain is discretized separately by an interface-fitted discretization, an explicit representation can be utilized. This approach is often applied to fluid domain decomposition applications (see e.g. the works of Massing *et al.* [151], Schott *et al.* [190, 191], Shahmiri [198]), and FSI related applications (see e.g. the works of Alauzet *et al.* [5], Burman and Fernández [42], Schott [187] and Schott *et al.* [192]), which are the focus of this thesis. Thus, an explicit approach for the representation of the interface $\Gamma_{\mathrm{h}}^{\mathrm{F,I}}$ is exclusively applied. Herein, the simultaneous solution of the structural or poroelastic equations and the fluid problem in an FSI/FPI setup allows using the explicit interface description given by the fitted discretizations of the domains $\Omega_{\mathrm{h}}^{\mathrm{S}}$ or $\Omega_{\mathrm{h}}^{\mathrm{P}}$. The deformation of the fluid-structure interface or fluid-poroelastic interface (for simplicity in the following considered as the general fluid interface $\Gamma_{\mathrm{h}}^{\mathrm{F,I}}$) is therefore given by the computed displacement vectors $\underline{\mathbf{u}}^{\mathrm{S}}$ or $\underline{\mathbf{u}}^{\mathrm{P}}$ and the initial geometry of the outer boundaries $\partial\Omega_{\mathrm{h}}^{\mathrm{S}}$ or $\partial\Omega_{\mathrm{h}}^{\mathrm{P}}$.

3.1.2 Unfitted Discretization

In case of unfitted interfaces, the discrete fluid domain $\Omega_{\mathrm{h}}^{\mathrm{F}}$ is not directly given by the domain covered by the computational mesh $\breve{\Omega}_{\mathcal{T}_{\mathrm{h}}}^{\mathrm{F}}$, as it is the case for boundary-fitted discretizations (compare to relation (2.99))

$$\text{unfitted: } \Omega_{\mathrm{h}}^{\mathrm{F}} \subseteq \breve{\Omega}_{\mathcal{T}_{\mathrm{h}}}^{\mathrm{F}}. \tag{3.1}$$

Making use of the explicit interface representation described in Section 3.1.1, the non-fluid part of the domain Ω_{h}^{0} is "cut" out of $\breve{\Omega}_{\mathcal{T}_{\mathrm{h}}}^{\mathrm{F}}$. In order to guarantee that the remaining domain equals the fluid domain $\Omega_{\mathrm{h}}^{\mathrm{F}}$, it has to be ensured that the computational mesh covers at least the entire fluid domain as specified in (3.1). The principal setup and notation for the CutFEM is presented in Figure 3.2. The governing equations of the fluid, given by the weak form (2.111), have to be fulfilled in the fluid domain solely. No interference from the non-fluid domain should occur. Specifying the nodal shape functions to depend on the position of the interface $\Gamma_{\mathrm{h}}^{\mathrm{F,I}}$ and to vanish in the non-fluid domain allows satisfying these criteria. By intersection of the computational fluid mesh with the interface $\Gamma_{\mathrm{h}}^{\mathrm{F,I}}$, the contained elements can be categorized into three different types: uncut fluid elements in $\breve{\Omega}_{\mathcal{T}_{\mathrm{h}},\setminus\Gamma^{\mathrm{F,I}}}^{\mathrm{F}}$, non-fluid elements in $\breve{\Omega}_{\mathcal{T}_{\mathrm{h}},\mathcal{I}}^{\mathrm{F}}$, and intersected elements in $\breve{\Omega}_{\mathcal{T}_{\mathrm{h}},\Gamma^{\mathrm{F,I}}}^{\mathrm{F}}$. First, the uncut fluid elements in the domain $\breve{\Omega}_{\mathcal{T}_{\mathrm{h}},\setminus\Gamma^{\mathrm{F,I}}}^{\mathrm{F}}$ are discretized in space similar to the boundary-fitted case with Lagrange polynomial-based shape functions as introduced in Section 2.2.2. For all elements in the domain $\breve{\Omega}_{\mathcal{T}_{\mathrm{h}},\mathcal{I}}^{\mathrm{F}}$, which are not part of the fluid domain, a vanishing contribution of the respective shape function at each node $j = 1...n_{\mathrm{nod}}^{\mathrm{F}}$ inside the element is utilized for the discretization in space

$$N_j\left(\underline{\boldsymbol{x}}\right)\big|_{\Omega_{\mathcal{T}_{\mathrm{h}},e}^{\mathrm{F}}} = 0 \;\text{ for }\; e \in [1, n_{\mathrm{ele}}^{\mathrm{F}}] \;\text{ with }\; \Omega_{\mathcal{T}_{\mathrm{h}},e}^{\mathrm{F}} \subseteq \breve{\Omega}_{\mathcal{T}_{\mathrm{h}},\mathcal{I}}^{\mathrm{F}}. \tag{3.2}$$

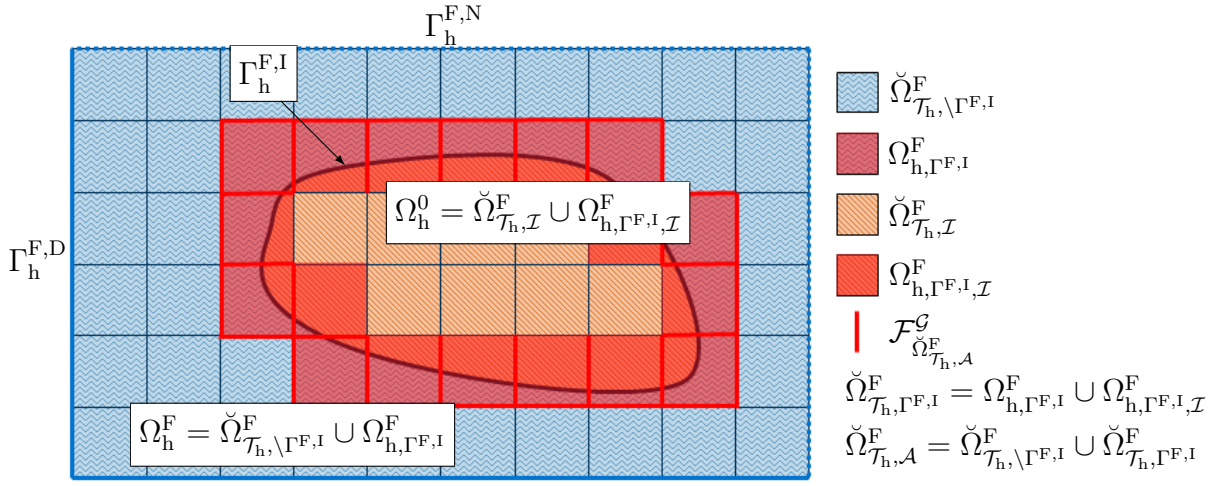

Figure 3.2: Basic concept for the applied CutFEM, where the discrete structural and/or the discrete poroelastic domains $\Omega_{\mathrm{h}}^{0} = \Omega_{\mathrm{h}}^{\mathrm{S}} \cup \Omega_{\mathrm{h}}^{\mathrm{P}}$ are embedded in the domain covered by the computational fluid mesh $\breve{\Omega}^{\mathrm{F}}_{\mathcal{T}_{\mathrm{h}}}$. This domain $\breve{\Omega}^{\mathrm{F}}_{\mathcal{T}_{\mathrm{h}}}$ can be segmented into the domain covered by uncut fluid elements $\breve{\Omega}^{\mathrm{F}}_{\mathcal{T}_{\mathrm{h}},\setminus\Gamma^{\mathrm{F,I}}}$, the domain covered by cut fluid elements $\breve{\Omega}^{\mathrm{F}}_{\mathcal{T}_{\mathrm{h}},\Gamma^{\mathrm{F,I}}}$ and the domain covered by inactive elements $\breve{\Omega}^{\mathrm{F}}_{\mathcal{T}_{\mathrm{h}},\mathcal{I}}$. The domain covered by interface intersected fluid elements $\breve{\Omega}^{\mathrm{F}}_{\mathcal{T}_{\mathrm{h}},\Gamma^{\mathrm{F,I}}}$ can be split into a subdomain which is part of the fluid domain $\Omega^{\mathrm{F}}_{\mathrm{h},\Gamma^{\mathrm{F,I}}}$ and a subdomain which is not part of the fluid domain $\Omega^{\mathrm{F}}_{\mathrm{h},\Gamma^{\mathrm{F,I}},\mathcal{I}}$. The domain covered by "inactive" elements of the computational mesh, which are not part of the fluid domain, is denoted by $\breve{\Omega}^{\mathrm{F}}_{\mathcal{T}_{\mathrm{h}},\mathcal{I}}$. The domain covered by "active" elements of the computational mesh is denoted by $\breve{\Omega}^{\mathrm{F}}_{\mathcal{T}_{\mathrm{h}},\mathcal{A}}$. On the set of faces $\mathcal{F}^{\mathcal{G}}_{\breve{\Omega}^{\mathrm{F}}_{\mathcal{T}_{\mathrm{h}},\mathcal{A}}}$, the ghost penalty stabilization operators are evaluated (see Section 3.1.3 for details).

Application of these shape functions results in a vanishing contribution in the weak form (2.112) inside of these elements, and thus, no artificial effect of the numerical method onto the fluid domain arises.

Finally, the group of cut elements in the domain $\breve{\Omega}^{\mathrm{F}}_{\mathcal{T}_{\mathrm{h}},\Gamma^{\mathrm{F,I}}}$, which is not entirely contained in the fluid domain due to the intersection by the interface $\Gamma_{\mathrm{h}}^{\mathrm{F,I}}$ is discussed. To represent sharp discontinuities of velocity and pressure at the interface inside these elements, the shape functions have to be modified. In the physical fluid part $\Omega^{\mathrm{F}}_{\mathrm{h},\Gamma^{\mathrm{F,I}}}$ of these elements, the standard shape functions as introduced in Section 2.2.2 are applied, whereas in the non-fluid subdomain $\Omega^{\mathrm{F}}_{\mathrm{h},\Gamma^{\mathrm{F,I}},\mathcal{I}}$ vanishing shape functions are used

$$N_j\left(\underline{\boldsymbol{x}}\right)|_{\Omega^{\mathrm{F}}_{\mathcal{T}_{\mathrm{h}},e}} = \begin{cases} N_j\left(\underline{\boldsymbol{x}}\right) & \text{in} \quad \Omega^{\mathrm{F}}_{\mathrm{h},\Gamma^{\mathrm{F,I}}} \\ 0 & \text{in} \quad \Omega^{\mathrm{F}}_{\mathrm{h},\Gamma^{\mathrm{F,I}},\mathcal{I}} \end{cases} \quad \text{for } e \in [1, n^{\mathrm{F}}_{\mathrm{ele}}] \text{ with } \Omega^{\mathrm{F}}_{\mathcal{T}_{\mathrm{h}},e} \subseteq \breve{\Omega}^{\mathrm{F}}_{\mathcal{T}_{\mathrm{h}},\Gamma^{\mathrm{F,I}}}. \tag{3.3}$$

Recalling the specification of the discrete spaces in (2.104) with the nodal shape functions defined beforehand, allows specifying the discrete test function and solution spaces for a CutFEM discretization as in (2.110). In the case of a moving boundary/interface problem, as this is the case for FSI, these spaces $\mathcal{S}_{\underline{\boldsymbol{v}}^{\mathrm{F}},\mathrm{h}}$, $\mathcal{S}_{p^{\mathrm{F}},\mathrm{h}}$, $\mathcal{T}_{\delta\underline{\boldsymbol{v}}^{\mathrm{F}},\mathrm{h}}$ and $\mathcal{T}_{\delta p^{\mathrm{F}},\mathrm{h}}$ change in time due to the dependence of the nodal shape function on the position of the interface $\Gamma_{\mathrm{h}}^{\mathrm{F,I}}$. This aspect is discussed in Section 3.2 concerning temporal discretization.

By making use of the previously defined shape functions for spatial discretization of the fluid problem, the resulting discrete weak form (2.111) has to be integrated solely in the fluid domain $\Omega_{\mathrm{h}}^{\mathrm{F}}$. For all elements in $\breve{\Omega}^{\mathrm{F}}_{\mathcal{T}_{\mathrm{h}},\setminus\Gamma^{\mathrm{F,I}}}$, the standard Gaussian quadrature rule for numerical integration of the $\mathcal{L}^2$-inner products is applied. Due to vanishing shape functions, no contributions to the fluid weak form arise from elements in $\breve{\Omega}^{\mathrm{F}}_{\mathcal{T}_{\mathrm{h}},\mathcal{I}}$ and therefore no integration rule needs to be specified on these elements. The most significant difference in the integration of the fluid weak form occurs for elements in $\breve{\Omega}^{\mathrm{F}}_{\mathcal{T}_{\mathrm{h}},\Gamma^{\mathrm{F,I}}}$ solely. Only the subdomain belonging to the fluid domain has to be integrated numerically, whereas the non-fluid subdomain does not contribute to the weak form (2.111). As the geometry of the physical part is given by the outer boundary of the respective element $\partial\Omega^{\mathrm{F}}_{\mathcal{T}_{\mathrm{h}},e}$ and the interface $\Gamma_{\mathrm{h}}^{\mathrm{F,I}}$, these volume cells are arbitrarily shaped polyhedrons. Therefore, no standard quadrature rule is available for the volume integration of the cells and an alternative approach is applied. This approach is described briefly in Section 3.1.4.

One aspect that should be highlighted considers all degrees of freedom $(\underline{\mathbf{v}}_j^{\mathrm{F}}, \underline{\mathbf{p}}_j^{\mathrm{F}})$ at node j, which do not have any support ($N_j\left(\underline{\boldsymbol{x}}\right) = 0$ in $\breve{\Omega}^{\mathrm{F}}_{\mathcal{T}_{\mathrm{h}}}$). Due to the vanishing support of the corresponding nodal test functions, vanishing equations in the discrete system (2.113) would occur. To avoid ill-conditioning, these vanishing equations are explicitly removed and the final system is not solved for these vanishing degrees of freedom. As a result, the number of fluid unknowns is smaller than $\left(n_{\mathrm{nod}}^{\mathrm{F}} \cdot (d+1)\right)$.

Remark 3.1 (Evaluation of the CIP stabilization for CutFEM)**.** *It should be highlighted that for the CutFEM the CIP fluid stabilizations* (2.114) *are only evaluated on the inner faces of the "active" part of the fluid discretization $\mathcal{F}_{\breve{\Omega}^{\mathrm{F}}_{\mathcal{T}_{\mathrm{h}},\mathcal{A},n+1}}$ instead of all inner faces of the full discretization $\mathcal{F}_{\breve{\Omega}^{\mathrm{F}}_{\mathcal{T}_{\mathrm{h}}}}$.*

Remark 3.2 (Number of Considered DOF-sets)**.** *In order to simplify the previous presentation, only one independent fluid state for the spatial discretization was considered at each computational node. In general, one computational node can have several shape functions corresponding to different fluid domains. Details on DOF-set strategies for multiple DOF-sets are presented by Schott [187], Schott and Wall [188]. These strategies are especially essential when considering thin structures in FSI or two-phase flow.*

3.1.3 Ghost Penalty Stabilization[1]

Due to the arbitrary position of the interface $\Gamma_{\mathrm{h}}^{\mathrm{F,I}}$, which is given by the motion and deformation of the embedded domains $\Omega_{\mathrm{h}}^{\mathrm{S}}$ or $\Omega_{\mathrm{h}}^{\mathrm{P}}$, relative to the elements of the computational fluid mesh, the numerical method has to be robust with respect to any intersection configuration. In particular, interface positions which lead to a very small contribution of single discrete degrees of freedom to the weak form (2.111), have to be treated properly. If not done so, such configurations can lead to an ill-conditioned system of equations due to the decreased influence of single degrees of freedom. Furthermore, a loss of discrete stability, due to the Nitsche-based approach for the imposition of interface conditions (see Section 3.3.2.1 and Section 3.3.3), which relies on sufficient control of the discrete fluid solution in the fluid domain $\Omega_{\mathrm{h}}^{\mathrm{F}}$ extended by the domain $\Omega^{\mathrm{F}}_{\mathrm{h},\Gamma^{\mathrm{F,I}},\mathcal{I}}$,

[1] This section is adapted from the author's publication [2].

could occur. The "ghost" domain $\Omega^{\mathrm{F}}_{\mathrm{h},\Gamma^{\mathrm{F,I}},\mathcal{I}}$ includes the non-fluid subdomain aggregated from all intersected elements.

Additional ghost penalty stabilization allows for the extension of the physical solution of the fluid domain into the "ghost" domain. This can be achieved by adding an additional symmetric and weakly consistent ghost penalty operator, similar to the CIP operators in (2.114), to the weak form (2.111). Such a stabilization technique was first presented by Burman [38] and analyzed by Burman and Hansbo [46] for the Poisson's problem, extended to the Stokes problem by Burman and Hansbo [47], Massing *et al.* [150], and to the Oseen problem by Massing *et al.* [149], Schott and Wall [188]. The additional ghost penalty operators applied for all numerical examples are

$$\begin{aligned}
&\mathcal{W}^{\mathrm{F}}_{\mathcal{G}_{\mathrm{h}},n+1}\left[\left(\delta\underline{\boldsymbol{v}}^{\mathrm{F}}_{\mathrm{h}},\delta p^{\mathrm{F}}_{\mathrm{h}}\right),\left(\underline{\boldsymbol{v}}^{\mathrm{F}}_{\mathrm{h},n+1},p^{\mathrm{F}}_{\mathrm{h},n+1}\right)\right]=\\
&\sum_{1\leq j\leq p}\left\langle\tau_p^{GP,j}\left[\!\left[\partial^j_{\underline{\boldsymbol{n}}}\delta p^{\mathrm{F}}_{\mathrm{h}}\right]\!\right],\left[\!\left[\partial^j_{\underline{\boldsymbol{n}}}p^{\mathrm{F}}_{\mathrm{h}}\right]\!\right]\right\rangle_{\mathcal{F}^{\mathcal{G}}_{\breve{\Omega}^{\mathrm{F}}_{\mathcal{T}_{\mathrm{h}},\mathcal{A},n+1}},n+1}\\
&+\left\langle\tau_{div}^{GP,1}\left[\!\left[\boldsymbol{\nabla}\cdot\delta\underline{\boldsymbol{v}}^{\mathrm{F}}_{\mathrm{h}}\right]\!\right],\left[\!\left[\boldsymbol{\nabla}\cdot\underline{\boldsymbol{v}}^{\mathrm{F}}_{\mathrm{h}}\right]\!\right]\right\rangle_{\mathcal{F}^{\mathcal{G}}_{\breve{\Omega}^{\mathrm{F}}_{\mathcal{T}_{\mathrm{h}},\mathcal{A},n+1}},n+1}\\
&+\sum_{1\leq j\leq p}\left\langle\tau_u^{GP,j}\left[\!\left[\partial^j_{\underline{\boldsymbol{n}}}\delta\underline{\boldsymbol{v}}^{\mathrm{F}}_{\mathrm{h}}\right]\!\right],\left[\!\left[\partial^j_{\underline{\boldsymbol{n}}}\underline{\boldsymbol{v}}^{\mathrm{F}}_{\mathrm{h}}\right]\!\right]\right\rangle_{\mathcal{F}^{\mathcal{G}}_{\breve{\Omega}^{\mathrm{F}}_{\mathcal{T}_{\mathrm{h}},\mathcal{A},n+1}},n+1}.
\end{aligned}\tag{3.4}$$

Herein, $\partial^j_{\underline{\boldsymbol{n}}}*$ denotes the j^{th} derivative of $*$ in face $\mathcal{F}$ normal direction. In principle, these operators penalize deviations from an extended smooth solution of an extension of the discrete fluid solution in $\Omega^{\mathrm{F}}_{\mathrm{h}}$ into the "ghost" domain $\Omega^{\mathrm{F}}_{\mathrm{h},\Gamma^{\mathrm{F,I}},\mathcal{I}}$. Contrary to the CIP operators (2.114), also jumps of higher order derivatives of the pressure and the velocity are penalized. To guarantee sufficient control of the solution in the "ghost" domain $\Omega^{\mathrm{F}}_{\mathrm{h},\Gamma^{\mathrm{F,I}},\mathcal{I}}$, all non-vanishing derivatives (up to polynomial order p) of the considered shape functions have to be considered. Furthermore, additional viscous and reactive parts compared to the CIP stabilization are required, which are included in the parameter $\tau_u^{GP,j}$. This operator is evaluated on all inner faces $\mathcal{F}_{\breve{\Omega}^{\mathrm{F}}_{\mathcal{T}_{\mathrm{h}},\mathcal{A}}}$ between "active" elements, with a least one element being a cut element in $\breve{\Omega}^{\mathrm{F}}_{\mathcal{T}_{\mathrm{h}},\Gamma^{\mathrm{F,I}}}$.

$$\mathcal{F}^{\mathcal{G}}_{\breve{\Omega}^{\mathrm{F}}_{\mathcal{T}_{\mathrm{h}},\mathcal{A}}}=\left\{\mathcal{F}^{\mathrm{F}}_{i,j}\in\mathcal{F}_{\breve{\Omega}^{\mathrm{F}}_{\mathcal{T}_{\mathrm{h}},\mathcal{A}}}\,\middle|\,\Omega^{\mathrm{F}}_{\mathcal{T}_{\mathrm{h}},i}\cap\Gamma^{\mathrm{F,I}}_{\mathrm{h}}\neq\emptyset\vee\Omega^{\mathrm{F}}_{\mathcal{T}_{\mathrm{h}},j}\cap\Gamma^{\mathrm{F,I}}_{\mathrm{h}}\neq\emptyset\right\}\tag{3.5}$$

Remark 3.3 (Detail on the set of faces for the evaluation of the ghost penalty operators)**.** *As this ghost penalty stabilization is only weakly consistent in case physically connected fluid regions are linked via this stabilization, a more restrictive selection of the stabilization faces is often performed. Hereby, all faces which are not connected to a fluid region on both sides are excluded from the set* $\mathcal{F}^{\mathcal{G}}_{\breve{\Omega}^{\mathrm{F}}_{\mathcal{T}_{\mathrm{h}},\mathcal{A}}}$*. Nevertheless, for single-phase flow and FSI in combination with "thick" structures (compared to the fluid element size), both variants vary only for some specific cases. The more restrictive approach is applied in all numerical examples presented in Chapters 3, 4, and 5 whereas definition* (3.5) *is directly applied in Chapters 6 and 7.*

The stabilization parameters of the ghost penalty stabilization are based on the CIP stabilization parameters given in (2.118),

$$\begin{aligned}
&\tau_p^{GP,1} = \tau_p^F, && \tau_p^{GP,2} = 0.05 h_{\mathcal{F}}^2 \tau_p^{GP,1},\\
&\tau_{div}^{GP,1} = \tau_{div}^F, &&\\
&\tau_u^{GP,1} = \tau_u^F + \gamma_\nu^{GP} h_{\mathcal{F}} \mu^{\mathrm{F}} + \gamma_t^{GP} h_{\mathcal{F}}^3 \frac{\rho^{\mathrm{F}}}{\theta \Delta t}, && \tau_u^{GP,2} = 0.05 h_{\mathcal{F}}^2 \left(\tau_u^{GP,1} + \tau_{div}^{GP,1} \right).
\end{aligned} \tag{3.6}$$

In the numerical examples presented in this thesis, either bi-linear quadrilateral elements for $d = 2$ or tri-linear hexahedral elements for $d = 3$ are used for the discretization of the fluid problem. Still, only derivatives up to order $p = 2$ are considered for the ghost penalty stabilization, as this turned out to be sufficient for all performed computations including also discretizations based on tri-linear hexahedral elements. The parameters for the derivatives of first order $\tau_p^{GP,1}, \tau_u^{GP,1}$ and $\tau_{div}^{GP,1}$ are chosen equally to the CIP parameters in (2.118), whereas the additional parameters in the viscous and reactive scaling are specified in the range $\gamma_\nu^{GP} \in [0.1, 0.5]$ and $\gamma_t^{GP} \in [0.001, 0.005]$ if not denoted otherwise. Stabilization parameters for 2^{nd} order derivatives are based on the first order parameters, but include an additional weighting and scaling with the mesh size parameter $h_{\mathcal{F}}$.

Combining the classical discrete weak form (2.112) with the additional ghost penalty contribution results in the weak form for a CutFEM fluid:

$$\begin{aligned}
&\mathcal{W}_{\mathrm{h},n+1}^{\mathrm{F,CUT}} \left[\left(\delta \underline{\boldsymbol{v}}_{\mathrm{h}}^{\mathrm{F}}, \delta p_{\mathrm{h}}^{\mathrm{F}} \right), \left(\underline{\boldsymbol{v}}_{\mathrm{h},n+1}^{\mathrm{F}}, p_{\mathrm{h},n+1}^{\mathrm{F}} \right) \right] =\\
&\mathcal{W}_{\mathrm{h},n+1}^{\mathrm{F}} \left[\left(\delta \underline{\boldsymbol{v}}_{\mathrm{h}}^{\mathrm{F}}, \delta p_{\mathrm{h}}^{\mathrm{F}} \right), \left(\underline{\boldsymbol{v}}_{\mathrm{h},n+1}^{\mathrm{F}}, p_{\mathrm{h},n+1}^{\mathrm{F}} \right) \right] + \mathcal{W}_{\mathcal{G}_{\mathrm{h}},n+1}^{\mathrm{F}} \left[\left(\delta \underline{\boldsymbol{v}}_{\mathrm{h}}^{\mathrm{F}}, \delta p_{\mathrm{h}}^{\mathrm{F}} \right), \left(\underline{\boldsymbol{v}}_{\mathrm{h},n+1}^{\mathrm{F}}, p_{\mathrm{h},n+1}^{\mathrm{F}} \right) \right].
\end{aligned} \tag{3.7}$$

Remark 3.4 (Choice of ghost penalty operators)**.** *In order to reduce the number of different ghost penalty operators, the velocity-based contributions related to the convective, viscous and reactive part are combined in the same operator* $\left\langle \left[\!\left[\partial_{\underline{\boldsymbol{n}}}^j \delta \underline{\boldsymbol{v}}^{\mathrm{F}} \right]\!\right], \left[\!\left[\partial_{\underline{\boldsymbol{n}}}^j \underline{\boldsymbol{v}}^{\mathrm{F}} \right]\!\right] \right\rangle_{\mathcal{F}_{\breve{\Omega}^{\mathrm{F}}_{\mathcal{T}_{\mathrm{h}},\mathcal{A}}}^{\mathcal{G}}}$ *in stabilization parameter* $\tau_u^{GP,1}$*. For derivatives of order* $j > 1$*, also the incompressibility contribution is combined into this operator, as can be seen in* $\tau_u^{GP,2}$ (3.6) *(see also the work of Massing* et al. *[149]).*

Remark 3.5 (Projection-based ghost penalty operators)**.** *In order to circumvent the necessity to considering all normal derivatives of higher order polynomial-based shape functions, the ghost penalty operator can also be constructed by local extrapolation-based ghost-penalty stabilization. Therein, the solution and its extrapolation from one element in a patch is penalized against the solution and the extrapolation of another element in the patch. For this approach, no derivatives of the solution need to be considered. This approach was analyzed by Schein [186].*

3.1.4 Numerical Integration and Geometric Intersection

As discussed in Section 3.1.2, for the numerical integration of the $\mathcal{L}^2$-inner products in intersected elements $\Omega_{\mathcal{T}_{\mathrm{h}},e}^{\mathrm{F}}$ which are part of the domain $\breve{\Omega}_{\mathcal{T}_{\mathrm{h}},\Gamma^{\mathrm{F,I}}}^{\mathrm{F}}$, the approach developed by Sudhakar [201], Sudhakar *et al.* [203] and Sudhakar and Wall [204] utilizing the divergence theorem, is applied. The basic algorithmic steps to apply this approach are elaborated in the following without going into detail. In order to enable a similar numerical integration procedure as the accumulative standard Gaussian quadrature, integration points (IPs) including a weight and position are

determined for these elements. To create these IPs for one of these arbitrary polyheadrons, all bounding polygonal surfaces (facets) defined by the intersection of the element boundary $\partial\Omega^{\mathrm{F}}_{\mathcal{T}_{\mathrm{h}},e}$ and the interface $\Gamma^{\mathrm{F,I}}_{\mathrm{h}}$ have to be determined. Then, 2D IPs on these facets (created by triangulation) are combined with 1D IPs on lines oriented in a predefined direction according to the detailed description by Sudhakar *et al.* [203]. For evaluation of these facets, all element boundary surfaces have to be geometrically intersected with the interface surfaces. To determine the intersection points the required geometric operations including all special cases can be broken down to the intersection of a single surface with a single line, the intersection of two lines, and the computation of the normal distance of a point to a surface. To enable a robust treatment of these basic geometric operations, critical configurations are treated by an increased computational precision (compared to double precision) making use of the CLN-library [108]. Without further geometric operations, facets can be created based on these intersection points, which are finally combined to the polyheadrons. As a subsequent step, a quadrature compression approach optionally allows reducing the number of required volume IPs as presented by Sudhakar *et al.* [205]. This compression strategy is not applied for the numerical examples presented in this thesis.

3.2 The Moving Boundary Problem

When applying the CutFEM for incorporation of discontinuities on fixed boundaries and therefore in a fixed reference domain, the classical time-discretization as for the boundary-fitted case (see Section 2.2.1 and 2.2.4) can be applied. In the case of moving boundaries or interfaces $\Gamma^{\mathrm{F,I}}_{\mathrm{h}}$ this is not possible anymore due to the time-dependent domain $\Omega^{\mathrm{F}}_{\mathrm{h},n+1} \neq \Omega^{\mathrm{F}}_{\mathrm{h},n}$ and the time-dependent test function and solution spaces. To retain usability of all formulations and algorithms developed for the unfitted fixed boundary problem, the temporal discretization based on Space-time approaches as analyzed by Lehrenfeld [140] and Frei and Richter [86] are not considered in the following. Time-stepping schemes for moving boundary problems in the context of XFEM are analyzed by Fries and Zilian [87]. An analysis of time-discretization based on the backward Euler for the moving boundary problem was presented by Zunino [240]. A semi-Lagrangian approach were a Lagrangian observer of the fluid problem is applied close to the moving interface for was introduced by Henke *et al.* [116]. As the focus of this thesis is on the application of CutFEM based fluid discretizations in the context of coupled problems, the development of highly accurate time-integration schemes for the CutFEM is not pursued herein and left to future work. Instead, a simple time stepping procedure will be applied. Therein, a constant fluid domain $\Omega^{\mathrm{F}}_{\mathrm{h},n+1}$ at t_{n+1} (in reference configuration for the ALE case) for every time interval $t \in]t_n, t_{n+1}]$ is assumed. This potentially limits the approach to first order convergence of the temporal error for the One-Step-θ scheme. A theoretical error analysis for this strategy is given by Lehrenfeld and Olshanskii [141]. Therein, a temporal convergence rate of order one for the One-Step-θ scheme with $\theta = 1.0$ and a temporal convergence rate of two for the second order Backward differentiation formula (BDF2) is observed. This approach allows applying the One-Step-θ time-discretization scheme as presented in Section 2.2.1 and 2.2.4. Therefore, all contributions to the fluid weak form (2.111) are evaluated in the current domain $\Omega^{\mathrm{F}}_{\mathrm{h},n+1}$, which is defined by the current interface position $\Gamma^{\mathrm{F,I}}_{\mathrm{h},n+1}$ and additionally by the vector containing all

fluid grid displacements $\underline{\mathbf{u}}^{\mathrm{G}}_{n+1}$ in the ALE case. The discrete test function and solution spaces $\mathcal{S}_{\underline{\boldsymbol{v}}^{\mathrm{F}},\mathrm{h},n+1}, \mathcal{S}_{p^{\mathrm{F}},\mathrm{h},n+1}, \mathcal{T}_{\delta\underline{\boldsymbol{v}}^{\mathrm{F}},\mathrm{h},n+1}$ and $\mathcal{T}_{\delta p^{\mathrm{F}},\mathrm{h},n+1}$ are defined at the end point $t = t_{n+1}$ of the considered interval. By applying temporal and spatial discretization, integrals of the following type required additional attention to be evaluated

$$\int_{\Omega^{\mathrm{F}}_{\mathrm{h},n+1}} \left(\left(\underline{\boldsymbol{a}}_{\mathrm{h}} \circ \Xi \right) \odot \left(\underline{\boldsymbol{a}}_{\mathrm{h}} \circ \Xi \right) \right)_n \circ \Xi^{-1}_{n+1} \, \mathrm{d}\Omega^{\mathrm{F}}. \tag{3.8}$$

Due to the equal reference domain at t_n and t_{n+1} in case the interface is not moving ($\Gamma^{\mathrm{F,I}}_{\mathrm{h},n} = \Gamma^{\mathrm{F,I}}_{\mathrm{h},n+1}$), the vector space containing $\underline{\boldsymbol{a}}_{\mathrm{h},n} \circ \Xi_n$ equals the one containing $\underline{\boldsymbol{a}}_{\mathrm{h},n+1} \circ \Xi_{n+1}$. Therefore, the term $\left(\underline{\boldsymbol{a}}_{\mathrm{h},n} \circ \Xi_n \right) \circ \Xi^{-1}_{n+1}$ can be evaluated. In the case of a moving interface ($\Gamma^{\mathrm{F,I}}_{\mathrm{h},n} \neq \Gamma^{\mathrm{F,I}}_{\mathrm{h},n+1}$), the vector space containing $\underline{\boldsymbol{a}}_{\mathrm{h},n} \circ \Xi_n$ is not equal to the one containing $\underline{\boldsymbol{a}}_{\mathrm{h},n+1} \circ \Xi_{n+1}$. In order to allow an evaluation of terms of type (3.8), a projection $\mathcal{P}^{\underline{\boldsymbol{a}}}_{n+1} \left[\underline{\boldsymbol{a}}_{\mathrm{h},n} \circ \Xi_n \right]$ from the vector spaces in reference configuration at $t = t_n$ to $t = t_{n+1}$ needs to be available.

It should be pointed out that in case an Eulerian observer is used (see Remark 2.1), the vector spaces containing $\left(\underline{\boldsymbol{a}}_{\mathrm{h},n} \circ \Xi_n \right) / \left(\underline{\boldsymbol{a}}_{\mathrm{h},n+1} \circ \Xi_{n+1} \right)$ are equal to the ones containing $\underline{\boldsymbol{a}}_{\mathrm{h},n} / \, \underline{\boldsymbol{a}}_{\mathrm{h},n+1}$. Therefore, in the case of interface motion, the vector spaces containing $\underline{\boldsymbol{a}}_{\mathrm{h},n}$ and $\underline{\boldsymbol{a}}_{\mathrm{h},n+1}$ are not equal. In the following, time integration is discussed for an Eulerian observer. Nevertheless, the following technique can be applied directly applied to the vector spaces in reference configuration for an ALE observer.

Considering the actual occurring terms arising from the fluid time-discretization instead of term (3.8), results in the required projection operators

$$\mathcal{P}^{\underline{\boldsymbol{v}}^{\mathrm{F}}}_{n+1} : \mathcal{S}_{\underline{\boldsymbol{v}}^{\mathrm{F}},\mathrm{h},n} \rightarrow \mathcal{S}_{\underline{\boldsymbol{v}}^{\mathrm{F}},\mathrm{h},n+1} \qquad \text{and} \qquad \mathcal{P}^{p^{\mathrm{F}}}_{n+1} : \mathcal{S}_{p^{\mathrm{F}},\mathrm{h},n} \rightarrow \mathcal{S}_{p^{\mathrm{F}},\mathrm{h},n+1} \tag{3.9}$$

between the fluid solution spaces.

The discrete approximation of any quantity $\underline{\boldsymbol{a}}_{\mathrm{h}} \left(\underline{\boldsymbol{x}} \right)$ in (2.103) is specified by its values $\underline{\boldsymbol{a}}_j$ at all global nodes j and the nodal support, which is the space created by its nodal shape functions $N_j \left(\underline{\boldsymbol{x}} \right)$. The change of nodal support at the two instances in time $t = t_n$ and $t = t_{n+1}$ for the moving interface problem is exemplary visualized in Figure 3.3. Therein, three different types of nodal support are distinguished. First, nodes with a cross do not have any support and therefore do not contribute to the weak form (2.111). Second, nodes marked by a ring do have nodal support in the cut domain $\breve{\Omega}^{\mathrm{F}}_{\mathcal{T}_{\mathrm{h}},\Gamma^{\mathrm{F,I}}}$ and therefore a time-dependent solution space. Finally, nodes with a bullet point have support solely in the uncut domain $\breve{\Omega}^{\mathrm{F}}_{\mathcal{T}_{\mathrm{h}},\Gamma^{\mathrm{F,I}}}$, and therefore, have a solution space that is constant in time (considering an ALE formulation this holds only true for the solution space expressed in reference configuration).

When the discussion is limited to a sufficiently small motion of the interface, seven cases for the change of nodal support can be identified based on these three different types of nodal support. These cases are given in Table 3.1. A projection operator $\mathcal{P}^{\underline{\boldsymbol{a}}}_{n+1}$, which is based on the projection of nodal quantities from $\underline{\mathbf{a}}_{j,n}$ to $\underline{\mathbf{a}}_{j,n+1}$ depending on the corresponding case, can be specified.

As there is no nodal support for nodes belonging to the cases "A" and "G" at t_{n+1}, no projection strategy has to specified. For nodes belonging to case "B" the nodal support does not change between both time steps and therefore the nodal values are kept. All nodes belonging to cases "D", "E" and "F" do contribute to the discrete approximation at both points in time t_n and t_{n+1}.

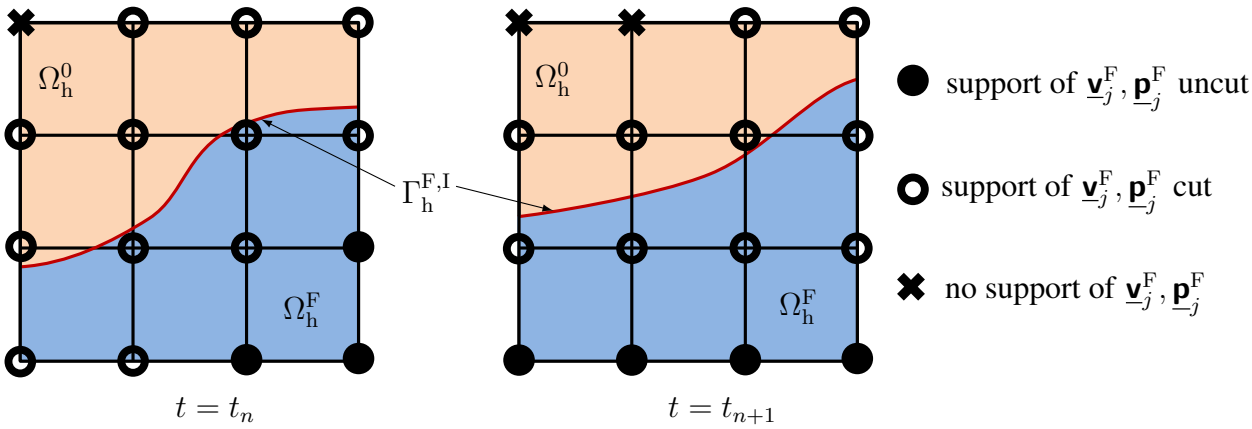

Figure 3.3: Transition of the degrees of freedoms of velocity and pressure at single computational nodes for the moving boundary problem.

Although the nodal support of these nodes potentially changes, a strategy where nodal values are kept is applied. Finally, nodes assignable to case "C" with vanishing nodal support at t_n and non-vanishing nodal support at t_{n+1} require an appropriate extension strategy. In the rightmost column of Table 3.1 the respective strategies are listed.

Table 3.1: Projection strategies for different occurring cases in the time-integration of the moving boundary problem

Case	Nodal support	Nodal support in domain	Strategy
A	$\times \longrightarrow \times$	$\breve{\Omega}^{\mathrm{F}}_{\mathcal{T}_{\mathrm{h}},\mathcal{I}} \longrightarrow \breve{\Omega}^{\mathrm{F}}_{\mathcal{T}_{\mathrm{h}},\mathcal{I}}$	none
B	$\bullet \longrightarrow \bullet$	$\breve{\Omega}^{\mathrm{F}}_{\mathcal{T}_{\mathrm{h}},\setminus\Gamma^{\mathrm{F,I}}} \longrightarrow \breve{\Omega}^{\mathrm{F}}_{\mathcal{T}_{\mathrm{h}},\setminus\Gamma^{\mathrm{F,I}}}$	keep
C	$\times \longrightarrow \circ$	$\breve{\Omega}^{\mathrm{F}}_{\mathcal{T}_{\mathrm{h}},\mathcal{I}} \longrightarrow \breve{\Omega}^{\mathrm{F}}_{\mathcal{T}_{\mathrm{h}},\Gamma^{\mathrm{F,I}}}$	extend
D	$\circ \longrightarrow \circ$	$\breve{\Omega}^{\mathrm{F}}_{\mathcal{T}_{\mathrm{h}},\Gamma^{\mathrm{F,I}}} \longrightarrow \breve{\Omega}^{\mathrm{F}}_{\mathcal{T}_{\mathrm{h}},\Gamma^{\mathrm{F,I}}}$	keep
E	$\circ \longrightarrow \bullet$	$\breve{\Omega}^{\mathrm{F}}_{\mathcal{T}_{\mathrm{h}},\Gamma^{\mathrm{F,I}}} \longrightarrow \breve{\Omega}^{\mathrm{F}}_{\mathcal{T}_{\mathrm{h}},\setminus\Gamma^{\mathrm{F,I}}}$	keep
F	$\bullet \longrightarrow \circ$	$\breve{\Omega}^{\mathrm{F}}_{\mathcal{T}_{\mathrm{h}},\setminus\Gamma^{\mathrm{F,I}}} \longrightarrow \breve{\Omega}^{\mathrm{F}}_{\mathcal{T}_{\mathrm{h}},\Gamma^{\mathrm{F,I}}}$	keep
G	$\circ \longrightarrow \times$	$\breve{\Omega}^{\mathrm{F}}_{\mathcal{T}_{\mathrm{h}},\Gamma^{\mathrm{F,I}}} \longrightarrow \breve{\Omega}^{\mathrm{F}}_{\mathcal{T}_{\mathrm{h}},\mathcal{I}}$	none

For strategy "keep", which implies

$$\mathcal{P}^{\underline{\boldsymbol{v}}^{\mathrm{F}}}_{n+1}\left[N_{j,n}\left(\underline{\boldsymbol{x}}\right)\underline{\mathbf{v}}^{\mathrm{F}}_{j,n}\right] := N_{j,n+1}\left(\underline{\boldsymbol{x}}\right)\underline{\mathbf{v}}^{\mathrm{F}}_{j,n}, \qquad \mathcal{P}^{p^{\mathrm{F}}}_{n+1}\left[N_{j,n}\left(\underline{\boldsymbol{x}}\right)\underline{\mathbf{p}}^{\mathrm{F}}_{j,n}\right] := N_{j,n+1}\left(\underline{\boldsymbol{x}}\right)\underline{\mathbf{p}}^{\mathrm{F}}_{j,n} \tag{3.10}$$

at global node j, no specific technique is required. The approach for all nodes requiring strategy "extend" is just briefly discussed in the following as details can be found in the work of Schott [187] and Schott *et al.* [192]. Therein, a system of equations inspired by the ghost penalty stabilization operators (equation (3.4)), is solved

$$\begin{aligned}\sum_{1\leq j\leq p}\left\langle h^2_{\mathcal{F}}\left[\left[\partial^j_{\underline{\boldsymbol{n}}}\delta\underline{\boldsymbol{v}}^{\mathrm{F}}_{\mathrm{h,n+1}}\right]\right],\left[\left[\partial^j_{\underline{\boldsymbol{n}}}\mathcal{P}^{\underline{\boldsymbol{v}}^{\mathrm{F}}}_{n+1}\left[\underline{\boldsymbol{v}}^{\mathrm{F}}_{\mathrm{h},n}\right]\right]\right]\right\rangle_{\mathcal{F}^{\mathcal{G}}_{\breve{\Omega}^{\mathrm{F}}_{\mathcal{T}_{\mathrm{h}},\mathcal{A},n+1}}}\\ +\sum_{1\leq j\leq p}\left\langle h^2_{\mathcal{F}}\left[\left[\partial^j_{\underline{\boldsymbol{n}}}\delta p^{\mathrm{F}}_{\mathrm{h,n+1}}\right]\right],\left[\left[\partial^j_{\underline{\boldsymbol{n}}}\mathcal{P}^{p^{\mathrm{F}}}_{n+1}\left[p^{\mathrm{F}}_{\mathrm{h},n}\right]\right]\right]\right\rangle_{\mathcal{F}^{\mathcal{G}}_{\breve{\Omega}^{\mathrm{F}}_{\mathcal{T}_{\mathrm{h}},\mathcal{A},n+1}}} = 0.\end{aligned} \tag{3.11}$$

Herein, all projections of nodal velocities or pressures, which where specified already by the strategy "keep" in (3.10), are directly incorporated in a strong sense. Solving this system of equations determines all remaining nodal values by a smooth spatial extension.

To simplify the presentation, only one set of degrees of freedom per node was considered in this section. For a detailed presentation on time-integration for the moving boundary problem considering multiple nodal DOF-sets the reader is referred to Schott [187], Schott and Wall [188]. Therein, also an additional distinction of nodal degrees of freedom with support in the cut domain into physical and "ghost" degrees of freedom is considered.

3.3 Weak Imposition of Interface Conditions

Combining the previously presented techniques allows tackling problems including fluid domains with moving boundaries unfitted to the computational mesh as well as solid domains fitted to the discretization as presented in the previous chapter. To include the interaction between both domains, approaches to incorporate the interface coupling between these two domains for unfitted FSI simulations, will be presented.

In general, different numerical approaches are applicable for the incorporation of interface conditions to an overall problem. For "matching-grid" interfaces a strong imposition of the condition into the discrete function space can be applied. Lagrange-multiplier-based methods suffer from the difficulty to guarantee Inf-Sup stability for unfitted discretization. Due to the successful application and mathematical analysis of the CutFEM with ghost penalty stabilization and the weak imposition of boundary/interface conditions by Nitsche-based methods (see e.g. the works of Burman and Fernández [42], Burman *et al.* [51] and Schott *et al.* [189, 190, 192]), this combination is also selected here. In this thesis, the weak imposition of interface conditions on $\Gamma_{\mathrm{h}}^{\mathrm{F,I}}$ is treated exclusively by Nitsche-based approaches. A main emphasis of the work in this thesis lies in the extension of existing approaches to various challenging problem setups. While no rigorous mathematical analysis is performed for these extensions, the findings from the analyses of the underlying formulations are considered for the construction of these extended formulations. Selected essential aspects for the application of Nitsche method are discussed first in a simple model problem, which enables the reader to understand the design of the developed Nitsche-based formulations. For complete analyses the reader is referred to the referenced literature.

This is followed by the presentation of two approaches for the fluid-structure interfaces and a formulation for a domain decomposition fluid-fluid interface. To put focus on the essential parts, the different interface terms arising from time-discretization are not explicitly specified in the following. All interface terms are considered in current configuration and thus, time-discrete $\mathcal{L}^2$-inner products of type (2.95) have to be evaluated.

3.3.1 Principles of Nitsche's Method for the CutFEM

In order to demonstrate the principles of Nitsche's method, a simple model problem is considered within the first part of this section. Therein, a Dirichlet-type boundary conditions is incorporated by the Nitsche method. This is the Poisson equation $-\alpha\boldsymbol{\Delta}a = 0$ with the positive constant $\alpha > 0$ in the domain Ω^{A} and the Dirichlet-type boundary condition $a = \hat{a}$ on $\Gamma^{\mathrm{A}} = \partial\Omega^{\mathrm{A}}$. The resulting weak form with test function δa_{h} and unit normal vector $\underline{\boldsymbol{n}}_{\mathrm{h}}$ on the boundary Γ^{A} including

the consistency boundary integral arising from partial integration without consideration of the boundary condition is

$$\mathcal{W}_{\mathrm{h}}^{\mathrm{A}}\left(\delta a_{\mathrm{h}}, a_{\mathrm{h}}\right) = \left(\boldsymbol{\nabla}\delta a_{\mathrm{h}}, \alpha\boldsymbol{\nabla}a_{\mathrm{h}}\right)_{\Omega_{\mathrm{h}}^{\mathrm{A}}} - \left\langle \delta a_{\mathrm{h}}, \alpha\boldsymbol{\nabla}a_{\mathrm{h}}\cdot\underline{\boldsymbol{n}}_{\mathrm{h}}\right\rangle_{\Gamma_{\mathrm{h}}^{\mathrm{A}}} = 0. \tag{3.12}$$

The discrete quantity a_{h} herein does not fulfill the Dirichlet-type boundary condition. To incorporate the boundary condition weakly by Nitsche's method, additional terms are added to the weak form.
Find $a_{\mathrm{h}} \in \mathcal{N}_{\mathrm{h}}\left(\Omega_{\mathrm{h}}^{\mathrm{A}}\right)$ *such that for all* $\delta a_{\mathrm{h}} \in \mathcal{N}_{\mathrm{h}}\left(\Omega_{\mathrm{h}}^{\mathrm{A}}\right)$:

$$\mathcal{W}_{\mathrm{h}}^{\mathrm{A,NIT}}\left(\delta a_{\mathrm{h}}, a_{\mathrm{h}}\right) = \mathcal{W}_{\mathrm{h}}^{\mathrm{A}}\left(\delta a_{\mathrm{h}}, a_{\mathrm{h}}\right) + \xi\left\langle\alpha\boldsymbol{\nabla}\delta a_{\mathrm{h}}\cdot\underline{\boldsymbol{n}}_{\mathrm{h}}, a_{\mathrm{h}}-\hat{a}\right\rangle_{\Gamma_{\mathrm{h}}^{\mathrm{A}}} + \gamma\left\langle\delta a_{\mathrm{h}}, a_{\mathrm{h}}-\hat{a}\right\rangle_{\Gamma_{\mathrm{h}}^{\mathrm{A}}} = 0. \tag{3.13}$$

First, it can be seen that these additional two terms are consistent as they vanish in the case the Dirichlet-type boundary condition is fulfilled. The parameter ξ of the adjoint-consistency term is typically chosen from $\xi \in \{-1, 0, 1\}$. The positive parameter $\gamma > 0$ of the penalty term has to be chosen sufficiently large. These terms are added to achieve existence and uniqueness of the discrete formulation. Therefore, it is required to fulfill a discrete Inf-Sup condition or the stronger criteria coercivity if possible, which directly implies the Inf-Sup condition

$$\mathcal{W}_{\mathrm{h}}^{\mathrm{A,NIT}}\left(a_{\mathrm{h}}, a_{\mathrm{h}}\right) \geq C_1\left(||\boldsymbol{\nabla}a_{\mathrm{h}}||^2_{\mathcal{L}^2,\Omega_{\mathrm{h}}^{\mathrm{A}}} + ||a_{\mathrm{h}}||^2_{\mathcal{L}^2,\Gamma_{\mathrm{h}}^{\mathrm{A}}}\right) \quad \text{with} \quad C_1 > 0 \neq f(h) \neq f(\alpha). \tag{3.14}$$

For $\xi = -1$ or $\xi = 0$, the critical aspect to fulfill coercivity is that the contribution of the boundary integral in (3.12) has to be balanced by other contributions in the weak form (3.13). The contribution arising from the consistency boundary integral in (3.12) can be split into two parts (for any $\delta > 0$). While one part can be balanced by the volumetric term the remaining contribution has to be compensated by the last term, called penalty term in (3.13) (see e.g. the work of Hansbo [111])

$$\begin{aligned} -\left\langle a_{\mathrm{h}}, \alpha\boldsymbol{\nabla}a_{\mathrm{h}}\cdot\underline{\boldsymbol{n}}_{\mathrm{h}}\right\rangle_{\Gamma_{\mathrm{h}}^{\mathrm{A}}} &\geq -||a_{\mathrm{h}}||_{\mathcal{L}^2,\Gamma_{\mathrm{h}}^{\mathrm{A}}}\cdot||\alpha\boldsymbol{\nabla}a_{\mathrm{h}}\cdot\underline{\boldsymbol{n}}_{\mathrm{h}}||_{\mathcal{L}^2,\Gamma_{\mathrm{h}}^{\mathrm{A}}} \\ &\geq -\underbrace{\frac{\delta}{2}||a_{\mathrm{h}}||^2_{\mathcal{L}^2,\Gamma_{\mathrm{h}}^{\mathrm{A}}}}_{\text{balanced by the penalty term}} - \underbrace{\frac{1}{2\delta}||\alpha\boldsymbol{\nabla}a_{\mathrm{h}}\cdot\underline{\boldsymbol{n}}_{\mathrm{h}}||^2_{\mathcal{L}^2,\Gamma_{\mathrm{h}}^{\mathrm{A}}}}_{\text{balanced by the volumetric term}}. \end{aligned} \tag{3.15}$$

To bound the contribution arising from the boundary by the volume contribution the following trace inequality is utilized

$$||\alpha\boldsymbol{\nabla}a_{\mathrm{h}}\underline{\boldsymbol{n}}_{\mathrm{h}}||^2_{\mathcal{L}^2,\Gamma_{\mathrm{h}}^{\mathrm{A}}\cap\Omega^{\mathrm{A}}_{\mathcal{T}_{\mathrm{h},e}}} \leq \alpha C^*_{2,e}\left|\left|\alpha^{1/2}\boldsymbol{\nabla}a_{\mathrm{h}}\right|\right|^2_{\mathcal{L}^2,\Omega_{\mathrm{h}}^{\mathrm{A}}\cap\Omega^{\mathrm{A}}_{\mathcal{T}_{\mathrm{h},e}}}. \tag{3.16}$$

The constant $C^*_{2,e}$ therein has to be considered for the definition of δ and consequently to specify the parameter γ in order to satisfy inequality (3.14). Three different specifications of the constant $C^*_{2,e}$ so that the trace inequality (3.16) is fulfilled are given in the following. For linear triangular or tetrahedral elements (with $\boldsymbol{\nabla}a_{\mathrm{h}} \neq f(\underline{\boldsymbol{x}})$), the element-wise constant factor $C^*_{2,e} = C^{\mathrm{S/V}}_{2,e}$ can be identified as surface to volume ratio

$$C^{\mathrm{S/V}}_{2,e} := \frac{\text{meas}\left(\Gamma_{\mathrm{h}}^{\mathrm{A}}\cap\Omega^{\mathrm{A}}_{\mathcal{T}_{\mathrm{h},e}}\right)}{\text{meas}\left(\Omega_{\mathrm{h}}^{\mathrm{A}}\cap\Omega^{\mathrm{A}}_{\mathcal{T}_{\mathrm{h},e}}\right)}. \tag{3.17}$$

For boundary-fitted shape regular meshes, the constant $C_{2,e}^{*} = C_{2,e}^{h}$ can be expressed by a characteristic element size h and the a positive constant $\tilde{C}_2$ with

$$C_{2,e}^{h} := \tilde{C}_2 h^{-1}. \tag{3.18}$$

Depending the on the polynomial degree and the number of spatial dimension of the utilized elements, the constant $\tilde{C}_2$ can be specified according to estimation presented by Burman and Ern [39]. For the computations presented in this work, an estimation of $\tilde{C}_2$ based on pre-estimated eigenvalue problems is utilized with the specific values given by Schott [187]. For more general cases, where the criteria of the previous special cases are not met or α is not a constant scalar in space, a generalized local eigenvalue problem can be solved for the maximum eigenvalue λ_e (see the work of Griebel and Schweitzer [103], Hansbo [111])

$$\begin{gathered} \underline{\boldsymbol{A}}_e \underline{\boldsymbol{X}}_e = \lambda_e \underline{\boldsymbol{B}}_e \underline{\boldsymbol{X}}_e \\ \langle \alpha \boldsymbol{\nabla} \delta a_{\mathrm{h}} \cdot \underline{\boldsymbol{n}}_{\mathrm{h}}, \alpha \boldsymbol{\nabla} a_{\mathrm{h}} \cdot \underline{\boldsymbol{n}}_{\mathrm{h}} \rangle_{\Gamma_{\mathrm{h}}^{\mathrm{A}} \cap \Omega_{\mathcal{T}_{\mathrm{h}},e}^{\mathrm{A}}} \longrightarrow \underline{\boldsymbol{A}}_e, \quad (\boldsymbol{\nabla} \delta a_{\mathrm{h}}, \alpha \boldsymbol{\nabla} a_{\mathrm{h}})_{\Omega_{\mathrm{h}}^{\mathrm{A}} \cap \Omega_{\mathcal{T}_{\mathrm{h}},e}^{\mathrm{A}}} \longrightarrow \underline{\boldsymbol{B}}_e, \end{gathered} \tag{3.19}$$

with the element matrices $\underline{\boldsymbol{A}}_e$ and $\underline{\boldsymbol{B}}_e$ - which are constructed from the respective forms, and the eigenvectors $\underline{\boldsymbol{X}}_e$. This allows computing an element-wise constant $C_{2,e}^{*} = C_{2,e}^{\mathrm{eig}}$ (see Dolbow and Harari [72])

$$\alpha C_{2,e}^{\mathrm{eig}} := \lambda_e. \tag{3.20}$$

As an alternative the maximum constant in the overall problem can be considered ([111]). By using one of the definitions (3.17), (3.18) or (3.20), the penalty scaling can be defined as

$$\gamma := \gamma_0 \alpha C_{2,e}^{*}, \quad \text{for (3.20)} \quad \gamma := \gamma_0 \lambda_e \tag{3.21}$$

with the constant γ_0 being sufficiently large to guarantee coercivity independent of the problem parameters (such as α) or the discretization parameters (such as the element size h).

For definition (3.17), it can be directly seen that in the unfitted case the constant $C_{2,e}^{*}$ is not bounded as the physical volume of an element $\mathrm{meas}\left(\Omega_{\mathrm{h}}^{\mathrm{A}} \cap \Omega_{\mathcal{T}_{\mathrm{h}},e}^{\mathrm{A}}\right)$ can vanish depending on the boundary/interface position. Using this definition directly for the CutFEM, can result in a large parameter γ and a resulting ill-conditioned system. This issue is cured by applying the ghost penalty stabilization operators on the faces of the intersected elements as introduced in Section 3.1.3. This additional stabilization allows recovering control in the "ghost" domain $\Omega_{\mathcal{T}_{\mathrm{h}},e}^{\mathrm{A}} \setminus \left(\Omega_{\mathrm{h}}^{\mathrm{A}} \cap \Omega_{\mathcal{T}_{\mathrm{h}},e}^{\mathrm{A}}\right)$. Thus, the required trace inequality (3.16) including the whole intersected element changes to

$$\left|\left|\alpha \boldsymbol{\nabla} a_{\mathrm{h}} \underline{\boldsymbol{n}}_{\mathrm{h}}\right|\right|_{\mathcal{L}^2, \Gamma_{\mathrm{h}}^{\mathrm{A}} \cap \Omega_{\mathcal{T}_{\mathrm{h}},e}^{\mathrm{A}}}^2 \leq \alpha C_{2,e}^{*} \left|\left|\alpha^{1/2} \boldsymbol{\nabla} a_{\mathrm{h}}\right|\right|_{\mathcal{L}^2, \Omega_{\mathcal{T}_{\mathrm{h}},e}^{\mathrm{A}}}^2. \tag{3.22}$$

As a consequence, the definitions (3.17), (3.18), and (3.20) can be modified for the application to CutFEM to take into account the entire element $\Omega_{\mathcal{T}_{\mathrm{h}},e}^{\mathrm{A}}$ instead of its restriction to the physical part $\Omega_{\mathrm{h}}^{\mathrm{A}} \cap \Omega_{\mathcal{T}_{\mathrm{h}},e}^{\mathrm{A}}$.

Remark 3.6 (Practical choice of penalty parameter definition)**.** *Although it is clear from a theoretical point of view which definition for the constant $C_{2,e}^{*}$ is valid for certain configurations, including a safety buffer in γ_0 allows extending the practical range of applicability of the definitions (e.g. using* (3.18) *for computational meshes undergoing moderate deformation).*

Up to now, the second term in (3.13), which is called adjoint-consistency term, was not discussed. By choosing $\xi = -1$, all interface terms are symmetric and therefore an originally symmetric bi-linear form remains symmetric.

By choosing $\xi = 1$, a skew-symmetric term is added, which allows for a direct compensation of the contributions of the consistency boundary integral on the interface. With this variant, no compensation of the consistency boundary integral by the penalty term is required. Still, a larger penalty parameter allows for an increased enforcement of the condition on the boundary. As a result, the ghost penalty stabilization is solely required to improve the problem conditioning for critical intersections.

The additional terms to incorporate the boundary condition in (3.13), build the basis also for the weak imposition of the interface condition as discussed in the following. In order to develop Nitsche-based approaches for coupled problems by analogy to the simple model problem, the consistency interface term in (3.12) has to be identified for the governing equations of increased complexity which allows assessing the design of the additional terms in (3.13). For all intermediate steps towards FSI based on the weak imposition of the interface condition by Nitsche's method, the reader is referred to the available literature. Starting from initial analysis for Poisson equation with CutFEM by Burman and Hansbo [46], which was extended to the Stokes equation by Burman and Hansbo [47], Massing *et al.* [150], and finally including advection, to the Oseen equation by Massing *et al.* [149], Schott and Wall [188]. Application of the CutFEM and weak imposition by Nitsche's method to the FSI interface conditions were presented by Burman and Fernández [42], Massing *et al.* [151], Schott *et al.* [192].

3.3.2 Nitsche-based FSI No-Slip Coupling

The weak imposition of the no-slip condition on the fluid-structure interface $\Gamma_{\mathrm{h}}^{\mathrm{FS}}$, as presented in Section 2.1.7, by a Nitsche-based approach is discussed in the following. The consistent contributions arising in the derivation of the weak formulation on the interface of the discrete structural weak form (2.108) and discrete fluid weak form (2.112) are

$$\begin{aligned}
&- \left\langle \delta\underline{\boldsymbol{u}}_{\mathrm{h}}^{\mathrm{S}}, \underline{\boldsymbol{h}}_{0,\mathrm{h}}^{\mathrm{S,I}} \right\rangle_{\Gamma_{0,\mathrm{h}}^{\mathrm{S,I}}} - \left\langle \delta\underline{\boldsymbol{v}}_{\mathrm{h}}^{\mathrm{F}}, \underline{\boldsymbol{h}}_{\mathrm{h}}^{\mathrm{F,I}} \right\rangle_{\Gamma_{\mathrm{h}}^{\mathrm{F,I}}} = \\
&- \left\langle \delta\underline{\boldsymbol{u}}_{\mathrm{h}}^{\mathrm{S}}, \underline{\boldsymbol{h}}_{\mathrm{h}}^{\mathrm{S,I}} \right\rangle_{\Gamma_{\mathrm{h}}^{\mathrm{FS}}} - \left\langle \delta\underline{\boldsymbol{v}}_{\mathrm{h}}^{\mathrm{F}}, \underline{\boldsymbol{h}}_{\mathrm{h}}^{\mathrm{F,I}} \right\rangle_{\Gamma_{\mathrm{h}}^{\mathrm{FS}}} - \left\langle \delta\underline{\boldsymbol{u}}_{\mathrm{h}}^{\mathrm{S}}, \underline{\boldsymbol{h}}_{\mathrm{h}}^{\mathrm{S,I}} \right\rangle_{\Gamma_{\mathrm{h}}^{\mathrm{S,I}} \setminus \Gamma_{\mathrm{h}}^{\mathrm{FS}}} - \left\langle \delta\underline{\boldsymbol{v}}_{\mathrm{h}}^{\mathrm{F}}, \underline{\boldsymbol{h}}_{\mathrm{h}}^{\mathrm{F,I}} \right\rangle_{\Gamma_{\mathrm{h}}^{\mathrm{F,I}} \setminus \Gamma_{\mathrm{h}}^{\mathrm{FS}}}.
\end{aligned} \tag{3.23}$$

The consistent stress representation on the structural boundary $\Gamma_{\mathrm{h}}^{\mathrm{S,I}}$ is $\underline{\boldsymbol{h}}_{\mathrm{h}}^{\mathrm{S,I}} := \underline{\boldsymbol{\sigma}}_{\mathrm{h}}^{\mathrm{S}} \cdot \underline{\boldsymbol{n}}_{\mathrm{h}}^{\mathrm{S}}$ and on the fluid boundary $\Gamma_{\mathrm{h}}^{\mathrm{F,I}}$ it is $\underline{\boldsymbol{h}}_{\mathrm{h}}^{\mathrm{F,I}} := \underline{\boldsymbol{\sigma}}_{\mathrm{h}}^{\mathrm{F}} \cdot \underline{\boldsymbol{n}}_{\mathrm{h}}^{\mathrm{F}}$. In the following, the interface terms on $\Gamma_{\mathrm{h}}^{\mathrm{FS}}$ will be taken into account exclusively, as interfaces between the fluid domain and the poroelastic domain as well as the different types of contact interfaces are discussed separately in the subsequent chapters. By utilizing the dynamic equilibrium (2.59) on the interface Γ^{FS}, the following relations hold true

$$\underline{\boldsymbol{h}}^{\mathrm{S,I}} = \underline{\boldsymbol{\sigma}}^{\mathrm{S}} \cdot \underline{\boldsymbol{n}}^{\mathrm{S}} = -\underline{\boldsymbol{h}}^{\mathrm{F,I}} - \hat{\underline{\boldsymbol{g}}}_{\sigma}^{\mathrm{FS}} = -\underline{\boldsymbol{\sigma}}^{\mathrm{F}} \cdot \underline{\boldsymbol{n}}^{\mathrm{F}} - \hat{\underline{\boldsymbol{g}}}_{\sigma}^{\mathrm{FS}} \tag{3.24}$$

$$\underline{\boldsymbol{h}}^{\mathrm{F,I}} = \underline{\boldsymbol{\sigma}}^{\mathrm{F}} \cdot \underline{\boldsymbol{n}}^{\mathrm{F}} = -\underline{\boldsymbol{h}}^{\mathrm{S,I}} + \hat{\underline{\boldsymbol{g}}}_{\sigma}^{\mathrm{FS}} = -\underline{\boldsymbol{\sigma}}^{\mathrm{S}} \cdot \underline{\boldsymbol{n}}^{\mathrm{S}} + \hat{\underline{\boldsymbol{g}}}_{\sigma}^{\mathrm{FS}}. \tag{3.25}$$

As a consequence, the choice whether the interface stress should be represented by the structural state or the fluid state can be made freely. In general, a combination of the corresponding

interface stress from both adjacent domains can be applied. The choice of the interface stress representation is expected to be essential when a high contrast in the material properties between both sides of the interface occurs. This aspect is analyzed for an advection-diffusion system by Burman and Zunino [49]. A specific weighting strategy of both interface contributions based on the interface location (see Hansbo and Hansbo [109]) allows the development of discrete formulations without a technique such as the ghost penalty stabilization if one discretization is applied for both adjacent domains. Annavarapu *et al.* [8] additionally included material parameters into the weighting strategy. To account for varying material parameters, a harmonic weighing is often applied when analyzing multiphase-flows (see e.g. the work of Schott *et al.* [189]). When considering fluid domain decomposition by including an fluid patch with interface-fitted discretization, an interface stress representation based on the non-intersected discretization can be considered (see e.g. the work of Schott *et al.* [190], Shahmiri [198]).

To limit the complexity of the considered Nitsche-based formulations for FSI, the interface stress is always based on one specific domain in the following. Nevertheless, if required for certain configurations, a weighted combination taking both interface stress representations into account could be considered in principle for the price of an extended computational workload for interface evaluations. First, the Nitsche-based formulation with a fluid state-based interface stress representation is presented. A solid state-based interface stress representation is considered subsequently.

3.3.2.1 Fluid-Sided Interface Stress Representation

All Nitsche-based formulations for FSI in combination with CutFEM are exclusively presented based on a fluid-sided interface stress representation (see e.g. the works of Alauzet *et al.* [5], Burman and Fernández [42], Schott [187], Schott *et al.* [191, 192]). Therefore, this approach is presented first, which leads to the following additional interface contributions of the weak form

$$\begin{aligned}\mathcal{W}_{\mathrm{h}}^{\mathrm{FSI,F}}\left[\left(\delta\underline{\boldsymbol{u}}_{\mathrm{h}}^{\mathrm{S}},\delta\underline{\boldsymbol{v}}_{\mathrm{h}}^{\mathrm{F}},\delta p_{\mathrm{h}}^{\mathrm{F}}\right),\left(\underline{\boldsymbol{u}}_{\mathrm{h}}^{\mathrm{S}},\underline{\boldsymbol{v}}_{\mathrm{h}}^{\mathrm{F}},p_{\mathrm{h}}^{\mathrm{F}}\right)\right] &= -\left\langle\delta\underline{\boldsymbol{v}}_{\mathrm{h}}^{\mathrm{F}}-\delta\underline{\boldsymbol{u}}_{\mathrm{h}}^{\mathrm{S}},\underline{\boldsymbol{\sigma}}_{\mathrm{h}}^{\mathrm{F}}\underline{\boldsymbol{n}}_{\mathrm{h}}^{\mathrm{F}}\right\rangle_{\Gamma_{\mathrm{h}}^{\mathrm{FS}}}\\ -\left\langle\delta\underline{\boldsymbol{u}}_{\mathrm{h}}^{\mathrm{S}},\hat{\underline{\boldsymbol{g}}}_{\sigma}^{\mathrm{FS}}\right\rangle_{\Gamma_{\mathrm{h}}^{\mathrm{FS}}} &- \left\langle\delta p_{\mathrm{h}}^{\mathrm{F}}\underline{\boldsymbol{n}}_{\mathrm{h}}^{\mathrm{F}}-2\xi^{\mathrm{FSI}}\mu^{\mathrm{F}}\underline{\boldsymbol{\epsilon}}^{\mathrm{F}}(\delta\underline{\boldsymbol{v}}_{\mathrm{h}}^{\mathrm{F}})\underline{\boldsymbol{n}}_{\mathrm{h}}^{\mathrm{F}},\underline{\boldsymbol{v}}_{\mathrm{h}}^{\mathrm{F}}-\tilde{\partial}_t\left[\underline{\boldsymbol{u}}_{\mathrm{h}}^{\mathrm{S}}\right]-\hat{\underline{\boldsymbol{g}}}_{v}^{\mathrm{FS}}\right\rangle_{\Gamma_{\mathrm{h}}^{\mathrm{FS}}}\\ &+\phi_{\Gamma}^{\mathrm{F}}\gamma_0^{\mathrm{FSI}}\left\langle\delta\underline{\boldsymbol{v}}_{\mathrm{h}}^{\mathrm{F}}-\delta\underline{\boldsymbol{u}}_{\mathrm{h}}^{\mathrm{S}},\underline{\boldsymbol{v}}_{\mathrm{h}}^{\mathrm{F}}-\tilde{\partial}_t\left[\underline{\boldsymbol{u}}_{\mathrm{h}}^{\mathrm{S}}\right]-\hat{\underline{\boldsymbol{g}}}_{v}^{\mathrm{FS}}\right\rangle_{\Gamma_{\mathrm{h}}^{\mathrm{FS}}}.\end{aligned}\tag{3.26}$$

The contributions in the first line consistently replace the terms on the interface $\Gamma_{\mathrm{h}}^{\mathrm{FS}}$ in (3.23) by representing the interface traction as the fluid stress. A comparison of this term with the corresponding last term in (3.12) of the simple Poisson problem in Section 3.3.1, allows understanding the principal construction of the two additional terms. One fundamental difference is that the fluid stress $\underline{\boldsymbol{\sigma}}_{\mathrm{h}}^{\mathrm{F}}$ not only consists of the fluid velocity gradient-based viscous stress but also contains a fluid pressure contribution. A second difference, which occurs for interface conditions in contrast to boundary conditions, is the "jump" of test the functions $\delta\underline{\boldsymbol{u}}^{\mathrm{S}}-\delta\underline{\boldsymbol{v}}^{\mathrm{F}}$ between the solid and fluid domain.

As this "jump" coincides with the no-slip constraint (2.60), a consistent adjoint-consistency term can be constructed as shown in the second line. Whereas the interface contribution of the pressure p^{F} is always compensated by a skew-symmetric adjoint-consistency contribution directly on the interface, the viscous part can be chosen to $\xi^{\mathrm{FSI}}\in\{-1,0,1\}$.

The consistent penalty term is required to enable a stable formulation as discussed for the Poisson equation in Section 3.3.1. When analyzing the prefactor, an increased complexity occurs due to the application of Nitsche's method for the Navier-Stokes equation. This includes a sufficiently large positive constant γ_0^{FSI} and an appropriate mesh size parameter h_Γ based on definition (3.18) (see Section 3.3.1). The mesh size parameter h_Γ is computed by the ratio of the element volume and the part of the area of interface $\Gamma_{\mathrm{h}}^{\mathrm{FS}}$ in the corresponding intersected element in $\Omega_{\mathcal{T}_{\mathrm{h}},e}^{\mathrm{F}}$. In the case an alternative definition based on the ratio of the element volume and the surface area of the largest element face is applied, depending on the intention of the corresponding numerical example this is denoted only if there is a relevant influence on the reported results.

The additive stabilization parameter ϕ_Γ^{F}, which considers the viscous, convective and temporal components of the discrete fluid equations:

$$\phi_\Gamma^{\mathrm{F}} = \frac{1}{h_\Gamma}\left(\mu^{\mathrm{F}} + h_\Gamma c_{v,\Gamma}\rho^{\mathrm{F}}\left|\left|\underline{\boldsymbol{v}}_{\mathrm{h}}^{\mathrm{F}}\right|\right|_{\infty,\Gamma} + h_\Gamma^2 c_{t,\Gamma}\frac{\rho^{\mathrm{F}}}{\theta\Delta t}\right), \tag{3.27}$$

is introduced to enable a stable numerical scheme in all regimes of the fluid equations (see Massing *et al.* [149], Schott [187]). A comparison to the simple formulation in Section 3.3.1, reveals the similarity to the viscous penalty component. The velocity norm $\left|\left|\underline{\boldsymbol{v}}_{\mathrm{h}}^{\mathrm{F}}\right|\right|_{\infty,\Gamma}$ is the maximum fluid velocity component at the current point in space on the interface $\Gamma_{\mathrm{h}}^{\mathrm{FS}}$. The convective and reactive constants are specified as: $c_{v,\Gamma} = 1/6, c_{t,\Gamma} = 1/12$.

To summarize the additional contribution in (3.26) (line two and three), all terms are consistent as they include the kinematic constraint (2.60) and are essential for the stability of the numerical scheme as well as the enforcement of the coupling conditions. For a clear presentation the straightforward temporal discretization is not explicitly specified in $\mathcal{W}_{\mathrm{h}}^{\mathrm{FSI,F}}$, (3.26). Whenever essential, an additional index in $\mathcal{W}_{\mathrm{h},n+1}^{\mathrm{FSI,F}}$ specifies that all interface terms $\langle *,*\rangle_{\Gamma_{\mathrm{h}}^{\mathrm{FS}}}$ are evaluated as $\langle *,*\rangle_{\Gamma_{\mathrm{h},n+1}^{\mathrm{FS}},n+\theta}$.

Remark 3.7 (Normal and tangential split of penalty term)**.** *Different components of the fluid stress contribute to the normal and tangential interface orientation. To account for this aspect, the penalty term can be split in these two orientations. Whereas all contributions of* (3.27) *need to be considered in normal direction, solely the viscous part is required in tangential direction*

$$\begin{aligned}
&\phi_\Gamma^{\mathrm{F}}\gamma_0^{\mathrm{FSI}}\left\langle \delta\underline{\boldsymbol{v}}_{\mathrm{h}}^{\mathrm{F}} - \delta\underline{\boldsymbol{u}}_{\mathrm{h}}^{\mathrm{S}}, \underline{\boldsymbol{v}}_{\mathrm{h}}^{\mathrm{F}} - \tilde{\partial}_t\left[\underline{\boldsymbol{u}}_{\mathrm{h}}^{\mathrm{S}}\right]\right\rangle_{\Gamma_{\mathrm{h}}^{\mathrm{FS}}} \longrightarrow \\
&\phi_\Gamma^{\mathrm{F}}\gamma_0^{\mathrm{FSI}}\left\langle \delta\underline{\boldsymbol{v}}_{\mathrm{h}}^{\mathrm{F}} - \delta\underline{\boldsymbol{u}}_{\mathrm{h}}^{\mathrm{S}}, \left(\underline{\boldsymbol{v}}_{\mathrm{h}}^{\mathrm{F}} - \tilde{\partial}_t\left[\underline{\boldsymbol{u}}_{\mathrm{h}}^{\mathrm{S}}\right]\right)\underline{\boldsymbol{P}}^n\right\rangle_{\Gamma_{\mathrm{h}}^{\mathrm{FS}}} + \frac{\mu^{\mathrm{F}}\gamma_0^{\mathrm{FSI}}}{h_\Gamma}\left\langle \delta\underline{\boldsymbol{v}}_{\mathrm{h}}^{\mathrm{F}} - \delta\underline{\boldsymbol{u}}_{\mathrm{h}}^{\mathrm{S}}, \left(\underline{\boldsymbol{v}}_{\mathrm{h}}^{\mathrm{F}} - \tilde{\partial}_t\left[\underline{\boldsymbol{u}}_{\mathrm{h}}^{\mathrm{S}}\right]\right)\underline{\boldsymbol{P}}^t\right\rangle_{\Gamma_{\mathrm{h}}^{\mathrm{FS}}}.
\end{aligned} \tag{3.28}$$

Due to increased cost for the evaluation of the penalty term, such a split will not be applied for the classical no-slip coupling condition. Nevertheless, in the case of an inherent split of the considered condition in normal and tangential direction, this strategy will be applied. This is the case for the considered coupling of fluid and poroelasticity in Chapters 4, 5 and 7, as well as the coupling of fluid and structures by the general Navier coupling condition in Chapter 6 and 7.

3.3.2.2 Solid-Sided Interface Stress Representation

In contrast to the previously discussed approach, a Nitsche-based FSI formulation for CutFEM-based on a solid-sided interface stress representation has, to the author's best knowledge, not been introduced so far. The principal possibility to choose the FSI interface stress from the solid domain instead of the fluid domain was already mentioned but not analyzed by Burman and Fernández [42] and Zonca *et al.* [239].

With this approach, the interface stress is based on a boundary-fitted discretization and the elements are therefore "uncut". This aspect is already presented for CutFEM domain decomposition (see e.g. the works of Hansbo *et al.* [110], Massing *et al.* [151], Schott [187], Schott *et al.* [190, 191]). In contrast to these works, the solid stress is nonlinear with respect to the primary unknowns, which has an essential effect on the design of the presented approach. From this point of view, the formulation is similar to the recently presented variant of Nitsche-based contact formulation (see the works of Mlika *et al.* [156], Seitz *et al.* [196]).

There are several promising aspects for developing this solid-sided Nitsche-based FSI formulation. Due to the boundary-fitted structural discretization, elements which provide the state for the interface stress are not intersected. As a result, the ghost penalty stabilization is solely required to improve the conditioning of the CutFEM formulation. This is potentially beneficial for "close-to-contact" configurations which include long sequences of intersected fluid elements. As the solid stress on a specific material point on the interface $\Gamma_{\mathrm{h}}^{\mathrm{FS}}$ is always related to the same solid element, possibly an improved continuity of utilized interface stress can be observed. Finally, for problems which include a large contrast of the material parameters related to the interface stress between fluid and solid this formulation can be beneficial. Especially for viscous fluid this is expected.

The additional interface contributions to the weak form for the Nitsche-based FSI-formulation with solid-side interface stress representation are

$$\begin{aligned}
\mathcal{W}_{\mathrm{h}}^{\mathrm{FSI,S}}\left[\left(\delta\underline{\boldsymbol{u}}_{\mathrm{h}}^{\mathrm{S}},\delta\underline{\boldsymbol{v}}_{\mathrm{h}}^{\mathrm{F}}\right),\left(\underline{\boldsymbol{u}}_{\mathrm{h}}^{\mathrm{S}},\underline{\boldsymbol{v}}_{\mathrm{h}}^{\mathrm{F}}\right)\right] &= \left\langle\delta\underline{\boldsymbol{v}}_{\mathrm{h}}^{\mathrm{F}}-\delta\underline{\boldsymbol{u}}_{\mathrm{h}}^{\mathrm{S}},\underline{\boldsymbol{\sigma}}_{\mathrm{h}}^{\mathrm{S}}\underline{\boldsymbol{n}}_{\mathrm{h}}^{\mathrm{S}}\right\rangle_{\Gamma_{\mathrm{h}}^{\mathrm{FS}}} \\
-\left\langle\delta\underline{\boldsymbol{v}}_{\mathrm{h}}^{\mathrm{F}},\hat{\underline{\boldsymbol{g}}}_{\sigma}^{\mathrm{FS}}\right\rangle_{\Gamma_{\mathrm{h}}^{\mathrm{FS}}} &- \phi_t^{\mathrm{S}}\left\langle\xi^{\mathrm{FSI}}\mathcal{D}_{\delta\underline{\boldsymbol{u}}_{\mathrm{h}}^{\mathrm{S}}}\left[\underline{\boldsymbol{\sigma}}_{\mathrm{h}}^{\mathrm{S}}\underline{\boldsymbol{n}}_{\mathrm{h}}^{\mathrm{S}}\right],\underline{\boldsymbol{v}}_{\mathrm{h}}^{\mathrm{F}}-\tilde{\partial}_t\left[\underline{\boldsymbol{u}}_{\mathrm{h}}^{\mathrm{S}}\right]-\hat{\underline{\boldsymbol{g}}}_{v}^{\mathrm{FS}}\right\rangle_{\Gamma_{\mathrm{h}}^{\mathrm{FS}}} \\
&+\phi_{\Gamma}^{\mathrm{S}}\gamma_0^{\mathrm{FSI}}\left\langle\delta\underline{\boldsymbol{v}}_{\mathrm{h}}^{\mathrm{F}}-\delta\underline{\boldsymbol{u}}_{\mathrm{h}}^{\mathrm{S}},\underline{\boldsymbol{v}}_{\mathrm{h}}^{\mathrm{F}}-\tilde{\partial}_t\left[\underline{\boldsymbol{u}}_{\mathrm{h}}^{\mathrm{S}}\right]-\hat{\underline{\boldsymbol{g}}}_{v}^{\mathrm{FS}}\right\rangle_{\Gamma_{\mathrm{h}}^{\mathrm{FS}}},
\end{aligned} \tag{3.29}$$

$$\phi_{\Gamma}^{\mathrm{S}}=\phi_t^{\mathrm{S}}\lambda_e,\quad \phi_t^{\mathrm{S}}=\theta\Delta t. \tag{3.30}$$

In the first line, the interface traction is represented by the solid stress. Therefore, this term consistently replaces the interface terms on $\Gamma_{\mathrm{h}}^{\mathrm{FS}}$ in (3.23). As this term can be identified as the corresponding interface term in (3.12), it motivates the construction of the Nitsche-based formulation in a similar way to Section 3.3.1.

One major difference compared to (3.12) are the nonlinear kinematics of the solid problem (considering relation (2.13) for the Cauchy stress) and the nonlinear constitutive law (2.16) (with e.g. the Neo-Hookean strain energy density function (2.17)). While interface terms including a linear stress representation (such as viscous fluid with constant viscosity) allow for a direct construction of adjoint-consistency terms, the directional derivative has to be utilized in case of a nonlinear stress representation (see Remark 3.11). The operator $\mathcal{D}_{\underline{\boldsymbol{v}}}\left[\underline{\boldsymbol{a}}\right]$ denotes the directional

derivative of a vector $\underline{\boldsymbol{a}}$ in direction of the vector $\underline{\boldsymbol{v}}$. Using this notation, an adjoint-consistency like term is added in the second line for the compensation of destabilizing effects introduced by the term in the first line for $\xi^{\mathrm{FSI}} = 1$. Also the variant without this term $\xi^{\mathrm{FSI}} = 0$ is promising as it avoids the evaluation of this term. The "symmetric variant" with $\xi^{\mathrm{FSI}} = -1$ is not considered in the following.

Finally, due to the nonlinearity of the solid stress, the scaling of the penalty term ϕ_Γ^{S} in the third line is based on a generalized eigenvalue problem as introduced in Section 3.3.1. Therein, the element matrices $\underline{\boldsymbol{A}}_e$ and $\underline{\boldsymbol{B}}_e$ are based on

$$\left\langle \mathcal{D}_{\delta\underline{\boldsymbol{u}}_{\mathrm{h}}^{\mathrm{S}}} \left[\underline{\boldsymbol{\sigma}}_{\mathrm{h}}^{\mathrm{S}} \underline{\boldsymbol{n}}_{\mathrm{h}}^{\mathrm{S}}\right], \underline{\boldsymbol{\sigma}}_{\mathrm{h}}^{\mathrm{S}} \underline{\boldsymbol{n}}_{\mathrm{h}}^{\mathrm{S}} \right\rangle_{\Gamma_{\mathrm{h}}^{\mathrm{FS}} \cap \Omega_{\mathcal{T}_{\mathrm{h}},e}^{\mathrm{S}}} \longrightarrow \underline{\boldsymbol{A}}_e, \left(\boldsymbol{\nabla}_0 \delta\underline{\boldsymbol{u}}_{\mathrm{h}}^{\mathrm{S}}, \underline{\boldsymbol{P}}_{\mathrm{h}}^{\mathrm{S}}\right)_{\Omega_{0,\mathrm{h}}^{\mathrm{S}} \cap \Omega_{\mathcal{T}_{\mathrm{h}},e}^{\mathrm{S}}} \longrightarrow \underline{\boldsymbol{B}}_e, \tag{3.31}$$

neglecting the derivatives of the normal vector $\underline{\boldsymbol{n}}_{\mathrm{h}}^{\mathrm{S}}$. The maximum eigenvalue λ_e of the generalized local eigenvalue problem (3.19) in element e, utilizing definitions (3.31), builds the basis for specifying the penalty scaling ϕ_Γ^{S}. To avoid incorrectly determined eigenvalues due to the not included rigid-body modes in both matrices $\underline{\boldsymbol{A}}_e$ and $\underline{\boldsymbol{B}}_e$, a contribution accounting for these modes is added to matrix $\underline{\boldsymbol{B}}_e$. Thus, the corresponding eigenvalues of the generalized eigenvalue problem vanish and do not have any effect on the maximum eigenvalue. Additionally, the time scaling ϕ_t^{S} in ϕ_Γ^{S} takes into account the relation by the discrete time derivative of the displacement-based elastic term in the domain $\Omega_{0,\mathrm{h}}^{\mathrm{S}}$ and the velocity-based penalty term on the interface $\Gamma_{\mathrm{h}}^{\mathrm{FS}}$. For a clear presentation, the straightforward temporal discretization is not explicitly specified in $\mathcal{W}_{\mathrm{h}}^{\mathrm{FSI,S}}$, (3.29). Whenever essential, an additional index in $\mathcal{W}_{\mathrm{h},n+1}^{\mathrm{FSI,S}}$ specifies that all interface terms $\langle *, * \rangle_{\Gamma_{\mathrm{h}}^{\mathrm{FS}}}$ are evaluated as $\langle *, * \rangle_{\Gamma_{\mathrm{h},n+1}^{\mathrm{FS}},n+\theta}$.

Remark 3.8 (Update strategy of Nitsche penalty scaling ϕ_Γ^{S})**.** *The scaling ϕ_Γ^{S} depends on the current deformation state $\underline{\boldsymbol{u}}_{\mathrm{h}}^{\mathrm{S}}$, and thus, needs to be updated in every iteration of the nonlinear solution procedure from a theoretical point of view. Nevertheless, alternative and computational less expensive strategies to update ϕ_Γ^{S} can be applied. In Section 3.5.2.2, numerical tests are performed to analyze different update strategies.*

Remark 3.9 (Evaluation of the directional derivative $\mathcal{D}_{\delta\underline{\boldsymbol{u}}_{\mathrm{h}}^{\mathrm{S}}} \left[\underline{\boldsymbol{\sigma}}_{\mathrm{h}}^{\mathrm{S}} \underline{\boldsymbol{n}}_{\mathrm{h}}^{\mathrm{S}}\right]$)**.** *For all numerical tests and examples presented in the following the direction derivative $\mathcal{D}_{\delta\underline{\boldsymbol{u}}_{\mathrm{h}}^{\mathrm{S}}} \left[\underline{\boldsymbol{\sigma}}_{\mathrm{h}}^{\mathrm{S}} \underline{\boldsymbol{n}}_{\mathrm{h}}^{\mathrm{S}}\right]$ does not include the derivative of the normal vector $\mathcal{D}_{\delta\underline{\boldsymbol{u}}_{\mathrm{h}}^{\mathrm{S}}} \left[\underline{\boldsymbol{\sigma}}_{\mathrm{h}}^{\mathrm{S}} \underline{\boldsymbol{n}}_{\mathrm{h}}^{\mathrm{S}}\right] \approx \mathcal{D}_{\delta\underline{\boldsymbol{u}}_{\mathrm{h}}^{\mathrm{S}}} \left[\underline{\boldsymbol{\sigma}}_{\mathrm{h}}^{\mathrm{S}}\right] \underline{\boldsymbol{n}}_{\mathrm{h}}^{\mathrm{S}}$.*

Remark 3.10 (Application of the formulation with $\xi^{\mathrm{FSI}} = 1$ including a small parameter γ_0^{FSI})**.** *The formulation including a skew-symmetric adjoint-consistency term ($\xi^{\mathrm{FSI}} = 1$) is applicable for certain problem configurations with small penalty parameters γ_0^{FSI} (see e.g. the numerical test presented in Section 3.5.2.2). Nevertheless, for general FSI configurations the displacement of the solid body has to be constrained often close to interface $\Gamma_{\mathrm{h}}^{\mathrm{FS}}$. If this condition is enforced in a strong node-wise sense, and constrained computational nodes are part of the interface $\Gamma_{\mathrm{h}}^{\mathrm{FS}}$, only the nodal contribution of the penalty term in $\mathcal{W}_{\mathrm{h}}^{\mathrm{FSI,S}}$ remains to enforce the no-slip constraint (as $\delta\underline{\boldsymbol{u}}^{\mathrm{S}} = 0$ on $\Gamma^{\mathrm{S,D}}$). In the case a small parameter γ_0^{FSI} is used (only applicable in combination with $\xi^{\mathrm{FSI}} = 1$), this leads to a significant violation of the no-slip constraint close to these nodes. For a larger parameter γ_0^{FSI} (as required for a stable formulation with $\xi^{\mathrm{FSI}} = 0$) this issues was found to be not critical for all numerical examples which were performed. Enforcing the constraints on $\Gamma^{\mathrm{S,D}}$ also weakly by the Nitsche method would solve this problem right away.*

Remark 3.11 (Construction of the skew-symmetric adjoint-consistency term)**.** *The consistent term in line one and the skew-symmetric adjoint-consistency term (with $\xi^{\mathrm{FSI}} = 1$) in line two of* (3.29) *are considered in the following. Analyzing the linearized system* (2.131) $\underline{\mathbf{C}}^i$ *of these two terms for a specific iteration step i (see Section 2.3), allows understanding the construction of the adjoint-consistency term. The linearized contributions, neglecting changes due to the interface deformation, of the first two terms in* (3.29)*, are*

$$\left\langle \delta\underline{\boldsymbol{v}}_{\mathrm{h}}^{\mathrm{F}} - \delta\underline{\boldsymbol{u}}_{\mathrm{h}}^{\mathrm{S}}, \mathcal{D}_{\Delta\underline{\boldsymbol{u}}_{\mathrm{h}}^{\mathrm{S},i}}\left[\underline{\boldsymbol{\sigma}}_{\mathrm{h}}^{\mathrm{S},i-1}\underline{\boldsymbol{n}}_{\mathrm{h}}^{\mathrm{S},i-1}\right]\right\rangle_{\Gamma_{\mathrm{h}}^{\mathrm{FS}}} - \phi_t^{\mathrm{S}}\left\langle \mathcal{D}_{\delta\underline{\boldsymbol{u}}_{\mathrm{h}}^{\mathrm{S}}}\left[\underline{\boldsymbol{\sigma}}_{\mathrm{h}}^{\mathrm{S},i-1}\underline{\boldsymbol{n}}_{\mathrm{h}}^{\mathrm{S},i-1}\right], \Delta\underline{\boldsymbol{v}}_{\mathrm{h}}^{\mathrm{F},i} - \tilde{\partial}_t\left[\Delta\underline{\boldsymbol{u}}_{\mathrm{h}}^{\mathrm{S},i}\right]\right\rangle_{\Gamma_{\mathrm{h}}^{\mathrm{FS}}}. \tag{3.32}$$

Following the basic concept of a coercivity analysis (as in (3.14) *for the Poisson problem) by testing the terms of the linearized system with*

$$\left[\left(\delta\underline{\boldsymbol{u}}_{\mathrm{h}}^{\mathrm{S}}, \delta\underline{\boldsymbol{v}}_{\mathrm{h}}^{\mathrm{F}}\right), \left(\Delta\underline{\boldsymbol{u}}_{\mathrm{h}}^{\mathrm{S},i}, \Delta\underline{\boldsymbol{v}}_{\mathrm{h}}^{\mathrm{F},i}\right)\right] := \left[\left(\tilde{\partial}_t\left[\underline{\boldsymbol{u}}_{\mathrm{h}}^{\mathrm{S},i}\right], \underline{\boldsymbol{v}}_{\mathrm{h}}^{\mathrm{F},i}\right), \left(\underline{\boldsymbol{u}}_{\mathrm{h}}^{\mathrm{S},i}, \underline{\boldsymbol{v}}_{\mathrm{h}}^{\mathrm{F},i}\right)\right], \tag{3.33}$$

motivates the factor ϕ_t^{S} and shows the direct compensation of the two linearized terms

$$\begin{aligned}\left\langle \underline{\boldsymbol{v}}_{\mathrm{h}}^{\mathrm{F},i} - \tilde{\partial}_t\left[\underline{\boldsymbol{u}}_{\mathrm{h}}^{\mathrm{S},i}\right], \mathcal{D}_{\underline{\boldsymbol{u}}_{\mathrm{h}}^{\mathrm{S},i}}\left[\underline{\boldsymbol{\sigma}}\,\underline{\boldsymbol{n}}\right]\right\rangle_{\Gamma_{\mathrm{h}}^{\mathrm{FS}}} - \phi_t^{\mathrm{S}}\left\langle \mathcal{D}_{\tilde{\partial}_t\left[\underline{\boldsymbol{u}}_{\mathrm{h}}^{\mathrm{S},i}\right]}\left[\underline{\boldsymbol{\sigma}}\,\underline{\boldsymbol{n}}\right], \underline{\boldsymbol{v}}_{\mathrm{h}}^{\mathrm{F},i} - \tilde{\partial}_t\left[\underline{\boldsymbol{u}}_{\mathrm{h}}^{\mathrm{S},i}\right]\right\rangle_{\Gamma_{\mathrm{h}}^{\mathrm{FS}}},\\ \text{with}\quad \mathcal{D}_{\underline{\boldsymbol{u}}_{\mathrm{h}}^{\mathrm{S},i}}\left[\underline{\boldsymbol{\sigma}}\,\underline{\boldsymbol{n}}\right] = \phi_t^{\mathrm{S}}\mathcal{D}_{\tilde{\partial}_t\left[\underline{\boldsymbol{u}}_{\mathrm{h}}^{\mathrm{S},i}\right]}\left[\underline{\boldsymbol{\sigma}}\,\underline{\boldsymbol{n}}\right], \quad \text{and}\quad \underline{\boldsymbol{\sigma}}\,\underline{\boldsymbol{n}} := \underline{\boldsymbol{\sigma}}_{\mathrm{h}}^{\mathrm{S},i-1}\underline{\boldsymbol{n}}_{\mathrm{h}}^{\mathrm{S},i-1}.\end{aligned} \tag{3.34}$$

Remark 3.12 (Directional derivatives for linear stress representation)**.** *The construction of the adjoint-consistency term in case of a nonlinear interface stress is based on the directional derivative in direction of the test function. As this coincides with the evaluation of the stress by the test function in case of a linear interface stress, e.g. for the fluid stress*

$$\underline{\boldsymbol{\sigma}}_{\mathrm{h}}^{\mathrm{F}}\left(\delta\underline{\boldsymbol{v}}_{\mathrm{h}}^{\mathrm{F}}, \delta p_{\mathrm{h}}^{\mathrm{F}}\right)\underline{\boldsymbol{n}}_{\mathrm{h}}^{\mathrm{F}} = \mathcal{D}_{\left(\delta\underline{\boldsymbol{v}}_{\mathrm{h}}^{\mathrm{F}}, \delta p_{\mathrm{h}}^{\mathrm{F}}\right)}\left[\underline{\boldsymbol{\sigma}}_{\mathrm{h}}^{\mathrm{F}}\left(\underline{\boldsymbol{v}}_{\mathrm{h}}^{\mathrm{F}}, p_{\mathrm{h}}^{\mathrm{F}}\right)\underline{\boldsymbol{n}}_{\mathrm{h}}^{\mathrm{F}}\right] \quad \forall \quad \left(\underline{\boldsymbol{v}}_{\mathrm{h}}^{\mathrm{F}}, p_{\mathrm{h}}^{\mathrm{F}}\right), \tag{3.35}$$

the direct evaluation is typically applied (see Section 3.3.2.1). This equality does not hold for a nonlinear interface stress, e.g. for the solid stress

$$\exists \quad \underline{\boldsymbol{u}}^{\mathrm{S}} \quad \text{such that} \quad \underline{\boldsymbol{\sigma}}_{\mathrm{h}}^{\mathrm{S}}\left(\delta\underline{\boldsymbol{u}}_{\mathrm{h}}^{\mathrm{S}}\right)\underline{\boldsymbol{n}}_{\mathrm{h}}^{\mathrm{S}} \neq \mathcal{D}_{\delta\underline{\boldsymbol{u}}_{\mathrm{h}}^{\mathrm{S}}}\left[\underline{\boldsymbol{\sigma}}_{\mathrm{h}}^{\mathrm{S}}\left(\underline{\boldsymbol{u}}_{\mathrm{h}}^{\mathrm{S}}\right)\underline{\boldsymbol{n}}_{\mathrm{h}}^{\mathrm{S}}\right]. \tag{3.36}$$

3.3.3 Nitsche-based Fluid Domain Decomposition

Finally, a Nitsche-based formulation which enables domain decomposition of the fluid domain Ω^{F} in the non-overlapping subdomains $\Omega^{\mathrm{F}_1} \cup \Omega^{\mathrm{F}_2}$ (with $\Omega^{\mathrm{F}_1} \cap \Omega^{\mathrm{F}_2} = \emptyset$) is presented briefly. Hereby, the subdomain Ω^{F_1} is discretized fitted to the arising fluid-fluid interface $\Gamma_{\mathrm{h}}^{\mathrm{FF}}$. The computational mesh of the subdomain Ω^{F_2} is unfitted to this interface and Ω^{F_1} is "cut" out as discussed in Section 3.1. Making use of unfitted fluid domain decomposition allows applying a local adjusted mesh resolution in the fluid domain depending on the complexity of the solution. The motivation for using such a domain decomposition formulation within this thesis is based on its capability to increase the fluid mesh resolution close to a moving interface ($\Gamma_{\mathrm{h}}^{\mathrm{FS}}$ or $\Gamma_{\mathrm{h}}^{\mathrm{FP}}$) without requiring remeshing procedures.

Fluid domain decomposition for interface-fitted discretizations of both subdomains which is enabled by the dual mortar Lagrange multiplier approach was treated by Ehrl *et al.* [78]. Shahmiri *et al.* [199] suggested a interface-unfitted domain decomposition approach based on a mixed/hybrid Lagrange multiplier technique for viscous flow. Domain decomposition based on the Nitsche method was presented for the Poisson problem by Hansbo *et al.* [110], for an advection-diffusion-reaction system by Burman and Zunino [48] and for the Stokes equation in fluid-structure interaction by Massing *et al.* [151]. The following Nitsche-based formulation was already presented and analyzed in Schott [187], Schott *et al.* [190, 191] and Shahmiri [198] and is given here for the sake of completeness. The Nitsche-based contributions added to the weak form are

$$\begin{aligned}
\mathcal{W}_{\mathrm{h}}^{\mathrm{FFI}}\left[\left(\delta\underline{\boldsymbol{v}}_{\mathrm{h}}^{\mathrm{F}},\delta p_{\mathrm{h}}^{\mathrm{F}}\right),\left(\underline{\boldsymbol{v}}_{\mathrm{h}}^{\mathrm{F}},p_{\mathrm{h}}^{\mathrm{F}}\right)\right] &= -\left\langle\delta\underline{\boldsymbol{v}}_{\mathrm{h}}^{\mathrm{F}_1}-\delta\underline{\boldsymbol{v}}_{\mathrm{h}}^{\mathrm{F}_2},\left[\kappa^1\underline{\boldsymbol{\sigma}}_{\mathrm{h}}^{\mathrm{F}_1}-\kappa^2\underline{\boldsymbol{\sigma}}_{\mathrm{h}}^{\mathrm{F}_2}\right]\underline{\boldsymbol{n}}_{\mathrm{h}}^{\mathrm{F}_1}\right\rangle_{\Gamma_{\mathrm{h}}^{\mathrm{FF}}} \\
-\left\langle\left[\left(\kappa^1\delta p_{\mathrm{h}}^{\mathrm{F}_1}-\kappa^2\delta p_{\mathrm{h}}^{\mathrm{F}_2}\right)-2\xi^{\mathrm{FFI}}\mu^{\mathrm{F}}\left(\kappa^1\underline{\boldsymbol{\epsilon}}^{\mathrm{F}}(\delta\underline{\boldsymbol{v}}_{\mathrm{h}}^{\mathrm{F}_1})-\kappa^2\underline{\boldsymbol{\epsilon}}^{\mathrm{F}}(\delta\underline{\boldsymbol{v}}_{\mathrm{h}}^{\mathrm{F}_2})\right)\right]\underline{\boldsymbol{n}}_{\mathrm{h}}^{\mathrm{F}_1},\underline{\boldsymbol{v}}_{\mathrm{h}}^{\mathrm{F}_1}-\underline{\boldsymbol{v}}_{\mathrm{h}}^{\mathrm{F}_2}\right\rangle_{\Gamma_{\mathrm{h}}^{\mathrm{FF}}} \\
&\quad+\phi_{\Gamma}^{\mathrm{F}}\gamma_0^{\mathrm{FFI}}\left\langle\delta\underline{\boldsymbol{v}}_{\mathrm{h}}^{\mathrm{F}_1}-\delta\underline{\boldsymbol{v}}_{\mathrm{h}}^{\mathrm{F}_2},\underline{\boldsymbol{v}}_{\mathrm{h}}^{\mathrm{F}_1}-\underline{\boldsymbol{v}}_{\mathrm{h}}^{\mathrm{F}_2}\right\rangle_{\Gamma_{\mathrm{h}}^{\mathrm{FF}}} \\
+\frac{1}{2}\rho^{\mathrm{F}}\left\langle\left|\underline{\boldsymbol{v}}^{\mathrm{F}_{[1,2]}}\cdot\underline{\boldsymbol{n}}^{\mathrm{F}_1}\right|\left(\delta\underline{\boldsymbol{v}}_{\mathrm{h}}^{\mathrm{F}_1}-\delta\underline{\boldsymbol{v}}_{\mathrm{h}}^{\mathrm{F}_2}\right)-\underline{\boldsymbol{v}}^{\mathrm{F}_{[1,2]}}\cdot\underline{\boldsymbol{n}}^{\mathrm{F}_1}\left(\delta\underline{\boldsymbol{v}}_{\mathrm{h}}^{\mathrm{F}_1}+\delta\underline{\boldsymbol{v}}_{\mathrm{h}}^{\mathrm{F}_2}\right),\underline{\boldsymbol{v}}_{\mathrm{h}}^{\mathrm{F}_1}-\underline{\boldsymbol{v}}_{\mathrm{h}}^{\mathrm{F}_2}\right\rangle_{\Gamma_{\mathrm{h}}^{\mathrm{FF}}}. &\quad (3.37)
\end{aligned}$$

Herein, all quantities corresponding to the fluid subdomain $\Omega^{\mathrm{F}_1}/\Omega^{\mathrm{F}_2}$ are indicated by the additionally index $1/2$. The weighting factors κ^1 and κ^2 (with $\kappa^1+\kappa^2=1$) determine if the interface stress representation is based on the fluid solution of Ω^{F_1} ($\kappa^1=1$), of Ω^{F_2} ($\kappa^2=1$), or a combination of both domains.

The terms of this formulation are analogous to the Nitsche-based formulations for the fluid-structure interface. The term in the first line consistently replaces the terms arising from partial integration in the derivation of the weak formulation (2.112). All additional terms include the kinematic continuity of the velocity and are therefore also consistent. The adjoint-consistency contribution in line two and the penalty term in line three were already discussed in Section 3.3.1. To ensure a robust formulation also for convection through the interface, the additional consistent inflow terms in the last line are added (for details see [187, 190, 191, 198]).

Analogous to the fluid-sided Nitsche-based formulation for the fluid-structure interface, the penalty term can be split into a normal and tangential part, considering only the viscous regime in tangential direction (see Remark 3.7). For a clear presentation, the straightforward temporal discretization is not explicitly specified in $\mathcal{W}_{\mathrm{h}}^{\mathrm{FFI}}$, (3.37). Whenever essential, an additional index in $\mathcal{W}_{\mathrm{h},n+1}^{\mathrm{FFI}}$ specifies that all interface terms $\langle *,*\rangle_{\Gamma_{\mathrm{h}}^{\mathrm{FF}}}$ are evaluated as $\langle *,*\rangle_{\Gamma_{\mathrm{h},n+1}^{\mathrm{FF}},n+\theta}$. For further details, the interested reader is referred to the cited references.

3.3.4 Coupled Discrete Formulation

To formulate the overall discrete system (including also a poroelastic domain), the discrete formulations (2.108), (2.112), and (2.121) of the respective domains are completed by the previously presented interface contributions (3.26), (3.29), and (3.37). The overall discrete solution space $\mathcal{S}_{\underline{\boldsymbol{x}},\mathrm{h},n+1}$ and discrete test function space $\mathcal{T}_{\delta\underline{\boldsymbol{x}},\mathrm{h},n+1}$ result from the discrete spaces of the underlying physical fields.

$$\begin{aligned}
\mathcal{S}_{\underline{\boldsymbol{x}},\mathrm{h},n+1} &:= \mathcal{S}_{\underline{\boldsymbol{u}}^{\mathrm{S}},\mathrm{h},n+1}\times\mathcal{S}_{\underline{\boldsymbol{v}}^{\mathrm{F}},\mathrm{h},n+1}\times\mathcal{S}_{p^{\mathrm{F}},\mathrm{h},n+1}\times\mathcal{S}_{\underline{\boldsymbol{u}}^{\mathrm{P}},\mathrm{h},n+1}\times\mathcal{S}_{\underline{\boldsymbol{v}}^{\mathrm{P}},\mathrm{h},n+1}\times\mathcal{S}_{p^{\mathrm{P}},\mathrm{h}} \\
\mathcal{T}_{\delta\underline{\boldsymbol{x}},\mathrm{h},n+1} &:= \mathcal{T}_{\delta\underline{\boldsymbol{u}}^{\mathrm{S}},\mathrm{h}}\times\mathcal{T}_{\delta\underline{\boldsymbol{v}}^{\mathrm{F}},\mathrm{h},n+1}\times\mathcal{T}_{\delta p^{\mathrm{F}},\mathrm{h},n+1}\times\mathcal{T}_{\delta\underline{\boldsymbol{u}}^{\mathrm{P}},\mathrm{h}}\times\mathcal{T}_{\delta\underline{\boldsymbol{v}}^{\mathrm{P}},\mathrm{h}}\times\mathcal{T}_{\delta p^{\mathrm{P}},\mathrm{h}} \qquad (3.38)
\end{aligned}$$

To allow for a compact notation, the overall discrete test function $\delta\underline{\boldsymbol{x}}_{\mathrm{h}}$ and discrete solution state $\underline{\boldsymbol{x}}_{\mathrm{h},n+1}$ are summarized by

$$\begin{aligned}\underline{\boldsymbol{x}}_{\mathrm{h},n+1} &:= \left(\underline{\boldsymbol{u}}^{\mathrm{S}}_{\mathrm{h},n+1}, \underline{\boldsymbol{v}}^{\mathrm{F}}_{\mathrm{h},n+1}, p^{\mathrm{F}}_{\mathrm{h},n+1}, \underline{\boldsymbol{v}}^{\mathrm{P}}_{\mathrm{h},n+1}, \underline{\boldsymbol{u}}^{\mathrm{P}}_{\mathrm{h},n+1}, p^{\mathrm{P}}_{\mathrm{h},n+1}\right), \\ \delta\underline{\boldsymbol{x}}_{\mathrm{h}} &:= \left(\delta\underline{\boldsymbol{u}}^{\mathrm{S}}_{\mathrm{h}}, \delta\underline{\boldsymbol{v}}^{\mathrm{F}}_{\mathrm{h}}, \delta p^{\mathrm{F}}_{\mathrm{h}}, \delta\underline{\boldsymbol{v}}^{\mathrm{P}}_{\mathrm{h}}, \delta\underline{\boldsymbol{u}}^{\mathrm{P}}_{\mathrm{h}}, \delta p^{\mathrm{P}}_{\mathrm{h}}\right). \end{aligned} \tag{3.39}$$

Making use of (3.38) and (3.39), the overall discrete formulation of the coupled CutFEM FSI problem is given by:

Find $\underline{\boldsymbol{x}}_{\mathrm{h},n+1} \in \mathcal{S}_{\underline{\boldsymbol{x}},\mathrm{h},n+1}$ *such that for all* $\delta\underline{\boldsymbol{x}}_{\mathrm{h}} \in \mathcal{T}_{\delta\underline{\boldsymbol{x}},\mathrm{h},n+1}$:

$$\mathcal{W}_{\mathrm{h},n+1}\left[\delta\underline{\boldsymbol{x}}_{\mathrm{h}}, \underline{\boldsymbol{x}}_{\mathrm{h},n+1}\right] = 0. \tag{3.40}$$

The underlying weak form results from a simple summation of the corresponding weak forms of all corresponding physical fields and interfaces.

$$\begin{aligned}&\mathcal{W}_{\mathrm{h},n+1}\left[\delta\underline{\boldsymbol{x}}_{\mathrm{h}}, \underline{\boldsymbol{x}}_{\mathrm{h},n+1}\right] = \\ &\quad \mathcal{W}^{\mathrm{S}}_{\mathrm{h},n+1}\left[\delta\underline{\boldsymbol{u}}^{\mathrm{S}}_{\mathrm{h}}, \underline{\boldsymbol{u}}^{\mathrm{S}}_{\mathrm{h},n+1}\right] + \mathcal{W}^{\mathrm{F,CUT}}_{\mathrm{h},n+1}\left[\left(\delta\underline{\boldsymbol{v}}^{\mathrm{F}}_{\mathrm{h}}, \delta p^{\mathrm{F}}_{\mathrm{h}}\right), \left(\underline{\boldsymbol{v}}^{\mathrm{F}}_{\mathrm{h},n+1}, p^{\mathrm{F}}_{\mathrm{h},n+1}\right)\right] + \\ &\quad \mathcal{W}^{\mathrm{FSI,o}}_{\mathrm{h},n+1}\left[\left(\delta\underline{\boldsymbol{u}}^{\mathrm{S}}_{\mathrm{h}}, \delta\underline{\boldsymbol{v}}^{\mathrm{F}}_{\mathrm{h}}, \delta p^{\mathrm{F}}_{\mathrm{h}}\right), \left(\underline{\boldsymbol{u}}^{\mathrm{S}}_{\mathrm{h},n+1}, \underline{\boldsymbol{v}}^{\mathrm{F}}_{\mathrm{h},n+1}, p^{\mathrm{F}}_{\mathrm{h},n+1}\right)\right] + \\ &\quad \mathcal{W}^{\mathrm{FFI}}_{\mathrm{h},n+1}\left[\left(\delta\underline{\boldsymbol{v}}^{\mathrm{F}}_{\mathrm{h}}, \delta p^{\mathrm{F}}_{\mathrm{h}}\right), \left(\underline{\boldsymbol{v}}^{\mathrm{F}}_{\mathrm{h},n+1}, p^{\mathrm{F}}_{\mathrm{h},n+1}\right)\right] + \\ &\quad \mathcal{W}^{\mathrm{P}}_{\mathrm{h},n+1}\left[\left(\delta\underline{\boldsymbol{v}}^{\mathrm{P}}_{\mathrm{h}}, \delta\underline{\boldsymbol{u}}^{\mathrm{P}}_{\mathrm{h}}, \delta p^{\mathrm{P}}_{\mathrm{h}}\right), \left(\underline{\boldsymbol{v}}^{\mathrm{P}}_{\mathrm{h},n+1}, \underline{\boldsymbol{u}}^{\mathrm{P}}_{\mathrm{h},n+1}, p^{\mathrm{P}}_{\mathrm{h},n+1}\right)\right] + \mathcal{W}^{**\mathrm{I}}_{\mathrm{h},n+1}\left[\delta\underline{\boldsymbol{x}}_{\mathrm{h}}, \underline{\boldsymbol{x}}_{\mathrm{h},n+1}\right] \\ &\quad \text{with} \quad \mathrm{o} = \{\mathrm{F}, \mathrm{S}\}, \quad \text{and with} \quad * = \{\mathrm{F}, \mathrm{S}, \mathrm{P}\} \end{aligned} \tag{3.41}$$

Herein, the contribution $\mathcal{W}^{\mathrm{P}}_{\mathrm{h},n+1}$ takes into account a potential poroelastic domain. The interface contribution $\mathcal{W}^{**\mathrm{I}}_{\mathrm{h},n+1}$ will be substituted in the following chapters to account for additional interface couplings. This includes the coupling on a fluid-poroelastic interface, a structure-structure contact interface, a structure-poroelastic contact interface, and a poroelastic-poroelastic contact interface. When considering pure CutFEM FSI, these two contributions vanish and are not evaluated in the solution procedure.

3.4 Nonlinear Solution Procedure

The numerical solution of the nonlinear problems of fluid (including potential mesh motion), poroelasticity, and structure, still neglecting the interaction of the different fields, was presented in Section 2.3. The application of analogous steps as discussed in Sections 2.2.3, 2.2.4, and 2.2.5 for the coupled discrete weak form (3.41), results in one coupled system of nonlinear equations. When using exclusively boundary-fitted discretization, such a system can be solved directly with the approach presented in Section 2.3.

This is not directly possible in case the CutFEM is applied for discretization of the fluid domain. The additional challenge for the nonlinear solution procedure arises from the changing discrete solution spaces and therefore the varying number of unknowns of the system that has to be solved. These changes occur between different discrete time steps as well as between different steps of the iterative procedure that is applied to solve the nonlinear system of equations.

In Algorithm 1, the principal solution steps are given. To avoid a recurring discussion of this approach in the subsequent chapters, also potential vectors of nodal unknowns that are arising from the discretization of a poroelastic domain ($\underline{\mathbf{u}}^{\mathrm{P}}, \underline{\mathbf{v}}^{\mathrm{P}}, \underline{\mathbf{p}}^{\mathrm{P}}$) are considered as this has no essential effect on the overall solution algorithm. When considering exclusively impermeable solids in the FSI, as presented in this chapter, these additional unknowns vanish. In the following, the essential steps of the algorithm are discussed.

Algorithm 1 Nonlinear solution procedure

1: Initialize: $n = 0; t = t_0;$
2: **while** $t < t_{\mathrm{E}}$ **do**
3: Update/Initialize: $t = t + \Delta t; i = 0;$
4: Get state: $\underline{\mathbf{x}}_n$
5: Predict state: $\underline{\mathbf{x}}^0_{n+1}$
6: **while not** converged **do**
7: Intersect $\Gamma^{\mathrm{FS}}_{\mathrm{h}}, \Gamma^{\mathrm{FP}}_{\mathrm{h}}, \Gamma^{\mathrm{FF}}_{\mathrm{h}}$ with $\breve{\Omega}^{\mathrm{F}}_{\mathcal{T}_{\mathrm{h}}} \rightarrow$ get "new" discrete solution space $\mathcal{S}^{i+1}_{\underline{\boldsymbol{x}},\mathrm{h},n+1}$
8: Get fluid state for t_n in current solution space with (3.9): $\underline{\mathbf{v}}^{\mathrm{F}}_n, \underline{\mathbf{p}}^{\mathrm{F}}_n \rightarrow \underline{\tilde{\mathbf{v}}}^{\mathrm{F}}_n, \underline{\tilde{\mathbf{p}}}^{\mathrm{F}}_n$
9: Get current fluid state in current solution space with (3.9): $\underline{\mathbf{v}}^{\mathrm{F},i}_{n+1}, \underline{\mathbf{p}}^{\mathrm{F},i}_{n+1} \rightarrow \underline{\tilde{\mathbf{v}}}^{\mathrm{F},i}_{n+1}, \underline{\tilde{\mathbf{p}}}^{\mathrm{F},i}_{n+1}$
10: Evaluate residual vector and linearization matrix $\underline{\mathbf{R}}^i_{n+1}, \underline{\mathbf{C}}^i_{n+1}$
11: Solve linear system $\underline{\mathbf{C}}^i_{n+1} \cdot \Delta\underline{\mathbf{x}}^{i+1}_{n+1} = -\underline{\mathbf{R}}^i_{n+1}$
12: Update $\underline{\mathbf{x}}^{i+1}_{n+1} = \underline{\tilde{\mathbf{x}}}^i_{n+1} + \omega^i \Delta\underline{\mathbf{x}}^{i+1}_{n+1}$
13: **end while** $i = i + 1;$
14: **end while** $n = n + 1;$

After the initialization and update procedures (Steps 1 to 3), the solution state (represented by the vector of nodal states $\underline{\mathbf{x}}_n := \left[\underline{\mathbf{u}}^{\mathrm{S}}_n, \underline{\mathbf{v}}^{\mathrm{F}}_n, \underline{\mathbf{p}}^{\mathrm{F}}_n, \underline{\mathbf{u}}^{\mathrm{G}}_n, \underline{\mathbf{u}}^{\mathrm{P}}_n, \underline{\mathbf{v}}^{\mathrm{P}}_n, \underline{\mathbf{p}}^{\mathrm{P}}_n\right]$) of the previous or initial time step t_n in the discrete function space of the previous time step $\mathcal{S}_{\underline{\boldsymbol{x}},\mathrm{h},n}$ is determined in Step 4. Based on this state $\underline{\mathbf{x}}_n$, in Step 5, the initial state $\underline{\mathbf{x}}^0_{n+1}$ in the function space $\mathcal{S}^0_{\underline{\boldsymbol{x}},\mathrm{h},n+1} := \mathcal{S}_{\underline{\boldsymbol{x}},\mathrm{h},n}$ that serves as the starting point for the iterative procedure is specified. The following Steps 6 to 13 are repeatedly performed as long as the procedure did not converge (see Section 2.3 for convergence criteria).

In Step 7, the deformed interfaces $\Gamma^{\mathrm{FS}}_{\mathrm{h}}$ (displacement state $\underline{\mathbf{u}}^{\mathrm{S},i}_{n+1}$), Γ^{FP} (displacement state $\underline{\mathbf{u}}^{\mathrm{P},i}_{n+1}$), and $\Gamma^{\mathrm{FF}}_{\mathrm{h}}$ (displacement state $\underline{\mathbf{u}}^{\mathrm{G},i}_{n+1}$) are intersected with the potentially deformed fluid mesh (displacement state $\underline{\mathbf{u}}^{\mathrm{G},i}_{n+1}$). This includes the determination of numerical integration points on the discrete interfaces $\Gamma^{\mathrm{FS}}_{\mathrm{h}}$, Γ^{FP}, $\Gamma^{\mathrm{FF}}_{\mathrm{h}}$, and in the intersected part of the fluid domain $\Omega^{\mathrm{F}}_{\mathrm{h},\Gamma^{\mathrm{F,I}}} \subseteq \Omega^{\mathrm{F}}_{\mathrm{h}}$. Additionally, the new discrete solution space $\mathcal{S}^{i+1}_{\underline{\boldsymbol{v}}^{\mathrm{F}},\mathrm{h},n+1} \times \mathcal{S}^{i+1}_{p^{\mathrm{F}},\mathrm{h},n+1} \longrightarrow \mathcal{S}^{i+1}_{\underline{\boldsymbol{x}},\mathrm{h},n+1}$ and the new discrete test function space $\mathcal{T}^{i+1}_{\delta\underline{\boldsymbol{v}}^{\mathrm{F}},\mathrm{h},n+1} \times \mathcal{T}^{i+1}_{\delta p^{\mathrm{F}},\mathrm{h},n+1} \longrightarrow \mathcal{T}^{i+1}_{\delta\underline{\boldsymbol{x}},\mathrm{h},n+1}$ are determined. Further details on this aspect can be found in Schott [187] and Schott *et al.* [192].

For the evaluation of the weak form (3.41), all states are required in the new discrete solution space $\mathcal{S}^{i+1}_{\underline{\boldsymbol{x}},\mathrm{h},n+1}$. Therefore, in Step 8, the fluid state $\underline{\mathbf{v}}^{\mathrm{F}}_n, \underline{\mathbf{p}}^{\mathrm{F}}_n$ corresponding to the previous time step t_n is projected from the solution space $\mathcal{S}_{\underline{\boldsymbol{x}},\mathrm{h},n}$ to $\mathcal{S}^{i+1}_{\underline{\boldsymbol{x}},\mathrm{h},n+1}$, by making use of the projection operator (3.9). The projected fluid state is denoted as $\underline{\tilde{\mathbf{v}}}^{\mathrm{F}}_n, \underline{\tilde{\mathbf{p}}}^{\mathrm{F}}_n$. The same procedure is performed in Step 9 on the fluid state $\underline{\mathbf{v}}^{\mathrm{F},i}_{n+1}, \underline{\mathbf{p}}^{\mathrm{F},i}_{n+1}$ corresponding to the previous iteration in the current

time step with solution space $\mathcal{S}^i_{\underline{\boldsymbol{x}},\mathrm{h},n+1}$. This state is projected to $\mathcal{S}^{i+1}_{\underline{\boldsymbol{x}},\mathrm{h},n+1}$ with operator (3.9) and denoted as $\tilde{\underline{\mathbf{v}}}^{\mathrm{F},i}_{n+1}, \tilde{\underline{\mathbf{p}}}^{\mathrm{F},i}_{n+1}$. The combination of these projected fluid states and all other states of the previous and current time step are denoted by $\tilde{\underline{\mathbf{x}}}_n := \left[\underline{\mathbf{u}}^{\mathrm{S}}_n, \tilde{\underline{\mathbf{v}}}^{\mathrm{F}}_n, \tilde{\underline{\mathbf{p}}}^{\mathrm{F}}_n, \underline{\mathbf{u}}^{\mathrm{G}}_n, \underline{\mathbf{u}}^{\mathrm{P}}_n, \underline{\mathbf{v}}^{\mathrm{P}}_n, \underline{\mathbf{p}}^{\mathrm{P}}_n\right]$ and $\tilde{\underline{\mathbf{x}}}^i_{n+1} := \left[\underline{\mathbf{u}}^{\mathrm{S},i}_{n+1}, \tilde{\underline{\mathbf{v}}}^{\mathrm{F},i}_{n+1}, \tilde{\underline{\mathbf{p}}}^{\mathrm{F},i}_{n+1}, \underline{\mathbf{u}}^{\mathrm{G},i}_{n+1}, \underline{\mathbf{u}}^{\mathrm{P},i}_{n+1}, \underline{\mathbf{v}}^{\mathrm{P},i}_{n+1}, \underline{\mathbf{p}}^{\mathrm{P},i}_{n+1}\right]$, respectively. This is possible due to the unchanging solution spaces $\mathcal{S}_{\underline{\boldsymbol{u}}^{\mathrm{S}},\mathrm{h},n+1}, \mathcal{S}_{\underline{\boldsymbol{u}}^{\mathrm{P}},\mathrm{h},n+1}, \mathcal{S}_{\underline{\boldsymbol{v}}^{\mathrm{P}},\mathrm{h},n+1}, \mathcal{S}_{p^{\mathrm{P}},\mathrm{h}}$.

In Step 10, the residual vector $\underline{\mathbf{R}}^i_{n+1}$ and the linearization matrix $\underline{\mathbf{C}}^i_{n+1}$ are computed by evaluation of the weak form (3.41). Herein, the state at $t = t_n$ is given by $\tilde{\underline{\mathbf{x}}}_n$ and the state at t_{n+1} by $\tilde{\underline{\mathbf{x}}}^i_{n+1}$.

Finally, in Step 11 the resulting linear system is solved and in Step 12 an update of the previous state is performed as already discussed in Section 2.3. Further details on this nonlinear solution strategy for FSI can be found in [187, 192].

Remark 3.13 (Time dependency of discrete solution space $\mathcal{S}_{\underline{\boldsymbol{x}},\mathrm{h},n+1}$)**.** *In definitions* (2.106)*,* (2.110)*,* (2.119)*, and in* (3.38) *it is denoted that almost all discrete solution spaces depend on time. Nevertheless, a projection of the solution state to the current solution space is performed only for the fluid velocity* $\underline{\mathbf{v}}^{\mathrm{F}}$ *and fluid pressure* $\underline{\mathbf{p}}^{\mathrm{F}}$ *(see Step 8 and 9 in Algorithm 1). The reason for this is that the time dependency of all other solution spaces arises solely from the time dependency of the prescribed states* $(\hat{\underline{\boldsymbol{u}}}^{\mathrm{S}}, \hat{\underline{\boldsymbol{v}}}^{\mathrm{F}}, \hat{\underline{\boldsymbol{u}}}^{\mathrm{P}}, \hat{v}^{\mathrm{P},n})$ *on the Dirichlet boundaries.*

Remark 3.14 (Comparison to Newton-Raphson procedure)**.** *The design of Algorithm 1 is motivated by a Newton-Raphson-based procedure. The algorithm differs by potentially changing unknowns of the system during the solution procedure from the well known procedure. Therefore, classical properties such as quadratic convergence of the residual close to the solution can not be guaranteed anymore. Nevertheless, in every iteration step with an projection operator equal to the identity in Step 9, the procedure equals a Newton-Raphson-based procedure. An alternative presentation of the algorithm, which includes a separation of these phases, can be found in [187, 192].*

Remark 3.15 (Neglected linearizations of the fluid equations with respect to the displacements)**.** *It should be pointed out that not all contributions of the linearization matrix* $\underline{\mathbf{C}}$ *in* (2.131) *are considered to solve the system for the numerical examples presented in this thesis. Especially, linearizations of the fluid weak form* $\mathcal{W}^{\mathrm{F,CUT}}_{\mathrm{h}}$ *and the interface contributions* $\mathcal{W}^{\mathrm{FSI,o}}_{\mathrm{h}}, \mathcal{W}^{\mathrm{FFI}}_{\mathrm{h}}$*,* $\mathcal{W}^{\mathrm{FPI},n}_{\mathrm{h}}, \mathcal{W}^{\mathrm{FPI},t,*}_{\mathrm{h}}$ *(see Chapter 4), with respect to the interface position are neglected and treated in a fixed-point fashion.*

3.5 Numerical Tests: CutFEM FSI

In the following section, the presented framework for CutFEM FSI is tested numerically. Special focus is put on the solid-sided interface stress representation as this formulation is analyzed for the first time. At first, a problem with known solution, enabled by the method of manufactured solution, is presented. This setup allows computing $\mathcal{L}^2$-error norms of the computed solution from the analytic solution. Three different sets of material parameters are considered and the spatial convergence of the formulation is analyzed. Additionally, the sensitivity of the formulation with solid-sided interface stress representation with respect to the Nitsche penalty parameter

is assessed. In the following two tests which are presented in Section 3.5.2, the influence of the interface stress representation on present discrete discontinuities is analyzed and different scaling strategies of the Nitsche penalty parameter with special focus on the nonlinearity of the solid stress, are validated. In order to make the presentation as clear as possible, the index h that specifies discrete quantities has been omitted for all numerical tests and examples as this is obvious anyway.

3.5.1 Problem Setup for the Method of Manufactured Solution

The analytic solution is chosen as

$$\underline{\boldsymbol{v}}^{\mathrm{F}}_{\mathcal{A}}(\underline{\boldsymbol{x}},t) = \begin{bmatrix} -A^{\mathrm{F}}\cos(B\,x)\sin(B\,y)\,g_u(t) \\ A^{\mathrm{F}}\sin(B\,x)\cos(B\,y)\,g_u(t) \end{bmatrix}, \tag{3.42}$$

$$p^{\mathrm{F}}_{\mathcal{A}}(\underline{\boldsymbol{x}},t) = -\left(\cos(2\,B\,x)+\cos(2\,B\,y)\right)g_p(t), \tag{3.43}$$

$$\underline{\boldsymbol{u}}^{\mathrm{S}}_{\mathcal{A}}(\underline{\boldsymbol{X}},t) = \begin{bmatrix} -A^{\mathrm{S}}\cos(B\,X)\sin(B\,Y)\,\frac{(1-g_u(t))}{-C^2} \\ A^{\mathrm{S}}\sin(B\,X)\cos(B\,Y)\,\frac{(1-g_u(t))}{-C^2} \end{bmatrix}, \tag{3.44}$$

with the time-dependent functions: $g_u(t) = e^{-C^2\,t}$ and $g_p(t) = 1/4\,e^{-2\,C^2\,t}$.

Herein, the analytic velocity and pressure solution in the fluid domain is denoted by $\underline{\boldsymbol{v}}^{\mathrm{F}}_{\mathcal{A}}$ and $p^{\mathrm{F}}_{\mathcal{A}}$. The analytic displacement solution in the structural domain is denoted by $\underline{\boldsymbol{u}}^{\mathrm{S}}_{\mathcal{A}}$. The components of the two-dimensional position vector $\underline{\boldsymbol{x}} = [x,y]^{\mathsf{T}}$ in current configuration are specified as x and y and the components of the material position vector $\underline{\boldsymbol{X}} = [X,Y]^{\mathsf{T}}$ as X and Y. The solution is chosen to fulfill the balance of fluid mass (equation (2.27)). The space constant B, and the time constant C influence the spatial and temporal gradients of the given solution. As the focus should be on the spatial errors in the following, $B = \pi$ is chosen to be larger than $C = \sqrt{2}\cdot 0.01\pi$.

The tests are performed for three different configurations, *C-mid*, *C-stiff*, and *C-visc* with varying material parameters and solution amplitudes. The dynamic viscosity μ^{F} of the fluid is specified in Table 3.2. The macroscopic deformation of the solid is given by a Neo-Hookean material model with the hyperelastic strain energy function (2.17) and the material constants Poisson ratio $\nu = 0.1$ and Young's modulus E which is given in Table 3.2. All solution amplitudes A^{F} and A^{S} are specified in Table 3.2. They are specified to retain an almost equivalent interface traction for all considered configurations.

Table 3.2: Parameters of the three different configurations

Configuration	μ^{F}	A^{F}	E	A^{S}
C-mid	1.0	1.0	100.0	1.0
C-stiff	1.0	1.0	10000.0	0.01
C-visc	100.0	0.01	100.0	1.0

The initial density of the solid is chosen to be equal to the fluid density $\rho^{\mathrm{S}}_0 = \rho^{\mathrm{F}} = 1.0$. In order to fulfill the balance of momentum, which is defined by equations (2.28) and (2.15), by the

analytic solutions (3.42)-(3.44), the following body forces are applied:

$$\rho^{\mathrm{F}}\hat{\underline{\boldsymbol{b}}}^{\mathrm{F}} = \rho^{\mathrm{F}}\frac{\partial \underline{\boldsymbol{v}}^{\mathrm{F}}_{\mathcal{A}}}{\partial t} + \rho^{\mathrm{F}}\underline{\boldsymbol{v}}^{\mathrm{F}}_{\mathcal{A}}\cdot\boldsymbol{\nabla}\underline{\boldsymbol{v}}^{\mathrm{F}}_{\mathcal{A}} - \boldsymbol{\nabla}\cdot\underline{\boldsymbol{\sigma}}^{\mathrm{F}}_{\mathcal{A}}, \quad \underline{\boldsymbol{\sigma}}^{\mathrm{F}}_{\mathcal{A}} = -p^{\mathrm{F}}_{\mathcal{A}}\underline{\boldsymbol{I}} + 2\mu^{\mathrm{F}}\underline{\boldsymbol{\epsilon}}^{\mathrm{F}}(\underline{\boldsymbol{v}}^{\mathrm{F}}_{\mathcal{A}}), \tag{3.45}$$

$$\rho^{\mathrm{S}}_0\hat{\underline{\boldsymbol{b}}}^{\mathrm{S}}_0 = \rho^{\mathrm{S}}_0\frac{\partial^2 \underline{\boldsymbol{u}}^{\mathrm{S}}_{\mathcal{A}}}{\partial t^2} - \boldsymbol{\nabla}_0\cdot\left(\underline{\boldsymbol{F}}^{\mathrm{S}}_{\mathcal{A}}\cdot\underline{\boldsymbol{S}}^{\mathrm{S}}_{\mathcal{A}}\right), \tag{3.46}$$

where the analytic deformation gradient is defined as $\underline{\boldsymbol{F}}^{\mathrm{S}}_{\mathcal{A}} = \underline{\boldsymbol{I}} + \partial\underline{\boldsymbol{u}}^{\mathrm{S}}_{\mathcal{A}}/\partial\underline{\boldsymbol{X}}^{\mathrm{S}}$, the corresponding determinate as $J^{\mathrm{S}}_{\mathcal{A}} = \det\left(\underline{\boldsymbol{F}}^{\mathrm{S}}_{\mathcal{A}}\right)$, the analytic second Piola-Kirchhoff stress tensor as $\underline{\boldsymbol{S}}^{\mathrm{S}}_{\mathcal{A}} = 2c\underline{\boldsymbol{I}} - 2c\left(J^{\mathrm{S}}_{\mathcal{A}}\right)^{-2\beta}\left(\underline{\boldsymbol{F}}^{\mathrm{S}}_{\mathcal{A}}\right)^{-1}\cdot\left(\underline{\boldsymbol{F}}^{\mathrm{S}}_{\mathcal{A}}\right)^{-\mathsf{T}}$, and the analytic Cauchy stress tensor as $\underline{\boldsymbol{\sigma}}^{\mathrm{S}}_{\mathcal{A}} = \left(J^{\mathrm{S}}_{\mathcal{A}}\right)^{-1}\underline{\boldsymbol{F}}^{\mathrm{S}}_{\mathcal{A}}\cdot\underline{\boldsymbol{S}}^{\mathrm{S}}_{\mathcal{A}}\cdot\left(\underline{\boldsymbol{F}}^{\mathrm{P}}_{\mathcal{A}}\right)^{\mathsf{T}}$. The analytic solution fulfills the interface conditions (2.59) and (2.60), if the constraint-jump $\hat{\underline{\boldsymbol{g}}}^{\mathrm{FS}}_{v}$ and the traction-jump $\hat{\underline{\boldsymbol{g}}}^{\mathrm{FS}}_{\sigma}$ are defined by the analytic solution as

$$\hat{\underline{\boldsymbol{g}}}^{\mathrm{FS}}_{\sigma} = \underline{\boldsymbol{\sigma}}^{\mathrm{F}}_{\mathcal{A}}\cdot\underline{\boldsymbol{n}}^{\mathrm{F}} - \underline{\boldsymbol{\sigma}}^{\mathrm{S}}_{\mathcal{A}}\cdot\underline{\boldsymbol{n}}^{\mathrm{F}}, \tag{3.47}$$

$$\hat{\underline{\boldsymbol{g}}}^{\mathrm{FS}}_{v} = \underline{\boldsymbol{v}}^{\mathrm{F}}_{\mathcal{A}} - \frac{\partial \underline{\boldsymbol{u}}^{\mathrm{S}}_{\mathcal{A}}}{\partial t}. \tag{3.48}$$

Remark 3.16 (Evaluation of the body force (3.45) and (3.46), the traction-jump (3.47), and the constraint-jump (3.48))**.** *All body force contributions* (3.45) *and* (3.46) *are evaluated at the computational nodes and re-interpolated with the standard shape functions of the corresponding finite elements. Compared to a direct volume integration, the additional error does not deteriorate the error convergence order of the subsequent computation. Contrary to this, the traction-jump and constraint-jump contributions are evaluated directly for the integration on the interface* Γ^{FS} *at every point in space. Hereby, the material position vector* $\underline{\boldsymbol{X}}^{\mathrm{S}}$ *is computed by re-interpolation of the initial nodal coordinates. All volume contributions* (3.45) *and* (3.46) *depend solely on the point in space and time for the given analytic solution, whereas the interface contribution* (3.46) *additionally depends on the normal vector* $\underline{\boldsymbol{n}}^{\mathrm{F}}$*. Therefore, contribution* (3.46) *was computed and simplified symbolically by Maple*$^{\mathrm{TM}}$ *[114] as a time- and space-dependent function in advance as far as possible. The evaluation of the function and the multiplication of the components with the discrete normal vector in each numerical integration point for the interface contributions is performed during the computation.*

These additional body force and jump contributions allow to fulfill the analytic solution, and thus, the application of the method of manufactured solution, independent of the alignment of the interface, the boundaries, and the domains. The setup, as shown in Figure 3.4, includes a wide variety of different intersections of single fluid elements by the interface Γ^{FS} for different mesh resolutions, while still enabling the use of structured discretizations. The solid domain Ω^{S} is a square of size 0.5×0.5, which is rotated by an angle of $\alpha = 30°$ around its center. The fluid domain Ω^{F} is described by a square with size 1.0×1.0, rotated by an angle of $\beta = 45°$ around its center, whereby the part occupied by the solid domain Ω^{S} is excluded. The size in the third spatial direction is 0.03125. On $\Gamma^{F,D}$, where the fluid discretization is matching the boundary, the analytic velocity (3.42) is prescribed as a Dirichlet boundary condition in a strong sense.

For the spatial discretization, four-noded, bi-linear, quadrilateral elements are used. This is accomplished through a discretization with one layer of eight-noded, tri-linear hexahedral elements. Discretization in time is performed by the backward Euler scheme ($\theta = 1$), with a time

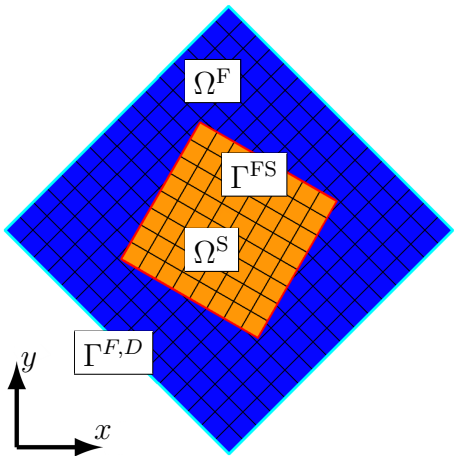

Figure 3.4: Geometric setup and computational meshes. The fluid domain Ω^{F}, the solid domain Ω^{S}, the common interface Γ^{FS}, and Dirichlet boundary condition $\Gamma^{F,D}$ are visualized here. Black lines indicate the computational mesh for a mesh size of $h = 0.0625$, corresponding to 16×16 bi-linear elements to discretize the fluid domain and 8×8 bi-linear elements to discretize the solid domain.

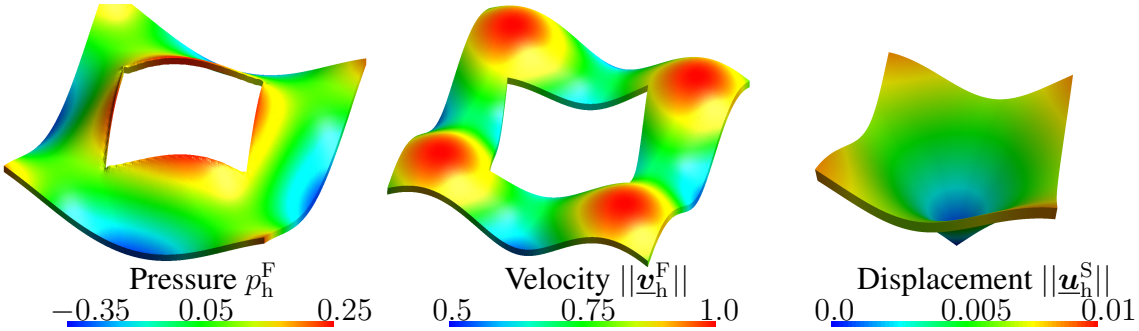

Figure 3.5: Computed pressure, velocity magnitude and displacement magnitude solution at $t = 0.01$ for $h = 0.0078125$, $\xi^{\mathrm{FSI}} = 1$, $\gamma_0^{\mathrm{FSI}} = 2.0$, solid-sided interface stress representation. Visualized by color-code and scalar warp in third direction.

step length of $\Delta t = 0.000625$. The final point in time of interest is set to $t_{\mathrm{E}} = 0.01$. The initial state is given by the analytic solution:

$$\mathring{\underline{\boldsymbol{v}}}^{\mathrm{F}}(\underline{\boldsymbol{x}}) = \underline{\boldsymbol{v}}_{\mathcal{A}}^{\mathrm{F}}(\underline{\boldsymbol{x}}, 0), \quad \mathring{\underline{\boldsymbol{u}}}^{\mathrm{S}}(\underline{\boldsymbol{X}}) = \underline{\boldsymbol{u}}_{\mathcal{A}}^{\mathrm{S}}(\underline{\boldsymbol{X}}, 0), \quad \mathring{\underline{\boldsymbol{v}}}^{\mathrm{S}}(\underline{\boldsymbol{X}}) = \underline{\boldsymbol{v}}_{\mathcal{A}}^{\mathrm{S}}(\underline{\boldsymbol{X}}, 0). \tag{3.49}$$

In Figure 3.5, the computed solution for a specific set of parameters is visualized for all computed unknowns, namely the pressure p^{F}, the velocity $\underline{\boldsymbol{v}}^{\mathrm{F}}$ and the displacement $\underline{\boldsymbol{u}}^{\mathrm{S}}$.

To quantify the performance of the proposed formulation, $\mathcal{L}^2$-error norms that are integrated in the domains Ω^{F} and Ω_0^{S} as well as on the interface Γ^{FS} are consulted. To enable a clear presentation of the computed results, the interface error is abbreviated in the following as

$$\mathcal{E} := \left|\left|\left(\underline{\boldsymbol{v}}^{\mathrm{F}} - \tilde{\partial}_t \left[\underline{\boldsymbol{u}}^{\mathrm{S}}\right]\right) - \left(\underline{\boldsymbol{v}}_{\mathcal{A}}^{\mathrm{F}} - \underline{\boldsymbol{v}}_{\mathcal{A}}^{\mathrm{S}}\right)\right|\right|_{\Gamma^{\mathrm{FS}}}. \tag{3.50}$$

The prefactor $\phi_\Gamma^{\mathrm{S}} \gamma_0^{\mathrm{FSI}}$ of the Nitsche penalty term for the solid-sided interface stress representation is computed only once per time step. The solution is computed for both, a formulation including a skew-symmetric adjoint-consistency term $\xi^{\mathrm{FSI}} = 1$ and a formulation which does not include an adjoint-consistency term $\xi^{\mathrm{FSI}} = 0$.

3.5.1.1 Spatial Convergence Analysis

In the following, the spatial convergence of the presented CutFEM FSI formulations are analyzed. For all considered configurations, the mesh size h, which equals the edge length of the quadrilateral elements of squared shape, is varied in $h \in [0.25, 0.0039062]$. The Nitsche penalty parameters are set to $\gamma_0^{\mathrm{FSI}} = 35.0$ for fluid-sided interface stress representation and to $\gamma_0^{\mathrm{FSI}} = 2.0$ for the solid-sided interface stress representation.

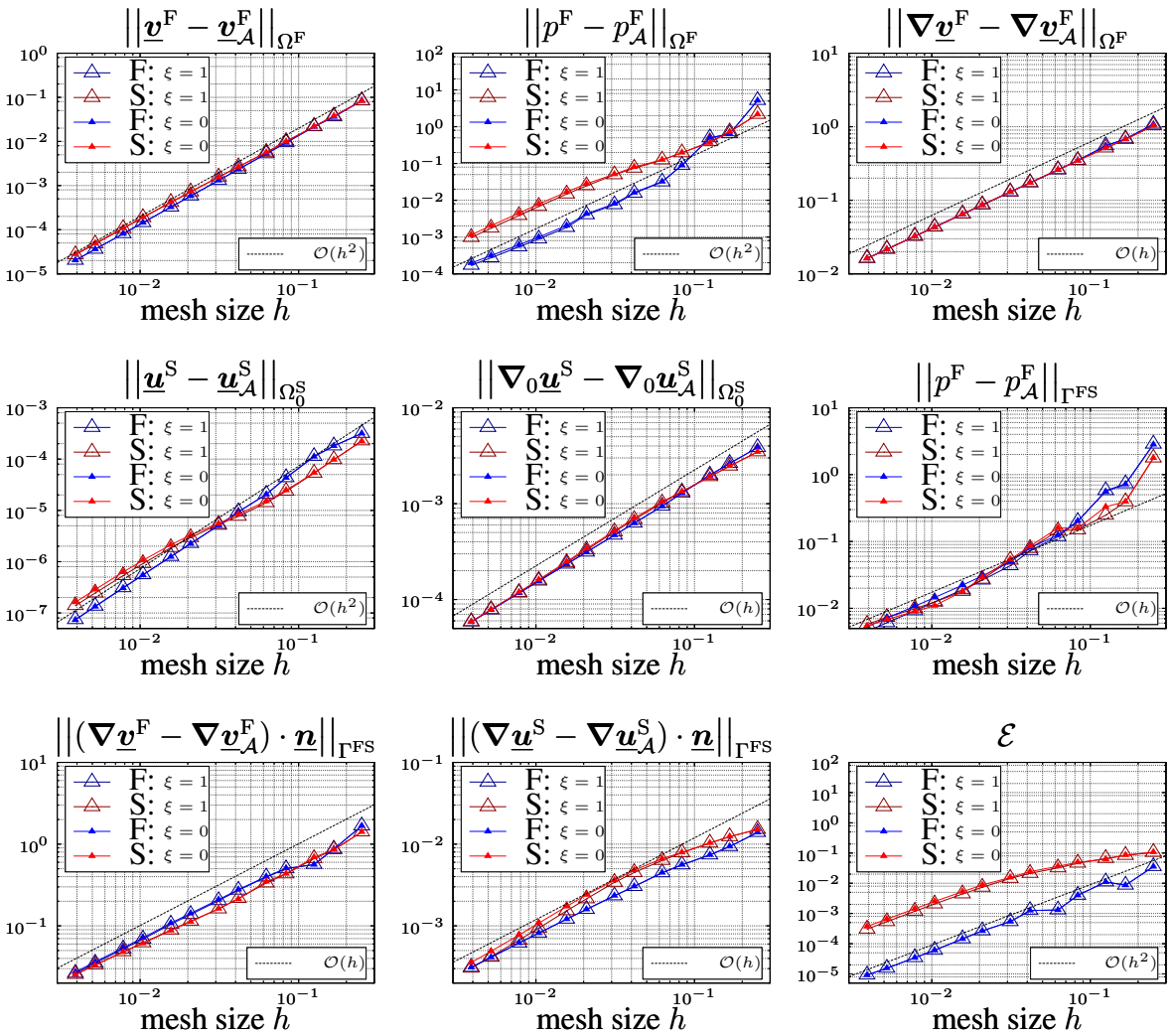

Figure 3.6: Computed domain and interface error norms for the spatial convergence study with configuration *C-mid* according to Table 3.2. (F: $\xi = 1$): fluid-sided interface stress representation with $\xi^{\mathrm{FSI}} = 1$; (S: $\xi = 1$): solid-sided interface stress representation with $\xi^{\mathrm{FSI}} = 1$; (F: $\xi = 0$): fluid-sided interface stress representation with $\xi^{\mathrm{FSI}} = 0$; (S: $\xi = 0$): solid-sided interface stress representation with $\xi^{\mathrm{FSI}} = 0$.

Configuration *C-mid* In Figure 3.6, the computed domain and interface error norms for the configuration *C-mid* are shown. All formulations converge with at least the expected convergence order as indicated by the dotted reference line. Comparing the variant with $\xi^{\mathrm{FSI}} = 1$ and without $\xi^{\mathrm{FSI}} = 0$ an adjoint-consistency term results in almost the same errors for all computed norms.

The pressure error in the fluid domain converges with an increased rate of $\mathcal{O}(h^2)$. This behavior is already well known and was often observed for incompressible flow as well as FSI.

The absolute value for most of the computed error norms is very similar for all tested variants. The first exception can be found for the interface error norm $\mathcal{E}$, where an increased error for the formulations with solid-sided interface representation can be observed. This difference results from the smaller prefactor of the Nitsche penalty term $\phi_\Gamma^{\mathrm{S}}\gamma_0^{\mathrm{FSI}}$ due to the included scaling with Δt compared to $\phi_\Gamma^{\mathrm{F}}\gamma_0^{\mathrm{FSI}}$ for the considered configuration. Therefore, the enforcement of the kinematic constraint (2.60) is reduced for the variant with solid-sided interface stress representation. As a second exception, the pressure error in Ω^{F} exhibits a different absolute error level. Still, this does not contradict the theoretical expectations as the error decreases almost with the same convergence rate.

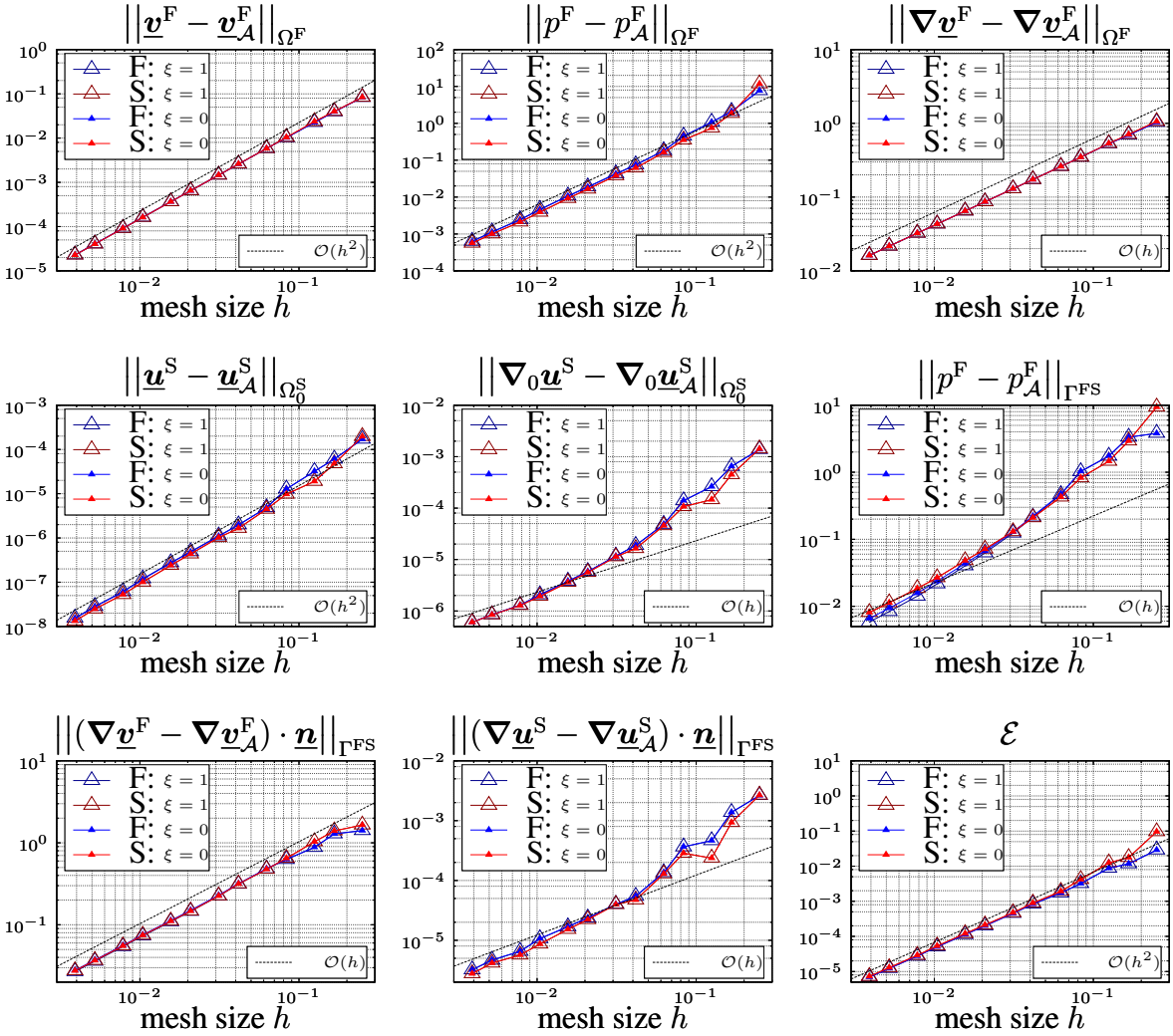

Figure 3.7: Computed domain and interface error norms for the spatial convergence study with configuration *C-stiff* according to Table 3.2. (F: $\xi = 1$): fluid-sided interface stress representation with $\xi^{\mathrm{FSI}} = 1$; (S: $\xi = 1$): solid-sided interface stress representation with $\xi^{\mathrm{FSI}} = 1$; (F: $\xi = 0$): fluid-sided interface stress representation with $\xi^{\mathrm{FSI}} = 0$; (S: $\xi = 0$): solid-sided interface stress representation with $\xi^{\mathrm{FSI}} = 0$.

Configuration *C-stiff* As described in Table 3.2 for configuration *C-stiff*, the stiffness of the solid domain is increased by a factor of 100 and at the same time the solid amplitude A^{S} is divided by the same factor to keep the solid interface stress approximately equal to the previously considered configuration.

The computed error norms are shown in Figure 3.7. Again a spatial convergence with at least the expected convergence order can be observed for all computed error norms. Compared to the results of configuration *C-mid*, the difference of the absolute error between fluid-sided and solid-sided interface stress representation disappeared. For the interface error $\mathcal{E}$, this behavior is expected due to the almost identical scaling of the prefactor of the Nitsche penalty term $\phi_{\Gamma}^{\mathrm{S}}\gamma_0^{\mathrm{FSI}}$ and $\phi_{\Gamma}^{\mathrm{F}}\gamma_0^{\mathrm{FSI}}$.

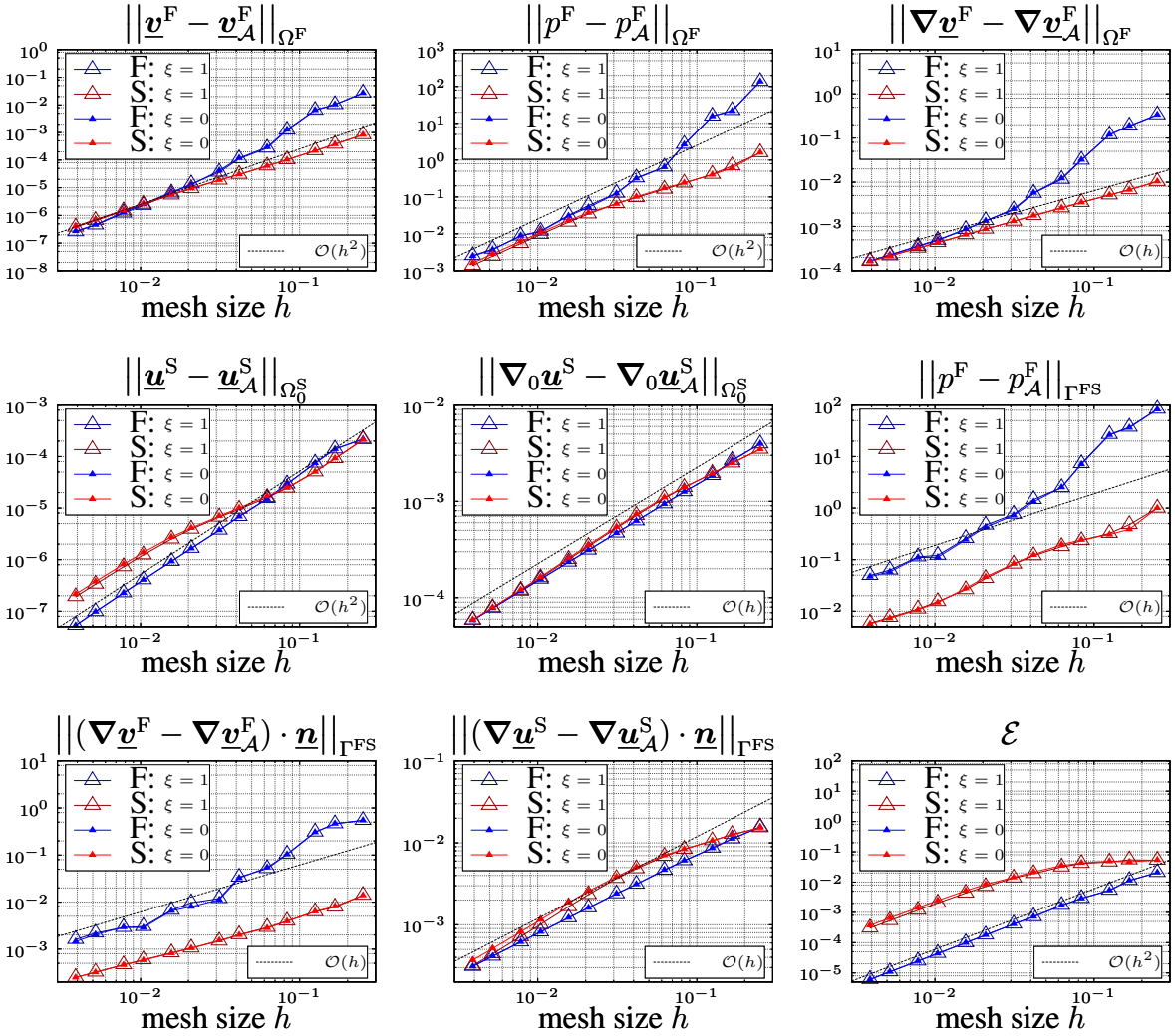

Figure 3.8: Computed domain and interface error norms for the spatial convergence study with configuration *C-visc* according to Table 3.2. (F: $\xi = 1$): fluid-sided interface stress representation with $\xi^{\mathrm{FSI}} = 1$; (S: $\xi = 1$): solid-sided interface stress representation with $\xi^{\mathrm{FSI}} = 1$; (F: $\xi = 0$): fluid-sided interface stress representation with $\xi^{\mathrm{FSI}} = 0$; (S: $\xi = 0$): solid-sided interface stress representation with $\xi^{\mathrm{FSI}} = 0$.

Configuration *C-visc* With a last configuration *C-visc*, the spatial convergence behavior for increased fluid viscosity is analyzed. Table 3.2 shows that the viscosity of the fluid domain is increased by a factor of 100 and at the same time the fluid amplitude A^{F} is divided by the same factor to keep the fluid interface stress approximately equal.

Figure 3.8 shows the computed error norms, which converge at least with the expected convergence orders. In contrast to the results of the configurations *C-mid* and *C-stiff*, the absolute error level differs between fluid-sided interface stress representation and solid-sided interface stress representation for almost all considered error norms. The error norms related to the fluid quantities $\underline{\boldsymbol{v}}^{\mathrm{F}}$ and p^{F} in the first line of Figure 3.8 reveal an increased error for the fluid-sided variant for coarse meshes. Due to a higher spatial convergence order for the fluid-sided variant, a similar absolute error level is obtained for both variants of interface stress representation for fine meshes. For the displacement $\underline{\boldsymbol{u}}^{\mathrm{S}}$ error in the solid domain the opposite behavior is observed. Whereas a similar error occurs for coarse discretizations, an increased error of the solid-sided variant compared to the fluid-sided variant is detected. The most significant deviation between these variants can be identified on the interface Γ^{FS} for the quantities related to the fluid stress $(\boldsymbol{\nabla}\underline{\boldsymbol{v}}^{\mathrm{F}}, p^{\mathrm{F}})$. The solid-sided interface representation performs essentially better. As the inverse effect could not be observed for the configuration with increased stiffness *C-stiff*, the varying sensitivity of the viscous stress compared to the fluid pressure for this configuration might lead to this result. Finally, the smaller prefactor of the Nitsche penalty term for the solid-sided interface stress representation leads to an increased error norm for the error $\mathcal{E}$.

The essential findings of the spatial convergence analysis can be summarized as follows. All computed error norms spatially converge for all considered configurations with at least the expected convergence orders. Depending on the specific problem setup, the fluid-sided interface stress representation and the solid-sided interface stress representation result in comparable (*C-mid*) absolute error norms or deviate significantly (*C-visc*). Still, in order to gain a deeper understanding on the influence of the choice of interface stress representation onto the error behavior for large contrast problems, validation tests which are based on physical relevant solutions seem beneficial.

3.5.1.2 Sensitivity of the Nitsche Penalty Parameter

In the following section, the sensitivity of the formulation with respect to the Nitsche penalty parameter γ_0^{FSI} for solid-sided interface stress representation is analyzed for the three configurations *C-mid*, *C-stiff*, and *C-visc*. Similar analyses for fluid-sided interface stress representation can be found e.g. in Schott [187], Schott and Wall [188] and Schott *et al.* [190]. In this computational test, the parameter γ_0^{FSI} is varied in the range $[10^{-4}, 10^{4}]$ and the resulting error norms are computed. A constant element size of $h = 0.015625$ is considered throughout this study.

In Figure 3.9, the computed results are shown. As expected, very large values of the parameter $\gamma_0^{\mathrm{FSI}} > 10^3$ lead to increasing error norms especially for the interface norms related to the solid or fluid stress $(p^{\mathrm{F}}, \boldsymbol{\nabla}\underline{\boldsymbol{v}}^{\mathrm{F}}, \boldsymbol{\nabla}\underline{\boldsymbol{u}}^{\mathrm{S}})$ with varying degrees of intensity for the different configurations. Due to the stronger enforcement of the kinematic constraint (2.60) for a large parameter γ_0^{FSI}, the interface error $\mathcal{E}$ decreases continuously. On the other hand, very small values of the parameter $\gamma_0^{\mathrm{FSI}} < 10^0$ lead to an increasing error for the Nitsche method not including an adjoint-consistency term ($\xi^{\mathrm{FSI}} = 0$) for all configurations. This increase in error is not so pronounced for the Nitsche method including a skew-symmetric adjoint-consistency term ($\xi^{\mathrm{FSI}} = 1$). Only

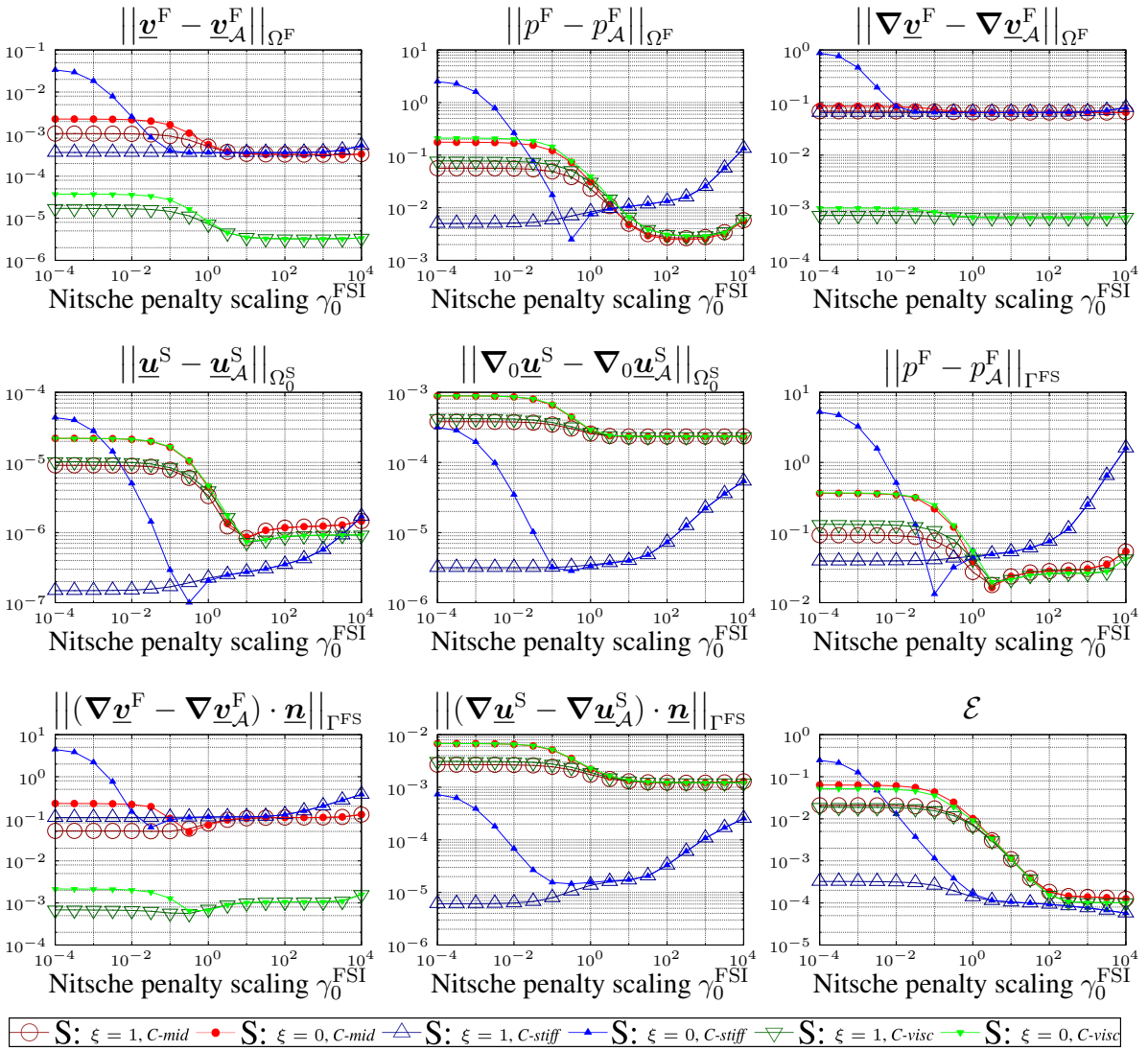

Figure 3.9: Computed domain and interface error norms for a varying Nitsche penalty scaling γ_0^{FSI}. The test is performed for the three configurations *C-mid*, *C-stiff*, and *C-visc* according to Table 3.2. (S: $\xi = 1$): solid-sided interface stress representation with $\xi^{\mathrm{FSI}} = 1$; (S: $\xi = 0$): solid-sided interface stress representation with $\xi^{\mathrm{FSI}} = 0$.

for the configuration *C-stiff* with $\xi^{\mathrm{FSI}} = 1$ no increase in error for small parameters γ_0^{FSI} can be observed.

To conclude, also the considered variant including a skew-symmetric adjoint-consistency term $\xi^{\mathrm{FSI}} = 1$ benefits from a Nitsche penalty term with a sufficiently large constant γ_0^{FSI}. The reason for this behavior could be found in the insufficient enforcement of the interface no-slip constraint for small parameters γ_0^{FSI}. This result was found for the configurations *C-mid* and *C-visc*. The qualitative different results for *C-stiff* might be related to the reduced amplitude A^{S}.

Taking all computed error norms into account, a value in the range $[1, 10^2]$ is suggested for the parameter γ_0^{FSI}. As expected, in the case the computed solution is spatially well resolved by the computational mesh the parameter is not very sensitive to variations if it is chosen large enough.

3.5.2 Problem Setup for Solid Cylinder Interaction Tests

In the following two tests, the interaction of a solid cylinder with fluid under varying boundary conditions is investigated. In the first test, a moving cylinder allows analyzing the influence of the interface stress representation on discrete discontinuities. The temporal and stress nonlinearity scaling of the prefactor in the Nitsche penalty term for solid-sided interface stress representation (3.30) is validated in a second test by a configuration compressing the cylinder.

The domain of interest is given by a rectangular box $\Omega = [0,1] \times [0,1]$ with outer fluid boundaries $\Gamma^{F,x-}$ on $x = 0$, $\Gamma^{F,x+}$ on $x = 1$, $\Gamma^{F,y-}$ on $y = 0$, and $\Gamma^{F,y+}$ on $y = 1$. On the boundary $\Gamma^{F,x-}$ a parabolic inflow $\underline{\boldsymbol{v}}^{\mathrm{F}} = [4(y - y^2), 0.0]$ and on the boundaries $\Gamma^{F,x+}$ and $\Gamma^{F,y+}$ zero fluid velocity is prescribed. The boundary condition on $\Gamma^{F,y-}$ will be altered and therefore specified in Sections 3.5.2.1 and 3.5.2.2. The domain of interest Ω embeds a solid domain Ω, which is initially a cylinder with radius $r^{\mathrm{S}} = 0.25$ and its center at $\underline{\boldsymbol{x}}^{\mathrm{S},mid} = [0.5, 0.5]$. The fluid domain is given by $\Omega^{\mathrm{F}} = \Omega \backslash \Omega^{\mathrm{S}}$ and thus the fluid-structure interface is given by $\Gamma^{\mathrm{FS}} = \partial\Omega^{\mathrm{S}}$. The solid and fluid material specifications are equal to Section 3.5.1 with configuration *C-mid*. The fluid domain is discretized by uniform bi-linear elements in domain Ω unfitted to the interface. Three discretization variants are utilized: *coarse* (16×16 fluid elements), *mid* (32×32 fluid elements), and *fine* (fluid 128×128 elements). The corresponding discretizations for the solid domain, which are fitted to Γ^{FS}, are shown in Figure 3.10. The discretization in time is performed by the backward Euler scheme $\theta = 1$, with a zero state as initial state.

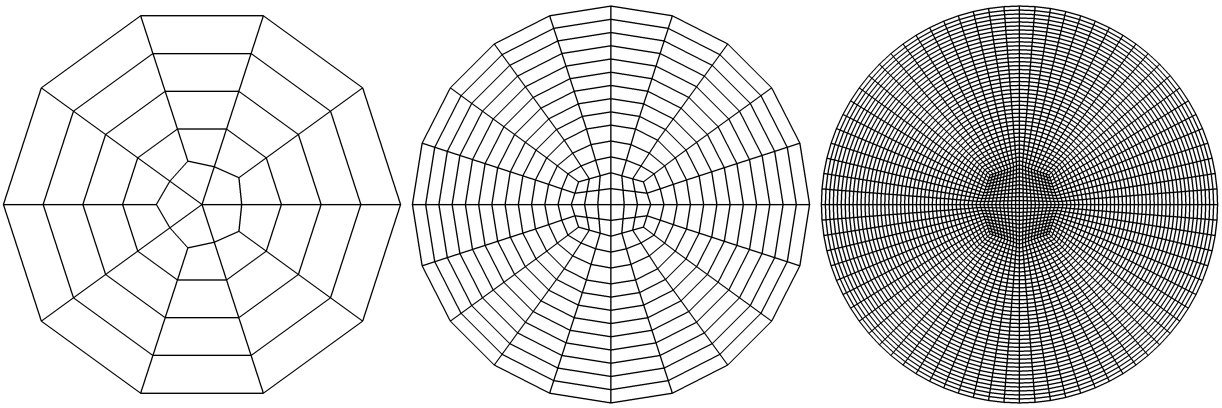

Figure 3.10: Three different discretizations of the solid cylinder domain Ω^{S}. Black lines indicate boundaries of the bi-linear elements. From left to right: *coarse*: 45 elements; *mid*: 264 elements; *fine*: 3600 elements.

3.5.2.1 Influence of Interface Stress Representation on Discrete Discontinuities

Due to the discontinuity of the discrete fluid velocity gradient when crossing fluid element boundaries, discontinuities in the solution can occur. In the case of a fluid-sided interface stress representation this discontinuity is directly incorporated by the viscous fluid stress on the interface. Since the interface traction in the case of solid-sided interface stress representation is continuous this effect possibly does not occur. These discontinuities are mainly noticeable for coarse discretizations. The following test is designed compare the appearance of this type of discontinuities in the computed solution for both types of interface stress representation.

The boundary condition on the outer fluid boundary $\Gamma^{F,y-}$ is specified as a zero-traction Neumann boundary condition resulting in a moving solid cylinder. Both Nitsche-based formulations on the FSI interface include a skew-symmetric adjoint-consistency term $\xi^{\mathrm{FSI}} = 1$. The penalty parameter is set to $\gamma_0^{\mathrm{FSI}} = 2$ for the solid-sided interface stress representation and to $\gamma_0^{\mathrm{FSI}} = 35$ for the fluid-sided interface stress representation. The time step length is $\Delta t = 0.00625$. This configuration is computed for the discretizations *coarse* and *mid*.

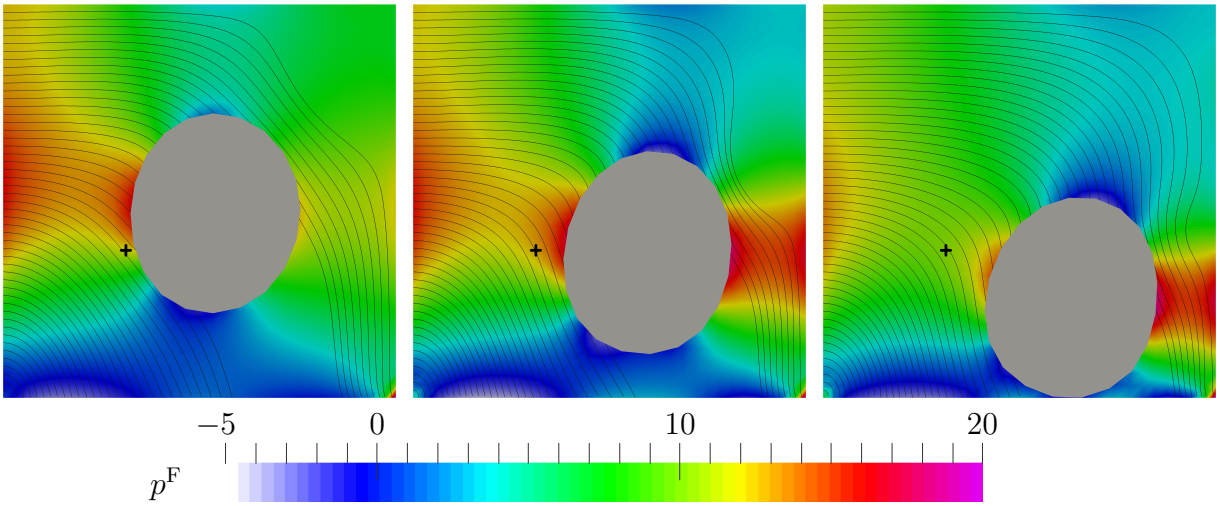

Figure 3.11: Computed solution of the moving cylinder problem with discretization *mid* and solid-sided interface stress representation for three instances in time, from left to right $t = 0.1, t = 0.3$, and $t = 0.5$. The black lines indicate streamlines given by the fluid velocity $\underline{\boldsymbol{v}}^{\mathrm{F}}$, the color-code in the fluid domain represents the fluid pressure p^{F}, and the gray domain corresponds to the current solid domain. The black cross indicates the point where the fluid quantities of all computed variants are compared in Figure 3.12.

Computed Results and Discussion The computed solution for solid-sided interface stress representation with discretization *mid* at three instances in time is shown in Figure 3.11. It can be seen that the fluid flow, which is indicated by the black streamlines, moves and deforms the solid from its initial position towards $\Gamma^{F,y-}$. The final point in time is set to $t_{\mathrm{E}} = 0.5$ before the solid leaves the fluid domain.

To quantify the effect of interface stress discontinuities on the computed solution, the velocity magnitude $||\underline{\boldsymbol{v}}^{\mathrm{F}}||$ and the fluid pressure p^{F} are evaluated at a specific position which is sensitive to discrete discontinuities. This point $\underline{\boldsymbol{x}} = [0.3125, 0.375]^{\mathsf{T}}$ is indicated by a black cross in Figure 3.11 and the computed quantities at $\underline{\boldsymbol{x}}$ are shown in Figure 3.12. Besides some smaller non-smooth points in time, a significant discontinuity of the velocity magnitude and the pressure can be observed at $t \approx 0.26$ for both variants of interface stress representation in combination with the *coarse* discretization. It is noteworthy that also the solid-sided interface stress representation, for which the stress is a continuous quantity on the interface Γ^{FS}, cannot resolve this issue in the case of coupled FSI.

Finally, both configurations are computed with the increased spatial resolution *mid* to verify the reduction of the discontinuities. For this refined discretization no clearly visible discontinuities can be seen in the computed solution.

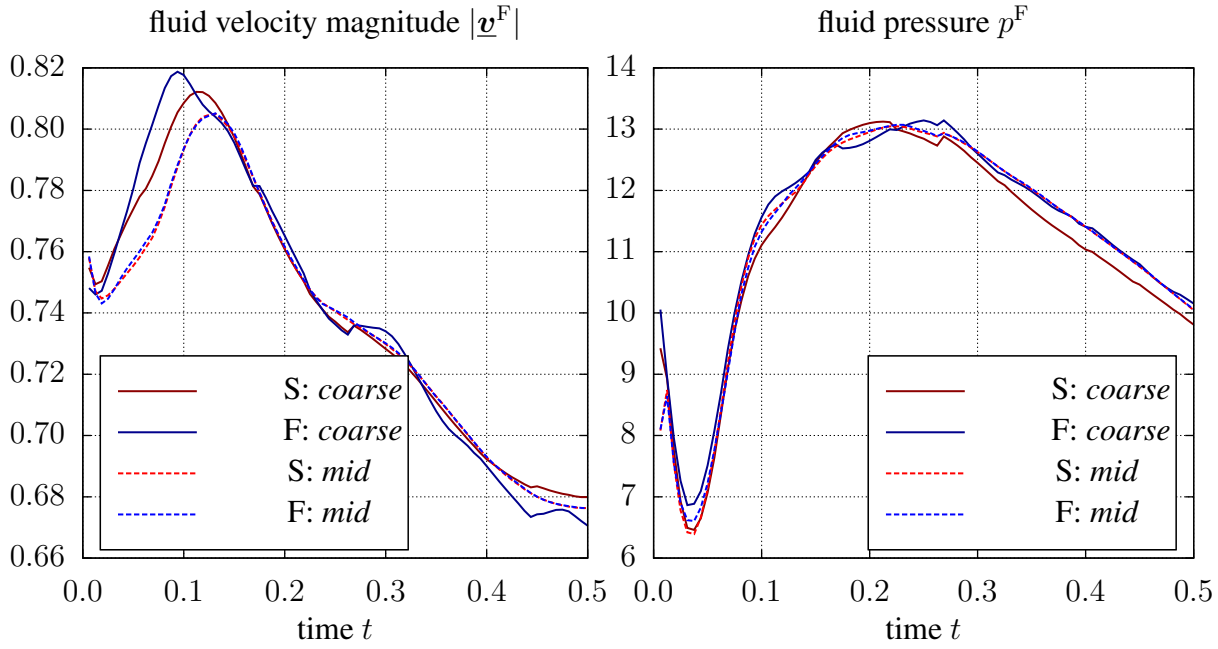

Figure 3.12: Computed fluid velocity magnitude $||\underline{\boldsymbol{v}}^{\mathrm{F}}||$ (left), and fluid pressure p^{F} (right) at a specific point in space $\underline{\boldsymbol{x}} = [0.3125, 0.375]^{\mathsf{T}}$. (S: *coarse*): solid-sided interface stress representation with discretization *coarse*; (F: *coarse*): fluid-sided interface stress representation with discretization *coarse*; (S: *mid*): solid-sided interface stress representation with discretization *mid*; (F: *mid*): fluid-sided interface stress representation with discretization *mid*;

3.5.2.2 Validation of Nitsche Penalty Scaling

In this second test, the scaling of the prefactor $\phi_{\Gamma}^{\mathrm{S}}\gamma_0^{\mathrm{FSI}}$ of the Nitsche penalty term in the case of solid-sided interface stress representation is analyzed. The focus is on analyzing the scaling coefficient $C_{2,e}^{\mathrm{eig}}$, computed by the local generalized eigenvalue problem as discussed in Section 3.3.2.2, and the scaling with Δt resulting from the temporal discretization. As the scaling coefficient $C_{2,e}^{\mathrm{eig}}$ takes into account, roughly speaking, the fraction "stiffness" divided by "element length", a test case which includes large changes in these two quantities is created. Therefore, the boundary conditions of the problem setup presented in Section 3.5.2 are chosen to result in a compression of the cylinder induced by the fluid. Additionally, two different time step lengths $\Delta t = 0.000625$ and $\Delta t = 0.0000625$ for the temporal discretization are tested.

On the outer fluid boundary $\Gamma^{F,y-}$, a zero velocity is prescribed as a Dirichlet boundary condition. Whereas the essential configuration for validation of the Nitsche penalty scaling $\phi_{\Gamma}^{\mathrm{S}}$ does not include an adjoint-consistency term $\xi^{\mathrm{FSI}} = 0$, the variant including a skew-symmetric adjoint-consistency term $\xi^{\mathrm{FSI}} = 1$ is presented for completeness. All variants are computed based on the discretization *fine* within this test.

Three different variants for updating the scaling coefficient $C_{2,e}^{\mathrm{eig}}$ are compared. *V-iter* denotes a variant with successive updating of $C_{2,e}^{\mathrm{eig}}$ in every iteration of the nonlinear solution procedure. Solving the local generalized eigenvalue problem to get $C_{2,e}^{\mathrm{eig}}$ only once at the beginning of each time step is denoted by *V-*Δt. Finally, in the variant *V-const* the scaling $C_{2,e}^{\mathrm{eig}}$ is evaluated only at the beginning of the computation with the given initial state. All variants are computed with three

different values of the constant $\gamma_0^{\mathrm{FSI}} = \{0.1, 1.0, 10.0\}$. Additionally, a reference computation is performed with fluid-sided interface stress representation and $\gamma_0^{\mathrm{FSI}} = 35$.

While from a theoretical point of view only the variant *V-iter* is sufficient to ensure a stable discrete formulations in all situations, it is assumed that also the variant *V-*Δt performs similarly good since typically only small changes of the discrete state occur during the nonlinear solution procedure. In contrast to that, for the variant *V-const* it is expected that discrete instabilities occur with progressing compression depending on the constant γ_0^{FSI}.

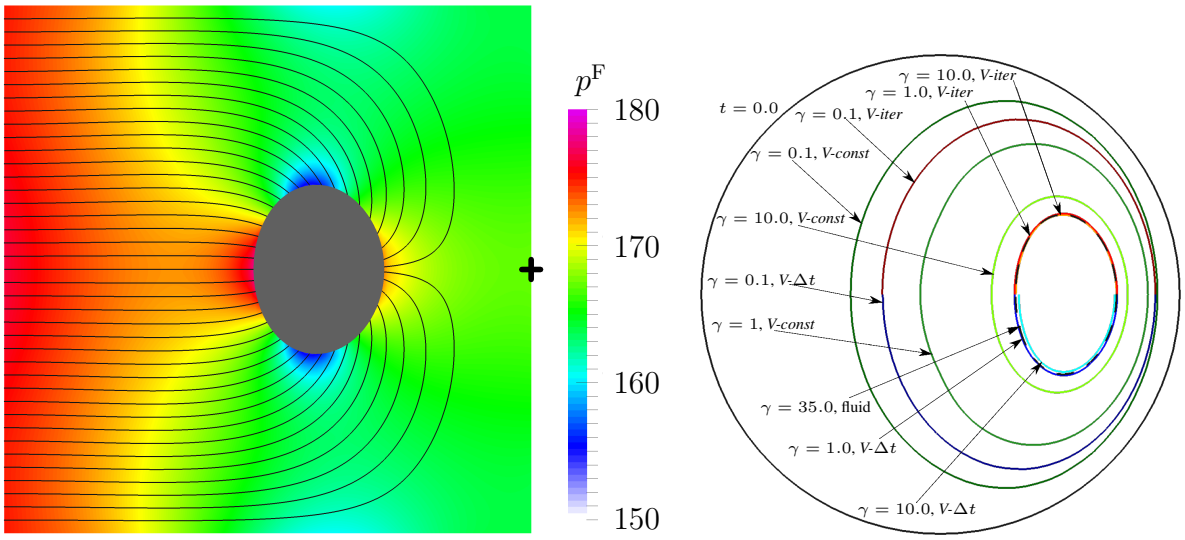

Figure 3.13: Computed solution at $t = 0.1$ for the variant *V-iter*, without an adjoint-consistency term $\xi^{\mathrm{FSI}} = 0$, with constant $\gamma_0^{\mathrm{FSI}} = 1$, and with time step length $\Delta t = 0.0000625$. The fluid pressure is represented by the color code, the black lines indicate the streamlines computed from the fluid velocity $\underline{\boldsymbol{v}}^{\mathrm{F}}$. The deformed solid cylinder Ω^{S} is visualized by the gray area. The black cross indicates the point where the fluid pressure of all computed variants is compared in Figure 3.14. (left) Visualization of the initial interface Γ^{FS} and deformed interface Γ^{FS} at the last computed time step for all considered configuration. To enable a clear presentation, only half the interface is shown for configuration *V-iter* ($y > 0.5$) and configuration *V-*Δt ($y < 0.5$). (right)

To depict the principal physical process of this test configuration, one exemplary computed solution is shown in Figure 3.13 (left). It can be seen, that fluid mass enters the fluid domain Ω^{F} through the boundary $\Gamma^{F,x-}$. As all other outer boundaries of the domain are "closed", the solid cylinder Ω^{S} is compressed. The majority of the interface traction on Γ^{FS} results from the fluid pressure p^{F} which increases in time. Viscous and inertia effects lead to local deviations of the pressure from a constant level in the domain Ω^{F}.

Figure 3.14 shows the computed horizontal diameter of the solid domain in relation to the fluid pressure at the specific point $\underline{\boldsymbol{x}} = [1.0, 0.5]^{\mathsf{T}}$, which is marked in Figure 3.13 (left), for the two considered time step lengths $\Delta t = 0.000625$ and $\Delta t = 0.0000625$. The maximal pressure (last time step) for which the nonlinear system with damped update strategy (see Sections 2.3 and 3.4 for details) of the respective variant could be solved with $\xi^{\mathrm{FSI}} = 0$, is marked by a circle. Additional, the maximal pressure for variant $\xi^{\mathrm{FSI}} = 1$ is indicated by a cross. This sec-

ond variant is given only as a reference and is not discussed in the following as it results in a solvable system independent of the prefactor of the Nitsche penalty term $\phi_\Gamma^{\mathrm{S}}\gamma_0^{\mathrm{FSI}}$. It should be highlighted, that the maximal pressure values indicated by the circles or crosses depend highly on the chosen approach and the specified termination criteria, but these values still allow for a relative comparison between the different variants. The presentation of the deformation (by the horizontal diameter) w.r.t. the fluid pressure allows making statements unaffected by the varying constraint enforcement for the different analyzed variants. The constraint violation increases for a low penalty scaling as shown in Section 3.5.1.2.

Computed Results and Discussion First, the results for the larger time step length $\Delta t = 0.000625$ with $\xi^{\mathrm{FSI}} = 0$ are discussed (circles in Figures 3.14 (top)). The computed reference configuration based on fluid-sided interface stress representation ($\gamma_0^{\mathrm{FSI}} = 35.0$) demonstrates that for a numerically stable formulation the system can be solved up to a maximal fluid pressure of $p^{\mathrm{F}} \approx 750$ before the nonlinearity of the system deteriorates the nonlinear solution procedure. The results of the simple scaling variant *V-const* show the expected behavior of not resulting in a stable formulation for a to small constant γ_0^{FSI}. With an increased constant γ_0^{FSI} a stable formulation can be established for an larger fluid load and as a consequence thereof for larger solid compression. Specifying the constant to $\gamma_0^{\mathrm{FSI}} = 10.0$ with *V-const* turns out to be sufficient to establish a stable formulation up to a fluid pressure load $p^{\mathrm{F}} \approx 550$. For the computationally most expensive variant *V-iter*, a constant of $\gamma_0^{\mathrm{FSI}} = 0.1$ is not sufficient to result in a stable formulation. However, increasing the value of the parameter to $\gamma_0^{\mathrm{FSI}} = 1.0$ and $\gamma_0^{\mathrm{FSI}} = 10.0$ results in robust formulations. The computed results for the variant *V-*Δt are similar to the variant *V-iter* in the respective considered configuration.

Comparing the previously discussed results for time step $\Delta t = 0.000625$ with the results for the smaller time step length $\Delta t = 0.0000625$, in Figure 3.14 (bottom), allows validating the temporal scaling of the Nitsche penalty parameter. The reference computation based on fluid-sided interface stress representation shows, that for the reduced time step length, the nonlinear solution procedure converges up to fluid pressure of $p^{\mathrm{F}} \approx 1200$. The enlarged solvable range of compression reveals that the variant *V-const* in combination with the largest constant $\gamma_0^{\mathrm{FSI}} = 10.0$ is by far not sufficient to guarantee stability of the formulation up to the maximal load and deformation anymore. In contrast to that, for the variants *V-iter* or *V-*Δt in combination with the scaling $\gamma_0^{\mathrm{FSI}} = 1.0$ and $\gamma_0^{\mathrm{FSI}} = 10.0$, the formulation is solvable up to the maximal fluid pressure. This confirms the temporal scaling in the factor ϕ_Γ^{S} as a stable formulation with the same parameter γ_0^{FSI} can be established for different time step lengths Δt.

Figure 3.13 (right) shows the resulting shape of the fluid-structure interface Γ^{FS} at the last solved point in time for all considered variants with $\xi^{\mathrm{FSI}} = 0$ and time step length $\Delta t = 0.0000625$. A comparison with the results presented in Figures 3.14 (bottom) reveals the inverse relation of the maximal fluid pressure and the remaining size of the solid domain.

In the following, the core statements of this computational test are summarized. The scaling of the Nitsche penalty parameter ϕ_Γ^{S} based on the generalized local eigenvalue problem (3.19) performs as expected. This scaling results in a stable formulation if the penalty constant is chosen large enough. A value of $\gamma_0^{\mathrm{FSI}} \geq 1.0$ was sufficient for all analyzed fluid pressure loads. Concerning the update strategies of ϕ_Γ^{S} it was found that evaluating ϕ_Γ^{S} solely at the beginning of the computation (*V-const*) does not reliably result in a stable formulation and therefore is

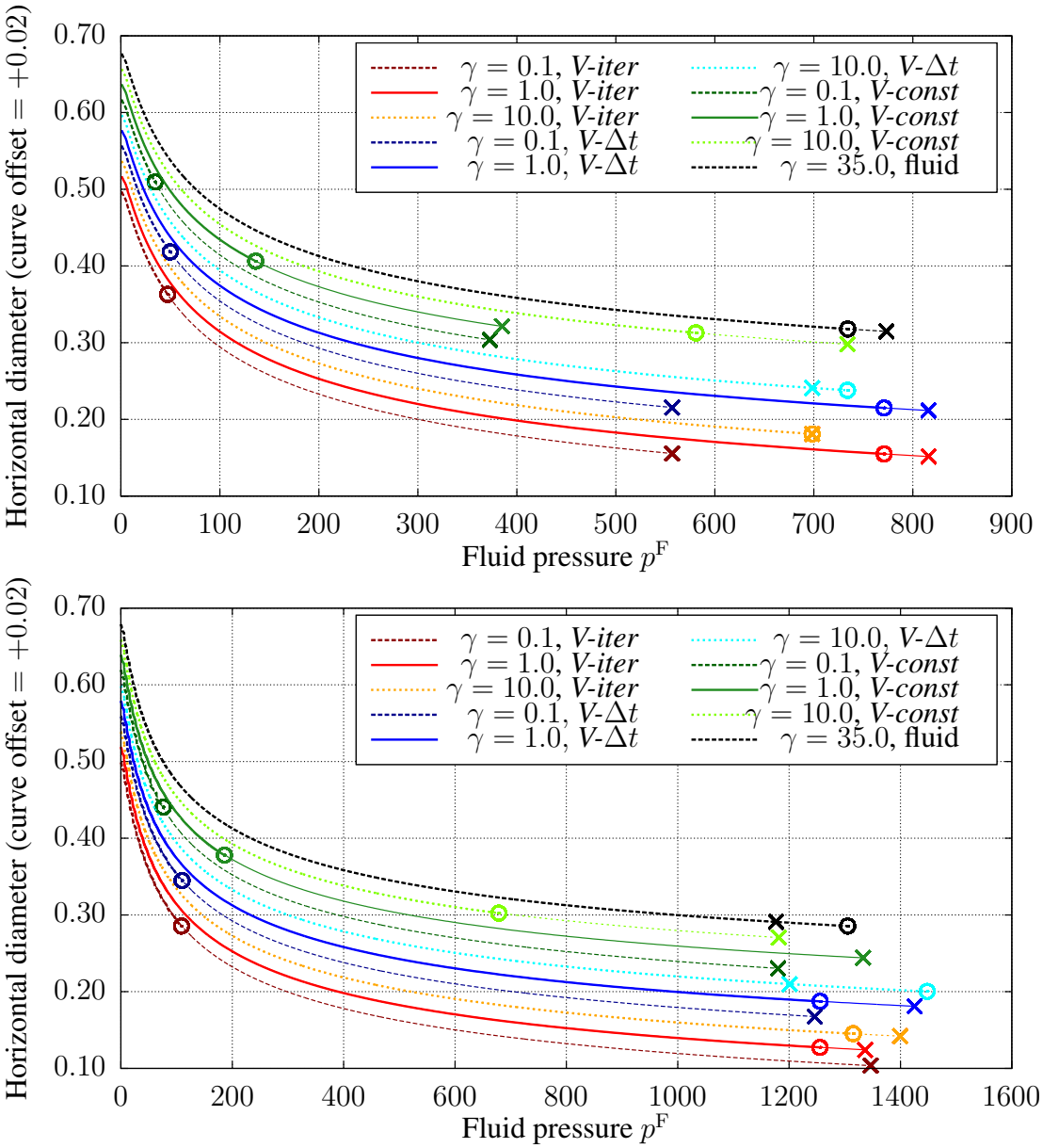

Figure 3.14: Computed horizontal diameter of the deformed solid domain in relation to the fluid pressure at point $\underline{\boldsymbol{x}} = [1.0, 0.5]^{\mathsf{T}}$. To enable a clear presentation, all curves are shifted by an offset of $+0.02$ from top-left to bottom-right according to the order of the lines in the legend. The value γ equals the constant γ_0^{FSI} and the considered variant is specified in the legend. The maximal pressure for which the nonlinear system could be solved is indicated by a circe ($\xi^{\mathrm{FSI}} = 0$) and a cross ($\xi^{\mathrm{FSI}} = 1$). The computed solution at the first computed time step is dominated by an initial shock, and thus, is not shown due to the irrelevance for this analysis. Computed for the large time step length $\Delta t = 0.000625$ (top), and computed for the small time step length $\Delta t = 0.0000625$ (bottom).

not recommended for such a configuration. Nevertheless, for cases with limited deformation or when including a skew-symmetric adjoint-consistency term $\xi^{\mathrm{FSI}} = 1$, this strategy can still be successful if a sufficiently large safety buffer is included in the constant γ_0^{FSI}. The continuous update strategy (*V-iter*) performs similar to the time step-wise update strategy (*V-*Δt), especially for small time step lengths. As the strategy strategy *V-*Δt is less computational costly and it reduces the nonlinearity of the system, for all computation with solid-sided interface stress representation this update strategy is recommened and thus it is applied for all computations which are presented in this thesis.

3.5.3 Convection-Dominated Flow around Solid Corners

For configurations which include convection-dominated fluid flow around sharp corners of soft solids, a significant difference between both variants of interface stress representation can be identified. Whereas the solution computed by the fluid-sided interface stress representation results in an solution accuracy as expected, an obviously non-physical deformation occurs close to the solid corner for the solid-sided interface stress representation. In the following, different solutions for the same problem configuration are shown, which are computed by various approaches to narrow down the causes for this issue. Not all details of the problem configuration are specified as they are not relevant for the illustration of this effect.

In Figure 3.15 (top), a comparison of the computed solution for CutFEM FSI in combination with both approaches of interface stress representation is given. The solid element at the corner shows non-physical deformation when applying the solid-sided interface stress representation. A similar non-physical deformation cannot be observed in the case fluid-sided interface stress representation is used.

In contrast to this observation for interface-unfitted CutFEM FSI, the non-physical deformation of the corner does not occur for neither variant of interface stress representation when applying interface-fitted matching grid ALE FSI as a numerical formulation to solve this type of problem (see Figure 3.15 (mid)).

Increasing the spatial resolution of the solid and fluid discretization simultaneously does not resolve this issue. However, for a finer fluid mesh in combination with the same solid discretization the effect disappears. This is shown for two different computational fluid mesh sizes in Figure 3.15 (bottom).

The previously presented computations indicate that this increased displacement error close to the corner is not related to the solid-sided interface stress representation only (see ALE FSI and refined fluid mesh). It is the combination of the discrete spaces provided by the CutFEM FSI approach with the solid-sided interface stress representation which leads to the problem. To fully understand this issue, which might get essential for FSI including high Reynolds number flows, further investigations are required. Nevertheless, for many configurations including all presented numerical examples, this effect is not very pronounced and thus does not lead to difficulties.

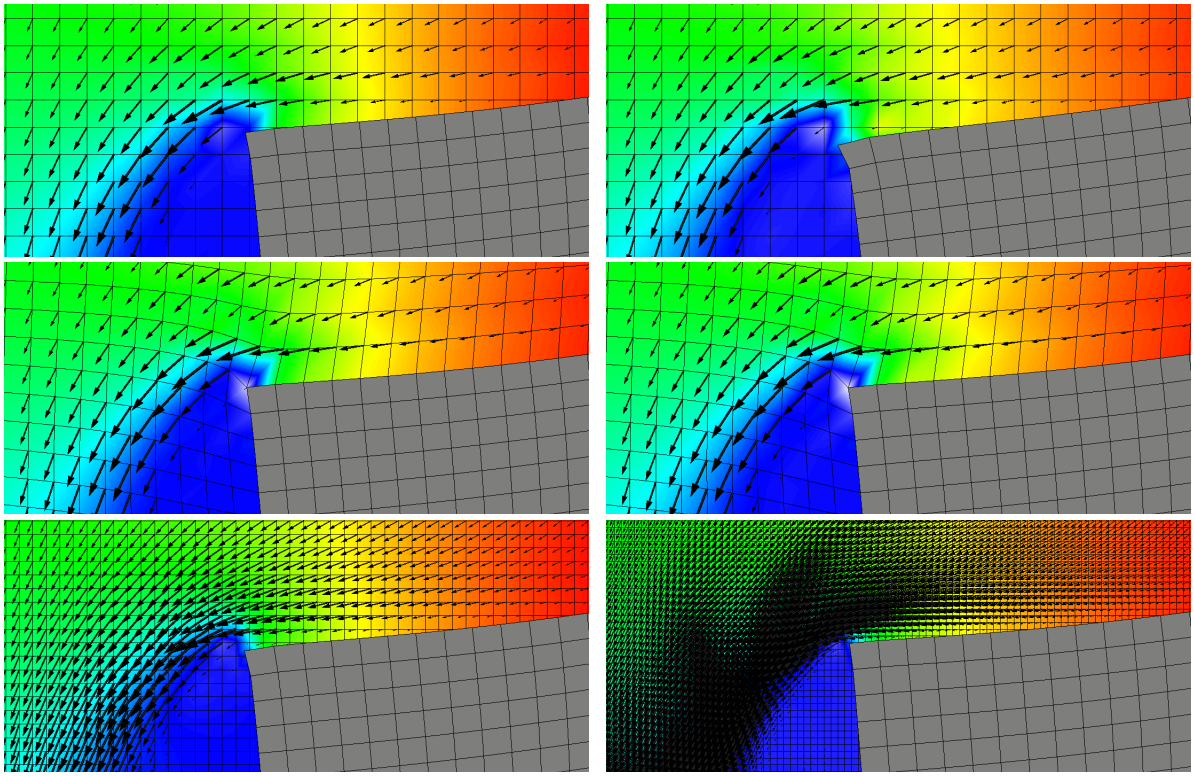

Figure 3.15: Visualization of the computed solution for convection-dominated fluid flow around a solid corner. The black arrows indicate the fluid velocity, the color code represents the fluid pressure, the black lines are the element boundaries, and the gray domain represents the solid domain. The characteristic properties of this configuration are the maximum velocity $||\underline{\boldsymbol{v}}^{\mathrm{F}}_{max}|| \approx 250$, the dynamic viscosity $\mu^{\mathrm{F}} = 0.1$, the fluid and solid density $\rho^{\mathrm{F}} = \rho^{\mathrm{S}}_0 = 1$, the Neo-Hookean material model (2.17) with Young's modulus $E = 5 \cdot 10^5$ and Poisson ratio $\nu = 0.3$, the element size $h \approx 0.03$, and no adjoint-consistency term $\xi^{\mathrm{FSI}} = 0$. The Nitsche penalty parameter for fluid-sided interface stress representation is $\gamma^{\mathrm{FSI}}_0 = 35$ and for solid-sided interface stress representation it is $\gamma^{\mathrm{FSI}}_0 = 5$. Computed by interface-unfitted CutFEM FSI with fluid-sided interface stress representation (top-left) and with solid-sided interface stress representation (top-right). Computed by interface-fitted ALE FSI with fluid-sided interface stress representation (mid-left) and with solid-sided interface stress representation (mid-right). Computed by interface-unfitted CutFEM FSI with solid-sided interface stress representation and reduced fluid element size $h^{\mathrm{F}} \approx 0.015$ (bottom-left) and $h^{\mathrm{F}} \approx 0.0075$ (bottom-right).

3.6 Numerical Example: 3D Spring-Damper System

To demonstrate the general applicability of the CutFEM FSI with both variants of interface stress representation, a 3D spring-damper system which dissipates mechanical energy by the motion of viscous fluid is analyzed.

Problem Description The principal geometry of the 3D spring-damper system is visualized in Figure 3.16. Therein, a (x, y, z)-coordinate system, which will be utilized in the following, is specified. The mechanical force is applied on top of a cylindrical stamp with radius $r_1 = 0.15$ and the vertical extension $z \in [0.07, 0.57]$. An attached solid disc with radius $r_2 = 0.5$ and the vertical extension $z \in [0.0, 0.07]$, including two cylindrical holes of radius $r_3 = 0.1$ with their axis crossing the positions $\underline{\boldsymbol{x}}^{hole} = (\pm 0.3, 0, 0)$, redirects the fluid flow. Two spiral springs

ensure a static load transmission of the system. The geometry of the first spring is defined by a vertical circle of radius $r_4 = 0.07$ in the $(y = 0)$-plane with midpoint position $\underline{\boldsymbol{x}}^{spring} = (-0.3, 0, -0.68)$ extruded along a helix with radius $r_5 = 0.3$, with a pitch of $h^{pitch} = 1.0$, and cropped at $z = 0$ and $z = -0.61$. The second spring is defined by rotation of the first spring with an angle of $\alpha^{spring} = \pi$ around the z-axis. The fluid domain Ω^{F} is specified by a cylinder with radius $r_6 = 0.55$ and the vertical extension $z \in [-0.61, 0.14]$ as well as the interface Γ^{FS} given by the deforming solid domain. On the fluid boundary at $z = 0.14$, a zero-traction condition

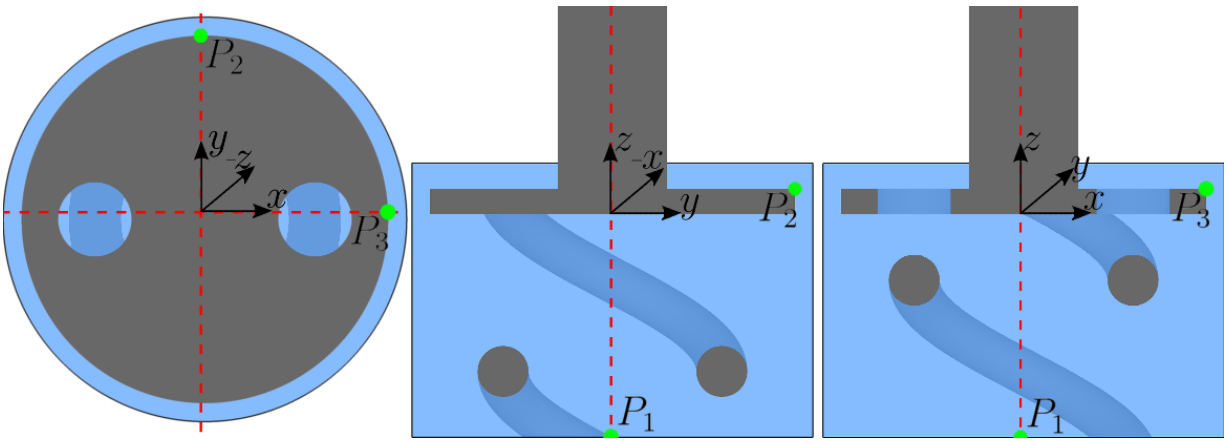

Figure 3.16: Geometric configuration of the 3D spring-damper system visualized by three cross-sectional views of the $(z = 0)$-, $(y = 0)$-, and $(x = 0)$-plane. The gray domain corresponds to the solid domain Ω^{S} whereas the blue domain corresponds to the fluid domain Ω^{F}. At the marked points P_1, P_2, and P_3 the computed fluid pressure and solid displacement solution is shown in Figure 3.19 and Figure 3.20.

is prescribed whereas on all other parts of the fluid boundary zero-velocity is specified. The springs are fixed at the bottom ($z = -0.61$) and the motion of the top surface of the cylindrical stamp ($z = 0.57$) is prescribed by $\hat{\underline{\boldsymbol{u}}}^{\mathrm{S}} = [0, 0, -0.125(1 - cos(10\pi t))]^{\mathsf{T}}$ for $t \in [0, 0.1]$ and $\hat{\underline{\boldsymbol{u}}}^{\mathrm{S}} = [0, 0, -0.25]^{\mathsf{T}}$ for $t > 0.1$. At the common interface of the fluid domain and the solid domain, the FSI-condition are enforced, whereas at the remaining unspecified part of the solid boundary (cylindrical surface of the stamp) zero-traction is prescribed.

The dynamic viscosity of the fluid is $\mu^{\mathrm{F}} = 0.1$ and the density is $\rho^{\mathrm{F}} = 0.1$. The material behavior of the solid is specified by a Neo-Hookean material model with the hyperelastic strain energy function (2.17) with a Young's modulus $E = 10^5$ and a Poisson ratio $\nu = 0.1$. The initial solid density is $\rho_0^{\mathrm{S}} = 1$. The discretization of the fluid domain, which is fitted to the outer boundaries but not to the interface Γ^{FS}, consists of 444600 tri-linear hexahedral element. The computational mesh of the solid domain consists of 73923 tri-linear hexahedral elements. An impression on the structure of the discretization is given in Figure 3.17 (top-left). Two computations are compared, wherein the incorporation of the FSI-condition on the interface Γ^{FS} is performed by the Nitsche-based method utilizing either the fluid-sided interface stress representation or the solid-sided interface stress representation. The computation with fluid-sided interface stress representation is specified by $\xi^{\mathrm{FSI}} = 1$ and $\gamma_0^{\mathrm{FSI}} = 35$. The computation with fluid-sided interface stress representation is specified by $\xi^{\mathrm{FSI}} = 0$ and $\gamma_0^{\mathrm{FSI}} = 1.5$. The discretization in time is performed by the backward Euler scheme ($\theta = 1$) with a time step length of $\Delta t = 10^{-4}$ for $t \in [0, 0.125]$ and an increased time step length in the relaxation phase of $\Delta t = 5 \cdot 10^{-4}$ for $t \in [0.125, 0.5]$. To improve the performance of the iterative procedure to solve the resulting linear system of equa-

tions, the constants specifying the relation of second and first order ghost penalty stabilization in (3.6) are increased to 5. The resulting linear system of equations which consists of approximately 1.85 million unknowns, is attacked by the iterative GMRES algorithm that is supported by preconditioning with a two block Gauss-Seidel iteration in combination with efficient algebraic multigrid applied on the fluid and solid block separately (details are given by Verdugo and Wall [214]).

Computed Results and Discussion To provide an impression of the overall behavior of the 3D spring-damper system, the computed solution for the solid-sided interface stress representation is shown in Figure 3.17. At the initial phase ($t = 0.025$ and $t = 0.05$), an axisymmetrical

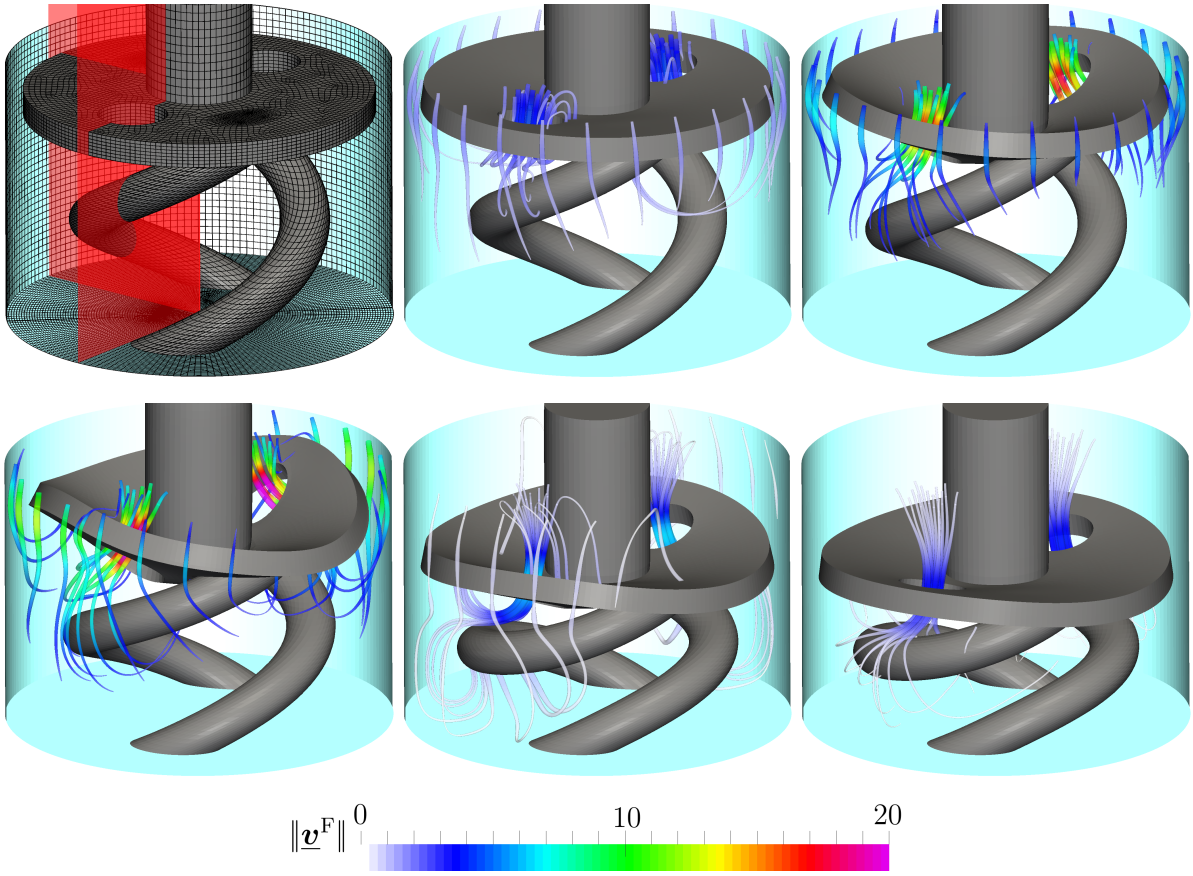

Figure 3.17: Computed deformation and fluid flow for solid-sided interface stress representation for different instances in time. The streamlines are based on the fluid velocity $\underline{\boldsymbol{v}}^{\mathrm{F}}$ and colored by the velocity magnitude. The points in time from top-left to bottom-right are: $t = 0.0, t = 0.025, t = 0.05, t = 0.07, t = 0.135$, and $t = 0.2$. The cyan-colored wall represents the boundary of the fluid domain. To enable a clear presentation, different minimal velocity magnitudes are specified to visualize the streamlines. The computational mesh and the planes on which the cross-sectional views of Figure 3.18 are based, are visualized in top-left figure.

deformation of the solid disc can be observed. As a result, an almost axisymmetrical fluid flow in the gap between the outer fluid boundary and the solid disc occurs. Additionally, an essential part of the fluid mass flows through the two holes in the solid disc. At $t = 0.07$, a transition of the disc deformation into a two-dimensional bending has occurred. As a result of the increased distance

between the solid disc and the fluid boundary close to the maximal bending, the main portion of the flow accumulates close to this position. In relaxation phase, for $t > 0.1$, a continuous decrease of all flow velocities and the solid disc deformation can be observed.

A more detailed view of the computed solution is given in Figure 3.18 by two cross-sectional views. These visualization reveals the working principle of the damper. Due to the acting mechanical load on the solid stamp the fluid pressure below the solid disk increases. As a result, a fluid flow through the holes and the gap between solid disc and flow boundary occurs. The predominate viscous stress dissipates the external mechanical energy added to the system on top of the solid stamp. Especially at the points in time with high fluid pressure the solid spring has an essential impact on the flow through the solid disc hole, and thus, on the damping behavior of the system (see the fluid flow in Figure 3.18 for $t = 0.055, t = 0.07$, and $t = 0.08$). A closer look at the connecting edge of the solid stamp and the disc reveals that a high fluid pressure is computed at this position. This effect is less pronounced for the computations based on the fluid-sided interface stress representation. Still, no essential impact on the overall computed solution could be identified.

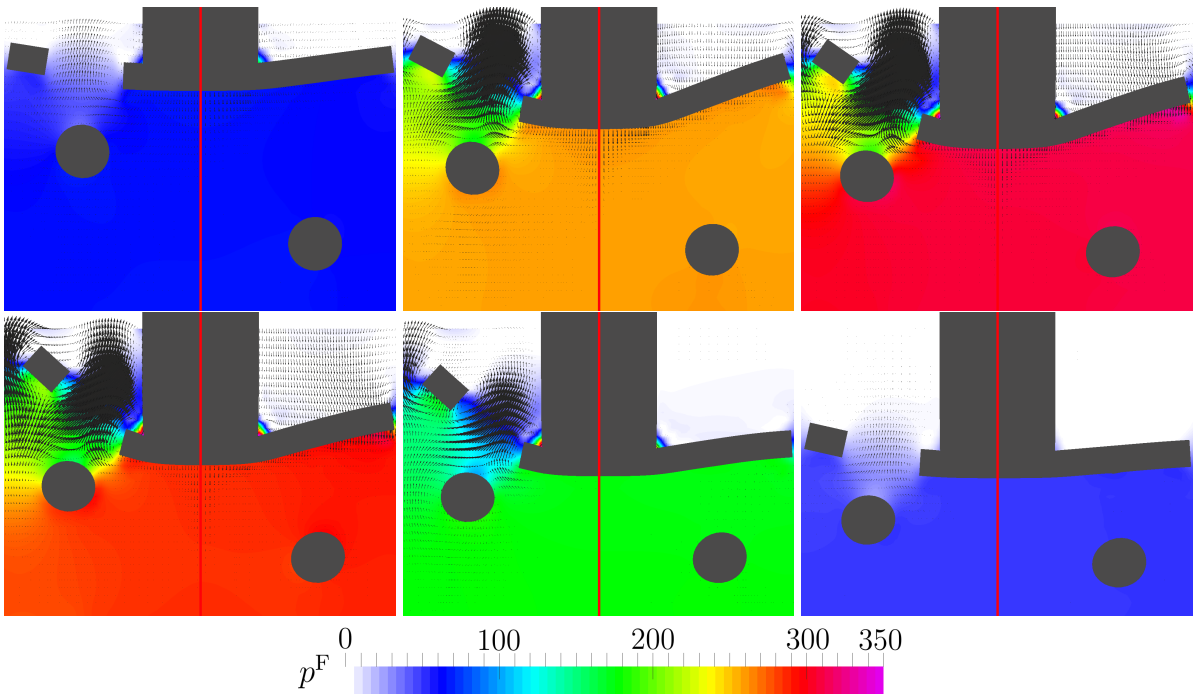

Figure 3.18: Computed deformation and fluid flow for solid-sided interface stress representation for different instances in time. The left half of each figure shows a cross-sectional view in the $(y = 0)$-plane and the right half a cross-sectional view in the $(x = 0)$-plane. These planes are visualized in Figure 3.17 (top-left). The fluid domain is colored based on the fluid pressure p^{F}. The points in time from top-left to bottom-right are: $t = 0.025, t = 0.055, t = 0.07, t = 0.08, t = 0.1$, and $t = 0.2$.

In Figure 3.19, a comparison of the computed vertical displacement at two characteristic points on the outer ring of the solid disc between the two approaches of interface stress representation is given. Both computations result in a similar temporal evolution of the displacement for both points P_2 and P_3. For the time interval $0.05 \lesssim t \lesssim 0.09$, a first noticeable difference between both approaches, which arises potentially due to the increased system dynamics and the

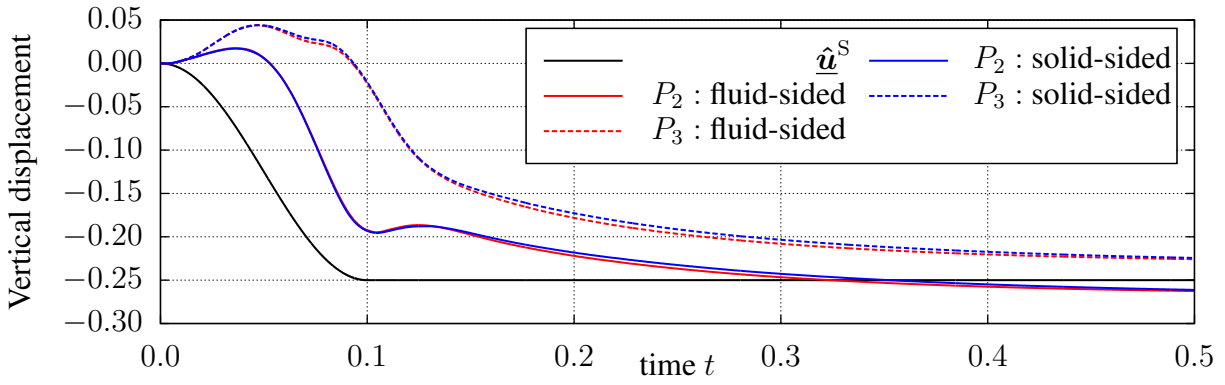

Figure 3.19: Comparison of the computed vertical displacement at two points P_2 and P_3 for the fluid-sided and the solid-sided interface stress representation. The reference coordinates of these points are: $P_2 : \underline{\boldsymbol{X}}^{\mathrm{S}} = [0.0, 0.5, 0.07]^{\mathrm{T}}$ and $P_3 : \underline{\boldsymbol{X}}^{\mathrm{S}} = [0.5, 0.0, 0.07]^{\mathrm{T}}$ and are marked by green points in Figure 3.16. The prescribed displacement $\underline{\boldsymbol{u}}^{\mathrm{S}}$ on the top surface of the cylindrical stamp is visualized as a reference.

complex fluid solution, can be observed at point P_3. The second observable difference occurs for $t > 0.125$ due to the increase of the time step length from $\Delta t = 10^{-4}$ to $\Delta t = 5 \cdot 10^{-4}$. The associated increase of the Nitsche penalty scaling $\phi_{\Gamma}^{\mathrm{S}}$ according to the temporal scaling in (3.30) for the solid-sided interface stress representation leads to a noticeable increase of the no-slip constraint enforcement for the utilized spatial resolution. This, of course, has an effect on the computed vertical displacement.

A comparison of the computed reaction force of the spring-damper system between both computations is shown in Figure 3.20 (top). Both approaches predict an almost identical temporal evolution of the reacting force. In accordance with the previously discussed displacement results, slight deviations between both approaches can be observed for the time interval $0.05 \lesssim t \lesssim 0.09$ and $t > 0.125$. At $t = 0.1$, a kink of the reaction force as a consequence of the instantaneous change of the prescribed solid acceleration on the top surface of the solid stamp occurs. Finally, in Figure 3.20 (bottom), the fluid pressure p^{F} at the bottom of the spring-damper system is shown. Besides the aspects already discussed for the reaction force, a short peak in the fluid pressure at $t = 0.125$ due to the change of the time step length can be observed for the solid-sided interface stress representation. Neglecting inertia and viscous fluid effects, the reaction force combines the load carried by the solid springs and the force transmitted by the fluid pressure. Thus, a comparison of the computed fluid pressure and the reaction force for the final point in time $t = 0.5$ reveals that the remaining reaction force is transmitted by the solid spring as the fluid pressure decreased almost to zero.

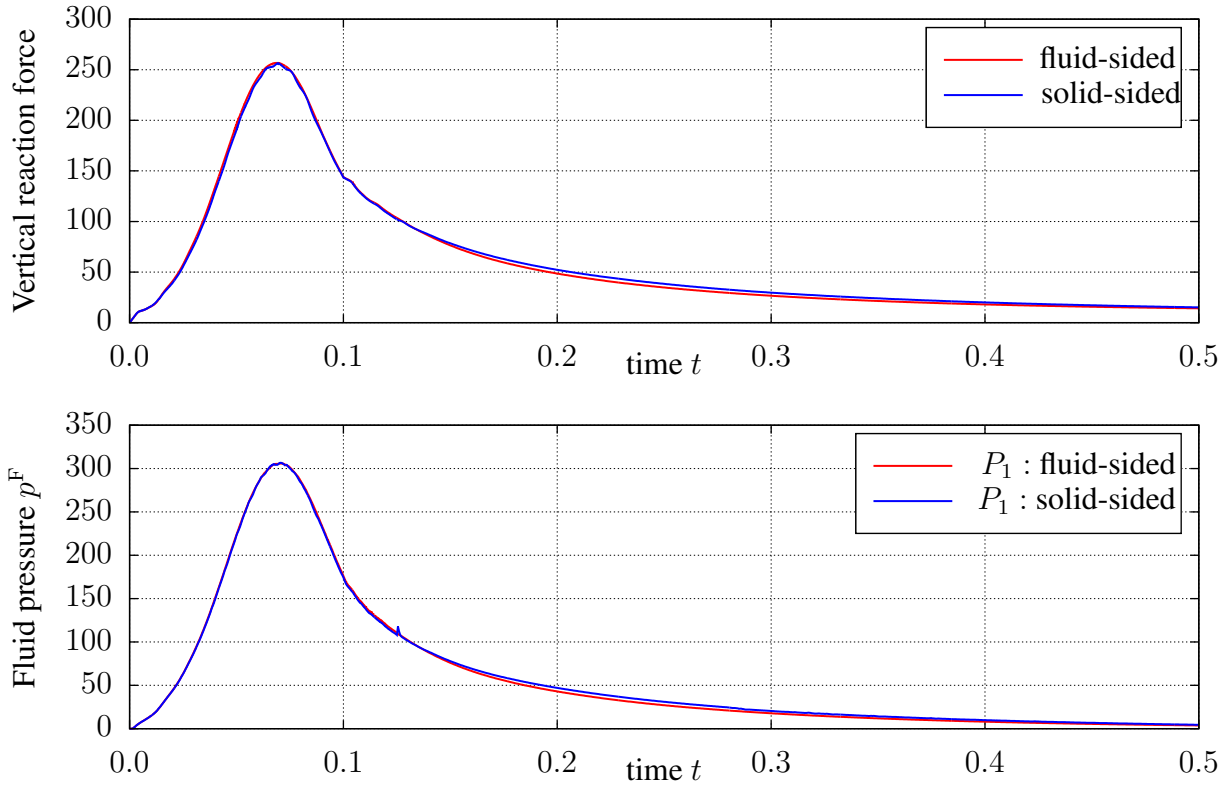

Figure 3.20: Comparison of the computed vertical reaction force on the top surface of the cylindrical solid stamp for the fluid-sided and the solid-sided interface stress representation. The reaction force is summed up from the nodal reaction forces to enforce the Dirichlet condition $\underline{\hat{\boldsymbol{u}}}^{\mathrm{S}}$ (top). Comparison of the computed fluid pressure p^{F} at the point P_1 for the fluid-sided and the solid-sided interface stress representation. The coordinates of the point, which is marked by a green point in Figure 3.16 (bottom), are: $P_1 : \underline{\boldsymbol{X}}^{\mathrm{S}} = [0.0, 0.0, -0.61]^{\mathsf{T}}$.

4 A Nitsche-based CutFEM for the Coupling of Incompressible Fluid Flow with Poroelasticity[1]

The focus of this chapter is the numerical treatment of interface-coupled problems concerning the interaction of incompressible fluid flow and permeable, elastic structures (FPI). The main emphasis is on extending the range of applicability of available formulations in three aspects: the incorporation of a more general poroelasticity formulation including a wide variety of material models by arbitrary strain energy density functions, the use of the CutFEM to allow for large interface motion and topological changes of the fluid domain, and the application of a novel Nitsche-based approach to incorporate the Beavers-Joseph (-Saffmann) tangential interface condition. This last aspect allows to extend the practicable range of applicability for the proposed formulation down to very low porosities and permeabilities which is important in several problem configurations in application. Different aspects of the above mentioned formulation are analyzed in a numerical example including spatial convergence, the sensitivity of the solution to the Nitsche penalty parameters, varying porosities and permeabilities, and a varying Beavers-Joseph interface model constant. Finally, two numerical examples analyzing the fluid induced bending of a poroelastic beam and the 3D interaction of a poroelastic plate and a fluid channel flow provide evidence of the general applicability of the presented approach.

The outline of this chapter is as follows. In Section 4.1, all essential formulations for the continuous and the discrete FPI problem, which were already discussed in the previous chapters, are referenced and briefly summarized. This is followed by a presentation of the applied numerical methods to weakly incorporate the interface conditions in normal and tangential orientation to the coupled problem, in Section 4.2. The coupled discrete formulation to be solved, is presented in Section 4.3. In Section 4.4, various aspects of the formulation are analyzed numerically by an example based on the method of manufactured solutions. The computational results of a general problem configuration, the fluid induced bending of a poroelastic beam, are presented in Section 4.5.1. In Section 4.5.2, the analysis of the 3D interaction of a poroelastic plate and a fluid channel flow highlight the applicability for more challenging 3D configurations.

4.1 Preliminaries for the Computational Solution of the FPI

Many aspects of treating the FPI problem numerically have already been presented in the previous chapters. In order to draw the readers attention to the most essential parts presented pre-

[1] This chapter is adapted from the author's publication [2].

viously, the most relevant sections are referenced and briefly recapitulated. First, the continuous FPI problem is discussed in Section 4.1.1, followed by a compact summary of already introduced approaches to numerically solve the discrete FPI problem, in Section 4.1.2.

4.1.1 The Continuous FPI Problem

The underlying physical problem, including all governing equations of FPI, was already introduced in Chapter 2 in a more general setup. The considered domains, interfaces, and boundaries are visualized in Figure 4.1. It should be highlighted that all discussions within this chapter are focused on this specific configuration, which include a fluid domain, a poroelastic domain, and their common interface. The application of the developed approach to more general problem configurations (see the generic overall problem presented in Section 2.1.1) is presented in Chapter 5 and 7.

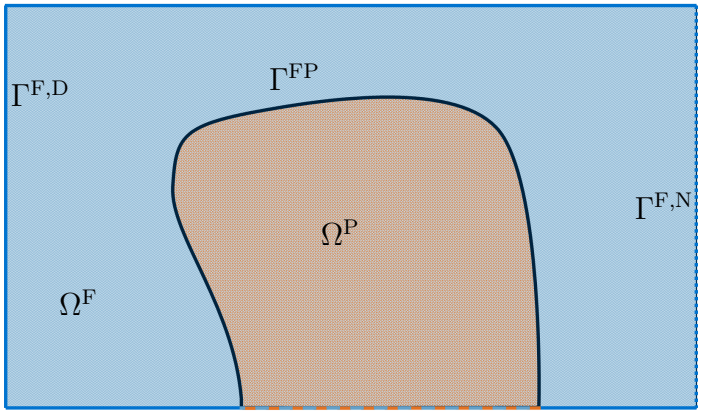

Figure 4.1: Fluid-Poroelastic interaction problem setup: fluid domain Ω^{F}, poroelastic domain Ω^{P}, common fluid-poroelastic interface Γ^{FP}, and boundaries $\Gamma^{\mathrm{F,D}}$, $\Gamma^{\mathrm{F,N}}$, $\Gamma^{\mathrm{P^F,D}}$, $\Gamma^{\mathrm{P^F,N}}$, $\Gamma^{\mathrm{P,D}}$, and $\Gamma^{\mathrm{P,N}}$ on the outer boundary of the FPI problem.

The overall domain $\Omega = \Omega^{\mathrm{F}} \cup \Omega^{\mathrm{P}}$ is given by the union of the fluid domain and the poroelastic domain. The outer boundary includes the union of all types of boundaries $\partial\Omega = \Gamma^{\mathrm{F,D}} \cup \Gamma^{\mathrm{F,N}} \cup \Gamma^{\mathrm{P,D}} \cup \Gamma^{\mathrm{P,N}} = \Gamma^{\mathrm{F,D}} \cup \Gamma^{\mathrm{F,N}} \cup \Gamma^{\mathrm{P^F,D}} \cup \Gamma^{\mathrm{P^F,N}}$. The governing equations in the fluid domain Ω^{F}, the Navier-Stokes equations including the balance of mass (2.27) and the balance of linear momentum (2.28), and additionally all required conditions on the boundaries $\Gamma^{\mathrm{F,D}}$ and $\Gamma^{\mathrm{F,N}}$ (2.31) were introduced in Section 2.1.5. The underlying system of equations for the poroelastic domain Ω^{P} including the balance of fluid mass (2.42), the balance of linear momentum for the fluid phase (2.43), and the balance of linear momentum for the porous mixture (2.46) was presented in Section 2.1.6. Therein, adequate boundary conditions (2.53) and (2.54) on the different boundaries $\Gamma^{\mathrm{P^F,D}}$, $\Gamma^{\mathrm{P^F,N}}$, $\Gamma^{\mathrm{P,D}}$, and $\Gamma^{\mathrm{P,N}}$ were also discussed. Describing the FPI system by the aforementioned equations, results in a system which has to be solved for the fluid velocity $\underline{\boldsymbol{v}}^{\mathrm{F}}$ and the fluid pressure p^{F} in the fluid domain Ω^{F} as well as the porous fluid velocity $\underline{\boldsymbol{v}}^{\mathrm{P}}$, the porous fluid pressure p^{P}, and the macroscopic displacement of the porous domain $\underline{\boldsymbol{u}}^{\mathrm{P}}$ in the poroelastic domain Ω^{P}.

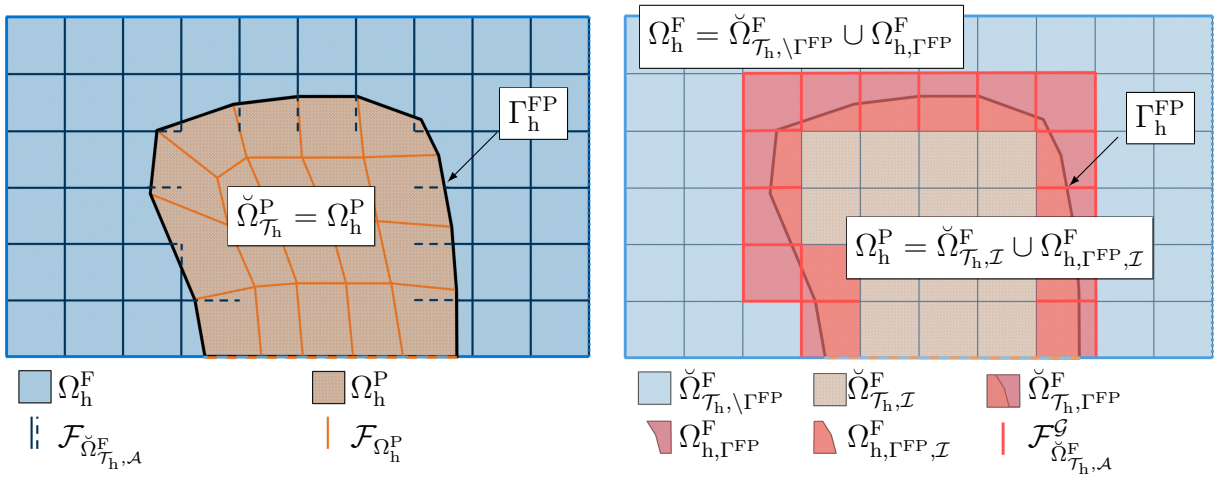

Figure 4.2: The domain covered by the boundary- and interface-fitted discretization $\breve{\Omega}_{\mathcal{T}_{\mathrm{h}}}^{\mathrm{P}}$ equals the discrete poroelastic domain $\Omega_{\mathrm{h}}^{\mathrm{P}}$. Visualization of the inner face sets ($\mathcal{F}_{\breve{\Omega}_{\mathcal{T}_{\mathrm{h}},\mathcal{A}}^{\mathrm{F}}}$ and $\mathcal{F}_{\Omega_{\mathrm{h}}^{\mathrm{P}}}$), where the CIP-stabilization is evaluated (left). The domain covered by the unfitted fluid discretization $\breve{\Omega}_{\mathcal{T}_{\mathrm{h}}}^{\mathrm{F}} = \breve{\Omega}_{\mathcal{T}_{\mathrm{h}},\backslash\Gamma^{\mathrm{FP}}}^{\mathrm{F}} \cup \breve{\Omega}_{\mathcal{T}_{\mathrm{h}},\mathcal{I}}^{\mathrm{F}} \cup \breve{\Omega}_{\mathcal{T}_{\mathrm{h}},\Gamma^{\mathrm{FP}}}^{\mathrm{F}}$ represents the fluid domain $\Omega_{\mathrm{h}}^{\mathrm{F}}$ through a set of elements covering the domain $\breve{\Omega}_{\mathcal{T}_{\mathrm{h}},\backslash\Gamma^{\mathrm{FP}}}^{\mathrm{F}}$ and the fluid subdomain $\Omega_{\mathrm{h},\Gamma^{\mathrm{FP}}}^{\mathrm{F}}$ of the domain $\breve{\Omega}_{\mathcal{T}_{\mathrm{h}},\Gamma^{\mathrm{FP}}}^{\mathrm{F}}$. The non-fluid domain, which equals the poroelastic domain $\Omega_{\mathrm{h}}^{\mathrm{P}}$, consists of the domain covering a set of elements in $\breve{\Omega}_{\mathcal{T}_{\mathrm{h}},\mathcal{I}}^{\mathrm{F}}$ and the non-fluid subdomain $\Omega_{\mathrm{h},\Gamma^{\mathrm{FP}},\mathcal{I}}^{\mathrm{F}}$ of the domain $\breve{\Omega}_{\mathcal{T}_{\mathrm{h}},\Gamma^{\mathrm{FP}}}^{\mathrm{F}}$. For all inner faces $\mathcal{F}_{\breve{\Omega}_{\mathcal{T}_{\mathrm{h}},\mathcal{A}}^{\mathrm{F}}}^{\mathcal{G}}$ of $\breve{\Omega}_{\mathcal{T}_{\mathrm{h}},\backslash\Gamma^{\mathrm{FP}}}^{\mathrm{F}} \cup \breve{\Omega}_{\mathcal{T}_{\mathrm{h}},\Gamma^{\mathrm{FP}}}^{\mathrm{F}}$, which are connected to one element in $\breve{\Omega}_{\mathcal{T}_{\mathrm{h}},\Gamma^{\mathrm{FP}}}^{\mathrm{F}}$, the ghost penalty stabilization is applied (right).

The missing piece to formulate the continuous FPI problem are the conditions on the common interface between the fluid domain and the poroelastic domain Γ^{FP}, which are discussed in Section 2.1.8. These interface conditions consist of the dynamic equilibrium of the fluid and the porous mixture (2.61), the dynamic equilibrium of the fluid and the porous fluid (2.62), the balance of mass on the interface (2.63), and the Beavers-Joseph (BJ) or Beavers-Joseph-Saffmann (BJS) condition (2.64). The latter condition takes effects of the porous flow close to the interface, which are not represented by the porous flow model, into account. Thus, the BJ or BJS condition, a general Navier type interface condition, is applied in tangential interface orientation.

4.1.2 The Discrete FPI Problem

The boundary-fitted FEM, as introduced in Section 2.2.2, is applied for the discretization of the poroelastic equations. The corresponding discrete weak form (2.120) including stabilization was discussed in Section 2.2.5. The discretization approach for the fluid domain is based on the CutFEM and was already presented with special focus on FSI in the previous chapter. In Figure 4.2, the discretization strategy for an FPI problem is shown. While the poroelastic domain is discretized by a boundary- and interface-fitted FEM discretization ($\breve{\Omega}_{\mathcal{T}_{\mathrm{h}}}^{\mathrm{P}} = \Omega_{\mathrm{h}}^{\mathrm{P}}$), the fluid domain is discretized unfitted to the interface ($\Omega_{\mathrm{h}}^{\mathrm{F}} \subset \breve{\Omega}_{\mathcal{T}_{\mathrm{h}}}^{\mathrm{F}}$). The geometric separation in the fluid domain $\Omega_{\mathrm{h}}^{\mathrm{F}} = \breve{\Omega}_{\mathcal{T}_{\mathrm{h}},\backslash\Gamma^{\mathrm{FP}}}^{\mathrm{F}} \cup \Omega_{\mathrm{h},\Gamma^{\mathrm{FP}}}^{\mathrm{F}}$ and the non-fluid domain $(\Omega_{\mathrm{h}}^{\mathrm{P}} =)\breve{\Omega}_{\mathcal{T}_{\mathrm{h}},\mathcal{I}}^{\mathrm{F}} \cup \Omega_{\mathrm{h},\Gamma^{\mathrm{FP}},\mathcal{I}}^{\mathrm{F}}$ is given by the intersection of the computational fluid mesh with the interface $\Gamma_{\mathrm{h}}^{\mathrm{FP}}$. Finally, the geometry of the interface $\Gamma_{\mathrm{h}}^{\mathrm{FP}}$ is given by the deformed boundary $\partial\Omega_{\mathrm{h}}^{\mathrm{P}} \supseteq \Gamma_{\mathrm{h}}^{\mathrm{FP}}$ of the boundary- and interface-fitted poroelastic discretization.

Taking this specific configuration into account, the approach discussed in detail in Section 3.1 can be directly applied. This includes especially the definition of all discrete fluid solution and test function spaces discussed in Section 3.1.2, the application of ghost penalty stabilization in Section 3.1.3, and the numerical integration of the $\mathcal{L}^2$-inner products of intersected elements in Section 3.1.4. The discretization in time is performed by the One-Step-θ scheme as discussed in Section 2.2.1, which is applied to the fluid domain in Section 2.2.4 and to the poroelastic domain in Section 2.2.5, and finally extended to the unfitted moving boundary configuration in Section 3.2. In the previous chapter, the weak imposition of the "no-slip" interface condition for the application in FSI by a Nitsche-based approach was discussed. To extend this towards FPI configurations, a novel Nitsche-based method for the weak imposition of all conditions (2.61)-(2.64) is discussed in the following.

4.2 The Nitsche-based Method on the Common Interface between Fluid and Poroelastic Domain

Up until now, the interface conditions between the fluid and the poroelastic domain on the interface $\Gamma_{\mathrm{h}}^{\mathrm{FP}}$ were not incorporated in the weak forms (3.7), (2.120). Due to the successful application of the CutFEM and the weak imposition of boundary/interface conditions by Nitsche-based methods for FSI (see e.g. the works of Alauzet *et al.* [5], Burman and Fernández [42], and Schott *et al.* [192]), this combination is also chosen to solve the problem of FPI in this chapter. Therefore, an additional integration on the discrete interface $\Gamma_{\mathrm{h}}^{\mathrm{FP}}$, which is given by the boundary of the deformed poroelastic domain $\partial\Omega_{\mathrm{h}}^{\mathrm{P}}$, has to be performed. Due to the different constraints in normal (2.63) and tangential (2.64) direction on the interface $\Gamma_{\mathrm{h}}^{\mathrm{FP}}$, separate treatment of both orientations is necessary.

4.2.1 Normal Direction

In normal direction, the additional contributions to the weak form for Nitsche's method includes a consistency, an adjoint-consistency and a penalty term, which are similar to the methods presented by Bukač *et al.* [37] and D'Angelo and Zunino [68].

$$\begin{aligned}
\mathcal{W}_{\mathrm{h}}^{\mathrm{FPI},n}\left[\left(\delta\underline{\boldsymbol{v}}_{\mathrm{h}}^{\mathrm{F}},\delta p_{\mathrm{h}}^{\mathrm{F}},\delta\underline{\boldsymbol{v}}_{\mathrm{h}}^{\mathrm{P}},\delta\underline{\boldsymbol{u}}_{\mathrm{h}}^{\mathrm{P}},\delta p_{\mathrm{h}}^{\mathrm{P}}\right),\left(\underline{\boldsymbol{v}}_{\mathrm{h}}^{\mathrm{F}},p_{\mathrm{h}}^{\mathrm{F}},\underline{\boldsymbol{v}}_{\mathrm{h}}^{\mathrm{P}},\underline{\boldsymbol{u}}_{\mathrm{h}}^{\mathrm{P}},p_{\mathrm{h}}^{\mathrm{P}}\right)\right] = \\
\left\langle\delta\underline{\boldsymbol{v}}_{\mathrm{h}}^{\mathrm{P}}+\delta\underline{\boldsymbol{u}}_{\mathrm{h}}^{\mathrm{P}}-\delta\underline{\boldsymbol{v}}_{\mathrm{h}}^{\mathrm{F}},\underline{\boldsymbol{\sigma}}_{\mathrm{h}}^{\mathrm{F}}\cdot\underline{\boldsymbol{n}}_{\mathrm{h}}^{\mathrm{F}}\cdot\underline{\boldsymbol{P}}^{n}\right\rangle_{\Gamma_{\mathrm{h}}^{\mathrm{FP}}}-\left\langle\delta\underline{\boldsymbol{v}}_{\mathrm{h}}^{\mathrm{P}},\hat{g}_{\sigma}^{\mathrm{FP},n}\underline{\boldsymbol{n}}_{\mathrm{h}}\cdot\underline{\boldsymbol{P}}^{n}\right\rangle_{\Gamma_{\mathrm{h}}^{\mathrm{FP}}}-\left\langle\delta\underline{\boldsymbol{u}}_{\mathrm{h}}^{\mathrm{P}},\hat{\underline{\boldsymbol{g}}}_{\sigma}^{\mathrm{FP}}\cdot\underline{\boldsymbol{P}}^{n}\right\rangle_{\Gamma_{\mathrm{h}}^{\mathrm{FP}}} \\
-\left\langle\delta p_{\mathrm{h}}^{\mathrm{F}}\cdot\underline{\boldsymbol{n}}_{\mathrm{h}}^{\mathrm{F}}+\xi^{\mathrm{FPI}}2\mu^{\mathrm{F}}\underline{\boldsymbol{\epsilon}}^{\mathrm{F}}(\delta\underline{\boldsymbol{v}}_{\mathrm{h}}^{\mathrm{F}})\cdot\underline{\boldsymbol{n}}_{\mathrm{h}}^{\mathrm{F}},\left[\underline{\boldsymbol{v}}_{\mathrm{h}}^{\mathrm{F}}-\tilde{\partial}_t\left[\underline{\boldsymbol{u}}_{\mathrm{h}}^{\mathrm{P}}\right]-\phi_{\mathrm{h}}\left(\underline{\boldsymbol{v}}_{\mathrm{h}}^{\mathrm{P}}-\tilde{\partial}_t\left[\underline{\boldsymbol{u}}_{\mathrm{h}}^{\mathrm{P}}\right]\right)-\hat{\underline{\boldsymbol{g}}}^{\mathrm{FP},n}\right]\cdot\underline{\boldsymbol{P}}^{n}\right\rangle_{\Gamma_{\mathrm{h}}^{\mathrm{FP}}} \\
+\frac{\phi_{\Gamma}^{\mathrm{F}}\gamma_0^{\mathrm{FPI},n}}{h_{\Gamma}}\left\langle\delta\underline{\boldsymbol{v}}_{\mathrm{h}}^{\mathrm{F}}-\delta\underline{\boldsymbol{v}}_{\mathrm{h}}^{\mathrm{P}}-\delta\underline{\boldsymbol{u}}_{\mathrm{h}}^{\mathrm{P}},\left[\underline{\boldsymbol{v}}_{\mathrm{h}}^{\mathrm{F}}-\tilde{\partial}_t\left[\underline{\boldsymbol{u}}_{\mathrm{h}}^{\mathrm{P}}\right]-\phi_{\mathrm{h}}\left(\underline{\boldsymbol{v}}_{\mathrm{h}}^{\mathrm{P}}-\tilde{\partial}_t\left[\underline{\boldsymbol{u}}_{\mathrm{h}}^{\mathrm{P}}\right]\right)-\hat{\underline{\boldsymbol{g}}}^{\mathrm{FP},n}\right]\cdot\underline{\boldsymbol{P}}^{n}\right\rangle_{\Gamma_{\mathrm{h}}^{\mathrm{FP}}}, \\
\phi_{\Gamma}^{\mathrm{F}}=\mu^{\mathrm{F}}+h_{\Gamma}c_{v,\Gamma}\rho^{\mathrm{F}}\left|\left|\underline{\boldsymbol{v}}^{\mathrm{F}}\right|\right|_{\infty,\Gamma}+h_{\Gamma}^2c_{t,\Gamma}\frac{\rho^{\mathrm{F}}}{\theta\Delta t}
\end{aligned} \tag{4.1}$$

As all terms are projected in the normal direction by the projection matrix $\underline{\boldsymbol{P}}^n := (\underline{\boldsymbol{n}}_{\mathrm{h}}\otimes\underline{\boldsymbol{n}}_{\mathrm{h}})$ herein, $\mathcal{W}_{\mathrm{h}}^{\mathrm{FPI},n}$ solely leads to contributions in the normal direction of the interface $\Gamma_{\mathrm{h}}^{\mathrm{FP}}$. The

terms in the second line originate from the integration by parts in the derivation of the weak form (2.112) and are therefore called consistency terms. Herein, the interface stress is chosen to be represented by the fluid stress. The last two terms in this line vanish for zero stress jumps in the dynamic equilibrium (2.61) and (2.62), which, in general, is the physical relevant case. All terms in the following lines are added in order to obtain a stable and convergent discrete numerical scheme and to enforce the kinematic constraint (2.63). Consistency is guaranteed due to the included kinematic constraint (2.63), wherefore these contributions vanish in the case of an exact constraint fulfillment. An additional adjoint-inconsistent pressure term in line three balances the pressure contribution of fluid stress in the consistency boundary integrals of line two. For the viscous adjoint-consistency term, an adjoint-consistent ($\xi^{\mathrm{FPI}} = 1$) or adjoint-inconsistent ($\xi^{\mathrm{FPI}} = -1$) variant can be chosen. Finally, in the last line, a penalty term guarantees the stability of the numerical method, if a sufficiently large constant $\gamma_0^{\mathrm{FPI},n}$ is chosen. The dependence of the resulting error norms of the numerical scheme on the penalty parameter $\gamma_0^{\mathrm{FPI},n}$ is analyzed in the numerical example presented in Section 4.4.3 for both choices of ξ^{FPI}. The additive scaling of ϕ_Γ^{F} aims for a stable numerical scheme in all regimes of the fluid equations, as discussed in the work by Massing *et al.* [149]. Herein, $\left|\left|\underline{\boldsymbol{v}}_{\mathrm{h}}^{\mathrm{F}}\right|\right|_{\infty,\Gamma}$ is the maximal fluid velocity component at the current point in space on the interface $\Gamma_{\mathrm{h}}^{\mathrm{FP}}$. The convective and reactive constants are specified to: $c_{v,\Gamma} = 1/6, c_{t,\Gamma} = 1/12$. The mesh size parameter h_Γ is computed by the ratio of the element volume and the part of the area of the interface $\Gamma_{\mathrm{h}}^{\mathrm{FP}}$ in the local intersected element in $\breve{\Omega}_{\mathcal{T}_{\mathrm{h}},\Gamma^{\mathrm{FP}}}$. Whenever essential, an additional index in $\mathcal{W}_{\mathrm{h},n+1}^{\mathrm{FPI},n}$ specifies that all interface terms $\langle *,*\rangle_{\Gamma_{\mathrm{h}}^{\mathrm{FP}}}$ are evaluated as $\langle *,*\rangle_{\Gamma_{\mathrm{h},n+1}^{\mathrm{FP}},n+\theta}$.

Remark 4.1 (Alternative scaling of the penalty terms)**.** *In the case that the partial integration of the porosity gradient is not performed in the derivation of the weak form of the balance of linear momentum for the poroelastic mixture* (2.46) *(weak form presented by Vuong* et al. *[216], basically $\boldsymbol{\nabla}\phi_{\mathrm{h}} \longrightarrow \boldsymbol{\nabla} p_{\mathrm{h}}^{\mathrm{P}}$ is not performed), a statement on the scaling of the penalty terms can be acquired. For this formulation, the consistency terms of the weak form of the mixture equation include only the averaged structural stress $\underline{\boldsymbol{\sigma}}_{\mathrm{h}}^{P^S} = \underline{\boldsymbol{\sigma}}_{\mathrm{h}}^{\mathrm{P}} + \phi_{\mathrm{h}} p_{\mathrm{h}}^{\mathrm{P}} \underline{\boldsymbol{I}}$, which results in the normal dynamic equilibrium (replacing constraint* (2.61) *in normal direction)*

$$0 = (1-\phi_{\mathrm{h}})\, \underline{\boldsymbol{n}}_{\mathrm{h}} \cdot \underline{\boldsymbol{\sigma}}_{\mathrm{h}}^{\mathrm{F}} \cdot \underline{\boldsymbol{n}}_{\mathrm{h}} - \underline{\boldsymbol{n}}_{\mathrm{h}} \cdot \underline{\boldsymbol{\sigma}}_{\mathrm{h}}^{P^S} \cdot \underline{\boldsymbol{n}}_{\mathrm{h}} \qquad \text{on } \Gamma_{\mathrm{h}}^{\mathrm{FP}} \times [t_0, t_{\mathrm{E}}]. \tag{4.2}$$

By an additional multiplication of the weak poroelastic fluid equation with the porosity ϕ_{h} (to result in a symmetric physical reactive contribution in domain $\Omega_{\mathrm{h}}^{\mathrm{P}}$ of the porous fluid phase and the porous solid phase), the resulting consistency terms in normal direction for an interface stress representation by the fluid stress are:

$$+\left\langle \phi_{\mathrm{h}} \delta\underline{\boldsymbol{v}}_{\mathrm{h}}^{\mathrm{P}} + (1-\phi_{\mathrm{h}})\, \delta\underline{\boldsymbol{u}}_{\mathrm{h}}^{\mathrm{P}} - \delta\underline{\boldsymbol{v}}_{\mathrm{h}}^{\mathrm{F}}, \underline{\boldsymbol{\sigma}}_{\mathrm{h}}^{\mathrm{F}} \cdot \underline{\boldsymbol{n}}_{\mathrm{h}}^{\mathrm{F}} \cdot \underline{\boldsymbol{P}}^{n} \right\rangle_{\Gamma_{\mathrm{h}}^{\mathrm{FP}}}. \tag{4.3}$$

Analogous to the coercivity analyses for the Nitsche's method for the weak imposition of boundary conditions (e.g. see the work of Burman and Hansbo [46]), it can be stated that the interface semi-norm specified by the left test function part $\left(\phi_{\mathrm{h}} \delta\underline{\boldsymbol{v}}_{\mathrm{h}}^{\mathrm{P}} + (1-\phi_{\mathrm{h}})\, \delta\underline{\boldsymbol{u}}_{\mathrm{h}}^{\mathrm{P}} - \delta\underline{\boldsymbol{v}}_{\mathrm{h}}^{\mathrm{F}}\right)$ of (4.3)*, should be balanced by an equal symmetric contribution of the penalty terms. Due to the same structure of this consistency test function part and the kinematic constraint* (2.63)*, an additional, multiplicative scaling of the penalty term including test function $\delta\underline{\boldsymbol{u}}_{\mathrm{h}}^{\mathrm{P}}$ with $(1-\phi_{\mathrm{h}})$ fulfills these*

requirements. A significant influence of this modification is expected for a vanishing solid phase close to the limit case $\phi_\mathrm{h} = 1$, which would result in a vanishing penalty contribution in the mixture equation. Nevertheless, due to the slightly different weak form applied here, this additional scaling is not applied.

4.2.2 Tangential Direction

For the weak imposition of the tangential constraint (2.64), two different methods, namely a substitution approach and a Nitsche-based approach, are presented. A comparison of both approach by a numerical test is presented in Sections 4.4.4 and 4.4.5.

4.2.2.1 Substitution Approach

The first method is presented for validation and comparison of the following Nitsche-based approach. Herein, the tangential interface traction is substituted by a kinematic relation making use of the BJ or BJS condition (2.64). Similar "Substitution" methods were applied in the works of Ambartsumyan *et al.* [7], Badia *et al.* [12] and Bukač *et al.* [37] to incorporate the BJ or the BJS condition. To enforce the tangential constraint by the "Substitution" method, the following contribution is added to the weak form

$$\begin{aligned}\mathcal{W}_\mathrm{h}^{\mathrm{FPI},t,Sub}\left[\left(\delta\underline{\boldsymbol{v}}_\mathrm{h}^\mathrm{F},\delta p_\mathrm{h}^\mathrm{F},\delta\underline{\boldsymbol{v}}_\mathrm{h}^\mathrm{P},\delta\underline{\boldsymbol{u}}_\mathrm{h}^\mathrm{P},\delta p_\mathrm{h}^\mathrm{P}\right),\left(\underline{\boldsymbol{v}}_\mathrm{h}^\mathrm{F},p_\mathrm{h}^\mathrm{F},\underline{\boldsymbol{v}}_\mathrm{h}^\mathrm{P},\underline{\boldsymbol{u}}_\mathrm{h}^\mathrm{P},p_\mathrm{h}^\mathrm{P}\right)\right] = \\ \left\langle \delta\underline{\boldsymbol{v}}_\mathrm{h}^\mathrm{F}-\delta\underline{\boldsymbol{u}}_\mathrm{h}^\mathrm{P},\frac{1}{\kappa}\left[\underline{\boldsymbol{v}}_\mathrm{h}^\mathrm{F}-\tilde{\partial}_t\left[\underline{\boldsymbol{u}}_\mathrm{h}^\mathrm{P}\right]-\beta_\mathrm{BJ}\phi\left(\underline{\boldsymbol{v}}_\mathrm{h}^\mathrm{P}-\tilde{\partial}_t\left[\underline{\boldsymbol{u}}_\mathrm{h}^\mathrm{P}\right]\right)-\hat{\underline{\boldsymbol{g}}}^{\mathrm{FP},t}\right]\cdot\underline{\boldsymbol{P}}^t\right\rangle_{\Gamma_\mathrm{h}^\mathrm{FP}} \\ -\left\langle \delta\underline{\boldsymbol{u}}_\mathrm{h}^\mathrm{P},\hat{\underline{\boldsymbol{g}}}_\sigma^\mathrm{FP}\cdot\underline{\boldsymbol{P}}^t\right\rangle_{\Gamma_\mathrm{h}^\mathrm{FP}}. \end{aligned} \tag{4.4}$$

As all terms are projected in the tangential plane by the projection matrix $\underline{\boldsymbol{P}}^t := (\underline{\boldsymbol{I}} - \underline{\boldsymbol{n}}_\mathrm{h}\otimes\underline{\boldsymbol{n}}_\mathrm{h})$ herein, $\mathcal{W}_\mathrm{h}^{\mathrm{FPI},t,Sub}$ solely leads to contributions in tangential orientation of the interface $\Gamma_\mathrm{h}^\mathrm{FP}$. For the "Substitution" method, the tangential boundary integrals, which arise from integration by parts when deriving (2.112) and (2.121), are substituted by the terms in (4.4). The principal structure and sign of this term equals a penalty term and therefore can be categorized as a positive contribution in a coercivity analysis. Due to the division by κ in the prefactor, this term starts to dominate the overall problem formulation for a decreasing κ. This worsens the conditioning of the discrete system of equations to solve and leads to increasing error norms, as analyzed in Section 4.4.4. The second term arises from the representation of the fluid interface stress by the kinematic constraint in (2.64) and due to the non vanishing stress jump $\hat{\underline{\boldsymbol{g}}}_\sigma^\mathrm{FP}$ in the dynamic equilibrium (2.61). Whenever essential, an additional index in $\mathcal{W}_{\mathrm{h},n+1}^{\mathrm{FPI},t,Sub}$ specifies that all interface terms $\langle *,*\rangle_{\Gamma_\mathrm{h}^\mathrm{FP}}$ are evaluated as $\langle *,*\rangle_{\Gamma_{\mathrm{h},n+1}^\mathrm{FP},n+\theta}$.

4.2.2.2 Nitsche-based Approach

The second presented method, which does not suffer from this conditioning problem for a small parameter κ, is based on the Nitsche method for general boundary conditions, which was first presented by Juntunen and Stenberg [132] for the Poisson problem. The extension to the Oseen problem is given by Winter *et al.* [226]. The tangential interface terms when applying this

approach are

$$\begin{aligned}
\mathcal{W}_{\mathrm{h}}^{\mathrm{FPI},t,Nit}\left[\left(\delta\underline{\boldsymbol{v}}_{\mathrm{h}}^{\mathrm{F}},\delta p_{\mathrm{h}}^{\mathrm{F}},\delta\underline{\boldsymbol{v}}_{\mathrm{h}}^{\mathrm{P}},\delta\underline{\boldsymbol{u}}_{\mathrm{h}}^{\mathrm{P}},\delta p_{\mathrm{h}}^{\mathrm{P}}\right),\left(\underline{\boldsymbol{v}}_{\mathrm{h}}^{\mathrm{F}},p_{\mathrm{h}}^{\mathrm{F}},\underline{\boldsymbol{v}}_{\mathrm{h}}^{\mathrm{P}},\underline{\boldsymbol{u}}_{\mathrm{h}}^{\mathrm{P}},p_{\mathrm{h}}^{\mathrm{P}}\right)\right] = \\
\left\langle\delta\underline{\boldsymbol{u}}_{\mathrm{h}}^{\mathrm{P}}-\delta\underline{\boldsymbol{v}}_{\mathrm{h}}^{\mathrm{F}},\underline{\boldsymbol{\sigma}}_{\mathrm{h}}^{\mathrm{F}}\cdot\underline{\boldsymbol{n}}_{\mathrm{h}}^{\mathrm{F}}\cdot\underline{\boldsymbol{P}}^{t}\right\rangle_{\Gamma_{\mathrm{h}}^{\mathrm{FP}}}-\left\langle\delta\underline{\boldsymbol{u}}_{\mathrm{h}}^{\mathrm{P}},\hat{\underline{\boldsymbol{g}}}_{\sigma}^{\mathrm{FP}}\cdot\underline{\boldsymbol{P}}^{t}\right\rangle_{\Gamma_{\mathrm{h}}^{\mathrm{FP}}} \\
+\xi^{\mathrm{FPI}}\frac{(\gamma_0^{\mathrm{FPI},t})^{-1}h_\Gamma}{\kappa\mu^{\mathrm{F}}+(\gamma_0^{\mathrm{FPI},t})^{-1}h_\Gamma}\left\langle-2\mu^{\mathrm{F}}\underline{\boldsymbol{\epsilon}}^{\mathrm{F}}(\delta\underline{\boldsymbol{v}}_{\mathrm{h}}^{\mathrm{F}})\cdot\underline{\boldsymbol{n}}_{\mathrm{h}}^{\mathrm{F}},\underline{\boldsymbol{c}}_{\mathrm{BJ}}\cdot\underline{\boldsymbol{P}}^{t}\right\rangle_{\Gamma_{\mathrm{h}}^{\mathrm{FP}}} \\
+\frac{\mu^{\mathrm{F}}}{\kappa\mu^{\mathrm{F}}+(\gamma_0^{\mathrm{FPI},t})^{-1}h_\Gamma}\left\langle\delta\underline{\boldsymbol{v}}_{\mathrm{h}}^{\mathrm{F}}-\delta\underline{\boldsymbol{u}}_{\mathrm{h}}^{\mathrm{P}},\underline{\boldsymbol{c}}_{\mathrm{BJ}}\cdot\underline{\boldsymbol{P}}^{t}\right\rangle_{\Gamma_{\mathrm{h}}^{\mathrm{FP}}},
\end{aligned}$$

$$\text{with}\quad \underline{\boldsymbol{c}}_{\mathrm{BJ}}=\underline{\boldsymbol{v}}_{\mathrm{h}}^{\mathrm{F}}-\tilde{\partial}_t\left[\underline{\boldsymbol{u}}_{\mathrm{h}}^{\mathrm{P}}\right]-\beta_{\mathrm{BJ}}\phi_{\mathrm{h}}\left(\underline{\boldsymbol{v}}_{\mathrm{h}}^{\mathrm{P}}-\tilde{\partial}_t\left[\underline{\boldsymbol{u}}_{\mathrm{h}}^{\mathrm{P}}\right]\right)+\kappa\underline{\boldsymbol{\sigma}}_{\mathrm{h}}^{\mathrm{F}}\cdot\underline{\boldsymbol{n}}_{\mathrm{h}}^{\mathrm{F}}-\hat{\underline{\boldsymbol{g}}}^{\mathrm{FP},t}. \tag{4.5}$$

Similar to the presented Nitsche method in normal direction, the interface stress is represented by the fluid stress. Therefore, the consistency integrals in tangential direction, which arise from the partial integration in the derivation of the weak forms (2.112) and (2.121), result in the contributions of line two. Again, a nonphysical contribution in the case $\hat{\underline{\boldsymbol{g}}}_{\sigma}^{\mathrm{FP}}\neq\underline{\mathbf{0}}$ arises from the interface stress representation as fluid stress. The following terms in line three and four are a consistent addition due to the inclusion of the BJ or the BJS condition (2.64), for what reason these contributions vanish in the case of the exact solution. In line three, an adjoint-consistent ($\xi^{\mathrm{FPI}}=1$) or an adjoint-inconsistent ($\xi^{\mathrm{FPI}}=-1$) term is added. As can be seen from the occurring prefactor, this term balances the consistency integrals in line two and the consistency like contribution $\left(\mu^{\mathrm{F}}\left(\kappa\mu^{\mathrm{F}}+(\gamma_0^{\mathrm{FPI},t})^{-1}h_\Gamma\right)^{-1}\left\langle\delta\underline{\boldsymbol{v}}_{\mathrm{h}}^{\mathrm{F}}-\delta\underline{\boldsymbol{u}}_{\mathrm{h}}^{\mathrm{P}},\kappa\underline{\boldsymbol{\sigma}}_{\mathrm{h}}^{\mathrm{F}}\cdot\underline{\boldsymbol{n}}_{\mathrm{h}}^{\mathrm{F}}\cdot\underline{\boldsymbol{P}}^{t}\right\rangle_{\Gamma_{\mathrm{h}}^{\mathrm{FP}}}\right)$ in the penalty terms. Finally, the penalty terms in line four aim for the stability of the numerical scheme for a sufficiently large penalty parameter $\gamma_0^{\mathrm{FPI},t}$. The prefactor of the penalty term also results from the two contributions of the consistency boundary integrals and the consistency like contribution in the penalty terms itself. In Section 4.4.3, the required penalty parameter $\gamma_0^{\mathrm{FPI},t}$ for the adjoint-consistent and adjoint-inconsistent variant is analyzed. Whenever essential, an additional index in $\mathcal{W}_{\mathrm{h},n+1}^{\mathrm{FPI},t,Nit}$ specifies that all interface terms $\langle*,*\rangle_{\Gamma_{\mathrm{h}}^{\mathrm{FP}}}$ are evaluated as $\langle*,*\rangle_{\Gamma_{\mathrm{h},n+1}^{\mathrm{FP}},n+\theta}$.

Remark 4.2 (Nonexistent tangential poroelastic fluid penalty contribution)**.** *By comparison of the Nitsche contributions in normal $\mathcal{W}_{\mathrm{h}}^{\mathrm{FPI},n}$ and tangential $\mathcal{W}_{\mathrm{h}}^{\mathrm{FPI},t,Nit}$ direction, it can be observed that the tangential penalty contribution of the poroelastic fluid equation is nonexistent. Considering the analogy to the coercivity analyses for general boundary conditions (see the work of Juntunen and Stenberg [132]), the interface semi-norm specified by the test functions in the consistency terms $\left(\delta\underline{\boldsymbol{u}}_{\mathrm{h}}^{\mathrm{P}}-\delta\underline{\boldsymbol{v}}_{\mathrm{h}}^{\mathrm{F}}\right)$ of* (4.5) *has to be balanced by a symmetric penalty contribution. By analyzing the Beaver-Joseph-Saffmann condition case ($\beta_{\mathrm{BJ}}=0$), the structure of the kinematic constraint* (2.64) *equals this contribution and therefore applying the same jump of test functions $\left(\delta\underline{\boldsymbol{u}}_{\mathrm{h}}^{\mathrm{P}}-\delta\underline{\boldsymbol{v}}_{\mathrm{h}}^{\mathrm{F}}\right)$ for the penalty terms results in the desired result. Also, from a modeling point of view, this "missing" tangential penalty is reasonable, as a Darcy fluid cannot compensate a tangential boundary stress. For the Beavers-Joseph condition, this argumentation does not directly hold anymore. Still, it can be clearly seen from computed results (not presented here) that a tangential penalty contribution tested on the Darcy-based equation should not be added to the weak form $\mathcal{W}_{\mathrm{h}}^{\mathrm{FPI},t,Nit}$. For example, one recognizes oscillations of the velocity $\underline{\boldsymbol{v}}_{\mathrm{h}}^{\mathrm{P}}$ in the porous domain close to the interface $\Gamma_{\mathrm{h}}^{\mathrm{FP}}$ even for a simple configuration such as the parallel flow of viscous and porous fluid when adding this penalty contribution.*

Remark 4.3 (Combination of projected consistency terms)**.** *In the case when the contributions* $\mathcal{W}_{\mathrm{h}}^{\mathrm{FPI},n}$ *and* $\mathcal{W}_{\mathrm{h}}^{\mathrm{FPI},t,Nit}$ *are combined, no projection of the fluid- and poroelastic consistency terms is required as they can be directly combined, and thus the implementation can be simplified*

$$\begin{aligned}
&\left\langle \delta\underline{\boldsymbol{u}}_{\mathrm{h}}^{\mathrm{P}} - \delta\underline{\boldsymbol{v}}_{\mathrm{h}}^{\mathrm{F}}, \underline{\boldsymbol{\sigma}}_{\mathrm{h}}^{\mathrm{F}} \cdot \underline{\boldsymbol{n}}_{\mathrm{h}}^{\mathrm{F}} \right\rangle_{\Gamma_{\mathrm{h}}^{\mathrm{FP}}} - \left\langle \delta\underline{\boldsymbol{u}}_{\mathrm{h}}^{\mathrm{P}}, \underline{\hat{\boldsymbol{g}}}_{\sigma}^{\mathrm{FP}} \right\rangle_{\Gamma_{\mathrm{h}}^{\mathrm{FP}}} = \\
&\left\langle \delta\underline{\boldsymbol{u}}_{\mathrm{h}}^{\mathrm{P}} - \delta\underline{\boldsymbol{v}}_{\mathrm{h}}^{\mathrm{F}}, \underline{\boldsymbol{\sigma}}_{\mathrm{h}}^{\mathrm{F}} \cdot \underline{\boldsymbol{n}}_{\mathrm{h}}^{\mathrm{F}} \cdot \underline{\boldsymbol{P}}^{n} \right\rangle_{\Gamma_{\mathrm{h}}^{\mathrm{FP}}} - \left\langle \delta\underline{\boldsymbol{u}}_{\mathrm{h}}^{\mathrm{P}}, \underline{\hat{\boldsymbol{g}}}_{\sigma}^{\mathrm{FP}} \cdot \underline{\boldsymbol{P}}^{n} \right\rangle_{\Gamma_{\mathrm{h}}^{\mathrm{FP}}} \\
+ &\left\langle \delta\underline{\boldsymbol{u}}_{\mathrm{h}}^{\mathrm{P}} - \delta\underline{\boldsymbol{v}}_{\mathrm{h}}^{\mathrm{F}}, \underline{\boldsymbol{\sigma}}_{\mathrm{h}}^{\mathrm{F}} \cdot \underline{\boldsymbol{n}}_{\mathrm{h}}^{\mathrm{F}} \cdot \underline{\boldsymbol{P}}^{t} \right\rangle_{\Gamma_{\mathrm{h}}^{\mathrm{FP}}} - \left\langle \delta\underline{\boldsymbol{u}}_{\mathrm{h}}^{\mathrm{P}}, \underline{\hat{\boldsymbol{g}}}_{\sigma}^{\mathrm{FP}} \cdot \underline{\boldsymbol{P}}^{t} \right\rangle_{\Gamma_{\mathrm{h}}^{\mathrm{FP}}}.
\end{aligned} \tag{4.6}$$

Due to the nonexistent viscosity and therefore tangential contribution of the Darcy-based fluid model in domain $\Omega_{\mathrm{h}}^{\mathrm{P}}$*, the projection of the consistency contributions in the poroelastic fluid equation* $\left\langle \delta\underline{\boldsymbol{v}}_{\mathrm{h}}^{\mathrm{P}}, \underline{\boldsymbol{\sigma}}_{\mathrm{h}}^{\mathrm{F}} \cdot \underline{\boldsymbol{n}}_{\mathrm{h}}^{\mathrm{F}} \cdot \underline{\boldsymbol{P}}^{n} \right\rangle_{\Gamma_{\mathrm{h}}^{\mathrm{FP}}} - \left\langle \delta\underline{\boldsymbol{v}}_{\mathrm{h}}^{\mathrm{P}}, \hat{g}_{\sigma}^{\mathrm{FP},n}\underline{\boldsymbol{n}} \cdot \underline{\boldsymbol{P}}^{n} \right\rangle_{\Gamma_{\mathrm{h}}^{\mathrm{FP}}}$ *has to remain untouched in* $\mathcal{W}_{\mathrm{h}}^{\mathrm{FPI},n}$*.*

4.3 The Coupled Discrete FPI Formulation

By summing up all contributions discussed and referenced beforehand, the final discrete weak form for the coupled fluid-poroelastic interaction problem is set. For the more general problem which was introduced in Section 2.1.1, this formulation has already been presented in Section 3.3.4, and in this section it will be specialized to the FPI application. The overall discrete solution space $\mathcal{S}_{\underline{\boldsymbol{x}}^{\mathrm{FPI}},\mathrm{h},n+1}$ and the discrete test function space $\mathcal{T}_{\delta\underline{\boldsymbol{x}}^{\mathrm{FPI}},\mathrm{h},n+1}$ result from the discrete spaces of the underlying physical fields, which were defined for the fluid problem in (2.110) and for the poroelastic problem in (2.119).

$$\begin{aligned}
\mathcal{S}_{\underline{\boldsymbol{x}}^{\mathrm{FPI}},\mathrm{h},n+1} &:= \mathcal{S}_{\underline{\boldsymbol{v}}^{\mathrm{F}},\mathrm{h},n+1} \times \mathcal{S}_{p^{\mathrm{F}},\mathrm{h},n+1} \times \mathcal{S}_{\underline{\boldsymbol{u}}^{\mathrm{P}},\mathrm{h},n+1} \times \mathcal{S}_{\underline{\boldsymbol{v}}^{\mathrm{P}},\mathrm{h},n+1} \times \mathcal{S}_{p^{\mathrm{P}},\mathrm{h}} \\
\mathcal{T}_{\delta\underline{\boldsymbol{x}}^{\mathrm{FPI}},\mathrm{h},n+1} &:= \mathcal{T}_{\delta\underline{\boldsymbol{v}}^{\mathrm{F}},\mathrm{h},n+1} \times \mathcal{T}_{\delta p^{\mathrm{F}},\mathrm{h},n+1} \times \mathcal{T}_{\delta\underline{\boldsymbol{u}}^{\mathrm{P}},\mathrm{h}} \times \mathcal{T}_{\delta\underline{\boldsymbol{v}}^{\mathrm{P}},\mathrm{h}} \times \mathcal{T}_{\delta p^{\mathrm{P}},\mathrm{h}}
\end{aligned} \tag{4.7}$$

The overall discrete test function $\delta\underline{\boldsymbol{x}}_{\mathrm{h}}^{\mathrm{FPI}}$ and the discrete solution state $\underline{\boldsymbol{x}}_{\mathrm{h},n+1}^{\mathrm{FPI}}$ are given by

$$\begin{aligned}
\underline{\boldsymbol{x}}_{\mathrm{h},n+1}^{\mathrm{FPI}} &:= \left(\underline{\boldsymbol{v}}_{\mathrm{h},n+1}^{\mathrm{F}}, p_{\mathrm{h},n+1}^{\mathrm{F}}, \underline{\boldsymbol{v}}_{\mathrm{h},n+1}^{\mathrm{P}}, \underline{\boldsymbol{u}}_{\mathrm{h},n+1}^{\mathrm{P}}, p_{\mathrm{h},n+1}^{\mathrm{P}}\right), \\
\delta\underline{\boldsymbol{x}}_{\mathrm{h}}^{\mathrm{FPI}} &:= \left(\delta\underline{\boldsymbol{v}}_{\mathrm{h}}^{\mathrm{F}}, \delta p_{\mathrm{h}}^{\mathrm{F}}, \delta\underline{\boldsymbol{v}}_{\mathrm{h}}^{\mathrm{P}}, \delta\underline{\boldsymbol{u}}_{\mathrm{h}}^{\mathrm{P}}, \delta p_{\mathrm{h}}^{\mathrm{P}}\right).
\end{aligned} \tag{4.8}$$

Making use of (4.7) and (4.8), the overall discrete formulation of the coupled CutFEM FPI problem is given by

$Find\ \underline{\boldsymbol{x}}_{\mathrm{h},n+1}^{\mathrm{FPI}} \in \mathcal{S}_{\underline{\boldsymbol{x}}^{\mathrm{FPI}},\mathrm{h},n+1}\ such\ that\ for\ all\ \delta\underline{\boldsymbol{x}}_{\mathrm{h}}^{\mathrm{FPI}} \in \mathcal{T}_{\delta\underline{\boldsymbol{x}}^{\mathrm{FPI}},\mathrm{h},n+1}$:

$$\mathcal{W}_{\mathrm{h},n+1}^{\mathrm{FPI}}\left[\delta\underline{\boldsymbol{x}}_{\mathrm{h}}^{\mathrm{FPI}}, \underline{\boldsymbol{x}}_{\mathrm{h},n+1}^{\mathrm{FPI}}\right] = 0. \tag{4.9}$$

The underlying weak form results from the combination of the corresponding weak forms of all corresponding physical fields and interfaces. This includes the discrete contributions arising from fluid discretized by the CutFEM in (3.7), for poroelasticity in (2.121), and for the incorporation

of the normal interface conditions in (4.1) and the tangential interface conditions in (4.4) or (4.5).

$$
\begin{aligned}
\mathcal{W}_{\mathrm{h},n+1}^{\mathrm{FPI}} \left[\delta\underline{\boldsymbol{x}}_{\mathrm{h}}^{\mathrm{FPI}}, \underline{\boldsymbol{x}}_{\mathrm{h},n+1}^{\mathrm{FPI}}\right] = \\
\quad \mathcal{W}_{\mathrm{h},n+1}^{\mathrm{F,CUT}} \left[\left(\delta\underline{\boldsymbol{v}}_{\mathrm{h}}^{\mathrm{F}}, \delta p_{\mathrm{h}}^{\mathrm{F}}\right), \left(\underline{\boldsymbol{v}}_{\mathrm{h},n+1}^{\mathrm{F}}, p_{\mathrm{h},n+1}^{\mathrm{F}}\right)\right] + \\
\quad \mathcal{W}_{\mathrm{h},n+1}^{\mathrm{P}} \left[\left(\delta\underline{\boldsymbol{v}}_{\mathrm{h}}^{\mathrm{P}}, \delta\underline{\boldsymbol{u}}_{\mathrm{h}}^{\mathrm{P}}, \delta p_{\mathrm{h}}^{\mathrm{P}}\right), \left(\underline{\boldsymbol{v}}_{\mathrm{h},n+1}^{\mathrm{P}}, \underline{\boldsymbol{u}}_{\mathrm{h},n+1}^{\mathrm{P}}, p_{\mathrm{h},n+1}^{\mathrm{P}}\right)\right] + \\
\quad \mathcal{W}_{\mathrm{h},n+1}^{\mathrm{FPI},n} \left[\left(\delta\underline{\boldsymbol{v}}_{\mathrm{h}}^{\mathrm{F}}, \delta p_{\mathrm{h}}^{\mathrm{F}}, \delta\underline{\boldsymbol{v}}_{\mathrm{h}}^{\mathrm{P}}, \delta\underline{\boldsymbol{u}}_{\mathrm{h}}^{\mathrm{P}}, \delta p_{\mathrm{h}}^{\mathrm{P}}\right), \left(\underline{\boldsymbol{v}}_{\mathrm{h},n+1}^{\mathrm{F}}, p_{\mathrm{h},n+1}^{\mathrm{F}}, \underline{\boldsymbol{v}}_{\mathrm{h},n+1}^{\mathrm{P}}, \underline{\boldsymbol{u}}_{\mathrm{h},n+1}^{\mathrm{P}}, p_{\mathrm{h},n+1}^{\mathrm{P}}\right)\right] + \\
\quad \mathcal{W}_{\mathrm{h},n+1}^{\mathrm{FPI},t,*} \left[\left(\delta\underline{\boldsymbol{v}}_{\mathrm{h}}^{\mathrm{F}}, \delta p_{\mathrm{h}}^{\mathrm{F}}, \delta\underline{\boldsymbol{v}}_{\mathrm{h}}^{\mathrm{P}}, \delta\underline{\boldsymbol{u}}_{\mathrm{h}}^{\mathrm{P}}, \delta p_{\mathrm{h}}^{\mathrm{P}}\right), \left(\underline{\boldsymbol{v}}_{\mathrm{h},n+1}^{\mathrm{F}}, p_{\mathrm{h},n+1}^{\mathrm{F}}, \underline{\boldsymbol{v}}_{\mathrm{h},n+1}^{\mathrm{P}}, \underline{\boldsymbol{u}}_{\mathrm{h},n+1}^{\mathrm{P}}, p_{\mathrm{h},n+1}^{\mathrm{P}}\right)\right]
\end{aligned} \tag{4.10}
$$

The "$*$"-symbol therein, specifies either the "Substitution" method by "Sub" or the Nitsche-based variant by "Nit" to enforce the tangential interface condition.

The Newton-Raphson like nonlinear solution procedure to solve the aforementioned system for the vector of unknown nodal states

$$
\underline{\mathbf{x}}_{n+1}^{\mathrm{FPI}} := \left[\left(\underline{\mathbf{v}}_{n+1}^{\mathrm{F}}\right)^{\mathsf{T}}, \left(\underline{\mathbf{p}}_{n+1}^{\mathrm{F}}\right)^{\mathsf{T}}, \left(\underline{\mathbf{u}}_{n+1}^{\mathrm{P}}\right)^{\mathsf{T}}, \left(\underline{\mathbf{v}}_{n+1}^{\mathrm{P}}\right)^{\mathsf{T}}, \left(\underline{\mathbf{p}}_{n+1}^{\mathrm{P}}\right)^{\mathsf{T}}\right]^{\mathsf{T}} \tag{4.11}
$$

was discussed, including poroelasticity, in Section 3.4.

In order to make the presentation as clear as possible, the index h, to specify discrete quantities, has been omitted for all numerical tests and examples in the following sections.

4.4 Numerical Tests: CutFEM FPI

In this section, the formulation presented in this chapter will be analyzed numerically. The aim is to verify that the expected properties that have already been analyzed in literature for the simplified variants of this problems, namely for the Stokes/Darcy coupling, the Stokes/Biot-system coupling, the CutFEM applied on the Oseen equations, the Nitsche's method for general Navier boundary condition, and the fluid-structure interaction are still valid for this problem configuration. Therefore, a problem setup that results in a known analytic solution is constructed by the method of manufactured solutions. Independent of the choice of the boundary and interface locations, this known solution should be valid in the respective domain. A comparison of the computed solutions to the analytic solution allows for an analysis of different aspects of the formulation.

In addition to the spatial convergence analysis for all essential domain and interface error norms, the behavior of the formulation for variations of the Nitsche penalty parameters is determined and a recommendation for the choice of these parameters is obtained. Furthermore, a test for varying porosity, and consequently varying the permeability through the Kozeny-Carman formula, allows comparing the presented novel Nitsche method and the predominant "Substitution" approach. This is performed for moderate, down to very small porosities/permeabilities and, therefore, allows for a fundamental comparison of both approaches. Finally, a comparison of the Beavers-Joseph (BJ) and Beavers-Joseph-Saffmann (BJS) condition for a variation of the interface model constant ranging from the limit cases "slip" to "no-slip" is performed.

4.4.1 Analytic Solution and Problem Setup

The analytic solution is chosen as follows

$$\underline{\boldsymbol{v}}_{\mathcal{A}}^{\mathrm{F}}(\underline{\boldsymbol{x}},t) = \begin{bmatrix} -A^{\mathrm{F}}\cos\left(B\,\pi\,x\right)\sin\left(B\,\pi\,y\right)g_u(t) \\ A^{\mathrm{F}}\sin\left(B\,\pi\,x\right)\cos\left(B\,\pi\,y\right)g_u(t) \end{bmatrix}, \tag{4.12}$$

$$p_{\mathcal{A}}^{\mathrm{F}}(\underline{\boldsymbol{x}},t) = -\frac{1}{4}\left(\cos\left(2\,B\,\pi\,x\right)+\cos\left(2\,B\,\pi\,y\right)\right)\rho^{\mathrm{F}}g_p(t), \tag{4.13}$$

$$\underline{\boldsymbol{v}}_{\mathcal{A}}^{\mathrm{P}}(\underline{\boldsymbol{x}},t) = \begin{bmatrix} -A^{\mathrm{P}}\cos\left(B\,\pi\,x\right)\sin\left(B\,\pi\,y\right)g_u(t) \\ A^{\mathrm{P}}\sin\left(B\,\pi\,x\right)\cos\left(B\,\pi\,y\right)g_u(t) \end{bmatrix}, \tag{4.14}$$

$$p_{\mathcal{A}}^{\mathrm{P}}(\underline{\boldsymbol{x}},t) = -\frac{1}{4}\left(\cos\left(2\,B\,\pi\,x\right)+\cos\left(2\,B\,\pi\,y\right)\right)\rho^{\mathrm{F}}g_p(t), \tag{4.15}$$

$$\underline{\boldsymbol{u}}_{\mathcal{A}}^{\mathrm{P}}(\underline{\boldsymbol{X}},t) = \begin{bmatrix} -A^{\mathrm{P^S}}\cos\left(B\,\pi\,X\right)\sin\left(B\,\pi\,Y\right)\frac{(1-g_u(t))}{-2\,C^2\,\pi^2\,\mu^{\mathrm{F}}(\rho^{\mathrm{F}})^{-1}} \\ A^{\mathrm{P^S}}\sin\left(B\,\pi\,X\right)\cos\left(B\,\pi\,Y\right)\frac{(1-g_u(t))}{-2\,C^2\,\pi^2\,\mu^{\mathrm{F}}(\rho^{\mathrm{F}})^{-1}} \end{bmatrix}, \tag{4.16}$$

with the time dependent functions: $g_u(t) = e^{-2\,C^2\,\pi^2\,\mu^{\mathrm{F}}\left(\rho^{\mathrm{F}}\right)^{-1}t}$ and $g_p(t) = e^{-4\,C^2\,\pi^2\,\mu^{\mathrm{F}}\left(\rho^{\mathrm{F}}\right)^{-1}t}$.

Herein, the analytic velocity and pressure solution in the fluid domain is denoted by $\underline{\boldsymbol{v}}_{\mathcal{A}}^{\mathrm{F}}$ and $p_{\mathcal{A}}^{\mathrm{F}}$. The analytic velocity, pressure, and displacement solution in the poroelastic domain is denoted by $\underline{\boldsymbol{v}}_{\mathcal{A}}^{\mathrm{P}}$, $p_{\mathcal{A}}^{\mathrm{P}}$, and $\underline{\boldsymbol{u}}_{\mathcal{A}}^{\mathrm{P}}$, respectively. The components of the two-dimensional position vector $\underline{\boldsymbol{x}} = [x,y]^{\mathsf{T}}$ in current configuration are specified as x and y and the components of the material position vector $\underline{\boldsymbol{X}} = [X,Y]^{\mathsf{T}}$ as X and Y. The solution is chosen in a way that fulfills the balance of fluid mass in the fluid domain (2.27) and in the poroelastic domain (2.43) in the case of a constant porosity ϕ. Additionally, by specifying the solution amplitudes to $A^{\mathrm{F}} = 0.1$, $A^{\mathrm{P}} = 0.21$, and $A^{\mathrm{P^S}} = -0.01$, the mass-balance (2.63) and the kinematic part of the BJ or BJS condition (2.64) on the interface Γ^{FP} are fulfilled without additional contributions $(\underline{\hat{\boldsymbol{g}}}^{\mathrm{FP},n}, \underline{\hat{\boldsymbol{g}}}^{\mathrm{FP},t})$ at the initial point in time due to the vanishing deformation. The space constant B, and the time constant C influence the spatial and temporal gradients of the given solution. As the focus in the following should be on spatial errors, $B = 1.0$ is chosen to be larger than $C = 0.01$.

The dynamic viscosity of the fluid is specified to $\mu^{\mathrm{F}} = 1.0$. To characterize the porous flow resistance, an isotropic material permeability $\underline{\boldsymbol{K}} = K \cdot \underline{\boldsymbol{I}}$, with scalar value $K = 0.1$, is prescribed. The porosity ϕ is constant in space and time to fulfill the balance of mass (2.43) by the analytic solution and is set to $\phi = 0.5$. Therefore, equation (2.51) is not evaluated, as the strain energy function $\psi^{\mathrm{P},vol}(J^{\mathrm{P}}(1-\phi))$ is defined implicitly. No penalty contribution of the strain energy function is considered, i.e. $\psi^{\mathrm{P},pen}(\underline{\boldsymbol{E}}^{\mathrm{P}}, J^{\mathrm{P}}(1-\phi)) = 0$. The macroscopic deformation of the solid phase is given by a Neo-Hookean material model with the hyperelastic strain energy function $\psi^{\mathrm{P},skel}$ specified in (2.17) and the constant parameters Young's modulus $E = 1000$ and Poisson ratio $\nu = 0.3$. The averaged initial density of the solid phase is chosen to be equal to the fluid density $\rho_0^{\mathrm{S}} = \rho^{\mathrm{F}} = 1.0$. If not denoted otherwise, the Beavers-Joseph coefficient on the interface Γ^{FP} is set to $\alpha_{\mathrm{BJ}} = 1.0$. In order to fulfill the balance of momentum defined by equations (2.28), (2.44), and (2.46) with the analytic solutions (4.12)–(4.16), the following body

force is applied

$$\rho^{\mathrm{F}}\hat{\underline{\boldsymbol{b}}}^{\mathrm{F}} = \rho^{\mathrm{F}}\frac{\partial \underline{\boldsymbol{v}}^{\mathrm{F}}_{\mathcal{A}}}{\partial t} + \rho^{\mathrm{F}}\underline{\boldsymbol{v}}^{\mathrm{F}}_{\mathcal{A}}\cdot\boldsymbol{\nabla}\underline{\boldsymbol{v}}^{\mathrm{F}}_{\mathcal{A}} - \boldsymbol{\nabla}\cdot\underline{\boldsymbol{\sigma}}^{\mathrm{F}}_{\mathcal{A}}, \quad \underline{\boldsymbol{\sigma}}^{\mathrm{F}}_{\mathcal{A}} = -p^{\mathrm{F}}_{\mathcal{A}}\underline{\boldsymbol{I}} + 2\mu^{\mathrm{F}}\underline{\boldsymbol{\epsilon}}^{\mathrm{F}}(\underline{\boldsymbol{v}}^{\mathrm{F}}_{\mathcal{A}}), \tag{4.17}$$

$$\rho^{\mathrm{F}}\hat{\underline{\boldsymbol{b}}}^{\mathrm{P}^{\mathrm{F}}} = \rho^{\mathrm{F}}\frac{\partial \underline{\boldsymbol{v}}^{\mathrm{P}}_{\mathcal{A}}}{\partial t}\bigg|_{\underline{\boldsymbol{X}}^{\mathrm{P}}} - \rho^{\mathrm{F}}\frac{\partial \underline{\boldsymbol{u}}^{\mathrm{P}}_{\mathcal{A}}}{\partial t}\cdot\boldsymbol{\nabla}\underline{\boldsymbol{v}}^{\mathrm{P}}_{\mathcal{A}} + \boldsymbol{\nabla}p^{\mathrm{P}}_{\mathcal{A}} + \mu^{\mathrm{F}}\mathring{\phi}\underline{\boldsymbol{k}}^{-1}_{\mathcal{A}}\cdot\left(\underline{\boldsymbol{v}}^{\mathrm{P}}_{\mathcal{A}} - \frac{\partial \underline{\boldsymbol{u}}^{\mathrm{P}}_{\mathcal{A}}}{\partial t}\right), \tag{4.18}$$

$$\tilde{\rho}^{\mathrm{P}^{\mathrm{S}}}_0\hat{\underline{\boldsymbol{b}}}^{\mathrm{P}}_0 = \tilde{\rho}^{\mathrm{P}^{\mathrm{S}}}_0\frac{\partial^2 \underline{\boldsymbol{u}}^{\mathrm{P}}_{\mathcal{A}}}{\partial t^2} - \boldsymbol{\nabla}_0\cdot\left(\underline{\boldsymbol{F}}^{\mathrm{P}}_{\mathcal{A}}\cdot\underline{\boldsymbol{S}}^{\mathrm{P}}_{\mathcal{A}}\right) + \left(1-\mathring{\phi}\right)J^{\mathrm{P}}_{\mathcal{A}}\boldsymbol{\nabla}p^{\mathrm{P}}_{\mathcal{A}} - \mu^{\mathrm{F}}J^{\mathrm{P}}_{\mathcal{A}}\mathring{\phi}^2\underline{\boldsymbol{k}}^{-1}_{\mathcal{A}}\cdot\left(\underline{\boldsymbol{v}}^{\mathrm{P}}_{\mathcal{A}} - \frac{\partial \underline{\boldsymbol{u}}^{\mathrm{P}}_{\mathcal{A}}}{\partial t}\right), \tag{4.19}$$

where the analytic deformation gradient is defined as $\underline{\boldsymbol{F}}^{\mathrm{P}}_{\mathcal{A}} = \underline{\boldsymbol{I}} + \partial\underline{\boldsymbol{u}}^{\mathrm{P}}_{\mathcal{A}}/\partial\underline{\boldsymbol{X}}^{\mathrm{P}}$, the determinate as $J^{\mathrm{P}}_{\mathcal{A}} = \det\underline{\boldsymbol{F}}^{\mathrm{P}}_{\mathcal{A}}$, the analytic homogenized second Piola-Kirchhoff stress tensor as $\underline{\boldsymbol{S}}^{\mathrm{P}}_{\mathcal{A}} = 2c\underline{\boldsymbol{I}} - 2c(J^{\mathrm{P}}_{\mathcal{A}})^{-2\beta}(\underline{\boldsymbol{F}}^{\mathrm{P}}_{\mathcal{A}})^{-1}\cdot(\underline{\boldsymbol{F}}^{\mathrm{P}}_{\mathcal{A}})^{-\mathsf{T}}$, the analytic Cauchy stress tensor as $\underline{\boldsymbol{\sigma}}^{\mathrm{P}}_{\mathcal{A}} = (J^{\mathrm{P}}_{\mathcal{A}})^{-1}\underline{\boldsymbol{F}}^{\mathrm{P}}_{\mathcal{A}}\cdot\underline{\boldsymbol{S}}^{\mathrm{P}}_{\mathcal{A}}\cdot(\underline{\boldsymbol{F}}^{\mathrm{P}}_{\mathcal{A}})^{\mathsf{T}}$, and the analytic inverse spatial permeability as $\underline{\boldsymbol{k}}^{-1}_{\mathcal{A}} = J^{\mathrm{P}}(\underline{\boldsymbol{F}}^{\mathrm{P}}_{\mathcal{A}})^{-\mathsf{T}}\cdot\underline{\boldsymbol{K}}^{-1}\cdot(\underline{\boldsymbol{F}}^{\mathrm{P}}_{\mathcal{A}})^{-1}$. The analytic solution fulfills the interface conditions (2.61) - (2.64), if the constraint-jumps and traction-jumps $\hat{\underline{\boldsymbol{g}}}^{\mathrm{FP}}_{\sigma}, \hat{g}^{\mathrm{FP},n}_{\sigma}, \hat{\underline{\boldsymbol{g}}}^{\mathrm{FP},n}, \hat{\underline{\boldsymbol{g}}}^{\mathrm{FP},t}$ are defined as

$$\hat{\underline{\boldsymbol{g}}}^{\mathrm{FP}}_{\sigma} = \underline{\boldsymbol{\sigma}}^{\mathrm{F}}_{\mathcal{A}}\cdot\underline{\boldsymbol{n}}^{\mathrm{F}} - \underline{\boldsymbol{\sigma}}^{\mathrm{P}}_{\mathcal{A}}\cdot\underline{\boldsymbol{n}}^{\mathrm{F}}, \tag{4.20}$$

$$\hat{g}^{\mathrm{FP},n}_{\sigma} = \underline{\boldsymbol{n}}^{\mathrm{F}}\cdot\underline{\boldsymbol{\sigma}}^{\mathrm{F}}_{\mathcal{A}}\cdot\underline{\boldsymbol{n}}^{\mathrm{F}} + p^{\mathrm{P}}_{\mathcal{A}}, \tag{4.21}$$

$$\hat{\underline{\boldsymbol{g}}}^{\mathrm{FP},n} = \underline{\boldsymbol{v}}^{\mathrm{F}}_{\mathcal{A}} - \frac{\partial \underline{\boldsymbol{u}}^{\mathrm{P}}_{\mathcal{A}}}{\partial t} - \phi\left(\underline{\boldsymbol{v}}^{\mathrm{P}}_{\mathcal{A}} - \frac{\partial \underline{\boldsymbol{u}}^{\mathrm{P}}_{\mathcal{A}}}{\partial t}\right), \tag{4.22}$$

$$\hat{\underline{\boldsymbol{g}}}^{\mathrm{FP},t} = \underline{\boldsymbol{v}}^{\mathrm{F}}_{\mathcal{A}} - \frac{\partial \underline{\boldsymbol{u}}^{\mathrm{P}}_{\mathcal{A}}}{\partial t} - \beta_{\mathrm{BJ}}\phi\left(\underline{\boldsymbol{v}}^{\mathrm{P}}_{\mathcal{A}} - \frac{\partial \underline{\boldsymbol{u}}^{\mathrm{P}}_{\mathcal{A}}}{\partial t}\right) + \kappa\underline{\boldsymbol{n}}^{\mathrm{F}}\cdot\underline{\boldsymbol{\sigma}}^{\mathrm{F}}_{\mathcal{A}}. \tag{4.23}$$

Remark 4.4 (Evaluation of the body force (4.17)-(4.19), the traction-jump (4.20)-(4.21), and the constraint-jump contributions (4.22)-(4.23))**.** *All body force contributions* (4.17)-(4.19) *are evaluated at the computational nodes and re-interpolated with the standard shape functions of the corresponding finite elements. Compared to a direct volume integration, the additional error does not deteriorate the error convergence order of the subsequent computation. Contrary to this, the traction-jump and constraint-jump contributions are considered directly for the integration on the interface* Γ^{FP} *at every point in space. Hereby, the material position vector* $\underline{\boldsymbol{X}}$ *is computed by re-interpolation of the initial nodal coordinates. For the given analytic solution, all volume contributions* (4.17)-(4.19) *depend solely on the point in space and time, whereas the interface contributions* (4.20)-(4.23) *additionally depend on the normal vector* $\underline{\boldsymbol{n}}^{\mathrm{F}}$*. Therefore, contributions* (4.17)-(4.23) *were computed and simplified symbolically by Maple*$^{\mathrm{TM}}$ *[114] as time- and space-dependent functions in advance as far as possible. The evaluation of these functions and the multiplication of the components with the discrete normal vector in each numerical integration point for the interface contributions is performed during the computation.*

These additional body force and jump contributions allows the analytic solution to be fulfilled, and therefore the application of the method of manufactured solution, independent of the alignment of the interface, the boundaries, and the domains. The setup, as shown in Figure 4.3, includes a wide variety of different intersections of single fluid elements by the interface Γ^{FP} for different mesh resolutions, while still allowing for the use of structured discretizations. The

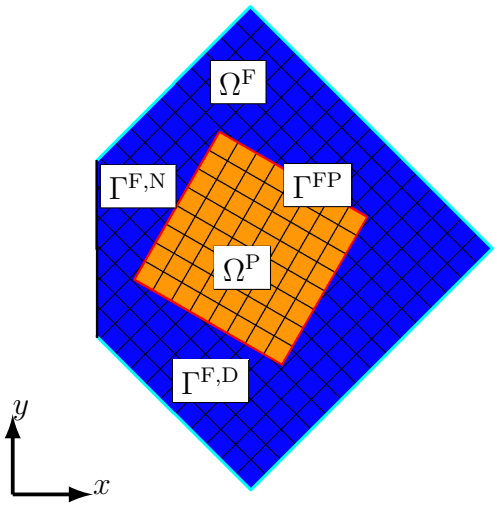

Figure 4.3: Geometric setup and computational meshes for the numerical test. The fluid domain Ω^{F}, the poroelastic domain Ω^{P}, the common interface Γ^{FP}, and the boundaries with Neumann boundary condition $\Gamma^{\mathrm{F,N}}$ or Dirichlet boundary condition $\Gamma^{\mathrm{F,D}}$ are visualized here. Black lines indicate the computational mesh for a mesh size of $h = 0.0625$, corresponding to 16×16 bi-linear elements to discretize the fluid domain and 8×8 bi-linear elements to discretize the poroelastic domain.

poroelastic domain Ω^{P} is a square of size 0.5×0.5, which is rotated by an angle of $\alpha = 30°$ around its center. The fluid domain Ω^{F} is described by a square with size 1.0×1.0, which is rotated by an angle of $\beta = 45°$ around its center, a part is removed by a vertical cut (horizontal distance from the square center $\Delta x = -0.45$), and the part occupied by the poroelastic domain Ω^{P} is excluded. On $\Gamma^{\mathrm{F,D}}$, where the fluid discretization is matching the boundary, the analytic velocity (4.12) is prescribed as a Dirichlet boundary condition. At $\Gamma^{\mathrm{F,N}}$, which is non-matching to the fluid discretization, the analytic fluid traction $\underline{\boldsymbol{\sigma}}^{\mathrm{F}}_{\mathcal{A}} \cdot \underline{\boldsymbol{n}}^{\mathrm{F}}$ is prescribed as a Neumann boundary condition.

For the spatial discretization, four-noded, bi-linear, quadrilateral elements are utilized. This is accomplished through a discretization with one layer of eight-noded, tri-linear hexahedral elements. The discretization in time is performed by the backward Euler scheme $\theta = 1$, with a time step length of $\Delta t = 0.05$ if not indicated otherwise. The last point of interest in time is $t_{\mathrm{E}} = 0.1$. The initial state is given by the analytic solution

$$\begin{aligned} \mathring{\underline{\boldsymbol{v}}}^{\mathrm{F}}(\underline{\boldsymbol{x}}) &= \underline{\boldsymbol{v}}^{\mathrm{F}}_{\mathcal{A}}(\underline{\boldsymbol{x}}, 0), \quad \mathring{\underline{\boldsymbol{v}}}^{\mathrm{P}}(\underline{\boldsymbol{x}}) = \underline{\boldsymbol{v}}^{\mathrm{P}}_{\mathcal{A}}(\underline{\boldsymbol{x}}, 0), \\ \mathring{\underline{\boldsymbol{u}}}^{\mathrm{P}}(\underline{\boldsymbol{X}}) &= \underline{\boldsymbol{u}}^{\mathrm{P}}_{\mathcal{A}}(\underline{\boldsymbol{X}}, 0), \quad \mathring{\underline{\boldsymbol{v}}}^{\mathrm{P^S}}(\underline{\boldsymbol{X}}) = \frac{\partial \underline{\boldsymbol{u}}^{\mathrm{P}}_{\mathcal{A}}}{\partial t}(\underline{\boldsymbol{X}}, 0). \end{aligned} \tag{4.24}$$

In Figure 4.4, the computed solution for a specific set of parameters is visualized for all computed unknowns, namely the pressure $(p^{\mathrm{F}}, p^{\mathrm{P}})$, the velocity $(\underline{\boldsymbol{v}}^{\mathrm{F}}, \underline{\boldsymbol{v}}^{\mathrm{P}})$, and the displacement $\underline{\boldsymbol{u}}^{\mathrm{P}}$.

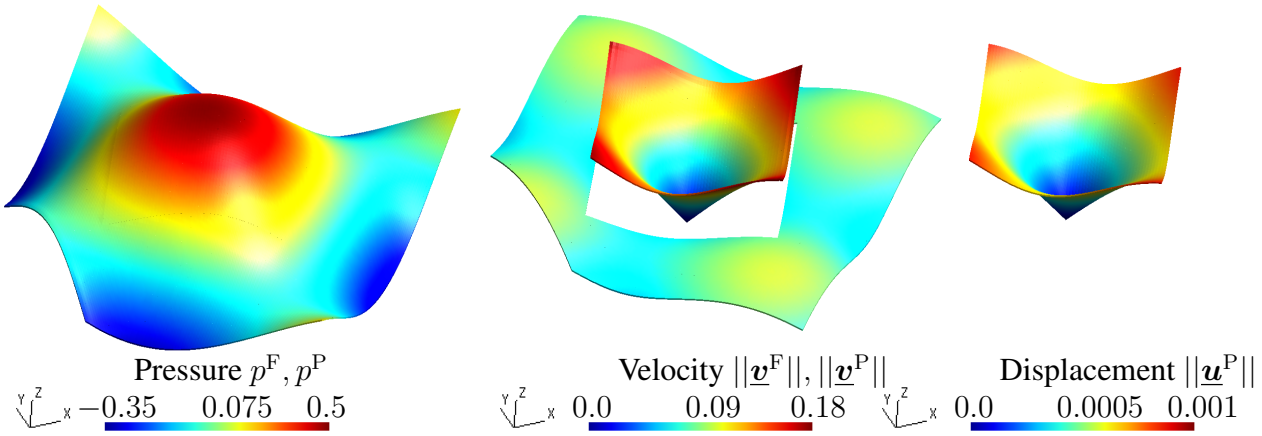

Figure 4.4: Computed pressure, velocity magnitude and displacement magnitude solution at $t = 0.1$ for $h = 0.0078125$, $\Delta t = 0.05$, $\xi = -1$, $\gamma_n^{-1} = 45.0$, $\gamma_t^{-1} = 45.0$, $\alpha_{\mathrm{BJ}} = 1.0$, Beavers-Joseph condition $\beta_{\mathrm{BJ}} = 1$ incorporated by (4.5). The solution is visualized by color-code and scalar warp in positive z-direction.

To quantify the performance of the proposed formulation, the following $\mathcal{L}^2$-error norms integrated in the domains Ω^{F} and Ω^{P}, as well as on the interface Γ^{FP} are consulted

$$
\begin{aligned}
&\left|\left|\underline{\boldsymbol{v}}^{\mathrm{F}} - \underline{\boldsymbol{v}}^{\mathrm{F}}_{\mathcal{A}}\right|\right|_{\Omega^{\mathrm{F}}}, \left|\left|p^{\mathrm{F}} - p^{\mathrm{F}}_{\mathcal{A}}\right|\right|_{\Omega^{\mathrm{F}}}, \left|\left|\boldsymbol{\nabla}\underline{\boldsymbol{v}}^{\mathrm{F}} - \boldsymbol{\nabla}\underline{\boldsymbol{v}}^{\mathrm{F}}_{\mathcal{A}}\right|\right|_{\Omega^{\mathrm{F}}}, \left|\left|\underline{\boldsymbol{v}}^{\mathrm{P}} - \underline{\boldsymbol{v}}^{\mathrm{P}}_{\mathcal{A}}\right|\right|_{\Omega^{\mathrm{P}}}, \left|\left|p^{\mathrm{P}} - p^{\mathrm{P}}_{\mathcal{A}}\right|\right|_{\Omega^{\mathrm{P}}},\\
&\left|\left|\underline{\boldsymbol{u}}^{\mathrm{P}} - \underline{\boldsymbol{u}}^{\mathrm{P}}_{\mathcal{A}}\right|\right|_{\Omega^{\mathrm{P}}_0}, \left|\left|\boldsymbol{\nabla}_0\underline{\boldsymbol{u}}^{\mathrm{P}} - \boldsymbol{\nabla}_0\underline{\boldsymbol{u}}^{\mathrm{P}}_{\mathcal{A}}\right|\right|_{\Omega^{\mathrm{P}}_0},\\
&\left|\left|p^{\mathrm{F}} - p^{\mathrm{F}}_{\mathcal{A}}\right|\right|_{\Gamma^{\mathrm{FP}}}, \left|\left|\left(\boldsymbol{\nabla}\underline{\boldsymbol{v}}^{\mathrm{F}} - \boldsymbol{\nabla}\underline{\boldsymbol{v}}^{\mathrm{F}}_{\mathcal{A}}\right)\cdot\underline{\boldsymbol{n}}\right|\right|_{\Gamma^{\mathrm{FP}}}, \left|\left|p^{\mathrm{P}} - p^{\mathrm{P}}_{\mathcal{A}}\right|\right|_{\Gamma^{\mathrm{FP}}}, \left|\left|\left(\boldsymbol{\nabla}\underline{\boldsymbol{u}}^{\mathrm{P}} - \boldsymbol{\nabla}\underline{\boldsymbol{u}}^{\mathrm{P}}_{\mathcal{A}}\right)\cdot\underline{\boldsymbol{n}}\right|\right|_{\Gamma^{\mathrm{FP}}},\\
&\mathcal{E}^n :=\\
&\left|\left|\left[\left(\underline{\boldsymbol{v}}^{\mathrm{F}} - \frac{\partial\underline{\boldsymbol{u}}^{\mathrm{P}}}{\partial t} - \phi\left(\underline{\boldsymbol{v}}^{\mathrm{P}} - \frac{\partial\underline{\boldsymbol{u}}^{\mathrm{P}}}{\partial t}\right)\right) - \left(\underline{\boldsymbol{v}}^{\mathrm{F}}_{\mathcal{A}} - \frac{\partial\underline{\boldsymbol{u}}^{\mathrm{P}}_{\mathcal{A}}}{\partial t} - \phi\left(\underline{\boldsymbol{v}}^{\mathrm{P}}_{\mathcal{A}} - \frac{\partial\underline{\boldsymbol{u}}^{\mathrm{P}}_{\mathcal{A}}}{\partial t}\right)\right)\right]\underline{\boldsymbol{P}}^n\right|\right|_{\Gamma^{\mathrm{FP}}},\\
&\mathcal{E}^t :=\\
&\left|\left|\left[\left(\underline{\boldsymbol{v}}^{\mathrm{F}} - \frac{\partial\underline{\boldsymbol{u}}^{\mathrm{P}}}{\partial t} - \phi\beta_{\mathrm{BJ}}\left(\underline{\boldsymbol{v}}^{\mathrm{P}} - \frac{\partial\underline{\boldsymbol{u}}^{\mathrm{P}}}{\partial t}\right)\right) - \left(\underline{\boldsymbol{v}}^{\mathrm{F}}_{\mathcal{A}} - \frac{\partial\underline{\boldsymbol{u}}^{\mathrm{P}}_{\mathcal{A}}}{\partial t} - \phi\beta_{\mathrm{BJ}}\left(\underline{\boldsymbol{v}}^{\mathrm{P}}_{\mathcal{A}} - \frac{\partial\underline{\boldsymbol{u}}^{\mathrm{P}}_{\mathcal{A}}}{\partial t}\right)\right)\right]\underline{\boldsymbol{P}}^t\right|\right|_{\Gamma^{\mathrm{FP}}}.
\end{aligned}
\tag{4.25}
$$

While the norms in the first two lines quantify the overall domain error, the specific interface error norms in line three quantify the components of the interface traction error, and, finally, the two norms $\mathcal{E}^n$ and $\mathcal{E}^t$ quantify the error of the kinematic components of constraints (2.63) and (2.64) in normal and tangential direction separately.

Remark 4.5 (Missing data points)**.** *For some of the following computations, data points are not plotted in the diagrams. These solutions were not computed, as a result of exceeding a maximum number of iterations in the Newton-Raphson like scheme or due to non-physical intermediate displacement states leading to problems in the geometric intersection algorithm. As neighboring points in the presented graphs already show an increase of the computed error and therefore this behavior is expected, this was not investigated further.*

4.4.2 Spatial Convergence Analysis

First, a spatial convergence analysis for the coupled FPI setup is performed. Indications for spatial convergence rates to be expected for the formulation, can be found in the contributions for the Stokes/Darcy coupling by Badia and Codina [13], Burman and Hansbo [45], for the Stokes/Biot-system coupling by Badia *et al.* [12], for the applied poroelastic formulation by Vuong *et al.* [217], for the CutFEM applied on the Stokes equation by Burman and Fernández [42] and applied on the Oseen equation by Massing *et al.* [149] including the general Navier boundary condition by Winter *et al.* [226], and for the CutFEM applied on the fluid-structure interaction by Massing *et al.* [151].

For this analysis, the Nitsche penalty parameters are set to $\gamma_0^{\mathrm{FPI},n} = \gamma_0^{\mathrm{FPI},t} = 45$ and the adjoint-inconsistent variant $\left(\xi^{\mathrm{FPI}} = -1\right)$ is applied. The mesh size h, which equals the edge length of the quadrilateral elements of squared shape, is varied in $h \in [0.25, 0.0039062]$. To prevent the temporal error from exceeding the spatial error, the two finest meshes $h = 0.0052083$ and $h = 0.0039062$ are discretized in time with half the time step length $\Delta t = 0.025$.

The error norms computed for the BJ and BJS interface condition are presented in Figure 4.5. For all domain error norms and almost all interface error norms, the expected convergence rates can be observed for a mesh size smaller than $h < 0.1$. No difference between both interface conditions occurs. An exception is the displacement domain error, where a difference between both methods can be observed potentially due to the small absolute error level. For the normal error $\mathcal{E}^n$, a noticeable kink can be observed, which occurs most likely due to the varying fluid element intersection configurations. Nevertheless, the overall convergence rate is not altered for both of these cases. The only significant difference can be observed in the tangential kinematic error $\mathcal{E}^t$. Here, a convergence rate of h^2 can only be observed for the BJS variant, while the BJ condition leads to $h^{3/2}$. This is a consequence of the additionally occurring tangential velocity in the poroelastic fluid constraint (2.64) in the case of BJ ($\beta_{\mathrm{BJ}} = 1$). Nevertheless, in the case the coefficient $\kappa\mu^{\mathrm{F}}$ is large enough, the full tangential constraint error will be dominated by the first order convergence of the fluid gradient for BJ and BJS anyway.

4.4.3 Sensitivity of the Formulation for Variations of the Nitsche Penalty Parameters $\gamma_0^{\mathrm{FPI},n}$ and $\gamma_0^{\mathrm{FPI},t}$

In the Nitsche-based formulations (4.1) and (4.5), the two penalty parameters $\gamma_0^{\mathrm{FPI},n}$ and $\gamma_0^{\mathrm{FPI},t}$ were introduced. For the weak imposition of boundary and interface conditions by the Nitsche-based method, it is expected that both parameters are required to be sufficiently large in the case of a formulation with the adjoint-consistent terms ($\xi^{\mathrm{FPI}} = 1$). In contrast to that, for the variant with the adjoint-inconsistent terms ($\xi^{\mathrm{FPI}} = -1$), a specific limit is not expected. Both parameters are varied independently to detect whether a different choice of both parameters is more beneficial. In Figure 4.6, a representative selection of the computed error norms dependent on the chosen penalty parameters is shown.

For the adjoint-inconsistent variant $\left(\xi^{\mathrm{FPI}} = -1\right)$, a smooth dependence of the computed error norms on the parameters $\gamma_0^{\mathrm{FPI},n}$ and $\gamma_0^{\mathrm{FPI},t}$ can be identified, which indicates a discrete stable formulation for the whole parameter range. Increasing error norms can be identified for the pressure and the normal constraint for decreasing penalty parameters. For the adjoint-consistent variant $\left(\xi^{\mathrm{FPI}} = 1\right)$, it can be observed that a penalty parameter smaller than $\gamma_0^{\mathrm{FPI},*} < 10$ results in large

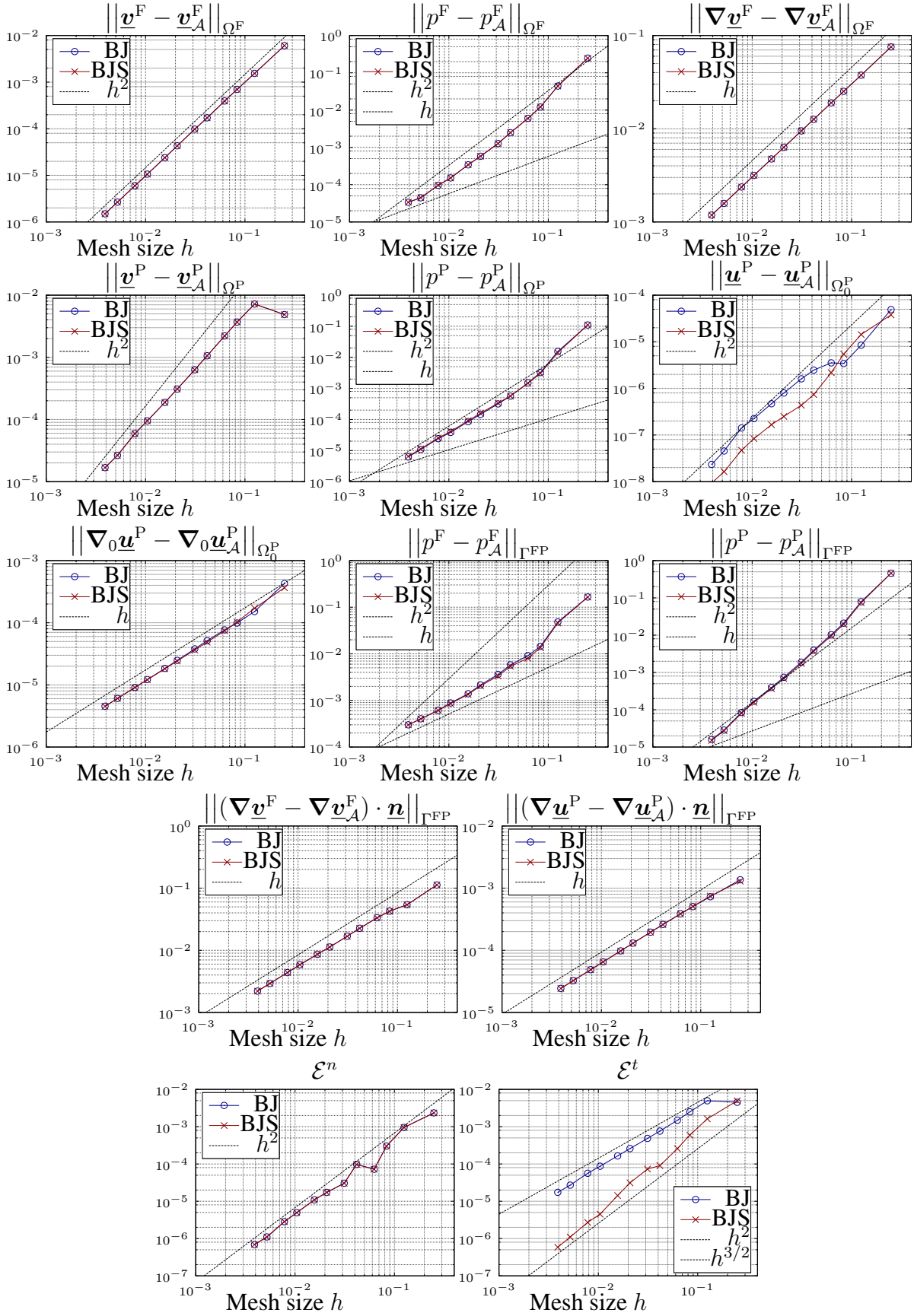

Figure 4.5: Computed domain and interface error norms for the spatial convergence study. Considered is the adjoint-inconsistent ($\xi^{\mathrm{FPI}} = -1$) Nitsche-based approach "Nit" with contribution (4.5) to the weak form and the penalty parameters $\gamma_0^{\mathrm{FPI},n} = \gamma_0^{\mathrm{FPI},t} = 45$.

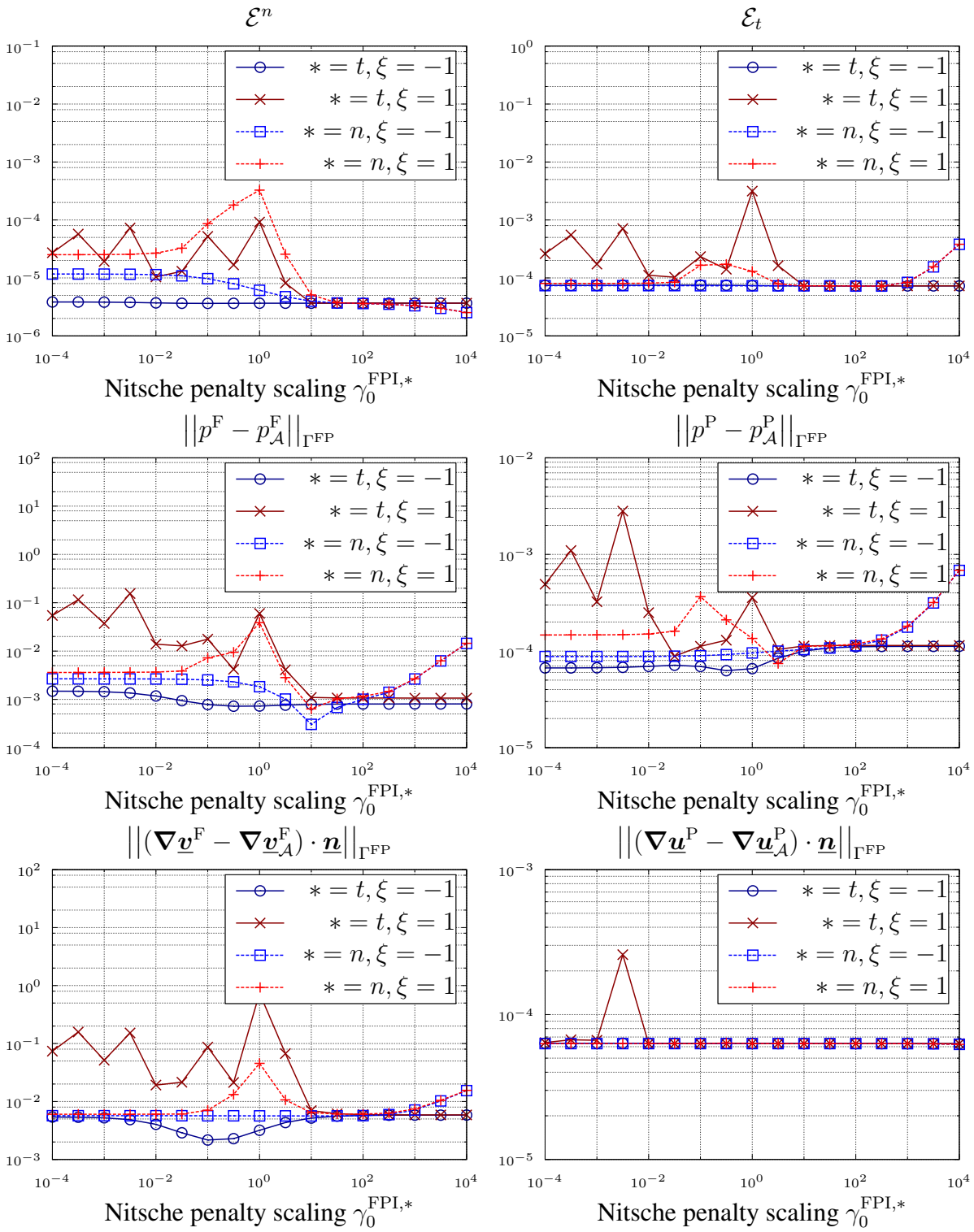

Figure 4.6: Computed interface error norms for varying the Nitsche penalty parameters $\gamma_0^{\mathrm{FPI},t}$ and $\gamma_0^{\mathrm{FPI},n}$. $(*=t,\xi=-1)$: adjoint-inconsistent variant, varying penalty parameter $\gamma_0^{\mathrm{FPI},t}$, fixed penalty parameter $\gamma_0^{\mathrm{FPI},n}=45$. $(*=t,\xi=1)$: adjoint-consistent variant, varying penalty parameter $\gamma_0^{\mathrm{FPI},t}$, fixed penalty parameter $\gamma_0^{\mathrm{FPI},n}=45$. $(*=n,\xi=-1)$: adjoint-inconsistent variant, varying penalty parameter $\gamma_0^{\mathrm{FPI},n}$, fixed penalty parameter $\gamma_0^{\mathrm{FPI},t}=45$. $(*=n,\xi=1)$: adjoint-consistent variant, varying penalty parameter $\gamma_0^{\mathrm{FPI},n}$, fixed penalty parameter $\gamma_0^{\mathrm{FPI},t}=45$. Computed for mesh size $h=0.0078125$.

variations of the error for small variations of the penalty parameter. This is in agreement with the expectation of a loss in coercivity for this formulation. Both variants show an increasing computed error for almost all error norms in the case of large normal penalty parameters. The sole exception is the error of kinematic constraint in normal direction $\mathcal{E}^n$, which is directly enforced by this penalty contribution, where a decreasing error for an increasing penalty parameter can be observed.

As a result of this computed study, a value for both penalty parameters $\gamma_0^{\mathrm{FPI},n}$ and $\gamma_0^{\mathrm{FPI},t}$ in the range of $(10, 100)$ is recommended, independent of the adjoint term symmetry. This ensures discrete stability and is a good compromise between kinematic constraint enforcement and errors of the pressure and velocity/displacement gradients. The parameter range and the dependence of the computed errors and penalty parameters is in good agreement with the results presented in the works of Massing *et al.* [149], Schott and Wall [188] and Winter *et al.* [226].

Remark 4.6 (Adjoint-inconsistent method with $\kappa^{-1} = 0$)**.** *From the results presented above, also a variant with $\gamma_0^{\mathrm{FPI},t} = 0$ for skew-symmetric adjoint terms $\xi^{\mathrm{FPI}} = -1$ seems possible. As already pointed out by Winter* et al. *[226], this is not possible when approaching the "full slip" limit $\kappa^{-1} = 0$, as the system to be solved becomes ill-conditioned. This can be directly seen in the second to last line of the tangential Nitsche terms in* (4.5)*, where the prefactor of the stress term $\left(\kappa(\gamma_0^{\mathrm{FPI},t})^{-1} h_\Gamma\right)\left(\kappa\mu^{\mathrm{F}} + (\gamma_0^{\mathrm{FPI},t})^{-1} h_\Gamma\right)^{-1}$ dominates the overall weak form.*

4.4.4 Comparison of Tangential "Substitution" and "Nitsche" Variant for Varying Porosity and Permeability

As presented in Section 4.2, two different approaches for incorporating the BJ or BJS condition in tangential direction are analyzed. First, the "Substitution" approach is analyzed, which is, to the best of the author's knowledge, exclusively applied in literature for this type of condition, due to its simplicity and good numerical stability. Nevertheless, when approaching the "no-slip"-limit ($\kappa = 0$), the κ^{-1} contribution leads to an ill-conditioned system for the "Substitution" approach. Therefore, the second approach based on the Nitsche method is compared to the "Substitution" approach for a wide range of the coefficient κ , which is specified by the relation (2.65): $\kappa = \left(\alpha_{\mathrm{BJ}}\mu^{\mathrm{F}}\sqrt{3}\right)^{-1}\sqrt{\mathrm{tr}(\underline{\boldsymbol{k}})}$.

To analyze the performance of both numerical approaches for varying physical parameters porosity ϕ and permeability $\underline{\boldsymbol{k}}$, a relation between the porosity ϕ and the permeability $\underline{\boldsymbol{k}}$ for the poroelastic medium is considered. One possibility is the Kozeny-Carman formula (see e.g. the textbook by Coussy [67]), which will be applied in the following by

$$\underline{\boldsymbol{K}} = K_{\mathrm{ref}} \frac{1-\phi_{\mathrm{ref}}^2}{\phi_{\mathrm{ref}}^3} \frac{\left(J^{\mathrm{P}}\phi\right)^3}{1-\left(J^{\mathrm{P}}\phi\right)^2} \underline{\boldsymbol{I}}, \tag{4.26}$$

with the reference porosity $\phi_{\mathrm{ref}} = 0.5$ and the scalar, material reference permeability $K_{\mathrm{ref}} = 0.1$ being prescribed. Then, by a reduction of the porosity ϕ, the trace of the material permeability $\mathrm{tr}(\underline{\boldsymbol{K}})$ and therefore the trace of the permeability $\mathrm{tr}(\underline{\boldsymbol{k}})$ decreases. This finally results in a shrinking coefficient κ. To investigate the difference in both formulations for a modification of solely physical parameters, the porosity is prescribed in the range of $\phi = [10^{-6}, 5 \cdot 10^{-1}]$ and the corresponding permeability is computed which leads to a modified coefficient κ. To analyze the

dependence of the numerical error on the Beavers-Joseph coefficient α_{BJ}, the computations are performed for $\alpha_{\mathrm{BJ}} = 1$ and $\alpha_{\mathrm{BJ}} = 10$.

Due to the considered low porosity and permeability, the relative velocity between the poroelastic fluid and poroelastic solid of the analytic solution is reduced. For this comparison, the amplitudes in the analytic solution (4.14) and (4.16) are chosen to an equal value of $A^{\mathrm{P}} = A^{\mathrm{PS}} = -10^{-5}$. As the solution (4.14) is given in the current configuration and the solution (4.16) in material configuration, a relative velocity for the deformed configuration still occurs.

A representative selection of the computed error norms is presented in Figure 4.7. First, when analyzing the Nitsche-based approach and comparing the computed results for the different coefficients $\alpha_{\mathrm{BJ}} = 1$ and $\alpha_{\mathrm{BJ}} = 10$, no dependence of the computed error norms can be observed. Moreover, the variation of the porosity does not lead to a significant change of the computed errors. Solely for large porosities, close to $\phi = 0.5$, an increasing error can be observed for all variants. This is likely due to the prescribed analytic solution with small relative velocity in the poroelastic domain, whereas the pressure gradient term cannot be balanced by the reactive term due to the moderate coefficient $\mu^{\mathrm{F}}\phi\underline{\boldsymbol{k}}^{-1}$. The "Substitution" approach, on the other hand, leads to increasing error norms for a small porosity (and permeability) for almost all quantities. This is the expected behavior, due to the scaling κ^{-1} of the substitution term. The kinematic tangential error $\mathcal{E}^t$, however, reduces for this approach in the small porosity limit, as the global system reduces to this constraint for $\kappa = 0$, which is the expected behavior.

Finally, one can conclude that both variants perform well for a wide range of the porosity ϕ and the permeability $\underline{\boldsymbol{k}}$. For the computed problem setup, the "Substitution" approach leads to a comparable error to the Nitsche-based approach for porosities down to $\phi = 10^{-3}$. Nevertheless, when it is essential to approach the impermeability limit $\phi = 0$ and $\underline{\boldsymbol{k}} = \underline{\mathbf{0}}$ (e.g. considering contacting rough surfaces by a poroelastic model as presented in the subsequent Chapter 5), the substitution approach fails due to ill-conditioning.

4.4.5 Comparison of Beavers-Joseph and Beavers-Joseph-Saffmann Interface Condition

To analyze the applicability of the BJ or the simplified BJS for the coupled FPI problem, a comparison of both approaches for a large range of $\alpha_{\mathrm{BJ}} = [10^{-8}, 10^{8}]$ is performed. For the sake of completeness, both formulations to enforce the tangential constraint are taken into account. In the works of Burman and Hansbo [45] and Gartling *et al.* [89], computations for the interface coupling of the Stokes and Darcy equation by the BJ condition with $\alpha_{\mathrm{BJ}}^{-1} = 0$ lead to an oscillatory velocity solution close to the interface. Mathematical analysis of the BJ condition for this problem setup was conducted by Cao *et al.* [54, 55].

The computed results are presented in Figure 4.8. As expected for small coefficients α_{BJ}, similar results for all variants are computed. Due to the vanishing kinematic contribution in (2.64), when approaching the "full slip" limit ($\kappa^{-1} = 0$), no difference between BJ and BJS occurs. Only the tangential kinematic error $\mathcal{E}^t$ differs due to the varying definition for the BJ and BJS case. For a growing coefficient, starting at around $\alpha_{\mathrm{BJ}} = 10.0$, a significant increase for almost all computed domain and interface errors can be observed for the BJ interface condition, which finally remain constant for large coefficients α_{BJ}. Solely the error $\mathcal{E}^t$ decreases towards the no-slip limit. In contrast, the BJS variant does not lead to a large change of the computed error

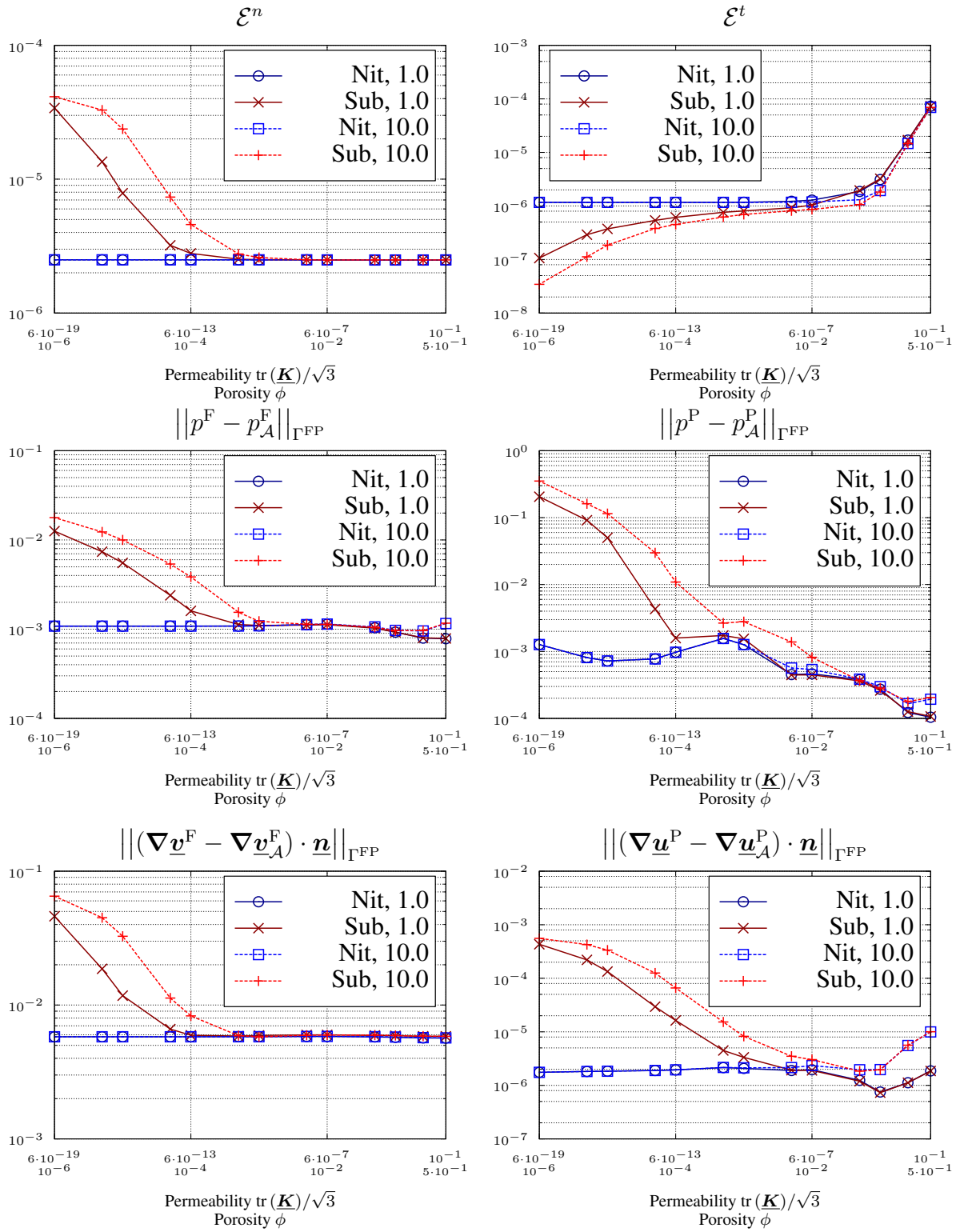

Figure 4.7: Computed interface error norms for varying porosity ϕ, varying material permeability $\underline{\boldsymbol{K}}$ according to the Kozeny-Carman formula (4.26), varying permeability $\underline{\boldsymbol{k}}$, and varying sliplength κ according to relation (2.65). The "Substitution" approach ("Sub") with contribution (4.4) to the weak form and the Nitsche-based approach ("Nit") with contribution (4.5) to the weak form are compared. The BJ condition is applied with coefficient $\alpha_{\mathrm{BJ}} = 1.0$: ("1.0") and $\alpha_{\mathrm{BJ}} = 10.0$: ("10.0"). Computed for mesh size $h = 0.0078125$, the adjoint-inconsistent variant ($\xi^{\mathrm{FPI}} = -1$) and the penalty parameters $\gamma_0^{\mathrm{FPI},n} = \gamma_0^{\mathrm{FPI},t} = 45$.

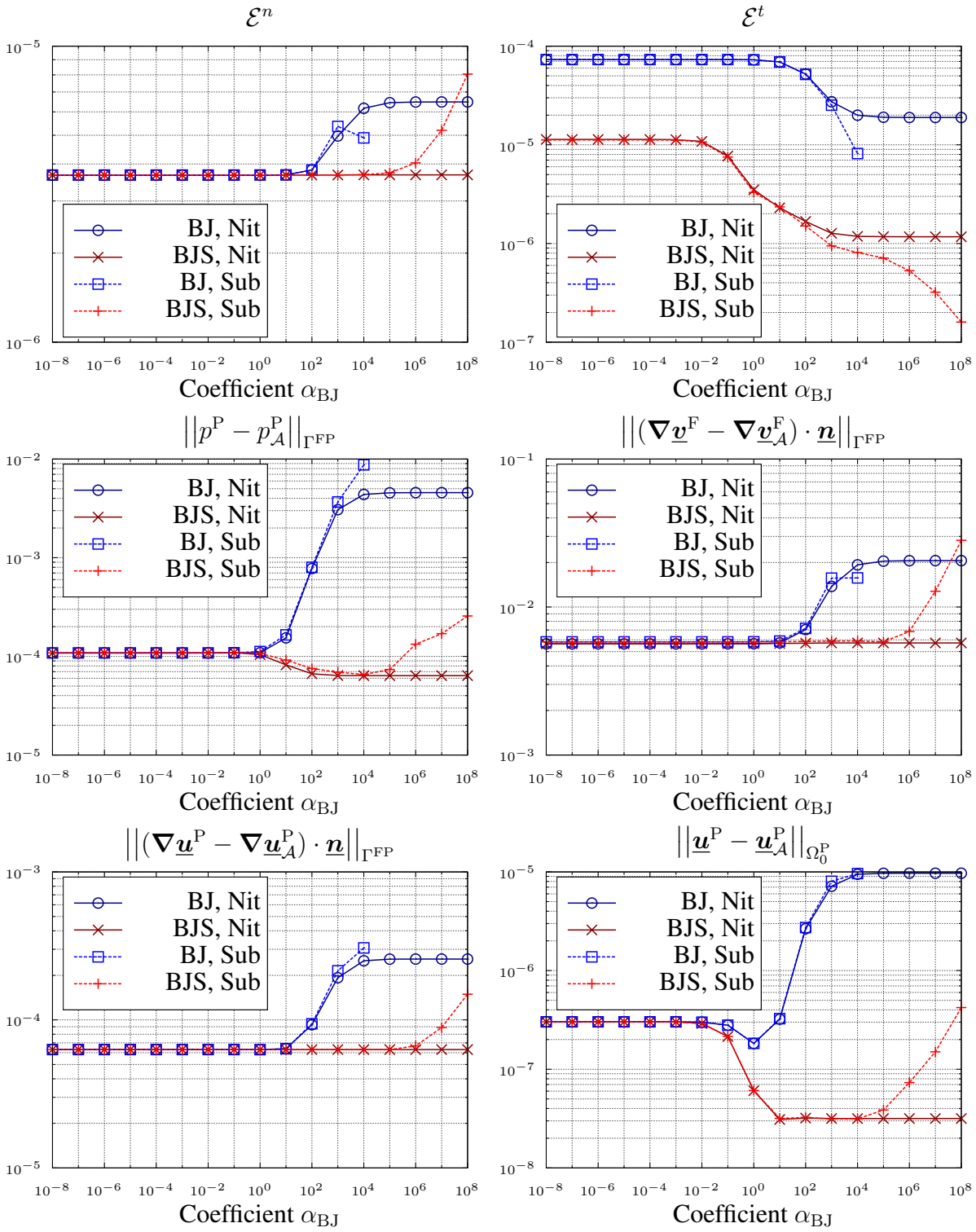

Figure 4.8: Computed domain and interface error norms for a varying coefficient α_{BJ}. The computations are performed for the Beavers-Joseph ("BJ", $\beta_{\mathrm{BJ}} = 1$) and the Beavers-Joseph-Saffmann ("BJS", $\beta_{\mathrm{BJ}} = 0$) interface condition (see (2.64)). The "Substitution" approach ("Sub") with contribution (4.4) to the weak form and the Nitsche-based approach ("Nit") with contribution (4.5) to the weak form are compared. Computed for mesh size $h = 0.0078125$, the adjoint-inconsistent variant ($\xi^{\mathrm{FPI}} = -1$) and the penalty parameters $\gamma_0^{\mathrm{FPI},n} = \gamma_0^{\mathrm{FPI},t} = 45$.

norms in the whole range of α_{BJ}. Only the error norm $\mathcal{E}^t$ behaves differently and shows similar behavior as for the BJ case. For the sake of completeness, the displacement domain error norm is shown in Figure 4.8, which decreases for large coefficients α_{BJ} and the BJS variant. The difference between the results computed for the Nitsche-based and the "Substitution" approach to enforce the BJ or the BJS conditions follows the same argumentation as in the previous section. For small values of α_{BJ}, both methods perform similarly, while for large values of the coefficient α_{BJ}, closer to the no-slip limit, only the Nitsche-based variant retains a well-conditioned system of equations. In contrast to the direct observation of oscillations of the velocity solution in the poroelastic domain for large coefficients α_{BJ} in the works of Burman and Hansbo [45] and Gartling *et al.* [89], for the considered mesh size parameter $h = 0.0078125$, these oscillations are not directly observable in a visualization such as Figure 4.4.

From these computed results, both interface conditions, the BJ and the BJS condition, confirm their applicability for the coupled FPI problem from a computational point of view for the whole relevant range of the coefficient α_{BJ}. Therefore, both conditions can be considered for upcoming computations, however, the BJ condition is preferred due to its experimental validation. For small values of $\alpha_{\mathrm{BJ}} < 10.0$, which includes the physical relevant range, no essential difference in the computed error norms can be observed.

4.5 Numerical Examples: CutFEM FPI

In the following, two numerical examples are presented to demonstrate the general applicability of the previously introduced approach.

4.5.1 Fluid Induced Bending of a Poroelastic Beam

In this section, the presented approach for solving the FPI is applied to the fluid induced dynamic bending process of a poroelastic beam. As this includes large deformation and motion, the benefits of the presented poroelasticity formulation and CutFEM approach are shown.

Problem Description The principal problem setup, including the geometry and basic boundary conditions, is visualized in Figure 4.9. It consists of a rectangular fluid domain and a poroelastic beam with a circular tip. On the Dirichlet boundary Γ^{in}, a parabolic velocity inflow profile is prescribed: $\underline{\hat{\boldsymbol{v}}}^{\mathrm{F}} = \left[0.2\left(y - y^2\right)\left(2 - 2\cos\left(0.5\pi t\right)\right), 0\right]^{\mathsf{T}}$ for $t \in [0.0, 2.0]$ and $\underline{\hat{\boldsymbol{v}}}^{\mathrm{F}} = \left[0.8\left(y - y^2\right), 0\right]^{\mathsf{T}}$ for $t \in [2.0, 10.0]$. On the boundary Γ^{out}, a zero-traction Neumann boundary condition in x-direction is combined with a zero velocity Dirichlet boundary condition in y-direction. The fluid is characterized by a dynamic viscosity of $\mu^{\mathrm{F}} = 0.01$ and a density of $\rho^{\mathrm{F}} = 0.1$. The initial porosity in the poroelastic beam is $\mathring{\phi} = 0.5$ and the initial isotropic material permeability is $\underline{\mathring{\boldsymbol{K}}} = \mathring{K} \cdot \underline{\boldsymbol{I}}$ with $\mathring{K} = 10^{-5}$. To consider the dependence of the permeability on the porosity, the Kozeny-Carman formula is applied

$$\underline{\boldsymbol{K}} = \underline{\mathring{\boldsymbol{K}}} \frac{1 - \mathring{\phi}^2}{\mathring{\phi}^3} \frac{\left(J^{\mathrm{P}}\phi\right)^3}{1 - \left(J^{\mathrm{P}}\phi\right)^2}. \tag{4.27}$$

Equal to the first example in Section 4.4, the macroscopic solid material behavior is given by a Neo-Hookean material model with the strain energy function $\psi^{\mathrm{P},skel}$ given in (2.17) and the

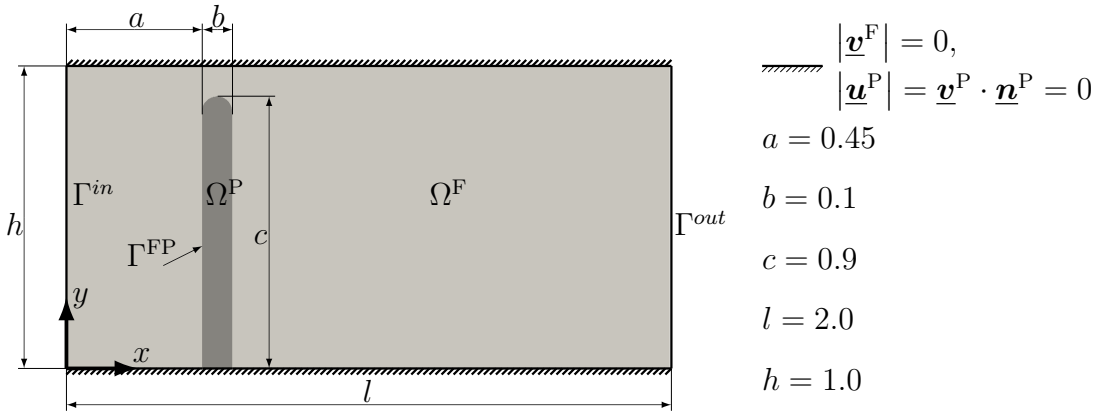

Figure 4.9: Geometry and boundary conditions for the fluid induced bending process of a poroelastic beam.

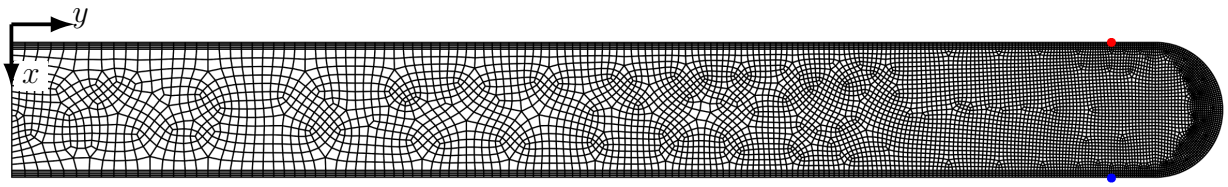

Figure 4.10: The boundary- and interface-fitted computational mesh consisting of 7880 bi-linear quadrilateral elements for the discretization of the poroelastic equations in the domain Ω^{P} (for visualization rotated by $-\pi/2$). The computed solution is visualized in Figure 4.12 at the position of the red marker (top) and at the position of the blue marker (bottom).

material parameters Young's modulus $E = 100$ and Poisson ration $\nu = 0.3$. To take the deformation and porous fluid pressure dependent varying porosity ϕ into account, the strain energy function $\psi^{\mathrm{P},vol}$ has to be considered as well. Here, the formulation which is specified in (2.48) is applied, with Bulk modulus $\kappa^{\mathrm{P}} = 100$. No contribution $\psi^{\mathrm{P},pen}$ is added to the overall strain energy function. The average initial density of the solid phase is set to $\rho_0^{\mathrm{S}} = 0.2$. On the interface Γ^{FP}, the BJ condition ($\beta_{\mathrm{BJ}} = 1$) with a coefficient of $\alpha_{\mathrm{BJ}} = 1.0$ is weakly imposed by the adjoint-inconsistent ($\xi^{\mathrm{FPI}} = -1$) Nitsche-based contribution (4.5) (penalty parameters $\gamma_0^{\mathrm{FPI},n} = \gamma_0^{\mathrm{FPI},t} = 45$).

The computational mesh for the discretization of the fluid equations in the domain Ω^{F}, which is only fitted to the outer boundaries but not to the interface Γ^{FP}, covers the whole rectangular domain visualized in Figure 4.9. It consists of $250 \times 120 = 30000$ structured, bi-linear, quadrilateral elements. Figure 4.10 shows the boundary- and interface-fitted, unstructured computational mesh for domain Ω^{P}. Analogous to the computations in Section 4.4, this is accomplished by a discretization with one layer of eight-noded, tri-linear hexahedral elements.

The discretization in time is performed by the backward Euler scheme $\theta = 1$ with a time step length of $\Delta t = 0.01$. The initial state of the problem is the zero-state: $\underline{\mathring{\boldsymbol{v}}}^{\mathrm{F}} = \underline{\mathring{\boldsymbol{u}}}^{\mathrm{P}} = \underline{\mathring{\boldsymbol{v}}}^{\mathrm{PS}} = \underline{\mathring{\boldsymbol{v}}}^{\mathrm{P}} = \underline{\mathbf{0}}$.

Computed Results and Discussion In Figure 4.11, the computed velocity and pressure solution for two instances in time is shown. At $t = 2$, the initiated bending motion of the poroelastic beam due to the fluid inflow, which leads to a pressure difference between the two interface sides, can be seen. The velocity in the fluid domain and the poroelastic domain is roughly continuous as the beam moves approximately with the same velocity as the fluid velocity. For

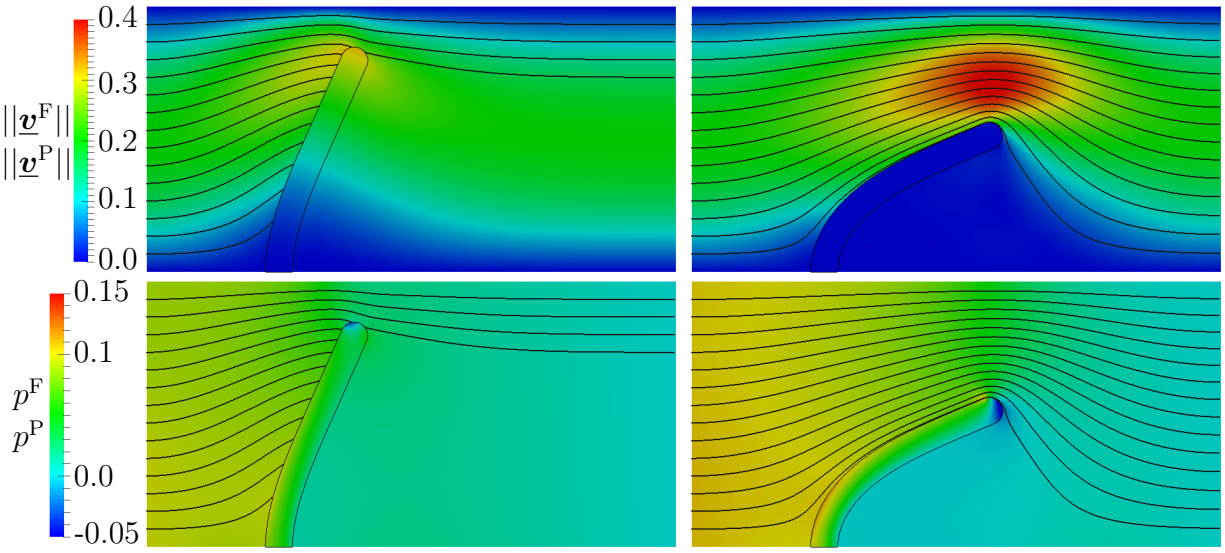

Figure 4.11: Computed velocity magnitude ($||\underline{\boldsymbol{v}}^{\mathrm{F}}||$ and $||\underline{\boldsymbol{v}}^{\mathrm{P}}||$) in the top row and pressure solution (p^{F} and p^{P}) in the bottom row at time $t = 2$ (left) and $t = 8$ (right). Black lines are the streamlines computed from the fluid velocity $\underline{\boldsymbol{v}}^{\mathrm{F}}$.

$t = 8$, the poroelastic beam is already in a stationary position and therefore the small remaining relative velocity in the poroelastic domain cannot be seen by the color code. The major part of the fluid mass flow does not pass the poroelastic beam, leading to the maximal velocity at the smallest constriction, which is located between the upper boundary of the fluid domain and the circular tip of the poroelastic beam.

In Figure 4.12, the computed solution at two selected points of the poroelastic domain is shown. At the point which is closer to the inflow boundary (top-left) a continuous increase of the pressure p^{P} during the bending motion can be observed. In contrast to that, at the point which is closer to the outflow boundary side (top-right) first an increase of the fluid pressure p^{P} due to the increasing inflow velocity followed by a decrease of the pressure due to the changing orientation caused by the bending motion of the beam occurs. At $t = 2$, a kink in the pressure curve forms due to the change in the inflow function. The porous fluid velocity $||\underline{\boldsymbol{v}}^{\mathrm{P}}||$ and the solid velocity $||\partial \underline{\boldsymbol{u}}^{\mathrm{P}}/\partial t||$ are almost equal and represent the initial acceleration phase, followed by the slowdown phase due to the increasing elastic stress balancing the fluid stress. A detailed view of the relative velocity $||\underline{\boldsymbol{v}}^{\mathrm{P}} - \partial \underline{\boldsymbol{u}}^{\mathrm{P}}/\partial t||$ for both selected points is given in Figure 4.12 (bottom). In the time interval from approximately $t = 2$ to $t = 6$, where a high solid velocity $||\partial \underline{\boldsymbol{u}}^{\mathrm{P}}/\partial t||$ is prevalent, oscillations of the relative velocity can be observed. Close inspection reveals that these oscillations also exist for the evolution of the pressure p^{P} in time at a specific material point $\underline{\boldsymbol{X}}^{\mathrm{P}}$ on the interface Γ^{FP}. This effect arises due to the frequently changing neighboring discrete fluid solution space (of the fixed background computational mesh) and the consequently varying computational error. In particular the discontinuous viscous fluid stress on the interface between single fluid elements is expected to have a large impact. This issue can be resolved by an increasing resolution of the computational fluid mesh close to the interface Γ^{FP} or by applying a hybrid approach as presented in the works of Schott *et al.* [190, 191]. To analyze the potential improvements, a Hybrid Eulerian-ALE fluid domain decomposition approach is applied in the following Section 4.5.1.1 to the same problem configuration.

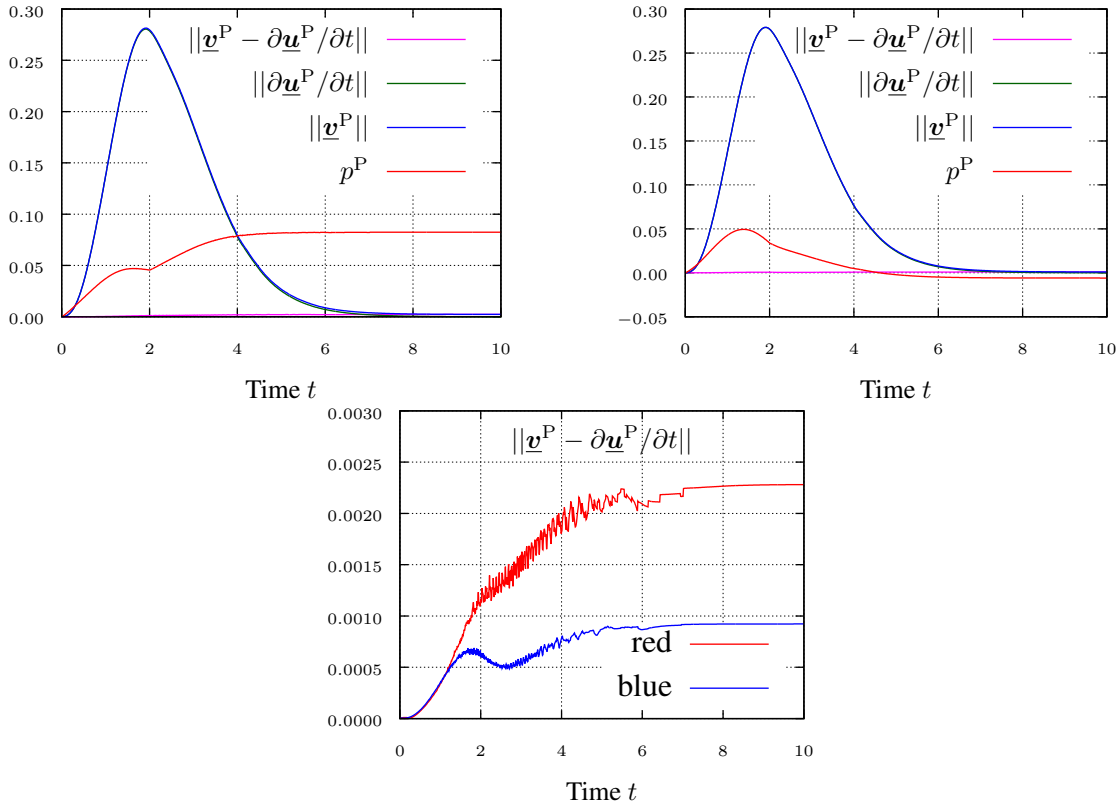

Figure 4.12: Computed porous fluid pressure p^{P}, porous fluid velocity magnitude $||\underline{\boldsymbol{v}}^{\mathrm{P}}||$, solid velocity magnitude $||\partial\underline{\boldsymbol{u}}^{\mathrm{P}}/\partial t||$, and relative velocity magnitude $||\underline{\boldsymbol{v}}^{\mathrm{P}} - \partial\underline{\boldsymbol{u}}^{\mathrm{P}}/\partial t||$ for two selected points. Computed solution at the position of the red marker (top-left) and the blue marker (top-right). The relative velocity magnitude is visualized in detail for both markers in the last graph (bottom). The markers can be found in Figure 4.10.

The computed porosity in the poroelastic domain is visualized at three instances in time in Figure 4.13 (left). Due to the expansion of the beam on the inflow side, an increase of the fluid

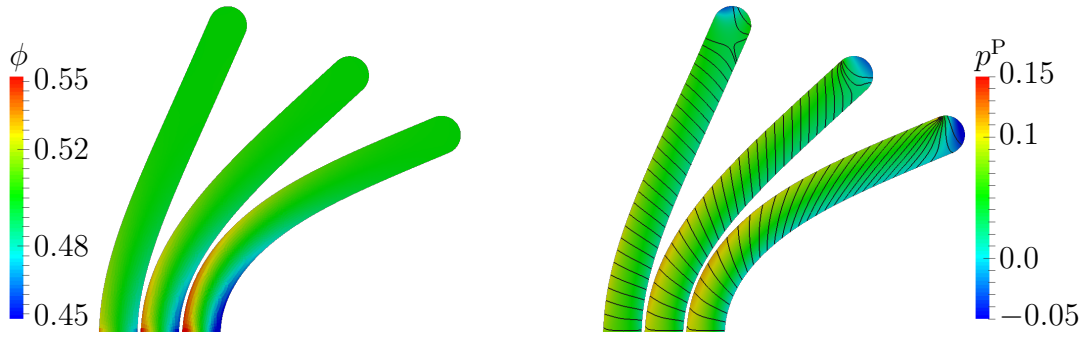

Figure 4.13: Computed porosity ϕ (element-wise constant visualization) in the poroelastic domain Ω^{P} at three instances in time from left to right $t = 2$, $t = 3$, and $t = 8$ (left). Computed pressure p^{P} and visualization of the seepage velocity $\left(\underline{\boldsymbol{v}}^{\mathrm{P}} - \partial\underline{\boldsymbol{u}}^{\mathrm{P}}/\partial t\right)$ by streamlines (black lines) in the poroelastic domain Ω^{P} at three instances in time from left to right $t = 2$, $t = 3$, and $t = 8$ (right).

fraction and therefore the porosity ϕ can be observed. On the other side, the compression leads to a reduction of the porosity. At the tip of the beam, no significant deformation occurs and the porosity is almost equal to its initial value of $\phi \approx \mathring{\phi} = 0.5$. It can be seen that for this problem setup, no significant influence of the fluid pressure on the porosity can be observed. In Figure 4.13 (right), the streamlines computed for the seepage velocity and the fluid pressure are visualized. As one would expect, a flow from the high pressure inflow side to the low pressure side can be observed for a large part of the beam. A fluid flow from the inside of the poroelastic domain leaving at the tip of the beam can be noticed solely at $t = 2$.

4.5.1.1 Application of Hybrid Eulerian-ALE Fluid Domain Decomposition for FPI

To increase the spatial resolution of the fluid discretization, a hybrid Eulerian-ALE approach for fluid domain decomposition is applied to the considered configuration. This approach is presented in detail for FSI in the work of Schott *et al.* [191] and is applied in the following to FPI. The principal idea is based on a domain decomposition approach for the fluid domain, where one moving and deforming fluid patch (in ALE formulation) is attached to the fluid interface of the (poroelastic) structure. This allows for refinement of the spatial resolution close to the deforming interface. Finally, this fluid patch is cut-out from a potentially coarse discretized non-moving "background" fluid domain. The resulting artificial fluid-fluid interface is treated as discussed in Section 3.3.3, where essential aspects of the works by Schott [187], Schott *et al.* [190, 191], Shahmiri [198] are summarized.

As shown in Figure 4.14 by the cyan colored elements, an additional computational mesh with its computational nodes matching on the interface Γ^{FP} with the poroelastic mesh is added. This additional mesh is utilized for the discretization of the fluid equations in the subdomain Ω^{F_1} of the overall fluid domain $\Omega^{\mathrm{F}_1} \subset \Omega^{\mathrm{F}}$. The remaining fluid domain $\Omega^{\mathrm{F}_2} = \Omega^{\mathrm{F}} \setminus \Omega^{\mathrm{F}_1}$ is discretized by the same fixed and structured mesh as described in Section 4.5.1. In domain Ω^{F_1}, the Navier-

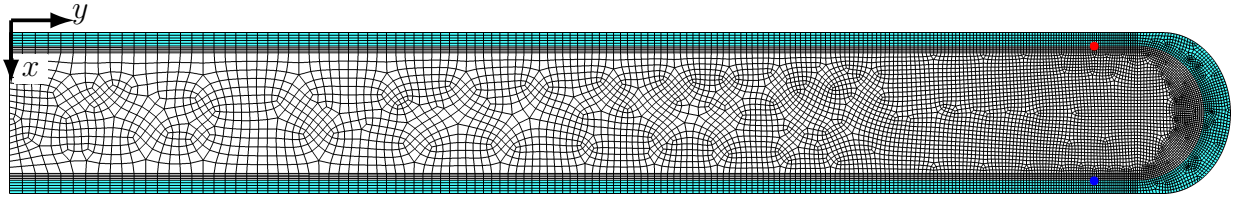

Figure 4.14: Boundary- and interface-fitted computational meshes consisting of 7880 and 2887 bi-linear, quadrilateral elements for the discretization of the domains Ω^{P} and Ω^{F_1}, respectively (for visualization rotated by $-\pi/2$). The computed solution is visualized in Figure 4.15 at the position of the red marker (top) and at the position of the blue marker (bottom).

Stokes equations are solved in the general ALE formulation. The mesh displacement $\underline{\boldsymbol{u}}^{\mathrm{G}}$ is set to zero on the bottom ($y = 0$) and is given by the displacement $\underline{\boldsymbol{u}}^{\mathrm{P}}$ of the poroelastic domain on the interface Γ^{FP} (for the incorporation in the overall system see Remark 2.12). The unconstrained mesh motion is computed by a pseudo-structural formulation (see Remark 2.11). For this discretization approach, the artificial interface Γ^{FF} between both fluid domains is unfitted in regard to the discretization of the domain Ω^{F_2}, whereas the interface Γ^{FP} is fitted to both adjacent computational meshes. The continuity of fluid velocity and pressure on the fluid decomposition interface Γ^{FF} is incorporated by the Nitsche-based contributions discussed in Section 3.3.3. The penalty parameter of the adjoint-inconsistent ($\xi^{\mathrm{FFI}} = 1$) Nitsche formulation is set to $\gamma_0^{\mathrm{FFI}} = 45$.

The terms accounting for convection through the interface (last line of equation (3.37)) are not considered in this example. Besides this modification of the spatial discretization approach, the setup remains as described in Section 4.5.1.

Computed Results and Discussion As the overall computed solution does not significantly differ from the discretization approach considered first (Section 4.5.1), the focus is put on presenting a comparison of detailed results between both discretization approaches. In Figure 4.15, the computed solution in the two selected points of the poroelastic domain is shown. A qualitative comparison of the computed pressure p^{P}, the fluid velocity magnitude $||\underline{\boldsymbol{v}}^{\mathrm{P}}||$, and the solid velocity magnitude $||\partial\underline{\boldsymbol{u}}^{\mathrm{P}}/\partial t||$ with the results presented in Figure 4.12 (top) shows that these quantities almost coincide. The oscillations of the computed relative velocity magnitude $||\underline{\boldsymbol{v}}^{\mathrm{P}} - \partial\underline{\boldsymbol{u}}^{\mathrm{P}}/\partial t||$, present in both considered points in space for the fixed-grid fluid discretization (see Figure 4.12 (bottom)), are significantly reduced by the Hybrid Eulerian-ALE fluid domain decomposition approach (see Figure 4.15 (bottom)). Still, the temporal average of the relative velocity is of comparable magnitude for both approaches.

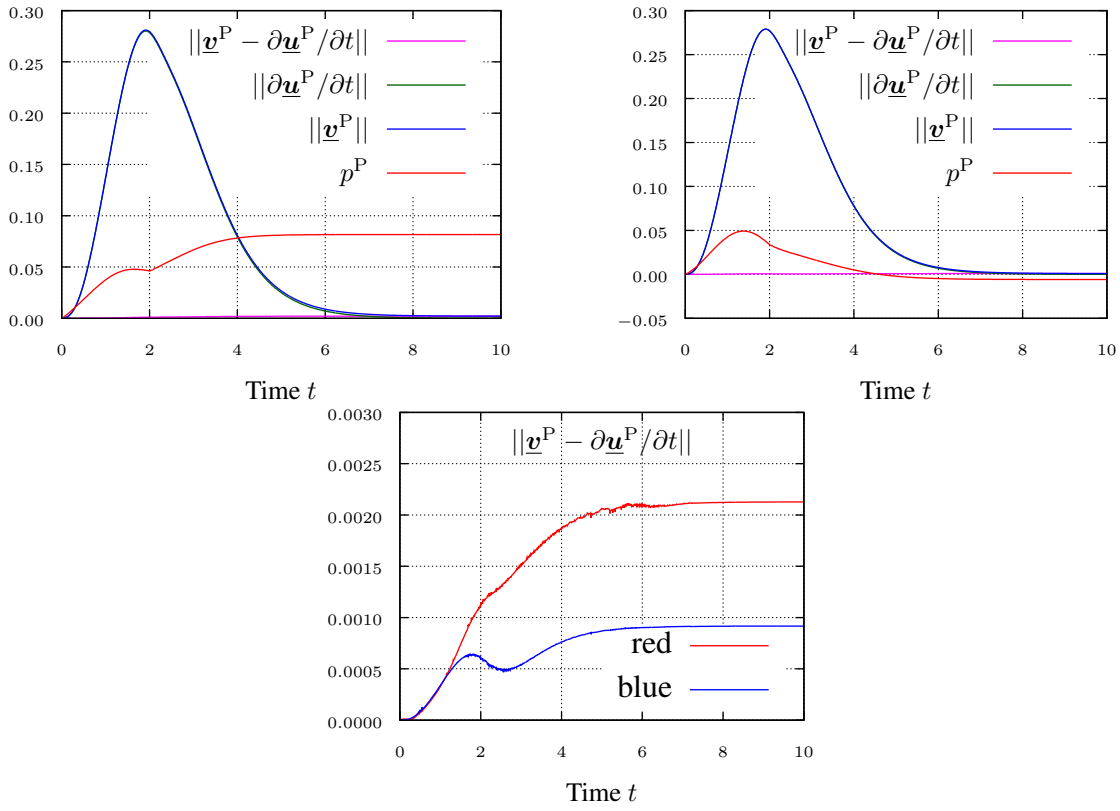

Figure 4.15: Computed porous fluid pressure p^{P}, porous fluid velocity magnitude $||\underline{\boldsymbol{v}}^{\mathrm{P}}||$, solid velocity magnitude $||\partial\underline{\boldsymbol{u}}^{\mathrm{P}}/\partial t||$, and relative velocity magnitude $||\underline{\boldsymbol{v}}^{\mathrm{P}} - \partial\underline{\boldsymbol{u}}^{\mathrm{P}}/\partial t||$ for two selected points. Computed solution at the position of the red marker (top-left) and the blue marker (top-right). The relative velocity magnitude is visualized in detail for both markers in the last graph (bottom). Computed with the Hybrid Eulerian-ALE fluid domain decomposition approach. The markers can be found in Figure 4.14.

In order to illustrate the differences between both discretization approaches, a comparison is presented in Figure 4.16. Herein, a detailed view on the most critical zone, the tip of the poro-

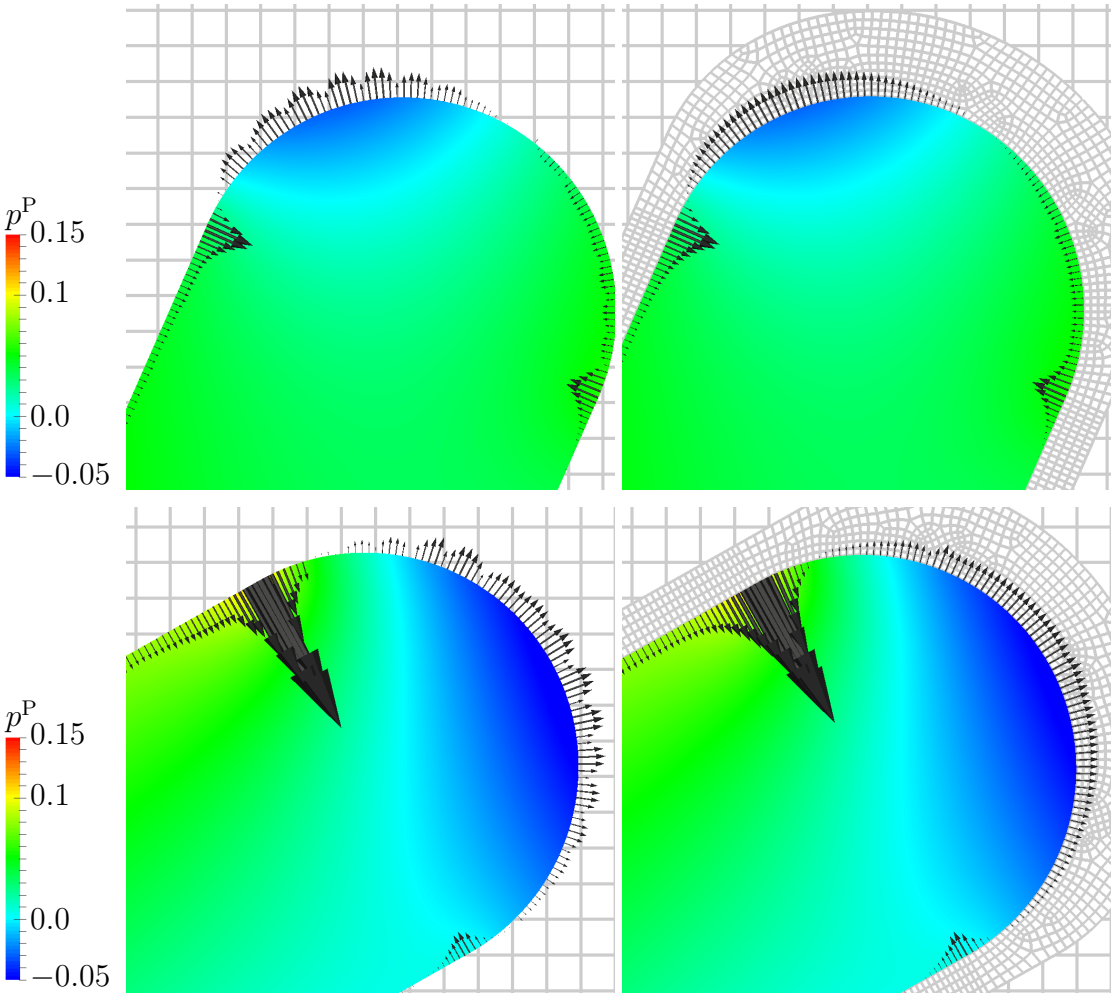

Figure 4.16: Detailed view on the tip of the bending beam for both discretization variants at two points in time. Time $t = 2.0$ in the first row and time $t = 4.0$ in the second row. The variant with a fixed computational fluid mesh as described in Section 4.5.1 is in the left column and the hybrid Eulerian-ALE approach as described in Section 4.5.1.1 is in the right column. The black arrows show the normal seepage velocity $\left(\underline{\boldsymbol{v}}^{\mathrm{P}} - \partial \underline{\boldsymbol{u}}^{\mathrm{P}}/\partial t\right) \cdot \underline{\boldsymbol{P}}^{n}$ on the interface Γ^{FP}. The color code represented the computed porous fluid pressure p^{P}.

elastic beam, is given. The computed porous fluid pressure p^{P} and the normal seepage velocity $\left(\underline{\boldsymbol{v}}^{\mathrm{P}} - \partial \underline{\boldsymbol{u}}^{\mathrm{P}}/\partial t\right) \cdot \underline{\boldsymbol{P}}^{n}$ on the interface Γ^{FP} is visualized for two instances in time. When analyzing the pressure, no significant difference between the two approaches is noticeable. In contrast to this, the velocity magnitude shows spatial oscillations due to a strong dependence on the background discretization for the fixed-grid fluid discretization (see Figure 4.16 (left)), which cannot be observed for the Hybrid Eulerian-ALE fluid domain decomposition approach (see Figure 4.16 (right)). Still, for time $t = 4.0$, a kink in the computed interface velocity magnitude close to an irregularity of the embedded fluid discretization can be observed. This observation indicates that the Hybrid Eulerian-ALE discretization approach also benefits from the predominate structure of

the discretization with respect to the interface Γ^{FP} in addition to the increased spatial resolution close to the interface Γ^{FP}.

4.5.2 3D Interaction of a Poroelastic Plate and Fluid Channel Flow

In this section, the interaction of a poroelastic plate, which is mounted on the downstream end of a poroelastic beam, and channel flow in a narrow channel is analyzed. This configuration is presented to highlight the applicability of the presented framework for more challenging 3D configurations.

Problem Description The geometric setup and all basic boundary conditions are shown in Figure 4.17. The poroelastic domain consists of a poroelastic crossbeam Ω^{P_1} which is mounted

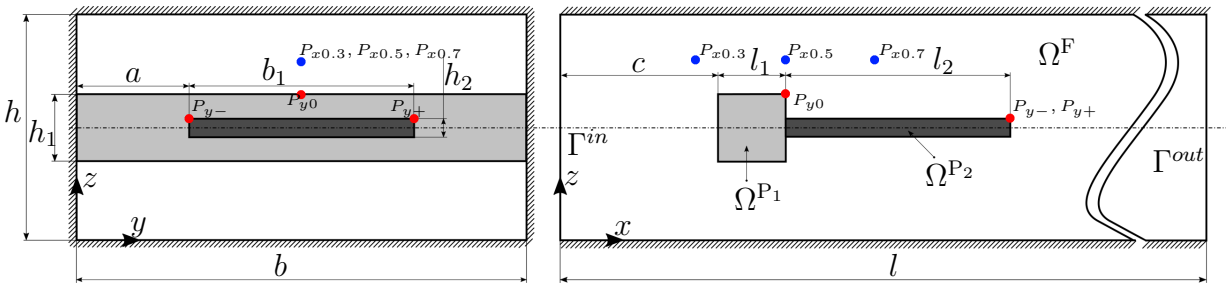

Figure 4.17: Geometry and boundary conditions for 3D interaction of poroelastic plate and fluid channel flow. On all boundaries which are marked by the diagonal lines the basic boundary conditions no-slip $|\underline{\boldsymbol{v}}^{\mathrm{F}}| = 0$, fixed $|\underline{\boldsymbol{u}}^{\mathrm{P}}| = 0$, or slip $\underline{\boldsymbol{v}}^{\mathrm{P}} \cdot \underline{\boldsymbol{n}}^{\mathrm{P}} = 0$, depending on the adjacent physical domain are prescribed. The lengths and distances are given by: $l = 8, b = 1, h = 0.5, l_1 = h_1 = 0.15, b_1 = 0.5, l_2 = 0.5, h_2 = 0.04, a = 0.251$, and $c = 0.35$. At the marked points $P_{y-}, P_{y+}, P_{y0}, P_{x0.3}, P_{x0.5}$, and $P_{x0.7}$, the computed poroelastic displacement and fluid velocity solution is shown in Figure 4.20.

on the channel walls. The poroelastic plate Ω^{P_2} is attached slightly asymmetrical (see distance a) to this beam. The remaining volume inside the channel of size $l \times b \times h$ specifies the considered fluid domain Ω^{F}. An elliptic paraboloid shape velocity profile with initial ramp up is prescribed on the inflow boundary Γ^{in}: $\hat{\underline{\boldsymbol{v}}}^{\mathrm{F}} = [300(4(z-0.25)^2 h^{-2} - 1)(4(y-0.5)^2 l^{-2} - 1)\hat{g}(t), 0, 0]^{\mathsf{T}}$ on Γ^{in} with $\hat{g}(t) = 1 - \cos(8\pi t)$ for $t \in [0, 0.125]$ and $\hat{g}(t) = 2.0$ for $t \in [0.125, 0.3]$. On the outflow boundary Γ^{out}, a zero-traction Neumann boundary condition is prescribed. The poroelastic matrix in both poroelastic domains is exposed to a body force in negative z-direction: $\tilde{\rho}_0^{\mathrm{PS}} \hat{\underline{\boldsymbol{b}}}_0^{\mathrm{P}} = [0, 0, -5000]^{\mathsf{T}}$ in $\Omega^{\mathrm{P}_1} \cup \Omega^{\mathrm{P}_2}$.

The material parameters to characterize the fluid behavior are the dynamic viscosity $\mu^{\mathrm{F}} = 0.1$ and the density $\rho^{\mathrm{F}} = 1$. The initial porosity in both poroelastic domains Ω^{P_1} and Ω^{P_2} is $\mathring{\phi} = 0.5$ and the initial isotropic material permeability is $\underline{\boldsymbol{\mathring{K}}} = \mathring{K} \cdot \underline{\boldsymbol{I}}$ with $\mathring{K} = 10^{-5}$. The averaged initial density of the solid phase is $\rho_0^{\mathrm{S}} = 20$. The dependence on the permeability by the porosity is given by the Kozeny-Carman formula (4.27). The macroscopic solid material behavior is given by a Neo-Hookean material model with the strain energy function $\psi^{\mathrm{P},skel}$ given in (2.17) with Young's modulus $E^1 = 10^7, E^2 = 10^6$ and Poisson ration $\nu^1 = \nu^2 = 0.33$ in the respective poroelastic domains. The strain energy function $\psi^{\mathrm{P},vol}$ as defined in (2.48) is considered with Bulk modulus $\kappa^{\mathrm{P}} = 10^7$. To guarantee a positive porosity, an additional penalty strain energy function $\psi^{\mathrm{P},pen}$ with parameter $\eta^{\mathrm{P}} = 1$, as specified in (2.49), is added. On the interface Γ^{FP},

the BJ condition ($\beta_{\mathrm{BJ}} = 1$) with a coefficient of $\alpha_{\mathrm{BJ}} = 1.0$ is weakly imposed by the adjoint-inconsistent ($\xi^{\mathrm{FPI}} = -1$) Nitsche-based contribution (4.5) with the penalty parameters $\gamma_0^{\mathrm{FPI},n} = \gamma_0^{\mathrm{FPI},t} = 35$.

The computational mesh which is applied for the discretization of the fluid domain, is not fitted to the interface Γ^{FP}, consists of 698400 tri-linear hexahedral elements and is refined in the region $0 \leq x \leq 1.7$. One single computational mesh for the discretization of both poroelastic domains, fitted to the interface Γ^{FP}, consisting of 62100 tri-linear hexahedral elements is applied. The discretization in time is performed by the backward Euler scheme $\theta = 1$ with a time step length of $\Delta t = 0.0005$ for $t \in]0, 0.195]$ and $\Delta t = 0.000125$ for $t \in]0.195, 0.3]$ to account for the changing system dynamics. The initial state of the problem is the zero-state: $\underline{\mathring{\boldsymbol{v}}}^{\mathrm{F}} = \underline{\mathring{\boldsymbol{u}}}^{\mathrm{P}} = \underline{\mathring{\boldsymbol{v}}}^{\mathrm{P^S}} = \underline{\mathring{\boldsymbol{v}}}^{\mathrm{P}} = \underline{\mathbf{0}}$. The monolithic linear system, which consists of approximately 3 million degrees of freedom, is attacked by the iterative GMRES algorithm, preconditioned by a three block Gauss-Seidel iteration in combination with efficient algebraic multigrid applied on the fluid, poroelastic fluid, and poroelastic mixture block separately (for details on the preconditioning approach see the work of Verdugo and Wall [214]).

Computed Results and Discussion Computed results for five different points in time are shown in Figure 4.18. In the initial phase, time $t = 0.04$, a symmetric deflection of the plate Ω^{P_2} due to the applied body force can be observed. The streamlines indicate that the outer flow follows basically the contour of the poroelastic body due to the low velocity. Triggered by the increased inflow velocity at $t = 0.14$, the flow is detached in downstream direction of Ω^{P_1} as indicated by the streamlines. This change in flow characteristics also results in a drop of the fluid pressure behind the poroelastic crossbeam. The flow induced displacement of the plate Ω^{P_2} in positive z-direction remains symmetric with respect to the $(y = 0.5)$-plane. For $t \geq 0.275$, this has changed and the plate deflects asymmetrically. Additionally, due to the oscillatory interaction of the fluid flow and the poroelastic crossbeam, a spatial variation of the pressure in x-direction can be observed.

A detailed view on the computed solution in the poroelastic domain is given in Figure 4.19. Due to the flow stagnation point in front of the poroelastic crossbeam, an increased pressure p^{P} can be observed. This induces a fluid flow through the poroelastic domain Ω^{P_1}. In contrast to the flow in the crossbeam, only very small velocities occur in the plate Ω^{P_2} due to the low pressure gradient of the surrounding flow. A comparison of the poroelastic fluid pressure in the plate between the early point in time $t = 0.08$ and the subsequent points in time $t = 0.28$ and $t = 0.3$ reveals that the pressure is essentially defined by the outer flow.

The computed vertical displacement at three selected points (marked by red points in Figure 4.17) is shown in Figure 4.20 (left). Therein, the points P_{y+} and P_{y-} correspond to the tips of the poroelastic plate Ω^{P_2}. It can be seen that in the initial phase $t < 0.10$, the plate deflects in negative z-direction due to the applied body force. During $0.10 < t < 0.15$, a symmetric deflection of the plate induced by the outer flow can be observed. After a transition phase, a periodically repeating asymmetrical deflection with increased amplitude of both tips can be observed for $t > 0.20$. The point P_{y0} is positioned in the center of the poroelastic crossbeam Ω^{P_1}. Whereas almost no vertical displacement occurs in the initial phase, for $t > 0.22$ a vibration of the crossbeam with higher frequency than the plate deflection can be observed. The computed fluid velocity magnitude at three selected points above the poroelastic crossbeam (marked by

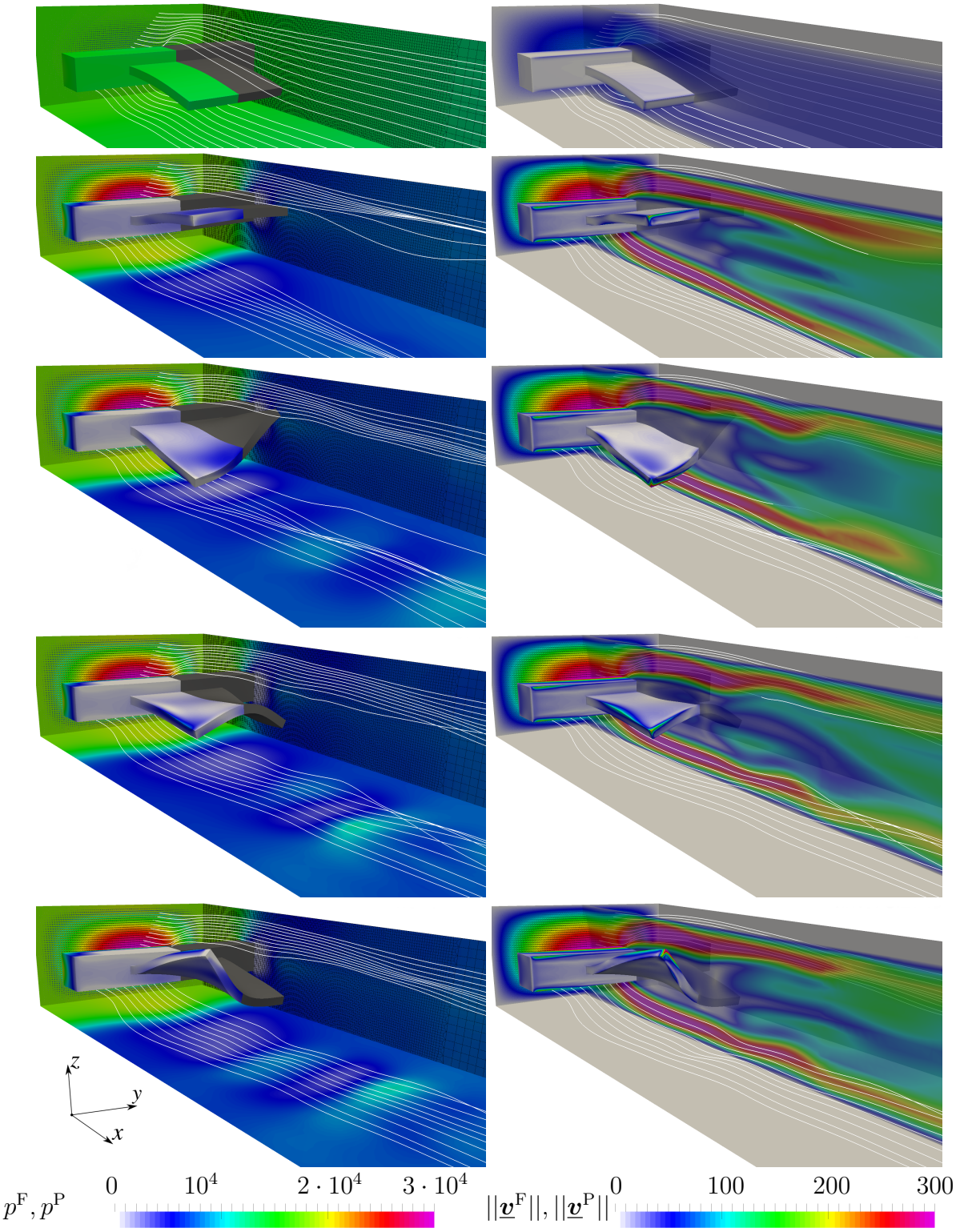

Figure 4.18: Computed pressure (p^{F} and p^{P}) in the left column and velocity magnitude ($||\underline{\boldsymbol{v}}^{\mathrm{F}}||$ and $||\underline{\boldsymbol{v}}^{\mathrm{P}}||$) in the right column at five instances in time. Time $t = 0.04$ (first row), $t = 0.14$ (second row), $t = 0.275$ (third row), $t = 0.287$ (fourth row), and $t = 0.294$ (last row). White lines show the streamlines computed from the fluid velocity $\underline{\boldsymbol{v}}^{\mathrm{F}}$. In the right column, the velocity magnitude is additionally visualized on the plane $y = b/2$. The computed fluid solution in the domains Ω^{P_1} and Ω^{P_2} is visualized solely for $y < b/2$ whereas the remaining part is colored gray to tidy up the presentation.

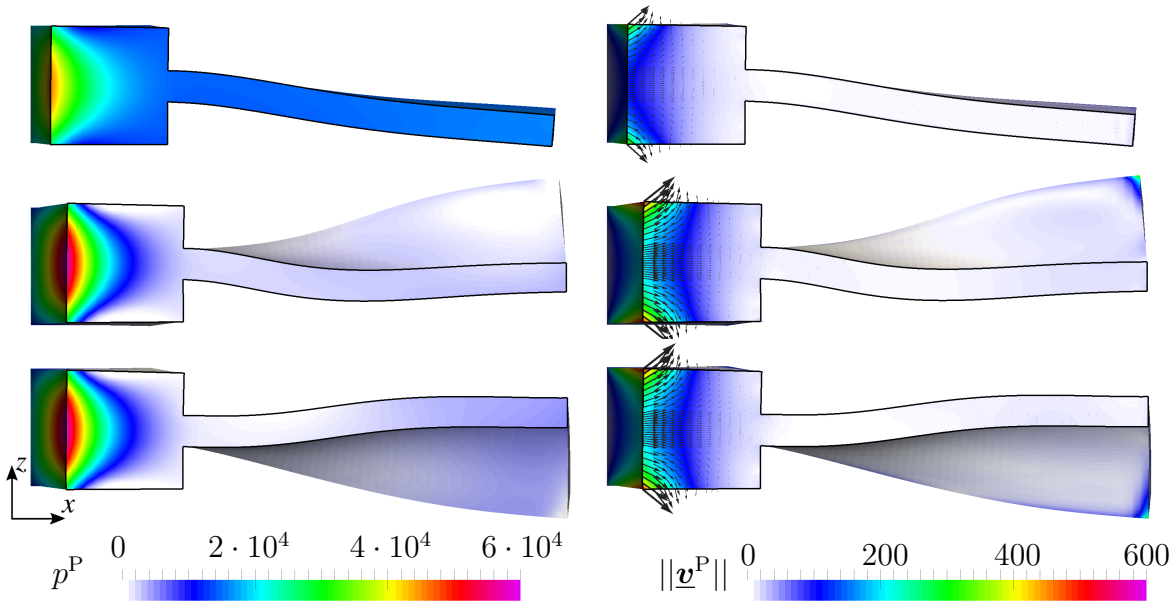

Figure 4.19: Detailed visualization of the half poroelastic domains Ω^{P_1} and Ω^{P_2} with $y > 0.5$. Computed pressure p^{P} in the left column and velocity magnitude $||\underline{\boldsymbol{v}}^{\mathrm{P}}||$ in the right column for time $t = 0.08$ (top row), $t = 0.28$ (mid row), and $t = 0.3$ (bottom row). The black arrows in the right column visualize the velocity $\underline{\boldsymbol{v}}^{\mathrm{P}}$.

blue points in Figure 4.17) is shown in Figure 4.20 (right). At all three points the velocity increases with the inflow velocities until $t = 0.125$. The highest velocity is reached at the point $P_{x0.5}$ which is situated directly above the deformed crossbeam. Starting from $t = 0.22$, oscillations at all three points can be observed. A comparison with the vibration frequency of the crossbeam (see displacement of point P_{y0}), reveals the interaction between the fluid flow and the vertical deformation of the crossbeam.

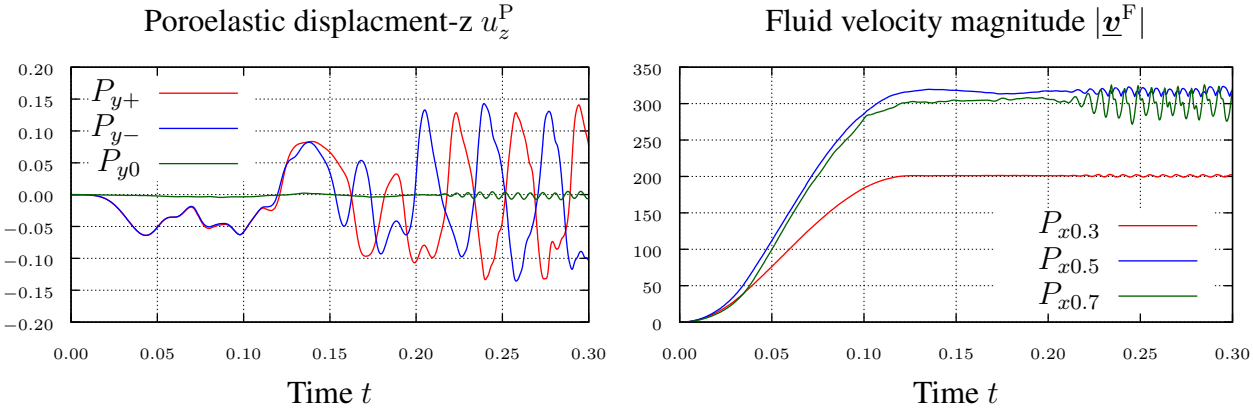

Figure 4.20: Computed vertical displacement u_z^{P} for three different points in space. The reference coordinates of the points are: $P_{y+} : \underline{\boldsymbol{X}}^{\mathrm{P}} = [1.0, 0.751, 0.27]^{\mathsf{T}}$, $P_{y-} : \underline{\boldsymbol{X}}^{\mathrm{P}} = [1.0, 0.251, 0.27]^{\mathsf{T}}$, and $P_{y0} : \underline{\boldsymbol{X}}^{\mathrm{P}} = [0.5, 0.5, 0.325]^{\mathsf{T}}$. These points are marked by red points in Figure 4.17 (left). Computed velocity magnitude $||\underline{\boldsymbol{v}}^{\mathrm{F}}||$ for three different points in space. The coordinates of the points are: $P_{x0.3} : \underline{\boldsymbol{x}} = [0.3, 0.5, 0.4]^{\mathsf{T}}$, $P_{x0.5} : \underline{\boldsymbol{x}} = [0.5, 0.5, 0.4]^{\mathsf{T}}$, $P_{x0.7} : \underline{\boldsymbol{x}} = [0.7, 0.5, 0.4]^{\mathsf{T}}$. These points are marked by blue points in Figure 4.17 (right).

5 A Consistent Approach for Fluid-Structure-Contact Interaction Based on a Porous Flow Model for Rough Surface Contact[1]

Simulation approaches for FSCI, especially if requested to be consistent even down to real contact scenarios, belong to the most challenging and still unsolved problems in computational mechanics. The main challenges are twofold – twofold one is to have an appropriate physical model for this scenario, and the other is to have a numerical method that is capable of working and being consistent down to a zero gap. When analyzing such challenging setups of FSI that include contact of submersed solid components it gets obvious that the influence of surface roughness effects is often essential for a physically consistent modeling of such configurations. Thus, a continuum mechanical model which is able to include the effects of the surface microstructure in a FSCI framework is presented in this chapter.

To reduce the high computational demands arising from a fully-resolving computation, as well as the necessity to know the exact microstructure, an averaged representation for the mixture of fluid and solid on the rough surfaces, which is of major interest for the macroscopic response of such a system, is introduced herein. This homogenized model includes the average physical behavior of the roughness layer into the FSCI framework. While this has not been done for real FSI so far, similar ideas have been successfully applied to consider roughness within Reynolds equation based formulations. Homogenizing a domain which consists of a fluid-filled deformable microstructure results in a poroelastic, fluid-saturated averaged domain. The basic idea of modeling surface roughness as a porous layer can already be found in the works of Li [143] and Tichy [210]. The novel approach is based on a similar idea but also works for general FSI problems, applicable for arbitrary shaped domains, including finite deformations of the solid, topological changes of the fluid domain and rearrangement of all interface conditions. Averaging the surface roughness as a poroelastic layer still enables accounting for many physically essential effects on a macroscopic level and, thus, in an averaged sense. Examples are the fluid pressure distribution between contacting bodies, stresses exchanged between contacting solids, the deformation of the roughness layer and the resulting fluid to solid fraction within the layer. Having this physical information available also allows including additional models to treat specific physical phenomena of the general problem of colliding bodies in fluid such as, for instance, friction of mixed lubrication contact or wear, which, however, are not in the focus of this thesis.

The inherent coupling of the macroscopic fluid flow and the flow inside the rough surfaces, the stress exchange of all contacting solid bodies that are involved, and the interaction between fluid

[1]This chapter is adapted from the author's publication [1].

and solid is included in the design of the model. Although the physical model is not restricted to finite element based methods, a numerical approach with its core based on the CutFEM, which is enabling topological changes of the fluid domain to solve the presented model numerically, is introduced. Such a CutFEM-based approach is able to deal with the numerical challenges mentioned above. Different test cases give a perspective towards the potential capabilities of the presented physical model and numerical approach.

This chapter is organized as follows: In Section 5.1, the porous flow based model for rough surface FSCI is introduced. The formulation of the overall coupled problem, including a brief recapitulation of already discussed fundamentals and a discussion of still missing interface conditions to incorporate contact between poroelastic and solid bodies is given in Section 5.2. In Section 5.3, the utilized approach for the numerical solution of the rough surface FSCI problem is presented. All applied numerical approaches which were already discussed in the previous chapters are reviewed. Subsequently, the formulation to take contact between poroelastic and solid bodies into account, is introduced. The overall discrete formulation to be solved by the nonlinear solution procedure is summarized in Section 5.4. Three configurations, including a leakage test, a rough surface contacting stamp and a non-return valve, are presented and analyzed in Section 5.5.

5.1 Rough Surface Contact Model

A typical configuration of FSCI problems, with fluid domain $\tilde{\Omega}^{\mathrm{F}}$ and structural bodies occupying domain $\tilde{\Omega}^{\mathrm{S}}$, is shown in Figure 5.1 (left). Herein, solid surfaces do not include any information about their present microstructure. This simplification is a good approximation for interfaces between structural bodies and the fluid such as Γ^{FS} in Figure 5.1 (left), where the distance to the next interface or boundary is large compared to the average height of surface asperities. In this case, the influence of surface roughness on the physical response of the fluid-structure interaction system is completely negligible. However, for interfaces such as $\Gamma^{\mathrm{FS},c}$ in Figure 5.1 (left), where the surfaces of solid bodies approach each other and the size of the fluid gap in between can get very small or even vanish, this argumentation does not hold anymore. In the following, the term "gap" or "fluid gap" is exclusively used to specify the normal distance between approaching or contacting surfaces. As soon as the gap is in the same order of magnitude as the roughness height (see Figure 5.1 (right)), effects caused by the microstructure of the surfaces will start to influence the macroscopic physical behavior of the system. Finally, when first surface asperities come into contact, assuming smooth surfaces is definitely far off from the physical response of such an FSCI system. As the prediction of effects dominated by rough surfaces such as, e.g. leakage or lubrication is of great importance, a model to include surface roughness of these contacting surfaces into an FSCI framework in an computationally efficient way will be presented in the following.

The domain of interest Ω^{P} consists of a part of the fluid domain $\hat{\Omega}^{\mathrm{F}}$ between the contacting surfaces, as well as the structural domain $\hat{\Omega}^{\mathrm{S}}$ in the neighborhood of the rough surface (see Figure 5.2). The overall domain $\Omega = \tilde{\Omega}^{\mathrm{S}} \cup \tilde{\Omega}^{\mathrm{F}} = \Omega^{\mathrm{S}} \cup \Omega^{\mathrm{F}} \cup \Omega^{\mathrm{P}}$ is composed of the fluid filled poroelastic domain $\Omega^{\mathrm{P}} = \hat{\Omega}^{\mathrm{S}} \cup \hat{\Omega}^{\mathrm{F}}$, the remaining solid domain $\Omega^{\mathrm{S}} = \tilde{\Omega}^{\mathrm{S}} \setminus \hat{\Omega}^{\mathrm{S}}$, and the remaining fluid domain $\Omega^{\mathrm{F}} = \tilde{\Omega}^{\mathrm{F}} \setminus \hat{\Omega}^{\mathrm{F}}$.

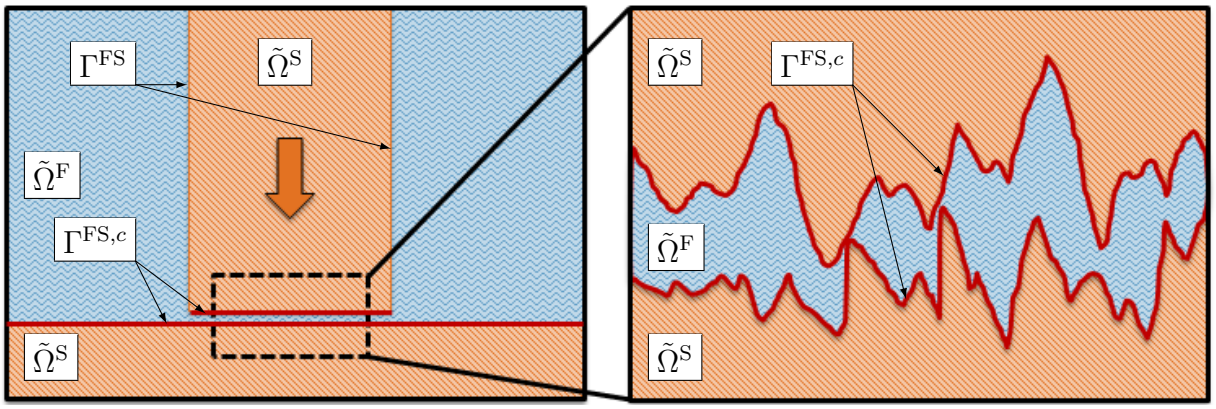

Figure 5.1: Typical configuration of an FSCI problem (left). Real surface geometry including the microstructure of rough bodies before contact (right).

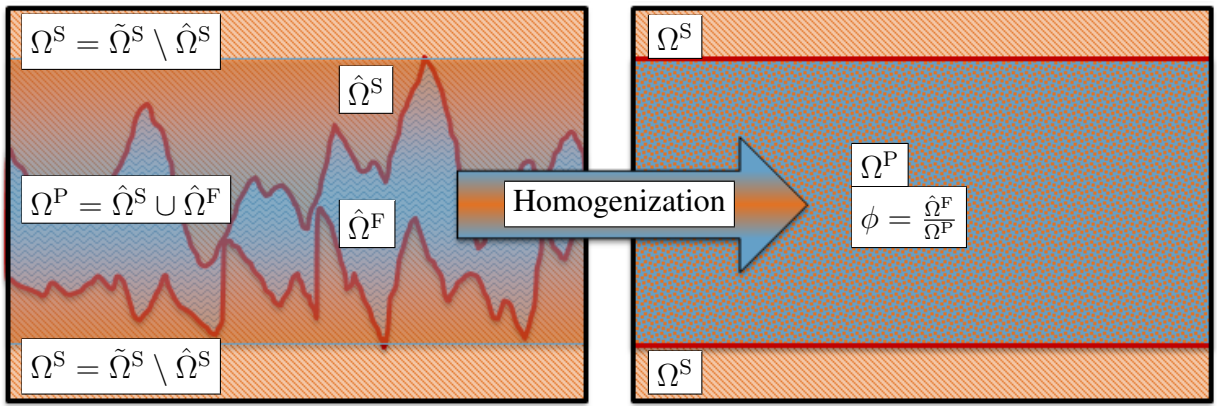

Figure 5.2: Detailed view of a potential microstructure between the contacting surfaces (left), represented by a homogenized poroelastic domain Ω^{P} with porosity ϕ in the proposed model (right).

This poroelastic region is modeled in an homogenized manner, an approach well known from porous media mechanics, see e.g. the related works of Chapelle and Moireau [57], Coussy [67], Lewis and Schrefler [142], Schrefler and Scotta [193] and Vuong *et al.* [216]. The resulting poroelastic layer describes the fluid flow and the structural elastodynamics in an averaged sense in every point of the poroelastic domain Ω^{P}. Herein, the porosity $\phi = \mathrm{vol}(\hat{\Omega}^{\mathrm{F}})/\mathrm{vol}(\Omega^{\mathrm{P}})$ specifies the ratio of fluid volume inside the poroelastic layer. The model describing this poroelastic layer should be able to represent the influence of structural deformation on the fluid flow and vice versa. Furthermore, the deformation of the roughness layer arising from applied external stress or external deformation on the outer boundaries of the poroelastic layer has to be considered. A coupling of the poroelastic layer to the outer fluid flow has to be guaranteed as well.

The height of this layer in the undeformed initial configuration is given by the state when first asperities establish contact (see domain Ω^{P} in Figure 5.2 (left)). Starting from this state, elastic forces can be transmitted via the poroelastic layer. Nevertheless, for the practical setup of such a problem, it is not necessary to accurately determine this height. The specified layer height needs to correspond rather to the average material model of the poroelastic layer. Considering the mechanical stiffness of the poroelastic layer as an example, a thicker layer with reduced initial stiffness can be comparable to a thinner layer with increased initial stiffness. In principle,

the chosen layer height only defines from which point on an elastic response occurs, but not how the stiffness changes when the layer is compressed. This last relation is included in the nonlinear material law of the poroelastic layer.

A poroelastic layer has to be added (at least on one of the contacting interfaces) to all interfaces $\Gamma^{\mathrm{FS},c}$, which potentially come into contact. The specification of the potentially contacting subset $\Gamma^{\mathrm{FS},c}$ of the interface Γ^{FS} has to be given by the user, just as in almost all other contact simulations, and allows reducing the cost of the performed computations. Adding a poroelastic layer to both contacting surfaces seems most natural from a modeling point of view. Such an approach could be mainly advantageous for representing processes occurring before contact establishes (Figure 5.4 (left)). Since the roughness is not expected to have a significant effect on the overall physical behavior of an FSI system in many cases, the two layer variant is not included in the presented numerical approach. Considering a poroelastic layer only on one of the contacting surfaces is capable of representing essential physical effects, such as leakage, in the case contact is established (Figure 5.4 (right)). From a computational point of view this choice simplifies the formulations as no contact formulation of two poroelastic bodies (including fluid mass transfer) is required. Additionally, only half or less of the interface area requires a poroelastic layer which is twice as high. The free choice, which one of the two contacting surfaces is supplemented by a roughness layer, is left to the user. A numerical formulation capable of consistently treating contact of two poroelastic bodies is presented in Chapter 7.

As the influence of the porous layer is negligibly small if bodies are not close to contact, a porous layer for all fluid structure interfaces Γ^{FS} does not seem to be necessary. To confirm this statement, the fluid velocity profiles for a fully developed parallel channel flow of a coupled "free" flow domain (Ω^{F}) and a porous flow domain (Ω^{P}) are shown in Figure 5.3. It can be seen that for an increasing ratio of fluid volume to porous volume, the velocity profile approaches the Poiseuille flow ("none"). This is equivalent to the statement that a porous layer can be neglected if it is sufficiently small compared to the distance to the next boundary in the adjacent "free" flow region.

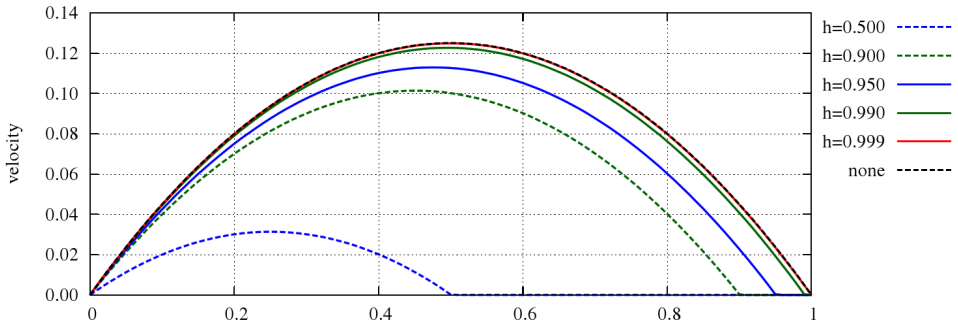

Figure 5.3: Velocity profiles for fully developed parallel 2D-flow of coupled "free" flow [0,h] and porous flow [h,1] in a channel of height 1. Five configurations with a different ratio of the fluid domain (height h) to the poroelastic domain (height 1-h) are shown. The configuration "none" considers free flow without a poroelastic domain (Poiseuille flow). The parameters of the flow are: dynamic viscosity $\mu^{\mathrm{F}} = 1$, porosity $\phi = 0.5$, permeability $K = 10^{-6}$, pressure gradient in flow direction $\partial p^{\mathrm{F}}/\partial x = \partial p^{\mathrm{P}}/\partial x = -1$, and coefficient $\alpha_{BJ} = 1$ on Γ^{FP}.

In Figure 5.4, a schematic sketch of the final model for the rough surface FSCI is presented, where all involved physical domains with different physical principles and the interfaces be-

tween these domains are shown. It should be pointed out that the fluid as well as the structural domain no longer include the volume occupied by the rough surface, as this is represented by the poroelastic model.

A review of the generic overall problem configuration introduced in Section 2.1.1 reveals, that the governing equations for the whole domain Ω, which is split into three resulting domains, namely the structural domain Ω^{S}, the fluid domain Ω^{F}, and the poroelastic domain Ω^{P} with appropriate boundary conditions on the outer boundary $\partial\Omega$, are already included in this generic problem setup. Thus, the governing equations in these domains, the conditions on the interfaces Γ^{FS} between the fluid domain and structural domain, and the conditions on the interfaces Γ^{FP} between the fluid domain and the poroelastic domain were already introduced in Chapter 2. The interface of closed contact between the poroelastic layer and the structural domain $\Gamma^{\mathrm{PS},c}$ and the change of interface conditions for the coupled problem to formulate the rough surface FSCI problem will be discussed in this chapter.

In contrast to the widely used Reynolds equation in elastohydrodynamic lubrication (EHL), where the no-slip condition is incorporated directly, the averaging procedure does not introduce any boundary conditions onto the fluid flow. This allows the incorporation of spatial and temporal changing boundary/coupling conditions during the computation. As a result, a representation of the different states of colliding solid bodies in surrounding fluid, which is continuous in time, is possible.

To illustrate this feature of the presented model, the impact of two submerged bodies serves as an example. As long as the distance between both structural bodies is large, the influence of the poroelastic layer is small and a “free-flowing” fluid similar to classical FSI problems is described. Once the gap between both contacting surfaces is in the same order of magnitude as the roughness height amplitude, a continuously increasing part of the fluid volume flow passes through the poroelastic layer. Further reduction of the fluid gap until first surface asperities start to contact is directly represented by contact between the poroelastic layer and the solid body. As soon as all of the fluid in the gap is inside the microstructure of the surfaces, the entire fluid flow passes through the poroelastic layer. Further increase of the contact pressure will result in progressing deformation of the poroelastic layer, which results in a reduction of the fluid fraction ϕ inside the layer. This goes along with an increase of fluid resistance and therefore reduced flow

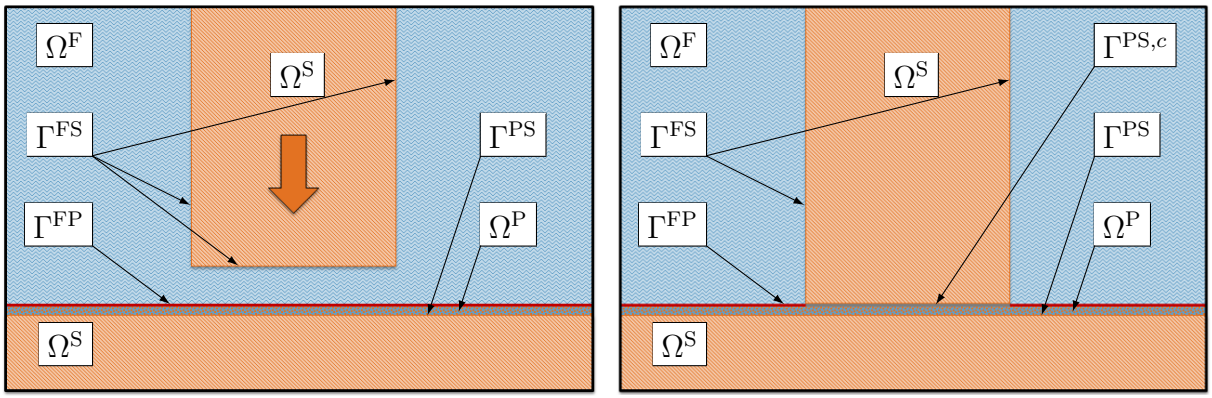

Figure 5.4: Proposed rough surface contact model for fluid-structure interaction, including all computationally essential domains $\Omega^{\mathrm{S}}, \Omega^{\mathrm{F}}, \Omega^{\mathrm{P}}$ and interfaces between these domains $\Gamma^{\mathrm{FS}}, \Gamma^{\mathrm{FP}}, \Gamma^{\mathrm{PS}}, \Gamma^{\mathrm{PS},c}$; not in contact (left), in contact (right).

or "leakage rate" for a specific fluid pressure gradient in the flow direction. Finally, for high loads in relation to the structural stiffness, the fluid fraction will approach the vanishing limit, whereby only the structural part is left between the contacting surfaces. It should be mentioned that this exemplary sequence of steps, which was described in detail, occurs just in the case that small variations in the fluid pressure and velocity far-fields arise during the approaching process of both structural bodies. If this is not the case, different pathways will be passed, for instance when an increasing fluid pressure deforms the poroelastic layer such that the contained fluid fraction is increased, which finally can lead to a "lift-off" of the contacting surfaces.

Remark 5.1 (The stiffness of the poroelastic layer)**.** *A comparison of the solid bulk material and the stiffness of rough contacting surfaces shows that the initial tangent stiffness is smaller due to the deformation of single contacting asperities. Increasing contact stress leads to a rapid increase in the tangent stiffness, as the porosity ϕ and therefore the fluid fraction decreases. This behavior is reflected by an increased nonlinearity of the strain energy function $\psi^{\mathrm{P},skel}$ compared to the bulk material and shown experimentally e.g. in the work of Zhai* et al. *[235].*

Remark 5.2 (A computationally assisted approach for the estimation of poroelastic material parameters)**.** *In the following, a computationally assisted way to determine a proper set of parameters for the poroelastic layer of a specific rough microstructure is presented. The parameters include the porosity ϕ, the permeability $\underline{\boldsymbol{k}}$, and the strain energy functions $\psi^{\mathrm{P},skel}$ and $\psi^{\mathrm{P},vol}$. To estimate the material parameters of the poroelastic layer for specific surfaces, the macroscopic material behavior of both contacting solid bodies as well as a resolved, representative microstructure geometry of the rough surfaces is required. First, performing direct contact simulations without any fluid pressure contribution for characteristic parts of the resolved rough surfaces allows specifying the material parameters of strain energy function $\psi^{\mathrm{P},skel}$ of the poroelastic layer. Measuring the void space allows the determination of the porosity ϕ. Furthermore, by including a predefined normal load, which represents the fluid pressure, on the contact interface of the direct contact simulations, the correlation of the fluid pressure and the solid phase compression can be analyzed. This allows identifying the parameters of the strain energy function $\psi^{\mathrm{P},vol}$. To specify the permeability $\underline{\boldsymbol{k}}$ numerically, a resolved computation of the fluid flow between the rough surfaces can be consulted. Performing these fluid flow simulations for several deformation states allows specifying the relation of permeability and porosity $\underline{\boldsymbol{k}} = \underline{\boldsymbol{k}}(\phi)$.*

5.2 The Continuous Rough Surface FSCI Problem

Many aspects to formulate the rough surface FSCI problem, presented in Section 5.1, have been already depicted in Chapter 2. In order to draw the attention of the reader to the essential parts presented previously, at first, the affected sections are referenced and briefly recapitulated in the following. Subsequently, appropriate coupling conditions on the "active" contact interface between the solid domain and the poroelastic domain $\Gamma^{\mathrm{PS},c}$ are discussed in Section 5.2.2. This is followed by an examination of the change of all prevalent interface coupling conditions in the context of the entire rough surface FSCI problem in Section 5.2.3.

5.2.1 Composition of Fundamentals for the Computational Solution of the Rough Surface FSCI

A comparison of the problem configuration in Figure 2.1 introduced in Section 2.1.1 with the rough surface FSCI problem configuration in Figure 5.4 reveals that the generic overall problem includes already all types of domains and interfaces to formulate the rough surface FSCI problem. Thus, most governing equations and underlying interface/boundary conditions of this abstract configuration were already discussed in Chapter 2.

The overall domain $\Omega = \Omega^{\mathrm{S}} \cup \Omega^{\mathrm{F}} \cup \Omega^{\mathrm{P}}$ is given by the union of the structural domain, the fluid domain, and the poroelastic domain. The outer boundary includes the union of all types of boundaries $\partial\Omega = \Gamma^{\mathrm{S,D}} \cup \Gamma^{\mathrm{S,N}} \cup \Gamma^{\mathrm{F,D}} \cup \Gamma^{\mathrm{F,N}} \cup \Gamma^{\mathrm{P,D}} \cup \Gamma^{\mathrm{P,N}} = \Gamma^{\mathrm{S,D}} \cup \Gamma^{\mathrm{S,N}} \cup \Gamma^{\mathrm{F,D}} \cup \Gamma^{\mathrm{F,N}} \cup \Gamma^{\mathrm{P^F,D}} \cup \Gamma^{\mathrm{P^F,N}}$. The balance of linear momentum (2.15) in the structural domain Ω^{S} as well as the conditions on the boundaries $\Gamma^{\mathrm{S,D}}$ and $\Gamma^{\mathrm{S,N}}$ (2.19) have to be fulfilled as explained in detail in Section 2.1.4. The governing equations in the fluid domain Ω^{F}, which are the Navier-Stokes equations including the balance of mass (2.27) and the balance of linear momentum (2.28), as well as all required conditions on the boundaries $\Gamma^{\mathrm{F,D}}$ and $\Gamma^{\mathrm{F,N}}$ (2.31), are discussed in Section 2.1.5. The underlying system of equations for the poroelastic domain Ω^{P}, including the balance of fluid mass (2.42), the balance of linear momentum for the fluid phase (2.43), and the balance of linear momentum for the porous mixture (2.46), is already presented in Section 2.1.6. Therein, adequate boundary conditions (2.53) and (2.54) on the different boundaries $\Gamma^{\mathrm{P^F,D}}$, $\Gamma^{\mathrm{P^F,N}}$, $\Gamma^{\mathrm{P,D}}$, and $\Gamma^{\mathrm{P,N}}$ are discussed. Describing the rough surface FSCI problem by the aforementioned equations results in a system which has to be solved for the structural displacement $\underline{\boldsymbol{u}}^{\mathrm{S}}$ in the structural domain Ω^{S}, the fluid velocity $\underline{\boldsymbol{v}}^{\mathrm{F}}$ and the fluid pressure p^{F} in the fluid domain Ω^{F}, and the porous fluid velocity $\underline{\boldsymbol{v}}^{\mathrm{P}}$, the porous fluid pressure p^{P}, and the macroscopic displacement of the porous domain $\underline{\boldsymbol{u}}^{\mathrm{P}}$ in the poroelastic layer Ω^{P}.

On the interface Γ^{FS} between the viscous fluid and the elastic structures, the dynamic equilibrium (2.59) (with $\underline{\hat{\boldsymbol{g}}}_{\sigma}^{\mathrm{FS}} = \underline{\mathbf{0}}$) and the kinematic no-slip condition (2.59) (with $\underline{\hat{\boldsymbol{g}}}_{v}^{\mathrm{FS}} = \underline{\mathbf{0}}$) have to be fulfilled as depicted in Section 2.1.7. The conditions on the interface between the viscous fluid and the poroelastic layer Γ^{FP} consist of the dynamic equilibrium of the fluid and the porous mixture (2.61) (with $\underline{\hat{\boldsymbol{g}}}_{\sigma}^{\mathrm{FP}} = \underline{\mathbf{0}}$), the dynamic equilibrium of the fluid and the porous fluid (2.62) (with $\hat{g}_{\sigma}^{\mathrm{FP},n} = \underline{0}$), the balance of mass on the interface (2.63) (with $\underline{\hat{\boldsymbol{g}}}^{\mathrm{FP},n} = \underline{\mathbf{0}}$), and the Beavers-Joseph (BJ) or Beavers-Joseph-Saffmann (BJS) condition (2.64) (with $\underline{\hat{\boldsymbol{g}}}^{\mathrm{FP},t} = \underline{\mathbf{0}}$), as discussed in Section 2.1.8.

In Section 2.1.10, general explanations concerning solid-solid contact, including the projection (2.68) and the geometric gap (2.69) between contacting interfaces as well as the balance of linear momentum on the contact interface (2.70) are given. In this chapter, the extension to solid-poroelastic contact including the representation of the "fictive" fluid traction $\underline{\tilde{\boldsymbol{h}}}^{\mathrm{F,I}}$ in the contact zone (see Section 2.1.10.2) by the porous fluid pressure p^{P} of the poroelastic layer is introduced.

5.2.2 Interface of Poroelastic Domain and Structural Domain in the Contact Case

The interfaces between the poroelastic layer and the structural domain $\Gamma^{\mathrm{PS}} \cup \Gamma^{\mathrm{PS},c} = \partial\Omega^{\mathrm{P}} \cap \partial\Omega^{\mathrm{S}} = \Gamma^{\mathrm{P,I}} \cap \Gamma^{\mathrm{S,I}}$ consist of a matching part Γ^{PS} and the contacting subset $\Gamma^{\mathrm{PS},c}$ (see Figure 5.4 (right)), which is only non-zero in the contact case. Here, the focus is on the contacting part only, since the physical and numerical treatment of interfaces such as Γ^{PS} can be found in the literature concerning domain decomposition (see e.g. the work of Wohlmuth [228]) for the coupling of displacement degrees of freedom and in the work of Vuong *et al.* [217] for the impermeability constraint. Considering frictionless contact, the following conditions need to be fulfilled

$$g^n := \left(\underline{\boldsymbol{x}}_{\Gamma}^{\mathrm{S}} - \underline{\boldsymbol{x}}_{\Gamma}^{\mathrm{P}}\right) \cdot \underline{\boldsymbol{n}} = 0 \qquad \text{on } \Gamma^{\mathrm{PS},c}, \tag{5.1}$$

$$\phi \left(\underline{\boldsymbol{v}}^{\mathrm{P}} - \frac{\partial \underline{\boldsymbol{u}}^{\mathrm{P}}}{\partial t}\right) \cdot \underline{\boldsymbol{n}} = 0 \qquad \text{on } \Gamma^{\mathrm{PS},c}, \tag{5.2}$$

$$\underline{\boldsymbol{n}} \cdot \underline{\boldsymbol{\sigma}}^{\mathrm{P}} \cdot \underline{\boldsymbol{n}} = \underline{\boldsymbol{n}} \cdot \underline{\boldsymbol{\sigma}}^{\mathrm{S}} \cdot \underline{\boldsymbol{n}} \qquad \text{on } \Gamma^{\mathrm{PS},c}. \tag{5.3}$$

$$\underline{\boldsymbol{t}}_i \cdot \underline{\boldsymbol{\sigma}}^{\mathrm{P}} \cdot \underline{\boldsymbol{n}} = \underline{\boldsymbol{t}}_i \cdot \underline{\boldsymbol{\sigma}}^{\mathrm{S}} \cdot \underline{\boldsymbol{n}} = 0 \quad i = 1,2 \qquad \text{on } \Gamma^{\mathrm{PS},c}. \tag{5.4}$$

Herein, (5.1) enforces the zero gap between the structural body and the porous layer, with $\underline{\boldsymbol{x}}_{\Gamma}^{\mathrm{P}}$ being the position on the interface $\Gamma^{\mathrm{P,I}}$ and $\underline{\boldsymbol{x}}_{\Gamma}^{\mathrm{S}} = \check{\underline{\boldsymbol{x}}}\left(\underline{\boldsymbol{x}}_{\Gamma}^{\mathrm{P}}\right)$ the projection of $\underline{\boldsymbol{x}}_{\Gamma}^{\mathrm{P}}$ in direction $\underline{\boldsymbol{n}}$ onto the interface $\Gamma^{\mathrm{S,I}}$ (see Section 2.1.10). Details concerning the utilized projection between both interfaces are given by Popp *et al.* [172]. Equation (5.2) represents the mass flow balance on the interface, where the relative fluid flow has to vanish due to the impermeability of the solid. Finally, conditions (5.3) and (5.4) reflect the dynamic equilibrium between poroelastic and solid domain in normal and tangential direction, respectively. The unit normal vector $\underline{\boldsymbol{n}}$ is chosen uniquely on the interface $\Gamma^{\mathrm{S},c}$ or $\Gamma^{\mathrm{P},c}$. For simplicity frictionless contact is considered in condition (5.4). Nevertheless, the presented framework can also be extended to the frictional case in a subsequent step. It should be mentioned that a portion of the contact traction in (5.3) is carried by the porous fluid pressure p^{P} as it forms a part of the poroelastic stress tensor $\underline{\boldsymbol{\sigma}}^{\mathrm{P}}$.

5.2.3 Change of Interface Conditions in the Coupled Problem

In the foregoing explanations, interfaces and their corresponding conditions were considered to be independent of each other. It is obvious that occurring contact between the poroelastic layer and the structural domain modifies not only the "active" contact interface $\Gamma^{\mathrm{PS},c}$, but also the interfaces between the fluid and the poroelastic domain Γ^{FP} as well as the fluid and the structural domain Γ^{FS}. The union of all three interfaces Γ is given by the current configuration of the solid and poroelastic domain, in particular of the respective parts of the outer boundaries $\Gamma = \Gamma^{\mathrm{PS},c} \cup \Gamma^{\mathrm{FS}} \cup \Gamma^{\mathrm{FP}} = \Gamma^{\mathrm{F,I}} \cup \Gamma^{\mathrm{P,I}} \cup \Gamma^{\mathrm{S,I}}$. The criteria specifying the different interface types on the interface Γ, are given by the following Karush-Kuhn-Tucker conditions, which need to be fulfilled

$$\left(\underline{\boldsymbol{x}}_{\Gamma}^{\mathrm{S}} - \underline{\boldsymbol{x}}_{\Gamma}^{\mathrm{P}}\right) \cdot \underline{\boldsymbol{n}}^{\mathrm{P}} \geq 0 \quad \text{on} \quad \Gamma, \tag{5.5}$$

$$\underline{\boldsymbol{h}}^{\mathrm{I}} \cdot \underline{\boldsymbol{n}}^{\mathrm{P}} \leq 0 \quad \text{on} \quad \Gamma, \tag{5.6}$$

$$\left[\left(\underline{\boldsymbol{x}}_{\Gamma}^{\mathrm{S}} - \underline{\boldsymbol{x}}_{\Gamma}^{\mathrm{P}}\right) \cdot \underline{\boldsymbol{n}}^{\mathrm{P}}\right] \left[\underline{\boldsymbol{h}}^{\mathrm{I}} \cdot \underline{\boldsymbol{n}}^{\mathrm{P}}\right] = 0 \quad \text{on} \quad \Gamma. \tag{5.7}$$

These conditions are in principal equal to (2.77)-(2.79), which are presented in Section 2.1.10.2. However, conditions (6.5)-(6.6) are modified for the case of poroelastic-solid contact. Herein, condition (6.5) guarantees that there is always a positive gap or no gap between potentially contacting bodies. Additionally, (6.6) restricts the minimal stress transferred directly by compression between the solid bodies to the surrounding fluid normal traction. Herein, $\underline{\boldsymbol{h}}^{\mathrm{I}}$ (e.g. $\underline{\boldsymbol{h}}^{\mathrm{I}} = \underline{\boldsymbol{\sigma}}^{\mathrm{P}} \cdot \underline{\boldsymbol{n}}^{\mathrm{P}} + p^{\mathrm{P}} \underline{\boldsymbol{n}}^{\mathrm{P}}$ (available on $\Gamma^{\mathrm{PS},c}$ and Γ^{FP}) or $\underline{\boldsymbol{h}}^{\mathrm{I}} = \underline{\boldsymbol{\sigma}}^{\mathrm{S}} \cdot \underline{\boldsymbol{n}}^{\mathrm{P}} - \underline{\boldsymbol{\sigma}}^{\mathrm{F}} \cdot \underline{\boldsymbol{n}}^{\mathrm{P}}$ (available on Γ^{FS})) is the traction difference between the total contact traction and the ambient fluid stress. This condition is a result of the assumption that the time interval for the formation of a fully covering fluid film on top of the rough microstructure is negligible and that this process does not need to be modeled. As soon as the local structural stress is smaller than the fluid stress (e.g. at single asperities), this fluid film will develop. In Figure 5.5, a schematic visualization of this process is given. Finally, (6.7) enforces either a zero gap between both interfaces (see equation (6.5)) or a vanishing relative traction (see equation (6.6)).

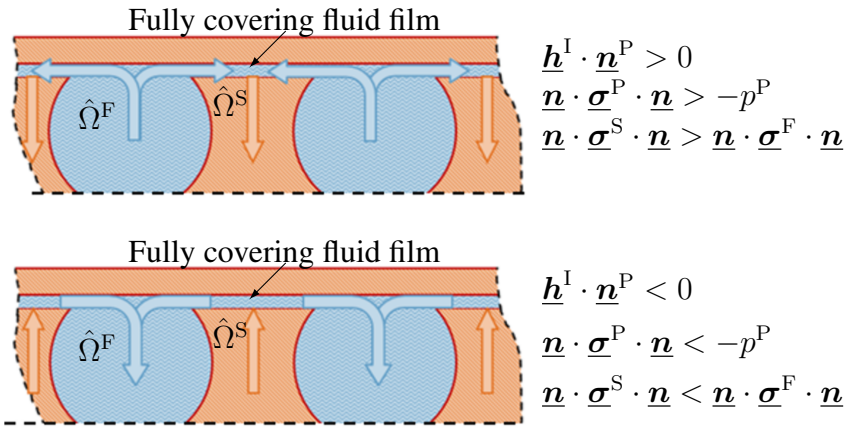

Figure 5.5: Detailed view on the condition transition point $\Gamma^{\mathrm{PS},c} \cap \Gamma^{\mathrm{FS}} \cap \Gamma^{\mathrm{FP}}$. Arrows indicate the process of generation (top) or degeneration (bottom) of a fully covering fluid film, depending on the traction difference between total contact traction and the ambient fluid stress.

Remark 5.3 (Fluid traction in contact zone $\Gamma^{\mathrm{PS},c}$)**.** *To compute the traction difference* $\underline{\boldsymbol{h}}^{\mathrm{I}}$*, which is required to formulate condition* (6.6)*, the physical model has to provide a reliable fluid traction on the overall interface* Γ*. This is especially critical in the contacting zone* $\Gamma^{\mathrm{PS},c}$*. The additional poroelastic layer on the contact interface comprises this fluid state by the porous fluid pressure* p^{P}*. If the physical model does not provide this information by nature, (implicit) assumptions or alternative modeling approaches are required to formulate the contact conditions* (6.5)-(6.7)*.*

The subset of the interface Γ where the first condition (6.5) is exactly zero and therefore fulfills (5.1) is the contact interface $\Gamma^{\mathrm{PS},c}$ between poroelastic domain and structural domain. The remaining parts, where the second condition (6.6) is exactly zero, are the interfaces between fluid domain and structural domain Γ^{FS} or between fluid domain and poroelastic domain Γ^{FP}, depending if it is a subset of the structural boundary or the poroelastic boundary.

In the following paragraph, the continuity of the formulation at the point or line of changing interface conditions (marked by the black cross in Figure 5.6) is discussed. To ensure continuity of the problem at this specific position, the conditions of all adjacent interfaces have to be

fulfilled simultaneously. To prove this, one type of interface conditions (e.g. contact) plus the criteria for transition to hold and verify the fulfillment of the other conditions (e.g. fluid-structure and fluid-poroelastic conditions) is assumed. The fulfillment of the different interface conditions in normal direction at the transition points from a contact interface ($\Gamma^{\mathrm{PS},c}$) to a non-contact interface (Γ^{FS} and Γ^{FP}) and vice versa is analyzed. These points are formed by the intersection of the interfaces $\Gamma^{\mathrm{PS},c}$, Γ^{FS} and Γ^{FP} and they satisfy the transition conditions, which are stated as the conditions (6.5) and (6.6) satisfied equal to zero. In order to enable a continuous transition of interface types, combining conditions on the contact interface $\Gamma^{\mathrm{PS},c}$ (conditions (5.1)-(5.4)) with the transition conditions has to fulfill conditions on the interfaces Γ^{FS} and Γ^{FP} (conditions (2.59)-(2.60) and (2.61)-(2.64)) by default (see upper red path in Figure 5.6). Therefore, it is assumed that the conditions of contact are satisfied and even for a vanishing fluid film the fluid state vectors ($\underline{\boldsymbol{v}}^{\mathrm{F}}$, p^{F}) and implicitly the corresponding fluid stress ($\underline{\boldsymbol{\sigma}}^{\mathrm{F}}$) are considered to result in continuous fulfillment of all interface conditions. Then, for the normal components of velocity and the normal traction difference, the following relations hold.

$$\text{kinematic constraints:} \quad \frac{\partial \underline{\boldsymbol{u}}^{\mathrm{S}}}{\partial t} \cdot \underline{\boldsymbol{n}} \overset{\text{condition (5.1)}}{=} \frac{\partial \underline{\boldsymbol{u}}^{\mathrm{P}}}{\partial t} \cdot \underline{\boldsymbol{n}} \overset{\text{condition (5.2)}}{=} \underline{\boldsymbol{v}}^{\mathrm{P}} \cdot \underline{\boldsymbol{n}} \overset{(*1)}{=} \underline{\boldsymbol{v}}^{\mathrm{F}} \cdot \underline{\boldsymbol{n}} \tag{5.8}$$

(*1) = normal velocity of emerging fluid film equals contact interface normal velocity

$$\begin{aligned}\text{stress equilibrium:} \quad \underline{\boldsymbol{h}}^{\mathrm{I}} \cdot \underline{\boldsymbol{n}} &\overset{\text{def.}}{=} 0 \overset{\text{transition point of (6.6)}}{=} \underline{\boldsymbol{n}} \cdot \underline{\boldsymbol{\sigma}}^{\mathrm{P}} \cdot \underline{\boldsymbol{n}} + p^{\mathrm{P}} \overset{\text{condition (5.3)}}{=} \underline{\boldsymbol{n}} \cdot \underline{\boldsymbol{\sigma}}^{\mathrm{S}} \cdot \underline{\boldsymbol{n}} + p^{\mathrm{P}} \\ &\overset{(*2)}{=} \underline{\boldsymbol{n}} \cdot \underline{\boldsymbol{\sigma}}^{\mathrm{S}} \cdot \underline{\boldsymbol{n}} - \underline{\boldsymbol{n}} \cdot \underline{\boldsymbol{\sigma}}^{\mathrm{F}} \cdot \underline{\boldsymbol{n}} \overset{\text{condition (5.3)}}{=} \underline{\boldsymbol{n}} \cdot \underline{\boldsymbol{\sigma}}^{\mathrm{P}} \cdot \underline{\boldsymbol{n}} - \underline{\boldsymbol{n}} \cdot \underline{\boldsymbol{\sigma}}^{\mathrm{F}} \cdot \underline{\boldsymbol{n}}\end{aligned} \tag{5.9}$$

(*2) = normal fluid stress of emerging fluid film in balance with fluid pressure in poroelastic layer

As a consequence of (5.8) and (5.9), the conditions on the interfaces Γ^{FS} and Γ^{FP} in normal direction (conditions (2.59)-(2.60) and (2.61)-(2.63)) are naturally fulfilled. For the change from the non-contact interfaces Γ^{FS} and Γ^{FP} to the contact interface $\Gamma^{\mathrm{PS},c}$, this can be shown analogously (see lower blue path in Figure 5.6).

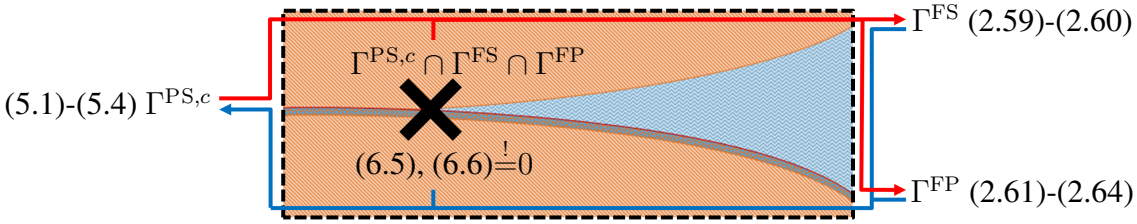

Figure 5.6: Visualization of the continuous transition of normal conditions at the point $\Gamma^{\mathrm{PS},c} \cap \Gamma^{\mathrm{FS}} \cap \Gamma^{\mathrm{FP}}$ which is marked by the black cross. Following the upper red path indicates the equivalence of the contact conditions by making use of the transition conditions and the normal conditions on the interfaces Γ^{FS} and Γ^{FP}. Following the lower blue path indicates the equivalence of the conditions on the interfaces Γ^{FS} and Γ^{FP} in normal direction by making use of the transition conditions and the contact conditions on $\Gamma^{\mathrm{PS},c}$.

Remark 5.4 (Continuity of the formulation for changing interface conditions in tangential direction)**.** *Considering frictionless contact at the contact interface $\Gamma^{\mathrm{PS},c}$ in combination with the*

no-slip condition at the interface Γ^{FS} and the Beavers-Joseph condition at the interface Γ^{FP} leads to a non-continuous change in the tangential component of the interface conditions. A continuous change between contact and non-contact interfaces for frictionless contact would require zero tangential stress ("full-slip" conditions) close to the contacting zone on the interfaces Γ^{FS} and Γ^{FP} as well. This non-continuous change of the tangential condition also holds true when considering frictional contact as the tangential stress resulting from macroscopic contact friction laws is in general not equal to the stress resulting from the viscous flow. It should be highlighted that this circumstance does not lead to a discontinuity in the formulation as long as there is a continuous change of the interface area on Γ^{FS}, Γ^{FP}, and $\Gamma^{\mathrm{PS},c}$. The only exception, where this is not the case, is the contact of two parallel plates. Nevertheless, contrary to the continuity of the normal component of the interface conditions (enabled by a proper consideration of the fluid traction in $\underline{\boldsymbol{h}}^{\mathrm{I}}$), the continuity of the tangential components turned out to be less essential for the performance of the nonlinear solution procedure for the presented numerical computations.

It should be pointed out that for a pure structural contact case with vanishing fluid, conditions (6.5), (6.6), and (6.7) reduce to the classical contact conditions, as the relative traction equals the absolute traction for vanishing fluid pressure.

5.3 The Discrete Rough Surface FSCI Problem

All fundamentals that are applied for the numerical solution of the rough surface FSCI problem which were already introduced previously are reviewed in Section 5.3.1. A dual mortar method to incorporate contact between the poroelastic layer and the structural domain is introduced subsequently. Finally, a Nitsche-based method is utilized to ensure the fluid mass balance on the interface of closed contact.

5.3.1 Review of Previously Introduced Numerical Approaches

For the discretization of the governing equations of the structural and poroelastic subproblem, the boundary-fitted FEM, as introduced in Section 2.2.2, is applied. The corresponding discrete weak forms (2.107) and (2.120) including stabilization have been discussed in Section 2.2.3 and Section 2.2.5, respectively. The discretization approach for the fluid domain is based on the CutFEM and has been presented in detail in Chapter 3. Details concerning the discrete fluid solution and fluid test function spaces are given in Section 3.1.2, the application of "ghost penalty" stabilization in Section 3.1.3, the numerical integration of the $\mathcal{L}^2$-inner products of intersected elements in Section 3.1.4, and the unfitted moving interface configuration in Section 3.2. The geometry of the discrete interface $\Gamma_{\mathrm{h}}^{\mathrm{F,I}}$, which completes the description of the outer boundary of the fluid domain $\Omega_{\mathrm{h}}^{\mathrm{F}}$, is based on the deformed discrete boundaries $\Gamma_{\mathrm{h}}^{\mathrm{F,I}} \subseteq \partial\Omega_{\mathrm{h}}^{\mathrm{S}} \cap \partial\Omega_{\mathrm{h}}^{\mathrm{P}}$ provided by the boundary-fitted discretizations.

The conditions on the interface of fluid and elastic structures $\Gamma_{\mathrm{h}}^{\mathrm{FS}}$ are imposed weakly by a Nitsche-based formulation (additional contribution to the weak form: $\mathcal{W}_{\mathrm{h}}^{\mathrm{FSI,F}}$ in (3.26)) discussed in detail in Section 3.3.2.1. Here, the fluid-sided interface stress representation with skew-symmetric adjoint-consistency contribution ($\xi^{\mathrm{FSI}} = 1$) is applied exclusively. The conditions on the interface of fluid and poroelastic structures $\Gamma_{\mathrm{h}}^{\mathrm{FP}}$ are imposed weakly by the novel

Nitsche-based formulation presented and analyzed in Chapter 4. This results in the additional contribution to the weak form $\mathcal{W}_{\mathrm{h}}^{\mathrm{FPI},n}$ in normal interface direction discussed in detail in Section 4.2.1 and the additional contribution to the weak form $\mathcal{W}_{\mathrm{h}}^{\mathrm{FPI},t,Nit}$ in tangential interface orientation discussed in detail in Section 4.2.2. Due to the beneficial discrete stability properties, the variant with a skew-symmetric adjoint-consistent contribution ($\xi^{\mathrm{FPI}} = -1$) is considered. To incorporate solid-poroelastic contact into the discrete formulation, a Dual Mortar method based on a Lagrange multiplier will be introduced in the following.

5.3.2 Dual Mortar Method on the Contact Interface between Poroelastic Domain and Structural Domain

To numerically handle contact between the poroelastic domain and the structural domain on the solid-poroelastic contact interface $\Gamma_{\mathrm{h}}^{\mathrm{PS},c}$, a Mortar segment-to-segment approach, where the no-penetration constraint (5.1) is enforced in a weak sense by a Lagrange multiplier, is applied. This approach is combined with a Nitsche-based method to guarantee fluid mass balance (5.2) between poroelastic domain and impermeable solid (see Section 5.3.3).

Details on Mortar based contact approaches can be found, e.g., in the works of Puso and Laursen [175] and Fischer and Wriggers [84] or for dual Mortar based methods by Hüeber *et al.* [127] and Popp *et al.* [171, 172], whereby the latter reference gives details on the specific method applied here. In the following, only a brief overview of the most important aspects of the method is presented.

In contrast to the continuous interfaces, the discrete contact interfaces arising from the poroelastic domain $\Gamma_{\mathrm{h}}^{\mathrm{P,I}}$ and the structural domain $\Gamma_{\mathrm{h}}^{\mathrm{S,I}}$ are geometrically not exactly overlapping. Therefore, the potential contact interfaces $\breve{\Gamma}_{\mathrm{h}}^{\mathrm{P},c}$ and $\breve{\Gamma}_{\mathrm{h}}^{\mathrm{S},c}$ respectively arising from the poroelastic domain $\Omega_{\mathrm{h}}^{\mathrm{P}}$ and the structural domain $\Omega_{\mathrm{h}}^{\mathrm{S}}$ are introduced. In addition, the contact interfaces restricted to the "active" contact zone are defined as $\Gamma_{\mathrm{h}}^{\mathrm{P},c} = \Gamma_{\mathrm{h}}^{\mathrm{P,I}} \setminus \Gamma_{\mathrm{h}}^{\mathrm{FP}}$ and $\Gamma_{\mathrm{h}}^{\mathrm{S},c} = \Gamma_{\mathrm{h}}^{\mathrm{S,I}} \setminus \Gamma_{\mathrm{h}}^{\mathrm{FS}}$. A Lagrange multiplier $\underline{\boldsymbol{\lambda}}_{\mathrm{h}}$, which is discretized on the interface $\breve{\Gamma}_{\mathrm{h}}^{\mathrm{P},c}$, represents the total traction between the contact interfaces.

In order to take the change in the contact state depending on the relative traction (see $\underline{\boldsymbol{h}}^{\mathrm{I}}$ in (6.6)) into account and to allow for a continuous transition between "active" dual Mortar contact nodes and the Nitsche coupling method on $\Gamma_{\mathrm{h}}^{\mathrm{FS}}$ or $\Gamma_{\mathrm{h}}^{\mathrm{FP}}$, the nodal fluid pressure force $\underline{\boldsymbol{f}}_{\mathrm{h}}^{j}$ and its normal component $f_{\mathrm{h}}^{n,j}$ are evaluated as

$$\underline{\boldsymbol{f}}_{\mathrm{h}}^{j} = \frac{\left\langle N_j, p_{\mathrm{h}}^{\mathrm{P}} \underline{\boldsymbol{n}}_{\mathrm{h}}^{\mathrm{P}} \right\rangle_{\Gamma_{\mathrm{h}}^{\mathrm{P},c}}}{\left\langle N_j, \psi_j \right\rangle_{\breve{\Gamma}_{\mathrm{h}}^{\mathrm{P},c}}}, \quad f_{\mathrm{h}}^{n,j} = \underline{\boldsymbol{f}}_{\mathrm{h}}^{j} \cdot \tilde{\underline{\boldsymbol{n}}}_{\mathrm{h}}^{j}. \tag{5.10}$$

Herein, N_j and ψ_j are the nodal shape functions applied for the discretization of the test function $\delta \underline{\boldsymbol{u}}_{\mathrm{h}}^{\mathrm{P}}$ and the Lagrange multiplier $\underline{\boldsymbol{\lambda}}_{\mathrm{h}}$ on the discrete boundary of the porous domain $\Omega_{\mathrm{h}}^{\mathrm{P}}$, respectively. It should be pointed out that $\underline{\boldsymbol{f}}_{\mathrm{h}}^{j}$ and $f_{\mathrm{h}}^{n,j}$ are non-zero just for nodes which are adjacent to contacting boundary elements due to the integration on the "active" part of the contact interface $\Gamma_{\mathrm{h}}^{\mathrm{P},c}$. The fluid pressure is represented by the porous pressure $p_{\mathrm{h}}^{\mathrm{P}}$ since this quantity is available on the overall interface $\breve{\Gamma}_{\mathrm{h}}^{\mathrm{P},c}$ in contrast to the alternative consistent choice based on the fluid stress $\underline{\boldsymbol{\sigma}}_{\mathrm{h}}^{\mathrm{F}}$.

The Karush-Kuhn-Tucker conditions (6.5) - (6.7) can be expressed by a complementary function $C\left(\lambda_{\mathrm{h}}^{n,j}, g_{\mathrm{h}}^{j}\right)$ (with an algorithmic constant $c^n > 0$), which has to be fulfilled for every node j.

$$\begin{aligned} \lambda_{\mathrm{h}}^{n,j} = \underline{\boldsymbol{\lambda}}_{\mathrm{h}}^{j} \cdot \tilde{\underline{\boldsymbol{n}}}_{\mathrm{h}}^{j}, \quad g_{\mathrm{h}}^{j} = \left\langle \psi_{\delta,j}, \left(\underline{\boldsymbol{x}}_{\Gamma,\mathrm{h}}^{\mathrm{S}} - \underline{\boldsymbol{x}}_{\Gamma,\mathrm{h}}^{\mathrm{P}}\right) \cdot \tilde{\underline{\boldsymbol{n}}}_{\mathrm{h}} \right\rangle_{\breve{\Gamma}_{\mathrm{h}}^{\mathrm{P},c}}, \\ C\left(\lambda_{\mathrm{h}}^{n,j}, g_{\mathrm{h}}^{j}\right) = \left(\lambda_{\mathrm{h}}^{n,j} - f_{\mathrm{h}}^{n,j}\right) - \max\left(0, \left(\lambda_{\mathrm{h}}^{n,j} - f_{\mathrm{h}}^{n,j}\right) - c^n g_{\mathrm{h}}^{j}\right) = 0 \end{aligned} \tag{5.11}$$

Herein, the index j specifies quantities which correspond to a specific computational node j. The smoothed normal vector field $\tilde{\underline{\boldsymbol{n}}}_{\mathrm{h}}$ is evaluated on the interface $\breve{\Gamma}_{\mathrm{h}}^{\mathrm{P},c}$ based on the unit outward-pointing normal $\underline{\boldsymbol{n}}_{\mathrm{h}}^{\mathrm{P}}$ of the poroelastic domain $\Omega_{\mathrm{h}}^{\mathrm{P}}$. This normal vector field is also utilized for all projections between the interfaces $\breve{\Gamma}_{\mathrm{h}}^{\mathrm{P},c}$ and $\breve{\Gamma}_{\mathrm{h}}^{\mathrm{S},c}$. Subsequently, $\tilde{\underline{\boldsymbol{n}}}_{\mathrm{h}}^{j}$ is the nodal smoothed normal vector, $\underline{\boldsymbol{\lambda}}_{\mathrm{h}}^{j}$ the nodal discrete component of the Lagrange multiplier $\underline{\boldsymbol{\lambda}}_{\mathrm{h}}$ with nodal shape function ψ_j, g_{h}^{j} the nodal weighted gap, and $\psi_{\delta,j}$ the nodal shape function of the test function $\delta\underline{\boldsymbol{\lambda}}_{\mathrm{h}}$ on the interface $\breve{\Gamma}_{\mathrm{h}}^{\mathrm{P},c}$. Details concerning $\underline{\tilde{\boldsymbol{n}}}_{\mathrm{h}}$, $\tilde{\underline{\boldsymbol{n}}}_{\mathrm{h}}^{j}$, g_{h}^{j},ψ_j, and $\psi_{\delta,j}$, including the utilized projection between both interfaces, can be found in the works of Popp [170], Popp *et al.* [172]. Therein, the contact interface adjacent to the poroelastic or solid domain is denoted as slave or master interface, respectively.

The contact constraints (6.5) - (6.7) are finally incorporated into the overall formulation by enforcing the complementary function (5.11) and vanishing tangential components of the Lagrange multiplier $\underline{\boldsymbol{\lambda}}_{\mathrm{h}}^{j}$ for all computational nodes on the interface $\breve{\Gamma}_{\mathrm{h}}^{\mathrm{P},c}$. Additionally, the boundary traction is substituted by the Lagrange multiplier $\underline{\boldsymbol{\lambda}}_{\mathrm{h}}$ in the respective interface integrals on $\breve{\Gamma}_{\mathrm{h}}^{\mathrm{P},c}$, which arise naturally in the derivation of the weak forms (2.22) and (2.57).

Nevertheless, an alternative but equivalent representation of the contact constraints is preferred at this point. This variant is closer to the actual implementation and clearer in combination with the treatment of the interface terms presented beforehand. Hereby, the complementary function and the restriction in normal direction are directly incorporated in the "active set" of the Lagrange multiplier $\underline{\boldsymbol{\lambda}}_{\mathrm{h}}^{\mathcal{A}}$ as well as its corresponding test function $\delta\underline{\boldsymbol{\lambda}}_{\mathrm{h}}^{\mathcal{A}}$.

$$\begin{aligned} \underline{\boldsymbol{\lambda}}_{\mathrm{h}}^{\mathcal{A}} &= \sum_j \psi_j \underline{\boldsymbol{\lambda}}_{\mathrm{h}}^{j} \text{ with } \underline{\boldsymbol{\lambda}}_{\mathrm{h}}^{j} \cdot \left(\underline{\boldsymbol{I}} - \tilde{\underline{\boldsymbol{n}}}_{\mathrm{h}}^{j} \otimes \tilde{\underline{\boldsymbol{n}}}_{\mathrm{h}}^{j}\right) = \underline{\mathbf{0}} \text{ and } \underline{\boldsymbol{\lambda}}_{\mathrm{h}}^{j} = \underline{\boldsymbol{f}}_{\mathrm{h}}^{j} \text{ if } \left(\lambda_{\mathrm{h}}^{n,j} - f_{\mathrm{h}}^{n,j} - c^n g_{\mathrm{h}}^{j}\right) < 0 \\ \delta\underline{\boldsymbol{\lambda}}_{\mathrm{h}}^{\mathcal{A}} &= \sum_j \psi_{\delta,j} \delta\underline{\boldsymbol{\lambda}}_{\mathrm{h}}^{j} \text{ with } \delta\underline{\boldsymbol{\lambda}}_{\mathrm{h}}^{j} \cdot \left(\underline{\boldsymbol{I}} - \tilde{\underline{\boldsymbol{n}}}_{\mathrm{h}}^{j} \otimes \tilde{\underline{\boldsymbol{n}}}_{\mathrm{h}}^{j}\right) = \underline{\mathbf{0}} \text{ and } \delta\underline{\boldsymbol{\lambda}}_{\mathrm{h}}^{j} = \underline{\mathbf{0}} \text{ if } \left(\lambda_{\mathrm{h}}^{n,j} - f_{\mathrm{h}}^{n,j} - c^n g_{\mathrm{h}}^{j}\right) < 0 \end{aligned} \tag{5.12}$$

Application of these restrictions specified in (5.12) to the discrete spaces constructed by the Lagrange multiplier shape functions (ψ_j and $\psi_{\delta,j}$) on the interface $\Gamma_{\mathrm{h}}^{\mathrm{PS},c}$, analogously to definitions (2.104), specifies the discrete "active" Lagrange multiplier solution space $\mathcal{S}_{\underline{\boldsymbol{\lambda}}^{\mathcal{A}},\mathrm{h}}$ and test function space $\mathcal{T}_{\delta\underline{\boldsymbol{\lambda}}^{\mathcal{A}},\mathrm{h}}$. Finally, the contribution of the contact constraints can be written as

$$\begin{aligned} \mathcal{W}_{\mathrm{h}}^{\mathrm{PS},c}\left[\left(\delta\underline{\boldsymbol{u}}_{\mathrm{h}}^{\mathrm{S}}, \delta\underline{\boldsymbol{u}}_{\mathrm{h}}^{\mathrm{P}}, \delta\underline{\boldsymbol{\lambda}}_{\mathrm{h}}^{\mathcal{A}}\right), \left(\underline{\boldsymbol{u}}_{\mathrm{h}}^{\mathrm{S}}, \underline{\boldsymbol{u}}_{\mathrm{h}}^{\mathrm{P}}, \underline{\boldsymbol{\lambda}}_{\mathrm{h}}^{\mathcal{A}}\right)\right] = \\ - \left\langle \delta\underline{\boldsymbol{u}}_{\mathrm{h}}^{\mathrm{P}} - \delta\underline{\boldsymbol{u}}_{\mathrm{h}}^{\mathrm{S}}, -\underline{\boldsymbol{\lambda}}_{\mathrm{h}}^{\mathcal{A}} \right\rangle_{\breve{\Gamma}_{\mathrm{h}}^{\mathrm{P},c}} + \left\langle \delta\underline{\boldsymbol{\lambda}}_{\mathrm{h}}^{\mathcal{A}}, \left(\underline{\boldsymbol{x}}_{\Gamma,\mathrm{h}}^{\mathrm{S}} - \underline{\boldsymbol{x}}_{\Gamma,\mathrm{h}}^{\mathrm{P}}\right) \right\rangle_{\breve{\Gamma}_{\mathrm{h}}^{\mathrm{P},c}}. \end{aligned} \tag{5.13}$$

Herein, the first term originates from the standard Galerkin interface terms corresponding to the governing equations (2.15) and (2.46) by inserting the dynamic equilibrium (5.3) and representing the interface traction as $\underline{\boldsymbol{\lambda}}_{\mathrm{h}}^{\mathcal{A}}$. It should be pointed out that the second term includes the

constraint (5.1) due to the restriction into normal direction (5.12) of the test function. Whenever essential, an additional index in $\mathcal{W}^{\mathrm{PS},c}_{\mathrm{h},n+1}$ specifies that both interface terms $\langle *,* \rangle_{\breve{\Gamma}^{\mathrm{P},c}_{\mathrm{h}}}$ are evaluated as $\langle *,* \rangle_{\breve{\Gamma}^{\mathrm{P},c}_{\mathrm{h},n+1},n+\theta}$.

For the discretization of the Lagrange multiplier, dual shape functions ψ_i as introduced by Wohlmuth [227] are applied. The dual shape functions provide the following property

$$\int_{\breve{\Gamma}^{\mathrm{P},c}_{\mathrm{h}}} \psi_i N_j \,\mathrm{d}\Gamma = \delta_{ij} \int_{\breve{\Gamma}^{\mathrm{P},c}_{\mathrm{h}}} N_j \,\mathrm{d}\Gamma \qquad i,j = 1...n_{\mathrm{nod},\breve{\Gamma}^{\mathrm{P},c}_{\mathrm{h}}}. \tag{5.14}$$

Therein, δ_{ij} is the Kronecker delta , $n_{\mathrm{nod},\breve{\Gamma}^{\mathrm{P},c}_{\mathrm{h}}}$ the number of computational nodes on the discrete interface $\breve{\Gamma}^{\mathrm{P},c}_{\mathrm{h}}$, N_j the classical shape function of interface node j as defined in (2.102), and ψ_i the dual shape function of interface node i. Thus, the evaluation of the term $-\left\langle \delta\underline{\boldsymbol{u}}^{\mathrm{P}}_{\mathrm{h}}, -\underline{\boldsymbol{\lambda}}^{\mathcal{A}}_{\mathrm{h}} \right\rangle_{\breve{\Gamma}^{\mathrm{P},c}_{\mathrm{h}}}$ in (5.13) finally results in a diagonal Mortar coupling matrix. This allows for an efficient condensation of the Lagrange multiplier from the final system as the inversion of the Mortar coupling matrix is trivial. The condensation provides a reduction of the final system size which is solved, as well as a removal of the saddlepoint structure of the final system. For the construction of dual shape functions ψ_i, which provide property (5.14), the reader is referred to the works of Flemisch and Wohlmuth [85], Lamichhane and Wohlmuth [137], Lamichhane *et al.* [138] and Wohlmuth [228]. For the discretization of the test function $\delta\underline{\boldsymbol{\lambda}}_{\mathrm{h}}$, standard shape functions are used, leading to a Petrov-Galerkin type of Lagrange multiplier interpolation. Details can be found in the work of Popp *et al.* [173].

Remark 5.5 (On the fluid pressure force $\underline{\boldsymbol{f}}^{j}_{\mathrm{h}}$)**.** *To explain the consideration of the fluid pressure force $\underline{\boldsymbol{f}}^{j}_{\mathrm{h}}$, it is assumed that $\underline{\boldsymbol{f}}^{j}_{\mathrm{h}}$ is added in the contact zone, where no fluid traction is applied by the Nitsche-based contributions $\mathcal{W}^{\mathrm{FSI,F}}_{\mathrm{h}}$ or $\mathcal{W}^{\mathrm{FPI},n}$ (see Sections 3.3.2.1 and 4.2.1):* $\left\langle \delta\underline{\boldsymbol{u}}^{\mathrm{P}}_{\mathrm{h}} - \delta\underline{\boldsymbol{u}}^{\mathrm{S}}_{\mathrm{h}}, \psi_j \underline{\boldsymbol{f}}^{j}_{\mathrm{h}} \right\rangle_{\Gamma^{\mathrm{P},c}_{\mathrm{h}}}$*. In this hypothetical case, the contact traction based on a Lagrange multiplier $\tilde{\underline{\boldsymbol{\lambda}}}_{\mathrm{h}}$ can be considered as an additional traction on top of the fluid traction:* $\left\langle \delta\underline{\boldsymbol{u}}^{\mathrm{P}}_{\mathrm{h}} - \delta\underline{\boldsymbol{u}}^{\mathrm{S}}_{\mathrm{h}}, \psi_j (\underline{\boldsymbol{f}}^{j}_{\mathrm{h}} + \tilde{\underline{\boldsymbol{\lambda}}}^{j}_{\mathrm{h}}) \right\rangle_{\Gamma^{\mathrm{P},c}_{\mathrm{h}}}$.
Therefore, this Lagrange multiplier directly equals the negative traction difference $\underline{\boldsymbol{h}}^{\mathrm{I}}_{\mathrm{h}} = -\tilde{\underline{\boldsymbol{\lambda}}}_{\mathrm{h}}$, and as a result such a configuration leads to the classical contact formulations without surrounding fluid. Nevertheless, to avoid integration of this contribution $\underline{\boldsymbol{f}}^{j}_{\mathrm{h}}$ on the overall interface $\Gamma^{\mathrm{P},c}_{\mathrm{h}}$, the nodal force is directly subtracted from the nodal Lagrange multiplier in the complementary function C: ($\tilde{\underline{\boldsymbol{\lambda}}}^{j}_{\mathrm{h}} = \underline{\boldsymbol{\lambda}}^{j}_{\mathrm{h}} - \underline{\boldsymbol{f}}^{j}_{\mathrm{h}}$). This prohibits a direct dependency of the contact traction on the fluid pressure for established contact, as the interface integrals on $\Gamma^{\mathrm{P},c}_{\mathrm{h}}$ are based on $\underline{\boldsymbol{\lambda}}^{j}_{\mathrm{h}}$ and do not include $\underline{\boldsymbol{f}}^{j}_{\mathrm{h}}$.

Remark 5.6 (Continuity of the formulation)**.** *Due to the continuity of the complementary function, the resulting formulation including contact is continuous. This is enabled by the consideration of the fluid pressure force $\underline{\boldsymbol{f}}^{j}_{\mathrm{h}}$. Definition* (5.12) *shows that $\underline{\boldsymbol{f}}^{j}_{\mathrm{h}}$ contributes only to the "inactive" contact part based on the complementary function* (5.11)*. At the same time, it can be seen in* (5.10) *that $\underline{\boldsymbol{f}}^{j}_{\mathrm{h}}$ vanishes for all nodes j with nonexistent support on $\Gamma^{\mathrm{P},c}_{\mathrm{h}}$. As a result, the nodal fluid force $\underline{\boldsymbol{f}}^{j}_{\mathrm{h}}$ does contribute to the overall formulation solely close to the condition*

transition point $\Gamma_{\mathrm{h}}^{\mathrm{P},c} \cap \Gamma_{\mathrm{h}}^{\mathrm{FP}}$ and, thus, can be considered as a transition contribution which guarantees continuity and consistency between the Nitsche- and Lagrange multiplier-based interface formulations (see also the previous remark).

5.3.3 Nitsche-based Method for Fluid Mass Balance on Contact Interface

In addition to the classical contact constraints, the fluid mass balance (5.2) on the contact interface has to be fulfilled. For this purpose, a Nitsche-based method with the following contributions to the weak form is applied

$$\begin{aligned}\mathcal{W}_{\mathrm{h}}^{\mathrm{PS},f}\left[\left(\delta\underline{\boldsymbol{v}}_{\mathrm{h}}^{\mathrm{P}},\delta\underline{\boldsymbol{u}}_{\mathrm{h}}^{\mathrm{P}},\delta p_{\mathrm{h}}^{\mathrm{P}}\right),\left(\underline{\boldsymbol{v}}_{\mathrm{h}}^{\mathrm{P}},\underline{\boldsymbol{u}}_{\mathrm{h}}^{\mathrm{P}},p_{\mathrm{h}}^{\mathrm{P}}\right)\right] &= \left\langle\delta\underline{\boldsymbol{v}}_{\mathrm{h}}^{\mathrm{P}},p_{\mathrm{h}}^{\mathrm{P}}\underline{\boldsymbol{n}}_{\mathrm{h}}^{\mathrm{P}}\right\rangle_{\Gamma_{\mathrm{h}}^{\mathrm{P},c}}\\ -\left\langle\delta p_{\mathrm{h}}^{\mathrm{P}},\phi_{\mathrm{h}}\left(\underline{\boldsymbol{v}}_{\mathrm{h}}^{\mathrm{P}}-\tilde{\partial}_t\left[\underline{\boldsymbol{u}}_{\mathrm{h}}^{\mathrm{P}}\right]\right)\cdot\underline{\boldsymbol{n}}_{\mathrm{h}}^{\mathrm{P}}\right\rangle_{\Gamma_{\mathrm{h}}^{\mathrm{P},c}} &+\gamma^{\mathrm{P}}\left\langle\left(\delta\underline{\boldsymbol{v}}_{\mathrm{h}}^{\mathrm{P}}-\delta\underline{\boldsymbol{u}}_{\mathrm{h}}^{\mathrm{P}}\right)\cdot\underline{\boldsymbol{n}}_{\mathrm{h}}^{\mathrm{P}},\left(\underline{\boldsymbol{v}}_{\mathrm{h}}^{\mathrm{P}}-\tilde{\partial}_t\left[\underline{\boldsymbol{u}}_{\mathrm{h}}^{\mathrm{P}}\right]\right)\cdot\underline{\boldsymbol{n}}_{\mathrm{h}}^{\mathrm{P}}\right\rangle_{\Gamma_{\mathrm{h}}^{\mathrm{P},c}}.\end{aligned} \tag{5.15}$$

Herein, the first term is the consistency term arising from the derivation of the weak form from (2.44). The second line includes a skew-symmetric adjoint-consistency term and a penalty term with a sufficiently large positive penalty parameter γ^{P}. The motivation for adding these different contributions is already depicted in Section 3.3.1. An additional index in $\mathcal{W}_{\mathrm{h},n+1}^{\mathrm{PS},f}$ specifies that all interface terms $\langle *,*\rangle_{\Gamma_{\mathrm{h}}^{\mathrm{P},c}}$ are evaluated as $\langle *,*\rangle_{\Gamma_{\mathrm{h},n+1}^{\mathrm{P},c},n+\theta}$.

5.4 The Coupled Discrete Rough Surface FSCI Formulation

By summing up all contributions discussed and referenced beforehand, the final discrete weak form for the coupled rough surface FSCI problem is set. Except for the Lagrange multiplier based contact contributions, this formulation has already been presented in Section 3.3.4 for a more general configuration. The overall discrete solution space $\mathcal{S}_{\underline{\boldsymbol{x}}^{\mathrm{rFSCI}},\mathrm{h},n+1}$ and the discrete test function space $\mathcal{T}_{\delta\underline{\boldsymbol{x}}^{\mathrm{rFSCI}},\mathrm{h},n+1}$ result from the discrete spaces of the underlying physical fields defined for the structural problem in (2.106), for the fluid problem in (2.110), and for the poroelastic problem in (2.119). Additionally, the discrete Lagrange multiplier space in (5.12) is included.

$$\begin{aligned}\mathcal{S}_{\underline{\boldsymbol{x}}^{\mathrm{rFSCI}},\mathrm{h},n+1} &:= \mathcal{S}_{\underline{\boldsymbol{u}}^{\mathrm{S}},\mathrm{h},n+1}\times\mathcal{S}_{\underline{\boldsymbol{v}}^{\mathrm{F}},\mathrm{h},n+1}\times\mathcal{S}_{p^{\mathrm{F}},\mathrm{h},n+1}\times\mathcal{S}_{\underline{\boldsymbol{u}}^{\mathrm{P}},\mathrm{h},n+1}\times\mathcal{S}_{\underline{\boldsymbol{v}}^{\mathrm{P}},\mathrm{h},n+1}\times\mathcal{S}_{p^{\mathrm{P}},\mathrm{h}}\times\mathcal{S}_{\underline{\boldsymbol{\lambda}}^{\mathcal{A}},\mathrm{h},n+1}\\ \mathcal{T}_{\delta\underline{\boldsymbol{x}}^{\mathrm{rFSCI}},\mathrm{h},n+1} &:= \mathcal{T}_{\delta\underline{\boldsymbol{u}}^{\mathrm{S}},\mathrm{h}}\times\mathcal{T}_{\delta\underline{\boldsymbol{v}}^{\mathrm{F}},\mathrm{h},n+1}\times\mathcal{T}_{\delta p^{\mathrm{F}},\mathrm{h},n+1}\times\mathcal{T}_{\delta\underline{\boldsymbol{u}}^{\mathrm{P}},\mathrm{h}}\times\mathcal{T}_{\delta\underline{\boldsymbol{v}}^{\mathrm{P}},\mathrm{h}}\times\mathcal{T}_{\delta p^{\mathrm{P}},\mathrm{h}}\times\mathcal{T}_{\delta\underline{\boldsymbol{\lambda}}^{\mathcal{A}},\mathrm{h},n+1}\end{aligned} \tag{5.16}$$

The overall discrete test function $\delta\underline{\boldsymbol{x}}_{\mathrm{h}}^{\mathrm{rFSCI}}$ and discrete solution state $\underline{\boldsymbol{x}}_{\mathrm{h},n+1}^{\mathrm{rFSCI}}$ are given by

$$\begin{aligned}\underline{\boldsymbol{x}}_{\mathrm{h},n+1}^{\mathrm{rFSCI}} &:= \left(\underline{\boldsymbol{u}}_{\mathrm{h},n+1}^{\mathrm{S}},\underline{\boldsymbol{v}}_{\mathrm{h},n+1}^{\mathrm{F}},p_{\mathrm{h},n+1}^{\mathrm{F}},\underline{\boldsymbol{v}}_{\mathrm{h},n+1}^{\mathrm{P}},\underline{\boldsymbol{u}}_{\mathrm{h},n+1}^{\mathrm{P}},p_{\mathrm{h},n+1}^{\mathrm{P}},\underline{\boldsymbol{\lambda}}_{\mathrm{h}}^{\mathcal{A}}\right),\\ \delta\underline{\boldsymbol{x}}_{\mathrm{h}}^{\mathrm{rFSCI}} &:= \left(\delta\underline{\boldsymbol{u}}_{\mathrm{h}}^{\mathrm{S}},\delta\underline{\boldsymbol{v}}_{\mathrm{h}}^{\mathrm{F}},\delta p_{\mathrm{h}}^{\mathrm{F}},\delta\underline{\boldsymbol{v}}_{\mathrm{h}}^{\mathrm{P}},\delta\underline{\boldsymbol{u}}_{\mathrm{h}}^{\mathrm{P}},\delta p_{\mathrm{h}}^{\mathrm{P}},\delta\underline{\boldsymbol{\lambda}}_{\mathrm{h}}^{\mathcal{A}}\right).\end{aligned} \tag{5.17}$$

Making use of (5.16) and (5.17), the overall discrete formulation of the coupled rough surface FSCI problem is given by

Find $\underline{\boldsymbol{x}}_{\mathrm{h},n+1}^{\mathrm{rFSCI}} \in \mathcal{S}_{\underline{\boldsymbol{x}}^{\mathrm{rFSCI}},\mathrm{h},n+1}$ *such that for all* $\delta\underline{\boldsymbol{x}}_{\mathrm{h}}^{\mathrm{rFSCI}} \in \mathcal{T}_{\delta\underline{\boldsymbol{x}}^{\mathrm{rFSCI}},\mathrm{h},n+1}$:

$$\mathcal{W}_{\mathrm{h},n+1}^{\mathrm{rFSCI}}\left[\delta\underline{\boldsymbol{x}}_{\mathrm{h}}^{\mathrm{rFSCI}}, \underline{\boldsymbol{x}}_{\mathrm{h},n+1}^{\mathrm{rFSCI}}\right] = 0. \tag{5.18}$$

The underlying weak form results from the combination of the weak forms of all corresponding physical fields and interfaces. This includes the discrete contributions for structures in (2.108), for fluid discretized by the CutFEM in (3.7), for poroelasticity in (2.121), for the interface conditions between fluid and structures in (3.26), for interface conditions between fluid and poroelastic layer in (4.1) and (4.5), and for the poroelastic-solid contact conditions in (5.13) and (5.15).

$$\begin{aligned}
&\mathcal{W}_{\mathrm{h},n+1}^{\mathrm{rFSCI}}\left[\delta\underline{\boldsymbol{x}}_{\mathrm{h}}^{\mathrm{rFSCI}}, \underline{\boldsymbol{x}}_{\mathrm{h},n+1}^{\mathrm{rFSCI}}\right] = \\
&\quad \mathcal{W}_{\mathrm{h},n+1}^{\mathrm{S}}\left[\delta\underline{\boldsymbol{u}}_{\mathrm{h}}^{\mathrm{S}}, \underline{\boldsymbol{u}}_{\mathrm{h},n+1}^{\mathrm{S}}\right] + \\
&\quad \mathcal{W}_{\mathrm{h},n+1}^{\mathrm{F,CUT}}\left[\left(\delta\underline{\boldsymbol{v}}_{\mathrm{h}}^{\mathrm{F}}, \delta p_{\mathrm{h}}^{\mathrm{F}}\right), \left(\underline{\boldsymbol{v}}_{\mathrm{h},n+1}^{\mathrm{F}}, p_{\mathrm{h},n+1}^{\mathrm{F}}\right)\right] + \\
&\quad \mathcal{W}_{\mathrm{h},n+1}^{\mathrm{P}}\left[\left(\delta\underline{\boldsymbol{v}}_{\mathrm{h}}^{\mathrm{P}}, \delta\underline{\boldsymbol{u}}_{\mathrm{h}}^{\mathrm{P}}, \delta p_{\mathrm{h}}^{\mathrm{P}}\right), \left(\underline{\boldsymbol{v}}_{\mathrm{h},n+1}^{\mathrm{P}}, \underline{\boldsymbol{u}}_{\mathrm{h},n+1}^{\mathrm{P}}, p_{\mathrm{h},n+1}^{\mathrm{P}}\right)\right] + \\
&\quad \mathcal{W}_{\mathrm{h},n+1}^{\mathrm{FSI,F}}\left[\left(\delta\underline{\boldsymbol{u}}_{\mathrm{h}}^{\mathrm{S}}, \delta\underline{\boldsymbol{v}}_{\mathrm{h}}^{\mathrm{F}}, \delta p_{\mathrm{h}}^{\mathrm{F}}\right), \left(\underline{\boldsymbol{u}}_{\mathrm{h},n+1}^{\mathrm{S}}, \underline{\boldsymbol{v}}_{\mathrm{h},n+1}^{\mathrm{F}}, p_{\mathrm{h},n+1}^{\mathrm{F}}\right)\right] + \\
&\quad \mathcal{W}_{\mathrm{h},n+1}^{\mathrm{FPI},n}\left[\left(\delta\underline{\boldsymbol{v}}_{\mathrm{h}}^{\mathrm{F}}, \delta p_{\mathrm{h}}^{\mathrm{F}}, \delta\underline{\boldsymbol{v}}_{\mathrm{h}}^{\mathrm{P}}, \delta\underline{\boldsymbol{u}}_{\mathrm{h}}^{\mathrm{P}}, \delta p_{\mathrm{h}}^{\mathrm{P}}\right), \left(\underline{\boldsymbol{v}}_{\mathrm{h},n+1}^{\mathrm{F}}, p_{\mathrm{h},n+1}^{\mathrm{F}}, \underline{\boldsymbol{v}}_{\mathrm{h},n+1}^{\mathrm{P}}, \underline{\boldsymbol{u}}_{\mathrm{h},n+1}^{\mathrm{P}}, p_{\mathrm{h},n+1}^{\mathrm{P}}\right)\right] + \\
&\quad \mathcal{W}_{\mathrm{h},n+1}^{\mathrm{FPI},t,Nit}\left[\left(\delta\underline{\boldsymbol{v}}_{\mathrm{h}}^{\mathrm{F}}, \delta p_{\mathrm{h}}^{\mathrm{F}}, \delta\underline{\boldsymbol{v}}_{\mathrm{h}}^{\mathrm{P}}, \delta\underline{\boldsymbol{u}}_{\mathrm{h}}^{\mathrm{P}}, \delta p_{\mathrm{h}}^{\mathrm{P}}\right), \left(\underline{\boldsymbol{v}}_{\mathrm{h},n+1}^{\mathrm{F}}, p_{\mathrm{h},n+1}^{\mathrm{F}}, \underline{\boldsymbol{v}}_{\mathrm{h},n+1}^{\mathrm{P}}, \underline{\boldsymbol{u}}_{\mathrm{h},n+1}^{\mathrm{P}}, p_{\mathrm{h},n+1}^{\mathrm{P}}\right)\right] + \\
&\quad \mathcal{W}_{\mathrm{h},n+1}^{\mathrm{PS},c}\left[\left(\delta\underline{\boldsymbol{u}}_{\mathrm{h}}^{\mathrm{S}}, \delta\underline{\boldsymbol{u}}_{\mathrm{h}}^{\mathrm{P}}, \delta\underline{\boldsymbol{\lambda}}_{\mathrm{h}}^{\mathcal{A}}\right), \left(\underline{\boldsymbol{u}}_{\mathrm{h},n+1}^{\mathrm{S}}, \underline{\boldsymbol{u}}_{\mathrm{h},n+1}^{\mathrm{P}}, \underline{\boldsymbol{\lambda}}_{\mathrm{h},n+1}^{\mathcal{A}}\right)\right] + \\
&\quad \mathcal{W}_{\mathrm{h},n+1}^{\mathrm{PS},f}\left[\left(\delta\underline{\boldsymbol{v}}_{\mathrm{h}}^{\mathrm{P}}, \delta\underline{\boldsymbol{u}}_{\mathrm{h}}^{\mathrm{P}}, \delta p_{\mathrm{h}}^{\mathrm{P}}\right), \left(\underline{\boldsymbol{v}}_{\mathrm{h},n+1}^{\mathrm{P}}, \underline{\boldsymbol{u}}_{\mathrm{h},n+1}^{\mathrm{P}}, p_{\mathrm{h},n+1}^{\mathrm{P}}\right)\right]
\end{aligned} \tag{5.19}$$

The Newton-Raphson like nonlinear solution procedure to solve the aforementioned system for the vector of unknown nodal states

$$\underline{\mathbf{x}}_{n+1}^{\mathrm{rFSCI}} := \left[\left(\underline{\mathbf{u}}_{n+1}^{\mathrm{S}}\right)^{\mathsf{T}}, \left(\underline{\mathbf{v}}_{n+1}^{\mathrm{F}}\right)^{\mathsf{T}}, \left(\underline{\mathbf{p}}_{n+1}^{\mathrm{F}}\right)^{\mathsf{T}}, \left(\underline{\mathbf{u}}_{n+1}^{\mathrm{P}}\right)^{\mathsf{T}}, \left(\underline{\mathbf{v}}_{n+1}^{\mathrm{P}}\right)^{\mathsf{T}}, \left(\underline{\mathbf{p}}_{n+1}^{\mathrm{P}}\right)^{\mathsf{T}} \left(\underline{\boldsymbol{\lambda}}_{n+1}^{\mathcal{A}}\right)^{\mathsf{T}}\right]^{\mathsf{T}} \tag{5.20}$$

is discussed in Section 3.4. As already mentioned in Section 5.3.2, the contact Lagrange multiplier is removed from the final system by a global condensation procedure and, thus, does not interfere with the nonlinear solution procedure from an algorithmic point of view. The only modification to Algorithm 1, which is presented in Section 3.4, is that the state vector $\underline{\boldsymbol{\lambda}}_{n+1}^{\mathcal{A},i+1}$ has to be recovered based on the states $\underline{\mathbf{v}}_{n+1}^{\mathrm{F},i+1}$, $\underline{\mathbf{p}}_{n+1}^{\mathrm{F},i+1}$, $\underline{\mathbf{u}}_{n+1}^{\mathrm{P},i+1}$, $\underline{\mathbf{v}}_{n+1}^{\mathrm{P},i+1}$, and $\underline{\mathbf{p}}_{n+1}^{\mathrm{P},i+1}$ after the solution of the linear system in every iteration i.

5.5 Numerical Examples: Rough Surface FSCI

In this section, numerical examples are presented to analyze the behavior of the proposed model. First, a configuration for a typical leakage flow scenario is analyzed, followed by a squeeze-out flow of two contacting bodies. Finally, a non-return valve with focus on the dynamic "closing" and "opening" behavior is investigated. All results presented in the following have been computed with the multiphysics code environment BACI [221].

In the following, some remarks on algorithmic details are given, which are applied to solve the numerical examples.

- Due to the weak enforcement of the contact constraints by the Mortar methods, the distance between both involved discrete contacting interfaces is not zero at every spatial point. As a result, tiny disconnected fluid domains would arise, which are just a numerical artifact. To avoid this issue, "islands" smaller than a specific size are neglected and do not contribute to the fluid interfaces $\Gamma_{\mathrm{h}}^{\mathrm{FS}}, \Gamma_{\mathrm{h}}^{\mathrm{FP}}$, but to the contact interface $\breve{\Gamma}_{\mathrm{h}}^{\mathrm{P},c}$.

- All numerical examples are discretized with 3D hexahedral trilinear elements. For 2D examples, one element layer in the third axial direction is applied. All degrees of freedom in the third direction are set to zero and removed from the final system of equations.

- To avoid non-essential geometric operations, the update of the geometric intersection of computational fluid mesh and the interfaces $\Gamma_{\mathrm{h}}^{\mathrm{FS}}$, $\Gamma_{\mathrm{h}}^{\mathrm{FP}}$ and $\breve{\Gamma}_{\mathrm{h}}^{\mathrm{P},c}$ during the nonlinear iterations is only performed as long as the displacement increments are above a specified tolerance.

To avoid multiple repetitions, in the following, some common setup details which apply to all three examples shown here are depicted first.

- The initial state of all examples in the following is the zero-state: $\mathring{\underline{\boldsymbol{u}}}^{\mathrm{S}} = \mathring{\underline{\boldsymbol{v}}}^{\mathrm{S}} = \mathring{\underline{\boldsymbol{v}}}^{\mathrm{F}} = \mathring{\underline{\boldsymbol{u}}}^{\mathrm{P}} = \mathring{\underline{\boldsymbol{v}}}^{\mathrm{P^S}} = \mathring{\underline{\boldsymbol{v}}}^{\mathrm{P}} = \underline{\mathbf{0}}$.

- The dependence of fluid resistance and deformation in the poroelastic medium is modeled by an adaption of the Kozeny-Carman formula (see e.g. the textbook of Coussy [67]). For the assumption of isotropy, the following relation holds for the material permeability

$$\underline{\boldsymbol{K}} = K\underline{\boldsymbol{I}} = \mathring{K}\frac{1-\mathring{\phi}^2}{\mathring{\phi}^3}\frac{\left(J^{\mathrm{P}}\phi\right)^3}{1-\left(J^{\mathrm{P}}\phi\right)^2}\underline{\boldsymbol{I}}, \tag{5.21}$$

  where $\mathring{K}$ is the initial scalar permeability.

- The proportionality factor of the Beavers-Joseph condition is computed based on the work of Beavers and Joseph [20] and modified for the 3D case as introduced in (2.65): $\kappa = \left(\alpha_{\mathrm{BJ}}\mu^{\mathrm{F}}\sqrt{3}\right)^{-1}\sqrt{\mathrm{tr}(\underline{\boldsymbol{k}})}$.

- The dual shape functions of the contact Lagrange multiplier ψ_j are based on the boundary elements of the poroelastic domain, where the index j identifies a specific computational node on this discrete boundary.

In the following, if not necessary, there is no distinct separation between solid $\underline{\boldsymbol{u}}^{\mathrm{S}}$ and poroelastic displacements $\underline{\boldsymbol{u}}^{\mathrm{P}}$, fluid $\underline{\boldsymbol{v}}^{\mathrm{F}}$ and porous flow $\underline{\boldsymbol{v}}^{\mathrm{P}}$ velocities, and fluid p^{F} and porous flow p^{P} pressure, as this eases the visualization and the interpretation of the computed results. In order to make the presentation as clear as possible, the index h to specify discrete quantities has been omitted for all numerical examples.

5.5.1 Leakage Test

The first example analyzes the properties of the presented model for leakage flows.

Problem Description The setup of the problem can be seen in Figure 5.7, where two fluid domains with different fluid pressure levels are connected solely by the fluid-saturated rough surface domain of two contacting elastic bodies.

To allow for a qualitative comparison with measurements, the dimension and material parameters of the problem are closely related to the experiment by Lorenz and Persson [145]. Therein, a water filled glass cylinder with a rubber ring on the bottom is pressed on a rough hard solid surface with a given force. A defined water column in the glass cylinder allows specifying the fluid pressure difference in the experimental setup. Here, a plane slice of the circular leakage configuration is investigated. All dimensions and basic boundary conditions can be found in Figure 5.7.

The pressure difference between inflow and outflow boundary is applied by a prescribed traction-Neumann boundary condition on Γ^{in} (see fluid stress in Figure 5.8 (left)) and a zero-Neumann boundary condition on Γ^{out}. Fluid velocities on both boundaries in tangential direction are prohibited by a tangential-Dirichlet boundary condition. To analyze the resulting leakage flow for a range of solid contact pressure, a time-dependent solid stress is prescribed on boundary Γ^{p} as a Neumann boundary condition (see solid stress in Figure 5.8 (left)). The motion in tangential direction on the boundary Γ^{p} is blocked. Interfaces Γ^{FS} and Γ^{FP} (with $\alpha_{\mathrm{BJ}} = 1.0$) are handled by the methods presented in Section 3.3.2.1, Section 4.2.1, and Section 4.2.2.2, respectively. As the focus of this example is on presenting the behavior of the poroelastic layer during rough surface contact, contact between the domains Ω^{S_1},Ω^{S_2}, and Ω^{P} is considered directly by matching of the computational nodes and the corresponding displacements $\underline{\boldsymbol{u}}^{\mathrm{S}}$ and $\underline{\boldsymbol{u}}^{\mathrm{P}}$ on the common interfaces Γ^{PS}.

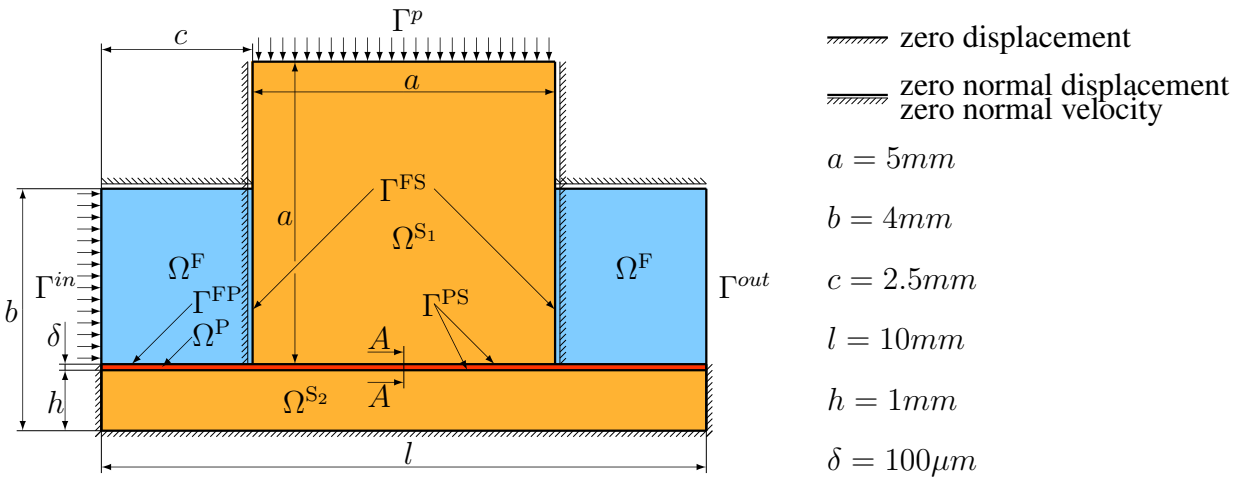

Figure 5.7: Geometry and boundary conditions for the leakage flow.

In domain Ω^{F}, water at a temperature of $20°C$ with fluid material properties, density $\rho^{\mathrm{F}} = 1000kg/m^3$, and dynamic viscosity $\mu^{\mathrm{F}} = 10^{-3}Pa \cdot s$ is considered. The material behavior of the solid domains Ω^{S_1} and Ω^{S_2} is modeled by the Neo-Hookean material model with the hyperelastic strain energy function ψ^{S} introduced in (2.17). In domain Ω^{S_1}, the Young's modulus is $E^1 = 2.3MPa$ and the Poisson ratio $\nu^1 = 0.49$. In domain Ω^{S_2}, $E^2 = 2300MPa$ and $\nu^2 = 0.3$ are given. The initial density is chosen to be equal to the fluid density in both solid domains

$\rho_0^{\mathrm{S}} = \rho^{\mathrm{F}} = 1000 kg/m^3$. As no direct computation of the poroelastic material parameters for these specific rough surfaces is performed, all parameters of the poroelastic layer are chosen in a physically plausible range. The initial porosity is set to $\mathring{\phi} = \phi(t=0) = 0.5$ in the entire poroelastic layer Ω^{P}. To describe a typical macroscopic material response for homogenized contact of rough surfaces, the macroscopic material behavior of the poroelastic layer is modeled by the following strain energy function (see Remark 5.1).

$$\psi^{\mathrm{P},skel} = c\left[\mathrm{tr}\left(\underline{\boldsymbol{C}}^{\mathrm{P}}\right) - 3\right] + \frac{c}{\beta}\left(\left(J^{\mathrm{P}}\right)^{-2\beta} - 1\right) + \tilde{c}^{\mathrm{P}}\left[\mathrm{tr}\left(\underline{\boldsymbol{C}}^{\mathrm{P}}\right) - 3\right]^{\alpha^{\mathrm{P}}},$$
$$c = \frac{E^{\mathrm{P}}}{4(1+\nu^{\mathrm{P}})}, \quad \beta = \frac{\nu^{\mathrm{P}}}{1-2\nu^{\mathrm{P}}} \tag{5.22}$$

Herein, the parameters are: $E^{\mathrm{P}} = 0.25 MPa$, $\nu^{\mathrm{P}} = 0.0$, $\tilde{c}^{\mathrm{P}} = 0.25 MPa$, $\alpha^{\mathrm{P}} = 8$. The additional contributions to the strain energy function $\psi^{\mathrm{P},vol}$ and $\psi^{\mathrm{P},pen}$ are specified in (2.48) and (2.49), respectively. The corresponding parameters are $\kappa^{\mathrm{P}} = 0.8 MPa$ and $\eta^{\mathrm{P}} = 1 kPa$. Taking into account the resulting leak rate of the rough microstructure in [145], the initial material permeability is set to $\mathring{K} = 4.6 \cdot 10^{-4} mm^2$.

For the temporal discretization, the backward Euler scheme ($\theta = 1.0$) with a time step length of $\Delta t = 0.05 s$ is applied. As the computation is performed with one layer of 3D hexahedral elements orthogonal to the 2D plane, all computed leak rates are divided by the thickness in this direction.

Computed Results and Discussion To allow for a comparison of the computed leak rate with the measured data presented in [145] for "sandpaper 120", measured leak rates are divided by the average circumference to compare the leak rate per unit depth. The computed leak rates are calculated in cross section $[A-A]$ of the poroelastic layer (see Figure 5.7)

$$\text{leak rate} = \int_{[A-A]} \phi\left(\underline{\boldsymbol{v}}^{\mathrm{P}} - \frac{\partial \underline{\boldsymbol{u}}^{\mathrm{P}}}{\partial t}\right) \cdot \underline{\boldsymbol{n}}^{[A-A]} \mathrm{d}[A-A]. \tag{5.23}$$

In Figure 5.8 (left), the computed temporal instationary leak rates are presented. After an instationary phase until $t = 5s$, the fluid stress is kept constant. The solid stress is increased discontinuously and kept constant for $\Delta t_{const} = 1s$. Figure 5.8 (right) shows a comparison of the computed stationary leak rates (last computed leak rate for each solid stress level), with the measured data presented in [145]. The excellent agreement shows that the influence of the elastic deformation due to the contact stress on the fluid flow in the rough layer can be modeled by the presented poroelastic model.

Figure 5.9 shows the overall pressure solution for the fluid domains as well as the displacement solution in the structural domains. As intended, there is no observable pressure gradient in the fluid domain Ω^{F} and the entire pressure drop takes place in the poroelastic layer.

Figure 5.10 visualizes the deformation of the poroelastic layer and the porosity at different solid stress levels. It can be observed that for small solid stress, hardly any deformation occurs and the porosity is close to the initial porosity. Increasing the solid stress leads to a compression of the layer and due to the relatively small fluid resistance, to a reduction of the porosity. The smaller cross section and the increased flow resistance (change in permeability) leads to a reduction of the leak rate for higher solid stress.

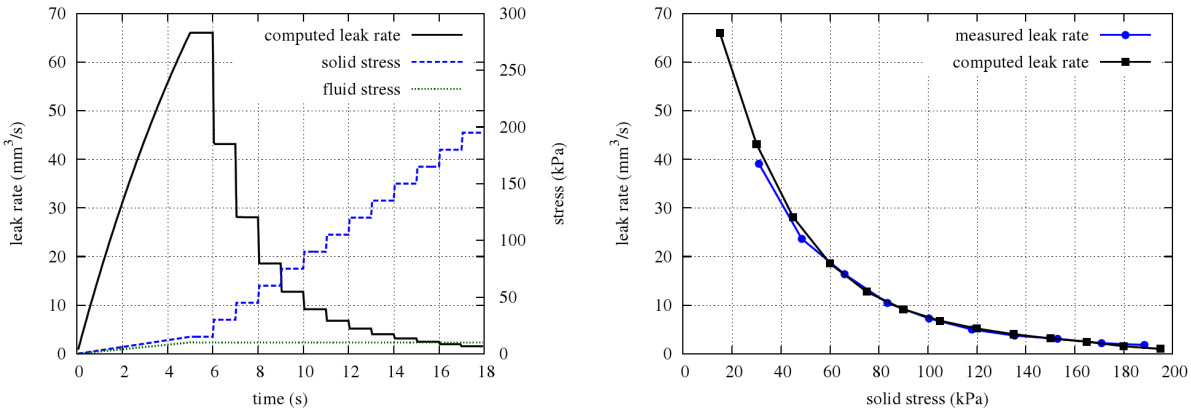

Figure 5.8: Applied solid stress on boundary Γ^{P}, fluid stress on boundary Γ^{in} and the computed leak rate in cross-section $A-A$ (left). Comparison of the computed stationary leak rates for different solid stresses and a constant fluid stress of $10kPa$ with measured leak rates from [145] (right).

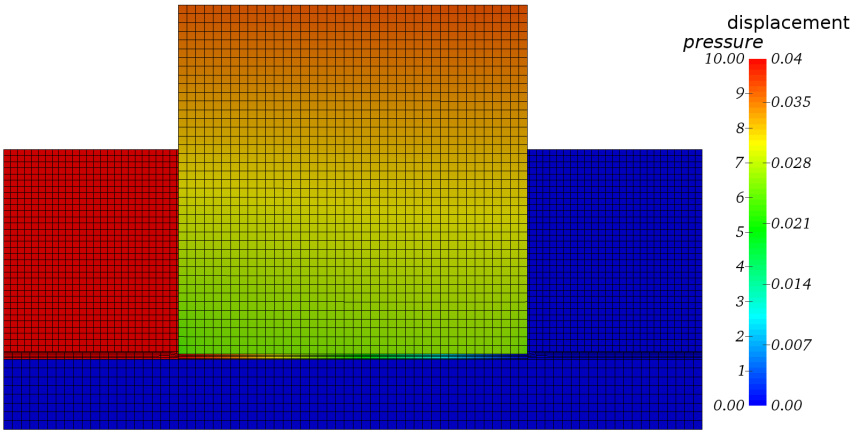

Figure 5.9: Pressure solution for the domains Ω^{F} and Ω^{P} and displacement solution for the domains Ω^{S_1} and Ω^{S_2} at a solid stress of $90kPa$ and t = 11s. The black lines indicate the discretization with trilinear hexahedral elements.

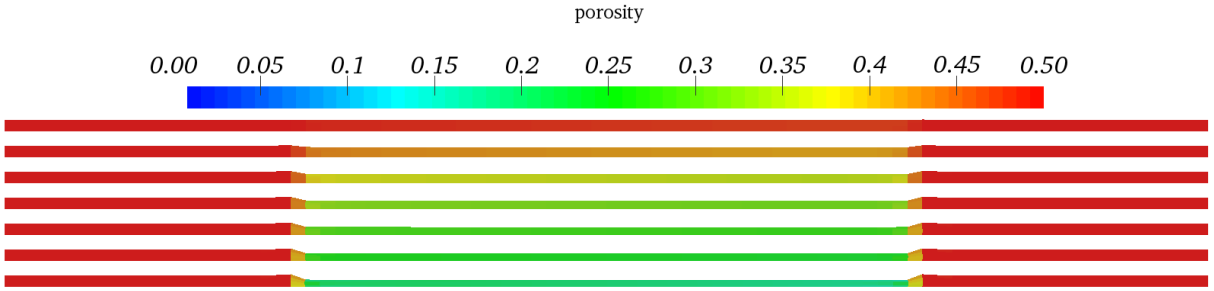

Figure 5.10: Porosity of the deformed poroelastic layer: from top to bottom solid stress = $15, 45, 75, 105, 135, 165, 195kPa$ (element-wise constant visualization).

5.5.2 Rough Surface Contacting Stamp

In a second numerical example, the rough surface contact behavior of an elastic stamp with a circular contacting surface impacting on a stiff but elastic foundation is analyzed.

Problem Description The setup consists of a stamp in solid domain Ω^{S_1} and the foundation in solid domain Ω^{S_2} coated with a poroelastic layer Ω^{P} to model the surface roughness. Both bodies are embedded in a fluid domain Ω^{F}. The geometry including all dimensions as well as the basic boundary conditions can be found in Figure 5.11. To allow a distinct evaluation of the

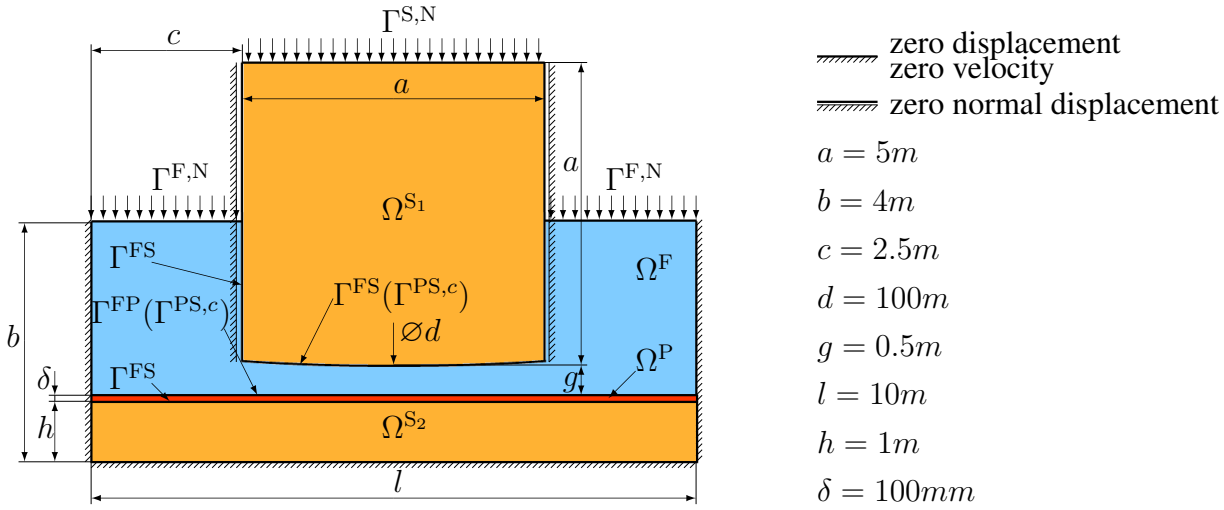

Figure 5.11: Geometry and boundary conditions of the rough surface contacting stamp example.

stamp impact as well as the lift off behavior, undesired vertical fluid loads acting on the stamp are prevented by a vertical linear slide. On the interfaces Γ^{FS}, Γ^{FP} (with $\alpha_{BJ} = 1.0$), Γ^{PS}, and $\Gamma^{PS,c}$, the interface conditions are incorporated by the methods presented in Sections 3.3.2.1, 4.2.1, 4.2.2.2, 5.3.2, and 5.3.3.

Starting from this initial configuration, an increasing solid stress of maximum $2kPa$ is applied on boundary $\Gamma^{S,N}$, which leads to a squeeze-out motion of the fluid, and finally contact occurs. Afterwards, the fluid stress is increased on boundaries $\Gamma^{F,N}$ with a maximum value of $2.02kPa$, which is slightly above the maximum solid stress. The time-dependent solid and fluid stress are shown in Figure 5.12 (left). As soon as the local fluid pressure in the poroelastic layer exceeds the contact stress, the bodies will lift off at this local position. As a higher fluid stress than solid stress is applied, the whole stamp lifts off and finally moves upwards.

The fluid material parameters are $\rho^{F} = 1.0kg/m^3$ and $\mu^{F} = 1.0Pa \cdot s$. The material behavior of the solid domains as well as the macroscopic material behavior of the poroelastic layer are modeled by the Neo-Hookean material model with the hyperelastic strain energy functions ψ^{S} and $\psi^{P,skel}$ as introduced in (2.17). The Young's modulus E and the Poisson ratio ν are $E^1 = 20kPa, \nu^1 = 0.3$ in the solid domain Ω^{S_1}, $E^2 = 2000kPa, \nu^2 = 0.3$ in the solid domain Ω^{S_2}, and $E^{P} = 10kP, \nu^{P} = 0.0$ on the poroelastic domain Ω^{P}. The additional volume and penalty contributions to the strain energy function of the poroelastic domain with parameters $\kappa^{P} = 1000kPa$, $\eta^{P} = 1.0Pa$ are specified in (2.48) and (2.49). The initial porosity and permeability is $\mathring{\phi} = 0.5$ and $\mathring{K} = 10^{-2}m^2$, respectively. The backward Euler scheme is applied for time

discretization, with an appropriate time step length of $\Delta t = 0.1s, 0.01s$ or $0.001s$, depending on the system dynamics.

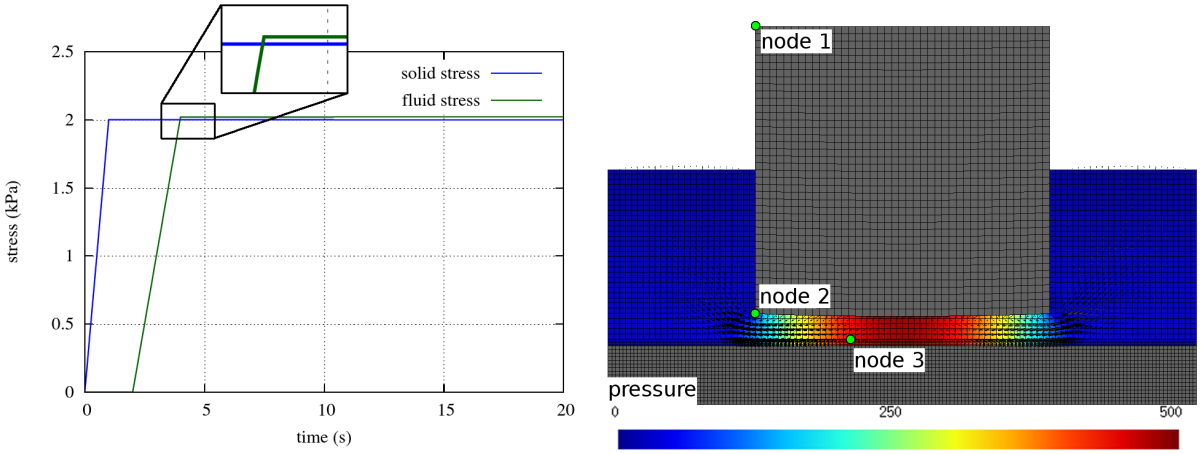

Figure 5.12: Time dependent solid and fluid stress on the boundaries $\Gamma^{S,N}$ and $\Gamma^{F,N}$ (left). Visualization of the fluid pressure, the fluid velocity (black arrows), the displacement (deformed domain) solution, and the computational mesh (element boundaries by black lines) for $t = 0.2s$ (right).

Computed Results and Discussion In Figure 5.12 (right) the spatial discretization (consisting of one layer of 3D trilinear hexahedral elements) is visualized. The solid and poroelastic elements "cut out" the non-physical part of the non-matching fluid elements. Furthermore, the overall computed solution for $t = 0.2s$ is visualized, where fluid outflow on $\Gamma^{F,N}$ occurs due to the pressure gradient which is induces by the structural motion.

An examination of the contacting phase at two different points in time is provided in Figure 5.13, which shows a detailed view of the contacting zone. It should be pointed out that in all following figures, the velocity amplitude is specified by the arrow length and the color code but not by the density of arrows. The zone with an increased density of arrows indicates the poroelastic layer, arising from the finer spatial resolution compared to the fluid domain. At $t = 0.2s$, the motion of the stamp, which is induced by the structural stress on $\Gamma^{S,N}$, displaces the fluid from the contacting zone. As the gap between stamp and foundation is still larger than the roughness height, the significant part of the fluid mass transport happens in the free fluid domain Ω^F. This is a result of the similar pressure gradient in the roughness layer and the free fluid. At $t = 0.71s$, there is already partial contact between the solid stamp and the poroelastic layer. The fluid pressure increased significantly, as the fluid mass transport happens mainly in the poroelastic roughness layer with a higher flow resistance than for the pure fluid in Ω^F. Compared to the velocities at $t = 0.2s$, the maximum value of the fluid velocity increased due to the higher pressure gradient. Until $t = 1.0s$, a compression of the poroelastic roughness, which leads to a reduction of the porosity and an outflow of fluid mass due to the increasing solid stress, can be observed. The increase of the fluid stress, starting at $t = 2.0s$, causes an inverse behavior with an inflow of fluid into the contacting area. Details of this lift-off phase can be seen in Figure 5.14. At $t = 4.005s$, the prescribed fluid stress reaches its maximum. Due to the flow resistance in the rough surface layer, the pressure in the contacting zone is still significantly lower than the prescribed fluid stress. As the lift-off occurs from outside to inside, most of the fluid flow occurs

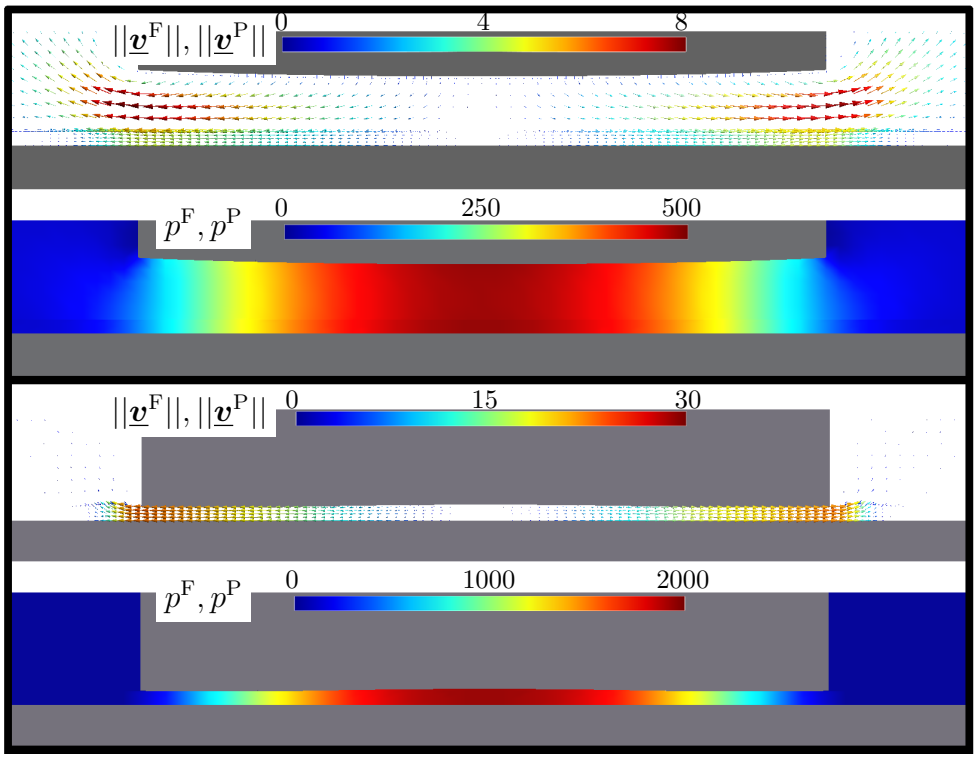

Figure 5.13: Fluid pressure $p^{\mathrm{F}}, p^{\mathrm{P}}$, fluid velocity $\underline{\boldsymbol{v}}^{\mathrm{F}}, \underline{\boldsymbol{v}}^{\mathrm{P}}$ (arrows), and displacement (deformed domain) solution in the contacting phase at time $t = 0.2$ (top) and $t = 0.71$ (bottom).

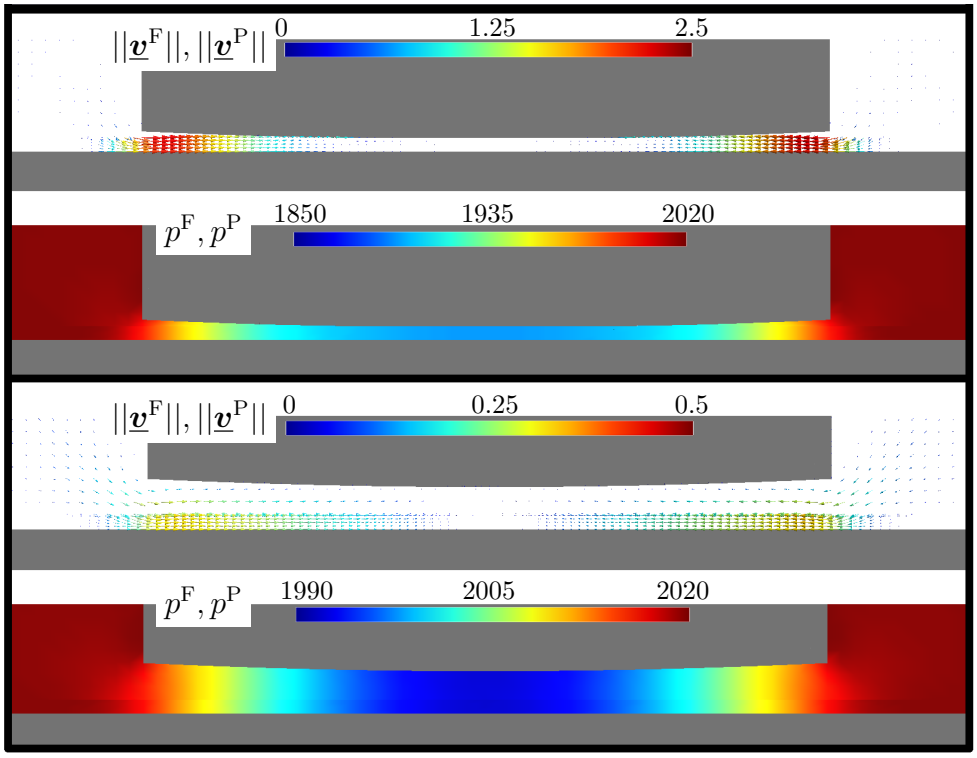

Figure 5.14: Fluid pressure $p^{\mathrm{F}}, p^{\mathrm{P}}$, fluid velocity $\underline{\boldsymbol{v}}^{\mathrm{F}}, \underline{\boldsymbol{v}}^{\mathrm{P}}$ (arrows), and displacement (deformed domain) solution in the lift-off phase at time $t = 4.005$ (top) and $t = 19.945$ (bottom).

on both outer regions. This leads to a very small pressure gradient and a negligible flow in the center of the contacting region. Advancing in time, the pressure in the center increases until the overall fluid force on the stamp exceeds the prescribed value of the solid force, and the solid bodies detach completely. For $t = 19.945s$, both bodies have reached a distance greater than the roughness layer height.

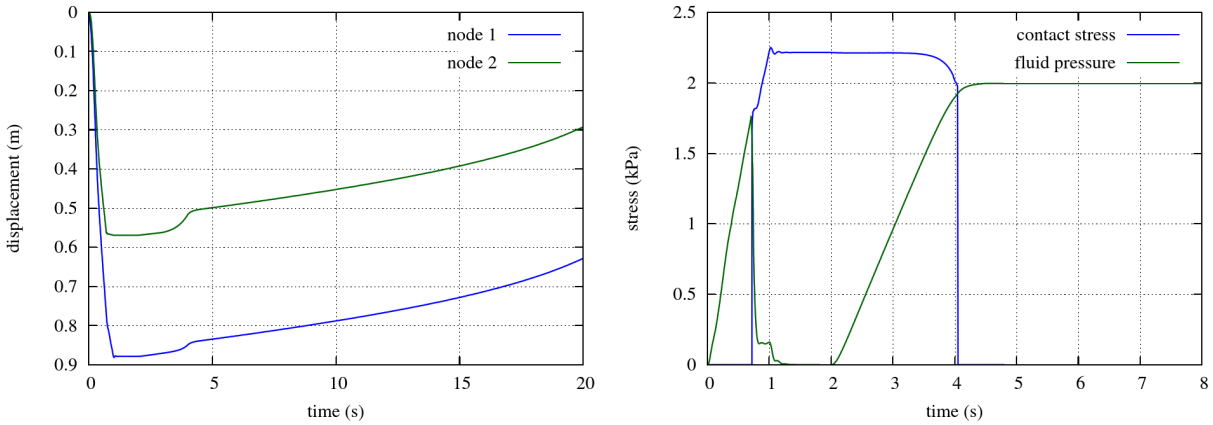

Figure 5.15: Displacement in vertical direction of two selected computational nodes (see Figure 5.12 (right) for the selected nodes) (left). Contact stress and fluid pressure at the selected node 3 (see Figure 5.12) (right).

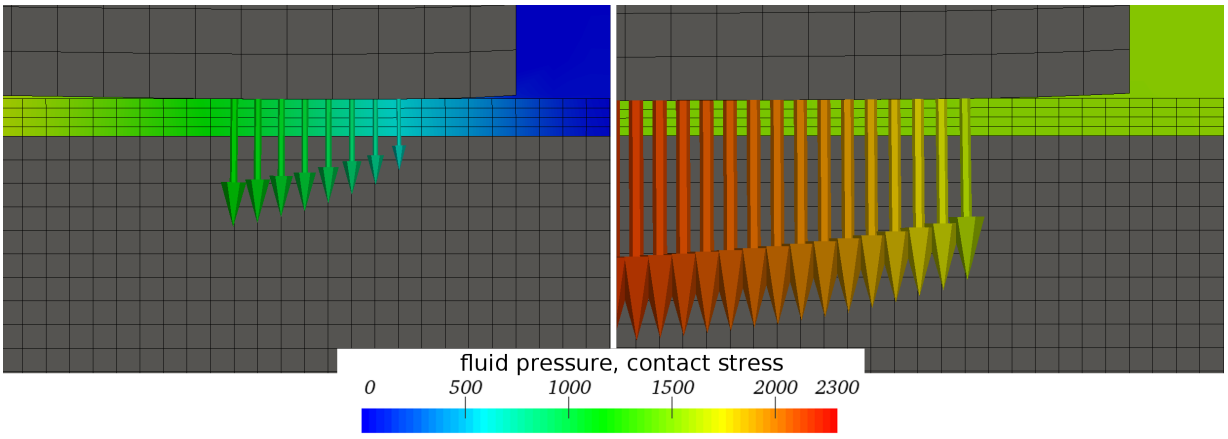

Figure 5.16: Visualization of the fluid pressure (background color) and the contact stress (arrows) for the right half in the proximity of the lower right of the stamp at two points in time $t = 0.702s$ (left) and $t = 3.515s$ (right).

In Figure 5.15 (left), the computed displacements for two selected nodes at the left side of the stamp are plotted. Due to the applied solid stress, both nodes moved down in vertical direction, until node 2 contacts with solid body Ω^{S_2} and, in the following, only a small motion of node 2 due to the compression of the poroelastic layer occurs. It can be observed that node 1 moved for a longer period in time and reaches a larger displacement maximum, due to the elastic deformation of the stamp. As there is an increase in fluid pressure for $2.0s \leq t \leq 4.0s$, both points start moving upwards again. After the velocity in both nodes increases due to the local deformation in this area, a smaller velocity, which is similar in both points, can be observed. Finally, the rising

distance between both bodies leads to an increase of the fluid force on the structural bodies and therefore an acceleration of the stamp.

Figure 5.15 (right) shows a comparison of the fluid pressure and the contact stress at the selected computational node 3. Starting from zero, the fluid pressure increases linearly due to the linearly rising prescribed solid stress on $\Gamma^{\mathrm{S,N}}$. As soon as contact occurs at this local point, the contact stress raises from zero to the current level of the fluid pressure and linearly increases in the following to the maximum stress in this computational node. The inherent reduction of the impact velocity and, therefore, the reduced fluid mass displacement in the poroelastic domain results in a significant reduction of fluid pressure. Until $t = 1.0s$, a smaller fluid pressure is still present due to the increasing solid stress and the corresponding deformation of the poroelastic domain. Starting from $t = 2.0s$, the fluid stress is increased, which leads to a local lift-off of the outer parts of the stamp, which also reduces the contact stress in node 3. As soon as the fluid pressure reaches the contact stress, this point gives up the contact constraint and the entire stress between the solid bodies is exchanged via the fluid.

In Figure 5.16, the area of the "active" contact constraint is visualized. Nodes of the interfaces, where the contact stress arrows are visible, are contained in the set of active Lagrange multipliers $\underline{\boldsymbol{\lambda}}^{\mathcal{A}}$. It can be seen that at the borders of this area, the values of fluid pressure and contact stress are almost equal. For $t = 0.702s$, which is during the contacting phase, one further aspect should be mentioned: At this point in time there is no contact in the center of the stamp. This results from the elastic deformation of the stamp, due to the maximum pressure in the center. This fluid island vanishes later by fluid mass flow through the poroelastic roughness layer.

5.5.3 Non-Return Valve

In the third example, a non-return valve is analyzed. This type of valve blocks the fluid flow in one direction, but enables the flow in the other direction. The fluid flow regulation of the valve is based on a deformable membrane, which adjusts according to the prevalent fluid pressure difference. To take into account the effect of the rough surface on the contacting membrane, a poroelastic layer is attached.

Problem Description All basic boundary conditions and the geometry can be found in Figure 5.17. The valve consists of an ellipsoidal shaped membrane $\Omega^{\mathrm{P}} \cup \Omega^{\mathrm{S}_1}$ and a solid support Ω^{S_2}. The volume which is not occupied by these domains is the domain Ω^{F}. In the following, its subdomains to the left and right of the membrane are referred to as inflow and outflow domain, respectively. Interfaces, boundary conditions, and dimensions are only defined once, but are still appropriate for the upper and lower part as the valve is symmetric. On the Neumann boundaries Γ^{F,N_1} and Γ^{F,N_2}, the fluid traction is prescribed, which leads to a flow through the valve. To depict the functional principle, the desired behavior for two different flow configurations is described. In the case that the fluid pressure on Γ^{F,N_1} is higher than on Γ^{F,N_2} ("open direction"), the elastic membrane deforms and increases the size of the smallest constriction between Ω^{P} and Ω^{S_2}. This reduces the flow resistance through the valve for an increasing pressure difference between inflow and outflow. If the fluid pressure on Γ^{F,N_2} is higher than on Γ^{F,N_1} ("blocking direction"), the deformation of the elastic membrane reduces the size of the smallest constriction and therefore increases the flow resistance. For a specific pressure difference, the membrane

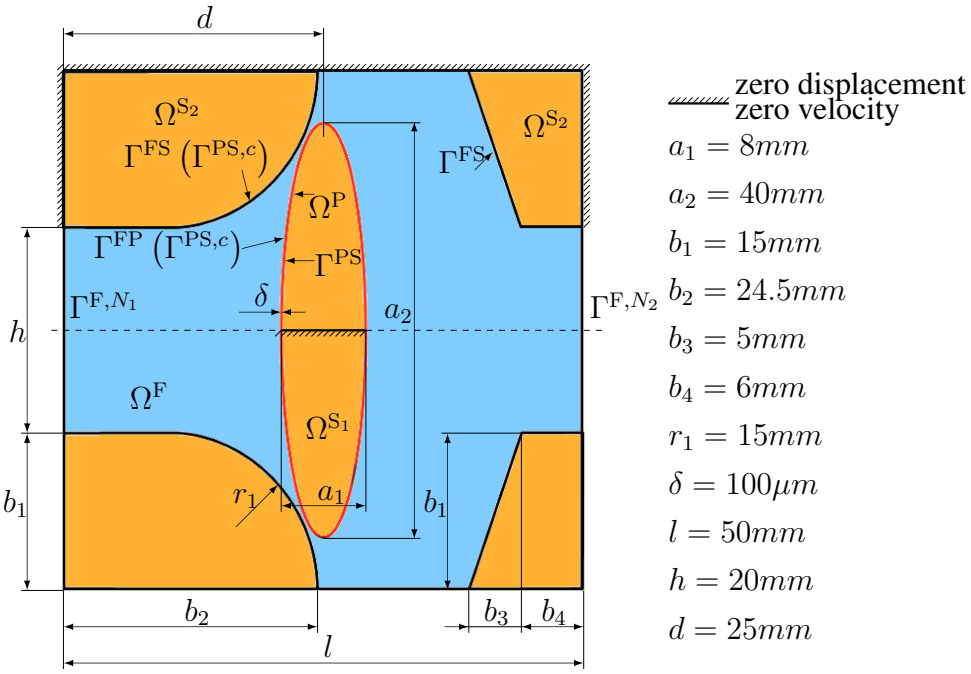

Figure 5.17: Boundary conditions and geometry of the non-return valve.

$\Omega^{S_1} \cup \Omega^{P}$ and the support Ω^{S_2} come into contact and, thus, the entire leakage flow has to pass through the rough layer. This flow rate is intended to be small compared to the flow rate in "open direction".

As fluid, water with the density $\rho^{F} = 1000kg/m^3$ and the dynamic viscosity $\mu^{F} = 10^{-3}Pa \cdot s$ is considered. A Neo-Hookean material (see equation (2.17)) is applied to model the solid behavior with Young's modulus and Poisson ratio of $E^1 = 2.3MPa, \nu^1 = 0.49$ and $E^2 = 2.3MPa, \nu^2 = 0.3$ in Ω^{S_1} and Ω^{S_2}, respectively. The initial density of the solid is equal to the fluid density $\rho_0^{S} = \rho^{F} = 1000kg/m^3$. The poroelastic layer Ω^{P} is specified by a spatially constant initial porosity $\mathring{\phi} = \phi(t = 0) = 0.5$ and a spatially constant initial material permeability $\mathring{K} = 4.6 \cdot 10^{-5}mm^2$. The macroscopic material response of the poroelastic layer is given by the strain energy functions (2.48) and (2.49) with parameters $E^{P} = 0.25MPa$, $\nu^{P} = 0.0$, $\tilde{c}^{P} = 0.25MPa$, $\alpha^{P} = 8, \kappa^{P} = 0.8MPa$, and $\eta^{P} = 1kPa$. For discretization in time, the backward Euler scheme is applied with time step lengths of $\Delta t = 2 \cdot 10^{-4}s$, $5 \cdot 10^{-5}s$, $2.5 \cdot 10^{-5}s$, or $1.25 \cdot 10^{-5}s$, depending on the dynamic response of the system.

The spatial discretization of all physical domains, consisting of one layer of 3D trilinear hexahedral elements, is visualized in Figure 5.18 (left). The poroelastic layer Ω^{P} with height δ is discretized by three layers of elements, which can be recognized in the detailed view in Figure 5.20. Due to the symmetric configuration, only one half of the domains is discretized and consulted for the computations. On the arising symmetry boundary, flow in normal direction is prohibited. In Figure 5.18 (right), the prescribed fluid stress for two different cases is plotted. The first case is designed to analyze the dynamic "valve closing" behavior. Additionally, it includes two sinusoidal-shaped peaks to determine the dynamic reaction of the valve on spurious pressure variations. The load peaks are initiated at $t = 0.075s$ and $t = 0.08s$ for a time span

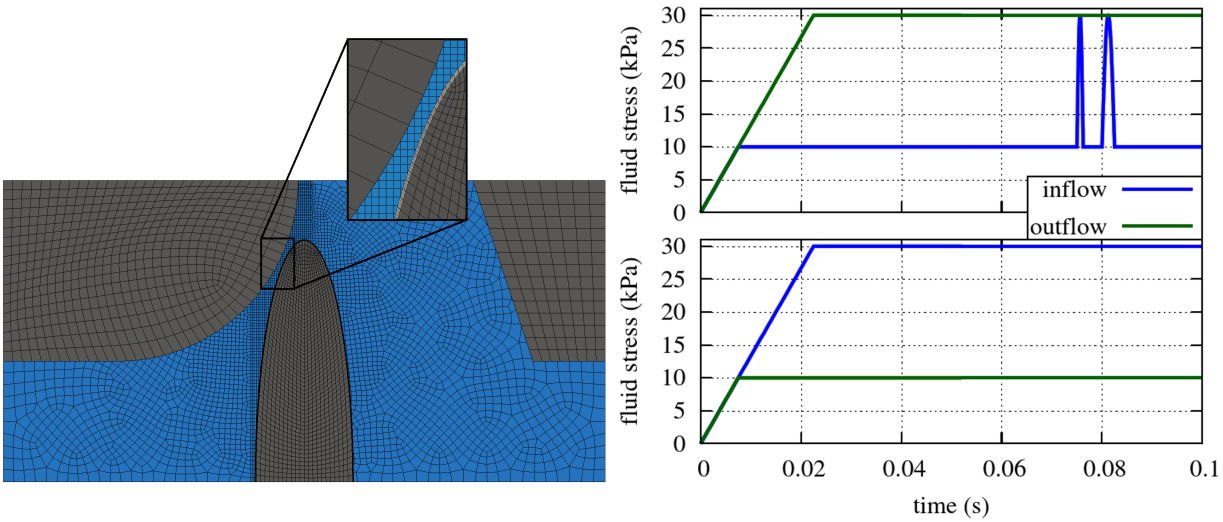

Figure 5.18: Computational mesh for all physical fields and detailed view of the smallest constriction. The hexahedral element boundaries are visualized by black lines (left). Prescribed time-dependent Neumann fluid stress on the inflow boundary Γ^{F,N_1} and the outflow boundary Γ^{F,N_2}. The upper diagram shows the applied load case to analyze a dynamic "valve closing" process. The lower diagram shows the prescribed load to analyze the valve behavior in "open direction" (right).

of $\Delta t_1 = 0.00125s$ and $\Delta t_1 = 0.0025s$, respectively. Case two analyzes the flow in "open direction" for a constant fluid stress difference between the inlet and the outlet boundary.

Computed Results and Discussion First, the computed results for the case "valve closing" are presented. Figure 5.19 shows the pressure field and the deformation of the valve for two instances in time. At $t = 0.07s$, an approximately stationary solution for the flow through the

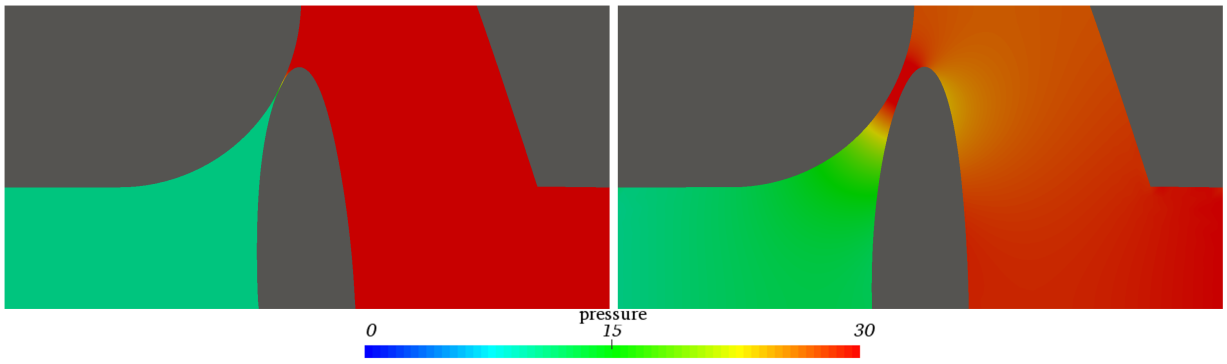

Figure 5.19: "Valve closing": Computed fluid pressure and solid deformation, $t = 0.07s$ (left), $t = 0.0836s$ (right).

closed valve can be observed. Contact occurs between the membrane and the support and the overall leakage flow through the valve is small. Thus, the pressure in the inflow and the outflow domain is almost constant and corresponds approximately to the applied boundary conditions. The pressure drop occurs mainly in the poroelastic layer. A lifting of the membrane from the support and therefore a temporal opening of the valve at $t = 0.0836s$ occurs due to the second applied sinusoidal-shaped fluid stress peak at the inflow boundary. Here, contrary to the station-

ary case ($t = 0.07s$), pressure gradients in the fluid domain can be observed. This originates from the fluid motion induced by deformation of membrane and support.

Figure 5.20 shows a detailed view on the smallest constriction between the membrane and the support. Due to the simultaneous increase in fluid stress (up to a value of $10kPa$) on the inflow

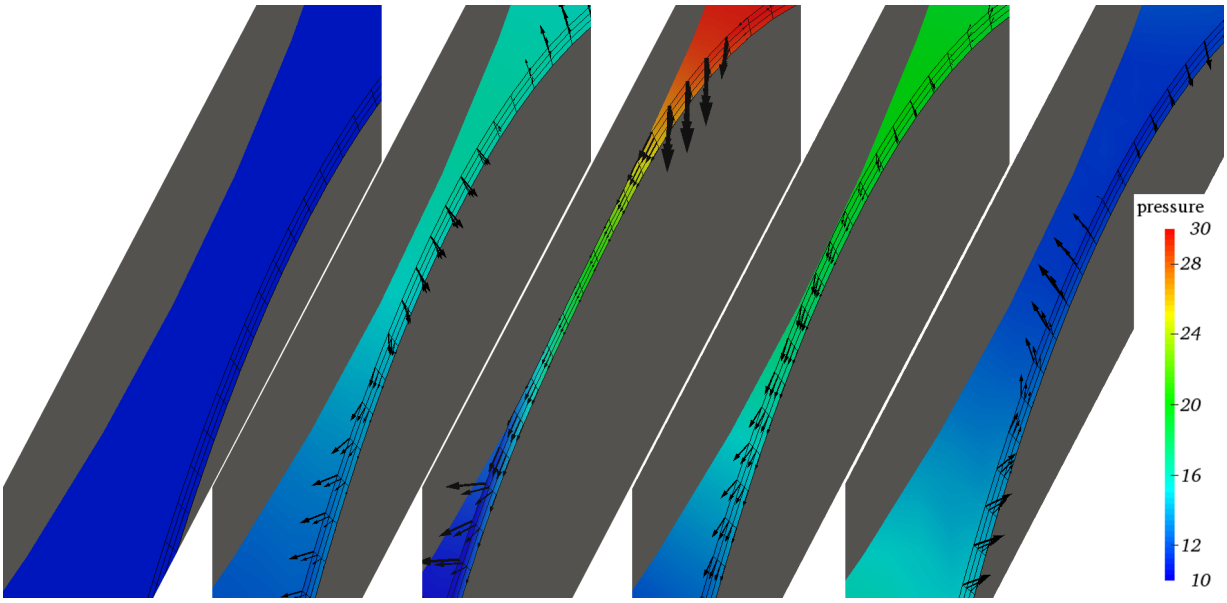

Figure 5.20: "Valve closing": Detailed view on the smallest constriction. The fluid pressure and the convective velocity (black arrows) $\left(\underline{\boldsymbol{v}}^{\mathrm{P}} - \partial\underline{\boldsymbol{u}}^{\mathrm{P}}/\partial t\right)$ in the poroelastic domain during the dynamic valve closing process is shown at five instances in time. The black lines indicate the computational mesh of the poroelastic layer. From left to right: $t = 0.008s$, $t = 0.012s$, $t = 0.07s$, $t = 0.077s$, and $t = 0.0827s$.

and the outflow boundary, mainly pure compression of all solid domains occurs, which leads to negligible fluid velocities (see $t = 0.008s$). At $t = 0.012s$, the membrane moves towards the solid support induced by the fluid pressure. This leads to a fluid flow through the roughness layer out of the narrowest position of the fluid domain. For the approximately stationary solution at $t = 0.07s$, a flow from the high pressure outflow domain through the poroelastic layer into the low pressure inflow domain can be observed. This flow corresponds to the leak rate of the investigated valve. The first fluid stress peak ($\Delta t_1 = 0.00125s$) leads to a loss of contact. At $t = 0.077s$, the maximum distance between the membrane and the solid support for this first peak occurs. Here, an increase of the fluid velocity through the poroelastic layer, which is expanded due to the vanishing contact stress, in comparison to the stationary situation can be observed. The second load peak leads to a pronounced lift-off of the membrane. During the lift-off phase at $t = 0.0827s$, fluid mass enters the smallest constriction. This corresponding fluid flow is split between the pure fluid domain and the poroelastic domain.

To quantify the performance of the non-return valve, the flow rates through the inflow $\Gamma^{N,1}$ and the outflow $\Gamma^{N,2}$ boundary are computed. In (6.36), a unique normal vector $\underline{\boldsymbol{n}}^{\Gamma^{N,1}->\Gamma^{N,2}}$, pointing in designated flow direction of the "open" valve, is applied for both boundaries.

$$\text{flow rate} = \int_{\Gamma^{N,i}} \underline{\boldsymbol{v}}^{\mathrm{F}} \cdot \underline{\boldsymbol{n}}^{\Gamma^{N,1}->\Gamma^{N,2}} \mathrm{d}\Gamma^{N,i}, \qquad i = 1, 2 \tag{5.24}$$

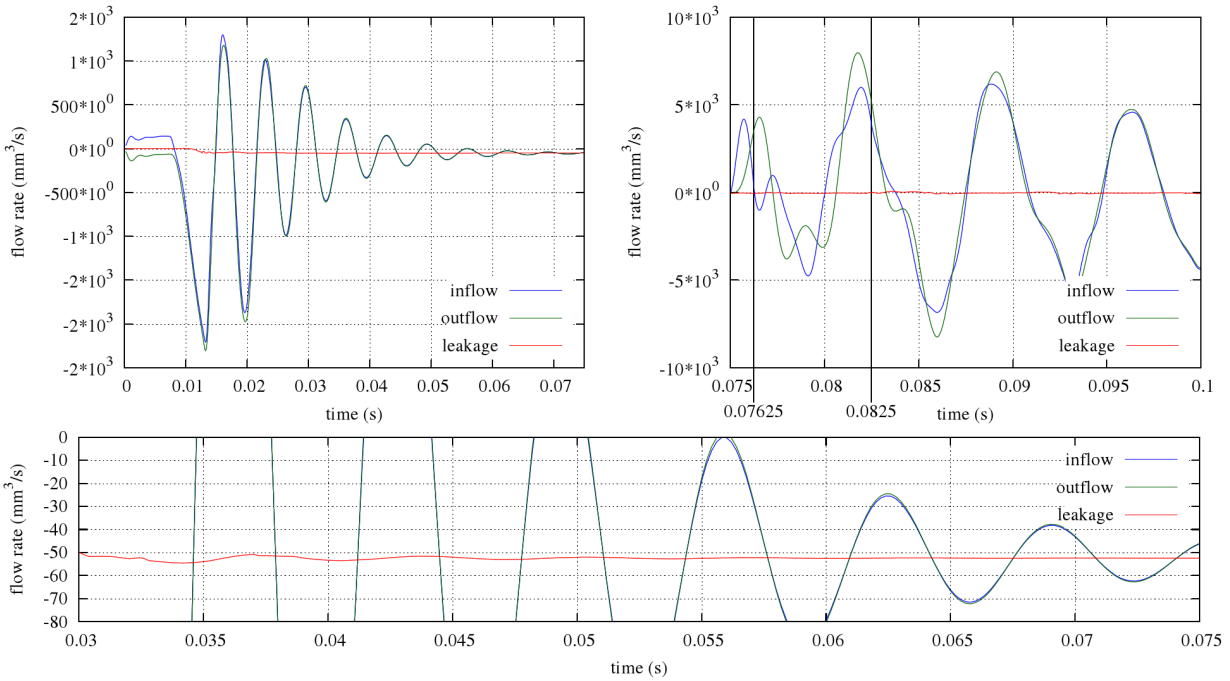

Figure 5.21: "Valve closing": Flow rate per unit depth on the inflow boundary Γ^{F,N_1} and the outflow boundary Γ^{F,N_2} and the computed leakage flow rate through the poroelastic layer.

The leakage flow rate through the poroelastic layer is computed based on the definition (5.23). Figure 5.21 (left) shows the computed flow rates during the dynamic closing process. Until $t = 0.0075s$, the compression of the solid bodies, which occurs due to the pressure increase, leads to inflow on both boundaries. Due to the dynamic impact of the membrane on the solid support, recurring deformation of the membrane is initiated. This causes a change in volume in the inflow and the outflow domain and, therefore, decaying oscillations of both measured flow rates. The average stationary flow rate computed between $t = 0.066s$ and $t = 0.0724s$ is $52.4mm^3/s$ and, thus, is almost equal to the directly computed (roughly constant) leakage flow rate (see detailed view in Figure 5.21 (bottom)). Figure 5.21 (right) shows the flow rates during and after the prescribed load peaks. Although the first stress peak does not lead to a significant lift-off of the membrane, its deformation and the associated change of volume in the inflow and the outflow domain generates high flow rates on both boundaries. Finally, due to the longer excitation phase, the second fluid load peak induces more pronounced flow rate peaks, which are decaying in time.

Figure 5.22 depicts the computed solution for the second case ("open direction") at four different instances in time. The present pressure difference deforms the membrane and increases the size of the smallest constriction. At $t = 0.026$, the evolution of a vortex behind the membrane can be observed. A movement of this vortex towards the symmetry plane of the valve can be seen at $t = 0.035s$. For $t = 0.05$ and $t = 0.09s$, a complex non-stationary flow pattern can be observed. It should be pointed out that assuming a symmetric flow field behind the membrane might influence the computed flow rates for this open valve configuration.

In Figure 5.23 (left), the computed flow rates on the inflow and outflow boundary are shown. After $t = 0.0075s$, the flow through the valve develops and similar flow rates for the inflow and

outflow boundary can be observed. Due to the previously described development of fluid vortices and their influence on the membrane deformation, no stationary flow rate can be observed. The average flow rate, evaluated between $t = 0.04s$ and $t = 0.1s$, is $8087mm^3/s$. Figure 5.23 (right) shows the difference between the inflow and outflow flow rate. This difference occurs due to the compression of the solid support and the membrane. In the initial phase, pure inflow into the system occurs due to the pressure increase until $t = 0.025s$. Later in time, oscillations with a vanishing mean value occur. This corresponds to a sequence of compression and expansion phases of the solid domains due to the time-dependent fluid loads.

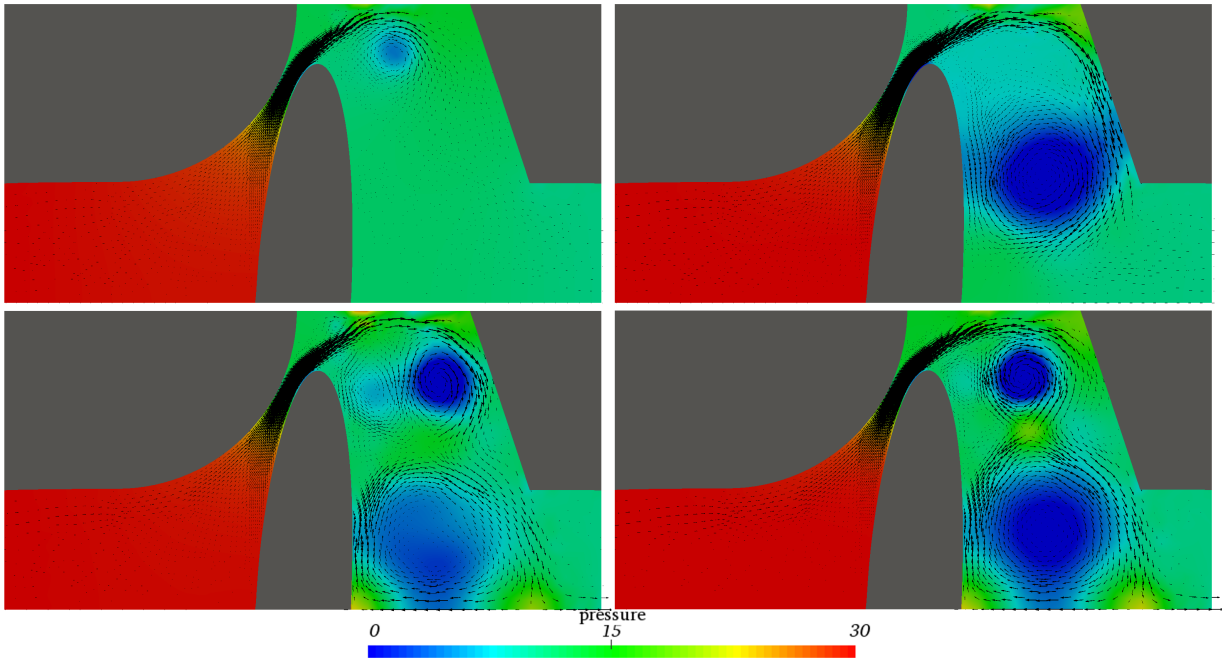

Figure 5.22: "Open direction": Fluid pressure and velocity (black arrows) at four different points in time. From top-left to bottom-right: $t_1 = 0.026s$, $t_2 = 0.035s$, $t_3 = 0.05$ and $t_4 = 0.09$.

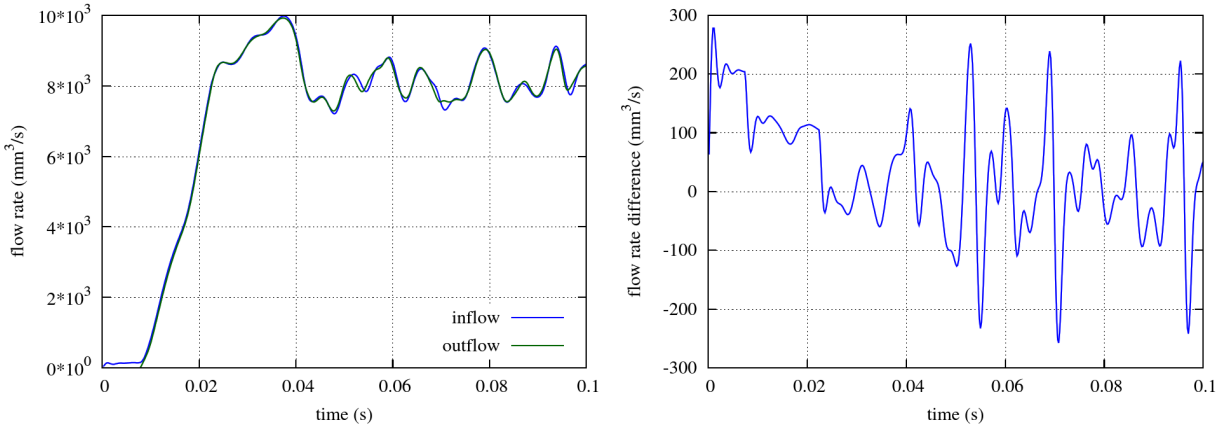

Figure 5.23: "Open direction": Flow rate per unit depth on the inflow boundary Γ^{F,N_1} and the outflow boundary Γ^{F,N_2} (left) and the flow rate difference between inflow and outflow (right).

6 A Consistent and Comprehensive Computational Approach for General Fluid-Structure-Contact Interaction Problems[1]

A consistent approach that allows solving challenging general nonlinear fluid-structure-contact interaction (FSCI) problems is presented in this chapter. In contrast to the formulation in Chapter 5, a simpler physical model, which does not directly take the effect of surface roughness into account, is considered. As a result, a more streamlined numerical approach can be developed, which is still applicable to many configurations where the rough surface microstructure does not dominate the overall physical response of the system and the physical processes of interest are not related to the effect of surface roughness.

The underlying continuous formulation includes both, ”no-slip” fluid-structure interaction as well as frictionless contact between multiple elastic bodies. The respective interface conditions in normal and tangential orientation and especially the role of the fluid stress within the region of closed contact are discussed for the general problem of FSCI. To ensure continuity of the tangential constraints from no-slip to frictionless contact, a transition is enabled by using the general Navier condition with varying slip length. Moreover, the fluid stress in the contact zone is obtained by an extension approach as it plays a crucial role for the lift-off behavior of contacting bodies. With the given continuity of the spatially continuous formulation, continuity of the discrete problem (which is essential for the convergence of Newton's method) is reached naturally. As topological changes of the fluid domain are an inherent challenge in FSCI configurations, a non-interface-fitted CutFEM is applied to discretize the fluid domain. All interface conditions, that are the “no-slip” FSI, the general Navier condition, and the frictionless contact are incorporated using Nitsche-based methods, thus retaining the continuity and consistency of the model. To account for the strong interaction between the fluid and solid domains, the overall coupled discrete system is solved monolithically. Numerical examples of varying complexity are presented to corroborate the developments. In a first example, the fundamental properties of the presented formulation such as the contacting and lift-off behavior, the mass conservation, and the influence of the slip length for the general Navier interface condition are analyzed. Beyond that, two more general examples demonstrate challenging aspects such as topological changes of the fluid domain, large contacting areas, and underline the general applicability of the presented method. Finally, the computational prediction of a double-leafed valve shows the applicability of the formulation to general 3D configurations.

[1] This chapter is adapted from the author's publication [3].

The chapter is organized as follows. In Section 6.1, the governing equations, which are comprised of the structural and fluid mechanics model as well as conditions on the interface in normal an tangential direction of the FSCI problem, are given. This is followed by a presentation of the discrete formulation, including all volume and interface contributions in Section 6.2. The coupled discrete FSCI problem and specific strategies utilized for the solution of the system are presented in Section 6.3. Finally, different numerical examples, which are capable of analyzing different aspects of the formulation, are presented in Section 6.4.

6.1 FSCI Problem Formulation

In this section, the governing equations and conditions for all physical domains and interfaces of the FSCI problem are briefly referenced. A typical configuration for such a problem is shown in Figure 6.1. The domain Ω of the overall FSCI problem includes the fluid domain Ω^{F} and the solid domain Ω^{S}. The overall coupling interface Γ consists of the fluid-structure interface Γ^{FS} and the active (closed) contact interface $\Gamma^{\mathrm{S},c}$.

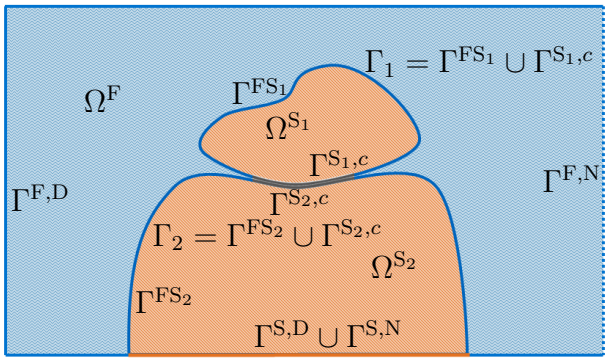

Figure 6.1: Fluid-structure-contact interaction (FSCI) problem setup for two contacting bodies Ω^{S_1} and Ω^{S_2}: the fluid domain Ω^{F}, the solid domain $\Omega^{\mathrm{S}} = \Omega^{\mathrm{S}_1} \cup \Omega^{\mathrm{S}_2}$, the fluid-structure interface $\Gamma^{\mathrm{FS}} = \Gamma^{\mathrm{FS}_1} \cup \Gamma^{\mathrm{FS}_2}$, the active (closed) contact interface $\Gamma^{\mathrm{S},c} = \Gamma^{\mathrm{S}_1,c} \cup \Gamma^{\mathrm{S}_2,c}$, the overall coupling interface $\Gamma = \Gamma_1 \cup \Gamma_2$, and the outer boundaries $\Gamma^{\mathrm{F,D}}, \Gamma^{\mathrm{F,N}}, \Gamma^{\mathrm{S,D}}, \Gamma^{\mathrm{S,N}}$.

The IBVP of nonlinear elastodynamics, which describes the physical behavior in the solid domain Ω^{S}, including especially the balance of linear momentum in (2.15), is discussed in detail in Section 2.1.4. In Section 2.1.5, the Navier-Stokes equations (2.27)-(2.28) and all condition to formulate the transient incompressible viscous flow problem in domain Ω^{F}, are introduced.

While all condition on the overall interface Γ are already discussed in Section 2.1.7 and Section 2.1.10.2 for the FSI- and the contact-interface, these conditions are reformulated, generalized, and expressed in normal and tangential interface orientation separately, such that the derivation of the Nitsche-based formulation, which is subsequently preformed, is more easily comprehensible. In the following, one set of conditions on the interface Γ is formulated which includes already the transition between the different types of interface conditions.

The Fluid Extension Operator In order to formulate the interface conditions at any point in space $\underline{\boldsymbol{x}}$ on the overall coupling interface, an extension operator $\mathcal{E}_{\underline{\boldsymbol{x}}} : \Gamma^{\mathrm{FS}} \longrightarrow \Gamma$ from the fluid-structure interface Γ^{FS} to the overall interface Γ is required. This extension is applied for

all quantities solely defined in the fluid domain Ω^{F} and, thus, for all quantities on the fluid-structure interface Γ^{FS} which are required for the formulation of the interface constraints on Γ. In the following, the extension of any quantity $*$ is denoted by an additional index $*_{\mathcal{E}}$. Exemplary, the extension of the normal fluid stress $\sigma^{\mathrm{F},nn}$ to a position $\underline{\boldsymbol{x}}$ on Γ is defined as follows:

$$\sigma_{\mathcal{E}}^{\mathrm{F},nn}\left(\underline{\boldsymbol{x}}\right) = \begin{cases} \sigma^{\mathrm{F},nn}\left(\underline{\boldsymbol{v}}^{\mathrm{F}}\left(\underline{\boldsymbol{x}}\right), p^{\mathrm{F}}\left(\underline{\boldsymbol{x}}\right)\right) & \text{on} \quad \Gamma^{\mathrm{FS}} \\ \mathcal{E}_{\underline{\boldsymbol{x}}}\left[\sigma^{\mathrm{F},nn}\left(\underline{\boldsymbol{v}}^{\mathrm{F}}\left(\underline{\boldsymbol{x}}_{\mathcal{E}}\right), p^{\mathrm{F}}\left(\underline{\boldsymbol{x}}_{\mathcal{E}}\right)\right)\right] & \text{on} \quad \Gamma^{\mathrm{S},c}, \end{cases}$$

$$\text{with} \quad \mathcal{E}_{\underline{\boldsymbol{x}}}\left[\sigma^{\mathrm{F},nn}\left(\underline{\boldsymbol{v}}^{\mathrm{F}}\left(\underline{\boldsymbol{x}}_{\mathcal{E}}\right), p^{\mathrm{F}}\left(\underline{\boldsymbol{x}}_{\mathcal{E}}\right)\right)\right] = \sigma^{\mathrm{F},nn}\left(\underline{\boldsymbol{v}}^{\mathrm{F}}\left(\underline{\boldsymbol{x}}\right), p^{\mathrm{F}}\left(\underline{\boldsymbol{x}}\right)\right) \quad \text{on} \quad \Gamma^{\mathrm{FS}} \cap \Gamma^{\mathrm{S},c}, \tag{6.1}$$

where the extension origin position $\underline{\boldsymbol{x}}_{\mathcal{E}}$ is properly chosen on Γ^{FS}. The last line in (6.1) represents the continuity of the extension operator. The applied extension operator for all presented numerical examples is discussed in Section 6.3.3. Alternative approaches to obtain fluid quantities on the overall interface Γ are briefly discussed in the Remarks 6.11 and 6.12.

6.1.1 Conditions on the Overall Coupling Interface Γ in Normal Direction

For the formulation of the interface constraints, which are split in the interface normal direction and in the tangential plane, the solid outward unit normal $\underline{\boldsymbol{n}} = \underline{\boldsymbol{n}}^{\mathrm{S}}$ will be considered. The normal component of the respective Cauchy stress is denoted as: $\sigma^{\mathrm{S},nn} = \underline{\boldsymbol{\sigma}}^{\mathrm{S}} : \underline{\boldsymbol{P}}^{n}$ and $\sigma^{\mathrm{F},nn} = \underline{\boldsymbol{\sigma}}^{\mathrm{F}} : \underline{\boldsymbol{P}}^{n}$, with the normal projection operator being specified as $\underline{\boldsymbol{P}}^{n} := \underline{\boldsymbol{n}} \otimes \underline{\boldsymbol{n}}$.

The conditions in the normal direction for purely non-adhesive structural contact configurations are given by the classical Hertz–Signiorini–Moreau (HSM) conditions

$$g^{n} := (\check{\underline{\boldsymbol{x}}}(\underline{\boldsymbol{x}}) - \underline{\boldsymbol{x}}) \cdot \underline{\boldsymbol{n}} \geq 0 \quad \text{on} \quad \Gamma, \tag{6.2}$$

$$\sigma^{\mathrm{S},nn} \leq 0 \quad \text{on} \quad \Gamma, \tag{6.3}$$

$$g^{n}\sigma^{\mathrm{S},nn} = 0 \quad \text{on} \quad \Gamma, \tag{6.4}$$

which ensure the non-penetration, the absence of adhesive contact forces, and the complementarity between the contact pressure and normal gap g^{n}. To obtain the normal gap g^{n}, the point $\check{\underline{\boldsymbol{x}}}(\underline{\boldsymbol{x}})$ is obtained as the projection of $\underline{\boldsymbol{x}}$ along its normal $\underline{\boldsymbol{n}}$ onto the opposite solid surface; in the case that no such projection exists, an infinite gap is assumed ($g^{n} \to \infty$). All quantities $*$ evaluated at this projection point will be denoted by a check $\check{*}$.

In the case contacting bodies are surrounded by fluid, the fluid flow in the contacting zone has to be considered properly as discussed in Section 2.1.10.2. Applying the classical HSM conditions (6.2)-(6.4) directly would result in the implicit assumption that fluid does not fill the contact zone. For such a configuration an instantaneous change from zero traction to the traction arising from the ambient fluid in the contact opening zone on the solid boundary would occur and thus the formulation of a continuous problem is prohibited. Considering, on the contrary, the presence of (physically reasonable) fluid in the contact zone (on a smaller length scale and not resolved but just modeled at the current macroscopic scale) leads to modified HSM conditions, where a lifting of both bodies occurs for vanishing relative traction of contact (solid) traction and ambient fluid traction. These conditions result in a continuous problem as the balance of solid

and fluid traction is essential on the common interface of a fluid and a solid. Then, the conditions on the interface Γ formulated for a specific point $\underline{\boldsymbol{x}}$ on Γ are

$$g^n \geq 0 \quad \text{on} \quad \Gamma, \tag{6.5}$$

$$\sigma^{\mathrm{S},nn} - \sigma_{\mathcal{E}}^{\mathrm{F},nn}\left(\underline{\boldsymbol{x}}\right) \leq 0 \quad \text{on} \quad \Gamma, \tag{6.6}$$

$$g^n \left[\sigma^{\mathrm{S},nn} - \sigma_{\mathcal{E}}^{\mathrm{F},nn}\left(\underline{\boldsymbol{x}}\right)\right] = 0 \quad \text{on} \quad \Gamma. \tag{6.7}$$

Condition (6.5) enforces a positive or vanishing gap g^n between two solid bodies. In condition (6.6), a negative or vanishing relative traction has to be guaranteed, at least in the case without adhesive forces that is considered here. Finally, in equation (6.7), either a vanishing gap in the contact case of solid-solid interaction or a vanishing relative traction in the case of fluid-structure interaction is enforced. Additionally, the dynamic equilibrium between two contacting bodies has to be formulated

$$\sigma^{\mathrm{S},nn} - \sigma_{\mathcal{E}}^{\mathrm{F},nn} = \sigma^{\check{\mathrm{S}},nn} - \sigma_{\mathcal{E}}^{\check{\mathrm{F}},nn} \qquad \text{on } \Gamma. \tag{6.8}$$

In the contact case, due to the vanishing gap g^n, the normal fluid traction equals its projection $\sigma_{\mathcal{E}}^{\mathrm{F},nn} = \sigma_{\mathcal{E}}^{\check{\mathrm{F}},nn}$ and, therefore, the classical dynamic equilibrium between both contacting bodies is recovered. Due to the vanishing relative traction $\sigma^{\mathrm{S},nn} = \sigma_{\mathcal{E}}^{\mathrm{F},nn}$ for the fluid-structure interaction case, both sides of the equilibrium vanish and as a result equation (6.8) is automatically fulfilled. Finally, the mass balance for the motion of solid bodies connected to a fluid domain is given as

$$v^{rel,n} := \left(\underline{\boldsymbol{v}}^{\mathrm{F}} - \frac{\partial \underline{\boldsymbol{u}}^{\mathrm{S}}}{\partial t}\right) \cdot \underline{\boldsymbol{n}} = 0 \qquad \text{on } \Gamma^{\mathrm{FS}}. \tag{6.9}$$

Herein, a vanishing normal relative velocity $v^{rel,n}$ is enforced solely on the interface Γ^{FS}, which is part of the fluid outer boundary $\partial\Omega^{\mathrm{F}}$. Applying an extension to the normal relative velocity $v_{\mathcal{E}}^{rel,n}$, this condition is automatically fulfilled on the remaining subset of the interface $\Gamma^{\mathrm{S},c}$ and hence on the entire Γ.

Remark 6.1 (Influence of the fluid extension operator)**.** *It should be highlighted, that conditions* (6.6)*,* (6.7)*, and* (6.8) *are expressed by an extension of the fluid stress from the fluid-structure interface* Γ^{FS} *to the contact interface* $\Gamma^{\mathrm{S},c}$*. The fluid stress extension has an essential influence only close to the condition changing point/curve* $(\Gamma^{\mathrm{FS}} \cap \Gamma^{\mathrm{S},c})$*. This point is contained in the origin from which the extension is constructed, namely the fluid domain. Thus, even the application of a simple continuous extension strategy of the fluid stress, which is by definition more accurate close to the fluid domain, provides a sufficiently accurate fluid stress representation for a wide range of problem configurations. Still, is should be emphasized that the continuous extension operator is considered in this chapter especially to enable a clear presentation due to its simplicity. In the case that a more accurate physical fluid solution is required in the contact zone, alternative extension based strategies can be considered or appropriate equations to describe the fluid flow in this zone can be solved.*

6.1.2 Conditions on the Overall Coupling Interface Γ in Tangential Direction

In the tangential direction, frictionless solid-solid contact in combination with the general Navier boundary condition as a kinematic constraint between the solid bodies and the fluid domain is considered for simplicity of presentation. Then, the following conditions have to be fulfilled on the interface Γ

$$\underline{\boldsymbol{\sigma}}^{\mathrm{S}} \cdot \underline{\boldsymbol{n}} \cdot \underline{\boldsymbol{P}}^{t} = \underline{\mathbf{0}} \qquad \text{on } \Gamma^{\mathrm{S},c}, \tag{6.10}$$

$$\left(\underline{\boldsymbol{\sigma}}^{\mathrm{F}} \cdot \underline{\boldsymbol{n}} - \underline{\boldsymbol{\sigma}}^{\mathrm{S}} \cdot \underline{\boldsymbol{n}}\right) \cdot \underline{\boldsymbol{P}}^{t} = \underline{\mathbf{0}} \qquad \text{on } \Gamma^{\mathrm{FS}}, \tag{6.11}$$

$$\left(\underline{\boldsymbol{v}}^{\mathrm{F}} - \frac{\partial \underline{\boldsymbol{u}}^{\mathrm{S}}}{\partial t} + \kappa \underline{\boldsymbol{\sigma}}^{\mathrm{F}} \cdot \underline{\boldsymbol{n}}^{\mathrm{F}}\right) \cdot \underline{\boldsymbol{P}}^{t} = \underline{\mathbf{0}} \qquad \text{on } \Gamma^{\mathrm{FS}}. \tag{6.12}$$

Herein, the tangential projection operator is specified by $\underline{\boldsymbol{P}}^{t} := \underline{\boldsymbol{I}} - \underline{\boldsymbol{n}} \otimes \underline{\boldsymbol{n}}$. While condition (6.10) represents the vanishing tangential traction component on the contact interface $\Gamma^{\mathrm{S},c}$, condition (6.11) enforces the dynamic equilibrium between solid and fluid on interface Γ^{FS}. As these two conditions can coincide at the common point $\Gamma^{\mathrm{S},c} \cap \Gamma^{\mathrm{FS}}$ only in the case of a vanishing tangential fluid traction $\left(\underline{\boldsymbol{\sigma}}^{\mathrm{F}} \cdot \underline{\boldsymbol{n}} \cdot \underline{\boldsymbol{P}}^{t} = \underline{\mathbf{0}}\right)$, the general Navier boundary condition (6.12) with a varying slip length is applied. This condition includes the no-slip boundary condition for a vanishing slip length $\kappa = 0$, which is the common interface condition, successfully applied for macroscopic problem setups. Nevertheless, on smaller scales, due to characteristics such as surface roughness or wettability, an interfacial velocity slip can be observed in a large number of experiments (see e.g. the review presented by Neto *et al.* [160]). The main emphasis of applying the general Navier boundary condition is to guarantee continuity for transitions between fluid-structure interaction and frictionless contact solid-solid interaction and to enable a relaxation of the tangential constraint close to the contacting zone. To obtain these properties, an infinite slip length $\kappa = \infty$ is specified close to the common point $\Gamma^{\mathrm{S},c} \cap \Gamma^{\mathrm{FS}}$, whereas a vanishing slip length still allows the consideration of the no-slip condition for the majority of the fluid-structure interface Γ^{FS} representing the macroscopic modeling point of view. Further details on the specification of the slip length κ for the presented formulation are given in Section 6.2.3. For the case of problems on small length scales where a certain amount of interfacial velocity slip occurs, the numerical approach allows specifying a physically substantiated slip length as well.

Remark 6.2 (Continuity of the formulation considering frictional contact)**.** *It should be pointed out that also for the case when frictional contact is considered, specific treatment of the tangential constraints will be required to result in a continuous problem. This issue arises due to the fact, that the fluid wall shear stress on a fluid-structure interface is not automatically equal to the tangential stress resulting from sliding friction of two contacting structures on a macroscopic view. In the case of a friction model with vanishing tangential interface traction at the condition changing point/curve $\Gamma^{\mathrm{FS}} \cap \Gamma^{\mathrm{S},c}$, applying the presented strategy directly results in a continuous problem also for frictional contact. The presented general Navier conditions yields a zero tangential fluid traction at the condition changing point $\Gamma^{\mathrm{FS}} \cap \Gamma^{\mathrm{S},c}$. Hence, to ensure continuity, a solid contact friction model has to provide a vanishing tangential traction at this point as well. For instance, this can be achieved using a Coulomb friction law (friction coefficient $\mathfrak{F}$) based on the relative normal stress with the total friction bound $\mathfrak{F} \cdot (\sigma^{\mathrm{S},nn} - \sigma_{\mathcal{E}}^{\mathrm{F},nn})$.*

6.2 Discrete Formulation

In this section, the discrete formulation that is applied to the numerical solution of the FSCI problem is presented. The temporal and spatial discretization of the continuous problem, which is presented in the previous section, is based on the One-Step-θ scheme as discussed in Section 2.2.1 and the FEM as discussed in Section 2.2.2. First, the discrete weak forms which are directly derived from the governing equations, including additional fluid stabilization operators, are referenced. To account for topological changes in the fluid domain, an elementary feature occurring for the FSCI problems, the CutFEM is applied to the discretization of the fluid equations. Details on the determination of a consistent discrete pair of the fluid domain and the fluid-structure interface for the contact case are given. The interface conditions, which are split in normal and tangential direction, are incorporated by Nitsche-based approaches. For the normal direction, a single continuous interface traction representation is proposed, which automatically incorporates the fluid-structure and contact conditions. A detailed explanation of the resulting contributions by this normal interface traction is given. Furthermore, a Nitsche-based formulation to incorporate the tangential fluid-structure interface condition including potential slip is presented. The specification of the slip length parameter on the interface to enable a continuous transition from fluid-structure coupling to frictionless contact is discussed. Finally, all contributions are treated in a single global system of equations and solved monolithically. Additional details on the solution procedure of the FSCI problem are given at the end of this section.

6.2.1 The Discrete Weak Form of the Coupled System

The discrete weak forms for the structural domain $\mathcal{W}_{\mathrm{h}}^{\mathrm{S}}$ and the fluid domain $\mathcal{W}_{\mathrm{h}}^{\mathrm{F,CUT}}$ utilizing the CutFEM are specified in (2.108) and in (3.7), respectively. The discrete weak form of the coupled system $\mathcal{W}_{\mathrm{h}}^{\mathrm{FS}}$ is composed of these two weak forms and the additional boundary integral on Γ_{h}, which arises naturally in the derivation of the weak forms.

$$\begin{aligned}\mathcal{W}_{\mathrm{h}}^{\mathrm{FS}}\left[\left(\delta\underline{\boldsymbol{u}}_{\mathrm{h}}^{\mathrm{S}},\delta\underline{\boldsymbol{v}}_{\mathrm{h}}^{\mathrm{F}},\delta p_{\mathrm{h}}^{\mathrm{F}}\right),\left(\underline{\boldsymbol{u}}_{\mathrm{h}}^{\mathrm{S}},\underline{\boldsymbol{v}}_{\mathrm{h}}^{\mathrm{F}},p_{\mathrm{h}}^{\mathrm{F}}\right)\right] = \\ \mathcal{W}_{\mathrm{h}}^{\mathrm{S}}\left[\delta\underline{\boldsymbol{u}}_{\mathrm{h}}^{\mathrm{S}},\underline{\boldsymbol{u}}_{\mathrm{h}}^{\mathrm{S}}\right]+\mathcal{W}_{\mathrm{h}}^{\mathrm{F,CUT}}\left[\left(\delta\underline{\boldsymbol{v}}_{\mathrm{h}}^{\mathrm{F}},\delta p_{\mathrm{h}}^{\mathrm{F}}\right),\left(\underline{\boldsymbol{v}}_{\mathrm{h}}^{\mathrm{F}},p_{\mathrm{h}}^{\mathrm{F}}\right)\right] \\ \underbrace{-\left\langle\delta\underline{\boldsymbol{u}}_{\mathrm{h}}^{\mathrm{S}},\overline{\boldsymbol{\sigma}}_{\mathrm{h}}^{n}\right\rangle_{\Gamma_{\mathrm{h}}}+\left\langle\delta\underline{\boldsymbol{v}}_{\mathrm{h},\emptyset}^{\mathrm{F}},\overline{\boldsymbol{\sigma}}_{\mathrm{h}}^{n}\right\rangle_{\Gamma_{\mathrm{h}}}}_{:=\mathcal{W}_{\mathrm{h},\Gamma}^{\mathrm{FS},n}+\mathcal{W}_{\mathrm{h},\Gamma}^{\mathrm{FS},t}}\end{aligned} \tag{6.13}$$

As introduced in the previous chapters, an interface-fitted discretization is applied for the structural domain. Details on the discretization of the fluid domain, which is non-interface-fitted, are given in Section 3.1 and with the focus on specific aspects for FSCI in Section 6.2.1.1 and Section 6.2.1.2.

Including the unique interface traction $\overline{\boldsymbol{\sigma}}_{\mathrm{h}}^{n}$, which will be specified in Section 6.2.2 and Section 6.2.3, the respective dynamic equilibrium in normal direction (6.6), (6.7), and (6.8), as well as in tangential direction (6.10), and (6.11) is incorporated directly into the weak form. As the interface conditions (6.5)-(6.12) require a separate treatment of the normal and the tangential constraints, the normal component $\overline{\sigma}_{\mathrm{h}}^{nn}$ and the tangential component $\overline{\boldsymbol{\sigma}}_{\mathrm{h}}^{n}\cdot\underline{\boldsymbol{P}}^{t}$ of the interface traction $\overline{\boldsymbol{\sigma}}_{\mathrm{h}}^{n}=\overline{\sigma}_{\mathrm{h}}^{nn}\cdot\underline{\boldsymbol{n}}_{\mathrm{h}}+\overline{\boldsymbol{\sigma}}_{\mathrm{h}}^{n}\cdot\underline{\boldsymbol{P}}^{t}$ are discussed separately in Sections 6.2.2 and 6.2.3.

To extend the interface contribution on $\Gamma_{\mathrm{h}}^{\mathrm{FS}}$ arising from partial integration of the viscous and pressure contributions in domain $\Omega_{\mathrm{h}}^{\mathrm{F}}$ formally to the overall interface Γ_{h}, an additional definition

of the fluid test functions $(\delta\underline{\boldsymbol{v}}^{\mathrm{F}}_{\mathrm{h},\emptyset}, \delta p^{\mathrm{F}}_{\mathrm{h},\emptyset})$ on the whole interface Γ_{h} is consulted. For the additional interface contributions in (6.13), vanishing fluid test functions outside of the fluid domain $\Omega^{\mathrm{F}}_{\mathrm{h}}$ are considered.

$$\left(\delta\underline{\boldsymbol{v}}^{\mathrm{F}}_{\mathrm{h},\emptyset}, \delta p^{\mathrm{F}}_{\mathrm{h},\emptyset}\right) = \begin{cases} \left(\delta\underline{\boldsymbol{v}}^{\mathrm{F}}_{\mathrm{h}}, \delta p^{\mathrm{F}}_{\mathrm{h}}\right) & \text{in} \quad \Omega^{\mathrm{F}}_{\mathrm{h}} \\ (\underline{\mathbf{0}}, 0) & \text{otherwise} \end{cases} \tag{6.14}$$

6.2.1.1 The CutFEM Utilized for FSCI

The CutFEM is applied for the discretization of the fluid domain allowing for a fixed Eulerian computational mesh. A visualization of the discretization concept is given for an exemplary contacting configuration in Figure 6.2. The typical small penetration of contacting solid bodies in the discrete solution is visualized exaggeratedly in this figure. This aspect is discussed in detail in Section 6.2.1.2. In the CutFEM, the fluid discretization in domain $\breve{\Omega}^{\mathrm{F}}_{\mathcal{T}_{\mathrm{h}}}$ is specified to cover the

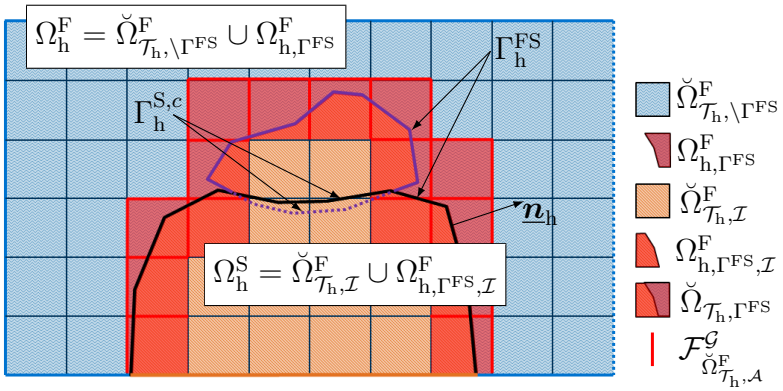

Figure 6.2: Basic problem setup for the applied CutFEM in a FSCI configuration, the structural domain $\Omega^{\mathrm{S}}_{\mathrm{h}} = \Omega^{\mathrm{S}_1}_{\mathrm{h}} \cup \Omega^{\mathrm{S}_2}_{\mathrm{h}}$ is embedded in the fluid domain $\Omega^{\mathrm{F}}_{\mathrm{h}}$. The domain covered by the non-interface-fitted discretization $\breve{\Omega}^{\mathrm{F}}_{\mathcal{T}_{\mathrm{h}}} = \breve{\Omega}^{\mathrm{F}}_{\mathcal{T}_{\mathrm{h}},\setminus\Gamma^{\mathrm{FS}}} \cup \breve{\Omega}^{\mathrm{F}}_{\mathcal{T}_{\mathrm{h}},\mathcal{I}} \cup \breve{\Omega}_{\mathcal{T}_{\mathrm{h}},\Gamma^{\mathrm{FS}}}$ represents the fluid domain $\Omega^{\mathrm{F}}_{\mathrm{h}}$ by a set of elements covering the domain $\breve{\Omega}^{\mathrm{F}}_{\mathcal{T}_{\mathrm{h}},\setminus\Gamma^{\mathrm{FS}}}$ and the fluid subdomain $\Omega^{\mathrm{F}}_{\mathrm{h},\Gamma^{\mathrm{FS}}}$ of the domain $\breve{\Omega}_{\mathcal{T}_{\mathrm{h}},\Gamma^{\mathrm{FS}}}$. The non-fluid domain, which equals the structural domain $\Omega^{\mathrm{S}}_{\mathrm{h}}$, consists of the domain covering the set of elements in $\breve{\Omega}^{\mathrm{F}}_{\mathcal{T}_{\mathrm{h}},\mathcal{I}}$ and the non-fluid subdomain $\Omega^{\mathrm{F}}_{\mathrm{h},\Gamma^{\mathrm{FS}},\mathcal{I}}$ of the domain $\breve{\Omega}^{\mathrm{F}}_{\mathcal{T}_{\mathrm{h}},\Gamma^{\mathrm{FS}}}$. For all inner element faces $\mathcal{F}^{\mathcal{G}}_{\breve{\Omega}^{\mathrm{F}}_{\mathcal{T}_{\mathrm{h}},\mathcal{A}}}$ of $\breve{\Omega}^{\mathrm{F}}_{\mathcal{T}_{\mathrm{h}},\setminus\Gamma^{\mathrm{FS}}} \cup \breve{\Omega}^{\mathrm{F}}_{\mathcal{T}_{\mathrm{h}},\Gamma^{\mathrm{FS}}}$, which are connected to one element in $\breve{\Omega}_{\mathcal{T}_{\mathrm{h}},\Gamma^{\mathrm{FS}}}$, the ghost penalty stabilization is applied.

entire fluid domain $\Omega^{\mathrm{F}}_{\mathrm{h}}$. The boundaries and interfaces of the fluid domain $\partial\Omega^{\mathrm{F}}_{\mathrm{h}}$ do not have to match the boundary of the computational discretization $\partial\breve{\Omega}^{\mathrm{F}}_{\mathcal{T}_{\mathrm{h}}}$. This beneficial feature of the CutFEM allows the direct handling of large motion or deformation of the solid domain $\Omega^{\mathrm{S}}_{\mathrm{h}}$ and even topological changes of the fluid domain $\Omega^{\mathrm{F}}_{\mathrm{h}}$ as it typically occurs in FSCI problems. As shown by the exemplary configuration in Figure 6.2, the outer boundaries of the fluid domain often match the discretization boundary, which does not necessarily have to be. The solid domains $\Omega^{\mathrm{S}_1}_{\mathrm{h}}$ and $\Omega^{\mathrm{S}_2}_{\mathrm{h}}$ are discretized matching to the boundaries and interfaces. Then, the discrete fluid domain $\Omega^{\mathrm{F}}_{\mathrm{h}}$ results from "cutting out" the non-fluid domain, which is specified by the current geometry of the fluid-structure interface $\Gamma^{\mathrm{FS}}_{\mathrm{h}}$. This interface is given by the boundary of the solid domain $\Gamma^{\mathrm{FS}}_{\mathrm{h}} \subseteq \partial\Omega^{\mathrm{S}}_{\mathrm{h}}$ and potential non-matching outer boundaries. All details concerning the numerical

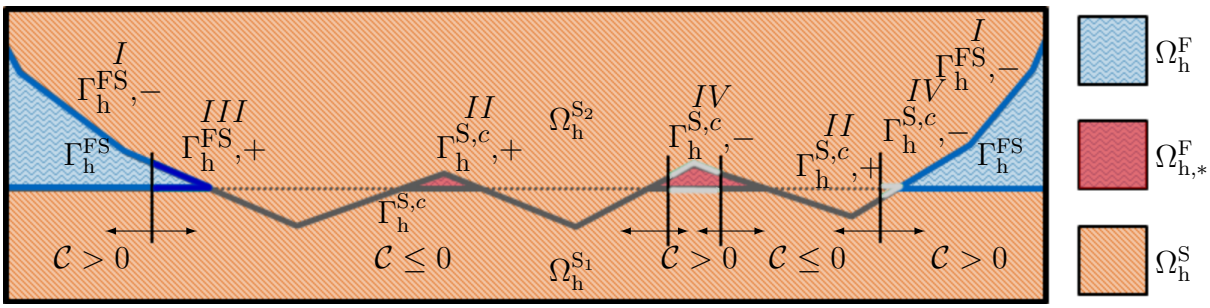

Figure 6.3: Detailed (exaggerated) view of the discrete contacting zone of two solid bodies $\Omega_{\mathrm{h}}^{\mathrm{S}_1}$ and $\Omega_{\mathrm{h}}^{\mathrm{S}_2}$. Due to the discrete contact formulation, small fluid fractions $\Omega_{\mathrm{h},*}^{\mathrm{F}}$ can emerge, which are not considered part of the fluid domain $\Omega_{\mathrm{h}}^{\mathrm{F}}$. The fluid-structure interface $\Gamma_{\mathrm{h}}^{\mathrm{FS}}$ (blue line) is constructed consistently to this fluid domain $\Omega_{\mathrm{h}}^{\mathrm{F}}$. The remaining part of the interface Γ_{h} is the contact interface $\Gamma_{\mathrm{h}}^{\mathrm{S},c}$. With the scalar value $\mathcal{C}$ introduced in Section 6.2.2, the interface is split into four cases $(I/\Gamma_{\mathrm{h}}^{\mathrm{FS}},-; II/\Gamma_{\mathrm{h}}^{\mathrm{S},c},+; III/\Gamma_{\mathrm{h}}^{\mathrm{FS}},+; IV/\Gamma_{\mathrm{h}}^{\mathrm{S},c},-)$.

integration of the weak form in the different types of elements ($\breve{\Omega}_{\mathcal{T}_{\mathrm{h}},\setminus\Gamma^{\mathrm{FS}}}^{\mathrm{F}}$, $\breve{\Omega}_{\mathcal{T}_{\mathrm{h}},\mathcal{I}}^{\mathrm{F}}$, and $\breve{\Omega}_{\mathcal{T}_{\mathrm{h}},\Gamma^{\mathrm{FS}}}$) and the applied ghost penalty stabilization can be found in Section 3.1.

Remark 6.3 (Existence of the discrete fluid test functions in the ghost domain)**.** *It should be highlighted that in contrary to definition* (6.14)*, the discrete test functions* $\left(\delta\underline{\boldsymbol{v}}_{\mathrm{h}}^{\mathrm{F}}, \delta p_{\mathrm{h}}^{\mathrm{F}}\right)$ *do not vanish in the ghost domain* $\Omega_{\mathrm{h},\Gamma^{\mathrm{FS}},\mathcal{I}}^{\mathrm{F}}$ *and are evaluated on the inter-element faces for the face-oriented stabilization and ghost penalty stabilization* (2.114) *and* (3.4) *outside of the physical fluid domain* $\Omega_{\mathrm{h}}^{\mathrm{F}}$.

6.2.1.2 Consistent Fluid Domain $\Omega_{\mathrm{h}}^{\mathrm{F}}$ and Fluid-Structure Interface $\Gamma_{\mathrm{h}}^{\mathrm{FS}}$ Representation for the Contacting Case

The weak form (2.112) is solely integrated in the physical domain $\Omega_{\mathrm{h}}^{\mathrm{F}}$. This domain is characterized by the non-moving outer boundaries $\Gamma_{\mathrm{h}}^{\mathrm{F,D}}$ and $\Gamma_{\mathrm{h}}^{\mathrm{F,N}}$ as well as the moving fluid-structure interface $\Gamma_{\mathrm{h}}^{\mathrm{FS}}$. The discrete motion of the interface $\Gamma_{\mathrm{h}}^{\mathrm{FS}}$ is given by the general interface Γ_{h} and hence by the motion of the solid domain $\Omega_{\mathrm{h}}^{\mathrm{S}}$. It is essential to evaluate the overall weak form on a consistent pair of domain $\Omega_{\mathrm{h}}^{\mathrm{F}}$ and interface $\Gamma_{\mathrm{h}}^{\mathrm{FS}}$. This aspect is straight-forward as long as no contact between solid bodies occurs, but should be discussed in detail for the case of contacting discrete bodies. The contacting scenario illustrated in Figure 6.3 results in partial overlap of both solid domains due to the discrete approximation. Therefore, in a first step all parts of the interface Γ_{h} which are overlapping - identified by the solid unit outward solid normal vector $\underline{\boldsymbol{n}}_{\mathrm{h}}$ - are removed from the "intersection" interface. The corresponding fluid domain $\Omega_{\mathrm{h}}^{\mathrm{F}} \cup \Omega_{\mathrm{h},*}^{\mathrm{F}}$ potentially includes small fluid fractions occurring from the discrete contact formulation. To avoid these "islands", the purely numerically occurring segments on the current "intersection" interface are removed additionally, leading to the consulted interface $\Gamma_{\mathrm{h}}^{\mathrm{FS}}$. For sufficiently spatially resolved computational meshes, the identification can be simply performed by a predefined maximal ratio of the element size compared to the actual size of the bounding box containing a single fluid fraction. Finally, the intersection of the computational fluid mesh is performed with this interface $\Gamma_{\mathrm{h}}^{\mathrm{FS}}$, resulting in a physical fluid domain $\Omega_{\mathrm{h}}^{\mathrm{F}}$ which does not include the domain $\Omega_{\mathrm{h},*}^{\mathrm{F}}$. The discrete contact interface is then defined by: $\Gamma_{\mathrm{h}}^{\mathrm{S},c} = \Gamma_{\mathrm{h}} \setminus \Gamma_{\mathrm{h}}^{\mathrm{FS}}$.

6.2.2 Nitsche-based Method on the Overall Coupling Interface Γ_{h} in Normal Direction

The representative interface traction $\overline{\sigma}_{\mathrm{h}}^{nn} = \underline{\overline{\boldsymbol{\sigma}}}_{\mathrm{h}}^{n} \cdot \underline{\boldsymbol{n}}_{\mathrm{h}}$ in normal direction needs to comply with all interface conditions (6.5)-(6.9). Defining the normal interface traction to

$$\overline{\sigma}_{\mathrm{h}}^{nn} = \min \left[(\sigma_{\mathrm{h},\mathcal{E}}^{\mathrm{F},nn} + \gamma_{\mathcal{E}}^{\mathrm{FSI}} v_{\mathrm{h},\mathcal{E}}^{rel,n}) \ , \ (\overline{\sigma}_{\mathrm{h}}^{\mathrm{S},nn} + \gamma^{\mathrm{S},c} g_{\mathrm{h}}^{n}) \right], \tag{6.15}$$

with two sufficiently large parameters $\gamma_{\mathcal{E}}^{\mathrm{FSI}} > 0$ and $\gamma^{\mathrm{S},c} > 0$, allows the fulfillment of these conditions as discussed in the following. The left-hand side of the minimum corresponds to enforcing the FSI conditions ((6.6) in the case equal to zero in combination with (6.9)) and the right-hand side of the minimum enforces the contact no-penetration condition in normal direction ((6.5) in the case equal to zero in combination with (6.8)). As a result, condition (6.7) is fulfilled automatically for both sides of the minimum.

In the case that the contact no-penetration condition is active, the balance of linear momentum across the closed contact interface, in which condition (6.8) reduces to $\sigma_{\mathrm{h}}^{\mathrm{S},nn} = \sigma_{\mathrm{h}}^{\check{\mathrm{S}},nn}$, is incorporated by using the same representative solid stress $\overline{\sigma}_{\mathrm{h}}^{\mathrm{S},nn}$ on both sides of the potential contact surfaces. In the most simple case, one of the two potentially contacting solids, e.g. $\Omega_{\mathrm{h}}^{\mathrm{S}_1}$ is designated as a so-called slave side and the representative solid stress is chosen as the discrete stress representation of that side $\overline{\sigma}_{\mathrm{h}}^{\mathrm{S},nn} = \sigma_{\mathrm{h}}^{\mathrm{S}_1,nn}$. An explicit choice of a slave side, however, results in an inherent bias between the two solid sides. To obtain an unbiased formulation, an arbitrary convex combination $\overline{\sigma}_{\mathrm{h}}^{\mathrm{S},nn} = \omega^c \sigma_{\mathrm{h}}^{\mathrm{S}_1,nn} + (1-\omega^c)\sigma_{\mathrm{h}}^{\mathrm{S}_2,nn}$ of the stress representations of the two solid sides can be used based on a weight $\omega^c \in [0,1]$. If this weight is determined independently of the numbering of the contacting solids (i.e. invariant with respect to flipping the slave and master side), the resulting algorithm is unbiased. Two possible choices for unbiased method are either choosing $\omega^c = 1/2$ (see the works of Chouly *et al.* [63] and Mlika *et al.* [156]) or using harmonic weights determined based on material parameters and mesh sizes (see the works of Burman and Zunino [49] and Seitz *et al.* [196]).

This formulation for Nitsche contact follows also the principles for Nitsche's method discussed in Section 3.3.1. Due to the nonlinearity of the constitutive relation and the deformation of the elements, an element-wise local generalized eigenvalue problem is solved to specify the Nitsche penalty parameter $\gamma^{\mathrm{S},c}$ by the maximum eigenvalue λ_e of the element $\Omega_{\mathcal{T}_{\mathrm{h}},e}^{\mathrm{S}}$. In contrast to the considered local generalized eigenvalue problem for solid-sided interface stress representation for the CutFEM FSI in (3.31), not all linearizations of the terms specified in (3.31) are considered for the evaluation of the element matrices matrices $\underline{\boldsymbol{A}}_e$ and $\underline{\boldsymbol{B}}_e$ in (3.19). The details of this definition, which turned out to perform best in the numerical examples of Seitz [195], can be found in the thesis of Seitz [195] for the Nitsche contact formulation. Nevertheless, for all numerical examples presented in this and the following chapter no noticeable difference between both definitions is expected. Based on the maximum eigenvalues λ_{e1} and λ_{e2} of two contacting elements $\Omega_{\mathcal{T}_{\mathrm{h}},e1}^{\mathrm{S}_1}$ and $\Omega_{\mathcal{T}_{\mathrm{h}},e2}^{\mathrm{S}_2}$ the harmonic weighting of the contact stress for this element pair can be specified. The weighting factor is given by

$$\omega^c = \frac{\lambda_{e2}}{\lambda_{e1} + \lambda_{e2}}, \tag{6.16}$$

and the corresponding harmonic combination of the Nitsche penalty parameter is

$$\gamma^{\mathrm{S},c} = \gamma_0^{\mathrm{S},c}\phi^{\mathrm{S},c} = \gamma_0^{\mathrm{S},c}\left[\omega^c\lambda_{e1} + (1-\omega^c)\lambda_{e2}\right]. \tag{6.17}$$

Further explanations and details concerning the formulation for Nitsche contact can be found in the thesis of Seitz [195].

Remark 6.4 (Independent interface condition transition)**.** *It should be highlighted that the specification of the representative interface traction in* (6.15) *results in a transition between the FSI and contact conditions independent on both potentially contacting interfaces. This is essential to result in a continuous formulation, since the numerical fluid stress* $\sigma_{\mathrm{h},\mathcal{E}}^{\mathrm{F},nn} + \gamma_{\mathcal{E}}^{\mathrm{FSI}} v_{\mathrm{h},\mathcal{E}}^{rel,n}$ *in general is not equal on both sides of potential contacting interfaces.*

Remark 6.5 (Self-contact)**.** *Since the contact formulation utilizing a harmonic weighting of the underlying solid stresses for the contact stress representations does not required a specification of a "master" and a "slave" contact interface, this formulation is directly well suited to treat self-contact of deformable bodies. For a self-contact problem, the contacting interface pairs change dynamically and thus cannot be defined beforehand.*

In the case that the FSI condition is enforced in (6.15), the normal interface traction is represented uniquely by the normal fluid traction $\sigma_{\mathrm{h}}^{\mathrm{F},nn}$. Thus, the essential dynamic equilibrium (6.6) in the case equal to zero and the equilibrium (6.8) due to vanishing contributions on both sides separately are fulfilled . For this choice, a properly scaled, consistent penalty contribution $\gamma^{\mathrm{FSI}} v_{\mathrm{h}}^{rel,n}$ is added to guarantee discrete stability of the formulation and to enforce the constraint (6.9). In addition to the resulting traction and the penalty contribution, a skew-symmetric adjoint-consistency term is added to the weak form (6.13)

$$\mathcal{W}_{\mathrm{h},\Gamma,\mathrm{Adj}}^{\mathrm{FS},n}\left[\left(\delta\underline{\boldsymbol{v}}_{\mathrm{h}}^{\mathrm{F}}, \delta p_{\mathrm{h}}^{\mathrm{F}}\right), \left(\underline{\boldsymbol{u}}_{\mathrm{h}}^{\mathrm{S}}, \underline{\boldsymbol{v}}_{\mathrm{h}}^{\mathrm{F}}\right)\right] = \left\langle \delta p_{\mathrm{h},\emptyset}^{\mathrm{F}}\underline{\boldsymbol{n}}_{\mathrm{h}} - 2\mu^{\mathrm{F}}\underline{\boldsymbol{\epsilon}}^{\mathrm{F}}(\delta\underline{\boldsymbol{v}}_{\mathrm{h},\emptyset}^{\mathrm{F}})\underline{\boldsymbol{n}}_{\mathrm{h}}, v_{\mathrm{h},\mathcal{E}}^{rel,n}\underline{\boldsymbol{n}}_{\mathrm{h}} \right\rangle_{\Gamma_{\mathrm{h}}}. \tag{6.18}$$

This term enables to directly balance the destabilizing effects of the fluid pressure and the viscous fluid stress, when introducing $\sigma_{\mathrm{h}}^{\mathrm{F},nn}$ in (6.13). Due to the inherent constraint (6.9), this additional contribution does not alter the consistency of the formulation. When enforcing the FSI conditions, also a representation of the interface traction by the corresponding solid stress as discussed in Section 3.3.2.2 would be possible, which is not considered in the following.

A Demonstration of the Different Resulting Interface Contributions To demonstrate the arising interface contributions from the incorporation of the normal interface traction (6.15) into the weak form (6.13), the boundary integral on the interface Γ_{h} is split into the solid-solid contact "+" and the fluid-structure interaction "−" parts

$$\langle *,*\rangle_{\Gamma_{\mathrm{h}},+} = \begin{cases} \langle *,*\rangle_{\Gamma_{\mathrm{h}}} & \text{if} \quad \mathcal{C} \leq 0 \\ 0 & \text{otherwise} \end{cases}, \qquad \langle *,*\rangle_{\Gamma_{\mathrm{h}},-} = \begin{cases} 0 & \text{if} \quad \mathcal{C} \leq 0 \\ \langle *,*\rangle_{\Gamma_{\mathrm{h}}} & \text{otherwise} \end{cases}, \tag{6.19}$$

$$\text{with} \quad \mathcal{C}\left(\underline{\boldsymbol{u}}_{\mathrm{h}}^{\mathrm{S}}, \underline{\boldsymbol{v}}_{\mathrm{h}}^{\mathrm{F}}, p_{\mathrm{h}}^{\mathrm{F}}\right) = \left(\overline{\sigma}_{\mathrm{h}}^{\mathrm{S},nn} + \gamma^{\mathrm{S},c} g_{\mathrm{h}}^{n}\right) - \left(\sigma_{\mathrm{h},\mathcal{E}}^{\mathrm{F},nn} + \gamma_{\mathcal{E}}^{\mathrm{FSI}} v_{\mathrm{h},\mathcal{E}}^{rel,n}\right).$$

Remark 6.6 (Relation between the interfaces $\Gamma_{\mathrm{h}}^{\mathrm{S},c}$, $\Gamma_{\mathrm{h}}^{\mathrm{FS}}$ and $\Gamma_{\mathrm{h}},+$, $\Gamma_{\mathrm{h}},-$)**.** *For the continuous problem presented in Section 6.1, integration on the interface subsets $\Gamma,+$ and $\Gamma,-$ coincidences with an integration on the contact interface $\Gamma^{\mathrm{S},c}$ and the fluid-structure interface Γ^{FS}, respectively. Due to the discrete error this relation does not hold for the discrete formulation, where in general a deviation between these interfaces will occur.*

In definition (6.19), the sign of the scalar $\mathcal{C}$ indicates, which side of the $\min[]$ function in (6.15) represents the normal interface traction. In addition to this split of interface Γ in the "$+$" and "$-$" parts, a purely geometric split into interfaces $\Gamma_{\mathrm{h}}^{\mathrm{FS}}$ and $\Gamma_{\mathrm{h}}^{\mathrm{S},c}$ was described in Section 6.2.1.2. As the interface $\Gamma_{\mathrm{h}}^{\mathrm{FS}}$ is part of the outer fluid boundary $\partial\Omega_{\mathrm{h}}^{\mathrm{F}}$, the fluid state $(\underline{\boldsymbol{v}}_{\mathrm{h}}^{\mathrm{F}}, p_{\mathrm{h}}^{\mathrm{F}})$ and the corresponding test functions $(\delta\underline{\boldsymbol{v}}_{\mathrm{h}}^{\mathrm{F}}, \delta p_{\mathrm{h}}^{\mathrm{F}})$ are directly defined on this interface without any extension required. Combining these two different subdivisions when performing the integration of the normal traction (6.13) on the interface Γ_{h}, leads to four cases $(I-IV)$ which finally needs to be dealt with

$$\begin{aligned}
&\left\langle \delta\underline{\boldsymbol{v}}_{\mathrm{h},\emptyset}^{\mathrm{F}} - \delta\underline{\boldsymbol{u}}_{\mathrm{h}}^{\mathrm{S}}, \overline{\sigma}_{\mathrm{h}}^{nn}\underline{\boldsymbol{n}}_{\mathrm{h}} \right\rangle_{\Gamma_{\mathrm{h}}} = \left\langle \delta\underline{\boldsymbol{v}}_{\mathrm{h},\emptyset}^{\mathrm{F}} - \delta\underline{\boldsymbol{u}}_{\mathrm{h}}^{\mathrm{S}}, \overline{\sigma}_{\mathrm{h}}^{nn}\underline{\boldsymbol{n}}_{\mathrm{h}} \right\rangle_{\Gamma_{\mathrm{h}},+} + \left\langle \delta\underline{\boldsymbol{v}}_{\mathrm{h},\emptyset}^{\mathrm{F}} - \delta\underline{\boldsymbol{u}}_{\mathrm{h}}^{\mathrm{S}}, \overline{\sigma}_{\mathrm{h}}^{nn}\underline{\boldsymbol{n}}_{\mathrm{h}} \right\rangle_{\Gamma_{\mathrm{h}},-} = \\
&\underbrace{\left\langle \delta\underline{\boldsymbol{v}}_{\mathrm{h},\emptyset}^{\mathrm{F}} - \delta\underline{\boldsymbol{u}}_{\mathrm{h}}^{\mathrm{S}}, \overline{\sigma}_{\mathrm{h}}^{nn}\underline{\boldsymbol{n}}_{\mathrm{h}} \right\rangle_{\Gamma_{\mathrm{h}}^{\mathrm{S},c},+}}_{\text{case } II} + \underbrace{\left\langle \delta\underline{\boldsymbol{v}}_{\mathrm{h},\emptyset}^{\mathrm{F}} - \delta\underline{\boldsymbol{u}}_{\mathrm{h}}^{\mathrm{S}}, \overline{\sigma}_{\mathrm{h}}^{nn}\underline{\boldsymbol{n}}_{\mathrm{h}} \right\rangle_{\Gamma_{\mathrm{h}}^{\mathrm{S},c},-}}_{\text{case } IV} \\
&+ \underbrace{\left\langle \delta\underline{\boldsymbol{v}}_{\mathrm{h},\emptyset}^{\mathrm{F}} - \delta\underline{\boldsymbol{u}}_{\mathrm{h}}^{\mathrm{S}}, \overline{\sigma}_{\mathrm{h}}^{nn}\underline{\boldsymbol{n}}_{\mathrm{h}} \right\rangle_{\Gamma_{\mathrm{h}}^{\mathrm{FS}},+}}_{\text{case } III} + \underbrace{\left\langle \delta\underline{\boldsymbol{v}}_{\mathrm{h},\emptyset}^{\mathrm{F}} - \delta\underline{\boldsymbol{u}}_{\mathrm{h}}^{\mathrm{S}}, \overline{\sigma}_{\mathrm{h}}^{nn}\underline{\boldsymbol{n}}_{\mathrm{h}} \right\rangle_{\Gamma_{\mathrm{h}}^{\mathrm{FS}},-}}_{\text{case } I}.
\end{aligned} \tag{6.20}$$

A visualization of these four cases for a specific discrete contact configuration is given in Figure 6.3. In the following, the resulting contributions, which have to be evaluated, are depicted. Vanishing contributions are not included and the extension operator is just applied in the case no direct representation of the corresponding quantity is available on the relevant segment. Further, the skew-symmetric adjoint-consistency term introduced in (6.18) is included, to include all interface contributions evaluated in the normal direction

$$\begin{aligned}
&\mathcal{W}_{\mathrm{h},\Gamma}^{\mathrm{FS},n}\left[\left(\delta\underline{\boldsymbol{u}}_{\mathrm{h}}^{\mathrm{S}}, \delta\underline{\boldsymbol{v}}_{\mathrm{h}}^{\mathrm{F}}, \delta p_{\mathrm{h}}^{\mathrm{F}}\right), \left(\underline{\boldsymbol{u}}_{\mathrm{h}}^{\mathrm{S}}, \underline{\boldsymbol{v}}_{\mathrm{h}}^{\mathrm{F}}, p_{\mathrm{h}}^{\mathrm{F}}\right)\right] + \mathcal{W}_{\mathrm{h},\Gamma,\mathrm{Adj}}^{\mathrm{FS},n}\left[\left(\delta\underline{\boldsymbol{v}}_{\mathrm{h}}^{\mathrm{F}}, \delta p_{\mathrm{h}}^{\mathrm{F}}\right), \left(\underline{\boldsymbol{u}}_{\mathrm{h}}^{\mathrm{S}}, \underline{\boldsymbol{v}}_{\mathrm{h}}^{\mathrm{F}}\right)\right] \\
&\quad = I + II + III + IV
\end{aligned}$$

with:

$$\begin{aligned}
I &= \left\langle \delta\underline{\boldsymbol{v}}_{\mathrm{h}}^{\mathrm{F}} - \delta\underline{\boldsymbol{u}}_{\mathrm{h}}^{\mathrm{S}}, \sigma_{\mathrm{h}}^{\mathrm{F},nn}\underline{\boldsymbol{n}}_{\mathrm{h}} \right\rangle_{\Gamma_{\mathrm{h}}^{\mathrm{FS}},-} + \left\langle \delta\underline{\boldsymbol{v}}_{\mathrm{h}}^{\mathrm{F}} - \delta\underline{\boldsymbol{u}}_{\mathrm{h}}^{\mathrm{S}}, \gamma^{\mathrm{FSI}} v_{\mathrm{h}}^{rel,n}\underline{\boldsymbol{n}}_{\mathrm{h}} \right\rangle_{\Gamma_{\mathrm{h}}^{\mathrm{FS}},-} \\
&\quad + \left\langle \delta p_{\mathrm{h}}^{\mathrm{F}}\underline{\boldsymbol{n}}_{\mathrm{h}} - 2\mu^{\mathrm{F}}\underline{\boldsymbol{\epsilon}}^{\mathrm{F}}(\delta\underline{\boldsymbol{v}}_{\mathrm{h}}^{\mathrm{F}})\underline{\boldsymbol{n}}_{\mathrm{h}}, v_{\mathrm{h}}^{rel,n}\underline{\boldsymbol{n}}_{\mathrm{h}} \right\rangle_{\Gamma_{\mathrm{h}}^{\mathrm{FS}},-},
\end{aligned} \tag{6.21}$$

$$II = \left\langle -\delta\underline{\boldsymbol{u}}_{\mathrm{h}}^{\mathrm{S}}, \overline{\sigma}_{\mathrm{h}}^{\mathrm{S},nn}\underline{\boldsymbol{n}}_{\mathrm{h}} \right\rangle_{\Gamma_{\mathrm{h}}^{\mathrm{S},c},+} + \left\langle -\delta\underline{\boldsymbol{u}}_{\mathrm{h}}^{\mathrm{S}}, \gamma^{\mathrm{S},c} g_{\mathrm{h}}^{n}\underline{\boldsymbol{n}}_{\mathrm{h}} \right\rangle_{\Gamma_{\mathrm{h}}^{\mathrm{S},c},+}, \tag{6.22}$$

$$III = \left\langle \delta\underline{\boldsymbol{v}}_{\mathrm{h}}^{\mathrm{F}} - \delta\underline{\boldsymbol{u}}_{\mathrm{h}}^{\mathrm{S}}, \overline{\sigma}_{\mathrm{h}}^{\mathrm{S},nn}\underline{\boldsymbol{n}}_{\mathrm{h}} \right\rangle_{\Gamma_{\mathrm{h}}^{\mathrm{FS}},+} + \left\langle \delta\underline{\boldsymbol{v}}_{\mathrm{h}}^{\mathrm{F}} - \delta\underline{\boldsymbol{u}}_{\mathrm{h}}^{\mathrm{S}}, \gamma^{\mathrm{S},c} g_{\mathrm{h}}^{n}\underline{\boldsymbol{n}}_{\mathrm{h}} \right\rangle_{\Gamma_{\mathrm{h}}^{\mathrm{FS}},+}, \tag{6.23}$$

$$IV = \left\langle -\delta\underline{\boldsymbol{u}}_{\mathrm{h}}^{\mathrm{S}}, \sigma_{\mathrm{h},\mathcal{E}}^{\mathrm{F},nn}\underline{\boldsymbol{n}}_{\mathrm{h}} \right\rangle_{\Gamma_{\mathrm{h}}^{\mathrm{S},c},-} + \left\langle -\delta\underline{\boldsymbol{u}}_{\mathrm{h}}^{\mathrm{S}}, \gamma_{\mathcal{E}}^{\mathrm{FSI}} v_{\mathrm{h},\mathcal{E}}^{rel,n}\underline{\boldsymbol{n}}_{\mathrm{h}} \right\rangle_{\Gamma_{\mathrm{h}}^{\mathrm{S},c},-}. \tag{6.24}$$

Herein, contribution I equals the classical Nitsche-based method for the imposition of the mass conservation on an fluid-structure interface as applied in Burman and Fernández [42] and Schott

et al. [192]. This method includes an interface traction representation by the fluid stress, a penalty term which is consistent due to the includes mass conservation (6.9), and the skew symmetric viscous and pressure adjoint-consistency term which also includes (6.9).

The evaluated terms in summand II coincide in principle with Nitsche-based methods for classical contact problems, e.g. applied in works of Chouly *et al.* [63], Mlika *et al.* [156] and Seitz *et al.* [196]. Here, the interface traction is represented by a one-sided or two-sided weighted solid stress of both contacting bodies with an additional penalty term including the no penetration condition included in (6.5) and (6.7). No adjoint-consistency terms are applied. Due to the vanishing fluid test functions $(\delta\underline{\boldsymbol{v}}^{\mathrm{F}}_{\mathrm{h},\emptyset}, \delta p^{\mathrm{F}}_{\mathrm{h},\emptyset})$, no contribution to the fluid weak form occurs.

Finally, contributions III and IV arise solely close to the condition changing point/curve $\mathcal{C} = 0$ and the common point/curve of both interface $\Gamma^{\mathrm{S},c}_{\mathrm{h}} \cap \Gamma^{\mathrm{FS}}_{\mathrm{h}}$. The impact of these summands compared to contributions I and II is relatively small and so making use of a simple extension of the fluid quantities in (6.24) is acceptable. Still, both contribution have to be applied to ensure a continuous discrete problem and guarantee geometrically fitting interface conditions applied onto the fluid domain.

Remark 6.7 (Application of a different representation for contribution III)**.** *For all numerical examples presented in Section 6.4, an alternative formulation of contribution III is applied due to algorithmic reasons. Therein, the contributions of Nitsche contact II are completed by a fluid-sided interface traction representation for the fluid domain.*

$$\begin{aligned} III = &\left\langle \delta\underline{\boldsymbol{v}}^{\mathrm{F}}_{\mathrm{h}}, \sigma^{\mathrm{F},nn}_{\mathrm{h}}\underline{\boldsymbol{n}}_{\mathrm{h}} \right\rangle_{\Gamma^{\mathrm{FS},+}_{\mathrm{h}}} + \left\langle \delta\underline{\boldsymbol{v}}^{\mathrm{F}}_{\mathrm{h}}, \gamma^{\mathrm{FSI}} v^{rel,n}\underline{\boldsymbol{n}} \right\rangle_{\Gamma^{\mathrm{FS},+}_{\mathrm{h}}} \\ &+ \left\langle \delta p^{\mathrm{F}}_{\mathrm{h}}\underline{\boldsymbol{n}}_{\mathrm{h}} - 2\mu^{\mathrm{F}}\underline{\boldsymbol{\epsilon}}^{\mathrm{F}}(\delta\underline{\boldsymbol{v}}^{\mathrm{F}}_{\mathrm{h}})\underline{\boldsymbol{n}}_{\mathrm{h}}, v^{rel,n}_{\mathrm{h}}\underline{\boldsymbol{n}}_{\mathrm{h}} \right\rangle_{\Gamma^{\mathrm{FS},+}_{\mathrm{h}}} \\ &+ \left\langle -\delta\underline{\boldsymbol{u}}^{\mathrm{S}}_{\mathrm{h}}, \overline{\sigma}^{\mathrm{S},nn}_{\mathrm{h}}\underline{\boldsymbol{n}}_{\mathrm{h}} \right\rangle_{\Gamma^{\mathrm{FS},+}_{\mathrm{h}}} + \left\langle -\delta\underline{\boldsymbol{u}}^{\mathrm{S}}_{\mathrm{h}}, \gamma^{\mathrm{S},c} g^{n}_{\mathrm{h}}\underline{\boldsymbol{n}}_{\mathrm{h}} \right\rangle_{\Gamma^{\mathrm{FS},+}_{\mathrm{h}}} \end{aligned} \tag{6.25}$$

By comparison of contributions (6.23) *and* (6.25)*, the coincidence of both formulations at the condition-changing point $\mathcal{C} = 0$ for a fulfilled mass balance* (6.9) *can be directly seen. As the impact of contribution III is generally small and arises solely close to $\mathcal{C} = 0$, this modification does not have a significant influence onto the performance of the presented formulation.*

Remark 6.8 (Specification of the solid penalty constant $\gamma^{\mathrm{S},c}_0$)**.** *For Nitsche's method, the parameter $\gamma^{\mathrm{S},c} = \gamma^{\mathrm{S},c}_0 \phi^{\mathrm{S},c}$ with a sufficiently large, positive constant $\gamma^{\mathrm{S},c}_0$ is required to establish discrete stability of the formulation. As previously discussed, material- and mesh-dependencies of $\gamma^{\mathrm{S},c}$ are already considered in $\phi^{\mathrm{S},c}$ by a local generalized eigenvalue problem. Larger values of the constant $\gamma^{\mathrm{S},c}_0$ improve the constraint enforcement $(g^n_{\mathrm{h}} = 0)$, while smaller values typically reduce the error of the consistent stress representation $(\overline{\sigma}^{\mathrm{S},nn}_{\mathrm{h}})$. For the FSCI problem, additional aspects have to be considered. The influence of case IV (see* (6.24)*) should be minimized, as it incorporates the extended fluid solution and switching between the cases II and IV during the nonlinear solution procedure should be reduced. A small penalty parameter $\gamma^{\mathrm{S},c}$ supports this behavior as it turns out to reduce the ratio of $\mathcal{C} \leq 0$ on the interface $\Gamma^{\mathrm{S},c}_{\mathrm{h}}$. As a result, a small but still numerical stable constant $\gamma^{\mathrm{S},c}_0$ is beneficial for solving the FSCI problem. This aspect is not critical as the constant $\gamma^{\mathrm{S},c}_0$ is not problem dependent for a properly defined scaling $\phi^{\mathrm{S},c}$ and the same value can be kept for all computation ($\gamma^{\mathrm{S},c}_0 = 1.0$ is used for all presented numerical examples).*

Remark 6.9 (Determination of the fluid penalty parameter γ^{FSI})**.** *The penalty term in* (6.15) *with the parameter* $\gamma^{\mathrm{FSI}} = \gamma_0^{\mathrm{FSI}} \phi_\Gamma^{\mathrm{F}}$ *balances viscous, convective and temporal contributions according to the work of Massing* et al. *[149] and so enables a discrete stable formulation. The additive stabilization parameter* ϕ_Γ^{F} *is specified in* (3.27)*. For the determination of the constant* γ_0^{FSI}*, which has to be sufficiently large for a stable discrete formulation, constraint enforcement as well as the resulting interface stress error is important. Additionally, for the computed numerical examples, it was observed, that a small penalty parameter* γ_0^{FSI} *is beneficial for the FSCI problem as it incorporates an inherent relaxation of the kinematic constraints especially close to the point of changing conditions (*$\mathcal{C} = 0$*) and, hence, improves the performance of the nonlinear solution procedure. The relevance of this aspect depends highly on the complexity of the considered problem configuration and increases for a reduced accuracy of the applied numerical integration procedure on the interface* Γ_{h}.

Remark 6.10 (Applied numerical integration procedure on the interface Γ_{h})**.** *For the numerical integration of the contributions* (6.21)-(6.25) *on the interface, non-smooth and non-continuous functions on single solid boundary elements have to be integrated. These kinks and jumps potentially occur due to element boundaries of the contact partner or on the intersection of the interface with fluid element boundaries. To enable an accurate numerical integration, each solid boundary element has to be split by all other element boundaries involved and a numerical integration rule has to be specified, e.g. by triangulation, on these segments (see e.g. the work of Farah* et al. *[82]). For the numerical examples presented in the following, this most accurate approach was not applied. Instead, the numerical integration points on the interface* Γ_{h} *are constructed to account for the intersection of the interface with fluid element boundaries solely. To account for the integration of the discontinuous solid stress in the contacting case, an increased number of integration points is applied.*

6.2.3 Nitsche-based Method on the Overall Coupling Interface Γ_{h} in Tangential Direction

The tangential component of the interface traction $\overline{\underline{\boldsymbol{\sigma}}}_{\mathrm{h}}^{n} \cdot \underline{\boldsymbol{P}}^{t}$ has to fulfill the traction free condition (6.10) due to the consideration of frictionless contact on the contact interface $\Gamma_{\mathrm{h}}^{\mathrm{S},c}$

$$\overline{\underline{\boldsymbol{\sigma}}}_{\mathrm{h}}^{n} \cdot \underline{\boldsymbol{P}}^{t} = \underline{\mathbf{0}} \quad \text{on} \quad \Gamma_{\mathrm{h}}^{\mathrm{S},c}. \tag{6.26}$$

Further, the dynamic equilibrium (6.11) and the Navier slip boundary condition (6.12) have to be fulfilled on the fluid-structure interface $\Gamma_{\mathrm{h}}^{\mathrm{FS}}$. A representation of the unique tangential interface traction by

$$\begin{aligned} &\overline{\underline{\boldsymbol{\sigma}}}_{\mathrm{h}}^{n} \cdot \underline{\boldsymbol{P}}^{t} = \\ &\left[-\frac{(\gamma_0^{\mathrm{FSI},t})^{-1} h_\Gamma}{\kappa \mu^{\mathrm{F}} + (\gamma_0^{\mathrm{FSI},t})^{-1} h_\Gamma} \underline{\boldsymbol{\sigma}}_{\mathrm{h}}^{\mathrm{F}} \cdot \underline{\boldsymbol{n}}_{\mathrm{h}}^{\mathrm{F}} + \frac{\mu^{\mathrm{F}}}{\kappa \mu^{\mathrm{F}} + (\gamma_0^{\mathrm{FSI},t})^{-1} h_\Gamma} \left(\underline{\boldsymbol{v}}_{\mathrm{h}}^{\mathrm{F}} - \tilde{\partial}_t \left[\underline{\boldsymbol{u}}_{\mathrm{h}}^{\mathrm{S}} \right] \right) \right] \cdot \underline{\boldsymbol{P}}^{t} \quad \text{on} \quad \Gamma_{\mathrm{h}}^{\mathrm{FS}}, \end{aligned} \tag{6.27}$$

complies with these condition. For the limit cases no-slip (slip length $\kappa = 0$) and free-slip (slip length $\kappa = \infty$), the tangential interface traction reduces to

$$\overline{\underline{\boldsymbol{\sigma}}}_{\mathrm{h}}^{n} \cdot \underline{\boldsymbol{P}}^{t} = \left[-\underline{\boldsymbol{\sigma}}_{\mathrm{h}}^{\mathrm{F}} \cdot \underline{\boldsymbol{n}}_{\mathrm{h}}^{\mathrm{F}} + \mu^{\mathrm{F}} \gamma_0^{\mathrm{FSI},t} / h_\Gamma \left(\underline{\boldsymbol{v}}_{\mathrm{h}}^{\mathrm{F}} - \tilde{\partial}_t \left[\underline{\boldsymbol{u}}_{\mathrm{h}}^{\mathrm{S}} \right] \right) \right] \cdot \underline{\boldsymbol{P}}^{t} \quad \text{and} \quad \overline{\underline{\boldsymbol{\sigma}}}_{\mathrm{h}}^{n} \cdot \underline{\boldsymbol{P}}^{t} = \underline{\mathbf{0}},$$

respectively. Incorporating of the tangential interface traction in the weak form (6.13) and adding an additional consistent skew-symmetric adjoint term results in the contributions

$$\mathcal{W}_{\mathrm{h},\Gamma}^{\mathrm{FS},t}\left[\left(\delta\underline{\boldsymbol{u}}_{\mathrm{h}}^{\mathrm{S}},\delta\underline{\boldsymbol{v}}_{\mathrm{h}}^{\mathrm{F}}\right),\left(\underline{\boldsymbol{u}}_{\mathrm{h}}^{\mathrm{S}},\underline{\boldsymbol{v}}_{\mathrm{h}}^{\mathrm{F}}\right)\right] = -\left\langle\delta\underline{\boldsymbol{v}}_{\mathrm{h}}^{\mathrm{F}}-\delta\underline{\boldsymbol{u}}_{\mathrm{h}}^{\mathrm{S}},\underline{\boldsymbol{\sigma}}_{\mathrm{h}}^{\mathrm{F}}\cdot\underline{\boldsymbol{n}}_{\mathrm{h}}^{\mathrm{F}}\cdot\underline{\boldsymbol{P}}^{t}\right\rangle_{\Gamma_{\mathrm{h}}^{\mathrm{FS}}}$$
$$+\frac{\mu^{\mathrm{F}}}{\kappa\mu^{\mathrm{F}}+(\gamma_0^{\mathrm{FSI},t})^{-1}h_\Gamma}\left\langle\delta\underline{\boldsymbol{v}}_{\mathrm{h}}^{\mathrm{F}}-\delta\underline{\boldsymbol{u}}_{\mathrm{h}}^{\mathrm{S}},\left[\underline{\boldsymbol{v}}_{\mathrm{h}}^{\mathrm{F}}-\tilde{\partial}_t\left[\underline{\boldsymbol{u}}_{\mathrm{h}}^{\mathrm{S}}\right]+\kappa\underline{\boldsymbol{\sigma}}_{\mathrm{h}}^{\mathrm{F}}\cdot\underline{\boldsymbol{n}}_{\mathrm{h}}^{\mathrm{F}}\right]\cdot\underline{\boldsymbol{P}}^{t}\right\rangle_{\Gamma_{\mathrm{h}}^{\mathrm{FS}}}, \tag{6.28}$$
$$\mathcal{W}_{\mathrm{h},\Gamma,\mathrm{Adj}}^{\mathrm{FS},t}\left[\delta\underline{\boldsymbol{v}}_{\mathrm{h}}^{\mathrm{F}},\left(\underline{\boldsymbol{u}}_{\mathrm{h}}^{\mathrm{S}},\underline{\boldsymbol{v}}_{\mathrm{h}}^{\mathrm{F}}\right)\right] =$$
$$-\frac{(\gamma_0^{\mathrm{FSI},t})^{-1}h_\Gamma}{\kappa\mu^{\mathrm{F}}+(\gamma_0^{\mathrm{FSI},t})^{-1}h_\Gamma}\left\langle-2\mu^{\mathrm{F}}\underline{\boldsymbol{\epsilon}}^{\mathrm{F}}(\delta\underline{\boldsymbol{v}}_{\mathrm{h}}^{\mathrm{F}})\cdot\underline{\boldsymbol{n}}_{\mathrm{h}}^{\mathrm{F}},\left[\underline{\boldsymbol{v}}_{\mathrm{h}}^{\mathrm{F}}-\tilde{\partial}_t\left[\underline{\boldsymbol{u}}_{\mathrm{h}}^{\mathrm{S}}\right]+\kappa\underline{\boldsymbol{\sigma}}_{\mathrm{h}}^{\mathrm{F}}\cdot\underline{\boldsymbol{n}}_{\mathrm{h}}^{\mathrm{F}}\right]\cdot\underline{\boldsymbol{P}}^{t}\right\rangle_{\Gamma_{\mathrm{h}}^{\mathrm{FS}}}. \tag{6.29}$$

It can be directly seen that this formulation is consistent, as the term in the first line includes the naturally arising fluid stress applied on fluid and solid boundary due to the balance (6.11) and the additional terms include directly the constraint (6.12). Theses additional terms are present to guarantee a discrete stable formulation and to enforce the kinematic constraint. They balance the destabilizing effects of the viscous boundary integral occurring in line one and the term of similar structure in line two. The penalty parameter in tangential direction $\gamma_0^{\mathrm{FSI},t}$ needs to be a positive and sufficiently large constant. This Nitsche-based contribution for the general Navier interface condition is based on the formulation presented and analyzed by Juntunen and Stenberg [132] for the Poisson problem and by Winter *et al.* [226] for the linearized fluid problem. It was successfully applied to enforce the coupling conditions between a poroelastic structure and fluid flow in Chapter 4 and Chapter 5.

Definition of the Slip Length κ As motivated already in Section 6.1.2 for the overall problem, the no-slip interface condition $\kappa = 0$ on Γ^{FS} has to be applied. Solely close to the contacting zone, a relaxation of this constraint is designated. A continuous transition between the tangential fluid-structure interaction condition (6.11)-(6.12) and the tangential frictionless contact condition (6.10) can be guaranteed for an infinite slip length $\kappa = \infty$ on $\Gamma_{\mathrm{h}}^{\mathrm{FS}} \cap \Gamma_{\mathrm{h}}^{\mathrm{S},c}$. The applied interpolation between these limiting points is given by

$$\kappa = \begin{cases} 0 & \text{if} \quad g_{\mathrm{h}}^n > h \\ \kappa_0 h\left[\frac{h}{g_{\mathrm{h}}^n}-1\right] & \text{if} \quad h \geq g_{\mathrm{h}}^n > 0. \\ \infty & \text{otherwise} \end{cases} \tag{6.30}$$

Herein, the minimal value of the gap g_{h}^n between two solid interfaces to apply the no-slip interface condition is specified by the fluid element size h. The interpolation function can be specified by the constant reference slip length κ_0. It should be pointed out that for a reduction of the fluid element size h, also the range of influence for this modification compared to a pure no-slip condition is reduced. For small scales, an alternative formulation for the slip length in relation (6.30) due to the underlying physical slip can improve the accuracy of the interface condition. A second advantage of allowing a certain amount of slip on the interface is to avoid blockage of single fluid elements between approaching surfaces due to the insufficient discrete solution space. This aspect is less essential for a weak enforcement of the interface condition by Nitsche's method with an appropriately chosen penalty parameter $\gamma_0^{\mathrm{FSI},t}$ than for a strong enforcement of interface

conditions (Bazilevs and Hughes [19] provide a comparison of strong enforcement and weak imposition of fluid boundary conditions). To give an example, van Loon *et al.* [213] resolved this issue by a modification of the fluid-structure interface constraint close to contact.

6.3 The Coupled Discrete FSCI Problem

The overall discrete solution space $\mathcal{S}_{\underline{\boldsymbol{x}}^{\mathrm{FSCI}},\mathrm{h},n+1}$ and the discrete test function space $\mathcal{T}_{\delta\underline{\boldsymbol{x}}^{\mathrm{FSCI}},\mathrm{h},n+1}$ result from the discrete spaces of the underlying physical fields defined for the structural problem in (2.106) and for the fluid problem in (2.110).

$$\begin{aligned}\mathcal{S}_{\underline{\boldsymbol{x}}^{\mathrm{FSCI}},\mathrm{h},n+1} &:= \mathcal{S}_{\underline{\boldsymbol{u}}^{\mathrm{S}},\mathrm{h},n+1} \times \mathcal{S}_{\underline{\boldsymbol{v}}^{\mathrm{F}},\mathrm{h},n+1} \times \mathcal{S}_{p^{\mathrm{F}},\mathrm{h},n+1} \\ \mathcal{T}_{\delta\underline{\boldsymbol{x}}^{\mathrm{FSCI}},\mathrm{h},n+1} &:= \mathcal{T}_{\delta\underline{\boldsymbol{u}}^{\mathrm{S}},\mathrm{h}} \times \mathcal{T}_{\delta\underline{\boldsymbol{v}}^{\mathrm{F}},\mathrm{h},n+1} \times \mathcal{T}_{\delta p^{\mathrm{F}},\mathrm{h},n+1}\end{aligned} \tag{6.31}$$

The overall discrete test function $\delta\underline{\boldsymbol{x}}_{\mathrm{h}}^{\mathrm{FSCI}}$ and discrete solution state $\underline{\boldsymbol{x}}_{\mathrm{h},n+1}^{\mathrm{FSCI}}$ are given by

$$\begin{aligned}\underline{\boldsymbol{x}}_{\mathrm{h},n+1}^{\mathrm{FSCI}} &:= \left(\underline{\boldsymbol{u}}_{\mathrm{h},n+1}^{\mathrm{S}}, \underline{\boldsymbol{v}}_{\mathrm{h},n+1}^{\mathrm{F}}, p_{\mathrm{h},n+1}^{\mathrm{F}}\right), \\ \delta\underline{\boldsymbol{x}}_{\mathrm{h}}^{\mathrm{FSCI}} &:= \left(\delta\underline{\boldsymbol{u}}_{\mathrm{h}}^{\mathrm{S}}, \delta\underline{\boldsymbol{v}}_{\mathrm{h}}^{\mathrm{F}}, \delta p_{\mathrm{h}}^{\mathrm{F}}\right).\end{aligned} \tag{6.32}$$

Making use of (6.31) and (6.32), the overall discrete formulation of the coupled FSCI problem is

Find $\underline{\boldsymbol{x}}_{\mathrm{h},n+1}^{\mathrm{FSCI}} \in \mathcal{S}_{\underline{\boldsymbol{x}}^{\mathrm{FSCI}},\mathrm{h},n+1}$ *such that for all* $\delta\underline{\boldsymbol{x}}_{\mathrm{h}}^{\mathrm{FSCI}} \in \mathcal{T}_{\delta\underline{\boldsymbol{x}}^{\mathrm{FSCI}},\mathrm{h},n+1}$:

$$\mathcal{W}_{\mathrm{h},n+1}^{\mathrm{FSCI}}\left[\delta\underline{\boldsymbol{x}}_{\mathrm{h}}^{\mathrm{FSCI}}, \underline{\boldsymbol{x}}_{\mathrm{h},n+1}^{\mathrm{FSCI}}\right] = 0. \tag{6.33}$$

The underlying weak form results from the combination of the weak forms of all corresponding physical fields and interfaces. This includes the discrete contributions for structures in (2.108) and for fluid discretized by the CutFEM in (3.7). By making use of the corresponding interface traction representations in normal (6.15) and in tangential (6.26) - (6.27) direction in the weak form (6.13), and summing up all additional contributions including interface adjoint-consistency terms, the weak form of the overall coupled discrete FSCI problem can be formulated as

$$\begin{aligned}\mathcal{W}_{\mathrm{h},n+1}^{\mathrm{FSCI}}&\left[\delta\underline{\boldsymbol{x}}_{\mathrm{h}}^{\mathrm{FSCI}}, \underline{\boldsymbol{x}}_{\mathrm{h},n+1}^{\mathrm{FSCI}}\right] = \\ &\mathcal{W}_{\mathrm{h},n+1}^{\mathrm{S}}\left[\delta\underline{\boldsymbol{u}}_{\mathrm{h}}^{\mathrm{S}}, \underline{\boldsymbol{u}}_{\mathrm{h},n+1}^{\mathrm{S}}\right] \\ &+\mathcal{W}_{\mathrm{h},n+1}^{\mathrm{F,CUT}}\left[\left(\delta\underline{\boldsymbol{v}}_{\mathrm{h}}^{\mathrm{F}}, \delta p_{\mathrm{h}}^{\mathrm{F}}\right), \left(\underline{\boldsymbol{v}}_{\mathrm{h},n+1}^{\mathrm{F}}, p_{\mathrm{h},n+1}^{\mathrm{F}}\right)\right] \\ &+\mathcal{W}_{\mathrm{h},\Gamma,n+1}^{\mathrm{FS},n}\left[\left(\delta\underline{\boldsymbol{u}}_{\mathrm{h}}^{\mathrm{S}}, \delta\underline{\boldsymbol{v}}_{\mathrm{h}}^{\mathrm{F}}\right), \left(\underline{\boldsymbol{u}}_{\mathrm{h},n+1}^{\mathrm{S}}, \underline{\boldsymbol{v}}_{\mathrm{h},n+1}^{\mathrm{F}}, p_{\mathrm{h},n+1}^{\mathrm{F}}\right)\right] \\ &+\mathcal{W}_{\mathrm{h},\Gamma,n+1}^{\mathrm{FS},t}\left[\left(\delta\underline{\boldsymbol{u}}_{\mathrm{h}}^{\mathrm{S}}, \delta\underline{\boldsymbol{v}}_{\mathrm{h}}^{\mathrm{F}}\right), \left(\underline{\boldsymbol{u}}_{\mathrm{h},n+1}^{\mathrm{S}}, \underline{\boldsymbol{v}}_{\mathrm{h},n+1}^{\mathrm{F}}\right)\right] \\ &+\mathcal{W}_{\mathrm{h},\Gamma,\mathrm{Adj},n+1}^{\mathrm{FS},n}\left[\left(\delta\underline{\boldsymbol{v}}_{\mathrm{h}}^{\mathrm{F}}, \delta p_{\mathrm{h}}^{\mathrm{F}}\right), \left(\underline{\boldsymbol{u}}_{\mathrm{h},n+1}^{\mathrm{S}}, \underline{\boldsymbol{v}}_{\mathrm{h},n+1}^{\mathrm{F}}\right)\right] \\ &+\mathcal{W}_{\mathrm{h},\Gamma,\mathrm{Adj},n+1}^{\mathrm{FS},t}\left[\delta\underline{\boldsymbol{v}}_{\mathrm{h}}^{\mathrm{F}}, \left(\underline{\boldsymbol{u}}_{\mathrm{h},n+1}^{\mathrm{S}}, \underline{\boldsymbol{v}}_{\mathrm{h},n+1}^{\mathrm{F}}\right)\right].\end{aligned} \tag{6.34}$$

The additional index "$n+1$" in $\mathcal{W}_{\mathrm{h},\Gamma,n+1}^{\mathrm{FS},n}$, $\mathcal{W}_{\mathrm{h},\Gamma,n+1}^{\mathrm{FS},t}$, $\mathcal{W}_{\mathrm{h},\Gamma,\mathrm{Adj},n+1}^{\mathrm{FS},n}$, and $\mathcal{W}_{\mathrm{h},\Gamma,\mathrm{Adj},n+1}^{\mathrm{FS},t}$ specifies that all interface terms $\langle *,*\rangle_{\Gamma_{\mathrm{h}}}$ are evaluated as $\langle *,*\rangle_{\Gamma_{\mathrm{h},n+1},n+\theta}$.

The Newton-Raphson like nonlinear solution procedure to solve the aforementioned system for the vector of unknown nodal states

$$\underline{\mathbf{x}}_{n+1}^{\mathrm{FSCI}} := \left[\left(\underline{\mathbf{u}}_{n+1}^{\mathrm{S}}\right)^{\mathsf{T}}, \left(\underline{\mathbf{v}}_{n+1}^{\mathrm{F}}\right)^{\mathsf{T}}, \left(\underline{\mathbf{p}}_{n+1}^{\mathrm{F}}\right)^{\mathsf{T}} \right]^{\mathsf{T}}, \tag{6.35}$$

is discussed in Section 3.4.

In the following, algorithmic details for the monolithic solution algorithm, which are applied for the computation of the subsequently presented numerical examples, are presented. These strategies enable a robust solution of the resulting highly nonlinear problems and were not introduced in Section 3.4.

6.3.1 Update Strategy for Geometric Intersection

A simple procedure to avoid deterioration of the convergence behavior in the Newton-Raphson procedure due to "algorithmic"-discontinuities arising from geometric tolerances in the algorithm intersecting the interface $\Gamma_{\mathrm{h}}^{\mathrm{FS}}$ and the computational fluid domain $\Omega_{\mathrm{h}}^{\mathrm{F}}$ is applied. Herein, the geometric intersection (includes the creation of numerical integration points in the physical fluid domain $\Omega_{\mathrm{h}}^{\mathrm{F}}$ and on the fluid-structure interface $\Gamma_{\mathrm{h}}^{\mathrm{FS}}$) is just updated as long as the maximal displacement increment $||\Delta\underline{\mathbf{u}}_{n+1}^{\mathrm{S},i+1}||_{\infty} > \epsilon_{\mathrm{geom}}$ in an iterations step exceeds a specified valued. For the remaining iteration steps, the intersection information of the previous iteration step is applied.

6.3.2 Solution Space Update Strategy

As explained in detail in Section 3.4 and by Schott *et al.* [192], the solution space is updated dynamically within the iterative solution procedure for solving the system of nonlinear equations. For classical FSI computations without structural contact, applying this procedure typically results in a constant solution space after few iterations. Nevertheless, including contact increases the sensitivity of the formulation with respect to changing solution spaces. This aspect can result in periodically repeating changes of the solution space within the iterative solution procedure for specific geometric configurations and so prohibits the convergence of the scheme. The reason for this behavior is a discontinuity in the discrete formulation, which arises due to the change in the considered set of faces in the weakly consistent ghost penalty stabilization (3.4), when changing the discrete fluid solution spaces. The influence of this effect onto the convergence of the Newton-Raphson based procedure is especially relevant in the case when two physical fluid domains are merged or separated. Thus, when exceeding a maximum number of iterations in the nonlinear solution procedure, no reduction in the computational nodes carrying fluid degrees of freedom is performed anymore. The fluid solution space is then just enlarged within the actual time step. To retain a solvable system of equations, the ghost penalty stabilization has to include the faces connecting all additional degrees of freedom to the physical domain. This strategy leads to a constant set of faces considered for the stabilization during the Newton-Raphson based procedure and, as a result, avoids the occurring discontinuity in the discrete formulation. With this modification, the consistency of the formulation is not touched. Only some additional fluid degrees of freedom, which represent an extension of the solution in the non-physical domain, are appended to the system. To ease the use of this strategy, the discrete fluid solution

space is constructed by a maximum of one set of fluid unknowns on each node in the presented computations. As long as no slender solid bodies are considered, this restriction still results in an appropriate discrete fluid solution space (for more details on multiple sets of fluid unknowns on single computational nodes see work of Schott and Wall [188]).

6.3.3 Applied Extension Operator

In Section 6.1.1 and Section 6.2.2, an extension operator $\mathcal{E}_{\underline{\boldsymbol{x}}}$ is required to extend the scalar fluid quantities, normal stress, relative normal velocity, and fluid Nitsche penalty parameter from the fluid-structure interface to the contact interface $\Gamma_{\mathrm{h}}^{\mathrm{FS}} \longrightarrow \Gamma_{\mathrm{h}}^{\mathrm{S},c}$. In the numerical examples presented, a very simple operator is applied. Herein, starting from the coordinate $\underline{\boldsymbol{x}}$ on the interface $\Gamma_{\mathrm{h}}^{\mathrm{S},c}$, the closest point $\underline{\boldsymbol{x}}_{\mathcal{E}}$ to $\Gamma_{\mathrm{h}}^{\mathrm{FS}} \cap \Gamma_{\mathrm{h}}^{c}$ is computed. In this point, the scalar quantity is evaluated. Then a constant extension is applied and as a result the computed value of the scalar quantity equals the extension.

Remark 6.11 (Alternatives to the proposed extension strategy for fluid filled contact zones)**.** *This kind of extension includes the modeling assumption that the contacting zone is filled with fluid. As long as the influence of this extension on the computational model is limited to the neighborhood of the fluid domain, this approximation of the fluid solution seems sufficient. If a better fluid solution on the contact interface is required, a physical model has to be solved to avoid the extension. Depending on the requirements for this solution, potential models are based on the Reynolds equation introduced by Reynolds [179] or a poroelastic layer as presented in Chapter 5.*

Remark 6.12 (Alternative to the proposed extension strategy for vanishing fluid in the contact zones)**.** *If vanishing fluid in the contact zone is modeled, a continuous extension from the physical fluid solution to a vanishing fluid solution (zero ambient pressure) depending on the distance to the fluid domain can be applied alternatively. When making use of this approach, it has to be guaranteed that gaps emerging from opening contact in this zone of vanishing fluid solution are not considered as part of the fluid domain $\Omega_{\mathrm{h}}^{\mathrm{F}}$ to avoid a non-physical model. Such a configuration equals classical structural contact mechanics and, therefore, is not considered in the following.*

6.4 Numerical Examples: General FSCI

In the following section, four numerical examples with focus on different aspects of computationally solving FSCI problems are presented. To start with, the falling, contacting, and lifting of a rounded stamp is analyzed to verify the principal processes present in all FSCI configurations. The examination of an elastic pump proves the applicability of the framework to handle topological changes of the fluid domain including significantly different fluid solutions between the separated domains. Further, a flow-driven squeezed elastic structure is analyzed, which includes highly dynamic mechanisms, large contact areas, and numerous contacting and lift-off processes. Finally, the numerical study of a double-leafed valve demonstrates the applicability of the presented formulation for 3D configurations. For the first three examples presented in

this section, four-noded bi-linear quadrilateral elements and for the last example eight-noded tri-linear hexahedral elements are applied for the spatial discretization of all solid domains and fluid domains. In order to make the presentation as clear as possible, the index h to specify discrete quantities has been omitted for all numerical examples.

The configurations of the presented examples (except for the first validation example) are chosen to challenge the presented FSCI formulation. To guarantee a strong interaction between the structures and the fluid, equal initial densities are considered within all domains. Thus, it is ensured that the fluid-structure coupling, the solid-solid contact, as well as the change between these conditions have an essential impact to the overall processes of the respective problem configuration.

6.4.1 Falling, Contacting, and Lifting of a Rounded Stamp

The first presented numerical example, a simple configuration including the falling, contacting, and lifting of a rounded stamp, is considered to analyze basic properties of the presented formulation. Due to the symmetry of this configuration, just the half rounded stamp Ω^{S_2} and fluid domain Ω^{F} are considered.

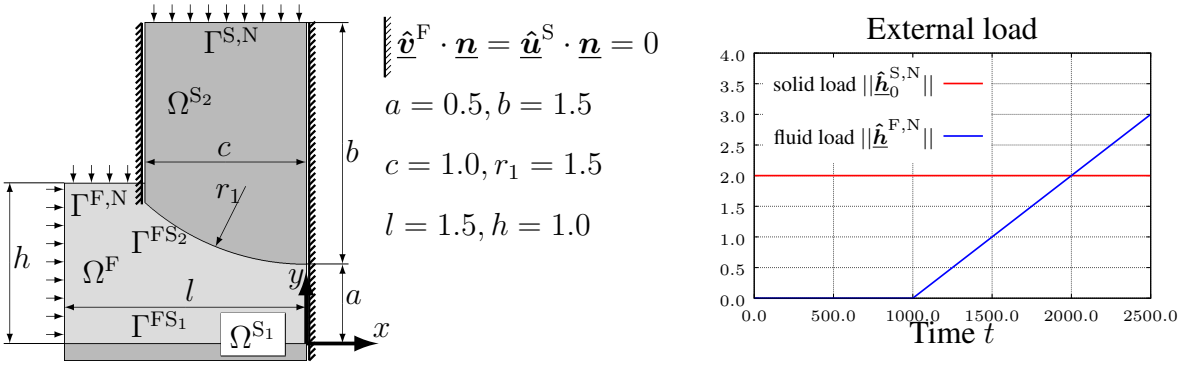

Figure 6.4: Geometry and boundary conditions for the falling, contacting, and lifting of a rounded stamp. Due to the symmetry of the configuration, only the part with $x \leq 0$ is considered (left). The prescribed, time-dependent external loads $\hat{\underline{\boldsymbol{h}}}_0^{\mathrm{S,N}}$ and $\hat{\underline{\boldsymbol{h}}}^{\mathrm{F,N}}$ are given in the diagram (right).

Problem Description The geometric setup and basic boundary conditions are visualized in Figure 6.4. The solid domain Ω^{S_1} is rigid and fixed in space by a Dirichlet boundary condition on the overall domain. In the initial phase, the stamp is exposed solely to a prescribed constant-in-time Neumann load on the boundary $\Gamma^{\mathrm{S,N}}$ in negative y-direction (see Figure 6.4 (right)), which induces the falling motion. After a certain time, contact between the solid domains Ω^{S_1} and Ω^{S_2} will occur and a stationary state will be established subsequently. Finally, after $t = 1000$ a Neumann fluid load is prescribed in the normal direction of the boundary $\Gamma^{\mathrm{F,N}}$. This load increases linearly in time as indicated in Figure 6.4 (right). The fluid material parameters are specified as density $\rho^{\mathrm{F}} = 10^{-3}$ and dynamic viscosity $\mu^{\mathrm{F}} = 1.0$. The solid density in the undeformed configuration is equal to the fluid density $\rho_0^{\mathrm{S}} = 10^{-3}$. A Neo-Hookean model with the hyperelastic strain energy function ψ^{S} specified in (2.17) describes the material behavior of the solid domain Ω^{S_2}, with with Young's modulus $E = 100$ and Poisson's ratio $\nu = 0.0$. To analyze the presented formulation, two different spatial resolutions are applied. For the "coarse"

variant, the fluid mesh consists of $16 \times 24 = 384$ elements and the solid mesh of domain Ω^{S_2} is created by 400 elements. In the "fine" variant, $64 \times 96 = 6144$ fluid elements and 6400 elastic solid elements are used. The weighting of the solid contact stress is purely based on the domain Ω^{S_2} due to the rigid domain Ω^{S_1}. The reference slip length is set to $\kappa_0 = 0.1$ for all computations including the Navier slip condition. The constants for the Nitsche penalty parameters are $\gamma_0^{S,c} = 1$ and $\gamma_0^{FSI} = \gamma_0^{FSI,t} = 35$ if not denoted otherwise. The discretization in time is performed with the Backward Euler scheme ($\theta = 1.0$), with three different sizes of the time step ($\Delta t = 0.01$ for $t \in [0, 20]$, $\Delta t = 0.2$ for $t \in [20, 420]$, $\Delta t = 2.0$ for $t \in [420, 2500]$) to account for the varying dynamic of the analyzed system.

Numerical Results and Discussion In Figure 6.5, the vertical displacement of the spatial point with initial position $\underline{\boldsymbol{X}}^S = (0, a)$ of the solid domain Ω^{S_2} is depicted. Comparing the "fine"

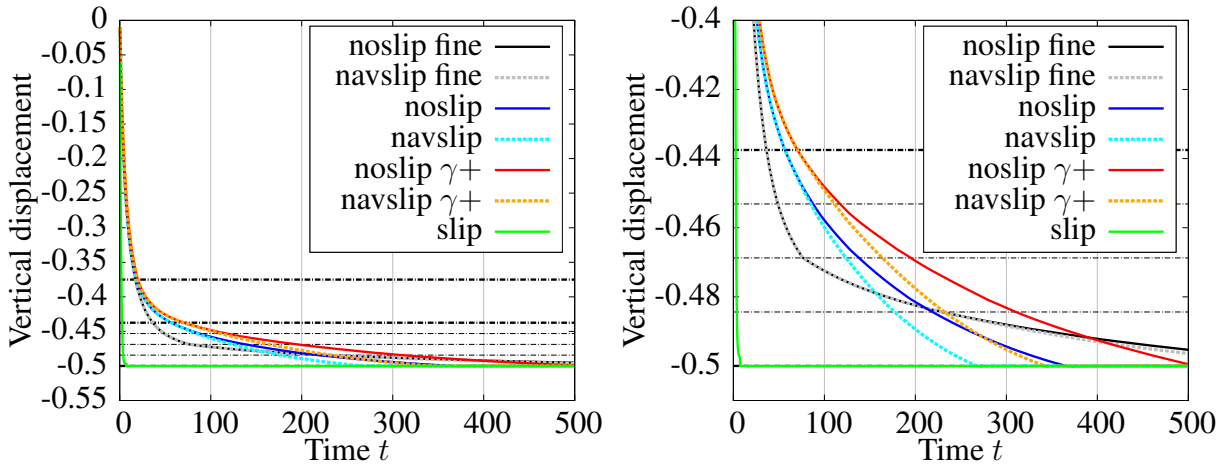

Figure 6.5: Vertical displacement of the spatial point with initial position $\underline{\boldsymbol{X}}^S = (0, a)$ of the solid domain Ω^{S_2} for different computed variants over time (left overview, right detail): "noslip fine" (slip length on the interface Γ^{FS} specified to $\kappa = 0$, computed with the "fine" discretization variant), "navslip fine" (slip length on the interface Γ^{FS} as defined in Section 6.2.3 ($\kappa_0 = 0.1$), computed with the "fine" discretization variant), "noslip" (slip length on the interface Γ^{FS} specified to $\kappa = 0$, computed with the "coarse" discretization variant), "navslip" (slip length on the interface Γ^{FS} as defined in Section 6.2.3 ($\kappa_0 = 0.1$), computed with the "coarse" discretization variant), "noslip $\gamma+$" (configuration as "noslip" with increased tangential Nitsche penalty constant $\gamma_0^{FSI,t} = 35000$), "navslip $\gamma+$" (configuration as "navslip" with increased tangential Nitsche penalty constant $\gamma_0^{FSI,t} = 35000$), "slip" (slip length on the interface Γ^{FS} specified to $\kappa = \infty$, computed with the "coarse" discretization variant). The horizontal black dash-dotted lines (thick lines for coarse mesh) indicate the fluid element boundaries.

and "coarse" discretizations shows a good agreement down to a gap of approximately two coarse fluid elements (vertical displacement $\underline{\boldsymbol{u}}_y^S(0, a) = -0.375$), where both variants start to deviate significantly. Solely the "slip" variant leads to a fundamentally different impact behavior, which is clear due to the non-physical boundary condition applied to the viscous fluid. All variants lead to contact in finite time, even though this phenomenon is not expected for the no-slip variants theoretically (see e.g. the works of Hillairet and Takahashi [119] and Gérard-Varet *et al.* [92]). The explanation for this (realistic) behavior lies in the inherent constraint relaxation arising from the weak imposition by Nitsche's method. As soon as the solution can no longer be resolved sufficiently, a tangential slip occurs numerically also for the no-slip model. To substantiate this

explanation, a variant with increased tangential penalty parameter $\gamma_0^{\mathrm{FSI},t} = 35000$ is computed, which reduces the numerical slip and, thus, results as expected in a slower approach velocity.

In the following, the difference between the no-slip condition and the Navier slip condition of the computed solution is discussed. As expected, the Navier slip variant results in an increased velocity, starting from fluid gaps smaller than one fluid element (see definition of the slip length in Section 6.2.3). Still, the difference between both approaches is not substantial (compared to the error between "coarse" and "fine" resolution). While this simple configuration allows solving the FSCI problem for both interface conditions, applying the Navier slip condition seems to be beneficial for general configurations in two aspects. Firstly, independent of the approach applied for the imposition of the interface condition, a controlled way of relaxation of the tangential constraint can be incorporated. Secondly, this type of condition is required to allow for a continuous problem formulation on the interface.

The overall flowrate on boundary $\Gamma^{\mathrm{F,N}}$ and two different flow rate errors are visualized in Figure 6.6 including the relaxation by the Navier slip interface condition and in Figure 6.7 applying the no-slip interface condition. Herein, the flow rate Φ through boundary $\Gamma^{\mathrm{F,N}}$, the fluid displacement rate on the interface Γ^{FS} given by the fluid velocity $\underline{\boldsymbol{v}}^{\mathrm{F}}$ or the solid velocity $\partial \underline{\boldsymbol{u}}^{\mathrm{S}}/\partial t$ is computed as

$$\Phi = \left| \int_{\Gamma^{\mathrm{F,N}}} \underline{\boldsymbol{v}}^{\mathrm{F}} \cdot \underline{\boldsymbol{n}} \, \mathrm{d}\Gamma^{\mathrm{F,N}} \right|, \quad \Phi^F_{\Gamma^{\mathrm{FS}}} = \left| \int_{\Gamma^{\mathrm{FS}}} \underline{\boldsymbol{v}}^{\mathrm{F}} \cdot \underline{\boldsymbol{n}} \, \mathrm{d}\Gamma^{\mathrm{FS}} \right|, \quad \Phi^S_{\Gamma^{\mathrm{FS}}} = \left| \int_{\Gamma^{\mathrm{FS}}} \frac{\partial \underline{\boldsymbol{u}}^{\mathrm{S}}}{\partial t} \cdot \underline{\boldsymbol{n}} \, \mathrm{d}\Gamma^{\mathrm{FS}} \right|. \tag{6.36}$$

Due to the fluid incompressibility, all three rates have to be equal when taking into account the exact solution of the underlying problem. Analyzing the flow rates Φ in Figure 6.6, an initial decrease of the fluid flow due to the deceleration of the structure in domain Ω^{S_2} for the approaching bodies can be observed. After a short-time raise at the point of first contact (at $t = 268.2$ for the coarse mesh and $t = 616$ for the fine mesh), the flow rate decreases to small magnitudes. At $t = 1000$, the fluid load at $\Gamma^{\mathrm{F,N}}$ starts linearly increasing, which results in a quick rise in the flow rate. As soon as contact is released (at $t = 2166$ for the coarse mesh and $t = 2290$ for the fine mesh), the structure in Ω^{S_2} moves in positive y-direction and so the flow increases. To quantify the numerical error, two flow rate errors are considered

$$\Phi^1_{err} = \left| \Phi^S_{\Gamma^{\mathrm{FS}}} - \Phi \right|, \quad \Phi^2_{err} = \left| \Phi^S_{\Gamma^{\mathrm{FS}}} - \Phi^F_{\Gamma^{\mathrm{FS}}} \right|. \tag{6.37}$$

Herein, Φ^1_{err} indicates errors in the overall mass balance, and Φ^2_{err} characterizes the mass balance errors due to the weak imposition of the interface condition by the Nitsche method. When analyzing the overall mass balance Φ^1_{err}, an unexpectedly small error for this mesh resolution can be observed. An explanation to this effect is given in the following. The discrete fluid mass balance is comprised of the divergence term in (2.112), the weakly consistent face-oriented stabilization operators and ghost penalty stabilization operators (2.114) and (3.4), and the skew-symmetric adjoint-consistency term on the interface (6.18). Partial integration of the divergence term in (2.112) for the fluid balance of mass is performed and the resulting terms are combined with the

adjoint-consistency term (6.18).

Discrete fluid balance of mass:

$$\underbrace{\left(\delta p_{\mathrm{h}}^{\mathrm{F}}, \boldsymbol{\nabla}\cdot\underline{\boldsymbol{v}}_{\mathrm{h}}^{\mathrm{F}}\right)_{\Omega_{\mathrm{h}}^{\mathrm{F}}}}_{\text{from (2.112)}} - \underbrace{\left\langle \delta p_{\mathrm{h}}^{\mathrm{F}}\underline{\boldsymbol{n}}_{\mathrm{h}}, v_{\mathrm{h}}^{rel,n}\underline{\boldsymbol{n}}_{\mathrm{h}}\right\rangle_{\Gamma_{\mathrm{h}}^{\mathrm{FS}}}}_{\text{from (6.18)}} + \underbrace{\mathcal{W}_{\mathcal{S}_{\mathrm{h}}}^{\mathrm{P}}}_{\text{from (2.114)}} + \underbrace{\mathcal{W}_{\mathcal{G}_{\mathrm{h}}}^{\mathrm{F}}}_{\text{from (3.4)}} =$$

$$- \left(\boldsymbol{\nabla}\delta p_{\mathrm{h}}^{\mathrm{F}}, \underline{\boldsymbol{v}}_{\mathrm{h}}^{\mathrm{F}}\right)_{\Omega_{\mathrm{h}}^{\mathrm{F}}} + \left\langle \delta p_{\mathrm{h}}^{\mathrm{F}}, \underline{\boldsymbol{v}}_{\mathrm{h}}^{\mathrm{F}}\cdot\underline{\boldsymbol{n}}_{\mathrm{h}}\right\rangle_{\partial\Omega_{\mathrm{h}}^{\mathrm{F}}} - \left\langle \delta p_{\mathrm{h}}^{\mathrm{F}}, v_{\mathrm{h}}^{rel,n}\underline{\boldsymbol{n}}_{\mathrm{h}}\cdot\underline{\boldsymbol{n}}_{\mathrm{h}}\right\rangle_{\Gamma_{\mathrm{h}}^{\mathrm{FS}}} + \mathcal{W}_{\mathcal{S}_{\mathrm{h}}}^{\mathrm{P}} + \mathcal{W}_{\mathcal{G}_{\mathrm{h}}}^{\mathrm{F}} =$$

$$- \left(\boldsymbol{\nabla}\delta p_{\mathrm{h}}^{\mathrm{F}}, \underline{\boldsymbol{v}}_{\mathrm{h}}^{\mathrm{F}}\right)_{\Omega_{\mathrm{h}}^{\mathrm{F}}} + \left\langle \delta p_{\mathrm{h}}^{\mathrm{F}}, \underline{\boldsymbol{v}}_{\mathrm{h}}^{\mathrm{F}}\cdot\underline{\boldsymbol{n}}_{\mathrm{h}}\right\rangle_{\partial\Omega_{\mathrm{h}}^{\mathrm{F}}\setminus\Gamma_{\mathrm{h}}^{\mathrm{FS}}} + \left\langle \delta p_{\mathrm{h}}^{\mathrm{F}}, \tilde{\partial}_t\left[\underline{\boldsymbol{u}}_{\mathrm{h}}^{\mathrm{S}}\right]\cdot\underline{\boldsymbol{n}}_{\mathrm{h}}\right\rangle_{\Gamma_{\mathrm{h}}^{\mathrm{FS}}} + \mathcal{W}_{\mathcal{S}_{\mathrm{h}}}^{\mathrm{P}} + \mathcal{W}_{\mathcal{G}_{\mathrm{h}}}^{\mathrm{F}} \qquad (6.38)$$

It can be observed that the fluid velocity in the boundary integral in the second line is replaced by the solid velocity on the interface Γ^{FS}. The skew-symmetric adjoint-consistency term (6.18) acts therefore as a compensation term for the violation of the balance of mass on the fluid-structure interface. Hence, the error Φ_{err}^1 is not influenced by the accuracy of the FSI constraint enforcement but is solely attributed to the stabilization terms from the CIP and the GP stabilization. In addition, the finite convergence tolerance of the nonlinear solution procedure yields perturbations in the error level depending on the remaining residual. Finally, the interface error Φ_{err}^2 is observed to be significantly larger than the overall error Φ_{err}^1. Comparing the "coarse" and the "fine" mesh resolution allows the analysis of the spatial convergence of this error. For the time range with similar flow rates (Φ coarse $\approx$ Φ fine), a reduction in the error, approximately of second order with respect to the fluid mesh element size h, can be observed. To give a compre-

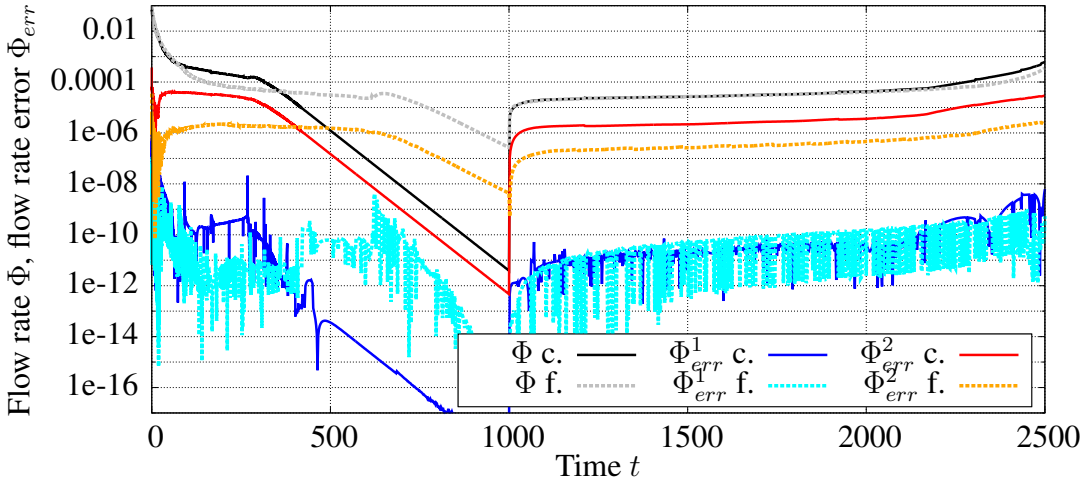

Figure 6.6: Comparison of computed flow rates and flow rate errors for the "c.": coarse and "f.": fine mesh resolution for the Navier slip interface condition. Herein, Φ is the flow rate on boundary $\Gamma^{\mathrm{F,N}}$, Φ_{err}^1 the overall flow rate error, and Φ_{err}^2 the flow rate error on the interface Γ^{FS}.

hensive view of the balance of mass for this FSCI formulation, the results for the application of the no-slip condition on the entire interface are also given in Figure 6.7. No significant difference between both results can be observed. Due to the logarithmic axis scaling, a deviation for the small flow rates ($600 \leq t \leq 1000$) after contact established can be observed. As this difference does not essentially influence the lift-off procedure afterwards, the principal discussion done for the Navier slip condition holds also for the no-slip condition.

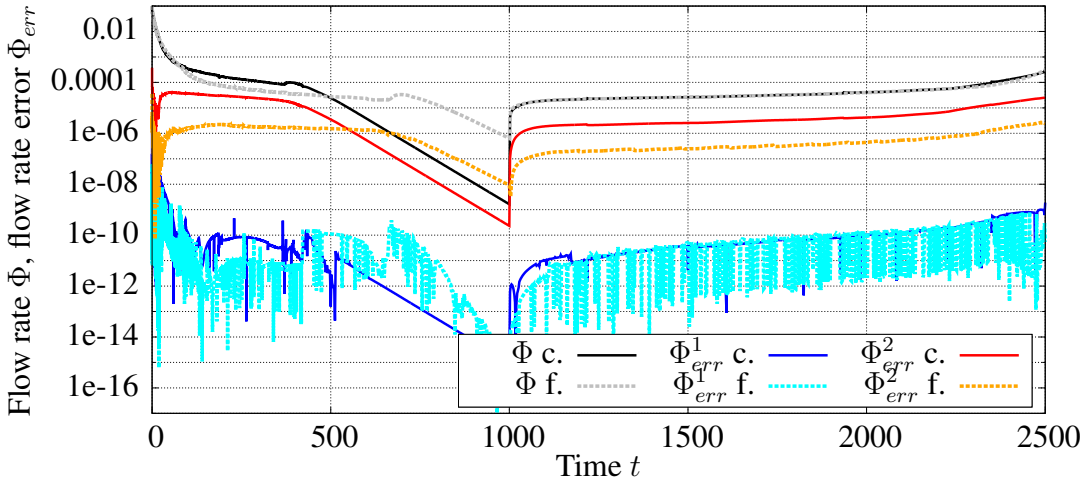

Figure 6.7: Comparison of computed flow rates and flow rate errors for the "c.": coarse and "f.": fine mesh resolution for the no-slip interface condition. Herein, Φ is the flow rate on boundary $\Gamma^{\mathrm{F,N}}$, Φ^1_{err} the overall flow rate error, and Φ^2_{err} the flow rate error on the interface Γ^{FS}.

In Figure 6.8, a detailed view of the contacting zone for different points in time is given. Three different types of traction are visualized by arrows, namely the overall traction, the FSI traction, and the contact traction. At $t = 100$ (first row in Figure 6.8), the body Ω^{S_2} approaches Ω^{S_1} and as a result a high pressure peak occurs in the smallest constriction. This peak is almost equal to the FSI traction concluding that viscous traction is not significant. At $t = 340$ (second row in Figure 6.8), the majority of the external load is carried by the contact traction. For the overall traction, the continuous transition of FSI traction and contact traction can be seen. An essential part of the external load at $t = 2020$ (third row in Figure 6.8) is carried by the FSI traction, but due to the fluid inertia there is still contact at the area around $x = 0$. Finally, at $t = 2420$ the structural body Ω^{S_2} completely lifted again and so the lowest pressure and FSI traction can be identified in the smallest constriction.

6.4.2 Elastic Pump

In the following example, an elastic fluid pump powered by an external load is analyzed. This configuration includes large deformation of the solid domain and a periodically changing topological connection of the fluid domain. Large fluid pressure discontinuities when crossing the valves occur, which need to be represented properly by the fluid solution space.

Problem Description The geometric setup and the basic boundary conditions are depicted in Figure 6.9. The geometry of the solid domain Ω^{S} is designed to pump fluid in the domain Ω^{F} from the fluid inflow boundary Γ^{in} to the fluid outflow boundary Γ^{out}. The structural part includes two valves consisting of two flaps each to control the flow direction. The fluid flow is driven by the change of volume in the fluid chamber placed between the two valves. The pump is powered by a time-dependent periodic traction in normal direction, which is prescribed as a Neumann condition on the circular solid boundary Γ^p as $\hat{\underline{\boldsymbol{h}}}^{\mathrm{S,N}} = -20A(1-\cos(40\pi t)) \cdot \underline{\boldsymbol{n}}$, with $A = 1.0$ for $t \in [0, 0.15]$ and $A = 1.5$ for $t \in [0.15, 0.3]$. In the tangential plane of Γ^p, zero-traction

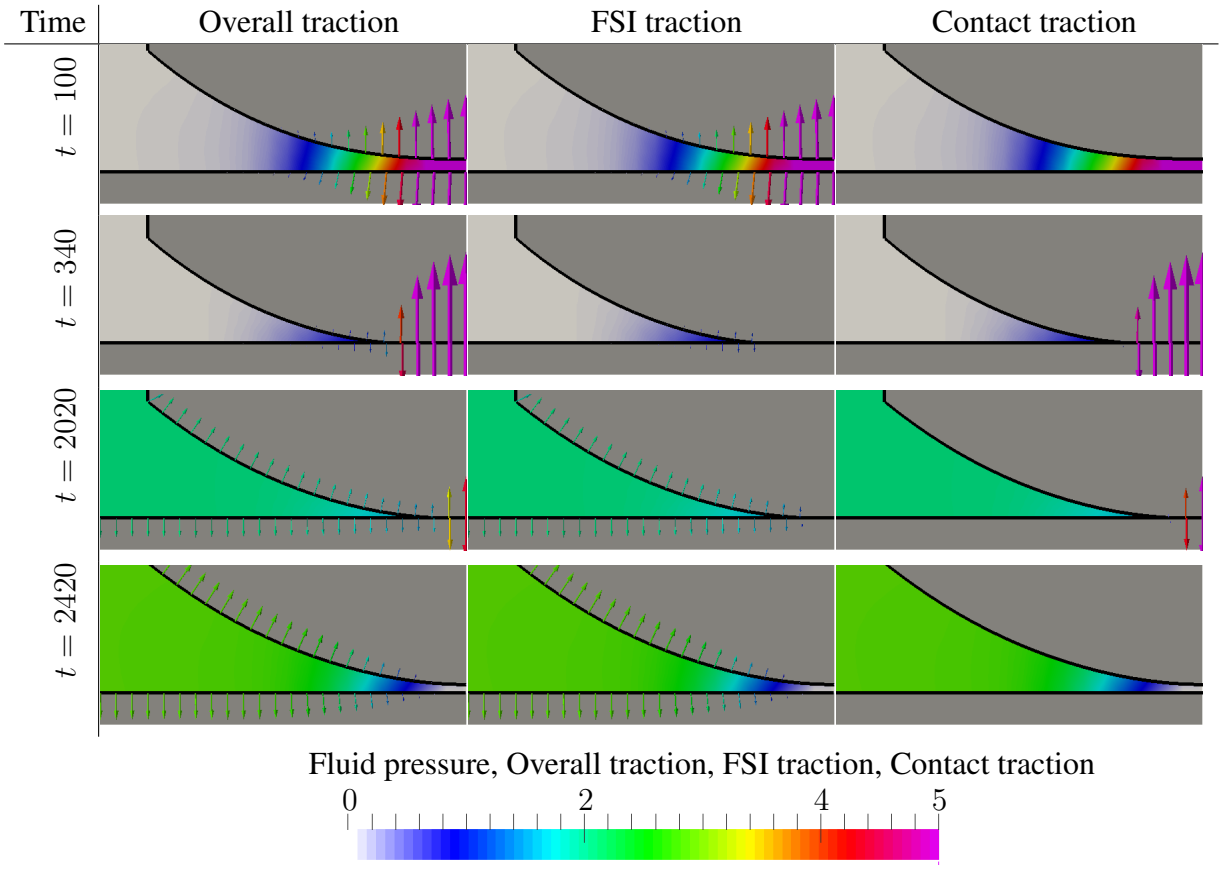

Figure 6.8: Visualization of the computed falling, contacting and lifting process of the rounded stamp for the Navier slip interface condition at four instances in time. The color code in the fluid domain visualizes the computed fluid pressure and the color code of the arrows the respective traction magnitude. The arrows visualize the interface traction separated in three groups. The overall traction includes all contributing of cases $I - IV$, the FSI traction includes case I, and the contact traction includes cases $II - IV$ (specified in the interface contributions (6.21)-(6.25)). The visualization of the traction is reconstructed from the nodal interface contributions of (6.21)-(6.25)) to the overall weak form on the solid mesh.

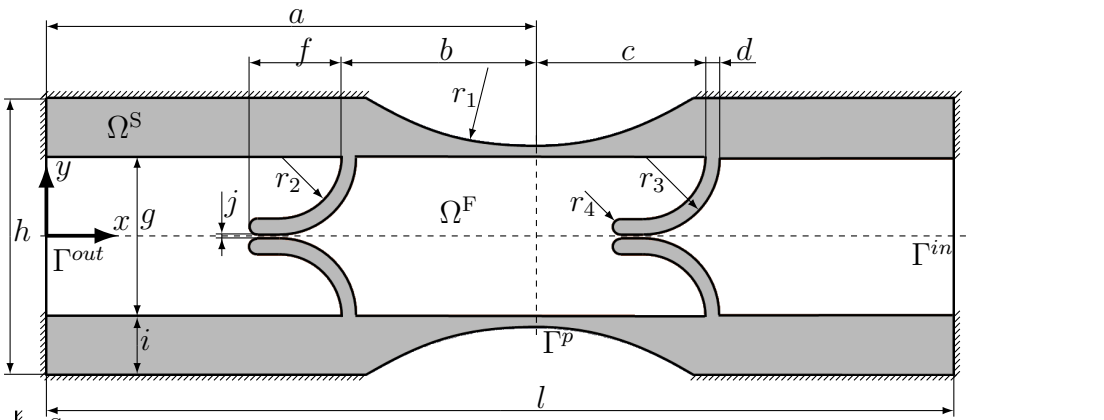

$\underline{\hat{\boldsymbol{u}}}^{\mathrm{S}} = \underline{\mathbf{0}}$, $a = 0.8$, $b = 0.3125$, $c = 0.2875$, $d = 0.025$, $f = 0.1525$, $g = 0.26$, $i = 0.1$
$j = 0.01$, $h = 0.46$, $l = 1.5$, $r_1 = 0.5$, $r_2 = 0.1$, $r_3 = 0.125$, $r_4 = 0.0125$

Figure 6.9: Geometry and boundary conditions for the elastic pump.

is prescribed. Therefore, the pump is driven for three periodic cycles with a constant amplitude of the external load, followed by three periodic cycles with an external load increased by 50%. Both, the solid and the fluid are subject to a gravitational body force in negative y-direction: $\rho_0^{\mathrm{S}}\hat{\underline{\boldsymbol{b}}}_0^{\mathrm{S}} = \rho^{\mathrm{F}}\hat{\underline{\boldsymbol{b}}}^{\mathrm{F}} = [0,-1]^{\mathsf{T}}$. On the fluid boundaries Γ^{in} and Γ^{out}, the hydrostatic pressure is prescribed by a Neumann boundary condition in x-direction ($\hat{\underline{\boldsymbol{h}}}^{\mathrm{F,N}} \cdot \underline{\boldsymbol{n}} = y$), whereas zero velocity in y-direction is prescribed by a Dirichlet-type boundary condition.

As material parameters, the fluid density is $\rho^{\mathrm{F}} = 10^{-3}$ and the dynamic viscosity is $\mu^{\mathrm{F}} = 10^{-4}$. The material behavior of the solid continuum is given by the Neo-Hookean model with the strain energy function (2.17) and a Young's modulus $E = 2000$ and Poisson's ration $\nu = 0.3$. The initial density in Ω^{S} equals the fluid density $\rho_0^{\mathrm{S}} = \rho^{\mathrm{F}} = 10^{-3}$.

The fluid domain is discretized by a structured mesh consisting of $240 \times 54 = 12960$ (with $0.0 \leq x \leq 1.5$ and $-0.1755 \leq y \leq 0.1755$) elements, which is unfitted to the interface Γ^{FS}. The solid domain is discretized fitted to the interface Γ^{FS} by 4648 elements (shown in Figure 6.10 (top-left)). A contact stress based on harmonic weighting between the stress representation of both solid domains, as discussed in Section 6.2.2, is applied. Due to the almost equal material parameters and mesh sizes of all contacting interfaces, this approach results approximately in a mean weighting $\omega^c \approx 0.5$. The reference slip length is set to $\kappa_0 = 0.1$. The constants for the Nitsche penalty parameters are $\gamma_0^{\mathrm{S},c} = 1$ and $\gamma_0^{\mathrm{FSI}} = \gamma_0^{\mathrm{FSI},t} = 35$. The temporal discretization is performed with $\theta = 1.0$ and a time step size of $\Delta t = 0.0002$ for $t \in [0, 0.1698]$ and $\Delta t = 0.0001$ for $t \in [0.1698, 0.3]$, to account for changing system dynamics, is applied.

Numerical Results and Discussion In Figure 6.10, the computed fluid velocity and pressure as well as the computed deformation for $t \in [0.1, 0.15]$ are presented. These results correspond with the third load cycle and already exhibit a periodic response to the periodic external load with an amplitude of $A = 1.0$. Starting with $t = 0.1$, where no external load on Γ^P is applied, the left valve is closed and, due to the pressure gradient in the right valve, a flow into the fluid chamber occurs. In the next point in time $t = 0.106$, a compression of the fluid chamber resulting in an increasing pressure due to the external load is observable. Due to the geometry of the two valves, an opening motion of the left valve and a closing motion of the right valve is induced. As both valves are still open at this point in time fluid, mass leaves the chamber through both valves and finally leads to an back flow at the inflow boundary. This behavior has changed at $t = 0.11$, where the right valve prevents fluid flow as it is closed. It can be seen that the occurring pressure jump between both sides of the right valve can be well represented by the provided fluid function space. The resulting force of the discontinuous fluid pressure leads to a deformation of the right valve into positive x-direction. At the same time, the flaps of the left valve are opened by the fluid pressure and allow for a large fluid flow which finally leads to a high flow rate at the boundary Γ^{out}. At $t = 0.125$, the volume in the chamber is almost minimal and as a consequence the structural velocity on Γ^p nearly vanishes. Therefore, the fluid pressure gradients decrease and both valves relax towards the initial geometry. At $t = 0.135$, the external load reduces and leads to an increasing volume in the fluid chamber. Consequently, the pressure in the chamber drops and induces a closing motion of the left valve. A peak of the fluid pressure between the two left flaps occurs due to the acceleration of fluid mass. The closed left valve prevents flow through the left valve, and the discontinuous pressure is carried elastically by the flaps. The right valve is opened by the pressure difference on both sides of the flaps and

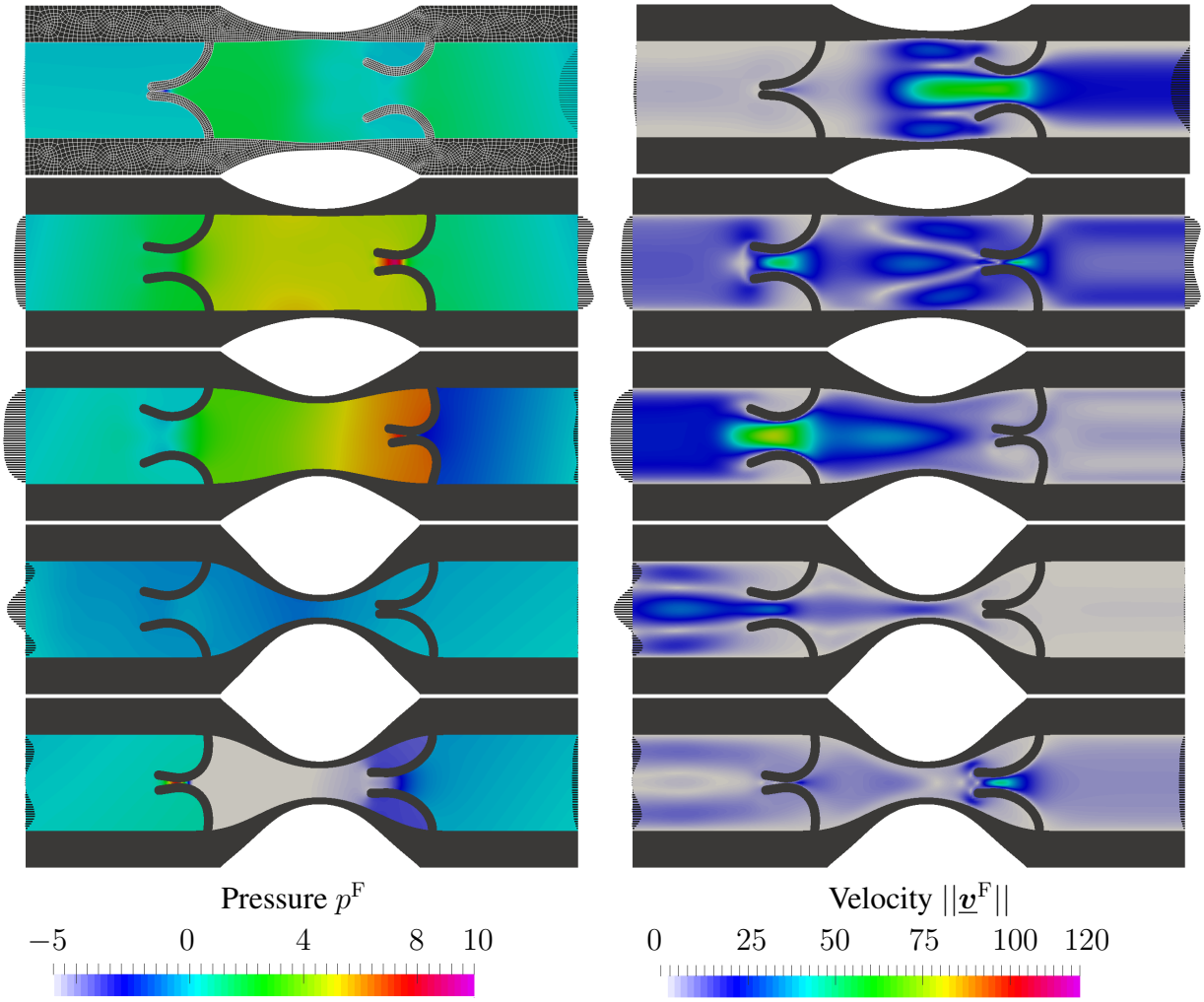

Figure 6.10: Visualization of the computed fluid velocity and pressure and the computed deformation of solid domain for $t \in [0.1, 0.15]$. In the left column, the color code represents the fluid pressure, whereas, in the right column, the fluid velocity magnitude is represented. Additionally, the black bars at the inflow boundary Γ^{in} and outflow boundary Γ^{out} indicate the computed fluid velocity at the corresponding boundary. Five points in time are represented by the rows, which are from top to bottom $t = 0.1, t = 0.106, t = 0.11, t = 0.125$, and $t = 0.135$.

allows for fluid flow into the chamber. As the pumping motion is almost periodical, the results computed for $t = 0.15$ are not distinguishable from the solution at $t = 0.1$ and, thus, are not shown.

To quantify the output of the examined pump, the computed flow rates at the inflow boundary Γ^{in} and outflow boundary Γ^{out} are presented in Figure 6.11 (left). First, the time interval $t \in$

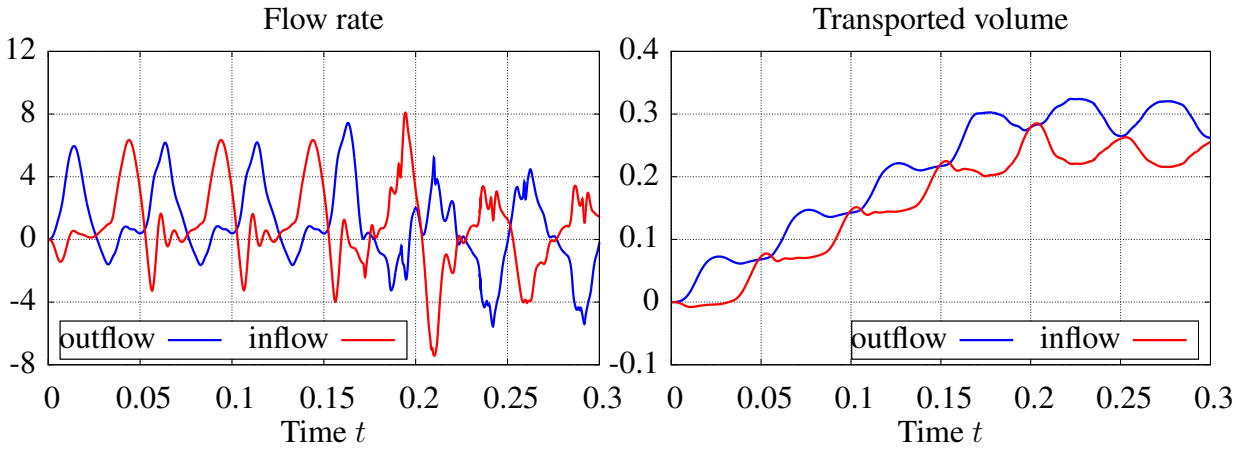

Figure 6.11: Computed flow rates at the inflow boundary Γ^{in} and the outflow boundary Γ^{out}. The normal vector therein is oriented in negative x-direction, which is the design flow direction of the pump (left). Transported volume through the inflow boundary Γ^{in} and the outflow boundary Γ^{out} computed in a post-processing step where an integration in time of the flow rates is performed (right).

$[0.1, 0.15]$, with a periodic external load of amplitude $A = 1$, is analyzed. While the first cycle is still dominated by the start-up process from a system initially in rest, the flow rates of the second and third cycle are very similar. Therefore, the cycle $t \in [0.1, 0.15]$ can be classified as the periodic response to the periodic load with $A = 1$ and was already discussed in detail previously. Now, analyzing the subsequent interval $t \in [0.15, 0.3]$ with $A = 1.5$, after a transition phase in the fourth load cycle the pump exhibits again an almost periodic behavior for the last two load cycles. It can be seen that oscillations with higher frequencies occur than for the smaller load amplitude, which are tackled by a reduced time step size in the time integration scheme.

To make a statement on the performance of the pump, the volume transported through the pump is presented in Figure 6.11 (right). It can be seen that in each cycle the transported volume through Γ^{in} at first is smaller than through Γ^{out} mainly due to the volume change in the fluid chamber. The difference in the transported volume is smaller for $A = 1$ than for $A = 1.5$ as larger deformations occur. Analyzing the transported volume per cycle, it can be seen that, for the smaller amplitude, each cycle transports approximately 0.074, whereas the higher load amplitude leads to a slight transport opposite to the design flow direction.

To generate understanding for this phenomenon, four exemplary points in time with load amplitude $A = 1.5$ are selected and shown in Figure 6.12. Compared to the load with amplitude $A = 1.0$, higher fluid velocities occur leading to higher pressures and finally an increase of the interface traction, at $t = 0.167$. This fluid state leads to a non-symmetric deformation of the flaps in the right valve. As it can be seen at $t = 0.174$, finally the lower flap snaps through and as a result the right valve does not prevent flow properly anymore. For $t \in [0.1791, 0.1822]$, contact between the upper and lower part of the fluid chamber occurs, prohibiting the flow in

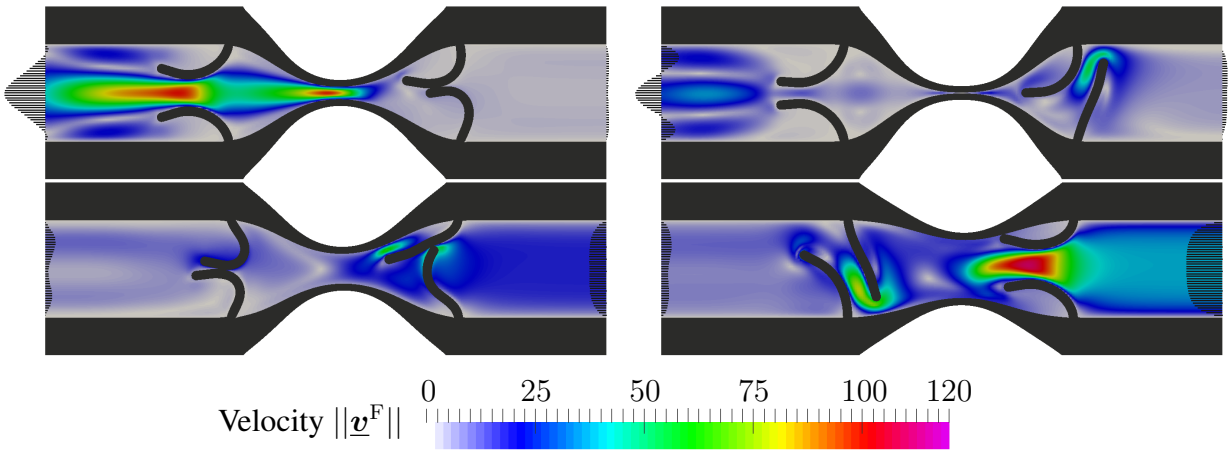

Figure 6.12: Visualization of the computed fluid velocity and pressure and the computed deformation of solid domain for $t \in [0.15, 0.2]$. The color code represents the fluid velocity magnitude, and the black bars at the inflow boundary Γ^{in} and outflow boundary Γ^{out} indicate the computed fluid velocity at the corresponding boundary. Four points in time are represented from top-left to bottom-right $t = 0.167, t = 0.174, t = 0.19$ and $t = 0.194$.

the chamber. At $t = 0.19$, the lower flap of the right valve starts to snap back, whereas the left valve is exposed to large non-symmetric deformation. Finally at $t = 0.194$, the left valve has snap-through, allowing for flow opposite to the design flow direction. In short, a load amplitude of $A = 1.5$ is beyond the maximal load resulting in a proper operation of the elastic pump.

Nevertheless, from a computational point of view, it is noteworthy that the presented formulation demonstrates to be applicable also for these rather complex scenarios and, hence, promises to be a rather general tool. Processes beyond the intended design can be computed without requiring changes to the problem setup. In this example, unexpected deformation and topological changes to the fluid domain were handled without any modifications to the problem setup.

6.4.3 Flow-Driven Squeezed Elastic Structure

In the following, a configuration is considered where an initially cylindrical elastic body Ω^{S_2} is squeezed through an elastic structure Ω^{S_1} by the load of the surrounding fluid flow. This configuration is designed to test the formulation's capability to handle frequent changes between the fluid-structure interface and the contact interface including large contacting areas and essential topological changes.

Problem Description The problem setup of this example, including all dimensions and basic boundary conditions, is visualized in Figure 6.13 (left). All dimensions of the solid body Ω^{S_1}, which are not explicitly indicated in this figure, are defined by symmetry and replication of the given dimensions (e.g. all unspecified radii are equal to r_2).

On the inflow boundary Γ^{in}, a time-dependent, parabolic velocity profile

$$\begin{aligned} \hat{\underline{\boldsymbol{v}}}^{\mathrm{F}} &= \left[0, -100(1-x^2)4000t\right]^{\mathsf{T}} && \text{for } t \in [0.0, 0.00025] \quad \text{and} \\ \hat{\underline{\boldsymbol{v}}}^{\mathrm{F}} &= \left[0, -100(1-x^2)\right]^{\mathsf{T}} && \text{for } t \in [0.00025, 0.016] \end{aligned}$$

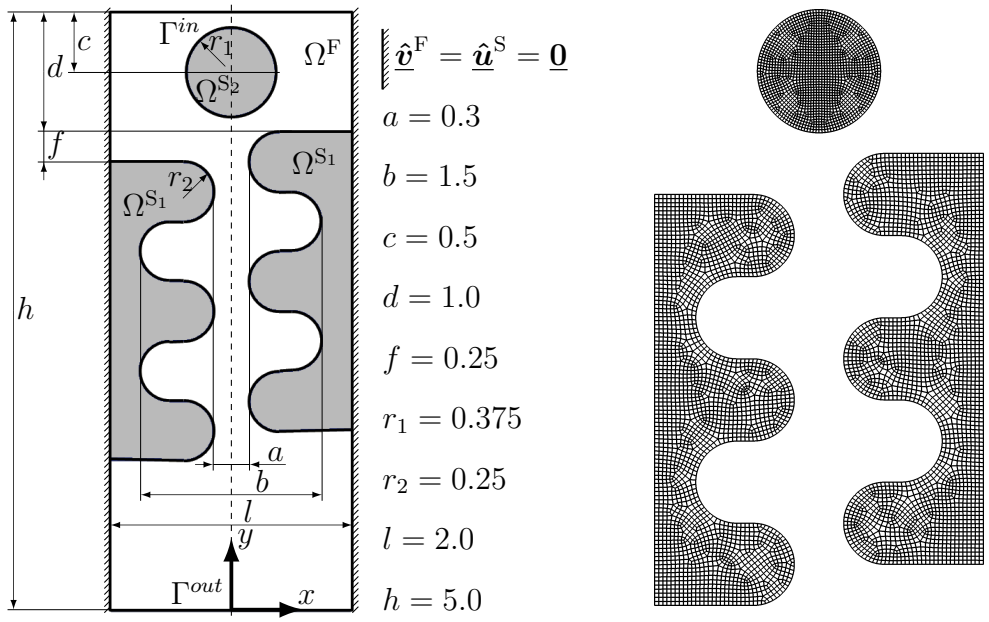

Figure 6.13: Geometry and boundary conditions for the flow-driven squeezed elastic structure (left). Visualization of the discretization for the solid domains Ω^{S_1} and Ω^{S_2} with black lines indicating element boundaries (right).

is prescribed as Dirichlet boundary condition. On the outflow boundary Γ^{out}, a zero-traction Neumann boundary condition is prescribed.

The material properties of the incompressible fluid are specified by the density $\rho^{\mathrm{F}} = 10^{-6}$ and the dynamic viscosity $\mu^{\mathrm{F}} = 10^{-5}$. The initial density in both solid domains equals the fluid density $\rho_0^{\mathrm{S}} = \rho^{\mathrm{F}} = 10^{-6}$. Similar to the numerical examples presented previously, a Neo-Hookean material model with strain energy function (2.17) is considered for both solids. The parameters of the material model in the squeezed domain Ω^{S_2} are given by $E^{\mathrm{S}_2} = 100$ and $\nu^{\mathrm{S}_2} = 0.3$, whereas the outer domain Ω^{S_1} has an increased stiffness by $E^{\mathrm{S}_1} = 200$ and $\nu^{\mathrm{S}_1} = 0.3$.

The structured computational mesh applied for the discretization of the fluid domain consists of $120 \times 300 = 36000$ bilinear elements. The solid domain is discretized fitted to the interface Γ^{FS} by 4890 elements in domain Ω^{S_1} and by 1562 elements in domain Ω^{S_2}. The solid discretization is given in Figure 6.13 (right). In contrast to the examples presented previously, the constants for the Nitsche penalty parameters are $\gamma_0^{\mathrm{S},c} = 1$ and $\gamma_0^{\mathrm{FSI}} = \gamma_0^{\mathrm{FSI},t} = 5$, in order to relax the kinematic constraints and, thus, support the nonlinear solution procedure (see Remark 6.9). With this modification, the penalty parameters are still large enough to provide discrete stability of the formulation. A contact stress based on harmonic weighting between the stress representation of both solid domains, as discussed in Section 6.2.2, is applied. The reference slip length is set to $\kappa_0 = 0.1$. The temporal discretization is preformed with $\theta = 1$ and a time step size of $\Delta t = 0.00002$ for $t \in [0, 0.0056]$ and $\Delta t = 0.000005$ for $t \in [0.0056, 0.016]$ to account for the varying dynamic of the coupled system.

Numerical Results and Discussion In Figure 6.14, the computed fluid velocity and the computed deformation of the solid domains are presented for different points in time. Following the different snapshots, the motion of the solid domain Ω^{S_2} can be observed. In the initial phase

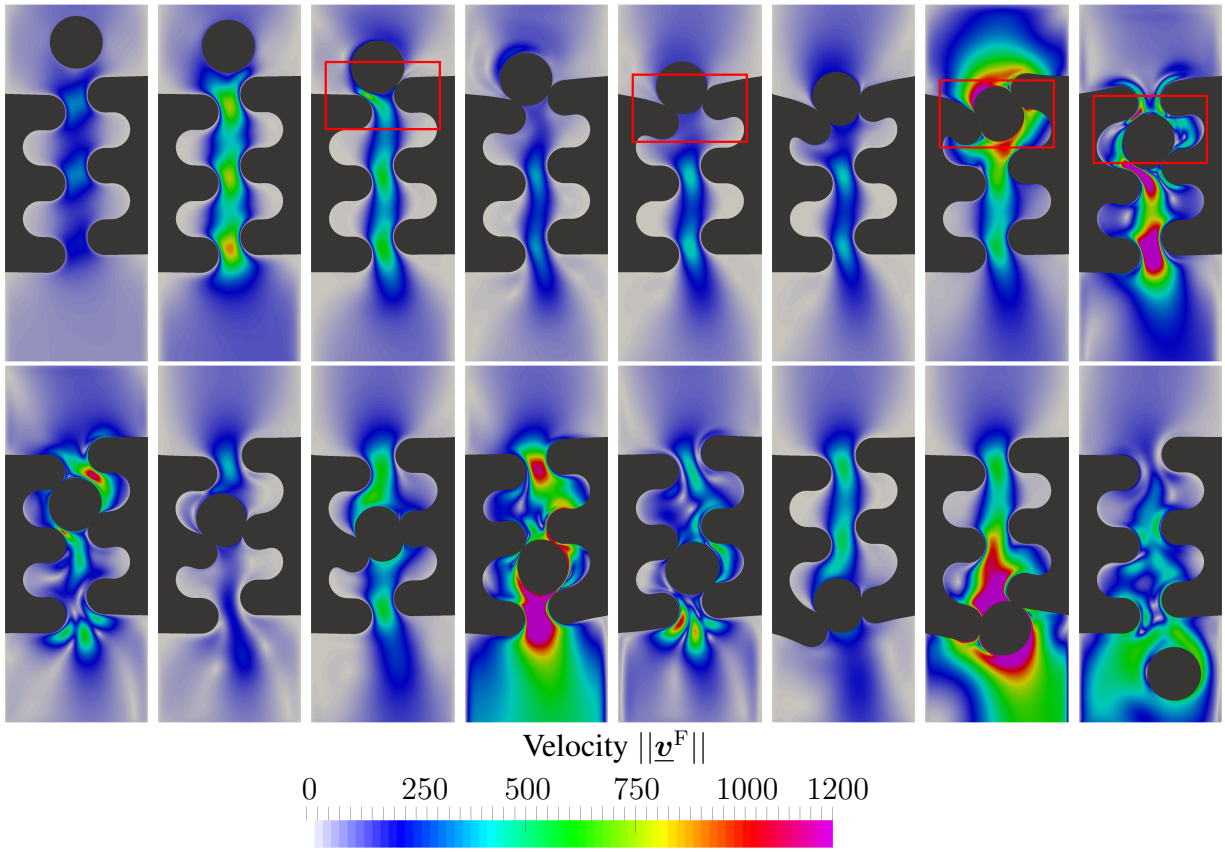

Figure 6.14: Visualization of the computed fluid velocity and the computed deformation of solid domains. The color code represents the fluid velocity magnitude. Different points in time are represented from top-left to bottom-right with $t = 0.0005, t = 0.001, t = 0.003, t = 0.004, t = 0.005, t = 0.006, t = 0.0065, t = 0.007$ in the first row and $t = 0.0075, t = 0.009, t = 0.01, t = 0.0105, t = 0.011, t = 0.0145, t = 0.015, t = 0.016$ in the second row. The red frame indicates the area of the detailed views in Figure 6.15.

$(0 < t < 0.00324)$, a vertical motion of Ω^{S_2} is induced by the fluid flow. At $t = 0.00324$, contact between Ω^{S_2} and the right part of Ω^{S_1} occurs. Starting from $t = 0.00386$, additional contact between Ω^{S_2} and the left part of Ω^{S_1} establishes. Therefore, the topology of the fluid domain changes from one connected domain, to two separated fluid domains. In the subsequent phase $(0.00386 < t < 0.006)$, the pressure in the upper fluid domain increases, which leads to a squeezing process of Ω^{S_2} and a deformation of Ω^{S_1} and, thus, to a storage of elastic energy. For $t > 0.0065$, an acceleration in vertical direction of Ω^{S_2} can be observed by the transfer of the elastic energy via contact forces. Finally at $t = 0.00668$, contact between both solid bodies is released and a single connected fluid domain reoccurs. Reestablishing contact at $t = 0.00713$ of Ω^{S_2} and the right part of Ω^{S_1}, this principal process repeats for two additional cycles. Nevertheless, due to the varying geometric setup around the three smallest constrictions, the physical process is not repeated exactly and, thus, the robustness of the algorithm is tested for this challenging configuration. Finally, at $t = 0.015155$, both solid domains separate for the last time. In the remaining period, the fluid traction is exclusively acting on the interface $\partial\Omega^{S_2}$.

To give a more detailed view of the computed process, the fluid solution as well as the interface traction for four exemplary points in time are shown in Figure 6.15. First, the point in time just

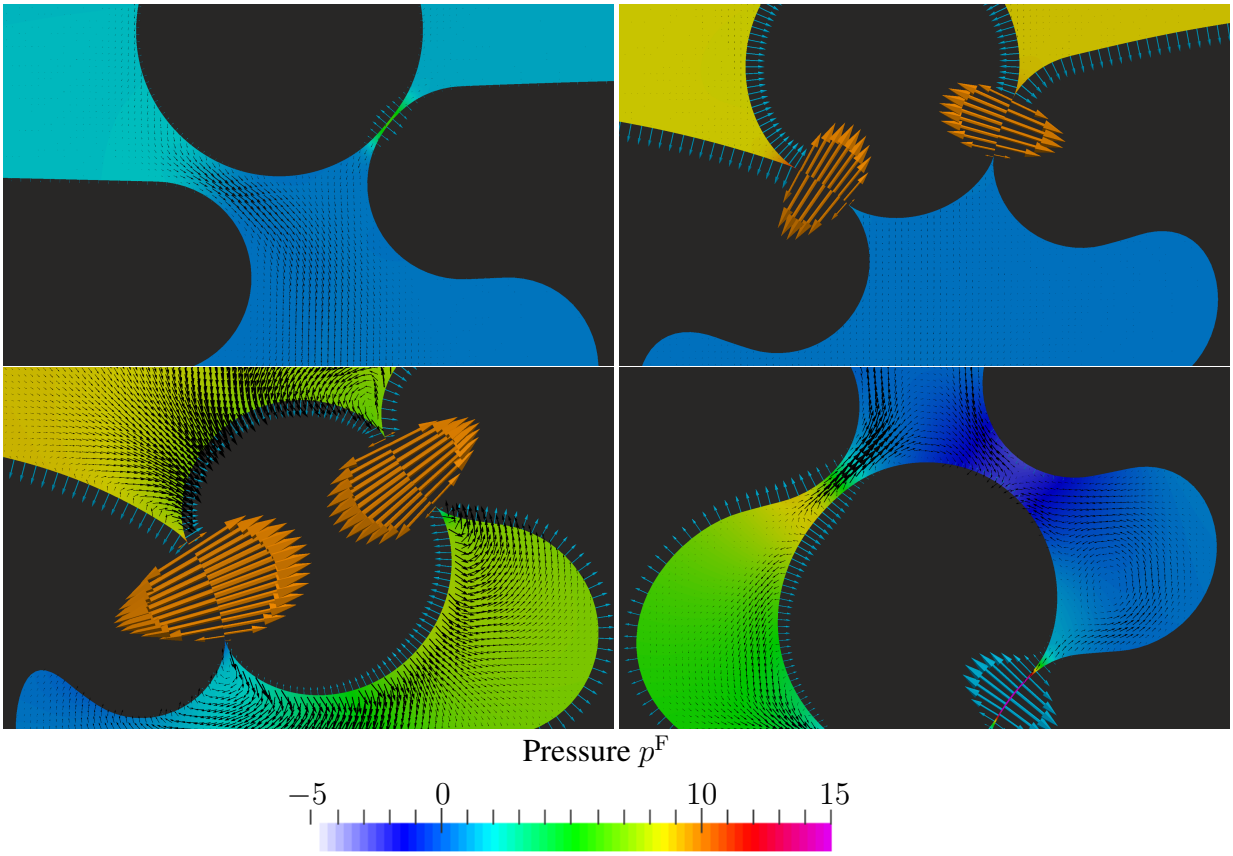

Figure 6.15: Visualization of the computed fluid velocity and pressure, the computed deformation of solid domains, and the interface traction. The color code represents the fluid pressure and the black arrows in domain Ω^{F} indicate the fluid velocity. The blue arrows on Γ represent the FSI traction (case I) and the orange arrows on Γ visualize the contact traction (case $II - IV$). The visualization of the traction is reconstructed from the nodal interface contributions of (6.21)-(6.25)) to the overall weak form on the solid mesh. Four points in time are represented from top-left to bottom-right $t = 0.003, t = 0.005, t = 0.0065$ and $t = 0.007$. The position of each detailed view in the overall problem is marked in Figure 6.14 by a red frame.

before contact occurs $t = 0.003$, is discussed. Due to the small cross-section of the connection between the upper and lower part of the fluid domain, the pressure in the upper part is already increased. Therefore, an essential fluid flow can be observed between Ω^{S_2} and the left part of Ω^{S_1}. The distance in the smallest constriction for the right part leads to an increased fluid pressure compared to the ambient pressure and, thus, to a separating FSI traction of the two solid bodies. At $t = 0.005$, contact between both solid domains is established in two positions. Due to the inflow on Γ^{in}, the pressure in the upper part of the fluid domain is increased, which leads to an increased FSI traction on the affected part of the interface. Although the maximal contact traction is significantly higher than the FSI traction, there is a continuous transition along the interface. The y-components of the resulting FSI force and contact force are almost in balance, and as a result only a very slow motion of the system (see fluid velocity) is observed, continuously adapting to the increasing pressure difference. At $t = 0.0065$ this state changes fundamentally. Due to the deformation based change of the contact interface orientation, the resulting contact force accelerates the solid body in Ω^{S_2}, and with it the surrounding fluid, in negative y-direction.

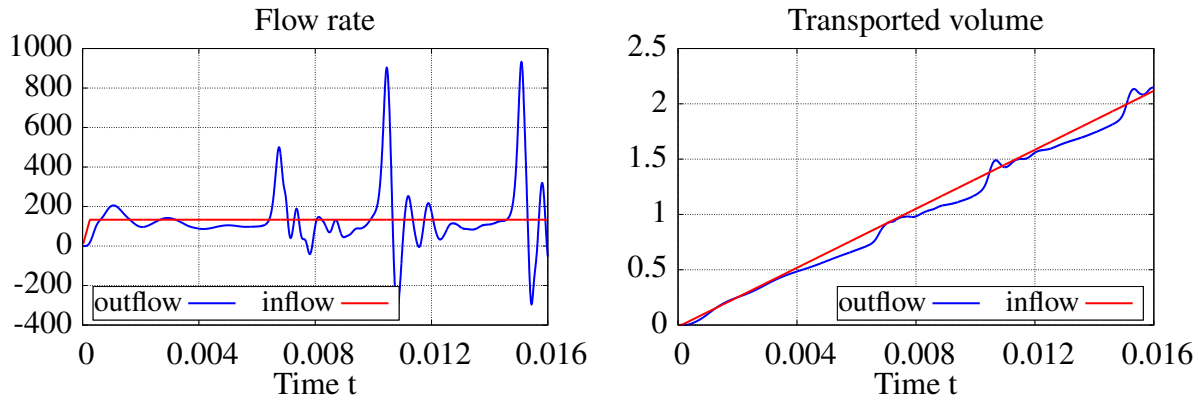

Figure 6.16: Computed flow rates at the inflow boundary Γ^{in} and the outflow boundary Γ^{out}. The normal vector therein is oriented in negative y-direction, which is the main flow direction of the overall configuration (left). Transported volume through the inflow boundary Γ^{in} and the outflow boundary Γ^{out} computed in a post-processing step where an integration in time of the flow rates is performed (right).

The fluid pressure in the upper part of the flow domain drops, whereas the pressure in the lower part increases resulting in an almost constant FSI traction acting on $\partial\Omega^{S_2}$. Finally at $t = 0.007$, contact is released and the structural body in Ω^{S_2} approaches the second barrier. This process leads again to an increased local fluid pressure and, thus, to a growth of the related FSI traction. Due to the structural motion the pressure in the left chamber is raised, which results in a fluid flow out of the fluid chamber. This description of the computed physical process highlights the capabilities of the presented formulation to predict the physical processes in FSCI without requiring a specific treatment whenever topological changes occur.

In Figure 6.16 (left), the computed flow rates at the inflow boundary and outflow boundary are presented. While the prescribed flow rate at the inflow is constant in time after the initial ramp up phase, the flow rate at the outflow boundary is massively influenced by the overall system. Three phases can be observed where a lower outflow rate (than the inflow rate) is followed by a peak of the flow rate. These can be identified as the phases where the solid domains are compressed due to increasing pressure as Ω^{S_2} blocks the flow. These phases are always followed by the highly dynamic process of squeezing through. To analyze the overall balance of mass, the transported volume through the inflow- and outflow-boundary is given in Figure 6.16 (right). The difference between the transported volume of outflow and inflow results from the compression or expansion of the solid domains. As no systematical increase of this difference in time can be recognized, no relevant loss in mass occurs. This behavior is expected as discussed in the first presented numerical example in Section 6.4.1.

6.4.4 3D Analysis of a Double-Leafed Valve

As a last numerical example for FSCI, the analysis of a double-leafed valve is presented to demonstrate the applicability to more general 3D configurations. In a first phase, an increased fluid traction on the outflow boundary is prescribed to analyze the valve closing behavior including contact. The application of an increased fluid traction on the inflow boundary in the subsequent phase allows investigating the processes of valve opening.

Problem Description The geometric setup and the basic boundary condition are shown in Figure 6.17. The solid domain $\Omega^{\mathrm{S}} = \Omega^1 \cup \Omega^2$ consists of an elastic cylindrical tube Ω^1 and two

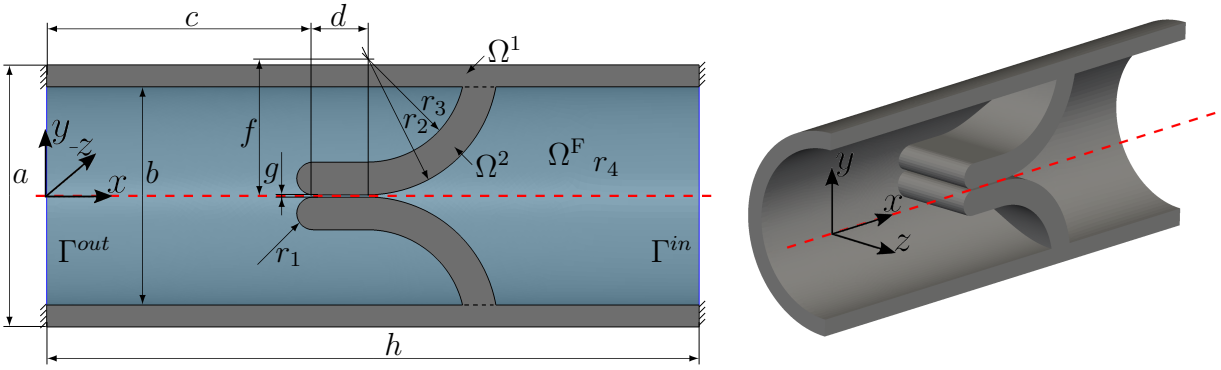

$\underline{\boldsymbol{u}}^{\mathrm{S}} = \hat{\underline{\boldsymbol{u}}}^{\mathrm{S}}$, $a = 0.12$, $b = 0.1$, $c = 0.1225$, $d = 0.025$, $f = 0.0605$,
$g = 0.001$, $h = 0.3$, $r_1 = 0.0075$, $r_2 = 0.06$, $r_3 = 0.045$

Figure 6.17: Geometry and basic boundary conditions for the double-leafed valve.

valve leaflets Ω^2. This solid tube is filled with fluid, which specifies the fluid domain Ω^{F}. On the cylindrical outer boundary of the solid tube Ω^1, a zero-traction condition is prescribed. To investigate the effect of external disturbances on the functionality of the valve, a rotational motion around the x-axis with an angle $\alpha = \pm\pi/12$ ('+' sign at $x = 0$, '-' sign at $x = h$) is prescribed on the solid Dirichlet boundaries. The prescribed displacement at the reference position $\underline{\boldsymbol{X}}^{\mathrm{S}} = [X, Y, Z]^{\mathsf{T}}$ is $\hat{\underline{\boldsymbol{u}}}^{\mathrm{S}} = [0, Y\cos(\alpha g(t)) + Z\sin(\alpha g(t)) - Y, -Y\sin(\alpha g(t)) + Z\cos(\alpha g(t)) - Z]^{\mathsf{T}}$, with the time-dependent function $g(t) = 0.004t$ for $t \in [0, 0.004]$ and $g(t) = 1$ for $t > 0.004$. This prescribes a rotational motion in the initial phase of the considered time interval that is kept constant for the remaining time. For comparison, also the symmetric configuration with fixed solid Dirichlet boundaries $\hat{\underline{\boldsymbol{u}}}^{\mathrm{S}} = \underline{\mathbf{0}}$ ($\alpha = 0$) is computed. The fluid flow is driven by a Neumann boundary condition with the time-dependent function $f(t) = 15[1 - \cos(50t\pi)]$:

$$\hat{\underline{\boldsymbol{h}}}^{\mathrm{F,N}} = \begin{cases} [f(t), 0, 0]^{\mathsf{T}}, & t \in [0, 0.04] \\ \underline{\mathbf{0}}, & t \in [0.04, 0.08] \end{cases} \text{ on } \Gamma^{out}, \quad \hat{\underline{\boldsymbol{h}}}^{\mathrm{F,N}} = \begin{cases} \underline{\mathbf{0}}, & t \in [0, 0.04] \\ [-f(t), 0, 0]^{\mathsf{T}}, & t \in [0.04, 0.08] \end{cases} \text{ on } \Gamma^{in}.$$

As a consequence, the valve is closed in the phase $t \in [0, 0.04]$ and opened for $t \in [0.04, 0.08]$. On both boundaries Γ^{out} and Γ^{in}, a zero-tangential velocity is prescribed.

The fluid is specified by a density of $\rho^{\mathrm{F}} = 10^{-3}$ and a dynamic viscosity of $\mu^{\mathrm{F}} = 10^{-4}$. The initial solid density is equal to the fluid density $\rho_0^{\mathrm{S}} = \rho^{\mathrm{F}} = 10^{-3}$ and a Neo-Hookean material model with strain-energy density function (2.17) including the Young's modulus $E = 2000$ and the Poisson ration $\nu = 0.3$ is used for the entire solid domain Ω^{S}. The solid domain is discretized with 191624 hexahedral tri-linear elements, which are fitted to the boundaries of the solid domain. A structured computational mesh with $90 \times 64 \times 30 = 172800$ hexahedral tri-linear elements in the domain $[0, 0.3] \times [-0.07, 0.07] \times [-0.06, 0.06]$ is utilized for the discretization of the fluid domain. The contact stress is weighted harmonically and the reference slip length is set to $\kappa_0 = 0.1$. The constants for the Nitsche penalty parameters are $\gamma_0^{\mathrm{S},c} = 1$ and $\gamma_0^{\mathrm{FSI}} = \gamma_{t,0}^{\mathrm{FSI}} = 35$. A time step length in the range $\Delta t = [2.5 \cdot 10^{-5}, 2 \cdot 10^{-4}]$ is utilized for the temporal discretization with the backward Euler scheme ($\theta = 1$).

Numerical Results and Discussion In Figure 6.18 and Figure 6.19, a visualization of the computed solution for the double-leafed valve at six points in time is given.

In the initial phase $t \in [0, 0.02]$, the fluid pressure in the left valve chamber increases, which leads to an extension of the circular tube. As a result, fluid mass enters the chamber through the boundary Γ^{out}. Due to the prevalent fluid pressure difference on both sides of the valve, contact between the lower an upper leaflet is established. Since the computed results in the following relaxation phase $t \in [0.02, 0.04]$ in principle show the same process in revers order, this is not visualized here. The process in the following phase $t \in [0.04, 0.06]$ is powered by an increasing fluid pressure on the boundary Γ^{in}. Besides the expansion of the right valve chamber, the present fluid pressure difference lifts both leaflets and, thus, contact is released. In the following, a fluid flow from the boundary Γ^{in} to Γ^{out} establishes.

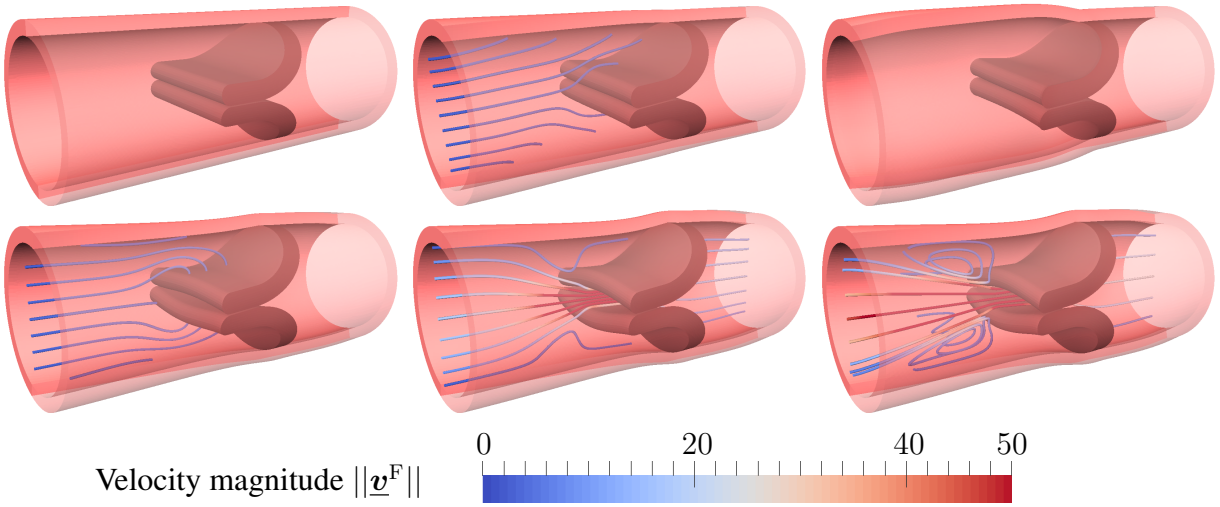

Figure 6.18: Visualization of the computed fluid velocity and deformation solution for the configuration with $\alpha = \pm\pi/12$ at six instances in time, from top-left to bottom-right: $t = 0.0, t = 0.005, t = 0.02, t = 0.05, t = 0.055$, and $t = 0.06$. The streamlines visualize the fluid velocity magnitude for $||\underline{\boldsymbol{v}}^{\mathrm{F}}|| \geq 0.8$.

In Figure 6.20 the computed flow rates at the inflow boundary Γ^{in} and the outflow boundary Γ^{out} are shown. For validation both variant with $\alpha = 0$ and $\alpha = \pm\pi/12$ are depicted therein. For $t \in [0, 0.04]$ a significant fluid flow occurs only through the boundary Γ^{out} due to the expansion of the cylindrical tube Ω^1. As a consequence of the deformation of the valve leaflets in positive x-direction, a relatively small fluid flow through the boundary Γ^{in} can be observed. Due to the opening of the valve and the associated reduction of the effective flow resistance in the time interval $t \in [0.04, 0.08]$, a significantly larger flow rate through both boundaries arises. Initiated by relaxation of the right valve chamber of Ω^1 for $t \gtrsim 0.07$, a fluid flow in positive x-direction occurs. A comparison of the symmetric $(\alpha = 0)$ and the rotated $(\alpha = \pm\pi/12)$ configuration reveals, that the disturbance by the rotation does not essentially deteriorate the process of the valve. The only significant difference can be observed in the initial phase ($t \in [0, 0.004]$), which is due to the prescribed rotational motion on Γ^{in} and Γ^{out}.

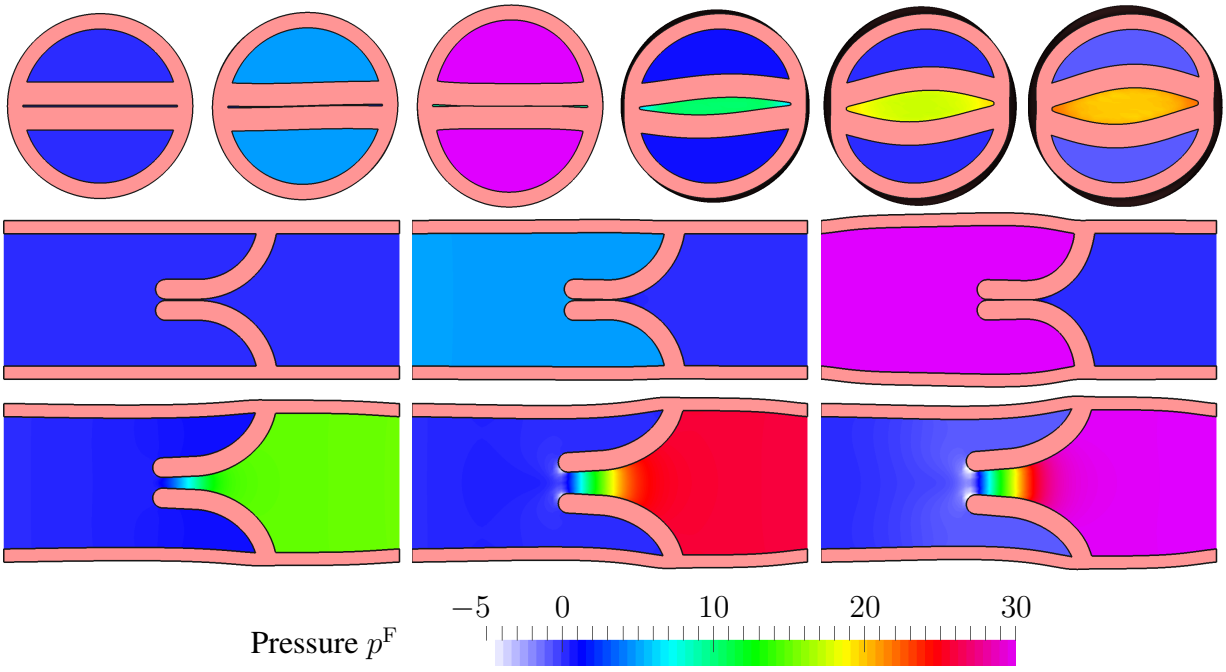

Figure 6.19: Computed fluid pressure and deformation solution for the configuration with $\alpha = \pm\pi/12$ at six instances in time from (top-)left to (bottom-)right: $t = 0.0, t = 0.005, t = 0.02, t = 0.05, t = 0.055$, and $t = 0.06$. Cross-sectional view at $x = 0.15$ in the first row. Cross-sectional view at $z = 0$ in row two and three.

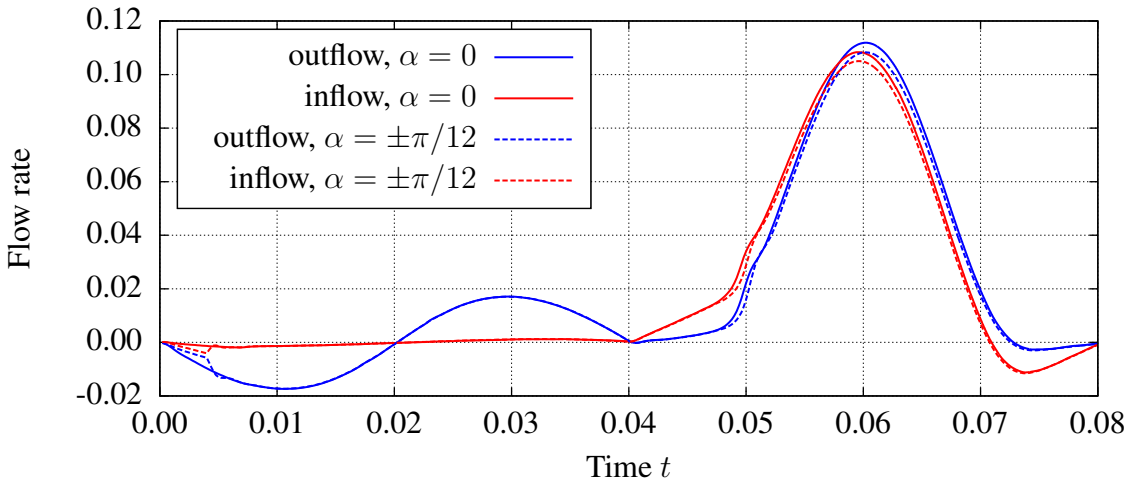

Figure 6.20: Computed flow rates at the inflow boundary Γ^{in} and the outflow boundary Γ^{out}. The normal vector is oriented in negative x-direction.

7 A Consistent Computational Approach for General Fluid-Poroelasticity-Structure-Contact Interaction Problems[1]

The focus of this chapter is the numerical treatment of interface-coupled problems concerned with the interaction of impermeable or permeable elastic bodies[2] and the surrounding fluid including the contact interaction of deformable bodies. The presented formulation is based on the approach for FSCI in Chapter 6, and consistently takes into account poroelastic bodies including the conditions of solid-poroelastic contact, poroelastic-poroelastic contact, and viscous flow poroelasticity interaction. Up to the author's best knowledge, this is the first formulation capable of solving the general FPSCI problem numerically.

The interface conditions in normal and tangential orientation to formulate this type of coupled problem based on the fundamental balances of mass and linear momentum, the no-slip condition, the Beavers Joseph condition, and the conditions for frictionless contact on the respective interfaces are discussed. A continuous transition of the different types of tangential conditions is enabled by application of the general Navier condition with varying slip length. All interface conditions are reformulated into one set of conditions in normal and tangential orientation which already include the continuous transition between the different types of interfaces. The fluid stress in the zone of closed contact, which is essential for the lift-off behavior of contacting bodies, is obtained by an extension approach augmented by the porous fluid state to ensure continuity and physical accuracy. To account for topological changes of the fluid domain, the numerical approach utilizes non-interface-fitted computational meshes for the fluid domain enabled by the CutFEM. All interface conditions are incorporated in a weak sense by Nitsche-based approaches.

All capabilities of the approach for FSCIwhich is presented in Chapter 6 are kept and united with the new developments into one single framework. Thus, the following presentation includes also all formulations depicted already in Chapter 6 to demonstrate the integration into the new framework. Besides the application of this computational approach to physical configurations which include poroelastic bodies such as biological soft tissue, it is also capable of solving the rough surface FSCI model presented in Chapter 5, which is based on a homogenized poroelastic layer.

Different numerical examples analyze the proper contacting and lift-off behavior for contact between the different pairs of impermeable and permeable bodies and demonstrate the robustness

[1] This chapter is adapted from the author's publication [4].

[2] Permeable elastic bodies in the surrounding of fluid are modeled by a fluid-saturated poroelastic medium.

for more challenging configurations, which include topological changes of the fluid domain, large contacting areas, and 3D configurations.

This chapter is organized as follows. In Section 7.1, the FPSCI problem formulation is presented. This includes mainly the specification of the set of interface conditions in normal direction and tangential direction. The discrete formulation is presented in Section 7.2. Besides a short depiction of the weak forms in the domains, special focus is put on the incorporation of all interface conditions by Nitsche-based methods. The coupled discrete FPSCI system is presented in Section 7.3. Finally, different numerical examples, which are presented in Section 7.4, analyze the introduced formulation and demonstrate its capabilities.

7.1 FPSCI Problem Formulation

In Figure 7.1, an exemplary configuration of the examined FPSCI problem is presented. The

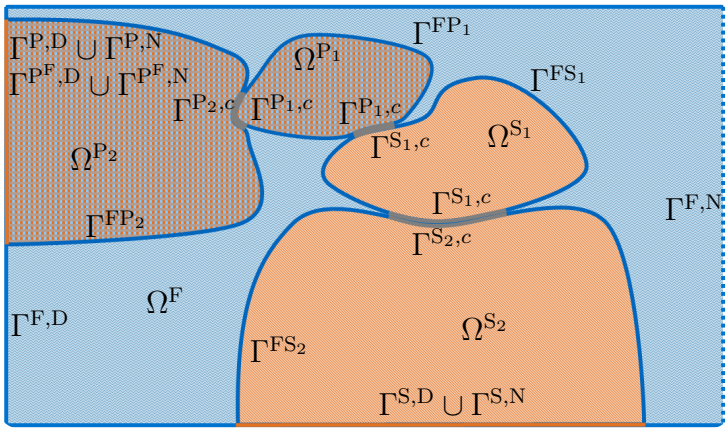

Figure 7.1: Fluid-poroelasticity-structure-contact interaction (FPSCI) problem setup in the domain Ω including two structural $\Omega^{\mathrm{S}_1}, \Omega^{\mathrm{S}_2}$ and two poroelastic $\Omega^{\mathrm{P}_1}, \Omega^{\mathrm{P}_2}$ contacting bodies. This configuration is composed of the fluid domain Ω^{F}, the solid domain $\Omega^{\mathrm{S}} = \Omega^{\mathrm{S}_1} \cup \Omega^{\mathrm{S}_2}$, the poroelastic domain $\Omega^{\mathrm{P}} = \Omega^{\mathrm{P}_1} \cup \Omega^{\mathrm{P}_2}$, the fluid-structure interface $\Gamma^{\mathrm{FS}} = \Gamma^{\mathrm{FS}_1} \cup \Gamma^{\mathrm{FS}_2}$, the fluid-poroelastic interface $\Gamma^{\mathrm{FP}} = \Gamma^{\mathrm{FP}_1} \cup \Gamma^{\mathrm{FP}_2}$, the active (closed) solid contact interface $\Gamma^{\mathrm{S},c} = \Gamma^{\mathrm{S}_1,c} \cup \Gamma^{\mathrm{S}_2,c}$, the active (closed) poroelastic contact interface $\Gamma^{\mathrm{P},c} = \Gamma^{\mathrm{P}_1,c} \cup \Gamma^{\mathrm{P}_2,c}$, and the outer boundaries $\Gamma^{\mathrm{F,D}}, \Gamma^{\mathrm{F,N}}, \Gamma^{\mathrm{S,D}}, \Gamma^{\mathrm{S,N}}, \Gamma^{\mathrm{P,D}}, \Gamma^{\mathrm{P,N}}, \Gamma^{\mathrm{P^F,D}}, \Gamma^{\mathrm{P^F,N}}$.

domain of interest $\Omega = \Omega^{\mathrm{F}} \cup \Omega^{\mathrm{S}} \cup \Omega^{\mathrm{P}}$ includes the fluid domain Ω^{F}, the solid domain Ω^{S}, and the poroelastic domain Ω^{P} which are potentially split into non overlapping subdomains. The boundaries of the respective domains are denoted as $\partial\Omega, \partial\Omega^{\mathrm{F}}, \partial\Omega^{\mathrm{S}}$, and $\partial\Omega^{\mathrm{P}}$. The overall coupling interface $\Gamma = \Gamma^{\mathrm{S,I}} \cup \Gamma^{\mathrm{P,I}}$ is specified by the solid interface $\Gamma^{\mathrm{S,I}} = \partial\Omega^{\mathrm{S}} \setminus \partial\Omega$ and the poroelastic interface $\Gamma^{\mathrm{P,I}} = \partial\Omega^{\mathrm{P}} \setminus \partial\Omega$. While the interface $\Gamma^{\mathrm{S,I}} = \Gamma^{\mathrm{FS}} \cup \Gamma^{\mathrm{S},c}$ consists of the fluid-structure interface Γ^{FS} and the active solid contact interface $\Gamma^{\mathrm{S},c}$, the interface $\Gamma^{\mathrm{P,I}} = \Gamma^{\mathrm{FP}} \cup \Gamma^{\mathrm{P},c}$ is composed of the fluid-poroelastic interface Γ^{FP} and the active poroelastic contact interface $\Gamma^{\mathrm{P},c}$. The potentially contacting part of the respective interfaces are denoted by $\breve{\Gamma}^{\mathrm{S},c}$ with $\Gamma^{\mathrm{S},c} \subseteq \breve{\Gamma}^{\mathrm{S},c} \subseteq \Gamma^{\mathrm{S,I}}$ and $\breve{\Gamma}^{\mathrm{P},c}$ with $\Gamma^{\mathrm{P},c} \subseteq \breve{\Gamma}^{\mathrm{P},c} \subseteq \Gamma^{\mathrm{P,I}}$. The parts on the outer boundary $\partial\Omega$ are denoted by $\Gamma^{\mathrm{F,D}}, \Gamma^{\mathrm{S,D}}, \Gamma^{\mathrm{P,D}}, \Gamma^{\mathrm{P^F,D}}$ for the Dirichlet-type boundaries and $\Gamma^{\mathrm{F,N}}, \Gamma^{\mathrm{S,N}}, \Gamma^{\mathrm{P,N}}, \Gamma^{\mathrm{P^F,N}}$ for the Neumann-type boundaries.

The governing equations and conditions in the respective domain including the definition of all quantities are discussed in Chapter 2. The IBVP to describe the transient behavior of elastic

structures in the domain Ω^{S} is depicted in Section 2.1.4, the problem formulation for transient, incompressible, viscous flow in the domain Ω^{F} is presented in Section 2.1.5, and the formulation applied for the poroelastic medium consisting of a homogenized impermeable structural phase and a fluid phase in domain Ω^{P} is discussed in Section 2.1.6.

7.1.1 Preliminaries for the Formulation of the Interface Conditions

In order to enable a more detailed subdivision of the contact interfaces $\Gamma^{\mathrm{S},c}$ and $\Gamma^{\mathrm{P},c}$, the normal projection is introduced. Hereby, a point with coordinate $\underline{\boldsymbol{x}}$ on an interface is projected in interface normal direction onto the opposite surface to coordinate $\check{\underline{\boldsymbol{x}}}(\underline{\boldsymbol{x}})$. All quantifies $*$ which are evaluated at this projection point will be denoted by a check $\check{*} = *(\check{\underline{\boldsymbol{x}}}) = *(\check{\underline{\boldsymbol{x}}}(\underline{\boldsymbol{x}}))$.

Depending on the physical type of the second contact interface, the solid contact interface $\Gamma^{\mathrm{S},c}$ can be subdivided into the solid-solid contact interface $\Gamma^{\mathrm{SS},c}$ and the solid-poroelastic contact interface $\Gamma^{\mathrm{SP},c}$ and the poroelastic contact interface $\Gamma^{\mathrm{P},c}$ can be subdivided into the poroelastic-poroelastic contact interface $\Gamma^{\mathrm{PP},c}$ and the poroelastic-solid contact interface $\Gamma^{\mathrm{PS},c}$

$$\Gamma^{\mathrm{AB},c} := \Gamma^{\mathrm{A},c}\big|_{\check{\underline{\boldsymbol{x}}}(\underline{\boldsymbol{x}}) \text{ on } \Gamma^{\mathrm{B,I}}}, \quad \text{with } \underline{\boldsymbol{x}} \text{ on } \Gamma^{\mathrm{A},c}, \quad \text{and } \mathrm{A},\mathrm{B} \in \{\mathrm{S},\mathrm{P}\}. \tag{7.1}$$

This partitioning is also applied to split the potentially contacting poroelastic interface $\breve{\Gamma}^{\mathrm{P},c}$ into $\breve{\Gamma}^{\mathrm{PP},c}$ and $\breve{\Gamma}^{\mathrm{PS},c}$. Combining the solid and the poroelastic interface traction allows specifying an interface traction defined on the entire interface

$$\underline{\boldsymbol{\sigma}}^{\mathrm{S/P}} := \begin{cases} \underline{\boldsymbol{\sigma}}^{\mathrm{S}} & \text{on} \quad \Gamma^{\mathrm{S,I}} \\ \underline{\boldsymbol{\sigma}}^{\mathrm{P}} & \text{on} \quad \Gamma^{\mathrm{P,I}} \end{cases}. \tag{7.2}$$

In the following the relative velocity in the porous medium, the seepage velocity is denoted as

$$\underline{\boldsymbol{v}}^{\mathrm{P},seepage} := \phi \left(\underline{\boldsymbol{v}}^{\mathrm{P}} - \frac{\partial \underline{\boldsymbol{u}}^{\mathrm{P}}}{\partial t} \right) \quad \text{on} \quad \Gamma^{\mathrm{P,I}}. \tag{7.3}$$

The effective interface fluid velocity $\underline{\boldsymbol{v}}^{\mathrm{S/P},\Gamma}$ allows formulating the kinematic constraints in a compact notation.

$$\underline{\boldsymbol{v}}^{\mathrm{S/P},\Gamma} := \begin{cases} \dfrac{\partial \underline{\boldsymbol{u}}^{\mathrm{S}}}{\partial t} & \text{on} \quad \Gamma^{\mathrm{S,I}} \\ \dfrac{\partial \underline{\boldsymbol{u}}^{\mathrm{P}}}{\partial t} + \underline{\boldsymbol{v}}^{\mathrm{P},seepage} & \text{on} \quad \Gamma^{\mathrm{P,I}} \end{cases} \tag{7.4}$$

To ease the formulation of the interface fluid mass balance, a relative interface velocity is defined as

$$\underline{\boldsymbol{v}}^{\mathrm{S/P},rel} := \underline{\boldsymbol{v}}^{\mathrm{F}} - \underline{\boldsymbol{v}}^{\mathrm{S/P},\Gamma} \quad \text{on} \quad \Gamma^{\mathrm{F,I}}. \tag{7.5}$$

The Fluid Extension Operator As it can be seen for the exemplary configuration in Figure 7.1, the interface Γ is not adjacent to the fluid domain in the contacting parts $\Gamma^{\mathrm{S},c}$ and $\Gamma^{\mathrm{P},c}$. Since fluid quantifies are required to formulate the interface conditions at any point in space $\underline{\boldsymbol{x}}$ on the overall coupling interface Γ, an extension operator $\mathcal{E}_{\underline{\boldsymbol{x}}} : \Gamma^{\mathrm{FS}} \cup \Gamma^{\mathrm{FP}} \longrightarrow \Gamma$ from the

fluid-structure interface Γ^{FS} and fluid-poroelastic interface Γ^{FP} to the overall interface Γ is required. This extension is applied for all quantities defined in the fluid domain Ω^{F} and, thus, for all quantities on the fluid-structure interface Γ^{FS} and the fluid-poroelastic interface Γ^{FP} which are required for the formulation of the interface constraints on Γ. In the following, the extension of any quantity $*$ is denoted by an additional index $*_{\mathcal{E}}$. Exemplary, the extension of the normal interface fluid velocity $v^{\mathrm{F},n} = \underline{\boldsymbol{v}}^{\mathrm{F}} \cdot \underline{\boldsymbol{n}}$ to a position $\underline{\boldsymbol{x}}$ on Γ is defined as follows

$$v_{\mathcal{E}}^{\mathrm{F},n}\left(\underline{\boldsymbol{x}}\right) = \begin{cases} v^{\mathrm{F},n}\left(\underline{\boldsymbol{v}}^{\mathrm{F}}\left(\underline{\boldsymbol{x}}\right)\right) & \text{on} \quad \Gamma^{\mathrm{FS}} \cup \Gamma^{\mathrm{FP}} \\ \mathcal{E}_{\underline{\boldsymbol{x}}}\left[v^{\mathrm{F},n}\left(\underline{\boldsymbol{v}}^{\mathrm{F}}\left(\underline{\boldsymbol{x}}_{\mathcal{E}}\right)\right)\right] & \text{on} \quad \Gamma^{\mathrm{S},c} \cup \Gamma^{\mathrm{P},c}, \end{cases}$$

$$\text{with} \quad \mathcal{E}_{\underline{\boldsymbol{x}}}\left[v^{\mathrm{F},n}\left(\underline{\boldsymbol{v}}^{\mathrm{F}}\left(\underline{\boldsymbol{x}}_{\mathcal{E}}\right)\right)\right] = v^{\mathrm{F},n}\left(\underline{\boldsymbol{v}}^{\mathrm{F}}\left(\underline{\boldsymbol{x}}\right)\right) \quad \text{on} \quad \left(\Gamma^{\mathrm{FS}} \cap \Gamma^{\mathrm{S},c}\right) \cup \left(\Gamma^{\mathrm{FP}} \cap \Gamma^{\mathrm{P},c}\right), \tag{7.6}$$

where the extension origin position $\underline{\boldsymbol{x}}_{\mathcal{E}}$ is properly chosen on $\Gamma^{\mathrm{FS}} \cup \Gamma^{\mathrm{FP}}$. The last lines in (7.6) represents the continuity of the extension operator. The applied extension operator for the presented numerical examples is discussed in Section 7.2.2.3.

7.1.2 Conditions on the Overall Coupling Interface Γ in Normal Direction

In this section, a set of interface conditions is formulated for the overall coupling interface Γ which connects the adjacent structural domain, poroelastic domain, or fluid domain. This set of conditions corresponds to the classical conditions for simplified configurations such as e.g. FSI, FPI, or contact discussed in Section 2.1.7, Section 2.1.8, and Section 2.1.10, but allows formulating the general problem of FPSCI.

The normal direction on the interface Γ is specified by the solid or poroelastic outward unit normal: $\underline{\boldsymbol{n}} = \underline{\boldsymbol{n}}^{\mathrm{S}}$ on $\Gamma^{\mathrm{S,I}}$ or $\underline{\boldsymbol{n}} = \underline{\boldsymbol{n}}^{\mathrm{P}}$ on $\Gamma^{\mathrm{P,I}}$. The normal component of the respective Cauchy stress is denoted as: $\sigma^{\mathrm{S},nn} = \underline{\boldsymbol{\sigma}}^{\mathrm{S}} : \underline{\boldsymbol{P}}^{n}$, $\sigma^{\mathrm{P},nn} = \underline{\boldsymbol{\sigma}}^{\mathrm{P}} : \underline{\boldsymbol{P}}^{n}$, $\sigma^{\mathrm{S/P},nn} = \underline{\boldsymbol{\sigma}}^{\mathrm{S/P}} : \underline{\boldsymbol{P}}^{n}$, and $\sigma^{\mathrm{F},nn} = \underline{\boldsymbol{\sigma}}^{\mathrm{F}} : \underline{\boldsymbol{P}}^{n}$, with the normal projection operator being specified as $\underline{\boldsymbol{P}}^{n} = \underline{\boldsymbol{n}} \otimes \underline{\boldsymbol{n}}$. The normal components of essential interface velocities are denoted by: $v^{\mathrm{P},seepage,n} = \underline{\boldsymbol{v}}^{\mathrm{P},seepage} \cdot \underline{\boldsymbol{n}}$, $v^{\mathrm{S/P},\Gamma,n} = \underline{\boldsymbol{v}}^{\mathrm{S/P},\Gamma} \cdot \underline{\boldsymbol{n}}$, and $v^{\mathrm{S/P},rel,n} = \underline{\boldsymbol{v}}^{\mathrm{S/P},rel} \cdot \underline{\boldsymbol{n}}$.

Balance of Linear Momentum and Kinematic Contact Condition At first, the following set of conditions, which is based on the classical Hertz–Signiorini–Moreau (HSM) conditions for contact, has to be fulfilled on the overall interface

$$g^{n}(\underline{\boldsymbol{x}}) := (\underline{\check{\boldsymbol{x}}}(\underline{\boldsymbol{x}}) - \underline{\boldsymbol{x}}) \cdot \underline{\boldsymbol{n}} \geq 0 \quad \text{on} \quad \Gamma, \tag{7.7}$$

$$\sigma^{\mathrm{S/P},nn}(\underline{\boldsymbol{x}}) - \sigma_{\mathcal{E}}^{\mathrm{F},nn}\left(\underline{\boldsymbol{x}}\right) \leq 0 \quad \text{on} \quad \Gamma, \tag{7.8}$$

$$g^{n}(\underline{\boldsymbol{x}}) \left[\sigma^{\mathrm{S/P},nn}(\underline{\boldsymbol{x}}) - \sigma_{\mathcal{E}}^{\mathrm{F},nn}\left(\underline{\boldsymbol{x}}\right)\right] = 0 \quad \text{on} \quad \Gamma. \tag{7.9}$$

Condition (7.7) ensures that no penetration of bodies occurs. With the second condition (7.8), a negative or vanishing relative traction of the contact stress and potential fluid traction is enforced. With this condition, it is ensured that contacting bodies lift-off e.g. in the case the fluid pressure raises in the contact zone even for a constant contact traction. A more detailed discussion concerning this condition can be found in Chapter 6 and in Section 2.1.10.2. Finally, in equation

(7.9), exclusively a vanishing gap or a vanishing relative traction is guaranteed. Whereas the first case can be identified as the kinematic condition for contact, the second case corresponds to the dynamic equilibrium on a fluid-structure or fluid-poroelastic interface.

Additionally, the dynamic equilibrium on the interface has to be fulfilled

$$\sigma^{\mathrm{S/P},nn} - \sigma_{\mathcal{E}}^{\mathrm{F},nn} = \sigma^{\mathrm{S/\check{P}},nn} - \sigma_{\mathcal{E}}^{\check{\mathrm{F}},nn} \quad \text{on } \Gamma. \tag{7.10}$$

In the case two bodies are in contact, the condition recovers the dynamic equilibrium between the contacting bodies since the fluid stress vanishes from the balance ($\sigma_{\mathcal{E}}^{\mathrm{F},nn} = \sigma_{\mathcal{E}}^{\check{\mathrm{F}},nn}$). For a fluid-structure or fluid-poroelastic interface both sides of the interface vanish separately due the fulfilled dynamic equilibrium by condition (7.9).

Balance of Mass Still missing are conditions to enforce the balance of mass on the interface. In contrast to the previous conditions, to improve comprehensibility, conditions for the contact interface $\Gamma^{\mathrm{P},c} \cup \Gamma^{\mathrm{S},c}$ and the interface connected to the fluid domain $\Gamma^{\mathrm{FS}} \cup \Gamma^{\mathrm{FP}}$ are presented separately. For all parts of the interface which are adjacent to the fluid domain, the normal fluid velocity is required to be equal to the effective normal interface velocity

$$v^{\mathrm{S/P},rel,n} = 0 \quad \text{on} \quad \Gamma^{\mathrm{FS}} \cup \Gamma^{\mathrm{FP}}. \tag{7.11}$$

This condition is equivalent to the interface normal part of the classical no-slip condition (2.60) on a fluid-structure interface and the mass balance on a fluid-poroelastic interface (2.63).

On the remaining part of the interface, i.e. the contact interface, the effective normal interface velocity has to be equal on both contact interfaces

$$v^{\mathrm{S/P},\Gamma,n} + v^{\mathrm{S/\check{P}},\Gamma,n} = 0 \quad \text{on} \quad \Gamma^{\mathrm{P},c} \cup \Gamma^{\mathrm{S},c}. \tag{7.12}$$

Depending on the physical types of contacting bodies, different versions of this condition can be formulated. Due to condition (7.9) in the contact case ($g^n = 0$), the normal velocity of the solid or the poroelastic matrix is equal on both contacting interfaces

$$\frac{\partial \underline{\boldsymbol{u}}^{\mathrm{A}}}{\partial t} \cdot \underline{\boldsymbol{n}} + \left(\frac{\partial \underline{\boldsymbol{u}}^{\check{\mathrm{B}}}}{\partial t} \cdot \underline{\boldsymbol{n}} \right) = 0 \quad \text{on} \quad \Gamma^{\mathrm{AB},c}, \quad \text{with } \mathrm{A}, \mathrm{B} \in \{\mathrm{S}, \mathrm{P}\}. \tag{7.13}$$

As a result, the normal velocity of the solid or poroelastic matrix cancels out from condition (7.12). Thus, condition (7.12) is automatically fulfilled on the solid-solid contact interface $\Gamma^{\mathrm{SS},c}$ by condition (7.9). On the solid-poroelastic contact interfaces $\Gamma^{\mathrm{SP},c}$ and $\Gamma^{\mathrm{PS},c}$ condition (7.12) is then equivalent to

$$v^{\mathrm{P},\check{seepage},n} = 0 \quad \text{on} \quad \Gamma^{\mathrm{SP},c}, \quad v^{\mathrm{P},seepage,n} = 0 \quad \text{on} \quad \Gamma^{\mathrm{PS},c}. \tag{7.14}$$

This condition is a no-outflow condition on the contact part of the poroelastic interface. Finally, on the contact interface of two poroelastic bodies, the fluid mass balance can be expressed as

$$v^{\mathrm{P},seepage,n} + v^{\mathrm{P},\check{seepage},n} = 0 \quad \text{on} \quad \Gamma^{\mathrm{PP},c}. \tag{7.15}$$

In principle, an equivalent, but not so obvious, single formulation of the conditions (7.11) and (7.12) on the overall interface Γ instead splitting into different interface types could be formulated as well.

Balance of Linear Momentum between Fluids As a last set of conditions in interface normal direction, the balance of linear momentum between the fluids has to be formulated. This is only relevant on the poroelastic interface $\Gamma^{\mathrm{P,I}}$ as this includes the traction arising from poroelastic fluid. On an interface between viscous flow and porous flow, the normal fluid stress is in balance with the porous fluid pressure

$$p^{\mathrm{P}} + \sigma^{\mathrm{F},nn} = 0 \quad \text{on } \Gamma^{\mathrm{FP}}. \tag{7.16}$$

This condition is already introduced in (2.62). The porous fluid pressure does not need to be specified for contact interfaces between an impermeable solid and a poroelastic body as it is implicitly specified by the no-outflow condition (7.14). In contrast to that, for two contacting poroelastic bodies a continuous poroelastic fluid pressure through the interface is enforced

$$p^{\mathrm{P}} = \check{p}^{\mathrm{P}} \quad \text{on } \Gamma^{\mathrm{PP},c}. \tag{7.17}$$

7.1.3 Conditions on the Overall Coupling Interface Γ in Tangential Direction

In tangential interface orientation, frictionless contact and the general Navier interface condition between the viscous fluid and the structural or poroelastic domain are applied. Frictionless contact is considered due to its simplicity for the presentation while still being a valid model for a large number of problem configurations. The general Navier condition allows capturing the classical condition of "no-slip" on the interface of impermeable structures and viscous fluids, a "slip" interface condition on the interface of poroelastic medium and viscous fluid, as well as the possibility to formulate a continuous problem even for the transition to contact. Then, the set of conditions to be fulfilled on the interface Γ is

$$\underline{\boldsymbol{\sigma}}^{\mathrm{S/P}} \cdot \underline{\boldsymbol{n}} \cdot \underline{\boldsymbol{P}}^{t} = \underline{\mathbf{0}} \qquad \text{on } \Gamma^{\mathrm{S},c} \cup \Gamma^{\mathrm{P},c}, \tag{7.18}$$

$$\left(\underline{\boldsymbol{\sigma}}^{\mathrm{F}} \cdot \underline{\boldsymbol{n}} - \underline{\boldsymbol{\sigma}}^{\mathrm{S/P}} \cdot \underline{\boldsymbol{n}}\right) \cdot \underline{\boldsymbol{P}}^{t} = \underline{\mathbf{0}} \qquad \text{on } \Gamma^{\mathrm{FS}} \cup \Gamma^{\mathrm{FP}}, \tag{7.19}$$

$$\left(\underline{\boldsymbol{v}}^{\mathrm{S/P},rel} + \kappa \underline{\boldsymbol{\sigma}}^{\mathrm{F}} \cdot \underline{\boldsymbol{n}}^{\mathrm{F}}\right) \cdot \underline{\boldsymbol{P}}^{t} = \underline{\mathbf{0}} \qquad \text{on } \Gamma^{\mathrm{FS}} \cup \Gamma^{\mathrm{FP}}. \tag{7.20}$$

Herein, the tangential projection operator is specified by $\underline{\boldsymbol{P}}^{t} := \underline{\boldsymbol{I}} - \underline{\boldsymbol{n}} \otimes \underline{\boldsymbol{n}}$. Condition (7.18) states the vanishing tangential traction component due to frictionless contact on the interfaces $\Gamma^{\mathrm{S},c}$ and $\Gamma^{\mathrm{P},c}$. The dynamic equilibrium in tangential direction on the interface between viscous fluid and the particular adjacent domain is represented by condition (7.19). As both of the first conditions are valid on the boundary line/point of contact $\Gamma^{\mathrm{S},c} \cap \Gamma^{\mathrm{FS}}$ and $\Gamma^{\mathrm{P},c} \cap \Gamma^{\mathrm{FP}}$, the tangential fluid traction has to vanish on this line ($\underline{\boldsymbol{\sigma}}^{\mathrm{F}} \cdot \underline{\boldsymbol{n}} \cdot \underline{\boldsymbol{P}}^{t} = 0$) to ensure continuity of the formulation. This aspect can be considered by the general Navier interface condition (7.20), when specifying the slip length close to this line to infinity $\kappa = \infty$. Starting at a particular distance to contact, the classic conditions on the interfaces Γ^{FS} and Γ^{FP} can be recovered by this condition. This is the "no-slip" condition with $\kappa = 0$ on Γ^{FS} and the Beavers-Joseph condition (see work of Beavers and Joseph [20]) with a specific slip length $\kappa = \kappa_{\mathrm{BJ}} = \left(\alpha_{\mathrm{BJ}} \mu^{\mathrm{F}} \sqrt{3}\right)^{-1} \sqrt{\mathrm{tr}(\underline{\boldsymbol{k}})}$, including the positive model parameter α_{BJ}, on Γ^{FP}. The specification of the slip length κ to account for these limiting cases, which is applied for all computed numerical examples, is given in Section 7.2.3.

7.2 Discrete Formulation

In this section, the discrete formulation which enables the numerical solution of the FPSCI problem is presented. The temporal discretization is performed by the One-Step-θ scheme as introduced in Section 2.2.1 and the spatial discretization by the FEM as introduced in Section 2.2.2. As utilized for all other formulations within this thesis, the fluid domain is discretized by a fixed computational mesh which is unfitted to the discrete overall interface Γ_h enabled by the CutFEM. Since no relevant difference in the application of CutFEM for the FPSCI problem as compared to the FSCI formulation presented in Chapter 6 occurs, no discussion concerning CutFEM is added in the following. The focus of this section is on the discrete formulation to incorporate all interface conditions in a weak sense by a consistent Nitsche-based approach. The approaches in normal and tangential interface orientation are presented separately to account for the different types of interface conditions as discussed in Section 7.1.2 and Section 7.1.3. In normal direction, the Nitsche-based method is introduced by one traction to represent the overall interface traction and one traction to represent the traction acting on the porous flow. Both tractions are formulated in a way to take into account all interface conditions directly while being continuous for any change of the system state. In tangential interface orientation, the Nitsche-based formulation allows incorporating a certain amount of fluid velocity slip. This is essential to ensure a continuous transition from the FSI and FPI coupling to frictionless contact and to formulate the BJ condition on the interface $\Gamma_\mathrm{h}^\mathrm{FP}$. Finally, all contributions are combined and treated in a single system of equations and solved by a monolithic procedure.

7.2.1 The Discrete Weak Form of the Coupled System

The discrete weak forms for the respective domains $\mathcal{W}_\mathrm{h}^\mathrm{S}, \mathcal{W}_\mathrm{h}^\mathrm{F,CUT}$, and $\mathcal{W}_\mathrm{h}^\mathrm{P}$ are already introduced in Section 2.2.3, Section 3.1, and Section 2.2.5, respectively. These discrete weak forms do not include the boundary integrals on the interfaces $\Gamma_\mathrm{h}^\mathrm{S,I}, \Gamma_\mathrm{h}^\mathrm{F,I}$, and $\Gamma_\mathrm{h}^\mathrm{P,I}$ of the respective domains, which arise naturally in the derivations of the weak form. Thus, these consistent integrals on the interface Γ_h are added for the coupled discrete weak form in the following.

$$
\begin{aligned}
\mathcal{W}_\mathrm{h}^\mathrm{FPS}\left[\left(\delta\underline{\boldsymbol{u}}_\mathrm{h}^\mathrm{S}, \delta\underline{\boldsymbol{v}}_\mathrm{h}^\mathrm{F}, \delta p_\mathrm{h}^\mathrm{F}, \delta\underline{\boldsymbol{u}}_\mathrm{h}^\mathrm{P}, \delta\underline{\boldsymbol{v}}_\mathrm{h}^\mathrm{P}, \delta p_\mathrm{h}^\mathrm{P}\right), \left(\underline{\boldsymbol{u}}_\mathrm{h}^\mathrm{S}, \underline{\boldsymbol{v}}_\mathrm{h}^\mathrm{F}, p_\mathrm{h}^\mathrm{F}, \underline{\boldsymbol{u}}_\mathrm{h}^\mathrm{P}, \underline{\boldsymbol{v}}_\mathrm{h}^\mathrm{P}, p_\mathrm{h}^\mathrm{P}\right)\right] &= \mathcal{W}_\mathrm{h}^\mathrm{S}\left[\delta\underline{\boldsymbol{u}}_\mathrm{h}^\mathrm{S}, \underline{\boldsymbol{u}}_\mathrm{h}^\mathrm{S}\right] + \\
\mathcal{W}_\mathrm{h}^\mathrm{F,CUT}\left[\left(\delta\underline{\boldsymbol{v}}_\mathrm{h}^\mathrm{F}, \delta p_\mathrm{h}^\mathrm{F}\right), \left(\underline{\boldsymbol{v}}_\mathrm{h}^\mathrm{F}, p_\mathrm{h}^\mathrm{F}\right)\right] + \mathcal{W}_\mathrm{h}^\mathrm{P}\left[\left(\delta\underline{\boldsymbol{v}}_\mathrm{h}^\mathrm{P}, \delta\underline{\boldsymbol{u}}_\mathrm{h}^\mathrm{P}, \delta p_\mathrm{h}^\mathrm{P}\right), \left(\underline{\boldsymbol{v}}_\mathrm{h}^\mathrm{P}, \underline{\boldsymbol{u}}_\mathrm{h}^\mathrm{P}, p_\mathrm{h}^\mathrm{P}\right)\right] \\
\underbrace{-\left\langle\delta\underline{\boldsymbol{u}}_\mathrm{h}^\mathrm{S/P}, \overline{\boldsymbol{\sigma}}_\mathrm{h}^n\right\rangle_{\Gamma_\mathrm{h}} + \left\langle\delta\underline{\boldsymbol{v}}_{\mathrm{h},\emptyset}^\mathrm{F}, \overline{\boldsymbol{\sigma}}_\mathrm{h}^n\right\rangle_{\Gamma_\mathrm{h}}}_{:=\mathcal{W}_{\mathrm{h},\Gamma}^{\mathrm{FPS},n}+\mathcal{W}_{\mathrm{h},\Gamma}^{\mathrm{FPS},t}} &\underbrace{+\left\langle\delta\underline{\boldsymbol{v}}_\mathrm{h}^\mathrm{P}, \overline{p}_\mathrm{h}^\mathrm{P}\cdot\underline{\boldsymbol{n}}_\mathrm{h}\right\rangle_{\Gamma_\mathrm{h}^\mathrm{P,I}}}_{\mathcal{W}_{\mathrm{h},\Gamma}^{\mathrm{P^F},c}}
\end{aligned}
\tag{7.21}
$$

Herein, the interface contributions on $\Gamma_\mathrm{h}^\mathrm{FS}$ and $\Gamma_\mathrm{h}^\mathrm{FP}$ arising from partial integration of the viscous and pressure contributions in domain Ω^F on $\Gamma_\mathrm{h}^\mathrm{F,I}$ are extended to the overall interface Γ_h by the definition (7.22) for the fluid test functions $\left(\delta\underline{\boldsymbol{v}}_{\mathrm{h},\emptyset}^\mathrm{F}, \delta p_{\mathrm{h},\emptyset}^\mathrm{F}\right)$ on the whole interface Γ_h. This definition ensures that fluid test functions are vanishing outside of the fluid domain. To enable a compact notation, a combined solid-poroelastic displacement test function $\delta\underline{\boldsymbol{u}}_\mathrm{h}^\mathrm{S/P}$ is introduced

in (7.22).

$$\left(\delta\underline{\boldsymbol{v}}_{\mathrm{h},\emptyset}^{\mathrm{F}}, \delta p_{\mathrm{h},\emptyset}^{\mathrm{F}}\right) = \begin{cases} \left(\delta\underline{\boldsymbol{v}}_{\mathrm{h}}^{\mathrm{F}}, \delta p_{\mathrm{h}}^{\mathrm{F}}\right) & \text{in} \quad \Omega_{\mathrm{h}}^{\mathrm{F}} \\ (\underline{\mathbf{0}}, 0) & \text{otherwise} \end{cases}, \quad \delta\underline{\boldsymbol{u}}_{\mathrm{h}}^{\mathrm{S/P}} = \begin{cases} \delta\underline{\boldsymbol{u}}_{\mathrm{h}}^{\mathrm{S}} & \text{in} \quad \Omega_{\mathrm{h}}^{\mathrm{S}} \\ \delta\underline{\boldsymbol{u}}_{\mathrm{h}}^{\mathrm{P}} & \text{in} \quad \Omega_{\mathrm{h}}^{\mathrm{P}} \end{cases} \tag{7.22}$$

By including the unique interface traction $\overline{\underline{\boldsymbol{\sigma}}}_{\mathrm{h}}^{n}$ for both the solid and the fluid boundary integral, which will be discussed in Sections 7.2.2.1 and 7.2.3, the dynamic equilibrium in normal direction (7.8), (7.9), and (7.10), as well as in tangential direction (7.18), and (7.19) is incorporated directly into the weak form. As the interface conditions (7.7)-(7.20) require a separate treatment of the normal and the tangential constraints, the normal component $\overline{\sigma}_{\mathrm{h}}^{nn}$ and the tangential component $\overline{\underline{\boldsymbol{\sigma}}}_{\mathrm{h}}^{n} \cdot \underline{\boldsymbol{P}}^{t}$ of the interface traction $\overline{\underline{\boldsymbol{\sigma}}}_{\mathrm{h}}^{n} = \overline{\sigma}_{\mathrm{h}}^{nn} \cdot \underline{\boldsymbol{n}} + \overline{\underline{\boldsymbol{\sigma}}}_{\mathrm{h}}^{n} \cdot \underline{\boldsymbol{P}}^{t}$ are treated separately in Sections 7.2.2.1 and 7.2.3. The application of a single interface fluid pressure $\overline{p}_{\mathrm{h}}^{\mathrm{P}}$ directly ensures the dynamic equilibrium (7.17) of the porous fluid for poroelastic-poroelastic contact and due to its definition in Section 7.2.2.2, which ensures the equality with $-\overline{\underline{\boldsymbol{\sigma}}}_{\mathrm{h}}^{n} \cdot \underline{\boldsymbol{n}}_{\mathrm{h}}$ on Γ^{FP}, also the dynamic equilibrium (7.16).

7.2.2 Nitsche-based Method on the Overall Coupling Interface Γ_{h} in Normal Direction

In the following, the numerical formulation to incorporate all interface normal conditions, discussed in Section 7.1.2, weakly by Nitsche-based methods is presented. First, the formulation taking into account all conditions (7.7)-(7.11) essential for the interaction of the fluid, the overall poroelastic mixture, and the structure is presented. Since these conditions are very similar to the ones for pure FSCI without considering poroelasticity, the approach is analogous to the presented formulation in Chapter 6.

7.2.2.1 Coupling between Fluid, Poroelastic Mixture, and Structure

To comply with all conditions specified in Section 7.1.2, the numerical normal interface traction $\overline{\sigma}_{\mathrm{h}}^{nn} = \overline{\underline{\boldsymbol{\sigma}}}_{\mathrm{h}}^{n} \cdot \underline{\boldsymbol{n}}_{\mathrm{h}}$, which is acting on the overall interface Γ_{h}, is constructed as

$$\overline{\sigma}_{\mathrm{h}}^{nn} = \min\left[(\sigma_{\mathrm{h}}^{\mathrm{F},nn} + \gamma^{\mathrm{FSI}} v_{\mathrm{h}}^{\mathrm{S/P},rel,n})_{\mathcal{E}} \ , \ (\overline{\sigma}_{\mathrm{h}}^{\mathrm{S/P},nn} + \gamma^{\mathrm{S/P},c} g_{\mathrm{h}}^{n})\right]. \tag{7.23}$$

This traction has to be included in the weak form (7.21) finally. The two additional numerical parameters $\gamma^{\mathrm{FSI}} > 0$ and $\gamma^{\mathrm{S/P},c} > 0$ are chosen sufficiently large (for details on the scaling of γ^{FSI} and $\gamma^{\mathrm{S/P},c}$ see e.g. the works of Massing *et al.* [149] and Seitz *et al.* [196]). The interface traction $\overline{\sigma}_{\mathrm{h}}^{nn}$ is composed of two separate contributions combined by the minimum function. As a result, the stress $\overline{\sigma}_{\mathrm{h}}^{nn}$ is continuous even for changes between these two contributions. First, the case with a smaller value of the left-hand side in (7.23) can be identified as enforcing the FSI or the FPI conditions (dynamic equilibrium (7.8) in the case equal to zero, a vanishing relative velocity (7.11), and a prevalent gap $g_{\mathrm{h}}^{n} > 0$ (7.7)). For a smaller value of right-hand side in (7.23), the contact conditions are applied (no-penetration condition (7.7) in the case equal to zero, the dynamic equilibrium (7.10) due to the chosen unique contact stress $\overline{\sigma}_{\mathrm{h}}^{\mathrm{S/P},nn}$, and a negative relative traction $(\overline{\sigma}_{\mathrm{h}}^{\mathrm{S/P},nn} - \sigma_{\mathrm{h}}^{\mathrm{F},nn}) < 0$ (7.8)). As a result, condition (7.9) is fulfilled for both cases automatically. In case no feasible projection exists, an infinite gap is assumed and thus the FSI or the FPI conditions are incorporated.

Remark 7.1 (Evaluation of the poroelastic Cauchy stress $\underline{\boldsymbol{\sigma}}_{\mathrm{h}}^{\mathrm{P}}$ in $\overline{\sigma}_{\mathrm{h}}^{\mathrm{S/P},nn}$)**.** *It can be directly seen from the definition of the second Piola-Kirchhoff stress tensor in* (2.50)*, that* $\underline{\boldsymbol{S}}_{\mathrm{h}}^{\mathrm{P}}$ *and thus also* $\underline{\boldsymbol{\sigma}}_{\mathrm{h}}^{\mathrm{P}}$ *includes, besides the deformation-dependent component, a porous fluid pressure-dependent contribution. Thus, also the normal poroelastic Cauchy stress* $\sigma_{\mathrm{h}}^{\mathrm{P},nn}$ *on the potential contact interface* $\breve{\Gamma}_{\mathrm{h}}^{\mathrm{P},c}$ *is porous fluid pressure* $p_{\mathrm{h}}^{\mathrm{P}}$*-dependent. This additional dependency is the main difference compared to the evaluation of the normal solid Cauchy stress* $\sigma_{\mathrm{h}}^{\mathrm{S},nn}$*.*

At first, the formulation when the contact conditions are enforced is discussed (left-hand side in (7.23)).To account for the balance of linear momentum on the interface (7.10), which reduces in the contact case to $\sigma_{\mathrm{h}}^{\mathrm{S/P},nn} = \sigma_{\mathrm{h}}^{\mathrm{S/\breve{P}},nn}$, a unique contact stress $\overline{\sigma}_{\mathrm{h}}^{\mathrm{S/P},nn}$ for both potentially contacting surfaces is applied. This means that always the same contact stress for both (potentially) contacting points (determined by the projection) on the contact interface is applied regardless on which side of the contact interface the term is evaluated. In principle, different weighting strategies to include the consistent stresses of the two adjacent domains are possible. The most simple one is to directly apply the consistent stress of one contact partner e.g. $\overline{\sigma}_{\mathrm{h}}^{\mathrm{S/P},nn} := \sigma_{\mathrm{h}}^{\mathrm{S}_1,nn}$ or $\overline{\sigma}_{\mathrm{h}}^{\mathrm{S/P},nn} := \sigma_{\mathrm{h}}^{\mathrm{P}_2,nn}$ leading to an inherent bias of the formulation. Taking into account the stress of both contacting sides, e.g. $\overline{\sigma}_{\mathrm{h}}^{\mathrm{S/P},nn} := \omega^c \sigma_{\mathrm{h}}^{\mathrm{S}_1,nn} + (1-\omega^c)\sigma_{\mathrm{h}}^{\mathrm{P}_2,nn}$, with the weighting factor $\omega^c \in [0,1]$ an unbiased method can be constructed. This is the case for the average weighting $\omega^c = 1/2$, which is applied in the works of Chouly *et al.* [63], Mlika *et al.* [156], and a harmonic weighting based on the material parameters and the mesh size of both contacting domains, which is applied in the works of Burman and Zunino [49], Seitz *et al.* [196] and in Chapter 6. The additional consistent penalty contribution $\gamma^{\mathrm{S/P},c} g_{\mathrm{h}}^n$ ensures enforcement of the no-penetration condition (7.7) and is required for a stable discrete formulation, as it is well-known from various studies on the Nitsche method for contact problems, see the work of Chouly and Hild [61].

In the following, the formulation when the FSI- or FPI-interface conditions are enforced is outlined (right-hand side in (7.23)). In this case, the normal fluid stress $\sigma_{\mathrm{h}}^{\mathrm{F},nn}$ represents the interface traction on all involved interfaces $\Gamma_{\mathrm{h}}^{\mathrm{S,I}}$, $\Gamma_{\mathrm{h}}^{\mathrm{P,I}}$, and $\Gamma_{\mathrm{h}}^{\mathrm{F,I}}$. Therefore, the balance of linear momentum specified by the inequality (7.8) in the case equal to zero and equation (7.9) for $g_{\mathrm{h}}^n \neq 0$, and as a result condition (7.10) for each side separately, are fulfilled. Again, a consistent and properly scaled penalty $\gamma^{\mathrm{FSI}} v_{\mathrm{h}}^{\mathrm{S/P},rel,n}$ contribution is added to enforce the kinematic constraint (7.11) and to stabilize the formulation. Additionally to this, a consistent skew-symmetric adjoint-consistency term is added to the weak form (7.21)

$$\begin{aligned} &\mathcal{W}_{\mathrm{h},\Gamma,\mathrm{Adj}}^{\mathrm{FPS},n}\left[\left(\delta\underline{\boldsymbol{v}}_{\mathrm{h}}^{\mathrm{F}}, \delta p_{\mathrm{h}}^{\mathrm{F}}\right), \left(\underline{\boldsymbol{u}}_{\mathrm{h}}^{\mathrm{S}}, \underline{\boldsymbol{v}}_{\mathrm{h}}^{\mathrm{F}}, \underline{\boldsymbol{u}}_{\mathrm{h}}^{\mathrm{P}}, \underline{\boldsymbol{v}}_{\mathrm{h}}^{\mathrm{P}}, p_{\mathrm{h}}^{\mathrm{P}}\right)\right] = \\ &\left\langle \delta p_{\mathrm{h}}^{\mathrm{F}} \underline{\boldsymbol{n}}_{\mathrm{h}} - 2\mu^{\mathrm{F}} \underline{\boldsymbol{\epsilon}}^{\mathrm{F}}(\delta\underline{\boldsymbol{v}}_{\mathrm{h}}^{\mathrm{F}})\underline{\boldsymbol{n}}_{\mathrm{h}}, v_{\mathrm{h}}^{\mathrm{S/P},rel,n}\underline{\boldsymbol{n}}_{\mathrm{h}} \right\rangle_{\Gamma_{\mathrm{h}}^{\mathrm{FS}} \cup \Gamma_{\mathrm{h}}^{\mathrm{FP}}}. \end{aligned} \tag{7.24}$$

This contribution enables a direct compensation of the destabilizing effects arising from the fluid pressure $p_{\mathrm{h}}^{\mathrm{F}}$, when representing the interface traction by the fluid stress $\sigma_{\mathrm{h}}^{\mathrm{F},nn}$. Also this term is consistent as it includes the constraint (7.11).

Remark 7.2 (Distinction of the different cases of the Nitsche-based contribution)**.** *The distinction between the contact- and the FSI/FPI-coupling based on the minimum function in* (7.23) *deviates from a classification based on a purely geometric criterion. A purely geometric criterion is used to specify the discrete fluid domain* $\Omega_{\mathrm{h}}^{\mathrm{F}}$ *and also the interface* $\Gamma_{\mathrm{h}}^{\mathrm{F,I}}$ *to ensure consistency between the two. Thus, combining the geometric classification of the fluid test functions*

$\left(\delta\underline{\boldsymbol{v}}^{\mathrm{F}}_{\mathrm{h},\emptyset}, \delta p^{\mathrm{F}}_{\mathrm{h},\emptyset}\right)$ *in* (7.22) *with the distinction in* (7.23)*, finally, four cases for the resulting interface contributions* $\mathcal{W}^{\mathrm{FPS},n}_{\mathrm{h},\Gamma}$ *to the weak form* (7.21) *can be distinguished. A more elaborate and detailed discussion on this aspect for FSCI can be found in Chapter 6.*

7.2.2.2 Coupling of the Porous Fluids

So far, only the coupling of the poroelastic mixture and the other domains is considered. The interaction of the porous fluid with the other domains is still missing. The resulting traction contributes to the weak form (7.21) by the last term on the interface $\Gamma^{\mathrm{P,I}}_{\mathrm{h}}$. To take into account all corresponding conditions (7.11) and (7.14)-(7.17), the following numerical porous interface pressure is applied in the weak form (7.21)

$$\overline{p}^{\mathrm{P}}_{\mathrm{h}} = \alpha^{\mathrm{P}}_{*} \left[\begin{cases} p^{\mathrm{P}}_{\mathrm{h}} & \text{on} \quad \breve{\Gamma}^{\mathrm{PS},c}_{\mathrm{h}} \\ \frac{1}{2}\left(p^{\mathrm{P}}_{\mathrm{h}} + \breve{p}^{\mathrm{P}}_{\mathrm{h}}\right) & \text{on} \quad \breve{\Gamma}^{\mathrm{PP},c}_{\mathrm{h}} \end{cases} \right] - \left(1-\alpha^{\mathrm{P}}_{*}\right)\left(\sigma^{\mathrm{F},nn}_{\mathrm{h}} + \gamma^{\mathrm{FSI}} v^{\mathrm{S/P},rel,n}_{\mathrm{h}}\right)_{\mathcal{E}}, \tag{7.25}$$

making use of the scalar porous interface type indicator $\alpha^{\mathrm{P}}_{*} \in [0,1]$. Herein, the representation of the pressure $\overline{p}^{\mathrm{P}}_{\mathrm{h}}$ is subdivided by the scalar α^{P}_{*} into the contact interface part $\Gamma^{\mathrm{P},c}_{\mathrm{h}}$ and the FPI interface part $\Gamma^{\mathrm{FP}}_{\mathrm{h}}$ of the porous interface $\Gamma^{\mathrm{P,I}}_{\mathrm{h}}$ to account for the varying prevalent conditions. Directly utilizing the geometry of the discrete interfaces results in a sharp interface indicator $\alpha^{\mathrm{P}}_{*} = \alpha^{\mathrm{P}}_{sharp}$

$$\alpha^{\mathrm{P}}_{sharp} = \begin{cases} 0.0 & \text{on} \quad \Gamma^{\mathrm{FP}}_{\mathrm{h}} \\ 1.0 & \text{on} \quad \Gamma^{\mathrm{P},c}_{\mathrm{h}}. \end{cases} \tag{7.26}$$

For the coupling of viscous fluid and porous fluid on $\Gamma^{\mathrm{FP}}_{\mathrm{h}}$ the same interface stress as presented in the previous Section 7.2.2.1 is applied. As a result, the effective numerical traction acting on both boundary integrals of the fluid and porous fluid interface is $(\sigma^{\mathrm{F},nn}_{\mathrm{h}} + \gamma^{\mathrm{FSI}} v^{\mathrm{S/P},rel,n}_{\mathrm{h}})_{\mathcal{E}}$ and, thus, the dynamic equilibrium between viscous and porous fluid (7.16) is fulfilled. The additional penalty contribution vanishes for a fulfilled mass balance (7.11) and thus it is consistent. Combining this contribution and the one elaborated in Section 7.2.2.1, results in the formulation for FPI presented and analyzed already in Chapter 4.

For the poroelastic contact case on $\Gamma^{\mathrm{P},c}_{\mathrm{h}}$, two different definitions for $\overline{p}^{\mathrm{P}}_{\mathrm{h}}$ are chosen depending whether the second participating domain is a solid domain or a poroelastic domain. Additional skew-symmetric adjoint-consistency like terms enforce the kinematic constraints and ensure a robust discrete formulation. This additional terms in the weak form (7.21) are consistent as they include the balance of mass on the interface (7.14) or (7.15)

$$\begin{aligned} &\mathcal{W}^{\mathrm{PF},c}_{\mathrm{h},\Gamma,\mathrm{Adj}}\left[\delta p^{\mathrm{P}}_{\mathrm{h}}, \left(\underline{\boldsymbol{u}}^{\mathrm{P}}_{\mathrm{h}}, \underline{\boldsymbol{v}}^{\mathrm{P}}_{\mathrm{h}}, p^{\mathrm{P}}_{\mathrm{h}}\right)\right] = \\ &- \alpha^{\mathrm{P}}_{*}\left\langle \delta p^{\mathrm{P}}_{\mathrm{h}}, v^{\mathrm{P},seepage,n}_{\mathrm{h}} \right\rangle_{\breve{\Gamma}^{\mathrm{PS},c}_{\mathrm{h}}} - \alpha^{\mathrm{P}}_{*}\left\langle \frac{1}{2}\left(\delta p^{\mathrm{P}}_{\mathrm{h}} + \delta\breve{p}^{\mathrm{P}}_{\mathrm{h}}\right), v^{\mathrm{P},seepage,n}_{\mathrm{h}} \right\rangle_{\breve{\Gamma}^{\mathrm{PP},c}_{\mathrm{h}}}. \end{aligned} \tag{7.27}$$

Herein, the scalar porous interface type indicator α^{P}_{*} is utilized in order to ensure that the contribution (7.27) is scaled to correspond to the first term in (7.25). In the case of poroelastic-solid contact on $\Gamma^{\mathrm{PS},c}_{\mathrm{h}}$, the pressure of the poroelastic domain is directly utilized as the representative

interface traction acting on the porous fluid. This is accompanied by the first term in (7.27), which includes the no-outflow condition (7.14). For the case of poroelastic-poroelastic contact on $\Gamma_{\mathrm{h}}^{\mathrm{PP},c}$, the mean porous pressure based on both contacting domains is used to account for the dynamic equilibrium (7.17). The corresponding second term in (7.27) is constructed by an average weighting of the pressure test function of both contacting interfaces. Due to the integration of this term on both contacting sides, this contribution is consistent as it includes the balance of mass (7.15).

While specification (7.25) results in a continuous pressure when considering the exact solution of the problem (as conditions (7.11), (7.16), and (7.17) are fulfilled), this is not true for the discrete formulation. To retain continuity of the formulation, which is essential for the gradient-based nonlinear solution strategy, an alternative definition for $\alpha_*^{\mathrm{P}} = \alpha_{smooth}^{\mathrm{P}} \in [0,1]$ is applied

$$\alpha_{smooth}^{\mathrm{P}} = \begin{cases} 0.0 & \text{on} \quad \Gamma_{\mathrm{h}}^{\mathrm{FP}} \setminus \breve{\Gamma}_{\mathrm{h}}^{\mathrm{P},c} \\ \max\left[0.0, 1.0 - g_{\mathrm{h}}^{n} \cdot (a \cdot h)^{-1}\right] & \text{on} \quad \breve{\Gamma}_{\mathrm{h}}^{\mathrm{P},c} \setminus \Gamma_{\mathrm{h}}^{\mathrm{P},c}, \\ 1.0 & \text{on} \quad \Gamma_{\mathrm{h}}^{\mathrm{P},c} \end{cases} \tag{7.28}$$

which includes a constant a, that is set to $a = 0.01$ for the presented numerical examples. This formulation ensures a continuous transition of the representative interface pressure $\overline{p}_{\mathrm{h}}^{\mathrm{P}}$ between contact and FPI. Based on the gap of the contacting interfaces a combination of both interface contributions is considered for: $0 < g_{\mathrm{h}}^{n} < a \cdot h$, while the formulation remains unaltered for the remaining range. Herein, h corresponds to a characteristic element size of the fluid discretization. For the numerical examples presented in this work, h is specified as the diagonal of the uniform elements.

Remark 7.3 (Discrete distinction of interface types for porous flow coupling)**.** *In contrast to the distinction between contact and FSI/FPI in Section 7.2.2.1, a purely geometrical criteria is applied to specify the numerical porous interface pressure* $\overline{p}_{\mathrm{h}}^{\mathrm{P}}$ (7.25)*. Computed results based on the direct application of the decision given by the "active" side of the min-function in* (7.23) *also for* $\overline{p}_{\mathrm{h}}^{\mathrm{P}}$*, do not fulfill the conditions of fluid mass balance* (7.14) *and* (7.15) *as prescribed. The reason for the behavior is that the decision in* (7.23) *can vary locally for some small areas on the contact interface, e.g. due to the discrete error of* $\overline{\sigma}_{\mathrm{h}}^{\mathrm{S/P},nn}$*. Due to the continuity of* $\overline{\sigma}_{\mathrm{h}}^{nn}$ *when changing the condition type in* (7.23) *this does not have a significant effect on terms including* $\overline{\sigma}_{\mathrm{h}}^{nn}$*. In contrast to this, due to the numerical error, the porous pressure and fluid stress based contributions in* (7.25) *are not equal at the points of changing conditions specified by* (7.23)*. Thus, a change from contact to FSI/FPI conditions can have an essential effect on terms including* $\overline{p}_{\mathrm{h}}^{\mathrm{P}}$*, and as a consequence on the fulfillment of the corresponding porous fluid mass balance.*

7.2.2.3 Fluid Stress Extension Approach

When evaluating (7.23) in the discrete weak form, the extension of the numerical fluid stress $(\sigma_{\mathrm{h}}^{\mathrm{F},nn} + \gamma^{\mathrm{FSI}} v_{\mathrm{h}}^{\mathrm{S/P},rel,n})$ has to be applied. From a physical point of view, this extended fluid stress has its main impact onto the response of such a system by specifying the state when contact is released.

As a first step to evaluate the extension, the extension origin position $\underline{\boldsymbol{x}}_{\mathcal{E}} \in \Gamma_{\mathrm{h}}^{\mathrm{FS}} \cup \Gamma_{\mathrm{h}}^{\mathrm{FP}}$ based on the position $\underline{\boldsymbol{x}} \in \Gamma_{\mathrm{h}}^{\mathrm{S},c} \cup \Gamma_{\mathrm{h}}^{\mathrm{P},c}$ to which the quantity of interest should be extended is computed.

This position $\underline{\boldsymbol{x}}_{\mathcal{E}}(\underline{\boldsymbol{x}})$ is determined as the closest point on the border line of contact $\left(\Gamma_{\mathrm{h}}^{\mathrm{FS}} \cup \Gamma_{\mathrm{h}}^{\mathrm{FP}}\right) \cap \left(\Gamma_{\mathrm{h}}^{\mathrm{S},c} \cup \Gamma_{\mathrm{h}}^{\mathrm{P},c}\right)$ to the position of interest $\underline{\boldsymbol{x}}$.

In the following, two approaches will be discussed. The first variant is a simple constant extension approach, applied to the extension of a scalar quantity $*$, as already presented and applied in Chapter 6

$$\mathcal{E}_{\underline{\boldsymbol{x}}}^{const.}\left[*\left(\underline{\boldsymbol{x}}_{\mathcal{E}}(\underline{\boldsymbol{x}})\right)\right] := *\left(\underline{\boldsymbol{x}}_{\mathcal{E}}(\underline{\boldsymbol{x}})\right). \tag{7.29}$$

The value of the scalar quantity $*$ evaluated at the extension origin position $\underline{\boldsymbol{x}}_{\mathcal{E}}$ is directly utilized as its extension. This simple approach is typically sufficient for configurations where contact is released solely close to the fluid domain. In the case a poroelastic domain is involved in contact, the porous fluid pressure $p_{\mathrm{h}}^{\mathrm{P}}$ provides a physically motivated and more accurate extension also far from the fluid domain. The physically motivated extension of the numerical fluid stress making use of the porous fluid pressure is specified as

$$\begin{aligned}
&\mathcal{E}_{\underline{\boldsymbol{x}}}^{\mathrm{F}-stress}\left[\sigma_{\mathrm{h}}^{\mathrm{F},nn} + \gamma^{\mathrm{FSI}} v_{\mathrm{h}}^{\mathrm{S/P},rel,n}\right] := \\
&(1-\alpha^{\mathcal{E}})\mathcal{E}_{\underline{\boldsymbol{x}}}^{const.}\left[\sigma_{\mathrm{h}}^{\mathrm{F},nn} + \gamma^{\mathrm{FSI}} v_{\mathrm{h}}^{\mathrm{S/P},rel,n}\right] - \alpha^{\mathcal{E}}\left[\begin{cases} p_{\mathrm{h}}^{\mathrm{P}} & \text{on} \quad \Gamma_{\mathrm{h}}^{\mathrm{PS},c} \\ \frac{1}{2}\left(p_{\mathrm{h}}^{\mathrm{P}} + \check{p}_{\mathrm{h}}^{\mathrm{P}}\right) & \text{on} \quad \Gamma_{\mathrm{h}}^{\mathrm{PP},c} \end{cases}\right](\underline{\boldsymbol{x}}).
\end{aligned} \tag{7.30}$$

Herein, the scalar weighting factor $\alpha^{\mathcal{E}} = \min\left[1, ||\underline{\boldsymbol{x}} - \underline{\boldsymbol{x}}_{\mathcal{E}}|| \cdot c \cdot h^{-1}\right] \in [0,1]$ (with $c = 1$) continuously combines the constant extension approach (7.29) with the physically motivated approach based on the porous fluid pressure. Combining these two approaches ensures that the extension is continuous (as it is based on the numerical fluid stress $(\sigma_{\mathrm{h}}^{\mathrm{F},nn} + \gamma^{\mathrm{FSI}} v_{\mathrm{h}}^{\mathrm{S/P},rel,n})$ close to the fluid domain) and on the other hand it is physically meaningful far from the fluid domain (as it is based on the porous fluid pressure far from the fluid domain). The interpolation zone between these two strategies is based on a characteristic element size h of the underlying fluid discretization. Depending on the number of involved poroelastic domains in the contact, either the porous fluid pressure is taken directly on $\Gamma_{\mathrm{h}}^{\mathrm{PS},c}$ or the mean porous fluid pressure of the two contacting bodies is used on $\Gamma_{\mathrm{h}}^{\mathrm{PP},c}$. Since no fluid pressure information in the contact zone is available on the solid-solid contact interface $\Gamma_{\mathrm{h}}^{\mathrm{SS},c}$, the constant extension approach (7.29) is utilized thereon.

7.2.3 Nitsche-based Method on the Overall Coupling Interface Γ_{h} in Tangential Direction

To incorporate the condition in tangential interface direction (7.18)-(7.20), a Nitsche-based method for the general Navier interface condition is applied. This formulation, which is robust for any slip length $\kappa \in [0, \infty]$, is based on the work Juntunen and Stenberg [132] for the Poisson problem and the work of Winter *et al.* [226] for the linearized fluid problem. This approach was already applied to FPI and FSCI problems in Chapter 4, Chapter 5, and Chapter 6. A common representation of the tangential interface stress $\overline{\boldsymbol{\sigma}}_{\mathrm{h}}^{n} \cdot \underline{\boldsymbol{P}}^{t}$ in both the fluid and the solid/poroelastic boundary integrals allows incorporating the dynamic equilibrium (7.19) directly. Due to the consideration of frictionless contact in (7.18), the numerical tangential interface traction vanishes

directly on the contacting part interface

$$\overline{\underline{\boldsymbol{\sigma}}}_{\mathrm{h}}^{n} \cdot \underline{\boldsymbol{P}}^{t} = \underline{\mathbf{0}} \quad \text{on} \quad \Gamma_{\mathrm{h}}^{\mathrm{S},c} \cup \Gamma_{\mathrm{h}}^{\mathrm{P},c}. \tag{7.31}$$

To incorporate the general Navier condition (7.20), the following specification of the interface stress on the interfaces $\Gamma_{\mathrm{h}}^{\mathrm{FS}}$ and $\Gamma_{\mathrm{h}}^{\mathrm{FP}}$ is consulted:

$$\overline{\underline{\boldsymbol{\sigma}}}_{\mathrm{h}}^{n} \cdot \underline{\boldsymbol{P}}^{t} = \frac{(\gamma_0^{\mathrm{FSI},t})^{-1} h_\Gamma}{\kappa \mu^{\mathrm{F}} + (\gamma_0^{\mathrm{FSI},t})^{-1} h_\Gamma} \left[-\underline{\boldsymbol{\sigma}}_{\mathrm{h}}^{\mathrm{F}} \cdot \underline{\boldsymbol{n}}_{\mathrm{h}}^{\mathrm{F}} + \frac{\mu^{\mathrm{F}}}{(\gamma_0^{\mathrm{FSI},t})^{-1} h_\Gamma} \underline{\boldsymbol{v}}_{\mathrm{h}}^{\mathrm{S/P},rel} \right] \cdot \underline{\boldsymbol{P}}^{t} \quad \text{on} \quad \Gamma_{\mathrm{h}}^{\mathrm{FS}} \cup \Gamma_{\mathrm{h}}^{\mathrm{FP}}. \tag{7.32}$$

Insertion of these interface stress definitions results in the following tangential contributions to the weak form (7.21)

$$\begin{aligned} \mathcal{W}_{\mathrm{h},\Gamma}^{\mathrm{FPS},t} \left[\left(\delta \underline{\boldsymbol{u}}_{\mathrm{h}}^{\mathrm{S}}, \delta \underline{\boldsymbol{v}}_{\mathrm{h}}^{\mathrm{F}}, \delta \underline{\boldsymbol{u}}_{\mathrm{h}}^{\mathrm{P}} \right), \left(\underline{\boldsymbol{u}}_{\mathrm{h}}^{\mathrm{S}}, \underline{\boldsymbol{v}}_{\mathrm{h}}^{\mathrm{F}}, \underline{\boldsymbol{u}}_{\mathrm{h}}^{\mathrm{P}}, \underline{\boldsymbol{v}}_{\mathrm{h}}^{\mathrm{P}}, p_{\mathrm{h}}^{\mathrm{P}} \right) \right] &= - \left\langle \delta \underline{\boldsymbol{v}}_{\mathrm{h}}^{\mathrm{F}} - \delta \underline{\boldsymbol{u}}_{\mathrm{h}}^{\mathrm{S/P}}, \underline{\boldsymbol{\sigma}}_{\mathrm{h}}^{\mathrm{F}} \cdot \underline{\boldsymbol{n}}_{\mathrm{h}}^{\mathrm{F}} \cdot \underline{\boldsymbol{P}}^{t} \right\rangle_{\Gamma_{\mathrm{h}}^{\mathrm{FS}} \cup \Gamma_{\mathrm{h}}^{\mathrm{FP}}} \\ + \frac{\mu^{\mathrm{F}}}{\kappa \mu^{\mathrm{F}} + (\gamma_0^{\mathrm{FSI},t})^{-1} h_\Gamma} \left\langle \delta \underline{\boldsymbol{v}}_{\mathrm{h}}^{\mathrm{F}} - \delta \underline{\boldsymbol{u}}_{\mathrm{h}}^{\mathrm{S/P}}, \left[\underline{\boldsymbol{v}}_{\mathrm{h}}^{\mathrm{S/P},rel} + \kappa \underline{\boldsymbol{\sigma}}_{\mathrm{h}}^{\mathrm{F}} \cdot \underline{\boldsymbol{n}}_{\mathrm{h}}^{\mathrm{F}} \right] \cdot \underline{\boldsymbol{P}}^{t} \right\rangle_{\Gamma_{\mathrm{h}}^{\mathrm{FS}} \cup \Gamma_{\mathrm{h}}^{\mathrm{FP}}}. \end{aligned} \tag{7.33}$$

Additionally, a skew-symmetric adjoint-consistency term is added

$$\begin{aligned} &\mathcal{W}_{\mathrm{h},\Gamma,\mathrm{Adj}}^{\mathrm{FPS},t} \left[\delta \underline{\boldsymbol{v}}_{\mathrm{h}}^{\mathrm{F}}, \left(\underline{\boldsymbol{u}}_{\mathrm{h}}^{\mathrm{S}}, \underline{\boldsymbol{v}}_{\mathrm{h}}^{\mathrm{F}}, \underline{\boldsymbol{u}}_{\mathrm{h}}^{\mathrm{P}}, \underline{\boldsymbol{v}}_{\mathrm{h}}^{\mathrm{P}}, p_{\mathrm{h}}^{\mathrm{P}} \right) \right] = \\ &- \frac{(\gamma_0^{\mathrm{FSI},t})^{-1} h_\Gamma}{\kappa \mu^{\mathrm{F}} + (\gamma_0^{\mathrm{FSI},t})^{-1} h_\Gamma} \left\langle -2\mu^{\mathrm{F}} \underline{\boldsymbol{\epsilon}}^{\mathrm{F}}(\delta \underline{\boldsymbol{v}}_{\mathrm{h}}^{\mathrm{F}}) \cdot \underline{\boldsymbol{n}}_{\mathrm{h}}^{\mathrm{F}}, \left[\underline{\boldsymbol{v}}_{\mathrm{h}}^{\mathrm{S/P},rel} + \kappa \underline{\boldsymbol{\sigma}}_{\mathrm{h}}^{\mathrm{F}} \cdot \underline{\boldsymbol{n}}_{\mathrm{h}}^{\mathrm{F}} \right] \cdot \underline{\boldsymbol{P}}^{t} \right\rangle_{\Gamma_{\mathrm{h}}^{\mathrm{FS}} \cup \Gamma_{\mathrm{h}}^{\mathrm{FP}}}. \end{aligned} \tag{7.34}$$

The first term in (7.33) shows that the tangential interface stress is represented by the fluid stress and, as a result, the dynamic equilibrium (7.19) is automatically fulfilled. It can be directly seen that the second, penalty like, term in (7.33) and the contribution (7.34) vanish in the case the tangential kinematic condition (7.20) is fulfilled and, thus, these terms are consistent. These two additional terms enforce the general Navier condition (7.20) and balance the destabilizing effect of the viscous stress on the interface introduced by the first term in (7.33). The constant tangential penalty parameter $\gamma_0^{\mathrm{FSI},t} > 0$ is specified sufficiently large.

Definition of the Slip Length κ As already discussed in Section 7.1.3, the general Navier interface condition is considered to result in a continuous formulation, while taking into account the different tangential interface conditions on an FSI ($\kappa = 0$), FPI ($\kappa = \kappa_{\mathrm{BJ}}$), or contact ($\kappa = \infty$) interface. To incorporate these conditions, the slip length κ on the fluid interface $\Gamma_{\mathrm{h}}^{\mathrm{F,I}}$ is specified as

$$\kappa := \begin{cases} \kappa^c & \text{on} \quad \Gamma_{\mathrm{h}}^{\mathrm{FS}} \\ \kappa_{\mathrm{BJ}} + \kappa^c & \text{on} \quad \Gamma_{\mathrm{h}}^{\mathrm{FP}} \end{cases}, \quad \text{with} \quad \kappa^c := \begin{cases} 0 & \text{if} \quad g_{\mathrm{h}}^{n} > h \\ \kappa_0 h \left[\frac{h}{g_{\mathrm{h}}^{n}} - 1 \right] & \text{if} \quad h \geq g_{\mathrm{h}}^{n} > 0. \\ \infty & \text{otherwise} \end{cases} \tag{7.35}$$

Herein, an interpolation, which is based on the normal gap g_{h}^{n}, of the slip length between the aforementioned limit cases depending on the spatial resolution of the computation fluid mesh is performed. The unmodified FSI/FPI interface conditions are applied down to a minimal distance specified by the fluid element size h. Thus, for refined computational discretizations the size of the interpolation zone decreases. The constant reference slip length κ_0 allows specifying the interpolation function.

7.3 The Coupled Discrete FPSCI Problem

Specified by the discrete solution spaces and discrete test functions spaces of the underlying physical fields, which are defined in (2.106) for the structural problem, in (2.110) for the fluid problem, and in (2.119) for the poroelastic problem, the overall discrete solution space $\mathcal{S}_{\underline{\boldsymbol{x}}^{\mathrm{FPSCI}},\mathrm{h},n+1}$ and the test function space $\mathcal{T}_{\delta\underline{\boldsymbol{x}}^{\mathrm{FPSCI}},\mathrm{h},n+1}$ is defined as

$$\begin{aligned}\mathcal{S}_{\underline{\boldsymbol{x}}^{\mathrm{FPSCI}},\mathrm{h},n+1} &:= \mathcal{S}_{\underline{\boldsymbol{u}}^{\mathrm{S}},\mathrm{h},n+1} \times \mathcal{S}_{\underline{\boldsymbol{v}}^{\mathrm{F}},\mathrm{h},n+1} \times \mathcal{S}_{p^{\mathrm{F}},\mathrm{h},n+1} \times \mathcal{S}_{\underline{\boldsymbol{u}}^{\mathrm{P}},\mathrm{h},n+1} \times \mathcal{S}_{\underline{\boldsymbol{v}}^{\mathrm{P}},\mathrm{h},n+1} \times \mathcal{S}_{p^{\mathrm{P}},\mathrm{h}} \\ \mathcal{T}_{\delta\underline{\boldsymbol{x}}^{\mathrm{FPSCI}},\mathrm{h},n+1} &:= \mathcal{T}_{\delta\underline{\boldsymbol{u}}^{\mathrm{S}},\mathrm{h}} \times \mathcal{T}_{\delta\underline{\boldsymbol{v}}^{\mathrm{F}},\mathrm{h},n+1} \times \mathcal{T}_{\delta p^{\mathrm{F}},\mathrm{h},n+1} \times \mathcal{T}_{\delta\underline{\boldsymbol{u}}^{\mathrm{P}},\mathrm{h}} \times \mathcal{T}_{\delta\underline{\boldsymbol{v}}^{\mathrm{P}},\mathrm{h}} \times \mathcal{T}_{\delta p^{\mathrm{P}},\mathrm{h}}\end{aligned} \tag{7.36}$$

The overall discrete test function $\delta\underline{\boldsymbol{x}}_{\mathrm{h}}^{\mathrm{FPSCI}}$ and discrete solution state $\underline{\boldsymbol{x}}_{\mathrm{h},n+1}^{\mathrm{FPSCI}}$ are given by

$$\begin{aligned}\underline{\boldsymbol{x}}_{\mathrm{h},n+1}^{\mathrm{FPSCI}} &:= \left(\underline{\boldsymbol{u}}_{\mathrm{h},n+1}^{\mathrm{S}}, \underline{\boldsymbol{v}}_{\mathrm{h},n+1}^{\mathrm{F}}, p_{\mathrm{h},n+1}^{\mathrm{F}}, \underline{\boldsymbol{v}}_{\mathrm{h},n+1}^{\mathrm{P}}, \underline{\boldsymbol{u}}_{\mathrm{h},n+1}^{\mathrm{P}}, p_{\mathrm{h},n+1}^{\mathrm{P}}\right), \\ \delta\underline{\boldsymbol{x}}_{\mathrm{h}}^{\mathrm{FPSCI}} &:= \left(\delta\underline{\boldsymbol{u}}_{\mathrm{h}}^{\mathrm{S}}, \delta\underline{\boldsymbol{v}}_{\mathrm{h}}^{\mathrm{F}}, \delta p_{\mathrm{h}}^{\mathrm{F}}, \delta\underline{\boldsymbol{v}}_{\mathrm{h}}^{\mathrm{P}}, \delta\underline{\boldsymbol{u}}_{\mathrm{h}}^{\mathrm{P}}, \delta p_{\mathrm{h}}^{\mathrm{P}}\right).\end{aligned} \tag{7.37}$$

By insertion of the interface traction $\overline{\boldsymbol{\sigma}}_{\mathrm{h}}^{n}$ in normal direction specified in (7.23) into $\mathcal{W}_{\mathrm{h},\Gamma}^{\mathrm{FPS},n}$ and in tangential direction specified in (7.31) and (7.32) into $\mathcal{W}_{\mathrm{h},\Gamma}^{\mathrm{FPS},t}$, and insertion of the interface fluid pressure $\overline{p}_{\mathrm{h}}^{\mathrm{P}}$ specified in (7.25) into $\mathcal{W}_{\mathrm{h},\Gamma,n+1}^{\mathrm{P^F},c}$ allows determining the coupled discrete weak form (7.21). Summing up the additional adjoint-consistency terms (7.24), (7.34), and (7.27), the following discrete weak form of the FPSCI problem, using definitions (7.36) and (7.37), has to be solved

$$\begin{aligned}&Find\ \underline{\boldsymbol{x}}_{\mathrm{h},n+1}^{\mathrm{FPSCI}} \in \mathcal{S}_{\underline{\boldsymbol{x}}^{\mathrm{FPSCI}},\mathrm{h},n+1}\ such\ that\ for\ all\ \delta\underline{\boldsymbol{x}}_{\mathrm{h}}^{\mathrm{FPSCI}} \in \mathcal{T}_{\delta\underline{\boldsymbol{x}}^{\mathrm{FPSCI}},\mathrm{h},n+1}\text{:} \\ &\mathcal{W}_{\mathrm{h},n+1}^{\mathrm{FPSCI}}\left[\delta\underline{\boldsymbol{x}}_{\mathrm{h}}^{\mathrm{FPSCI}}, \underline{\boldsymbol{x}}_{\mathrm{h},n+1}^{\mathrm{FPSCI}}\right] = \\ &\quad \mathcal{W}_{\mathrm{h},n+1}^{\mathrm{S}}\left[\delta\underline{\boldsymbol{u}}_{\mathrm{h}}^{\mathrm{S}}, \underline{\boldsymbol{u}}_{\mathrm{h},n+1}^{\mathrm{S}}\right] \\ &\quad + \mathcal{W}_{\mathrm{h},n+1}^{\mathrm{F,CUT}}\left[\left(\delta\underline{\boldsymbol{v}}_{\mathrm{h}}^{\mathrm{F}}, \delta p_{\mathrm{h}}^{\mathrm{F}}\right), \left(\underline{\boldsymbol{v}}_{\mathrm{h},n+1}^{\mathrm{F}}, p_{\mathrm{h},n+1}^{\mathrm{F}}\right)\right] \\ &\quad + \mathcal{W}_{\mathrm{h},n+1}^{\mathrm{P}}\left[\left(\delta\underline{\boldsymbol{v}}_{\mathrm{h}}^{\mathrm{P}}, \delta\underline{\boldsymbol{u}}_{\mathrm{h}}^{\mathrm{P}}, \delta p_{\mathrm{h}}^{\mathrm{P}}\right), \left(\underline{\boldsymbol{v}}_{\mathrm{h},n+1}^{\mathrm{P}}, \underline{\boldsymbol{u}}_{\mathrm{h},n+1}^{\mathrm{P}}, p_{\mathrm{h},n+1}^{\mathrm{P}}\right)\right] + \\ &\quad + \mathcal{W}_{\mathrm{h},\Gamma,n+1}^{\mathrm{FPS},n}\left[\left(\delta\underline{\boldsymbol{u}}_{\mathrm{h}}^{\mathrm{S}}, \delta\underline{\boldsymbol{v}}_{\mathrm{h}}^{\mathrm{F}}, \delta\underline{\boldsymbol{u}}_{\mathrm{h}}^{\mathrm{P}}\right), \left(\underline{\boldsymbol{u}}_{\mathrm{h},n+1}^{\mathrm{S}}, \underline{\boldsymbol{v}}_{\mathrm{h},n+1}^{\mathrm{F}}, p_{\mathrm{h},n+1}^{\mathrm{F}}, \underline{\boldsymbol{u}}_{\mathrm{h},n+1}^{\mathrm{P}}, \underline{\boldsymbol{v}}_{\mathrm{h},n+1}^{\mathrm{P}}, p_{\mathrm{h},n+1}^{\mathrm{P}}\right)\right] \\ &\quad + \mathcal{W}_{\mathrm{h},\Gamma,n+1}^{\mathrm{FPS},t}\left[\left(\delta\underline{\boldsymbol{u}}_{\mathrm{h}}^{\mathrm{S}}, \delta\underline{\boldsymbol{v}}_{\mathrm{h}}^{\mathrm{F}}, \delta\underline{\boldsymbol{u}}_{\mathrm{h}}^{\mathrm{P}}\right), \left(\underline{\boldsymbol{u}}_{\mathrm{h},n+1}^{\mathrm{S}}, \underline{\boldsymbol{v}}_{\mathrm{h},n+1}^{\mathrm{F}}, \underline{\boldsymbol{u}}_{\mathrm{h},n+1}^{\mathrm{P}}, \underline{\boldsymbol{v}}_{\mathrm{h},n+1}^{\mathrm{P}}, p_{\mathrm{h},n+1}^{\mathrm{P}}\right)\right] \\ &\quad + \mathcal{W}_{\mathrm{h},\Gamma,\mathrm{Adj},n+1}^{\mathrm{FPS},n}\left[\left(\delta\underline{\boldsymbol{v}}_{\mathrm{h}}^{\mathrm{F}}, \delta p_{\mathrm{h}}^{\mathrm{F}}\right), \left(\underline{\boldsymbol{u}}_{\mathrm{h},n+1}^{\mathrm{S}}, \underline{\boldsymbol{v}}_{\mathrm{h},n+1}^{\mathrm{F}}, \underline{\boldsymbol{u}}_{\mathrm{h},n+1}^{\mathrm{P}}, \underline{\boldsymbol{v}}_{\mathrm{h},n+1}^{\mathrm{P}}, p_{\mathrm{h},n+1}^{\mathrm{P}}\right)\right] \\ &\quad + \mathcal{W}_{\mathrm{h},\Gamma,\mathrm{Adj},n+1}^{\mathrm{FPS},t}\left[\delta\underline{\boldsymbol{v}}_{\mathrm{h}}^{\mathrm{F}}, \left(\underline{\boldsymbol{u}}_{\mathrm{h},n+1}^{\mathrm{S}}, \underline{\boldsymbol{v}}_{\mathrm{h},n+1}^{\mathrm{F}}, \underline{\boldsymbol{u}}_{\mathrm{h},n+1}^{\mathrm{P}}, \underline{\boldsymbol{v}}_{\mathrm{h},n+1}^{\mathrm{P}}, p_{\mathrm{h},n+1}^{\mathrm{P}}\right)\right] \\ &\quad + \mathcal{W}_{\mathrm{h},\Gamma,n+1}^{\mathrm{P^F},c}\left[\delta\underline{\boldsymbol{v}}_{\mathrm{h}}^{\mathrm{P}}, \left(\underline{\boldsymbol{u}}_{\mathrm{h},n+1}^{\mathrm{S}}, \underline{\boldsymbol{v}}_{\mathrm{h},n+1}^{\mathrm{F}}, p_{\mathrm{h},n+1}^{\mathrm{F}}, \underline{\boldsymbol{u}}_{\mathrm{h},n+1}^{\mathrm{P}}, \underline{\boldsymbol{v}}_{\mathrm{h},n+1}^{\mathrm{P}}, p_{\mathrm{h},n+1}^{\mathrm{P}}\right)\right] \\ &\quad + \mathcal{W}_{\mathrm{h},\Gamma,\mathrm{Adj},n+1}^{\mathrm{P^F},c}\left[\delta p_{\mathrm{h}}^{\mathrm{P}}, \left(\underline{\boldsymbol{u}}_{\mathrm{h},n+1}^{\mathrm{P}}, \underline{\boldsymbol{v}}_{\mathrm{h},n+1}^{\mathrm{P}}, p_{\mathrm{h},n+1}^{\mathrm{P}}\right)\right].\end{aligned} \tag{7.38}$$

The additional index $n+1$ in $\mathcal{W}_{\mathrm{h},\Gamma,n+1}^{\mathrm{FPS},n}$, $\mathcal{W}_{\mathrm{h},\Gamma,n+1}^{\mathrm{FPS},t}$, $\mathcal{W}_{\mathrm{h},\Gamma,\mathrm{Adj},n+1}^{\mathrm{FPS},n}$, $\mathcal{W}_{\mathrm{h},\Gamma,\mathrm{Adj},n+1}^{\mathrm{FPS},t}$, $\mathcal{W}_{\mathrm{h},\Gamma,n+1}^{\mathrm{P^F},c}$, and $\mathcal{W}_{\mathrm{h},\Gamma,\mathrm{Adj},n+1}^{\mathrm{P^F},c}$ specifies that the terms which are integrated on the interface $\langle *,*\rangle_{\Gamma_{\mathrm{h}}}$ are evaluated as $\langle *,*\rangle_{\Gamma_{\mathrm{h},n+1},n+\theta}$ according to the utilized notation for the temporal discretization introduced in Section 2.2.1.3.

The Newton-Raphson like nonlinear solution procedure to solve the aforementioned system for the vector of unknown nodal states

$$\underline{\mathbf{x}}_{n+1}^{\mathrm{FPSCI}} := \left[\left(\underline{\mathbf{u}}_{n+1}^{\mathrm{S}}\right)^{\mathsf{T}}, \left(\underline{\mathbf{v}}_{n+1}^{\mathrm{F}}\right)^{\mathsf{T}}, \left(\underline{\mathbf{p}}_{n+1}^{\mathrm{F}}\right)^{\mathsf{T}}, \left(\underline{\mathbf{u}}_{n+1}^{\mathrm{P}}\right)^{\mathsf{T}}, \left(\underline{\mathbf{v}}_{n+1}^{\mathrm{P}}\right)^{\mathsf{T}}, \left(\underline{\mathbf{p}}_{n+1}^{\mathrm{P}}\right)^{\mathsf{T}}\right]^{\mathsf{T}}, \tag{7.39}$$

is discussed in Section 3.4. The algorithmic details presented in Chapter 6, in Section 6.3.1 and Section 6.3.2 are applied for the monolithic solution procedure of the subsequently presented numerical examples.

7.4 Numerical Examples: General FPSCI

In the following, three numerical examples to analyze the introduced formulation and to demonstrate its capabilities are presented. In order to make the presentation as clear as possible, the index h to specify discrete quantities has been omitted for all numerical examples.

7.4.1 Falling, Contacting, and Lifting of a Rounded Poroelastic Stamp

To analyze basic properties of the presented formulation for FPSCI, a simple configuration which includes the falling, the contacting, and the lifting process of a rounded poroelastic stamp is investigated. A similar configuration is already analyzed for FSCI in Chapter 6. However, to show specific aspects of contact with poroelastic bodies a configuration with a reduced radius of the stamp and an additional hole in the stamp is considered. To verify both contact configurations, the poroelastic-solid contact and the poroelastic-poroelastic contact, two varying setups including a impermeable and a porous permeable foundation in combination with the poroelastic stamp are taken into account. By making use of the symmetry of this configuration, just the half domain of interest is solved in the following.

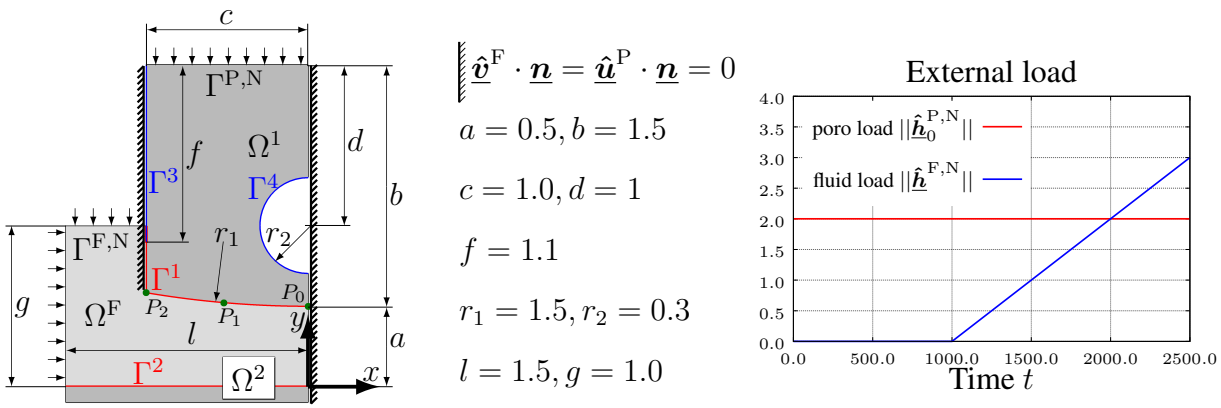

Figure 7.2: Geometry and basic boundary conditions for the falling, contacting, and lifting of a rounded poroelastic stamp. The overall interface is marked by the red lines. Due to the symmetry of the configuration, only the part with $x \leq 0$ is considered. The three points P_0, P_1 and P_2, marked by the green circles, will be used to discuss the deformation of the interface (left). The time-dependent external loads, the fluid load $\hat{\underline{\boldsymbol{h}}}^{\mathrm{F,N}}$ acting on the boundary $\Gamma^{\mathrm{F,N}}$ and the poroelastic mixture load $\hat{\underline{\boldsymbol{h}}}_0^{\mathrm{P,N}}$ acting on the boundary $\Gamma_0^{\mathrm{P,N}}$, are given in the diagram (right).

Problem Description The geometry and the basic boundary conditions of the considered configuration are visualized in Figure 7.2 (left), where the coupling interface Γ is marked by the red boundary. While the domain Ω^1 is a poroelastic domain $\Omega^1 \subseteq \Omega^{\mathrm{P}}$ for all considered setups, the second domain Ω^2 is specified either as a solid domain $\Omega^2 = \Omega^{\mathrm{S}}$ (variant *V-SP*) or a

poroelastic domain $\Omega^2 \subset \Omega^{\mathrm{P}}$ (variant *V-PP*). The domain Ω^2 is rigid, which is taken into account by a zero displacement Dirichlet in this domain. On the overall coupling interface $\Gamma = \Gamma^1 \cup \Gamma^2$, all conditions are incorporated according to the formulations presented in Sections 7.2.2 and 7.2.3. On the entire boundary of the poroelastic domain ($\partial\Omega^{\mathrm{P}} = \partial\Omega^1$ for *V-SP*, $\partial\Omega^{\mathrm{P}} = \partial\Omega^1 \cup \partial\Omega^2$ for *V-PP*) excluding most of the coupling interface ($\Gamma^1 \cup \Gamma^2 \setminus \Gamma^3$), a no-outflow condition on the poroelastic fluid ($v^{\mathrm{P},seepage,n} = 0$) is prescribed. Whereas this condition is enforced by a Dirichlet boundary condition for $\hat{v}^{\mathrm{P},n} = 0$ on boundaries which are fixed in normal direction $\underline{\hat{\boldsymbol{u}}}^{\mathrm{P}} \cdot \underline{\boldsymbol{n}} = 0$, a weak imposition (by a formulation similar to solid-poroelastic contact in Section 7.2.2.2) of this condition is applied for the remaining boundaries. The stamp Ω^1 is exposed to a constant-in-time Neumann load in negative $y-$direction on boundary $\Gamma^{\mathrm{P,N}}$ which induces the falling motion (see Figure 7.2 (right)). This will finally lead to a contacting of both domains Ω^1 and Ω^2. For $t > 1000$, a linearly increasing fluid Neumann load is prescribed on boundary $\Gamma^{\mathrm{F,N}}$ causing the lifting motion of the poroelastic stamp.

The density of the fluid is $\rho^{\mathrm{F}} = 10^{-3}$ and the dynamic viscosity is $\mu^{\mathrm{F}} = 1$. In the poroelastic domains the initial porosity is $\mathring{\phi} = 0.5$ and the isotrope material permeability $\underline{\boldsymbol{K}} = K \cdot \underline{\boldsymbol{I}}$ is specified by the scalar permeability K. As the flow resistance (given by the permeability) in the porous medium has an essential impact on the contacting and lifting behavior of the stamp, the solution is computed for two specifications of the permeability $K = 10^{-3}$ or $K = 10^{-4}$. The initial density $\rho_0^{\mathrm{S}} = 10^{-3}$ in the solid domain Ω^{S} and the macroscopic averaged initial density of the solid phase $\tilde{\rho}_0^{\mathrm{P^S}} = 10^{-3}$ in the poroelastic domain Ω^{P} are equal to the fluid density. A Neo-Hookean material model (2.17), with Young's modulus $E = 50$ and Poisson's ratio $\nu = 0$ accounts for the strain energy due to the macroscopic deformation of the solid phase ($\psi^{P,skel}(\underline{\boldsymbol{C}}^{\mathrm{P}}, J^{\mathrm{P}})$). Additionally, the volumetric contribution (2.48) with parameter $\kappa^{\mathrm{P}} = 100$ and a penalty contribution (2.49) with parameter $\eta^{\mathrm{P}} = 1$ are applied.

The computational meshes of the domains Ω^1 and Ω^2, which are fitted to the boundaries and interfaces, consist of 710 and 175 elements, respectively. To discretize the fluid domain, a structured grid with $16 \times 24 = 384$ elements is used. This computational mesh is not fitted to the interface Γ but fitted to the boundaries. Taking into account the rigid domain Ω^2, the contact interface stress $\overline{\sigma}^{\mathrm{S/P},nn}$ is exclusively based on the states of domain Ω^1. The reference slip length is specified to $\kappa_0 = 0.1$ and the model parameter for the BJ condition is $\alpha_{\mathrm{BJ}} = 1$. The constants for the Nitsche penalty parameters are $\gamma_0^{\mathrm{S/P},c} = 1$ and $\gamma_0^{\mathrm{FSI}} = \gamma_0^{\mathrm{FSI},t} = 35$. To reflect the varying dynamics of the system in the temporal discretization, three different sizes of the time step ($\Delta t = 0.01$ for $t \in [0, 20]$, $\Delta t = 0.2$ for $t \in [20, 420]$, $\Delta t = 2.0$ for $t > 420$) are applied in the Backward Euler scheme ($\theta = 1.0$).

Numerical Results and Discussion First, the computed results for both variants *V-SP* and *V-PP* in combination with the larger permeability $K = 10^{-3}$ are analyzed. In Figure 7.3, the computed vertical gap between both contacting interfaces is presented. It can be directly seen that the no-penetration condition of contact (7.7) is fulfilled as no negative values of the gap occur. At the initial phase the gap shrinks due to the vertical motion of the upper domain Ω^1. A zero gap, and thus contact between interfaces Γ^1 and Γ^2, occurs first for the mid point P_1. Contact of the right-most point P_0 is established later, and thus, in the meantime, a fluid subdomain not connected to the main part of the fluid domain occurs temporary close to P_0. Due to the permeability of the poroelastic domain, the fluid in this "island" is transported through

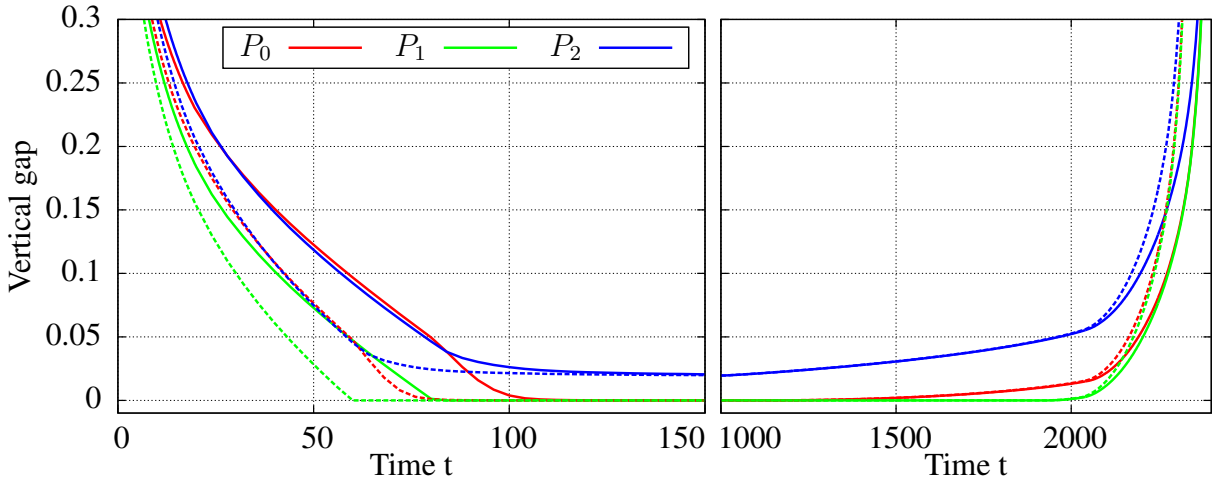

Figure 7.3: Computed vertical gap between the potentially contacting interfaces Γ^1 and Γ^2 at three positions for the scalar permeability $K = 10^{-3}$. The continuous lines show the results for variant *V-SP* while the dotted lines show the computed results for *V-PP*. The time interval $t \in [150, 1000]$ is not shown since the system is almost in rest. The positions P_0, P_1 and P_2 in the undeformed configuration are marked in Figure 7.2 (left) by green circles.

the poroelastic medium back to the main part of the fluid domain. For $t \approx 150$, where the vertical motion of domain Ω^1 almost finished, the left-most point P_2 did not contact the lower interface Γ^1. Due to the applied fluid load for $t > 1000$, a lifting domain Ω^1 can be observed. As expected, the separation of both contacting domains occurs for $t > 2000$ due to the fluid inertia. A comparison of both variants *V-SP* and *V-PP* reveals that all occurring processes are faster for the variant including two poroelastic domains. Nevertheless, the principal processes are similar and for low values of the fluid pressure (see Figure 7.3) in $t \in [100, 1500]$, as expected, almost equal.

In Figure 7.4, the average interface traction on the circular part of interface Γ^1 is shown. These quantities allow to analyze the correct contacting and lift-off behavior. At the initial phase, the overall traction which equals the FPI traction, evolves towards 2.0, which is the external load $||\hat{\underline{\boldsymbol{h}}}_0^{\mathrm{P,N}}||$. Due to the subsequent contacting process, an increasing fraction of the overall traction is transmitted by the contact traction. In the following period, the system comes to rest, and thus all fluid forces including the pressure vanish. As a result, the overall interface traction equals the contact traction. For $t > 1000$, due to the increasing fluid pressure an increasing fraction of overall traction is transmitted by the FPI traction. Finally, at the point in time where the average fluid pressure reaches the value 2.0 ($= ||\hat{\underline{\boldsymbol{h}}}_0^{\mathrm{P,N}}||$), contact between both domains releases, which is indicated by the vanishing contact traction. Due to the fluid dynamics, this lift-off occurs slightly after $t = 2000$, the point in time when the external load which is acting on the fluid boundary $\Gamma^{\mathrm{F,N}}$, reaches the value 2.0.

A more detailed look at Figure 7.4 reveals an additional aspect. At $t \approx 1400$, a discontinuity of the FPI traction and the contact traction can be observed. This occurs due to a simultaneous change of the interface conditions (from contact to FPI) on a large area in the neighborhood of position $x = 0$. As a result of the definition of the numerical interface traction in (7.23), still,

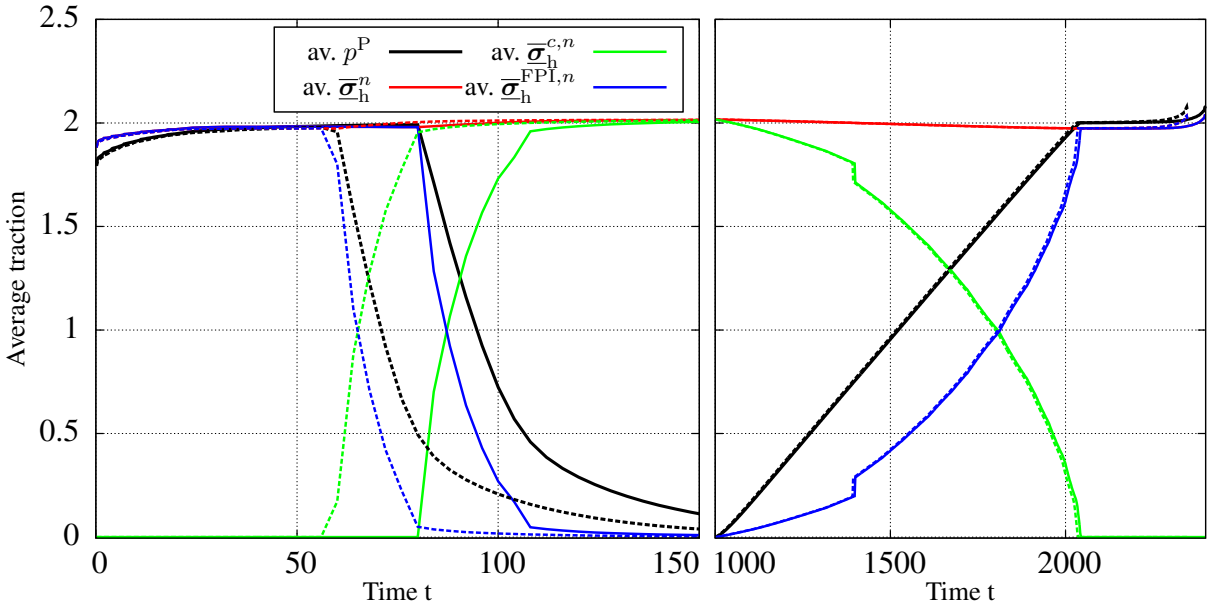

Figure 7.4: Computed average traction on the circular part of interface Γ^1 for the scalar permeability $K = 10^{-3}$. The average traction is computed in a post processing step by integration of the respective quantity (expressed by the nodal contributions on the poroelastic discretization) on the interface and division by the interface area. Shown are, "av. p^{P}", the average fluid pressure: based on the porous fluid pressure p^{P}, "av. $\overline{\boldsymbol{\sigma}}_{\mathrm{h}}^{n}$", the average overall traction: based on numerical interface traction (7.23) and (7.32), "av. $\overline{\boldsymbol{\sigma}}_{\mathrm{h}}^{c,n}$", the average contact traction: based only on the right-hand side of numerical normal interface traction (7.23), "av. $\overline{\boldsymbol{\sigma}}_{\mathrm{h}}^{\mathrm{FPI},n}$", the average FPI traction: based only on the left-hand side of numerical normal interface traction (7.23) and the tangential interface traction (7.32). The continuous lines show the results for variant *V-SP* while the dotted lines show the computed results for *V-PP*. The time interval $t \in [150, 1000]$ is not shown since the system is almost in rest.

there is no discontinuity in the overall traction and thus on the effect of interface treatment on the overall FPSCI system.

To give a comprehensive view on the presented formulation for FPSCI, the previously presented computations where also performed with a reduced permeability $K = 10^{-4}$, which has a significant influence on the system behavior. The computed vertical gap at three positions on the interface is shown in Figure 7.5. While contact and a lift-off process of the domains Ω^1 and Ω^2 still occurs, all processes are slowed down and the system does not completely come to rest after contact is established. A comparison of the computed vertical gap for $K = 10^{-3}$ and $K = 10^{-4}$ at $t \approx 1000$ reveals that the deformation of the interface is almost equal. This behavior is expected due to the low fluid pressure.

In Figure 7.6, the average interface traction on the circular part of interface Γ^1 computed for the permeability $K = 10^{-4}$ is shown. The discussion of the principal processes for the case with the higher permeability applies also for this case and, thus, only differences are mentioned here. In contrast to the computed results shown in Figure 7.4, at $t \approx 450$ and $t \approx 600$, the discontinuity of the FPI traction and the contact traction can be observed already in the contacting phase. Still, the computed overall traction is continuous also for this point in time. Due to the increased fluid resistance for this configuration, the porous pressure on the interface does not reach zero at $t = 1000$.

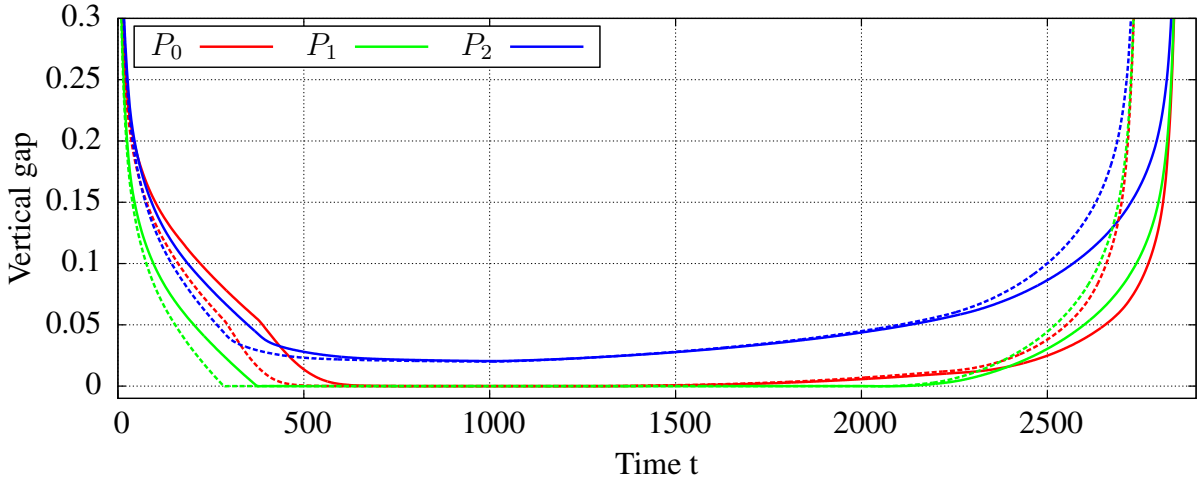

Figure 7.5: Computed vertical gap between the potentially contacting interfaces Γ^1 and Γ^2 at three positions for the scalar permeability $K = 10^{-4}$. The continuous lines show the results for variant *V-SP* while the dotted lines show the computed results for *V-PP*. The positions P_0, P_1 and P_2 in the undeformed configuration are marked in Figure 7.2 (left) by green circles.

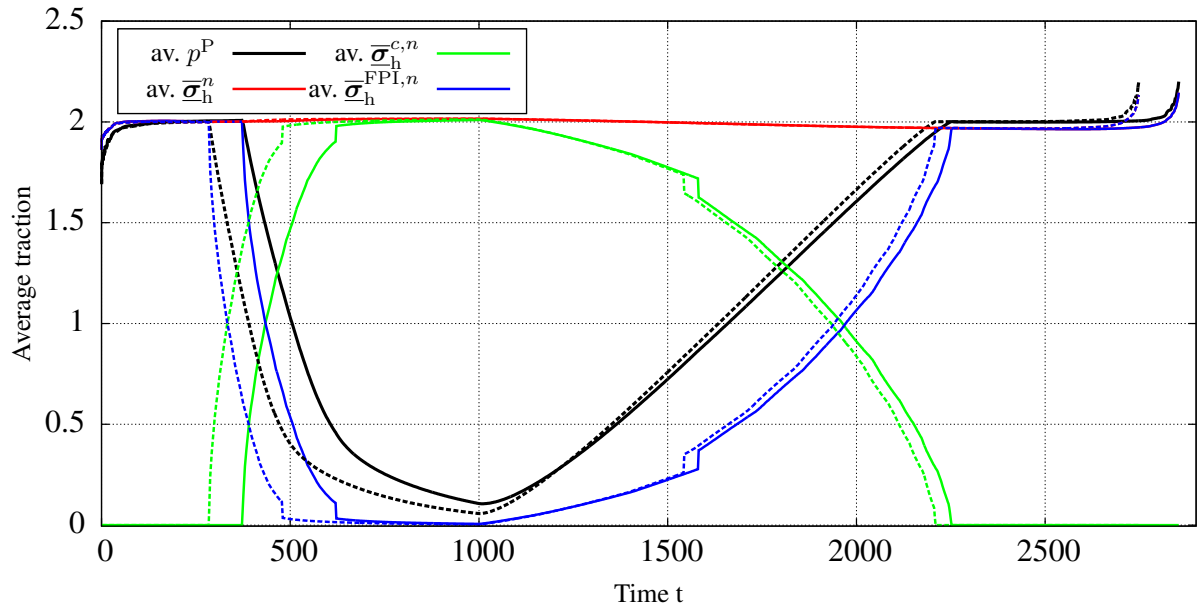

Figure 7.6: Computed average traction on the circular part of interface Γ^1 for the scalar permeability $K = 10^{-4}$. The average traction is computed in a post processing step by integration of the respective quantity (expressed by the nodal contributions on the poroelastic discretization) on the interface and division by the interface area. Shown are, "av. p^{P}", the average fluid pressure: based on the porous fluid pressure p^{P}, "av. $\overline{\boldsymbol{\sigma}}_{\mathrm{h}}^{n}$", the average overall traction: based on numerical interface traction (7.23) and (7.32), "av. $\overline{\boldsymbol{\sigma}}_{\mathrm{h}}^{c,n}$", the average contact traction: based only on the right-hand side of numerical normal interface traction (7.23), "av. $\overline{\boldsymbol{\sigma}}_{\mathrm{h}}^{\mathrm{FPI},n}$", the average FPI traction: based only on the left-hand side of numerical normal interface traction (7.23) and the tangential interface traction (7.32). The continuous lines show the results for variant *V-SP* while the dotted lines show the computed results for *V-PP*.

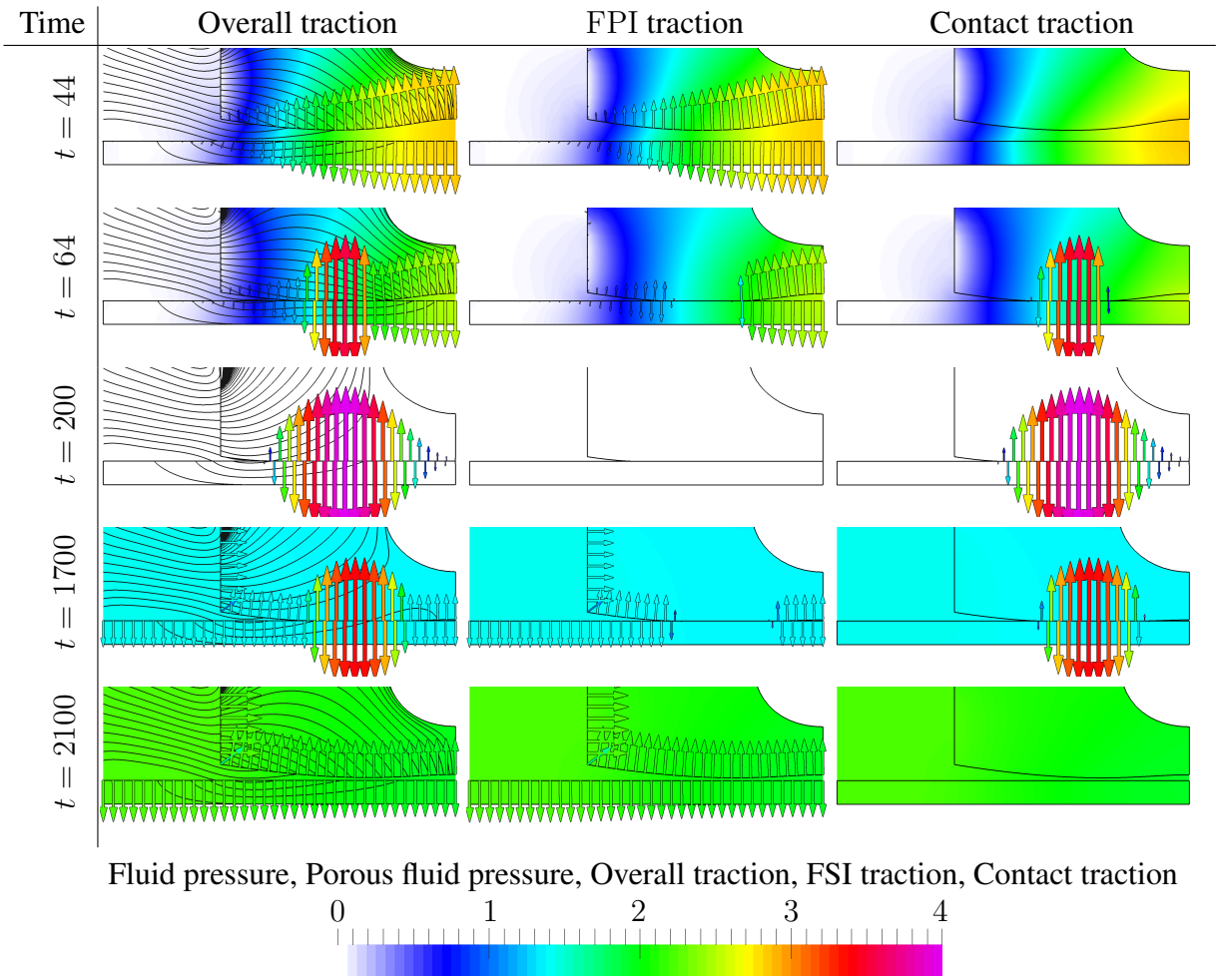

Figure 7.7: Visualization of the computed falling, contacting, and lifting of a rounded poroelastic stamp for variant *V-PP* with permeability $K = 10^{-3}$ at five instances in time $t = 44, t = 64, t = 200, t = 1700$, and $t = 2100$. The color code in the fluid domain and poroelastic domain illustrates the fluid pressure or the porous fluid pressure, respectively. The arrows represent the interface traction and are colored according to the color code. The contact traction includes the right-hand side of numerical normal interface traction (7.23). The overall traction includes all contributions to $\overline{\underline{\boldsymbol{\sigma}}}^n_{\mathrm{h}}$ ((7.23) and (7.32)). The FPI traction equals the overall traction minus the contact traction. The traction arrows are based on the nodal contributions of the interface traction to the weak form of the poroelastic domain. In the left-most column, the fluid flow is visualized by black streamlines which are based on $\underline{\boldsymbol{v}}^{\mathrm{F}}$ in the fluid domain and on $\underline{\boldsymbol{v}}^{\mathrm{P},seepage}$ in the poroelastic domain, respectively.

To illustrate the results, a detailed view of the computed solution for variant *V-PP* with permeability permeability $K = 10^{-3}$ is given in Figure 7.7. It can be seen that for all instances in time, the FPI traction equals the surrounding fluid pressure (cf. middle column) as the normal viscous interface traction is negligible for this problem setup. In the transition zone to contact, a smaller nodal FPI traction can be observed which is a result of the contact enforcement in the support of this node (see contact traction arrows). On the other hand, the contact traction is always larger than the fluid pressure (excluding the transition zone, where nodes get both the FPI and the contact traction contributions). This is a result of condition (7.8) and reproduced by the numerical procedure. The overall traction, which is finally effecting the poroelastic domains, combines the FPI traction and the contact traction. It can be observed that the overall traction curve is continuous also in the transition zone between contact and FPI.

Investigation of the Fluid Stress Extension Strategy In Section 7.2.2.3, a physically motivated extension of the fluid stress based on the porous fluid pressure is presented. While this seems more complex than the constant extension, which is applied in Chapter 6, it is advantageous for certain configuration due to the improved physical foundation. To demonstrate such a situation, the configuration variant *V-PP* with permeability $K = 10^{-3}$ considered previously is slightly modified. For $t > 1000$, instead of the no-outflow condition on the porous boundary Γ^4, a fluid load, with the same time-dependent absolute value for $\hat{h}^{\mathrm{P^F,N}}$ as shown in Figure 7.2, is prescribed. On the fluid boundary $\Gamma^{\mathrm{F,N}}$ a zero-traction boundary condition is applied.

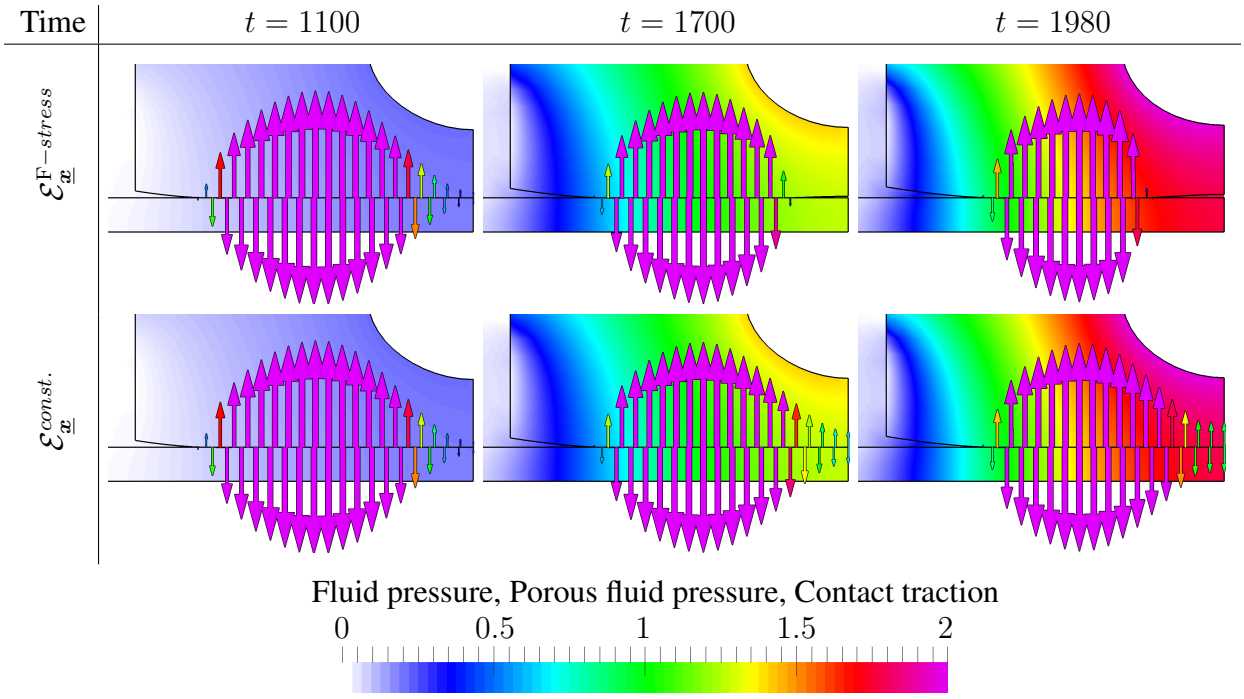

Figure 7.8: Detailed view on the computed solution for the modified configuration to test the fluid stress extension strategy at three instances in time $t = 1100, t = 1700$, and $t = 1980$. In the top row the physically motivated fluid stress extension approach (7.30) is applied. In the bottom row the constant fluid stress extension approach (7.29) is applied. The color code in the fluid domain and the poroelastic visualizes the fluid pressure. The arrows represent the contact traction and are colored by its magnitude.

In Figure 7.8, a comparison of the computed results for the physically motivated fluid stress extension approach (7.30) and the constant fluid stress extension approach (7.29) is given. The difference between both configurations occurs close to the position $x = 0$. For $t = 1100$, there is no difference between both extension strategies since the porous fluid pressure p^{P} is smaller than the contact traction in the entire contact zone. This changed at $t = 1700$, here the right-most part of the stamp releases contact due to the increasing fluid pressure when using the physically motivated extension approach. In contrast to that, when applying the constant extension strategy no release occurs. This is expected since the fluid pressure in the fluid domain, which is extended by this approach, is lower than the porous pressure at $x = 0$. It can be seen that the contact traction around $x = 0$ is lower than the fluid pressure, and thus it is non-physical as it violates the contact condition (7.8). Note that the contact traction and fluid traction have a negative sign. In principle the same, yet more pronounced, configuration can be observed for the point in time $t = 1980$.

This difference between the two extension approaches is a result of the large distance between the contact release zone and the fluid domain as well as the prevalent pressure gradient. For configurations where one of these two criteria is not fulfill, the error introduce by the constant extension approach will be less pronounced or even not observable. Still, for more complex configurations this cannot be ruled out in general and, thus, the physical motivated extension strategy which utilizes the porous pressure will be applied for all computations.

7.4.2 Flow-Driven Squeezed Elastic Structure

The computational analysis of the squeezing of an initially cylindrical elastic body Ω^2 through a second elastic body Ω^1 in surrounding fluid, is the second numerical example considered for FPSCI. Different configurations with one or two permeable poroelastic bodies allow to demonstrate the capability of the formulation to handle frequent changes between contact and $\mathrm{FSI/FPI}$ including large contacting areas and essential topological changes. The same problem configuration was already analyzed for FSCI with impermeable solids in Chapter 6.

Problem Description The geometric problem configuration as well as all basic boundary conditions are shown in Figure 7.9 (left). Three variants with a different classification of poroelastic and impermeable elastic domains are taken into account. In variant *V-PP*, both domains $\Omega^1 \cup \Omega^2 = \Omega^{\mathrm{P}}$ are poroelastic, in variant *V-SP*, the first domain is an impermeable elastic solid $\Omega^1 = \Omega^{\mathrm{S}}$ while the second domain is poroelastic $\Omega^2 = \Omega^{\mathrm{P}}$, and finally in variant *V-PS*, the reverse configuration $\Omega^1 = \Omega^{\mathrm{P}}$ and $\Omega^2 = \Omega^{\mathrm{S}}$ is considered. The variant *V-SS* including impermeable solids in both domains $\Omega^1 \cup \Omega^2 = \Omega^{\mathrm{S}}$ was already presented in Chapter 6 and the results will be included in the discussion for comparison. On the inflow boundary Γ^{in}, a parabolic velocity profile including an initial ramp-up phase $\underline{\hat{\boldsymbol{v}}}^{\mathrm{F}} = [0, -100(1-x^2)4000t]^{\mathsf{T}}$ for $t \in [0.0, 0.00025]$ and $\underline{\hat{\boldsymbol{v}}}^{\mathrm{F}} = [0, -100(1-x^2)]^{\mathsf{T}}$ for $t \in [0.00025, 0.02]$ is prescribed as Dirichlet boundary condition. On the outflow boundary Γ^{out}, a zero-traction Neumann boundary condition is applied.

The density and dynamic viscosity of the incompressible fluid is $\rho^{\mathrm{F}} = 10^{-6}$ and $\mu^{\mathrm{F}} = 10^{-5}$, respectively. The initial density in the solid domain $\rho_0^{\mathrm{S}} = 10^{-6}$ in Ω^{S} and the macroscopic averaged initial density of the solid phase in the poroelastic domain $\tilde{\rho}^{\mathrm{PS}} = 10^{-6}$ are equal to the fluid density. In the poroelastic domain Ω^{P}, the initial porosity is $\mathring{\phi} = 0.5$ and,

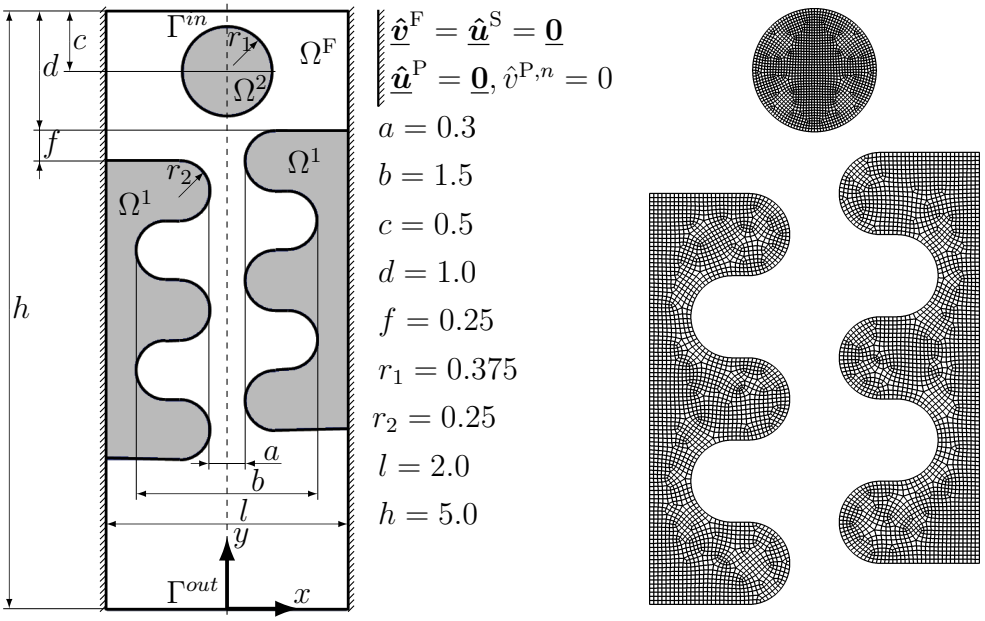

Figure 7.9: Geometry and boundary conditions for the flow driven squeezed elastic structure. Different problem configurations with poroelastic (Ω^{P}) or impermeable elastic (Ω^{S}) domains Ω^1 and Ω^2 are considered. All geometric dimensions which are not explicitly specified in domain Ω^1, are defined by symmetry and replication of the given dimensions (left). Visualization of the discretization for the domains Ω^1 and Ω^2 (right).

to account for changes of the porous flow resistance, the material permeability is based on an adaption of the Kozeny-Carman formula (see e.g. the textbook of Coussy [67]) $\underline{\boldsymbol{K}} = K\underline{\boldsymbol{I}} = \mathring{K}(1-\mathring{\phi}^2)\mathring{\phi}^{-3}(J^{\mathrm{P}}\phi)^3(1-\left(J^{\mathrm{P}}\phi\right)^2)^{-1}\underline{\boldsymbol{I}}$ with the initial scalar permeability $\mathring{K} = 10^{-5}$. The strain energy density function to characterize the elastic behavior in the solid domains ($\psi^{\mathrm{S}} = \psi_{NH}(\underline{\boldsymbol{C}}^{\mathrm{S}}, J^{\mathrm{S}})$) as well as the macroscopic behavior of the solid phase in the poroelastic domain ($\psi^{\mathrm{P},skel} = \psi_{NH}(\underline{\boldsymbol{C}}^{\mathrm{P}}, J^{\mathrm{P}})$) is given by a Neo-Hookean model (2.17). In the domain Ω^1, the Young's modulus is $E^{\Omega^1} = 200$ and Poisson's ratio is $\nu^{\Omega^1} = 0.3$, whereas the initially circular domain Ω^2 has a lower stiffness, with Young's modulus $E^{\Omega^2} = 100$ and Poisson's ratio $\nu^{\Omega^2} = 0.3$. In in the poroelastic domain Ω^{P} the additional contributions to the strain energy density function are the volumetric contribution (2.48) with parameter $\kappa^{\mathrm{P}} = 40$ and the penalty contribution (2.49) with parameter $\eta^{\mathrm{P}} = 1$.

The fluid domain is discretized structured and unfitted to the interface by a discretization with $120 \times 300 = 36000$ bilinear elements in the domain $[-1, 1] \times [0, 5]$. The interface-fitted discretizations of the domains Ω^1 and Ω^2 is depicted in Figure 7.9 (right) and consists of 4890 and 1562 bilinear elements, respectively. The contact stress $\overline{\sigma}^{\mathrm{S/P},nn}$ is based on a harmonic weighting between the stress representation of the adjacent contacting domains. The reference slip length is specified to $\kappa_0 = 0.1$ and the model parameter for the BJ condition is $\alpha_{\mathrm{BJ}} = 1$. The constants for the Nitsche penalty parameters are $\gamma_0^{\mathrm{S/P},c} = 1$ and $\gamma_0^{\mathrm{FSI}} = \gamma_0^{\mathrm{FSI},t} = 1$. The discretization in time is performed with $\theta = 1$ and the time step size $\Delta t = 2 \cdot 10^{-5}$ for the initial phase and a varying time step size $\Delta t \in [5 \cdot 10^{-6}, 2 \cdot 10^{-7}]$ for the subsequent processes to account for the changes of the dynamic of the investigated system.

Numerical Results and Discussion In Figure 7.10, an overview of the entire computed process for variant *V-PP* is given by a series of snapshots. The fluid flow induces a vertical motion

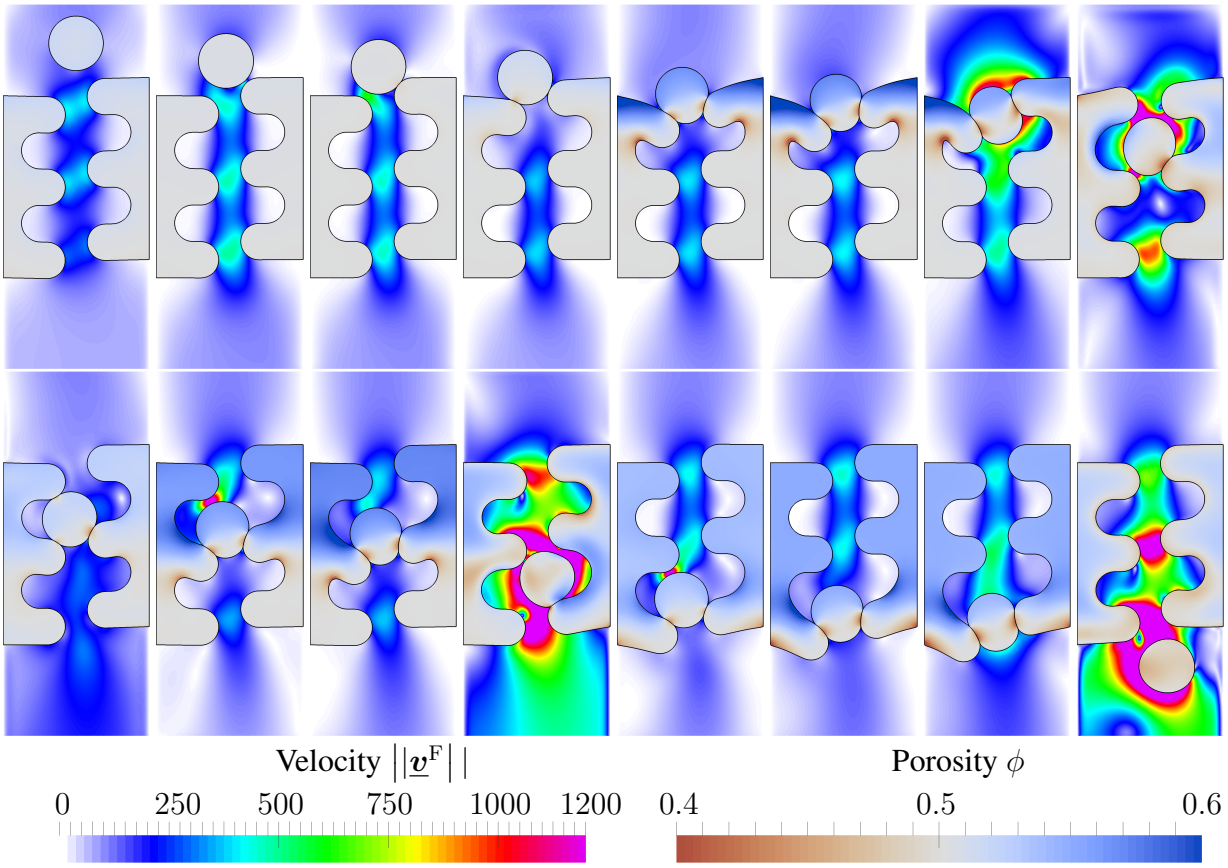

Figure 7.10: Visualization of the computed fluid velocity in the fluid domain Ω^{F} and the computed porosity in the deformed poroelastic domain Ω^{P} for variant *V-PP*. The color code represents the fluid velocity magnitude in the fluid domain and the porosity (element-wise constant visualization) in the poroelastic domain. Different points in time are represented from top-left to bottom-right with $t = \{0.0005, 0.0025, 0.003, 0.004, 0.007, 0.008, 0.0085, 0.009\}$ in the first row, and $t = \{0.01, 0.012, 0.013, 0.014, 0.0165, 0.0185, 0.019, 0.0195\}$ in the second row.

of the poroelastic domain Ω^2 in the initial phase $(0 < t < 0.00288)$. First contact between the domains Ω^1 and Ω^2 establishes at $t = 0.00288$, which is followed by a second contacting event at $t = 0.00364$. As a result, the topology of the fluid domain Ω^{F} is separated into a lower and upper subdomain. In the subsequent phase $(0.00364 < t < 0.008)$, the pressure in the upper fluid domain increases which leads to a squeezing of Ω^2 and deformation of Ω^1. The porosity in the poroelastic domain increases close to the regions of high pressure, whereas a locally reduced porosity can be observed at locations including compression of the poroelastic medium. In the phase $t > 0.0084$, the domain Ω^2 is accelerated rapidly by the release of the elastic energy stored in the deformation of the poroelastic medium. Within this highly dynamic process contact on the side $x > 0$ releases and the fluid domain is recombined. By reestablishing contact at $t = 0.0087$, the general process starts again by passing through similar steps as described above. Nevertheless, due to the varying initial conditions and the varying geometric setup the

process does not repeat exactly and, thus, allows demonstrating the robustness of the presented formulation for this challenging configuration.

A more detailed view on the computed process comparing all considered variants *V-PS*, *V-SP*, and *V-PP* is given in Figure 7.11. In the first row, the initial contacting process for all three variants can be observed. Compared to the contact of impermeable bodies (*V-SS*), the inflow of fluid mass in the poroelastic domains leads to a lower pressure and as a result to a less pronounced reduction of the relative velocity between both bodies. Contact establishes faster for all variants including contact with a permeable body than for contact between impermeable bodies. The second row shows a state where the fluid domain is separated into a upper subdomain with high pressure level and a lower subdomain with low pressure by the squeezed domain Ω^2 . Due to the significantly higher flow resistance in the poroelastic domain compared to the fluid domain, almost the entire drop in the fluid pressure occurs in the poroelastic domains. The fluid flow from the upper fluid subdomain passes through the poroelastic domain and enters the lower fluid subdomain as indicated by the streamlines and arrows. In the third row, the dynamic process where the domain Ω^2 deforms and squeezes through the narrowest constriction is shown. Due to the relative tangential velocity of Ω^1 and Ω^2 and the associated local compression and expansion, a high seepage velocity $\underline{\boldsymbol{v}}^{\mathrm{P},seepage}$ occurs on the interface Γ^{FP} close to the contact zone. This effect is especially pronounced for the variants *V-PS* and *V-SP*. As a result of the dynamic process, a local maximum of the pressure can be identified in the domain Ω^2 for variants *V-SP* and *V-PP*. The corresponding pressure gradient leads to a fluid flow through the poroelastic contact interface for variant *V-PP*. Finally, the last row shows the computed states of the system for a point in time which is minimally later. Due to the high fluid pressure in the fluid domain, a high seepage velocity $\underline{\boldsymbol{v}}^{\mathrm{P},seepage}$ can be observed for all configurations.

In Figure 7.12, a comparison of the temporal evolution of the vertical displacement at the lowest point (in y-direction) of domain Ω^2, the fluid pressure at a specific point on the inflow boundary Γ^{in}, the fluid flow rate through the outflow boundary Γ^{out}, and the transported fluid volume through the outflow boundary Γ^{out} including all variants *V-SS*, *V-PS*, *V-SP*, and *V-PP* is given. While the process is similar for all variants, these curves reveal that the overall process is slowed down by the poroelastic medium. This is expected as a part of the fluid volume passes through the poroelastic medium. While the permeability in domain Ω^2 has only a small effect on the overall process (compare variants *V-SS* and *V-SP*), the permeability of domain Ω^1 is crucial. The flow rate at the outflow boundary, shown in Figure 7.12 (third row), is subject to strong fluctuations around the average flow rate at the inflow boundary due to the volume change of the domains Ω^1 and Ω^2. A comparison of the transported fluid volume through the outflow boundary with the transported volume through the inflow boundary, shown in Figure 7.12 (bottom row), reveals that no relevant loss in mass occurs. While temporary deviations arise due to the compression and expansion of the domains Ω^1 and Ω^2, no increase in the difference of the time averaged values between inflow and outflow can be identified.

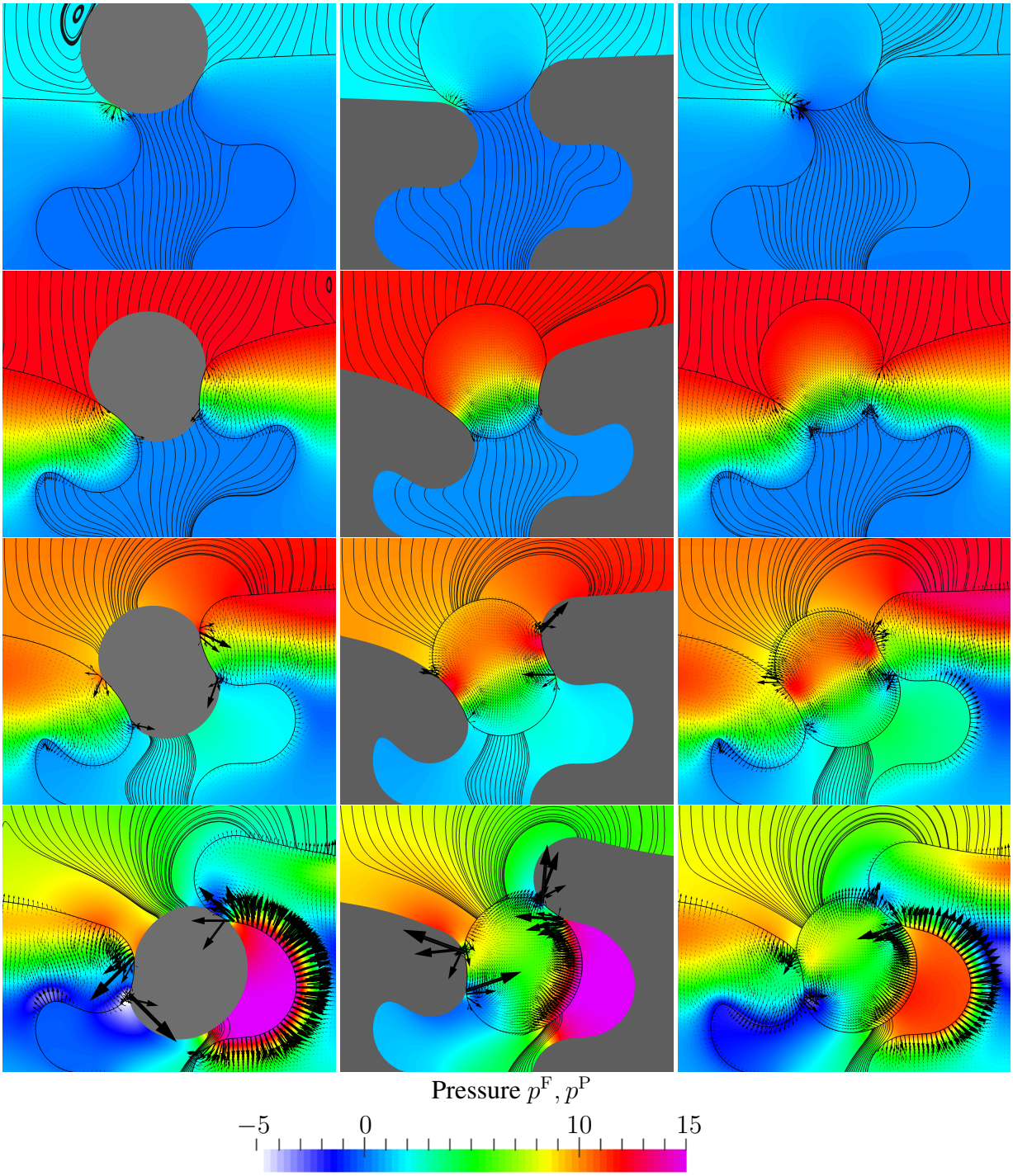

Figure 7.11: Visualization of the computed fluid velocity and pressure in the fluid domain Ω^{F}, the computed deformation of the solid domain Ω^{S}, and the computed pressure and seepage velocity in the poroelastic domain Ω^{P}. The color code represents the pressure p^{F} and p^{P} in the fluid and poroelastic domain, respectively. The black streamlines in the fluid domain Ω^{F} are computed by based on the velocity $\underline{\boldsymbol{v}}^{\mathrm{F}}$. The black arrows in the poroelastic domain indicate the seepage velocity $\underline{\boldsymbol{v}}^{\mathrm{P},seepage}$. The computed solution at four characteristic points in time from top-row to bottom-row are represented for each variant: *V-PS*: $t = 0.0037, t = 0.0071, t = 0.0077$, and $t = 0.0079$ (left-column); *V-SP*: $t = 0.0034, t = 0.0060, t = 0.0066$, and $t = 0.0068$ (mid-column); *V-PP*: $t = 0.0036, t = 0.0071, t = 0.0085$, and $t = 0.0086$ (right-column). The points in time are selected to compare the three variants based on a similar deformation state.

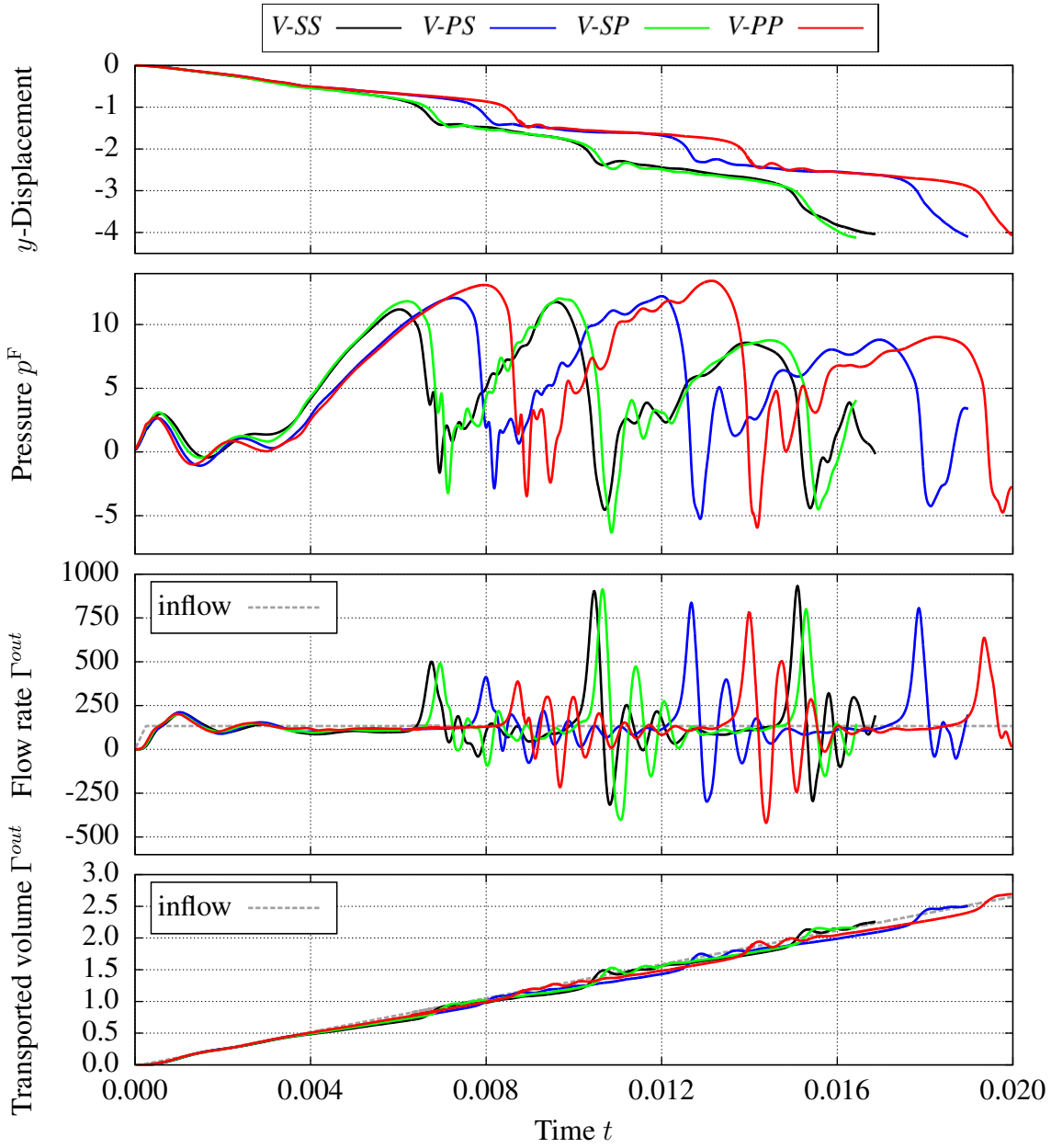

Figure 7.12: Comparison of the computed temporal evolution of different characteristic scalar quantities for the variants *V-SS*, *V-PS*, *V-SP*, and *V-PP*. Computed vertical displacement of a point in Ω^2 with the initial coordinate $\underline{\boldsymbol{X}} = [0, 4.4125]^{\mathsf{T}}$ (top row). The fluid pressure at the point with coordinate $\underline{\boldsymbol{x}} = [0, 5.0]^{\mathsf{T}}$ on the inflow boundary Γ^{in} of the fluid domain (second row). The flow rate through the outflow boundary Γ^{out} and the prescribed flow rate through the inflow boundary Γ^{in} (third row). The transported fluid volume through the outflow boundary Γ^{out} and the prescribed transported fluid volume through the inflow boundary Γ^{in} (bottom row). The entire domain Ω^2 is inside the computational discretization of the fluid domain Ω^{F} for the visualized time interval.

7.4.3 3D Analysis of a Double-Leafed Valve with Poroelastic Leaflets

As a last numerical example for FPSCI, the analysis of a double-leafed valve with poroelastic leaflets is presented to demonstrate the applicability to more general 3D configurations. In order to investigate the closing as well as the opening of the valve, the problem configuration can be split in two phases. In the first phase, the closing of the valve including contact of the leaflets is analyzed by prescribing an increasing fluid traction on the outflow boundary. The process of the valve opening is investigated in the subsequent phase by a prescribed increasing fluid traction on the inflow boundary.

Problem Description The problem setup is identical to the configuration presented in Section 6.4.4 including the geometric setup given in Figure 6.17 with the exception that the leaflets are not modeled impermeable but as fluid-saturated poroelastic structures. Therefore, the two valve leaflets characterize the poroelastic domain $\Omega^{\mathrm{P}} = \Omega^2$ and only the cylindrical tube represents the solid domain $\Omega^{\mathrm{S}} = \Omega^1$. All boundary conditions and material parameters already specified in Section 6.4.4 also apply to this configuration. Thus, only additional specification are given in the following. On the common boundary of the solid and the poroelastic domain $\partial\Omega^{\mathrm{S}} \cap \partial\Omega^{\mathrm{P}}$, a vanishing normal seepage velocity $v^{\mathrm{P},seepage,n} = 0$ is prescribed by an approach similar to the porous flow formulation for solid-poroelastic contact presented in Section 7.2.2.2.

In the poroelastic domain Ω^{P}, the initial porosity is $\mathring{\phi} = 0.5$, the constant material permeability $\underline{\boldsymbol{K}} = K \cdot \underline{\boldsymbol{I}}$ is specified by the scalar permeability $K = 10^{-5}$, and the macroscopic averaged initial density of the solid phase is $\tilde{\rho}_0^{\mathrm{PS}} = 10^{-3}$. A Neo-Hookean material model (2.17), with Young's modulus $E = 2000$ and Poisson's ratio $\nu = 0.3$ accounts for the strain energy due to the macroscopic deformation of the solid phase ($\psi^{P,skel}(\underline{\boldsymbol{C}}^{\mathrm{P}}, J^{\mathrm{P}})$) in the poroelastic domain. Additionally, the volumetric contribution (2.48) with parameter $\kappa^{\mathrm{P}} = 1000$ and a penalty contribution (2.49) with parameter $\eta^{\mathrm{P}} = 1$ are applied. The solid domain is discretized with 132727 hexahedral tri-linear elements and the poroelastic domain with 58897 hexahedral tri-linear elements, which are fitted to the boundaries of the corresponding domain. The contact stress $\overline{\sigma}^{\mathrm{S/P},nn}$ is weighted harmonically between the stress representation of the contacting poroelastic domains. The reference slip length is specified to $\kappa_0 = 0.1$ and the model parameter for the BJ condition is $\alpha_{\mathrm{BJ}} = 1$. The constants for the Nitsche penalty parameters are $\gamma_0^{\mathrm{S/P},c} = 1$ and $\gamma_0^{\mathrm{FSI}} = \gamma_0^{\mathrm{FSI},t} = 35$. A time step length in the range $\Delta t = [10^{-4}, 2 \cdot 10^{-4}]$ is utilized for the temporal discretization with the backward Euler scheme ($\theta = 1$).

Numerical Results and Discussion In Figure 7.13 and Figure 7.14, a visualization of the computed solution for the double-leafed valve with poroelastic leaflets at six points in time is given. A comparison with the results computed for the impermeable leaflets in Section 6.4.4 reveals that the process does not change fundamentally due to the permeability. As a consequence of the significantly higher fluid resistance in the poroelastic domain, the drop in pressure for the closed valve ($t \in [0, 0.04]$) occurs mainly in the leaflets, whereas a constant pressure can be observed in both fluid chambers of the valve. In contrast to the impermeable configuration, for $t = 0.02$, a fluid flow in the valve occurs due to the permeability of the leaflets, which is visualized in Figure 7.13. In the valve opening phase ($t \in [0.04, 0.08]$), the distance between both

leaflets is smaller than for the impermeable configuration. This is expected since the difference of the fluid pressure between the two sides of the leaflets is reduced due to the permeability and the interface velocity slip due to the BJ condition.

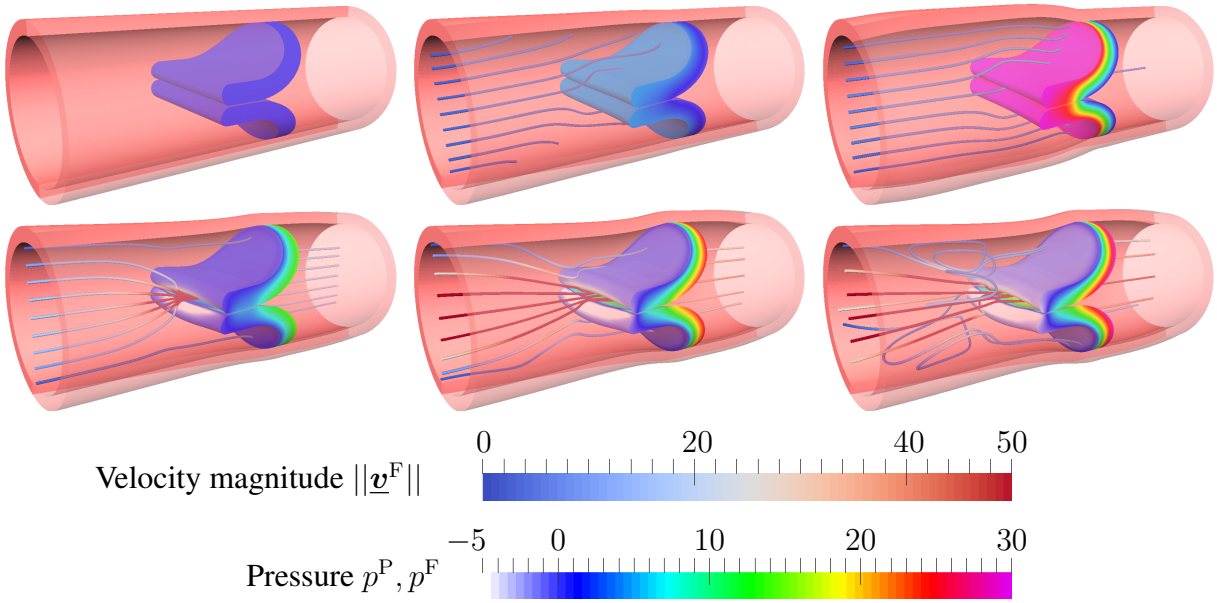

Figure 7.13: Visualization of the computed fluid velocity and deformation solution for the configuration with $\alpha = \pm\pi/12$ at six instances in time, from top-left to bottom-right: $t = 0.0, t = 0.005, t = 0.02, t = 0.05, t = 0.055$, and $t = 0.06$. The streamlines visualize the fluid velocity magnitude for $||\underline{\boldsymbol{v}}^{\mathrm{F}}|| \geq 0.8$.

In Figure 7.15, the computed flow rates at the inflow boundary Γ^{in} and the outflow boundary Γ^{out} are shown. For validation, both variant with $\alpha = 0$ and $\alpha = \pm\pi/12$ and also the flow rates computed for the impermeable configuration in Section 6.4.4 are depicted therein. Contrary to the impermeable configuration, in the valve closing phase $t \in [0, 0.04]$, an effective fluid flow from Γ^{out} to Γ^{in} due the permeability of the leaflets can be observed. The flow rate through the boundary Γ^{out} additionally includes the superimposed fluid flow due to the volumetric change of the left valve chamber. In the valve opening phase $t \in [0.04, 0.08]$, a significantly higher flow rate compared to the impermeable configuration can be observed. This increased flow rate results from the flow through the leaflets and the velocity slip on the interface Γ^{FP} due to the BJ condition. Comparing the symmetric $(\alpha = 0)$ and the rotated $(\alpha = \pm\pi/12)$ configuration reveals, that the disturbance by the rotation does not essentially deteriorate the process of the valve. Only in the initial phase ($t \in [0, 0.004]$) a difference can be observed, which is due to the prescribed rotational motion on Γ^{in} and Γ^{out}.

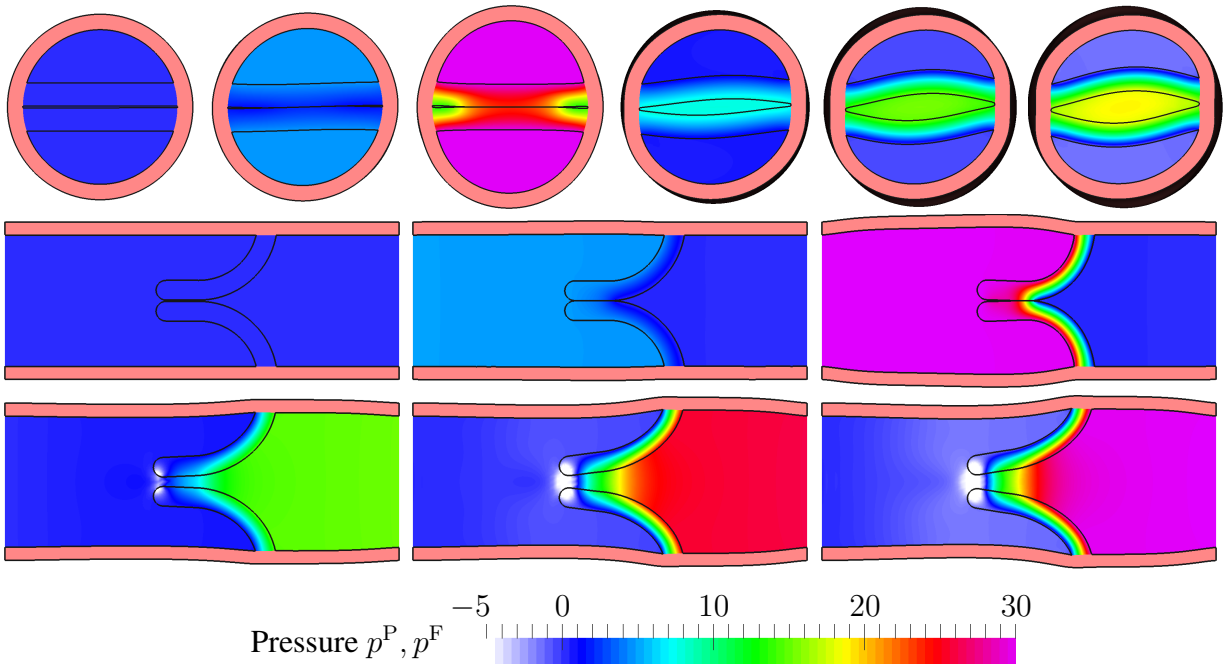

Figure 7.14: Computed fluid pressure and deformation solution for the configuration with $\alpha = \pm\pi/12$ at six instances in time from (top-)left to (bottom-)right: $t = 0.0, t = 0.005, t = 0.02, t = 0.05, t = 0.055$, and $t = 0.06$. Cross-sectional view at $x = 0.15$ in the first row. Cross-sectional view at $z = 0$ in row two and three.

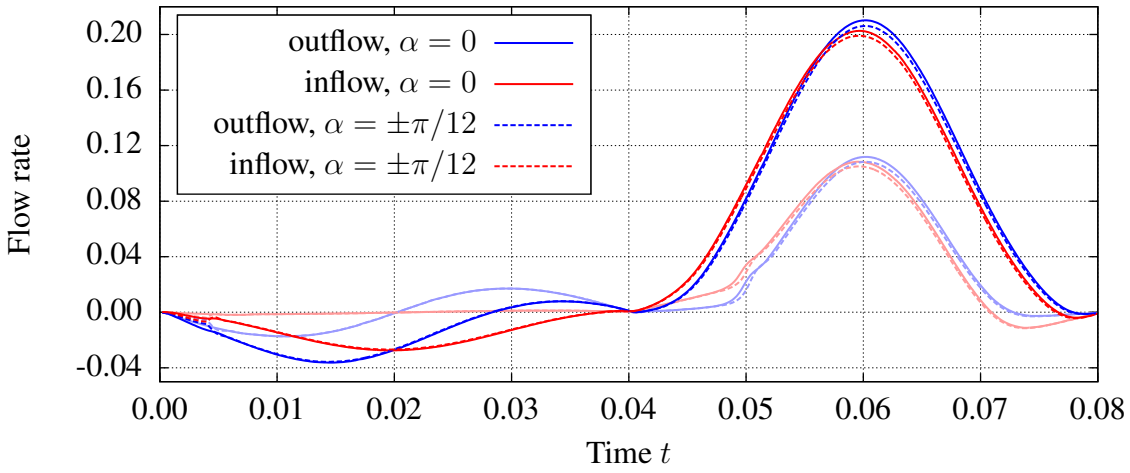

Figure 7.15: Computed flow rates at the inflow boundary Γ^{in} and the outflow boundary Γ^{out}. The normal vector is oriented in negative x-direction. For comparison, the computed flow rates of the impermeable configuration, which were already presented in Section 6.4.4, are additionally shown by the light-red and light-blue curves.

8 Summary and Outlook

Summary In this thesis, a group of computational methods to predict the mechanical processes of complex systems, which include the general interaction of impermeable and permeable structures with surrounding fluid is developed. Potential contact interaction between the structures as well as the strong interaction of the fluid with the structures are the central challenges for the design of such numerical methods. The developed formulations resolve limitations of previously presented approaches such as general applicability, consistency down to a vanishing fluid gap including topological changes of the fluid domain, and use of appropriate discrete fluid solution spaces especially for the fluid pressure.

Since the underlying physical processes of contact vary depending on the microstructure of the contact surfaces, different physical models are introduced that take rough and smooth surfaces into account. For the development of the required numerical formulations, computational approaches known from problems with reduced complexity are extended and adapted or new methods are formulated to result in a coherent framework of fluid-structure-contact interaction (FSCI) or fluid-poroelasticity-structure-contact interaction (FPSCI). Formulations which are valid for large deformations and nonlinear constitutive relations are utilized for the impermeable and permeable structures. The governing equations for the permeable poroelastic domains include incompressible pore flow based on the Darcy equation and a deformation-dependent porosity and permeability. To account for the inherent topological changes of the fluid domain, which naturally arise as a consequence of contact between structural bodies, the CutFEM is utilized for the discretization of the Navier-Stokes equations in the fluid domain. This includes the well-known ghost penalty stabilization, a technique that ensures a robust numerical formulation for arbitrarily aligned intersections of the fluid elements with embedded boundaries or interfaces. The CutFEM enables the application of computational meshes which are not fitted to the embedded interfaces and, thus, require no movement of the fluid discretization to accurately capture the different types of interfaces. As a result, issues arising from the distortion of fluid elements in the contact zone are avoided beforehand. Interface conditions between the viscous fluid and the respective structures are incorporated in a weak sense by various formulations of Nitsche-based methods. To incorporate the contact conditions, numerical formulations based on a dual Mortar Lagrange multiplier technique and the Nitsche method are developed. Since the focus of this thesis is on configurations with strongly interacting domains, a simultaneous monolithic solution approach for the coupled system is utilized in all formulations. It should be stressed that a comprehensive testing of all presented formulations by numerical tests and examples is carried out in order to demonstrate the broad applicability of the numerical approaches which are not limited to specific configurations.

In order to provide a solid foundation for the development of numerical approaches for FSCI and FPSCI, the CutFEM FSI formulation is introduced and validated. In addition to the commonly used representation of the FSI interface traction by the fluid stress, a formulation which utilizes the solid stress is developed. Such a formulation is promising for certain combinations

of solid and fluid material parameters (large contrast problems) and advantageous due to the fact that the solid stress is not based on intersected elements. A local generalized eigenvalue problem is utilized to ensure a stable discrete formulation for the Nitsche-based method with solid-sided interface stress representation especially when taking nonlinear solid constitutive relations and the deformation of the computational mesh into account. Various numerical tests demonstrate the optimal spatial convergence behavior and the proper scaling of all numerical parameters of the CutFEM FSI formulation. The numerical prediction of a 3D spring-damper system demonstrates the general applicability of both Nitsche-based formulations.

A first extension of this CutFEM FSI framework consists in the inclusion of permeable poroelastic structures by introducing a CutFEM FPI formulation. Besides the consideration of the general poroelastic formulation, a novel Nitsche-based approach to incorporate the conditions on the interface of the viscous fluid and the poroelastic structures is developed. In addition to the balance of mass and the balance of linear momentum on this interface, the Beavers-Joseph or Beavers-Joseph-Saffmann condition, which allows for a velocity slip in tangential interface orientation, is utilized. In contrast to the classical approaches to incorporate this slip condition, the novel Nitsche-based formulation is robust for the entire range of the slip length parameter. Rigorous numerical tests demonstrate the optimal spatial convergence orders of the CutFEM FPI formulation, analyze the optimal interval to specify the Nitsche penalty parameter, and confirm the expected advantages, such as the applicability for the entire range of the slip length, of the novel formulation compared to traditional approaches. Numerical examples highlight the flexibility of the CutFEM FPI formulation by the application of a Hybrid Eulerian-ALE fluid domain decomposition approach to increase the spatial resolution close to the interface. The investigation of the 3D interaction of a poroelastic plate and a fluid channel flow demonstrates the applicability to more general configurations.

The computational prediction of FSCI systems, which are characterized by an essential roughness of the contacting surfaces, is pursued thereafter. Since a resolved direct consideration of the rough microstructure is computationally expensive and not required for many applications, a physical model which includes an average representation in the vicinity of the rough interface by a poroelastic layer is introduced. The conditions on all occurring types of interfaces are discussed and special focus is put on the continuous transition between these conditions. For the numerical solution of this model, the previously developed numerical formulations for unfitted FSI and unfitted FPI are utilized. Additionally, a solid-poroelastic contact formulation based on the dual Mortar Lagrange multiplier method and a Nitsche-based approach for the porous fluid mass balance, which is applied on the contact interface, are developed. A validation against experimental data for a leakage configuration showed that the elastic deformation of the rough layer and the corresponding change of the leak rate can be successfully modeled by the introduced rough surface FSCI approach. Additional numerical examples prove that the correct contacting and lift-off behavior is predicted by the formulation. The computational study of a non-return valve indicates the usability of the approach for more complex problem configurations.

Since the surface roughness does not have a significant effect on the contacting process for all configurations, a simpler computational framework, which does not require the treatment of permeable poroelastic structures, for general FSCI problems is developed subsequently. Herein, a set of conditions to be fulfilled on the interface is formulated. This set of conditions directly includes the classical conditions of fluid-structure interaction and frictionless solid-solid contact as well as the continuous transition between them. The fluid state in the area of closed contact is re-

constructed from the closest fluid domain based on a simple extension approach. A novel numerical formulation to incorporate all conditions by a Nitsche-based approach is developed. Therein, an unbiased contact formulation, which is based on integrating the corresponding contact terms on both contacting interfaces, enables a continuous transition between the different underlying types of conditions also for the discrete formulation. Based on a simple numerical example, basic properties such as the contacting and lift-off behavior, the conservation of fluid mass, and the continuous transition of the effective interface traction are analyzed. The numerical study of an elastic pump and the processes of a flow-driven squeezed elastic structure demonstrate the suitability of the formulation for challenging configurations. Among other critical aspects, these configurations include frequent dynamic changes of the different types of interface conditions, various changes of the fluid domain topology, and also large contacting areas. To highlight the applicability to general 3D configurations, a double-leafed valve is numerically analyzed with the presented formulation.

As an extension to this FSCI formulation, a method to numerically solve general FPSCI problems, is developed. Besides the introduction of the general formulation for poroelastic permeable bodies, the additional conditions of viscous fluid-poroelasticity interaction, solid-poroelastic contact, and poroelastic-poroelastic contact are treated. One set of conditions, which also includes the porous fluid mass balance on potential contact interfaces, is formulated on the overall coupling interface. This set directly includes all types of conditions for a FPSCI problem and the transition between these conditions. All interface conditions are incorporated by Nitsche-based approaches, utilizing an interpolation technique to ensure a continuous transition also for the conditions corresponding to the porous flow. The extension approach to determine the fluid state in the contact zone developed for general FSCI is enriched by the porous fluid pressure, a physically more sophisticated approach. Finally, fundamental properties such as the contacting and lift-off behavior, the continuous transition of the acting interface traction, and the accuracy of the fluid stress extension strategy are numerically analyzed for a simple FPSCI configuration. The formulation is applied to solve the challenging configuration of a flow-driven squeezed elastic structure, which was already analyzed for FSCI, for different configurations of impermeable and permeable poroelastic domains. This gives evidence that also the FPSCI formulation is capable of treating frequent topological changes of the fluid domain and large contacting areas in a robust way. The applicability for 3D configurations is demonstrated by the numerical study of a poroelastic double-leafed valve.

Outlook As summarized previously, an essential progress toward the solution of general FSCI and FPSCI problems has been achieved within this thesis. Based on the developments in this thesis, the following promising improvements and extensions of the physical models, algorithms, and numerical formulations are worth to be addressed in future works.

While the spatial resolution close to the interface is in general a critical aspect for unfitted FSI formulations, when analyzing problems which include contact, this becomes even more important due to the prevalent thin fluid channels. The Hybrid Eulerian-ALE fluid domain decomposition approach, which allows attaching a deforming computational fluid mesh to the interface and which is applied in Section 4.5.1.1 to CutFEM FPI or in Schott *et al.* [191] to CutFEM FSI, could be extended towards FSCI or FPSCI. This extension requires the intersection of the interfaces

with the deformable fluid elements as demonstrated in Schott *et al.* [192] and the intersection of the domain decomposition interface with the physical interface, e.g. the fluid-structure interface.

Besides this increase in flexibility for the spatial fluid discretization, the numerical examples which were analyzed in this thesis revealed that an adaptive time stepping procedure is highly beneficial for such FSCI problems. Since impact events essentially require a small time step length, a simple strategy based on the interface position or a more general error indicator could be utilized to automatically control the variable time step length.

The presented fluid stress extension approach for FSCI in Chapter 6 could be replaced by a more physically meaningful alternative to determine the fluid state on the contact interface. Solving a reduced fluid equation, e.g. the Reynolds equation, in the zone of closed contact and coupling this reduced equation to the outer fluid state is a promising approach.

For FSI and FPI problems including thin bodies, the application of multiple DOF-sets per node in the fluid domain is essential. It is expected that this DOF-set strategy leads to a strong increase in DOF-set transitions during the nonlinear solution procedure for complex configurations. To ensure that the nonlinear system of equations can be solved, this aspect has to be analyzed and, potentially, the dynamic DOF-set-assignment strategy and the solution procedure have to be enhanced.

From an algorithmic point of view, different steps can improve the computational efficiency significantly. While all algorithms were implemented fully parallel, there is potential to improve the workload balance on the different processors. By introducing a sophisticated load balancing algorithm for the unfitted fluid formulation, computational resources can be used more efficiently, especially for computations which allocate a large number of processors.

For the Nitsche-based formulations presented in Chapter 6 and Chapter 7, a large number of numerical integration points on the interface are used to ensure an accurate integration. By utilizing appropriate triangulation algorithms that take the discontinuities and kinks of the integrated term on the different element boundaries into account and an adaptive strategy close to the condition transition zone of the Nitsche method, a significant reduction of the numerical integration points can be achieved.

Certain potential for improvements in terms of efficiency is provided by determining the optimal parametrization of the preconditioners utilized for the iterative GMRES procedure to solve the monolithic linear system of equations.

Most numerical examples presented in this thesis were performed for common and simple material models. For analyzing FSCI and FPSCI systems in biomechanics, more advanced material models, e.g. representing fibers, could improve the representation of the underlying physical processes. In this thesis, frictionless contact was exclusively considered due to its simplicity and the large number of problems where this is a sufficiently accurate physical model. Nevertheless, the extension of the presented physical models and numerical approaches to frictional contact allows broadening the range of problems to be predicted accurately.

In conclusion, the numerical formulations developed in this thesis build a solid basis and can be used to acquire insight for various questions of interest related to FSCI and FPSCI systems, which can only be investigated using sophisticated computational methods.

Bibliography

[1] C. Ager, B. Schott, A.-T. Vuong, A. Popp, and W. A. Wall, A consistent approach for fluid-structure-contact interaction based on a porous flow model for rough surface contact, *International Journal for Numerical Methods in Engineering* **119**, 1345–1378, 2019.

[2] C. Ager, B. Schott, M. Winter, and W. A. Wall, A Nitsche-based cut finite element method for the coupling of incompressible fluid flow with poroelasticity, *Computer Methods in Applied Mechanics and Engineering* **351**, 253 – 280, 2019.

[3] C. Ager, A. Seitz, and W. A. Wall, A consistent and versatile computational approach for general fluid-structure-contact interaction problems, *International Journal for Numerical Methods in Engineering*, 1 – 34, 2020.

[4] C. Ager, A. Seitz, and W. A. Wall, A consistent computational approach for general Fluid-Poroelasticity-Structure-Contact Interaction problems, *in preparation*, 2021.

[5] F. Alauzet, B. Fabrèges, M. A. Fernández, and M. Landajuela, Nitsche-XFEM for the coupling of an incompressible fluid with immersed thin-walled structures, *Computer Methods in Applied Mechanics and Engineering* **301**, 300–335, 2016.

[6] T. Almqvist, A. Almqvist, and R. Larsson, A comparison between computational fluid dynamic and Reynolds approaches for simulating transient EHL line contacts, *Tribology International* **37**, 61–69, 2004.

[7] I. Ambartsumyan, E. Khattatov, I. Yotov, and P. Zunino, A Lagrange multiplier method for a Stokes–Biot fluid–poroelastic structure interaction model, *Numerische Mathematik* **140**, 513–553, 2018.

[8] C. Annavarapu, M. Hautefeuille, and J. E. Dolbow, A robust Nitsche's formulation for interface problems, *Computer Methods in Applied Mechanics and Engineering* **225**, 44–54, 2012.

[9] M. Astorino, J.-F. Gerbeau, O. Pantz, and K.-F. Traoré, Fluid–structure interaction and multi-body contact: Application to aortic valves, *Computer Methods in Applied Mechanics and Engineering* **198**, 3603–3612, 2009.

[10] G. A. Ateshian, S. Maas, and J. A. Weiss, Finite Element Algorithm for Frictionless Contact of Porous Permeable Media Under Finite Deformation and Sliding, *Journal of Biomechanical Engineering* **132**, 061006–1–13, 2010.

[11] F. P. Baaijens, A fictitious domain/mortar element method for fluid–structure interaction, *International Journal for Numerical Methods in Fluids* **35**, 743–761, 2001.

[12] S. Badia, A. Quaini, and A. Quarteroni, Coupling Biot and Navier-Stokes equations for modelling fluid-poroelastic media interaction, *Journal of Computational Physics* **228**, 7986–8014, 2009.

[13] S. Badia and R. Codina, Unified Stabilized Finite Element Formulations for the Stokes and the Darcy Problems, *SIAM Journal on Numerical Analysis* **47**, 1971–2000, 2009.

[14] S. Badia, A. F. Martin, and F. Verdugo, Mixed Aggregated Finite Element Methods for the Unfitted Discretization of the Stokes Problem, *SIAM Journal on Scientific Computing* **40**, B1541–B1576, 2018.

[15] S. Badia, F. Verdugo, and A. F. Martín, The aggregated unfitted finite element method for elliptic problems, *Computer Methods in Applied Mechanics and Engineering* **336**, 533–553, 2018.

[16] R. W. Barber and D. R. Emerson, Challenges in Modeling Gas-Phase Flow in Microchannels: From Slip to Transition, *Heat Transfer Engineering* **27**, 3–12, 2006.

[17] T. P. Barrios, J. M. Cascón, and M. González, A posteriori error analysis of an augmented mixed finite element method for Darcy flow, *Computer Methods in Applied Mechanics and Engineering* **283**, 909–922, 2015.

[18] G. Bayada and M. Chambat, Homogenization of the Stokes system in a thin film flow with rapidly varying thickness, *ESAIM: Mathematical Modelling and Numerical Analysis* **23**, 205–234, 1989.

[19] Y. Bazilevs and T. J. R. Hughes, Weak imposition of Dirichlet boundary conditions in fluid mechanics, *Computers and Fluids* **36**, 12 – 26, 2007.

[20] G. S. Beavers and D. D. Joseph, Boundary conditions at a naturally permeable wall, *Journal of Fluid Mechanics* **30**, 197–207, 1967.

[21] F. B. Belgacem, The Mortar finite element method with Lagrange multipliers, *Numerische Mathematik* **84**, 173–197, 1999.

[22] T. Belytschko and T. Black, Elastic crack growth in finite elements with minimal remeshing, *International Journal for Numerical Methods in Engineering* **45**, 601–620, 1999.

[23] T. Belytschko, J. M. Kennedy, and D. Schoeberle, Quasi-Eulerian Finite Element Formulation for Fluid-Structure Interaction, *Journal of Pressure Vessel Technology* **102**, 62–69, 1980.

[24] T. Belytschko, N. Moës, S. Usui, and C. Parimi, Arbitrary discontinuities in finite elements, *International Journal for Numerical Methods in Engineering* **50**, 993–1013, 2001.

[25] T. Belytschko, W. K. Liu, B. Moran, and K. Elkhodary, *Nonlinear Finite Elements for Continua and Structures*, John Wiley & Sons, 2013.

[26] M. A. Biot, General Theory of Three-Dimensional Consolidation, *Journal of Applied Physics* **12**, 155–164, 1941.

[27] A. E. Bogaers, S. Kok, B. D. Reddy, and T. Franz, An evaluation of quasi-Newton methods for application to FSI problems involving free surface flow and solid body contact, *Computers & Structures* **173**, 71–83, 2016.

[28] L. Boilevin-Kayl, M. A. Fernández, and J.-F. Gerbeau, Numerical methods for immersed FSI with thin-walled structures, *Computers & Fluids* **179**, 744–763, 2019.

[29] M. Böl, R. B. Möhle, M. Haesner, T. R. Neu, H. Horn, and R. Krull, 3D finite element model of biofilm detachment using real biofilm structures from CLSM data, *Biotechnology and Bioengineering* **103**, 177–186, 2009.

[30] J. Bonet and R. D. Wood, *Nonlinear Continuum Mechanics for Finite Element Analysis*, Cambridge University Press, 1997.

[31] I. Borazjani, Fluid–structure interaction, immersed boundary-finite element method simulations of bio-prosthetic heart valves, *Computer Methods in Applied Mechanics and Engineering* **257**, 103–116, 2013.

[32] B. Bou-Said, A Comparison of Homogenization and Direct Techniques for the Treatment of Roughness in Incompressible Lubrication, *Journal of Tribology* **126**, 1–5, 2004.

[33] B. P. Boudreau, The diffusive tortuosity of fine-grained unlithified sediments, *Geochimica et Cosmochimica Acta* **60**, 3139–3142, 1996.

[34] M. Braack, E. Burman, V. John, and G. Lube, Stabilized finite element methods for the generalized Oseen problem, *Computer Methods in Applied Mechanics and Engineering* **196**, 853–866, 2007.

[35] S. Brandstaeter, S. L. Fuchs, R. C. Aydin, and C. J. Cyron, Mechanics of the stomach: A review of an emerging field of biomechanics, *GAMM-Mitteilungen*, e201900001, 2019.

[36] M. Budt, I. Temizer, and P. Wriggers, A computational homogenization framework for soft elastohydrodynamic lubrication, *Computational Mechanics* **49**, 749–767, 2012.

[37] M. Bukač, I. Yotov, R. Zakerzadeh, and P. Zunino, Partitioning strategies for the interaction of a fluid with a poroelastic material based on a Nitsche's coupling approach, *Computer Methods in Applied Mechanics and Engineering* **292**, 138–170, 2015.

[38] E. Burman, Ghost penalty, *Comptes Rendus Mathematique* **348**, 1217–1220, 2010.

[39] E. Burman and A. Ern, Continuous interior penalty hp-finite element methods for advection and advection-diffusion equations, *Mathematics of Computation* **76**, 1119–1140, 2007.

[40] E. Burman and M. A. Fernández, Continuous interior penalty finite element method for the time-dependent Navier–Stokes equations: space discretization and convergence, *Numerische Mathematik* **107**, 39–77, 2007.

[41] E. Burman and M. A. Fernández, Finite element methods with symmetric stabilization for the transient convection–diffusion–reaction equation, *Computer Methods in Applied Mechanics and Engineering* **198**, 2508–2519, 2009.

[42] E. Burman and M. A. Fernández, An unfitted Nitsche method for incompressible fluid–structure interaction using overlapping meshes, *Computer Methods in Applied Mechanics and Engineering* **279**, 497–514, 2014.

[43] E. Burman and P. Hansbo, Edge stabilization for Galerkin approximations of convection–diffusion–reaction problems, *Computer Methods in Applied Mechanics and Engineering* **193**, 1437–1453, 2004.

[44] E. Burman and P. Hansbo, Edge stabilization for the generalized Stokes problem: A continuous interior penalty method, *Computer Methods in Applied Mechanics and Engineering* **195**, 2393–2410, 2006.

[45] E. Burman and P. Hansbo, A unified stabilized method for Stokes' and Darcy's equations, *Journal of Computational and Applied Mathematics* **198**, 35–51, 2007.

[46] E. Burman and P. Hansbo, Fictitious domain finite element methods using cut elements: II. A stabilized Nitsche method, *Applied Numerical Mathematics* **62**, 328–341, 2012.

[47] E. Burman and P. Hansbo, Fictitious domain methods using cut elements: III. A stabilized Nitsche method for Stokes problem, *ESAIM: Mathematical Modelling and Numerical Analysis* **48**, 859–874, 2014.

[48] E. Burman and P. Zunino, A Domain Decomposition Method Based on Weighted Interior Penalties for Advection-Diffusion-Reaction Problems, *SIAM Journal on Numerical Analysis* **44**, 1612–1638, 2006.

[49] E. Burman and P. Zunino, Numerical Approximation of Large Contrast Problems with the Unfitted Nitsche Method, In *Frontiers in Numerical Analysis-Durham 2010*, pages 227–282, Springer, 2011.

[50] E. Burman, M. A. Fernández, and P. Hansbo, Continuous Interior Penalty Finite Element Method for Oseen's Equations, *SIAM Journal on Numerical Analysis* **44**, 1248–1274, 2006.

[51] E. Burman, S. Claus, P. Hansbo, M. G. Larson, and A. Massing, CutFEM: Discretizing geometry and partial differential equations, *International Journal for Numerical Methods in Engineering* **104**, 472–501, 2015.

[52] E. Burman, P. Hansbo, and M. G. Larson, The Penalty-Free Nitsche Method and Nonconforming Finite Elements for the Signorini Problem, *SIAM Journal on Numerical Analysis* **55**, 2523–2539, 2017.

[53] E. Burman, M. A. Fernández, and S. Frei, A Nitsche-based formulation for fluid-structure interactions with contact, *ESAIM: M2AN* **54**, 531–564, 2020.

[54] Y. Cao, M. Gunzburger, X. Hu, F. Hua, X. Wang, and W. Zhao, Finite Element Approximations for Stokes-Darcy Flow with Beavers-Joseph Interface Conditions, *SIAM Journal on Numerical Analysis* **47**, 4239–4256, 2010.

[55] Y. Cao, M. Gunzburger, F. Hua, and X. Wang, Coupled Stokes-Darcy model with Beavers–Joseph interface boundary condition, *Communications in Mathematical Sciences* **8**, 1–25, 2010.

[56] C. Cawthorn and N. Balmforth, Contact in a viscous fluid. Part 1. A falling wedge, *Journal of Fluid Mechanics* **646**, 327–338, 2010.

[57] D. Chapelle and P. Moireau, General coupling of porous flows and hyperelastic formulations – From thermodynamics principles to energy balance and compatible time schemes, *European Journal of Mechanics-B\Fluids* **46**, 82–96, 2014.

[58] X. Chen, Y. Chen, and T. Hisada, Development of a Finite Element Procedure of Contact Analysis for Articular Cartilage with Large Deformation Based on the Biphasic Theory, *JSME International Journal Series C Mechanical Systems, Machine Elements and Manufacturing* **48**, 537–546, 2005.

[59] J. Chessa and T. Belytschko, An Extended Finite Element Method for Two-Phase Fluids, *Journal of Applied Mechanics* **70**, 10–17, 2003.

[60] F. Chouly, An adaptation of Nitsche's method to the Tresca friction problem, *Journal of Mathematical Analysis and Applications* **411**, 329–339, 2014.

[61] F. Chouly and P. Hild, A Nitsche-Based Method for Unilateral Contact Problems: Numerical Analysis, *SIAM Journal on Numerical Analysis* **51**, 1295–1307, 2013.

[62] F. Chouly, P. Hild, and Y. Renard, Symmetric and non-symmetric variants of Nitsche's method for contact problems in elasticity: theory and numerical experiments, *Mathematics of Computation* **84**, 1089–1112, 2015.

[63] F. Chouly, R. Mlika, and Y. Renard, An unbiased Nitsche's approximation of the frictional contact between two elastic structures, *Numerische Mathematik* **139**, 593 – 631, 2018.

[64] H. Christensen and K. Tonder, The Hydrodynamic Lubrication of Rough Bearing Surfaces of Finite Width, *Journal of Lubrication Technology* **93**, 324–329, 1971.

[65] J. Chung and G. Hulbert, A Time Integration Algorithm for Structural Dynamics With Improved Numerical Dissipation: The Generalized-α Method, *Journal of Applied Mechanics* **60**, 371–375, 1993.

[66] M. Coroneo, L. Yoshihara, and W. A. Wall, Biofilm growth: A multi-scale and coupled fluid-structure interaction and mass transport approach, *Biotechnology and Bioengineering* **111**, 1385–1395, 2014.

[67] O. Coussy, *Poromechanics*, John Wiley & Sons, West Sussex, 2004.

[68] C. D'Angelo and P. Zunino, Robust numerical approximation of coupled Stokes' and Darcy's flows applied to vascular hemodynamics and biochemical transport, *ESAIM: Mathematical Modelling and Numerical Analysis* **45**, 447–476, 2011.

[69] R. H. Davis, Y. Zhao, K. P. Galvin, and H. J. Wilson, Solid–solid contacts due to surface roughness and their effects on suspension behaviour, *Philosophical Transactions of the Royal Society of London A: Mathematical, Physical and Engineering Sciences* **361**, 871–894, 2003.

[70] J. De Hart, G. Peters, P. Schreurs, and F. Baaijens, A three-dimensional computational analysis of fluid–structure interaction in the aortic valve, *Journal of Biomechanics* **36**, 103–112, 2003.

[71] M. Discacciati and A. Quarteroni, Navier-Stokes/Darcy coupling: modeling, analysis, and numerical approximation, *Revista Matemática Complutense* **22**, 315–426, 2009.

[72] J. Dolbow and I. Harari, An efficient finite element method for embedded interface problems, *International Journal for Numerical Methods in Engineering* **78**, 229–252, 2009.

[73] J. Donea and A. Huerta, *Finite Element Methods for Flow Problems*, John Wiley & Sons, 2003.

[74] J. Donea, P. Fasoli-Stella, and S. Giuliani, Lagrangian and Eulerian Finite Element Techniques for Transient Fluid-Structure Interaction Problems, *Transactions of the 4th Int. Conference on SMIRT, San Francisco. B1/2.*, 1977.

[75] P. S. Donzelli and R. L. Spilker, A contact finite element formulation for biological soft hydrated tissues, *Computer Methods in Applied Mechanics and Engineering* **153**, 63–79, 1998.

[76] N. D. Dos Santos, J.-F. Gerbeau, and J.-F. Bourgat, A partitioned fluid–structure algorithm for elastic thin valves with contact, *Computer Methods in Applied Mechanics and Engineering* **197**, 1750–1761, 2008.

[77] J. Douglas and T. Dupont, Interior Penalty Procedures for Elliptic and Parabolic Galerkin Methods, In *Computing Methods in Applied Sciences*, pages 207–216, Springer, 1976.

[78] A. Ehrl, A. Popp, V. Gravemeier, and W. A. Wall, A dual mortar approach for mesh tying within a variational multiscale method for incompressible flow, *International Journal for Numerical Methods in Fluids* **76**, 1–27, 2014.

[79] D. M. Espino, D. E. Shepherd, and D. W. Hukins, Evaluation of a transient, simultaneous, arbitrary Lagrange–Euler based multi-physics method for simulating the mitral heart valve, *Computer Methods in Biomechanics and Biomedical Engineering* **17**, 450–458, 2014.

[80] D. M. Espino, D. E. Shepherd, and D. W. Hukins, Transient large strain contact modelling: A comparison of contact techniques for simultaneous fluid–structure interaction, *European Journal of Mechanics-B/Fluids* **51**, 54–60, 2015.

[81] P. Farah, *Mortar Methods for Computational Contact Mechanics Including Wear and General Volume Coupled Problems*, Phd thesis, Institute for Computational Mechanics, Technical University of Munich, 2018.

[82] P. Farah, A. Popp, and W. A. Wall, Segment-based vs. element-based integration for mortar methods in computational contact mechanics, *Computational Mechanics* **55**, 209–228, 2015.

[83] C. Farhat and V. K. Lakshminarayan, An ALE formulation of embedded boundary methods for tracking boundary layers in turbulent fluid–structure interaction problems, *Journal of Computational Physics* **263**, 53–70, 2014.

[84] K. Fischer and P. Wriggers, Frictionless 2D contact formulations for finite deformations based on the mortar method, *Computational Mechanics* **36**, 226–244, 2005.

[85] B. Flemisch and B. I. Wohlmuth, Stable Lagrange multipliers for quadrilateral meshes of curved interfaces in 3D, *Computer Methods in Applied Mechanics and Engineering* **196**, 1589–1602, 2007.

[86] S. Frei and T. Richter, A second order time-stepping scheme for parabolic interface problems with moving interfaces, *ESAIM: Mathematical Modelling and Numerical Analysis* **51**, 1539–1560, 2017.

[87] T.-P. Fries and A. Zilian, On time integration in the XFEM, *International Journal for Numerical Methods in Engineering* **79**, 69–93, 2009.

[88] F. Galbusera, M. Bashkuev, H.-J. Wilke, A. Shirazi-Adl, and H. Schmidt, Comparison of various contact algorithms for poroelastic tissues, *Computer Methods in Biomechanics and Biomedical Engineering* **17**, 1323–1334, 2014.

[89] D. Gartling, C. Hickox, and R. Givler, Simulation of Coupled Viscous and Porous Flow Problems, *International Journal of Computational Fluid Dynamics* **7**, 23–48, 1996.

[90] M. W. Gee, U. Küttler, and W. A. Wall, Truly monolithic algebraic multigrid for fluid-structure interaction, *International Journal for Numerical Methods in Engineering* **85**, 987–1016, 2011.

[91] D. Gérard-Varet and M. Hillairet, Regularity Issues in the Problem of Fluid Structure Interaction, *Archive for Rational Mechanics and Analysis* **195**, 375–407, 2010.

[92] D. Gérard-Varet, M. Hillairet, and C. Wang, The influence of boundary conditions on the contact problem in a 3D Navier–Stokes flow, *Journal de Mathématiques Pures et Appliquées* **103**, 1–38, 2015.

[93] A. Gerstenberger, *An XFEM based fixed-grid approach to fluid-structure interaction*, Phd thesis, Institute for Computational Mechanics, Technical University of Munich, 2010.

[94] A. Gerstenberger and W. A. Wall, An eXtended Finite Element Method/Lagrange multiplier based approach for fluid-structure interaction, *Computer Methods in Applied Mechanics and Engineering* **197**, 1699 – 1714, 2008.

[95] M. Gitterle, *A dual mortar formulation for finite deformation frictional contact problems including wear and thermal coupling*, Phd thesis, Institute for Computational Mechanics, Technical University of Munich, 2012.

[96] R. Glowinski, T.-W. Pan, and J. Periaux, A fictitious domain method for external incompressible viscous flow modeled by Navier–Stokes equations, *Computer Methods in Applied Mechanics and Engineering* **112**, 133–148, 1994.

[97] R. Glowinski, T.-W. Pan, and J. Periaux, A fictitious domain method for Dirichlet problem and applications, *Computer Methods in Applied Mechanics and Engineering* **111**, 283–303, 1994.

[98] G. M. Goldin, A. M. Colclasure, A. H. Wiedemann, and R. J. Kee, Three-dimensional particle-resolved models of Li-ion batteries to assist the evaluation of empirical parameters in one-dimensional models, *Electrochimica Acta* **64**, 118–129, 2012.

[99] W. G. Gray and B. A. Schrefler, Thermodynamic approach to effective stress in partially saturated porous media, *European Journal for Mechanics A/Solids* **20**, 521–538, 2001.

[100] W. G. Gray and C. T. Miller, A generalization of averaging theorems for porous medium analysis, *Advances in Water Resources* **62, Part B**, 227 – 237, 2013.

[101] W. G. Gray and C. T. Miller, Thermodynamically constrained averaging theory approach for modeling flow and transport phenomena in porous medium systems: 5. Single-fluid-phase transport, *Advances in water resources* **32**, 681–711, 2009.

[102] W. G. Gray, C. T. Miller, and B. A. Schrefler, Averaging theory for description of environmental problems: What have we learned?, *Advances in water resources* **51**, 123–138, 2013.

[103] M. Griebel and M. A. Schweitzer, A Particle-Partition of Unity Method Part V: Boundary Conditions, In *Geometric Analysis and Nonlinear Partial Differential Equations*, pages 519–542, Springer, 2003.

[104] S. Groß and A. Reusken, An extended pressure finite element space for two-phase incompressible flows with surface tension, *Journal of Computational Physics* **224**, 40–58, 2007.

[105] H. Guo and R. L. Spilker, Biphasic Finite Element Modeling of Hydrated Soft Tissue Contact Using an Augmented Lagrangian Method, *Journal of Biomechanical Engineering* **133**, 111001, 2011.

[106] H. Guo and R. L. Spilker, An augmented Lagrangian finite element formulation for 3D contact of biphasic tissues, *Computer Methods in Biomechanics and Biomedical Engineering* **17**, 1206–1216, 2014.

[107] H. Guo, S. A. Maher, and R. L. Spilker, Biphasic finite element contact analysis of the knee joint using an augmented Lagrangian method, *Medical engineering & physics* **35**, 1313–1320, 2013.

[108] B. Haible and R. B. Kreckel. CLN, a Class Library for Numbers. URL `https://ginac.de/CLN/cln.html#Index`.

[109] A. Hansbo and P. Hansbo, An unfitted finite element method, based on Nitsche's method, for elliptic interface problems, *Computer Methods in Applied Mechanics and Engineering* **191**, 5537–5552, 2002.

[110] A. Hansbo, P. Hansbo, and M. G. Larson, A finite element method on composite grids based on Nitsche's method, *ESAIM: Mathematical Modelling and Numerical Analysis* **37**, 495–514, 2003.

[111] P. Hansbo, Nitsche's method for interface problems in computational mechanics, *GAMM-Mitteilungen* **28**, 183–206, 2005.

[112] P. Hansbo, M. G. Larson, and S. Zahedi, A cut finite element method for a Stokes interface problem, *Applied Numerical Mathematics* **85**, 90–114, 2014.

[113] S. Hartmann, S. Brunssen, E. Ramm, and B. I. Wohlmuth, Unilateral non-linear dynamic contact of thin-walled structures using a primal-dual active set strategy, *International Journal for Numerical Methods in Engineering* **70**, 883–912, 2007.

[114] A. Heck and A. Heck, *Introduction to MAPLE*, Volume 1993, Springer-Verlag New York, 1993.

[115] M. Heil, An efficient solver for the fully coupled solution of large-displacement fluid–structure interaction problems, *Computer Methods in Applied Mechanics and Engineering* **193**, 1–23, 2004.

[116] F. Henke, M. Winklmaier, V. Gravemeier, and W. A. Wall, A semi-Lagrangean time-integration approach for extended finite element methods, *International Journal for Numerical Methods in Engineering* **98**, 174–202, 2014.

[117] D. Herwartz, A. Pack, B. Friedrichs, and A. Bischoff, Identification of the giant impactor Theia in lunar rocks, *Science* **344**, 1146–1150, 2014.

[118] P. Hild, Numerical implementation of two nonconforming finite element methods for unilateral contact, *Computer Methods in Applied Mechanics and Engineering* **184**, 99–123, 2000.

[119] M. Hillairet and T. Takahashi, Collisions in Three-Dimensional Fluid Structure Interaction Problems, *SIAM Journal on Mathematical Analysis* **40**, 2451–2477, 2009.

[120] C. W. Hirt and B. D. Nichols, Volume of fluid (VOF) method for the dynamics of free boundaries, *Journal of computational physics* **39**, 201–225, 1981.

[121] C. W. Hirt, A. A. Amsden, and J. Cook, An arbitrary Lagrangian-Eulerian computing method for all flow speeds, *Journal of Computational Physics* **14**, 227–253, 1974.

[122] L. M. Hocking, The effect of slip on the motion of a sphere close to a wall and of two adjacent spheres, *Journal of Engineering Mathematics* **7**, 207–221, 1973.

[123] G. A. Holzapfel, *Nonlinear Solid Mechanics*, Volume 24, Wiley Chichester, 2000.

[124] J. Hou, M. Holmes, W. Lai, and V. Mow, Boundary Conditions at the Cartilage-Synovial Fluid Interface for Joint Lubrication and Theoretical Verifications, *Journal of Biomechanical Engineering* **111**, 78–87, 1989.

[125] Z. Huang, P. Avery, C. Farhat, J. Rabinovitch, A. Derkevorkian, and L. D. Peterson, Simulation of Parachute Inflation Dynamics Using an Eulerian Computational Framework for Fluid-Structure Interfaces Evolving in High-Speed Turbulent Flows, In *2018 AIAA Aerospace Sciences Meeting*, page 1540, 2018.

[126] S. Hüeber and B. I. Wohlmuth, A primal–dual active set strategy for non-linear multibody contact problems, *Computer Methods in Applied Mechanics and Engineering* **194**, 3147–3166, 2005.

[127] S. Hüeber, G. Stadler, and B. I. Wohlmuth, A Primal-Dual Active Set Algorithm for Three-Dimensional Contact Problems with Coulomb Friction, *SIAM Journal on Scientific Computing* **30**, 572–596, 2008.

[128] T. J. Hughes, G. Scovazzi, and L. P. Franca, Multiscale and Stabilized Methods, *Encyclopedia of Computational Mechanics Second Edition*, 1–64, 2018.

[129] M. Jai and B. Bou-Said, A Comparison of Homogenization and Averaging Techniques for the Treatment of Roughness in Slip-Flow-Modified Reynolds Equation, *Journal of Tribology* **124**, 327–335, 2002.

[130] K. E. Jansen, C. H. Whiting, and G. M. Hulbert, A generalized-α method for integrating the filtered Navier–Stokes equations with a stabilized finite element method, *Computer Methods in Applied Mechanics and Engineering* **190**, 305–319, 2000.

[131] I. Jones, Low Reynolds number flow past a porous spherical shell, In *Mathematical Proceedings of the Cambridge Philosophical Society*, Volume 73, pages 231–238. Cambridge University Press, 1973.

[132] M. Juntunen and R. Stenberg, Nitsche's method for general boundary conditions, *Mathematics of Computation* **78**, 1353–1374, 2009.

[133] D. Kamensky, M.-C. Hsu, D. Schillinger, J. A. Evans, A. Aggarwal, Y. Bazilevs, M. S. Sacks, and T. J. Hughes, An immersogeometric variational framework for fluid–structure interaction: Application to bioprosthetic heart valves, *Computer Methods in Applied Mechanics and Engineering* **284**, 1005–1053, 2015.

[134] T. Klöppel, A. Popp, U. Küttler, and W. A. Wall, Fluid-structure interaction for non-conforming interfaces based on a dual mortar formulation, *Computer Methods in Applied Mechanics and Engineering* **200**, 3111 – 3126, 2011.

[135] U. Küttler, M. W. Gee, C. Förster, A. Comerford, and W. A. Wall, Coupling strategies for biomedical fluid-structure interaction problems, *International Journal for Numerical Methods in Biomedical Engineering* **26**, 305–321, 2010.

[136] A. Laadhari and A. Quarteroni, Numerical modeling of heart valves using resistive Eulerian surfaces, *International Journal for Numerical Methods in Biomedical Engineering* **32**, e02743, 2016.

[137] B. P. Lamichhane and B. I. Wohlmuth, Biorthogonal bases with local support and approximation properties, *Mathematics of Computation* **76**, 233–249, 2007.

[138] B. P. Lamichhane, R. P. Stevenson, and B. I. Wohlmuth, Higher Order Mortar Finite Element Methods in 3D with Dual Lagrange Multiplier Bases, *Numerische Mathematik* **102**, 93–121, 2005.

[139] T. A. Laursen, *Computational Contact and Impact Mechanics*, Springer-Verlag Berlin Heidelberg, 2002.

[140] C. Lehrenfeld, The Nitsche XFEM-DG Space-Time Method and its Implementation in Three Space Dimensions, *SIAM Journal on Scientific Computing* **37**, A245–A270, 2015.

[141] C. Lehrenfeld and M. Olshanskii, An Eulerian finite element method for PDEs in time-dependent domains, *ESAIM: Mathematical Modelling and Numerical Analysis* **53**, 585–614, 2019.

[142] R. W. Lewis and B. A. Schrefler, *The Finite Element Method in the Static and Dynamic Deformation and Consolidation of Porous Media*, John Wiley & Sons, 1998.

[143] W.-L. Li, Derivation of Modified Reynolds Equation – A Porous Media Model, *Journal of Tribology* **121**, 823–829, 1999.

[144] X. Liu and L. Liu, Effect of valve lesion on venous valve cycle: A modified immersed finite element modeling, *PloS one* **14**, 1–26, 2019.

[145] B. Lorenz and B. N. Persson, Leak rate of seals: Effective-medium theory and comparison with experiment, *The European Physical Journal E: Soft Matter and Biological Physics* **31**, 159–167, 2010.

[146] P. Luo, C. Rodrigo, F. Gaspar, and C. Oosterlee, Monolithic multigrid method for the coupled Stokes flow and deformable porous medium system, *Journal of Computational Physics* **353**, 148–168, 2018.

[147] A. Main and G. Scovazzi, The shifted boundary method for embedded domain computations. Part I: Poisson and Stokes problems, *Journal of Computational Physics* **372**, 972–995, 2018.

[148] A. Main and G. Scovazzi, The shifted boundary method for embedded domain computations. Part II: Linear advection–diffusion and incompressible Navier–Stokes equations, *Journal of Computational Physics* **372**, 996–1026, 2018.

[149] A. Massing, B. Schott, and W. A. Wall, A stabilized Nitsche cut finite element method for the Oseen problem, *Computer Methods in Applied Mechanics and Engineering* **328**, 262–300, 2018.

[150] A. Massing, M. G. Larson, A. Logg, and M. E. Rognes, A Stabilized Nitsche Fictitious Domain Method for the Stokes Problem, *Journal of Scientific Computing* **61**, 604–628, 2014.

[151] A. Massing, M. G. Larson, A. Logg, and M. E. Rognes, A Nitsche-based cut finite element method for a fluid-structure interaction problem, *Communications in Applied Mathematics and Computational Science* **10**, 97–120, 2015.

[152] U. M. Mayer, A. Popp, A. Gerstenberger, and W. A. Wall, 3D fluid–structure-contact interaction based on a combined XFEM FSI and dual mortar contact approach, *Computational Mechanics* **46**, 53–67, 2010.

[153] M. Mayr, *A Monolithic Solver for Fluid-Structure Interaction with Adaptive Time Stepping and a Hybrid Preconditioner*, Phd thesis, Technical University of Munich, 2016.

[154] M. Mayr, T. Klöppel, W. A. Wall, and M. W. Gee, A Temporal Consistent Monolithic Approach to Fluid-Structure Interaction Enabling Single Field Predictors, *SIAM Journal on Scientific Computing* **37**, B30–B59, 2015.

[155] V. Meschini, M. De Tullio, G. Querzoli, and R. Verzicco, Flow structure in healthy and pathological left ventricles with natural and prosthetic mitral valves, *Journal of Fluid Mechanics* **834**, 271–307, 2018.

[156] R. Mlika, Y. Renard, and F. Chouly, An unbiased Nitsche's formulation of large deformation frictional contact and self-contact, *Computer Methods in Applied Mechanics and Engineering* **325**, 265–288, 2017.

[157] N. Moës, J. Dolbow, and T. Belytschko, A finite element method for crack growth without remeshing, *International Journal for Numerical Methods in Engineering* **46**, 131–150, 1999.

[158] V. C. Mow, W. Y. GU, and H. C. Faye, Structure and Function of Articular Cartilage and Meniscus, pages 181–258, *Basic Orthopaedic Biomechanics & Bechano-Biology*, V. C. Mow and R. Huiskes (eds.), Lippincott Williams & Wilkins, 2005.

[159] S. Nagrath, K. E. Jansen, and R. T. Lahey, Computation of incompressible bubble dynamics with a stabilized finite element level set method, *Computer Methods in Applied Mechanics and Engineering* **194**, 4565–4587, 2005.

[160] C. Neto, D. R. Evans, E. Bonaccurso, H.-J. Butt, and V. S. Craig, Boundary slip in Newtonian liquids: a review of experimental studies, *Reports on Progress in Physics* **68**, 2859, 2005.

[161] J. Nitsche, Über ein Variationsprinzip zur Lösung von Dirichlet-Problemen bei Verwendung von Teilräumen, die keinen Randbedingungen unterworfen sind, *Abhandlungen aus dem Mathematischen Seminar der Universität Hamburg* **36**, 9–15, 1971.

[162] Y. Öngün, M. André, D. Bartel, and L. Deters, An axisymmetric hydrodynamic interface element for finite-element computations of mixed lubrication in rubber seals, *Proceedings of the Institution of Mechanical Engineers, Part J: Journal of Engineering Tribology* **222**, 471–481, 2008.

[163] N. Patir and H. Cheng, An Average Flow Model for Determining Effects of Three-Dimensional Roughness on Partial Hydrodynamic Lubrication, *Journal of Lubrication Technology* **100**, 12–17, 1978.

[164] J. D. Pauw, L. Veggi, O. J. Haidn, C. Wagner, T. Thümmel, D. J. Rixen, C. Ager, A. Wirtz, A. Popp, W. A. Wall, and B. Wagner, An academic approach to the multidisciplinary development of liquid-oxygen turbopumps for space applications, *CEAS Space Journal* **11**, 193–203, 2019.

[165] C. S. Peskin, Flow patterns around heart valves: A numerical method, *Journal of Computational Physics* **10**, 252–271, 1972.

[166] C. S. Peskin, Numerical analysis of blood flow in the heart, *Journal of Computational Physics* **25**, 220–252, 1977.

[167] C. S. Peskin, The immersed boundary method, *Acta numerica* **11**, 479–517, 2002.

[168] M. R. Pfaller, J. M. Hörmann, M. Weigl, A. Nagler, R. Chabiniok, C. Bertoglio, and W. A. Wall, The importance of the pericardium for cardiac biomechanics: from physiology to computational modeling, *Biomechanics and Modeling in Mechanobiology* **18**, 503–529, 2019.

[169] P. Pibarot and J. G. Dumesnil, Prosthetic Heart Valves: Selection of the Optimal Prosthesis and Long-Term Management, *Circulation* **119**, 1034–1048, 2009.

[170] A. Popp, *Mortar Methods for Computational Contact Mechanics and General Interface Problems*, Phd thesis, Institute for Computational Mechanics, Technical University of Munich, 2012.

[171] A. Popp, M. W. Gee, and W. A. Wall, A finite deformation mortar contact formulation using a primal–dual active set strategy, *International Journal for Numerical Methods in Engineering* **79**, 1354–1391, 2009.

[172] A. Popp, M. Gitterle, M. W. Gee, and W. A. Wall, A dual mortar approach for 3D finite deformation contact with consistent linearization, *International Journal for Numerical Methods in Engineering* **83**, 1428–1465, 2010.

[173] A. Popp, A. Seitz, M. W. Gee, and W. A. Wall, Improved robustness and consistency of 3D contact algorithms based on a dual mortar approach, *Computer Methods in Applied Mechanics and Engineering* **264**, 67–80, 2013.

[174] M. Prat, F. Plouraboué, and N. Letalleur, Averaged Reynolds Equation for Flows between Rough Surfaces in Sliding Motion, *Transport in Porous Media* **48**, 291–313, 2002.

[175] M. A. Puso and T. A. Laursen, A mortar segment-to-segment frictional contact method for large deformations, *Computer Methods in Applied Mechanics and Engineering* **193**, 4891–4913, 2004.

[176] M. A. Puso and T. A. Laursen, A mortar segment-to-segment contact method for large deformation solid mechanics, *Computer Methods in Applied Mechanics and Engineering* **193**, 601–629, 2004.

[177] U. Rasthofer, *Computational Multiscale Methods for Turbulent Single and Two-Phase Flows*, Phd thesis, Institute for Computational Mechanics, Technical University of Munich, 2015.

[178] U. Rasthofer, F. Henke, W. A. Wall, and V. Gravemeier, An extended residual-based variational multiscale method for two-phase flow including surface tension, *Computer Methods in Applied Mechanics and Engineering* **200**, 1866–1876, 2011.

[179] O. Reynolds, On the Theory of Lubrication and its Application to Mr. Beauchamp Tower's Experiments, including an Experimental Determination of the Viscosity of Olive Oil, *Philosophical Transactions of the Royal Society of London* **177**, 157–234, 1886.

[180] H. Sabetamal, M. Nazem, S. W. Sloan, and J. P. Carter, Frictionless contact formulation for dynamic analysis of nonlinear saturated porous media based on the mortar method, *International Journal for Numerical and Analytical Methods in Geomechanics* **40**, 25–61, 2016.

[181] P. G. Saffman, On the Boundary Condition at the Surface of a Porous Medium, *Studies in Applied Mathematics* **50**, 93–101, 1971.

[182] F. Sahlin, R. Larsson, P. Marklund, A. Almqvist, and P. Lugt, A mixed lubrication model incorporating measured surface topography. Part 2: Roughness treatment, model validation, and simulation, *Proceedings of the Institution of Mechanical Engineers, Part J: Journal of Engineering Tribology* **224**, 353–365, 2010.

[183] S. Sathe and T. E. Tezduyar, Modeling of fluid–structure interactions with the space–time finite elements: contact problems, *Computational Mechanics* **43**, 51–60, 2008.

[184] R. A. Sauer and L. De Lorenzis, An unbiased computational contact formulation for 3D friction, *International Journal for Numerical Methods in Engineering* **101**, 251–280, 2015.

[185] H. Sauerland and T.-P. Fries, The extended finite element method for two-phase and free-surface flows: A systematic study, *Journal of Computational Physics* **230**, 3369–3390, 2011.

[186] A. Schein. Analysis of a Cut Finite Element Method for Lubrication Gap Flows and Implementation of a Ghost-Penalty Stabilization for High Order Elements. Master's thesis, Institute for Computational Mechanics, Technical University of Munich, 2017.

[187] B. Schott, *Stabilized Cut Finite Element Methods for Complex Interface Coupled Flow Problems*, Phd thesis, Institute for Computational Mechanics, Technical University of Munich, 2017.

[188] B. Schott and W. A. Wall, A new face-oriented stabilized XFEM approach for 2D and 3D incompressible Navier–Stokes equations, *Computer Methods in Applied Mechanics and Engineering* **276**, 233–265, 2014.

[189] B. Schott, U. Rasthofer, V. Gravemeier, and W. A. Wall, A face-oriented stabilized Nitsche-type extended variational multiscale method for incompressible two-phase flow, *International Journal for Numerical Methods in Engineering* **104**, 721–748, 2015.

[190] B. Schott, S. Shahmiri, R. Kruse, and W. A. Wall, A stabilized Nitsche-type extended embedding mesh approach for 3D low-and high-Reynolds-number flows, *International Journal for Numerical Methods in Fluids* **82**, 289–315, 2016.

[191] B. Schott, C. Ager, and W. A. Wall, A monolithic approach to fluid-structure interaction based on a hybrid Eulerian-ALE fluid domain decomposition involving cut elements, *International Journal for Numerical Methods in Engineering* **119**, 208–237, 2019.

[192] B. Schott, C. Ager, and W. A. Wall, Monolithic cut finite element-based approaches for fluid-structure interaction, *International Journal for Numerical Methods in Engineering* **119**, 757–796, 2019.

[193] B. A. Schrefler and A. Scotta, A fully coupled dynamic model for two-phase fluid flow in deformable porous media, *Computer Methods in Applied Mechanics and Engineering* **190**, 3223–3246, 2001.

[194] P. Schulte, L. Alegret, I. Arenillas, J. A. Arz, P. J. Barton, P. R. Bown, T. J. Bralower, G. L. Christeson, P. Claeys, C. S. Cockell, G. S. Collins, A. Deutsch, T. J. Goldin, K. Goto, J. M. Grajales-Nishimura, R. A. F. Grieve, S. P. S. Gulick, K. R. Johnson, W. Kiessling, C. Koeberl, D. A. Kring, K. G. MacLeod, T. Matsui, J. Melosh, A. Montanari, J. V. Morgan, C. R. Neal, D. J. Nichols, R. D. Norris, E. Pierazzo, G. Ravizza, M. Rebolledo-Vieyra, W. U. Reimold, E. Robin, T. Salge, R. P. Speijer, A. R. Sweet, J. Urrutia-Fucugauchi, V. Vajda, M. T. Whalen, and P. S. Willumsen, The Chicxulub Asteroid Impact and Mass Extinction at the Cretaceous-Paleogene Boundary, *Science* **327**, 1214–1218, 2010.

[195] A. Seitz, *Computational Methods for Thermo-Elasto-Plastic Contact*, Phd thesis, Institute for Computational Mechanics, Technical University of Munich, 2019.

[196] A. Seitz, W. A. Wall, and A. Popp, Nitsche's method for finite deformation thermomechanical contact problems, *Computational Mechanics* **63**, 1091–1110, 2018.

[197] J. Sethian, *Level Set Methods and Fast Marching Methods: Evolving Interfaces in Computational Geometry, Fluid Mechanics, Computer Vision, and Material Science*, Cambridge University Press, New York, 1999.

[198] S. Shahmiri, *A Hybrid Fixed-Grid-ALE Approach for Fluid-Structure Interaction*, Phd thesis, Institute for Computational Mechanics, Technical University of Munich, 2014.

[199] S. Shahmiri, A. Gerstenberger, and W. A. Wall, An XFEM-based embedding mesh technique for incompressible viscous flows, *International Journal for Numerical Methods in Fluids* **65**, 166–190, 2011.

[200] R. E. Showalter, Poroelastic Filtration Coupled to Stokes Flow, *Lecture Notes in Pure and Applied Mathematics* **242**, 229, 2005.

[201] Y. Sudhakar, *An embedded interface finite element method for fluid-structure-fracture interaction*, Phd thesis, Institute for Computational Mechanics, Technical University of Munich, 2015.

[202] Y. Sudhakar and W. A. Wall, A strongly coupled partitioned approach for fluid-structure-fracture interaction, *International Journal for Numerical Methods in Fluids* **87**, 90–108, 2018.

[203] Y. Sudhakar, J. M. De Almeida, and W. A. Wall, An accurate, robust, and easy-to-implement method for integration over arbitrary polyhedra: Application to embedded interface methods, *Journal of Computational Physics* **273**, 393–415, 2014.

[204] Y. Sudhakar and W. A. Wall, Quadrature schemes for arbitrary convex/concave volumes and integration of weak form in enriched partition of unity methods, *Computer Methods in Applied Mechanics and Engineering* **258**, 39–54, 2013.

[205] Y. Sudhakar, A. Sommariva, M. Vianello, and W. A. Wall, On the Use of Compressed Polyhedral Quadrature Formulas in Embedded Interface Methods, *SIAM Journal on Scientific Computing* **39**, B571–B587, 2017.

[206] N. Sukumar, N. Moës, B. Moran, and T. Belytschko, Extended finite element method for three-dimensional crack modelling, *International Journal for Numerical Methods in Engineering* **48**, 1549–1570, 2000.

[207] D. Taherzadeh, C. Picioreanu, U. Küttler, A. Simone, W. A. Wall, and H. Horn, Computational study of the drag and oscillatory movement of biofilm streamers in fast flows, *Biotechnology and Bioengineering* **105**, 600–610, 2010.

[208] T. E. Tezduyar and S. Sathe, Modelling of fluid–structure interactions with the space–time finite elements: Solution techniques, *International Journal for Numerical Methods in Fluids* **54**, 855–900, 2007.

[209] T. E. Tezduyar, S. Aliabadi, and M. Behr, Enhanced-Discretization Interface-Capturing Technique (EDICT) for computation of unsteady flows with interfaces, *Computer Methods in Applied Mechanics and Engineering* **155**, 235–248, 1998.

[210] J. Tichy, A Porous Media Model for Thin Film Lubrication, *Journal of Tribology* **117**, 16–21, 1995.

[211] J. Tripp, Surface Roughness Effects in Hydrodynamic Lubrication: The Flow Factor Method, *Journal of Lubrication Technology* **105**, 458–465, 1983.

[212] M. Tur, F. Fuenmayor, and P. Wriggers, A mortar-based frictional contact formulation for large deformations using Lagrange multipliers, *Computer Methods in Applied Mechanics and Engineering* **198**, 2860–2873, 2009.

[213] R. van Loon, P. D. Anderson, and F. N. van de Vosse, A fluid–structure interaction method with solid-rigid contact for heart valve dynamics, *Journal of Computational Physics* **217**, 806–823, 2006.

[214] F. Verdugo and W. A. Wall, Unified computational framework for the efficient solution of n-field coupled problems with monolithic schemes, *Computer Methods in Applied Mechanics and Engineering* **310**, 335–366, 2016.

[215] A.-T. Vuong, *A Computational Approach to Coupled Poroelastic Media Problems*, Phd thesis, Institute for Computational Mechanics, Technical University of Munich, 2016.

[216] A.-T. Vuong, L. Yoshihara, and W. A. Wall, A general approach for modeling interacting flow through porous media under finite deformations, *Computer Methods in Applied Mechanics and Engineering* **283**, 1240 – 1259, 2015.

[217] A.-T. Vuong, C. Ager, and W. A. Wall, Two finite element approaches for Darcy and Darcy–Brinkman flow through deformable porous media – Mixed method vs. NURBS based (isogeometric) continuity, *Computer Methods in Applied Mechanics and Engineering* **305**, 634–657, 2016.

[218] A.-T. Vuong, A. Rauch, and W. A. Wall, A biochemo-mechano coupled, computational model combining membrane transport and pericellular proteolysis in tissue mechanics, *Proceedings of the Royal Society A: Mathematical, Physical and Engineering Science* **473**, 20160812, 2017.

[219] G. J. Wagner, S. Ghosal, and W. K. Liu, Particulate flow simulations using lubrication theory solution enrichment, *International Journal for Numerical Methods in Engineering* **56**, 1261–1289, 2003.

[220] W. A. Wall, P. Gamnitzer, and A. Gerstenberger, Fluid–structure interaction approaches on fixed grids based on two different domain decomposition ideas, *International Journal of Computational Fluid Dynamics* **22**, 411–427, 2008.

[221] W. A. Wall, C. Ager, M. Grill, M. Kronbichler, C. Meier, and C. Schmidt, BACI: A multiphysics simulation environment, Technical report, Institute for Computational Mechanics, Technical University of Munich, 2019.

[222] S. Whitaker, Flow in porous media III: Deformable media, *Transport in Porous Media* **1**, 127–154, 1986.

[223] S. Whitaker, Flow in porous media II: The governing equations for immiscible, two-phase flow, *Transport in Porous Media* **1**, 105–125, 1986.

[224] S. Whitaker, Flow in porous media I: A theoretical derivation of Darcy's law, *Transport in Porous Media* **1**, 3–25, 1986.

[225] T. Wick, Flapping and contact FSI computations with the fluid–solid interface-tracking/interface-capturing technique and mesh adaptivity, *Computational Mechanics* **53**, 29–43, 2014.

[226] M. Winter, B. Schott, A. Massing, and W. A. Wall, A Nitsche cut finite element method for the Oseen problem with general Navier boundary conditions, *Computer Methods in Applied Mechanics and Engineering* **330**, 220–252, 2018.

[227] B. I. Wohlmuth, A Mortar Finite Element Method Using Dual Spaces for the Lagrange Multiplier, *SIAM Journal on Numerical Analysis* **38**, 989–1012, 2000.

[228] B. I. Wohlmuth, Discretization Techniques Based on Domain Decomposition, In *Discretization Methods and Iterative Solvers Based on Domain Decomposition*, pages 1–84, Springer, 2001.

[229] P. Wriggers and G. Zavarise, A formulation for frictionless contact problems using a weak form introduced by Nitsche, *Computational Mechanics* **41**, 407–420, 2008.

[230] P. Wriggers, *Computational Contact Mechanics*, Springer-Verlag Berlin Heidelberg, 2006.

[231] B. Yang and T. A. Laursen, A mortar-finite element approach to lubricated contact problems, *Computer Methods in Applied Mechanics and Engineering* **198**, 3656–3669, 2009.

[232] B. Yang, T. A. Laursen, and X. Meng, Two dimensional mortar contact methods for large deformation frictional sliding, *International Journal for Numerical Methods in Engineering* **62**, 1183–1225, 2005.

[233] T. Yang and R. L. Spilker, A Lagrange Multiplier Mixed Finite Element Formulation for Three-Dimensional Contact of Biphasic Tissues, *Journal of Biomechanical Engineering* **129**, 457–471, 2007.

[234] R. Zakerzadeh, M. Bukac, and P. Zunino, Computational analysis of energy distribution of coupled blood flow and arterial deformation, *International Journal of Advances in Engineering Sciences and Applied Mathematics* **8**, 70–85, 2016.

[235] C. Zhai, Y. Gan, D. Hanaor, G. Proust, and D. Retraint, The Role of Surface Structure in Normal Contact Stiffness, *Experimental Mechanics* **56**, 359–368, 2016.

[236] O. C. Zienkiewicz, R. L. Taylor, and D. Fox, *The Finite Element Method for Solid & Structural Mechanics*, Butterworth-Heinemann, 2013.

[237] O. C. Zienkiewicz, R. L. Taylor, and P. Nithiarasu, *The Finite Element Method for Fluid Dynamics*, Butterworth-Heinemann, 2013.

[238] O. C. Zienkiewicz, R. L. Taylor, and J. Zhu, *The Finite Element Method: Its Basis & Fundamentals*, Butterworth-Heinemann, 2013.

[239] S. Zonca, C. Vergara, and L. Formaggia, An Unfitted Formulation for the Interaction of an Incompressible Fluid with a Thick Structure via an XFEM/DG Approach, *SIAM Journal on Scientific Computing* **40**, B59–B84, 2018.

[240] P. Zunino, Analysis of backward Euler/extended finite element discretization of parabolic problems with moving interfaces, *Computer Methods in Applied Mechanics and Engineering* **258**, 152–165, 2013.

VERZEICHNIS DER BETREUTEN STUDIENARBEITEN

Im Rahmen dieser Dissertation entstanden am Lehrstuhl für Numerische Mechanik (LNM) in den Jahren von 2013 bis 2019 unter wesentlicher wissenschaftlicher, fachlicher und inhaltlicher Anleitung des Autors die im Folgenden aufgeführten studentischen Arbeiten. Der Autor dankt allen Studierenden für Ihr Engagement bei der Unterstützung dieser wissenschaftlichen Arbeit.

Studierende(r)	**Studienarbeit**
Harald Willmann	*Finite Element Formulation for Mesh-Tying and Contact Problems in Nonlinear Poroelasticity*, Masterarbeit, 2015
Alexander Schein	*Analysis of a Cut Finite Element Method for Lubrication Gap Flows and Implementation of a Ghost-Penalty Stabilization for High Order Elements*, Masterarbeit, 2016
Philip Bilfinger	*Numerical Stability Analysis of Transport Processes with interface-coupled Discretizations*, Bachelorarbeit, 2016
Gašper Odar	*Finite element analysis of frictional contact using Nitsche's method*, Semesterarbeit, 2017
Julian Christian Metken	*Direkte Numerische Kontaktsimulation elastischer Körper mit rauen Oberflächen*, Bachelorarbeit, 2017